Novel Near-Infrared-Emitting (Nano)Materials for Bioimaging

Dissertation
for the award of the degree
"*Doctor rerum naturalium*"
of the Georg-August-Universität Göttingen

within the doctoral program of Chemistry
of the Georg-August University School of Science (GAUSS)

submitted by
Gabriele Selvaggio
from Monfalcone, Italy

Göttingen, 2022

Thesis Advisory Committee (TAC) & Examination Board

Prof. Dr. Sebastian Kruss (1st Referee)
Physical Chemistry II
Ruhr University of Bochum

Prof. Dr. Dietmar Stalke (2nd Referee)
Institute of Inorganic Chemistry
Georg-August University of Göttingen

Jun.-Prof. Dr. Franziska Thomas
Institute of Organic Chemistry
University of Heidelberg

Further Members of the Examination Board

Prof. Dr. Timo Betz
Faculty of Physics
Georg-August University of Göttingen

Prof. Dr. Jörg Großhans
Department of Biology
Philipps University of Marburg

Jun.-Prof. Dr. Anna Krawczuk
Institute of Inorganic Chemistry
Georg-August University of Göttingen

Date of the oral examination: 22/08/2022

Dedicated to Nicole, my haven of peace and biggest fan

“All seed answer light, but the color is different”

Egyptian proverb

Table of Contents

1 | Abstract

The scientific interest around *in vivo* biomedical imaging has strongly increased in recent years due to its benefits compared to other diagnostic tools. Fluorophores that emit in the near-infrared region of the electromagnetic spectrum (700 nm < λ < 1700 nm, NIR) present optimal features for bioimaging due to the higher tissue penetration, better contrasts and lower phototoxicity. Unfortunately, compared to the more established visible fluorophores, the library of NIR emitters is scarce. For these reasons, the interest in designing novel NIR-emitting platforms is very high. This doctoral thesis is dedicated to near-infrared fluorescent materials and most importantly a fluorescent silicate: Egyptian Blue ($CaCuSi_4O_{10}$, EB). Thanks to its layered crystal structure, this phyllosilicate could be easily exfoliated into 2D nanomaterials (*i.e.* nanosheets, NS) of dimensions well below the micron range. Most importantly, these EB-NS retained the bright, long-lived NIR emission of the bulk counterparts down to particles of just few tenths of nm in size. Furthermore, this NIR fluorescence proved to be highly photostable, as it did not bleach and was not significantly affected by quenching molecules, pH or ionic environments. Next to the study of the photophysical properties of these novel 2D nanomaterials, *in vivo* fluorescence microscopy and remote detection were demonstrated for the first time. Furthermore, successful covalent surface functionalization by Si-H activation of hydrosilanes was performed. In this way, colloidal stability could be enhanced and targeted bioimaging of cancer cells could be demonstrated. Given the versatility of the chosen surface chemistry, the biocompatible nature of EB-NS as well as the multiple outstanding properties of this material, the work in this doctoral thesis robustly established a novel NIR fluorophore for biophotonics. Besides EB-NS, similar materials were investigated in this doctoral thesis, too. Han Blue ($BaCuSi_4O_{10}$, HB) and Han Purple ($BaCuSi_2O_6$, HP) display similarity to EB in terms of crystal structure and photophysical properties. NS of all three silicates were therefore successfully prepared. As previously reported for EB-NS, also HB-NS and HP-NS retained their NIR fluorescence and displayed superior brightness and photostability under continuous illumination compared to state-of-the-art fluorophores. *Via* fluorescence lifetime imaging and spectroscopy tools, proof-of-principle experiments in the direction of NS lifetime detection and engineering were carried out as well. Finally, the potential held by another group of NIR fluorophores, *i.e.* the hexameric (*H*) and octameric (*O*) forms of extended benzene-fused oligo-BODIPYs, was investigated. For the first time, the NIR fluorescence features of these BODIPY-derivatives were presented and studied. The bright and tunable fluorescence of *H*- and *O*-oligo-BODIPYs displayed high promises for both remote detection and microscopy fluorescence imaging. Furthermore, *H*-coated microbeads were successfully employed for colocalized imaging and microrheology of actin networks, whose filaments displayed limited degradation despite prolonged excitation of the embedded *H*-dye. In summary, this thesis provides insights into preparation, surface chemistry and photophysics of NIR fluorescent materials and shows their potential in (bio)photonics.

2 | Abbreviations

0D	zero-dimensional
1D	one-dimensional
2D	two-dimensional
3D	three-dimensional
3C-PP	EB-NS-decorated polymeric scaffold
AC	alternating current
ACN	acetonitrile
ACQ	aggregation-caused quenching
AD	*anno Domini*
AIE	aggregation-induced emission
AIEgens	aggregation-induced emission luminogens
AFM	atomic force microscopy
AFS	acoustic force spectroscopy
Alloc	allyloxycarbonyl
AM	antimonene
APTES	(3-aminopropyl)triethoxy silane
Ar	aryl
BC	before Christ
BF	bright-field
BODIPY	boron-dipyrromethene
BOIMPY	BOron complexes of IMinoPYrrolide ligands
BP	black phosphorus
CaP	polymeric scaffold
CaPCu	EB-NS-decorated polymeric scaffold
CAT	catalyst
CBS	circular backscatter detector
CCD	charge-coupled device
CHP	*N*-cyclohexyl-2-pyrrolidone
CLSM	confocal laser scanning microscopy
CMOS	complementary metal-oxide-semiconductor
COOH-preSil	(3-chloropropyl)dimethylsilane
COOH-Sil	4-(dimethylsilyl)butyric acid
CP	cross-polarization
CT	computed tomography

CTAB	cetrimonium bromide
Ctrl	control
CUP	cuprorivaite (EB-NS)
CVD	chemical vapor deposition
Cy	cyanine
D-A	donor-acceptor
DBE	1,2-dibromoethane
DCC	*N*,*N′*-dicyclohexylcarbodiimide
DCM	dichloromethane
DIPEA	*N*,*N*-diisopropylethylamine
DLR	dual lifetime referencing
DLS	dynamic light scattering
DMF	dimethyl formamide
DMSO	dimethyl sulfoxide
DNA	deoxyribonucleic acid
DOI	digital object identifier
DLVO	Derjaguin-Landau-Verwey-Overbeek
e.g.	*exempli gratia*
EB	Egyptian Blue
EB-NS	Egyptian Blue nanosheet(s)
EBfunc	functionalized EB-NS
EDC·HCl	*N*-ethyl-*N′*-(3-dimethylaminopropyl)-carbodiimide hydrochloride
EDTA	ethylenediaminetetraacetic acid
EDX	energy-dispersive X-ray spectroscopy
EI-MS	electron ionization mass spectrometry
ESI-MS	electrospray ionization mass spectrometry
ETD	Everhart-Thornley detector
FA	folic acid
FDA	U.S. Food and Drug Administration
FLIM	fluorescence lifetime imaging
FLIR	forward-looking infrared
fMRI	functional magnetic resonance imaging
fNIRS	functional near-infrared spectroscopy
fps	frames per second
FR	folate receptor
FTIR	Fourier transform infrared spectroscopy
FWHM	full width at half maximum

g-C_3N_4	graphitic carbon nitride
GFP	green fluorescent protein
GO	graphene oxide
h-BN	hexagonal boron nitride
***H*(-oligo-BODIPY)**	hexamer(-oligo-BODIPY)
HATU	1-[bis(dimethylamino)methylene]-1*H*-1,2,3-triazolo-[4,5-*b*]pyridinium hexafluorophosphate
HB	Han Blue
HB-NS	Han Blue nanosheet(s)
HG	hydrogel
HOBt	1-hydroxybenzotriazole hydrate
HOMO	highest occupied molecular orbital
HOPG	highly-oriented pyrolytic graphite
HP	Han Purple
HP-NS	Han Purple nanosheet(s)
HR	high resolution
i.e.	*id est*
ICG	indocyanine green
ICP-MS	inductively coupled plasma mass spectrometry
ICP-OES	inductively coupled plasma optical emission spectrometry
IFPs/iRFPs	infrared fluorescent proteins
IR	infrared
IRF	instrument response function
LDH	layered double hydroxide
LDPS(A)	laser diffraction particles size analyzer
LED	light-emitting diode
LPE	liquid-phase exfoliation
LUMO	lowest unoccupied molecular orbital
MAS NMR	magic-angle spinning nuclear magnetic resonance
MB	methylene blue
MC	McCrone
MCP	m-cresol purple
MDCK	Madin-Darby canine kidney
MOF	metal-organic framework
MRI	magnetic resonance imaging
mRNA	messenger ribonucleic acid
MS	mass spectrometry
MSD	mean squared displacement

MTS	3-(4,5-dimethylthiazol-2-yl)-5-(3-carboxymethoxyphenyl)-2-(4-sulfophenyl)-2H-tetrazolium
MXene	2D transition metal carbide/carbonitride/nitride
n.a.	not available
n-DA	n-dodecylamine
NA	numerical aperture
NADH	nicotinamide adenine dinucleotide
NHS	*N*-hydroxysuccinimide
NIR	near-infrared
NIR-I	first near-infrared window for (bio)imaging
NIR-II	second near-infrared window for (bio)imaging
NMP	*N*-methyl-2-pyrrolidone
NMR	nuclear magnetic resonance
noCAT	control sample without catalyst
NP	nanoparticle
NS	nanosheet(s)
NVP	*N*-vinylpyrrolidone
***O*(-oligo-BODIPY)**	octamer(-oligo-BODIPY)
OLED	organic light-emitting diode
OM	optical microscopy
OS	osteosarcoma
PA	palmitic acid
PB	planetary ball
PBS	phosphate-buffered saline
PCA	principal component analysis
PCL	polycaprolactone
PDMS	polydimethylsiloxane
PDT	photodynamic therapy
PET	positron emission tomography
PIDS	polarization intensity differential scattering
PL	photoluminescence
PP	poly(*ε*-caprolactone)+poly(*D*,*L*-lactic acid)
PS	polystyrene
pSi	porous silicon
PT	poly(*D*,*L*-lactide-co-trimethylene carbonate)
PTT	photothermal therapy
Pyr	pyrene
Pyr-Sil	1-(dimethylsilyl)pyrene

QD	quantum dot
QY	quantum yield
R.I.	refractive index
R-SiI	hydrosilane(s)
RBF	round-bottom flask
RCF	relative centrifugal force
ref.	reference(s)
RENP	rare earth-doped nanoparticle
RGD	arginine-glycine-aspartic sequence
rGO	reduced graphene oxide
RNA	ribonucleic acid
ROI	region of interest
ROS	reactive oxygen species
rpm	revolutions per minute
RUB	Ruhr-University of Bochum
SAED	selected area electron-diffraction
SANS	small-angle neutron scattering
SBR	signal-to-background ratio
SC	strontium copper tetrasilicate
SC-NS	strontium copper tetrasilicate nanosheet(s)
sCMOS	scientific complementary metal-oxide-semiconductor
SEM	scanning electron microscopy
SMD	small-molecule dye
SMP	shape-memory polymer
SPAD	single-photon avalanche diode
SPECT	single-photon emission computed tomography
ssDNA	single-stranded DNA
ssNMR	solid-state nuclear magnetic resonance
STEM	scanning transmission electron microscopy
SWCNT	single-walled carbon nanotube
TCSPC	time-correlated single photon counting
TEM	transmission electron microscopy
THF	tetrahydrofuran
TICT	twisted intramolecular charge transfer
TMD	transition metal dichalcogenide
TMO	transition metal oxide
TMSCl	trimethylsilyl chloride

US	ultrasound scanners
UV	ultraviolet
Vis	visible
VPT	video particle tracking
vs.	*versus*
WD	working distance
XAS	X-ray absorption spectroscopy
Xene	2D monoelemental material
XPS	X-ray photoelectron spectroscopy
XRD	X-ray diffractometry

3 | Introduction

3.1 Motivations

Fluorescence biomedical imaging offers multiple advantages for *in vivo* fundamental and clinical studies due to optimal features such as high spatial and temporal resolution, high sensitivity, low invasiveness and reduced toxicity[1–3]. Although multiple visible fluorophores have been established and are extensively used, they present clear limitations. Above all, autofluorescence of biological samples as well as absorption and scattering events are pronounced at visible wavelengths and, thus, lead to low contrasts and tissue penetration[1,2]. Clear improvements with regards to these issues have been displayed since the developing of fluorophores characterized by emission wavelengths in the near-infrared (NIR). These can indeed outperform visible fluorophores, given the excellent properties for bioimaging in the so-called “biological transparency NIR window”[3,4]. While this window has been later on extended to longer NIR wavelengths leading to enhanced tissue penetration results, unfortunately some challenges that hinder clinical translation of NIR fluorophores still remain. These issues typically concern low quantum yields (QYs), low photostability and biocompatibility, which are aspects of paramount importance for *in vivo* fluorescence biological imaging. Furthermore, although the field of NIR bioimaging has already demonstrated its high potential with several groundbreaking studies, its technology, both in terms of fluorophores and detection systems, is younger than the visible counterpart and has thus not evolved to the same extent. Concerning the fluorophores, this implies that the library of available NIR emitters is currently scarce. For this reason, the interest in designing novel NIR platforms of promising chemical and photophysical properties is very high within the scientific community. The motivation behind the works presented in this doctoral thesis was therefore to establish new promising candidates for NIR fluorescence bioimaging. Above all, the focus was set on the layered silicates Egyptian Blue (EB), Han Blue (HB) and Han Purple (HP). These materials were already known to display a bright, long-lived NIR fluorescence, next to multiple other chemical and photophysical properties outlined in previous studies[5]. Given their layered crystal structures, one of the main goals of this doctoral thesis was to understand whether the stable NIR fluorescence of the bulk materials could be retained after exfoliation into 2D nanomaterials (*i.e.* nanosheets, NS). Slightly different questions guided the investigations that were performed on the hexameric and octameric forms of extended benzene-fused oligo-BODIPYs[6]. The shorter oligomers of this class of BODIPY-derivatives reported high tunability of their fluorescence features, suggesting that the larger conjugated structures (*i.e.* the *H*- and *O*-oligo-BODIPYs) could display fluorescence in the NIR. Next to the exploration of fundamental photophysical properties of these novel materials, the showcasing of their employment in proof-of-principle applications was also a major aim of this work. Biocompatible traits and the ability to emit a stable and intense NIR fluorescent signal after introduction into biological systems represent clear requirements for a NIR labelling agent of high profile. Furthermore, if successful functionalization were to be performed on the surface without compromising the NIR optical properties, such novel imaging platform could specifically target biological features of interest and further biomedical questions could, thus, be addressed.

3.2 Outline

The structure of this doctoral thesis is cumulative, *i.e.* it is built around manuscripts published during my PhD or currently in preparation. In order to provide the Reader with the necessary tools to evaluate the reported studies, an overview of the scientific background is presented in the upcoming chapter **(Chapter 4)**. This chapter first describes NIR bioimaging and summarizes the main features of the most common NIR fluorophores **(Section 4.1)**. Within **Section 4.1.5**, BODIPY-derivatives are explained in more detail for a better understanding of the studies performed during my PhD on extended benzene-fused oligo-BODIPYs. Next, in **Section 4.2** the attention is shifted to 2D nanomaterials, with particular focus on their applications in biomedicine and their exfoliation routes. **Section 4.3** then presents the central players of this dissertation: EB, HB and HP. Within this section, a self-written **Review Manuscript** is embedded **(Section 4.3.2)**: here, the most relevant photophysical properties of the three layered silicates are described, as well as their established exfoliation routes and applications in a plethora of technological fields. Some of my own findings, which are also reported in this publication, are explained in more detail in the following chapter of this doctoral thesis **(Chapter 5)**, which guides the Reader through the most important results of my PhD. This chapter is divided into four sections centered around four manuscripts. Each manuscript is introduced by an introductory section and followed by a synopsis of the publication. **Section 5.1** presents **Manuscript I**, which focused on characterization and proof-of-principle applications of *H*- and *O*-oligo-BODIPYs. **Section 5.2** includes **Manuscript II**, which presented for the first time EB-NS as novel NIR fluorophore for biophotonics. **Section 5.3** presents **Manuscript III**, where the high promises of EB-NS, HB-NS and HP-NS for (bio)imaging were outlined. Finally **Section 5.4** contains **Manuscript IV**, which established covalent functionalization of EB-NS for targeted bioapplications. **Chapter 6** then provides a more detailed discussion of the findings reported in the previous manuscripts and suggests possible future directions of research. Finally, the conclusions of this doctoral thesis are presented in **Chapter 7**.

4 | Scientific Background

4.1 A (Bio)Window of Possibilities: The Near-Infrared (NIR) and its Fluorophores

4.1.1 Fluorescence Biological Imaging: Goals and Challenges

In the last decades, *in vivo* biomedical imaging has gained an increasing relevance, ranging from fundamental scientific research to clinical practice. Clinical imaging of human patients is increasingly employed in hospitals, enabling guided-surgical interventions as well as assessment of treatment efficacy and prognosis. Since the publication of the first X-ray photograph by Wilhelm Röntgen, several imaging modalities have been discovered and have undergone important technological developments, exploiting the full wavelength range of the electromagnetic spectrum. These techniques either rely on endogenous contrast from biological tissue (*e.g.* non-contrast X-ray computed tomography (CT), ultrasound scanners (US), functional magnetic resonance imaging (fMRI) and functional near-infrared spectroscopy (fNIRS)), or on externally introduced contrast agents (*e.g.* contrast-enhanced CT, positron emission tomography (PET) and single-photon emission CT (SPECT))[1–3,7]. Although most of them are to be considered as mature imaging methods which have resulted very successful in clinical applications, they suffer from major limitations: among them, intrinsically limited spatial resolutions (MRI and PET), reconstruction-dependent poor temporal resolution (CT, MRI, PET and SPECT), use of hazardous ionizing radiation (CT, PET and SPECT), lack of exogenous and endogenous probes, and expensive instrumentations (MRI, PET, SPECT and CT)[1,3]. Differently from the above-listed imaging modalities, *in vivo* fluorescence imaging does not suffer from these drawbacks. Indeed, it allows down to diffraction-limited high spatial resolution, real-time dynamics image acquisition, high sensitivity and multiple signal acquisition. Furthermore, it makes use of non-hazardous optical radiation, it benefits from a wide library of functional and molecular markers, and is more economically affordable in terms of instrumentations and probes[1–3]. However, *in vivo* fluorescence imaging using traditional wavelengths in the visible spectrum ($400 \text{ nm} < \lambda < 700 \text{ nm}$) suffers from poor photon penetration depth in tissue (typically < 3 mm)[2]. This major issue, which leads to a significant loss of resolution and contrast, can be fully understood if the general dynamics of light-tissue interactions are considered **(Figure 4.1a)**[8]. Besides the emission from the fluorescent labels, four main processes are indeed playing a major role in this regard: these are interface reflection, in-tissue scattering, in-tissue absorption and tissue autofluorescence. Reflections originate from the different refractive indexes (n) of the medium (*e.g.* air, $n \approx 1.0$) and superficial tissue of the imaged sample (*e.g.* dermis, $n \approx 1.4$)[1]: besides from the difference in n itself, this process strongly depends on the incidence angle of the photons, while being wavelength-independent (Fresnel equations). An inversely proportional dependence from the photon wavelength is instead observable in the case of photon scattering ($\mu_s' \propto \lambda^{-\alpha}$, with α = 0.2-4[1]). This process represents a direct consequence of the heterogeneous nature of tissue: indeed, its diverse biological components (*e.g.* water, lipid membrane and subcellular organelles) are characterized by different *n* values which lead to deviations of photons from their original paths *via* scattering events **(Figure 4.1b)**. Furthermore, numerous endogenous biomolecules can absorb light and lead to heat dissipation, thus further hindering the travel of inbound and outbound photons through tissue. Molecules such as hemoglobin **(Figure 4.1c)**, melanins, reduced nicotinamide adenine dinucleotide (NADH) and flavins indeed absorb in the ultraviolet-visible (UV-Vis) range of light, whereas water molecules present vibrational overtone bands and combination transitions in the near-infrared (NIR, **Figure 4.1d**). When excited by the incoming photons, some of the endogenous chromophores (*e.g.* flavins and NADH) and several pigmented cellular structures can additionally emit fluorescence: this so-produced non-specific background signal (*i.e.* autofluorescence) has been shown to decrease at longer photon wavelengths **(Figure 4.1e)**[1,2]. We can thus conclude that an ideal spectral window for bioimaging should feature low scattering, absorption and autofluorescence in order to achieve a high signal-to-background ratio (SBR).

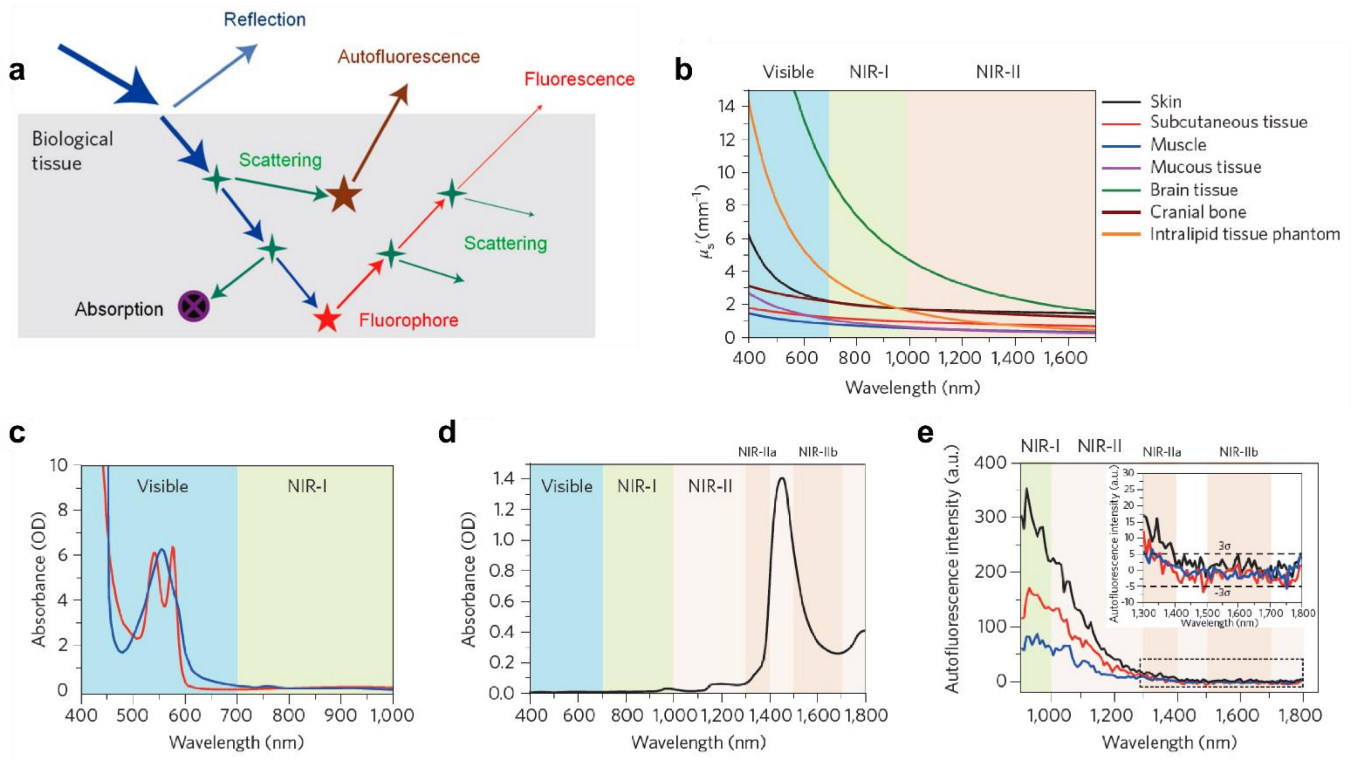

Figure 4.1 The benefits of fluorescence imaging in the near-infrared (NIR). a *Illustration showing the typical interactions that take place between an incoming photon and the imaged tissue.* ***b*** *Reduced scattering coefficient (μ_s') of exemplary biological tissues and intralipid tissue phantom at visible wavelengths (Vis) and over the first and second NIR windows (NIR-I and NIR-II, respectively).* ***c*** *Absorption features of oxygenated (red line) and deoxygenated (blue line) hemoglobin through a 1-mm-long path in human blood.* ***d*** *Absorption spectrum of water (again through a 1-mm-long path).* ***e*** *Autofluorescence detected from ex vivo mouse liver (black line), spleen (red line) and heart tissue (blue line) in the NIR-I and NIR-II windows ($\lambda_{exc} = 808$ nm). The dotted rectangle highlights the region where the magnified spectra (top-right corner) were extracted from. Adapted with permission from ref.* [2]*. Copyright 2020 American Chemical Society. Adapted with permission from ref.* [1]*. Copyright 2017 Springer Nature. Adapted with permission from ref.* [9]*. Copyright 2015 Springer Nature.*

4.1.2 Bioimaging in the NIR

Considered the light-tissue interactions described above, two main options are therefore possible: the development of new imaging instrumentation (*e.g.* confocal microscopy, two- and multi-photon microscopy, light-sheet microscopy, adaptive optical microscopy, optical coherence tomography, fluorescence-mediated tomography, *etc.*) or the design of new probes with more favorable spectral properties **(Figure 4.2)**[1]. The second approach is the one followed in this doctoral dissertation, whose focus is set on near-infrared light (NIR, $700\text{ nm} < \lambda < 3000\text{ nm}$[3,4]). Compared to the traditional visible regime, the NIR range of wavelengths $700\text{ nm} < \lambda < 1700\text{ nm}$ has shown to enable reduced photon scattering, tissue autofluorescence and absorption **(Figure 4.1b-e)**[1,2,7,10]. In this way, deeper tissue optical imaging with enhanced SBR can be achieved. Within this broad NIR region, two main sub-regions can be defined: the first NIR window (NIR-I, typically 700 nm < λ < 1000 nm) and the second NIR window (NIR-II, typically 1000 nm < λ < 1700 nm)[1,2,4,11–13]. The traditional NIR-I window has been the first to be investigated by the scientific community and is typically referred to as the "biological transparency NIR window". A technological advantage of the NIR-I window over the NIR-II one is that low-cost and commonly employed detectors such as silicon-based charge-coupled device (CCD) cameras can still detect NIR-I fluorophores with high enough sensitivity (quantum efficiency ≈ 60-80%[4]). The same cannot be said for fluorescence detection of the more recent NIR-II window, which instead requires the more expensive NIR-optimized cameras: these are based on semiconductor alloys with narrower bandgaps such as indium gallium arsenide (InGaAs) and mercury cadmium telluride (HgCdTe). The main advantage of NIR-II fluorophores, however, is that, compared to NIR-I, even better results in terms of deep tissue imaging can be obtained. Indeed, although water overtones are present in that region and define the borders of the NIR-IIa (1300 nm < λ < 1400 nm[14]) and NIR-IIb (1500 nm < λ < 1700 nm[15]) sub-windows, scattering and tissue autofluorescence are drastically reduced. Considered that the benefits of lower scattering and autofluorescence significantly outweigh the slightly stronger absorption in the NIR-II window, most of the scientific endeavors are nowadays dedicated to the design of NIR-II fluorophores and the optimization of the corresponding excitation/emission features[16]. However, as will be described in the next sections, the NIR-II field has not matured yet to the level of NIR-I, and the current clinical trials are focused on NIR-I dyes (*e.g.* IRDye800CW[1]). Furthermore, in-depth toxicological studies on most of these fluorophores are either lacking/incomplete or present clear limitations for clinical translation[1,2,17]. It should therefore not appear surprising that, despite the high promises of NIR bioimaging, only few (2) NIR-I fluorophores have been approved to the present day for in-human clinical use.

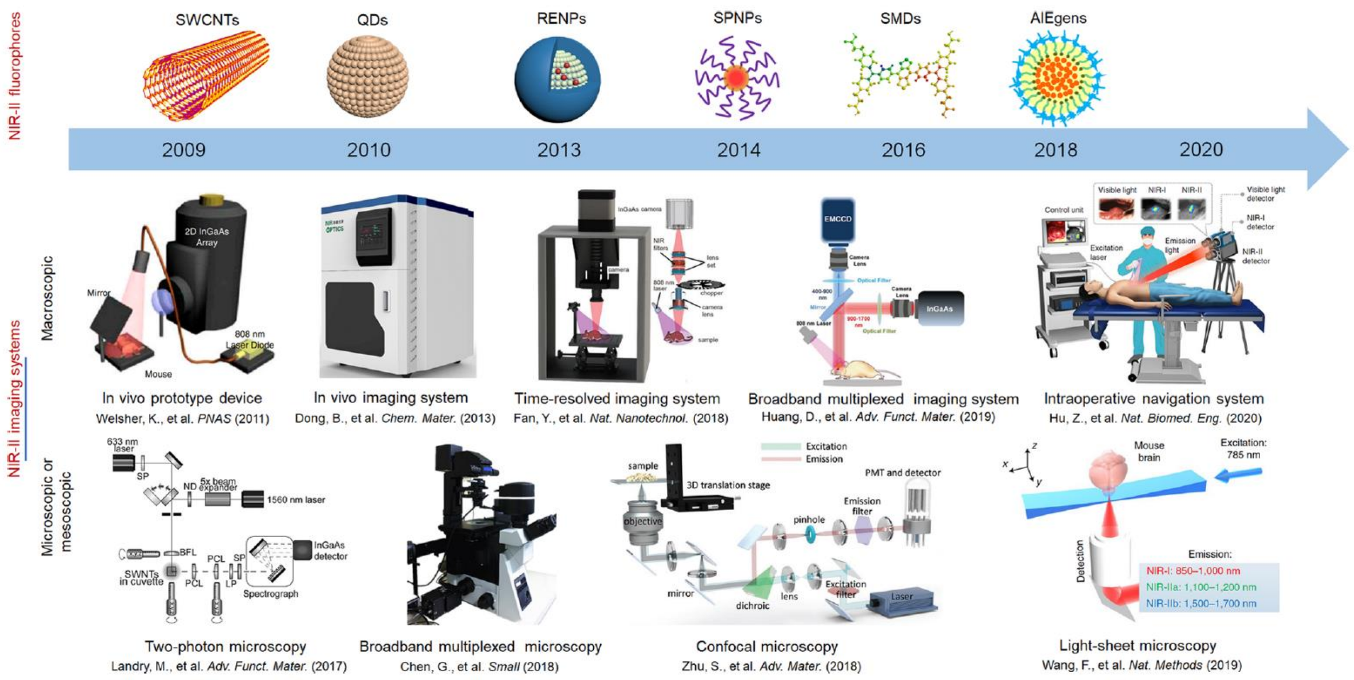

Figure 4.2 Evolution of NIR-II fluorescence imaging technology. *In recent years, new imaging setups and novel fluorescent probes for detection at near-infrared wavelengths have been developed, leading to groundbreaking studies in the fields of bioimaging and biosensing. Reproduced with permission from ref.* [2]*. Copyright 2020 American Chemical Society. Adapted with permission from ref.* [18]*. Copyright 2011 National Academy of Sciences. Adapted with permission from ref.* [19]*. Copyright 2017 Wiley-VCH. Adapted with permission from ref.* [20]*. Copyright 2013 American Chemical Society. Adapted with permission from ref.* [21]*. Copyright 2017 Wiley-VCH. Adapted with permission from ref.* [22]*. Copyright 2018 Springer Nature. Adapted with permission from ref.* [23,24]*. Copyright 2018 Wiley-VCH. Adapted with permission from ref.* [25,26]*. Copyright 2019 Springer Nature.*

4.1.3 State-of-the-art NIR-I Fluorophores

The “holy grail” of a (fluorescent) probe designed for clinical use is supposed to display high stability, high sensitivity, high specificity, favorable delivery to the target across biological barriers, as well as favorable pharmacokinetics and metabolism, and low toxicity[27]. With these criteria in mind, researchers have put significant efforts during the last years into designing novel platforms for bioimaging in the NIR, given the benefits of such wavelengths over traditional visible ones **(Section 4.1.1, Section 4.1.2)**[1,2,7,12,17]. In 1958, the first NIR fluorophore was approved by the U.S. Food and Drug Administration (FDA): indocyanine green (ICG)[8,28–30]. This tricarbocyanine is negatively charged, amphiphilic but more hydrophobic, and emits fluorescence at $\lambda \approx 800$ nm with a maximum quantum yield (QY) in serum of ≈ 9-12%[1,31–34]. ICG has been extensively employed in human patients for intra-operative imaging of anatomical features (*e.g.* fundus angiography and lymphography[2]) and image-guided surgical removal of diseased tissues. Similar clinical applications have been carried out some years later with methylene blue (MB)[29,35,36], a positively charged thiazine dye which is currently the second and latest FDA-approved NIR fluorophore. Even in the case of MB, fluorescence lies in the NIR-I window ($\lambda \approx 700$ nm, QY ≈ 4-10% in serum[1,37,38]). Despite the successful employment of ICG and MB in clinical studies, these organic dyes display clear limitations: these include the fact that they fluoresce well below the better performing NIR-II regime, that the labeling of lumen structures is mostly performed by passively dying the fluids, and that their net charges lead to a high background fluorescence signal due to non-specific binding to proteins[1]. For these reasons, the upcoming years have witnessed an increasing scientific interest around the search for new NIR fluorophores with improved characteristics. In the following part of this section, several important examples of novel NIR emitters will be shortly discussed. For instance, reported NIR-I charged dyes with higher QYs include IRDye800CW (negative charge, QY ≈ 13% in serum[1,11,31,34,39]) and non-sulfonated cyanine dyes (*e.g.* Cy5.5 and Cy7, positive charge, QY ≈ 22%[1,38,39] and ≈ 28%[1,11,39] in phosphate-buffered saline, respectively). Zwitterionic cyanine dyes, on the other side, display a neutral net charge, can target tumors expressing the integrin $\alpha_v\beta_3$ even without functionalization and have reported QY ≈ 15-20%[1,34,38]. Inherent targeting ability is also shown by other cyanine-based variants such as phosphonated and quaternary ammonium cyanine dyes, which also display enhanced solubility owing to the sulfonate, pamidronate and methoxy groups[1]. Very versatile and promising NIR-I dyes are the ones deriving from 4,4-difluoro-4-bora-3a,4a-diaza-*s*-indacene (*i.e.* boron-dipyrromethene, BODIPY): this broad class of organic molecules can feature really high QY (normally ≈ 60-90%, but also up to ≈ 99% even in water[1,40–43]) and has been used *e.g.* for targeted imaging of amyloid beta plaques in mouse brain for the study of Alzheimer's disease[40]. As for other classes of organic fluorophores, the emission wavelengths of BODIPY-based dyes can be tailored so to red-shift into the NIR-II window **(Section 4.1.4, Section 4.1.5)**. Other NIR-I players with a peculiar working principle are aggregation-induced emission (AIE) dots (QY ≈ 0.2-15%[1,2,44,45]), whose luminogens (AIEgens) become fluorescent in the far red to NIR-I region only in their aggregated state. The AIE fluorogens build up the dense core of these small-sized organic nanoparticles, which are then typically embedded in biocompatible matrices that act as protective shells. Conjugated copolymers, on the other side, stand out due to the tunability of both excitation and emission features up to the NIR-II window: their spectral range is indeed very broad (typically 500 nm < λ_{exc} < 1100 nm, 700 nm < λ_{em} < 1400 nm[1]) as are the achievable quantum yields (0.5% < QYs < 50%[1,46,47]). Among organic NIR-I fluorophores there are not, however, only exogenous contrast agents. Infrared fluorescent proteins (labelled as IFPs or iRFPs) are characterized by average QYs typically ≈ 6-11%[1,11,48,49], but, differently from the fluorophores described so far, they are endogenous. This means that they can be expressed in mammalian cells through genetic manipulation *via e.g.* viral vectors or plasmid transfection.

Besides photophysical features (*e.g.* QY) and chemical composition, also other parameters describing the interaction with the biological system are of great importance. In this regard, although organic molecules and dyes have been extensively employed and tend to present the fastest excretion kinetics (sizes are typically below the renal cut-off size, which is ≈ 5.5 nm[50,51]), they are not the only players with remarkable renal clearance. For instance, metal (*e.g.* Au, Ag and Cu) nanoclusters are highly water-soluble and benefit from efficient ("molecular") pharmacokinetics due to their extremely reduced dimensions (QY ≈ 1%[1,52,53] and ≈ 17%[1,54,55] for Au and Ag, respectively). Most inorganic fluorophores are however mostly appreciated for their spectral features, including longer emission wavelengths, higher QYs and/or better photostability[7]. Such properties are clearly provided by quantum dots (QDs): these zero-dimensional (0D) nanostructures comprise extensively used systems such as cadmium telluride (CdTe), cadmium selenide (CdSe), cadmium sulfide (CdS), lead sulfide (PbS), zinc sulfide (ZnS), silver sulfide (Ag_2S), silver selenide (Ag_2Se), silicon (Si), *etc.* These nanoparticles typically present sizes between 5-10 nm and good hydrophilicity. One of the reasons for the great success of QDs is given by the very high QYs ($2\% < QY < 30\%$[1,2,61,7,11,17,56–60]); these values can be reached thanks to the often employed core-shell geometry, which allows shielding of the particle's core from water. The choice of the materials and particle sizes furthermore allows to flexibly shift both excitation and emission of QDs to longer wavelengths (NIR-II). Most importantly, QDs are among the few players who display high resistance to photobleaching, meaning that the fluorescence intensity does not significantly decrease over prolonged excitation. Despite their high potential, most QDs face serious challenges in terms of clinical translation due to the presence of highly toxic heavy metals (*e.g.* Pb, Cd and Hg) in several of its most successful nanoparticles. Besides, inorganic probes in general tend to be retained indefinitely in the organs of the reticuloendothelial system (*e.g.* liver and spleen) due to their larger sizes and can also produce a large number of oxidative free radicals (reactive oxygen species, ROS), leading to toxicity during imaging. For these reasons, additional care must be taken in the design of such probes in terms of surface coatings (*e.g.* shells for QDs) and functionalization strategies[1,2,7,17].

4.1.4 State-of-the-art NIR-II Fluorophores

Although the QYs tend to decrease at longer wavelengths, the achievable deep tissue penetration and better contrasts result in the NIR-II fluorophores being nowadays the most researched systems for biological imaging. Furthermore, higher contrasts and better SBR values can be achieved if both excitation and emission photons present NIR-II wavelengths, as displayed by some of the established platforms. Most of the previously mentioned NIR-I fluorophores can be employed in the NIR-II window either by detection of their off-peak tail emissions or as a result of compositional and/or structural modifications **(Section 4.1.5)**[12]. Additional representative NIR-II fluorophores include single-walled carbon nanotubes (SWCNTs, **Figure 4.3a-d**), rare earth-doped nanoparticles (RENPs, **Figure 4.3e-h**) and small-molecule dyes (SMDs)[1,2,7]. Just slightly more than five years ago, CH1055 (QY ≈ 0.3%[62]) was reported as the first SMD for *in vivo* NIR-II fluorescence imaging. Since then, numerous SMDs have been discovered and/or further optimized to enhance QY, water solubility and biocompatibility **(Section 4.1.5)**[2]. In terms of photostability, however, RENPs, SWCNTs and the above described QDs outperform other players because of their shared high resistance to photobleaching (which is completely lacking in the case of SWCNTs). RENPs display broad ranges of wavelengths (typically 1000 nm < λ_{em} < 1800 nm[1]) and quantum yields (in most cases 1% < QY < 13%, but QY up to 90% has been reported, too[1,17,63–65]). The luminescence of these particles is the result of up- or down-conversion from resonant energy transfer between lanthanide ions (Ln^{3+}) within an inorganic crystalline host matrix (*e.g.* sodium yttrium fluoride, $NaYF_4$). The characteristic narrow and sharp emission peaks of RENPs can be tuned through the NIR-II region, allowing multispectral NIR-II imaging. The typically long excited state lifetime (τ) of RENPs (in the µs-ms range[22]) furthermore allows to benefit from the higher resolution typical of fluorescence lifetime imaging (FLIM) acquisitions **(Figure 4.3e-h)**. FLIM can indeed cut-off short-lived background signals and, in general, enables sensing and labeling strategies that would not be realizable with the traditional intensity-based measurements **(Section 5.3)**[66]. Compared to RENPs, much shorter lifetimes (in the range of 10-100 ps[67]) and much lower quantum yields (QY ≈ 0.1-1%[4,7,17,68–70]) are reported for SWCNTs. Nevertheless, these 1D nanomaterials play a role of paramount importance in the field of NIR-II fluorescence bioimaging and sensing[71]. SWCNTs can be broadly excited and their emission spectral features (900 nm < λ_{em} < 1800 nm[1]) appear in the form of multibands. These depend on the distribution of carbon lattice structures (*i.e.* chiralities) and diameters, and thus require purification steps to yield single bands[72]. Among other established sensing mechanisms, it has been quite recently demonstrated that specialized DNA-coating of SWCNTs can endow these nanostructures with promising sensing abilities for biomolecules of relevance (*e.g.* neurotransmitters, nitric oxide and bacteria metabolites)[67,71]. Thanks to their long wavelengths, their sensor properties, their versatile functionalization strategies and their excellent mechanical and photophysical stability, SWCNTs have starred in numerous studies of high scientific impact: these include imaging of both non-specifically and specifically targeted tumors, through-skin brain vasculature **(Figure 4.3a-d),** bacterial infections and much more[1,11,17,67,71]. Unfortunately, despite their enormous success, the biocompatibility of SWCNTs is still an extremely controversial topic which has so far represented the main obstacle for their employment in human patients[71,73–76]. Similar challenges are also faced by other inorganic probes (*e.g.* QDs and RENPs), as briefly mentioned at the end of **Section 4.1.3**[1,2,7,17].

Considered the overview on benefits and limitations of the commonly employed fluorophores described in **Section 4.1.3** and **Section 4.1.4**, it can be easily understood why the search for the “holy grail” of a NIR fluorophore is still ongoing.

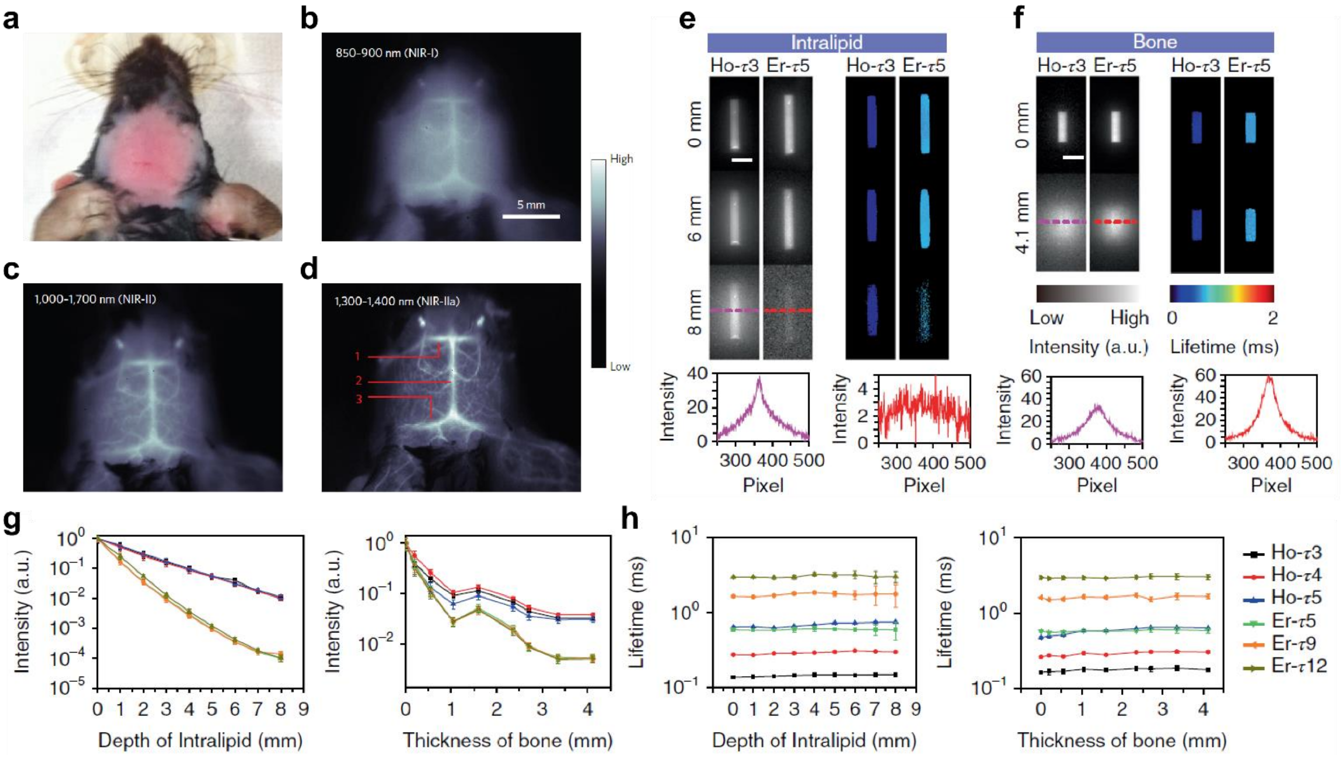

***Figure 4.3 The benefits of NIR-II intensity- and lifetime-based imaging. a** Top view picture of a hairless mouse head after injection of a conjugate composed by single-walled carbon nanotubes (SWCNTs) and a NIR-I dye (IRDye800). **b-d** Fluorescence images of the mouse from **a** in the NIR-I **(b)**, NIR-II **(c)** and NIR-IIa **(d)** windows. The inferior cerebral vein (1), superior sagittal sinus (2) and transverse sinus (3) are observable with increasing resolution. Adapted with permission from ref.* [14]*. Copyright 2014 Nature Publishing Group. **e-f** Comparison between fluorescence intensity-based (grayscale) and fluorescence lifetime-based (blue) images of capillary tubes containing holmium- (Ho^{3+}) and erbium (Er^{3+})-doped NIR-II nanoparticles with selected lifetime values (τ). To simulate the signal attenuation by biological tissue, intralipid medium **(e)** and bovine bones **(f)** were employed. Scale bar = 2 mm. **g-h** Normalized intensities **(g)** and lifetimes **(h)** for various holmium and erbium-doped nanoparticles with respect to depth of the intralipid solution and bone thickness as defined in **e-f**. Adapted with permission from ref.* [22]*. Copyright 2018 Springer Nature.*

4.1.5 Design Strategies for NIR-II Organic Fluorophores and the High Promises of the BODIPY Family

As mentioned in the previous sections **(Section 4.1.3, Section 4.1.4)**, the interest towards NIR-II fluorophores is very high. In this regard, organic dyes have shown high promises especially thanks to their compact molecular structures, rapid metabolism, synthetic reproducibility and facile derivatization[1,7,12]. NIR-II luminescent organic molecules are generally classified, according to their chemical structures, within two main classes of fluorophores: donor-acceptor-donor (D-A-D) type and polymethines (D-π-A)[12]. A lot of efforts have been made to improve the performance of such push-pull conjugate systems for bioimaging and biosensing applications. These mainly focused on the absorption and emission wavelengths, the NIR-II fluorescence brightness (*i.e.* product of QY and extinction coefficient ε), and the chemo- and photostability. With regards to the bathochromic shift to longer NIR-II wavelengths, several strategies have resulted successful: these include elongation of the conjugated chain, donor modification by increasing the electron density, acceptor modification by decreasing the electron density, exchange of heteroatoms and formation of J-aggregates[12]. For example, ICG-derivatives could be extended from the NIR-I to the NIR-II window (up to $\lambda \approx 1300$ nm) thanks to the lengthening of the polymethyl chain[7]. Next to the red-shifted wavelengths, J-aggregates (*i.e.* head-to-tail oriented aggregates of fluorophores with conjugated plane structure) present optimal characteristics for *in vivo* bioimaging, including enhanced ε and lower τ. Unfortunately, however, both their preparation and stabilization procedures are typically cumbersome[12,77]. In terms of brightness improvement in the NIR-II window, it has been demonstrated that the reduction of intermolecular interactions with *e.g.* water by means of steric hindrance plays a key role. Steric hindrance can be introduced either covalently (*e.g. via* donor modification) or by forming protein-fluorophore complexes *via* supramolecular interactions. Additionally, as briefly mentioned in **Section 4.1.3**, structural modifications to generate AIE fluorophores can overcome the aggregation-caused quenching (ACQ) which is typical of most (NIR-II) systems in aqueous solutions[12]. It must be kept in mind, though, that some strategies that work well for the brightness are detrimental to the bathochromic shifting cause and *vice versa*: for instance, higher quantum yields are obtainable at lower emission wavelengths and by suppressing the excited state twisted intramolecular charge transfer (TICT, process which can otherwise lead to red-shifts)[12,17]. Finally, multiple studies have focused on the molecular engineering of NIR-II fluorophores to improve their stability by implementing steric hindrance (*e.g.* micelles), more rigid conjugated planes and protein-fluorophore complexes. In this way, protection of the organic molecules from reactive species can be significantly enhanced[12].

Based on general molecular engineering concepts as the ones outlined above, numerous NIR-emitting fluorophores with molecular skeletons such as cyanines[30,78], BODIPYs[42,43], rhodamines[79,80], porphyrins[81–83] and squaraines[84,85] have been prepared in recent years[2]. Among them, the BODIPY scaffold has recently grown very popular and its functional derivatives have shown high potential for numerous technological fields besides bioimaging, such as chemosensing, photodynamic therapy, tunable laser dyes, organic light-emitting diodes (OLEDs) and organic photovoltaics[6,86]. The success of BODIPY derivatives should not be surprising, considered their multiple appealing properties: these include overall excellent thermal stability, chemical robustness, high fluorescence quantum yields, and relatively sharp and intense absorption and emission spectra. Quite interestingly, the characteristic negligible formation of triplet-states enables a minimized production of singlet molecular oxygen, thus preventing photodegradation of the dye[43]. The remarkable (photo)stability is further proven by the discrete insensitivity to environmental polarity and pH, as well as the decent stability to physiological conditions[42,43,87]. Although the fluorescence emission maxima of BODIPY dyes is originally relatively short ($\lambda_{\max} < 600$ nm[88]), these organic fluorophores present tunable emission wavelengths that can lead to bathochromic shifts into the NIR-I and NIR-II regions, as briefly outlined in **Section 4.1.3**. Indeed, these spectral features can be modified *via* extension of the delocalized π-conjugation system: possible routes to this end consist in production of ring-fused systems **(Figure 4.4, Section 5.1)**, attachment of aromatic groups (preferably with electron-donating substituents), rigidification of rotatable moieties and electronic stabilization of the *meso*-position[1,42,86,87]. The latter strategy can consist, for example, in the replacement of the carbon atom with nitrogen, leading to the formation of the aza-dipyrromethene boron difluoride (aza-BODIPY) dyes. These emit fluorescence in the NIR-II region (1000 nm < λ_{em} < 1200 nm) and have already shown high potential for bioapplications[7,12]. Additionally, other BODIPY-inspired scaffolds exists, such as bis(borondifluoride)-8-imidazodipyrromethene (BOIMPY) dyes: these novel platforms have shown great promise for the biomedical field, too, as styryl-containing BOIMPYs prepared by Knoevenagel-type condensations can display NIR-I emission[89]. In a more recent work, it was also reported that electronic saturation of the highly electron-depleted (aza-)BOIMPY skeleton by *β*-alkoxy/*α*-aryl groups can also yield wavelength shifts to the NIR-I region[86]. Unfortunately, despite the high promises, most of the BODIPY derivatives synthesized so far are not water-soluble. Additionally, the number of NIR-emitting dyes is still not comparable to the Vis counterparts[7,42,87]. It is therefore of high interest to expand the library of BODIPY-based fluorophores for efficient NIR fluorescence bioimaging.

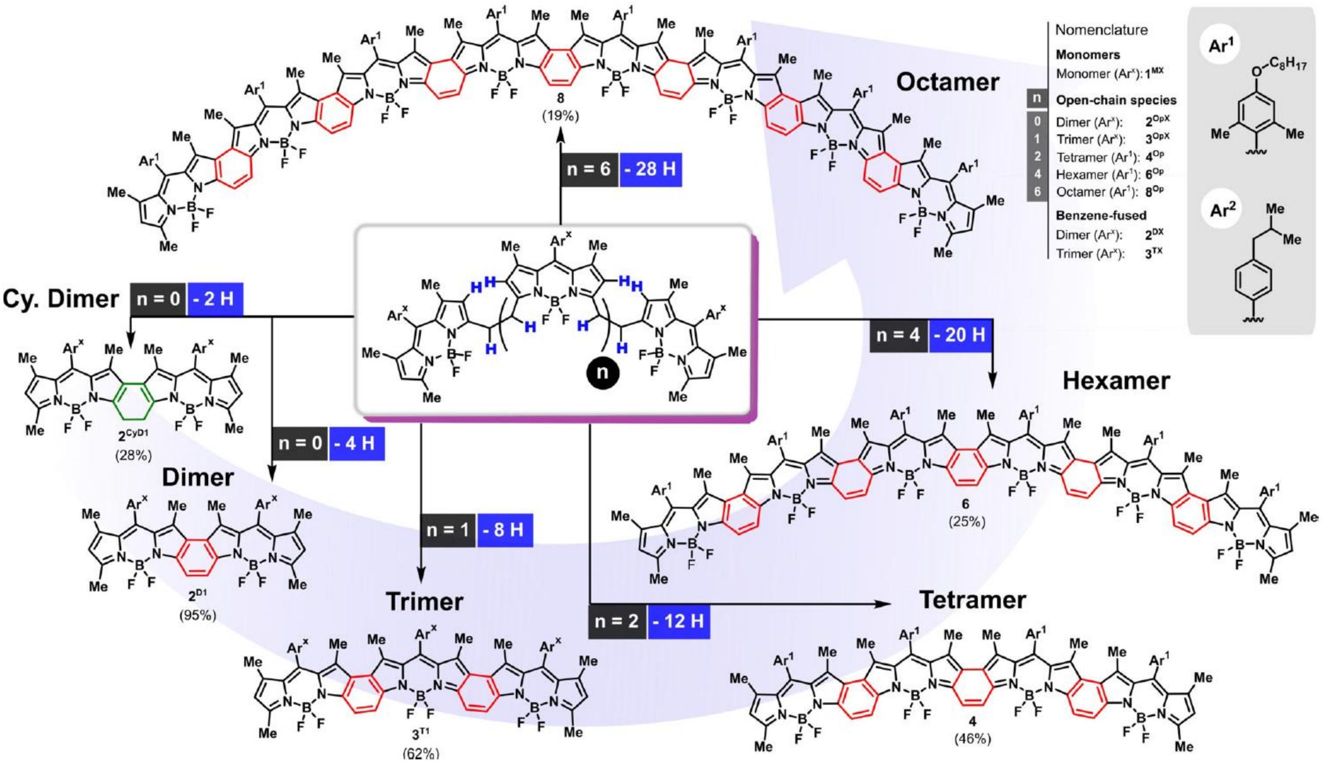

__Figure 4.4 Extended benzene-fused oligo-BODIPYs.__ Scheme illustrating the series of oligo-BODIPYs obtainable according to the protocol established by Patra et al. The reported yields correspond to molecules synthesized from their corresponding open-chain species (middle frame) with aryl groups Ar^1 *as meso-substituent (top-right panel). Reproduced with permission from ref.* [6]*. Copyright 2020 Wiley-VCH.*

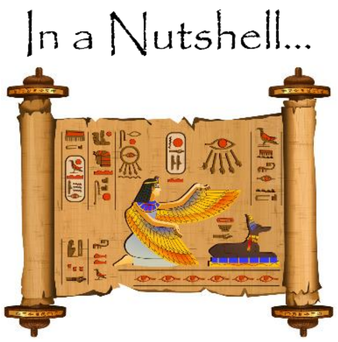

- ✓ Fluorescence imaging presents numerous advantages over other standard techniques for biological imaging.
- ✓ At near-infrared (NIR) wavelengths (700 nm < λ < 1700 nm) deep-tissue imaging is possible due to reduced absorption, scattering and autofluorescence events.
- ✓ Although the imaging contrast of NIR fluorophores outperforms the one obtainable with the more traditional visible emitters, not as many NIR systems have been established so far and only two have been approved for in-human clinical use.
- ✓ Organic and inorganic NIR fluorophores have shown their potential through several high-impact studies, however clinical translation is currently hindered by the limitations displayed by most NIR labels (*e.g.* toxicity, low (photo)stability, low quantum yields).
- ✓ Given the excellent features of NIR bioimaging, the scientific interest in developing novel NIR-emitting nanomaterials and dyes is nowadays very high.
- ✓ Among the organic fluorophores, the BODIPY scaffold appears very promising thanks to properties such as its versatile chemistry, high quantum yields and tunable spectral features.

In the first part of the results section of this dissertation **(Section 5.1)**, the focus is set on promising NIR organic fluorophores as the ones outlined in the current section. BODIPY derivatives such as extended benzene-fused oligo-BODIPYs are indeed players of optimal characteristics for biophotonics. The photophysical properties and bioimaging potential of some of these samples, which were kindly provided by the research group of Prof. Werz (Technical University of Braunschweig), have been investigated as promising organic emitters, potentially extending the toolbox of NIR fluorophores researchers could choose from.

As described in **Section 4.1.3** and **Section 4.1.4**, NIR-emitting nanoparticles can present very promising features in terms of *e.g.* (photo)stability. Among them, two-dimensional (2D) nanomaterials can display additional benefits thanks to their high aspect ratio, biocompatibility, biodegradability and exceptional chemical and physical properties. This doctoral thesis indeed mostly focuses on a novel class of such materials which is introduced in **Section 4.3** and more specifically described in the corresponding review article **(Review Manuscript**, **Section 4.3.2)**. However, for a better understanding of the general picture, the Reader is invited to first check the upcoming **Section 4.2** for an overview on the most promising characteristics and (bio)technological applications of established 2D “nanosheets”.

4.2 The Importance of Being 2D: The Legacy of Graphene

4.2.1 2D Nanomaterials as Versatile Platforms for Multiple Technologies

Two-dimensional (2D) nanomaterials (*i.e.* nanosheets, NS) provide a full toolbox of chemical and photophysical properties which are the reason for their huge success in numerous state-of-the-art technological fields. With "2D nanomaterial" is meant a high aspect ratio nanostructure whose thickness is in the nanometer regime, thus much smaller than the size along the other two dimensions (which can normally extend to the micrometer range)[90]. Within this context, the first groundbreaking step was taken with the discovery of graphene: most likely the most popular 2D material among scientists and not only, graphene consists of a single layer of sp^2-hybridized carbon atoms, obtainable from graphite *via* a facile exfoliation technique (so called "Scotch tape method")[91–97]. Since 2004, *i.e.* when Geim and Novoselov managed for the first time to isolate graphene, multiple works by research groups all over the world have been published on this material. These studies have underlined several aspects of this material's unprecedented properties: among them, optical transmittance of 97.7%, impermeability to any gases, carrier mobility reaching 200000 $cm^2\,v^{-1}\,s^{-1}$ at room temperature (larger than 10^6 $cm^2\,v^{-1}\,s^{-1}$ at 2 K) and a Young modulus of ≈ 0.5-1 TPa[90–94,96–99]. Following graphene, a second, wide class of 2D materials has been discovered and studied in detail: transition metal dichalcogenides (TMDs). This term comprises bulk materials of diverse properties, ranging from insulators (*e.g.* HfS_2), semiconductors (*e.g.* MoS_2 and WS_2), semimetals (*e.g.* WTe_2 and $TiSe_2$) to true metals (*e.g.* NbS_2 and VSe_2)[95,97,100]. Differently from graphene which is intrinsically chemically inert (*i.e.* lacks a band-gap), single layers of 2D TMDs exhibit versatile chemistry[97,98]. The quantum confinement effect, which implies that the electronic wavefunction is constrained to two dimensions in a NS, makes it possible to tailor the band structure of these materials, allowing the creation and tuning of novel optical and electronic properties[90,101,102]. For this reason, graphite and graphene display completely different properties[92]. Furthermore, the band-gap of a typical semiconductor TMD like MoS_2 is sizable, varying from 1.3 eV (indirect band-gap) to 1.9 eV (direct band-gap) after exfoliation; bulk properties of TMDs can be preserved, or exfoliation can lead to novel characteristics, like photoluminescence in MoS_2 monolayers[90,95,97,103–105]. Also thanks to the very high surface area displayed by these nanostructures, employment of TMD NS has been demonstrated in the fields of energy storage, sensing, catalysis and electronics[90,95,97,98,100,101,106–108]. Other examples of explored 2D materials with novel and interesting features comprise semiconducting IV-VI compounds, transition metal halides, metal oxides, hexagonal boron nitride (h-BN), graphitic carbon nitride (g-C_3N_4), transition metal carbides and carbonitrides (MXenes), the 2D counterpart of layered black phosphorus (BP, *i.e.* phosphorene), antimonene, silicene, honeycomb-like binary compounds of group IV elements, (alumino)silicates, layered double hydroxides (LDHs) and many more **(Figure 4.5a)**[97,99].

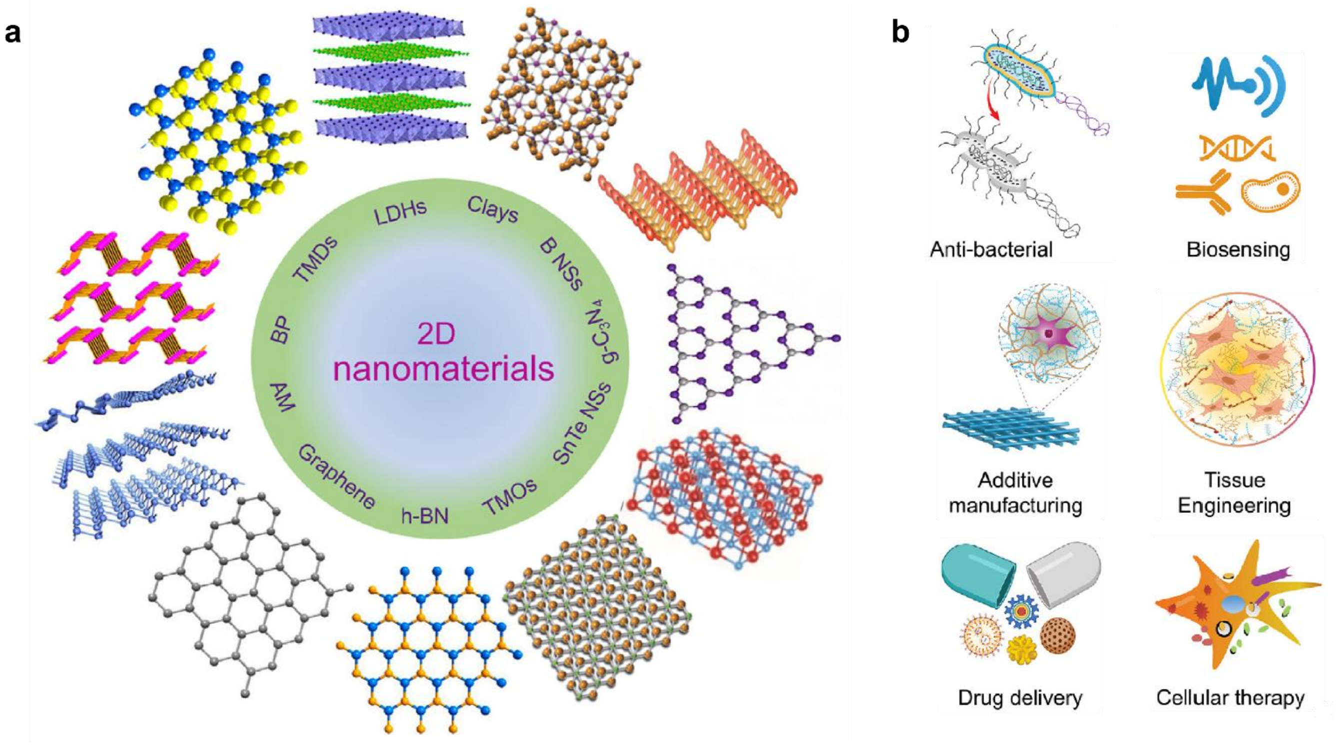

***Figure 4.5 Two-dimensional** (**2D) nanomaterials. a** Schematic illustration with the crystal structures of some of the most investigated 2D nanostructures beyond graphene. These include transition metal dichalcogenides (TMDs), layered double hydroxides (LDHs), clays, boron (B) and tin telluride (SnTe) nanosheets, graphitic carbon nitride (g-C_3N_4), transition metal oxides (TMOs), hexagonal boron nitride (h-BN), antimonene (AM) and black phosphorus (BP). Reproduced with permission from ref. [109]. Copyright 2019 Elsevier. **b** Illustration of various biomedical applications where 2D nanomaterials have been successfully employed. Adapted with permission from ref. [110]. Copyright 2021 Elsevier.*

4.2.2 Nanosheets in Biomedicine

As this dissertation mostly focuses on biomedical applications of 2D silicate nanomaterials, it is worth mentioning that such nanostructures in general present ideal features for biomedicine **(Figure 4.5b)**[109,111,112]. For instance, their high specific surface area and their surface functionalization chemistries are very suitable for drug/gene delivery systems[113–115]: indeed, molecules of interest (*e.g.* drug molecules) can in this way adsorb in high numbers and release kinetics can be tailored. Furthermore, the outstanding surface area to volume ratios, the high modulus values and/or the (bio)degradability of some 2D systems can be exploited in biomedical nanocomposites for *e.g.* tissue engineering and antimicrobial coatings[116–118]. Additionally, the extremely low thickness of most NS has proven to play a role of paramount importance for biosensing and gene sequencing applications[119,120]. The high aspect ratio of 2D nanomaterials also enables light, ultrasonic and magnetic responses of these materials to external stimuli, making their employment for multimodal imaging and photothermal/photodynamic therapy (PTT/PDT) possible[121–125]. NS size and shape, however, also strongly influence the interactions of those nanostructures with the biological environment. Given the complexity of response reactions of living tissues, as well as the heterogeneity of manufacturing processes and potential presence of impurities, there is up to now a lack of in-depth studies that address biocompatibility of 2D nanomaterials[109,111,112,126]. General observations suggest, however, that nanomaterial size, surface area and composition have great impact in terms of (cyto)toxicity, and must therefore be carefully designed[111]. In this regard, some 2D materials more than others present biocompatible traits and highly promising characteristics for biomedical applications. For example, the exceptional chemical, physical, electrical and biological properties of graphene, graphene oxide (GO) and reduced graphene oxide (rGO), that were partially mentioned in **Section 4.2.1**, have been widely implemented for tissue engineering, drug delivery, bioimaging and biosensing[96,127–134]. The shape and surface charge of silicate clays, on the other side, has favored interaction of such NS structures with biomolecules, thus enabling successful applications for drug/gene delivery, stem cell differentiation, controlled cell adhesion and hemostatic wound dressings[135–140]. LDHs present excellent biocompatibility and anion exchange capacity which explain their promising results in drug delivery applications and tissue engineering[116,141,142]. TMDs, as described in **Section 4.2.1**, display a uniquely versatile optoelectronic nature, besides having high absorption at near-infrared (NIR) wavelengths and being mechanically robust platforms: for these reasons, they result extremely appealing for drug delivery, bioimaging, biosensing and PTT/PDT[143–148]. Similar potential in such fields has been observed for TMOs, which are characterized by favorable cation exchange capabilities, redox activity and diverse electrical and optical properties[149–153]. Phosphorene has been widely employed for drug delivery, theranostics, tissue engineering and biosensing, however synthetical challenges and instability in air and water limit its applicability[121,154–156]. Finally, also other 2D materials such as h-BN[157,158], g-C_3N_4[159–161], tin telluride (SnTe)[162], MXenes[163,164], other monoelemental Xenes (*e.g.* silicene, antimonene, germanene, borophene)[165–167] and metal-organic frameworks (MOFs)[168–170] have recently been classified as promising 2D biomaterials for the mentioned biological applications, however for most of them more studies are needed to optimize their synthesis, fully exploit their outstanding properties and address the missing steps towards clinical translation.

4.2.3 Exfoliation of 2D Materials

Efforts have been made not only to better understand the chemical and optoelectronic properties of 2D materials, but also to optimize and scale-up their preparation. Analogously to other categories of nanomaterials, bottom-up and top-down routes can be defined. The former techniques (*e.g.* chemical vapor deposition (CVD), epitaxial growth and wet chemical methods[101,102]) can lead to large-scale device fabrication of large-area, ultrathin and uniform layers; processes result, however, expensive and complicated, due to *e.g.* the requirements of high temperatures and vacuum[98,99]. In the top-down category, instead, we deal with exfoliation (or delamination). A material prone to exfoliation should display a layered crystal structure where out-of-plane bonds are far weaker than in-plane ones (*e.g.* Van der Waals *vs.* covalent bonds). Several layered materials are known and have been exfoliated so far, including the already mentioned graphene, TMDs, h-BN, metal halides, layered metal oxides, layered double hydroxides and layered silicates (clays), to mention a few[90,100]. The two main kinds of exfoliation are micromechanical cleavage (*e.g.* the mentioned adhesive tape method) and liquid-phase exfoliation (LPE, **Figure 4.6**)[98]. While mechanical cleavage can produce single-crystal flakes of high purity, it is not scalable and control of flake thickness and lateral size is cumbersome[99]. LPE is mostly performed *via* ion intercalation, ion exchange and ultrasonication[90,98]. The latter typically yields flakes of sizes around few hundred nanometers, however the amount of monolayers is normally lower than *e.g.* ion intercalation[98], and (edge) defects can be induced after prolonged ultrasonication[99,171]. Next to ultrasonic exfoliation, it is worth mentioning scalable techniques which exploit high shear processing (*i.e.* wet ball milling and high-pressure homogenization) and electrochemistry (*i.e.* electrochemical exfoliation)[99,171]. In most of the mentioned techniques, solvents such as *N*-methyl-2-pyrrolidone (NMP), *N*-cyclohexyl-2-pyrrolidone (CHP), dimethyl formamide (DMF) and dimethyl sulfoxide (DMSO) are known to work efficiently for the exfoliation of several materials[95,99,105]. If the solvents are not characterized by appropriate surface energy, the exfoliated NS will then tend to reaggregate, leading to sedimentation. In this case, the addition of stabilizers can limit the action of these "bad" solvents: in aqueous solutions, surfactants such as sodium cholate, sodium deoxycholate, cetyltrimethylammonium bromide (CTAB) are indeed typically employed[99]. Post-exfoliation treatments such as centrifugation[172,173] and syringe-filtration are normally recommended to increase the monodispersity of the final NS sample. Among the benefits of LPE, it is noteworthy to mention that subsequent chemical modification of the exfoliated nanosheets, fundamental *e.g.* for drug delivery and sensing applications, is here possible. This technique also allows an easy and scalable deposition of NS on diverse surfaces *via* solution-based techniques such as inkjet printing and spray coating; these are known to be very useful tools for large-area electronics and the preparation of thin or free-standing films, heterostructured solids and fillers[90,98,99]. LPE of layered crystal structures holds therefore high promises for industrial applications in fields such as multifunctional composites, electronics, biomedicine, energy generation and storage[90,98]. It is therefore of great scientific interest to investigate new 2D materials.

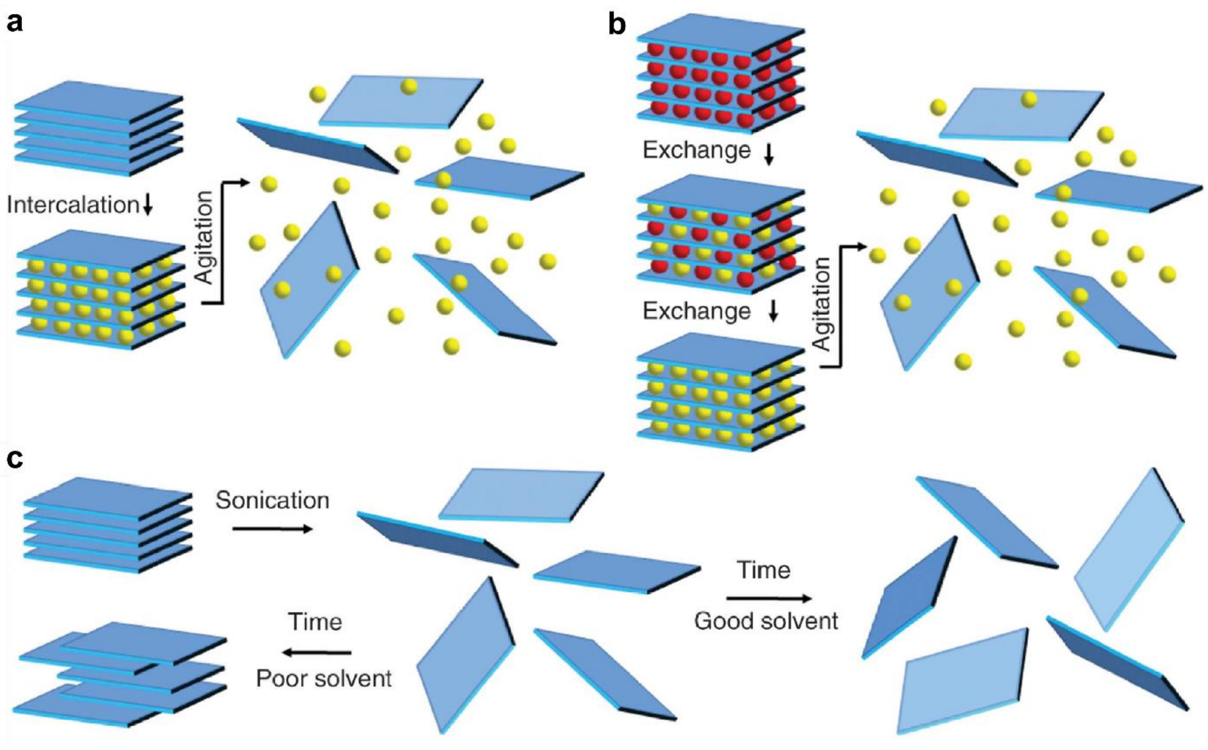

Figure 4.6 Liquid phase exfoliation (LPE) of 2D materials. *Schematic of the main routes for liquid exfoliation: ion intercalation* ***(a)****, ion exchange* ***(b)*** *and sonication-assisted exfoliation* ***(c)****. Ions are represented as yellow and red spheres. Reproduced with permission from ref.* [90]*. Copyright 2013 AAAS.*

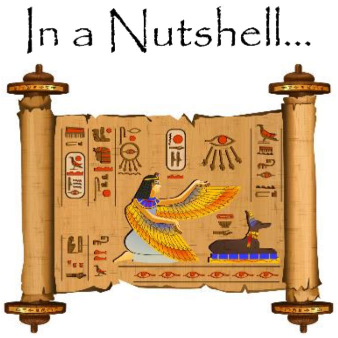

- ✓ Due to their high aspect ratio and their outstanding chemical and physical properties, 2D nanomaterials (*i.e.* nanosheets, NS) are promising platforms for multiple state-of-the-art technologies.
- ✓ Different classes of NS have shown high promise in the biomedical field for numerous applications.
- ✓ Despite the biocompatible nature of some materials, in-depth (cyto)toxicity studies lack for most, thus slowing down clinical translation.
- ✓ Liquid-phase exfoliation (LPE) presents promising features in terms of scalability and processability of the so-prepared NS.

The Reader is invited to check the next section and the corresponding **Review Manuscript (Section 4.3.2)** for more detailed insights on a novel class of 2D nanomaterials: the silicates Egyptian Blue, Han Blue and Han Purple, *i.e.* the main players of this dissertation.

4.3 Ancient Pigments for Novel (Bio)Technologies: Nanosheets of Egyptian Blue (EB-NS), Han Blue (HB-NS) and Han Purple (HP-NS)

4.3.1 Introduction

The silicates Egyptian Blue ($CaCuSi_4O_{10}$, EB), Han Blue ($BaCuSi_4O_{10}$, HB) and Han Purple ($BaCuSi_2O_6$, HP) represent at the same time materials of fascinating history and working platforms of apparently endless possibilities for multiple technological fields. These blue and purple powders **(Figure 4.7a)** were originally synthesized several centuries ago in Ancient Egypt and China (≈ 2500 BC and ≈ 220 BC-220 AD, respectively)[174–179]. Their original purpose was to be employed as pigments for artworks, given the scarce availability of blue and purple minerals in nature[180]. Throughout the years, EB, HB and HP have been intensively employed and their presence is still detectable in world-famous pieces of art such as the Bust of Queen Nefertiti and the Terracotta Warriors of the tomb of Emperor Qin Shihuangdi in Xi’an **(Figure 4.7b)**. Several studies have shown, however, that the “know-how” necessary to synthesize these beautiful pigments could cross borders in history: for instance, the high stability of EB has allowed the documentation of its presence in several territories of the Roman Empire, ranging from Spain to North Africa, western Asia and Europe[175].

Although these pigments clearly hold extraordinary value in the field of history of art, there is much more to that. Several studies have focused on the evolution over the centuries of the synthesis of EB, HB, HP, leading to the establishment of alternative preparation routes[174,180,181]. The impact of *e.g.* different starting materials and contaminants on the morphology of the synthesized silicates has indeed been thoroughly investigated. However, the spotlight has also been set on the numerous outstanding properties exhibited by such materials, some of which are intrinsically linked to their crystal structures. Indeed, the copper ion (Cu^{2+}), which acts as color center in all three silicates, presents a square planar (D_{4h}) coordination geometry **(Figure 4.7c)**[182]. Here we can observe that, due to extreme symmetry distortions (*i.e.* Jahn-Teller effect), the d_{z^2} orbital lies at a lower energy than the d_{xy}, d_{xz} and d_{yz} ones. As a result of an electron being promoted from lower energy levels in the *d*-shell to the $d_{x^2-y^2}$ one, three absorption bands stretching through a broad range of visible (Vis) and NIR wavelengths are obtained **(Figure 4.7d)**. Despite the parity-forbidden nature of the mentioned *d-d* transitions, vibronic coupling with unsymmetrical vibrational modes allows a significant amount of absorption to take place. Most interestingly, however, only the $B_{2g} \rightarrow B_{1g}$ transition determines emission, because non-radiative relaxations are much more effective from higher energy levels to B_{2g}[174,182]. Furthermore, the so-obtained fluorescence is centered in the NIR range and is characterized by high brightness, remarkable photostability and long excited state lifetime. Although these photophysical properties already define EB, HB and HP as materials of high impact for diverse fields, their potential can be further expanded in the nanoscaled form. As described in **Section 4.2**, 2D nanomaterials display several outstanding qualities that make them ideal candidates for numerous technological applications. In the case of EB, HB and HP, exfoliation to nanosheets (NS) is easily achievable due to the weak out-of-plane bonds that hold the silicate layers together. Most importantly, as outlined in **Section 4.3.2** and in the own contributions embedded in **Chapter 5**, the broad excitation range and, above all, the bright and stable NIR fluorescence of the bulk materials are retained after down-scaling the silicates to NS[183–185]. This recent finding has determined increasing scientific interest around such novel class of nanomaterials, especially in the biomedical field. Indeed, EB-NS, HB-NS and HP-NS also display additional features which are optimal for biomedicine, above all a biocompatible nature. All considered, EB-NS, HB-NS and HP-NS therefore seem to possess all the required traits of promising NIR fluorophores for (bio)photonics.

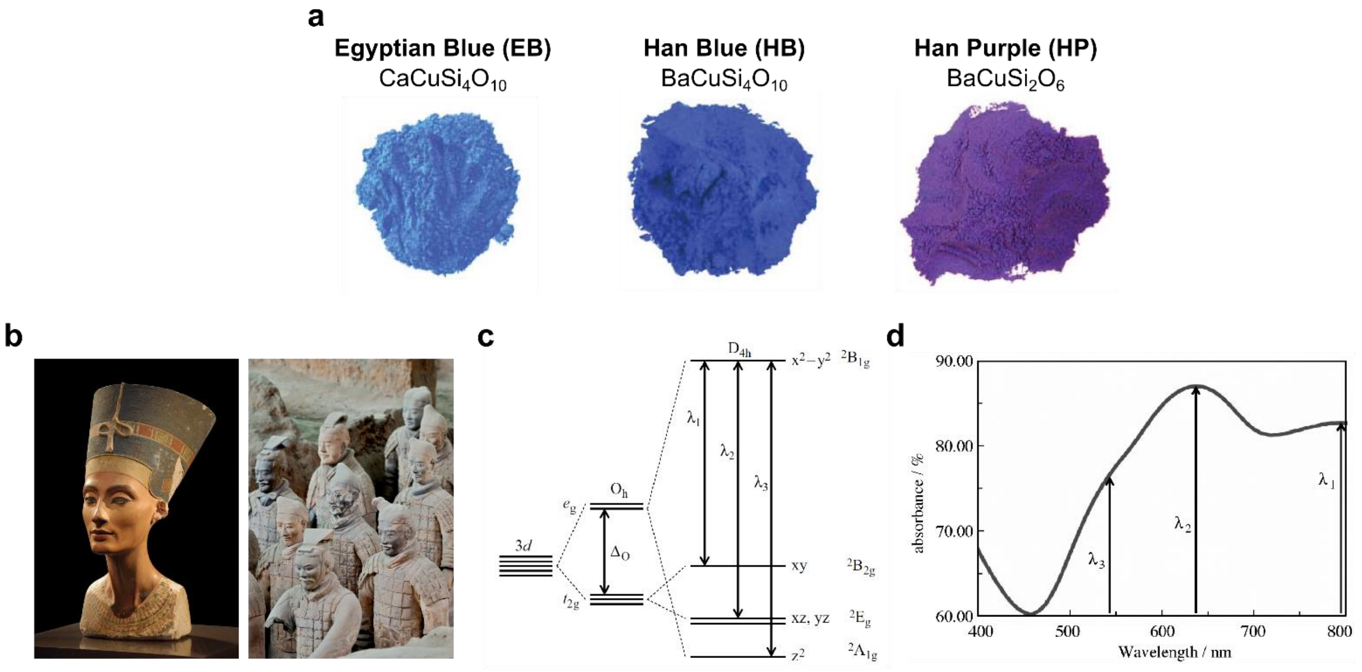

Figure 4.7 Egyptian Blue ($CaCuSi_4O_{10}$, EB), Han Blue ($BaCuSi_4O_{10}$, HB) and Han Purple ($BaCuSi_2O_6$, HP). a *Picture of bulk powders of EB, HB and HP. Adapted with permission from ref.* [180]*. Copyright 2007 Royal Society of Chemistry.* ***b*** *The Egyptian Bust of Queen Nefertiti and the Chinese Terracotta Warriors are two of the most significant examples of employments of these pigments in historical pieces of art. Adapted with permission from ref.* [186]*. Copyright 2009 Philip Pikart. Adapted with permission from ref.* [187]*. Copyright 2011 Kevin A. McGill.* ***c*** *Energy diagram of the electronic transitions of the copper ion (Cu^{2+}) in square-planar (D_{4h}) coordination geometry. Reproduced with permission from ref.* [174]*. Copyright 2011 Wiley-VCH.* ***d*** *Representative diffuse absorption spectrum of bulk EB synthesized via the salt-flux method. The band maxima are highlighted by the arrows: $\lambda_1(^2B_{1g} \rightarrow {}^2B_{2g})$ = 800 nm, $\lambda_2(^2B_{1g} \rightarrow {}^2E_g)$ = 630 nm, $\lambda_3(^2B_{1g} \rightarrow {}^2A_{1g})$ = 540 nm. Reproduced with permission from ref.* [174]*. Copyright 2011 Wiley-VCH.*

An extensive overview on EB-NS, HB-NS and HP-NS is to be found in the self-written review article embedded in this section **(Review Manuscript)**. Here, detailed descriptions and relevant scientific references are provided with regards to the crystal structures, the synthesis routes, the exfoliation protocols, the chemical and photophysical properties of interest and, finally, the broad spectrum of technological applications where EB-NS, HB-NS and HP-NS have been successfully employed. My own published works are also covered in this review article, however a more detailed discussion about these topics is to be found in the corresponding sections of this doctoral thesis (**Section 5.2** for **Manuscript II**, **Section 5.3** for **Manuscript III**). **Section 5.4** will instead describe the endeavors in the direction of functionalization of EB-NS: the results of this project are summarized in a paper draft **(Manuscript IV)**.

4.3.2 Preparation, Properties and Applications of Near-Infrared Fluorescent Silicate Nanosheets (Review Manuscript)

Publication Details

Title: “Preparation, properties and applications of near-infrared fluorescent silicate nanosheets”

Authors: **Gabriele Selvaggio** and Sebastian Kruss

Journal: *Nanoscale*, Advance Article (2022)

DOI: 10.1039/D2NR02967G

Nanoscale

REVIEW

View Article Online
View Journal

Cite this: DOI: 10.1039/d2nr02967g

Preparation, properties and applications of near-infrared fluorescent silicate nanosheets

Gabriele Selvaggio [a] and Sebastian Kruss *[a,b,c]

The layered silicates Egyptian Blue ($CaCuSi_4O_{10}$, EB), Han Blue ($BaCuSi_4O_{10}$, HB) and Han Purple ($BaCuSi_2O_6$, HP) are known as historic pigments, but they also possess novel optoelectronic properties with great potential for fundamental research and technology. They fluoresce in the near-infrared (NIR) range and can be exfoliated into two-dimensional (2D) nanomaterials (*i.e.* nanosheets, NS) which retain the photophysical properties of the bulk materials. These and other characteristics fuel the growing excitement of the scientific community about these materials. EB-, HB- and HP-NS have been used in various applications ranging from smart inks, energy storage, bioimaging, to phototherapy and more. In this review article, we report the fundamental properties of these low-dimensional silicate nanomaterials, discuss applications and outline perspectives for the future.

Received 29th May 2022,
Accepted 21st June 2022

DOI: 10.1039/d2nr02967g

rsc.li/nanoscale

Introduction

Two-dimensional (2D) nanomaterials (*i.e.* nanosheets, NS) have gained a lot of interest in light of their exceptional photophysical properties and their potential for many applications. The first established and up to now mostly investigated 2D material is graphene.[1–7] Since its isolation in 2004 by Geim and Novoselov, several theoretical and experimental studies have followed, which have underlined this material's interesting optoelectronic properties.[1–4,6–10] Following graphene, several new classes of 2D materials have been discovered and studied in detail. Above all, a versatile chemistry and novel properties could be unraveled by transition metal dichalcogenides (TMDs),[1,5,71] whose (single) layers displaying high surface area have allowed applications in several fields, including catalysis, energy storage, sensing and electronics.[5,7–9,11–15] Next to the TMDs, numerous other classes of promising 2D materials have been established.[7,10] With regards to the biomedical field, successful applications and high promises for *e.g.* drug and gene delivery, biosensing, tissue engineering, imaging and photo-

---

[a] *Department of Chemistry, Bochum University, Bochum, 44801, Germany.
E-mail: sebastian.kruss@rub.de*
[b] *Fraunhofer Institute for Microelectronic Circuits and Systems, Duisburg, 47057, Germany*
[c] *Center for Nanointegration Duisburg-Essen (CENIDE), Duisburg, 47057, Germany*

Gabriele Selvaggio

Gabriele Selvaggio received his BSc degree in Industrial Engineering at the University of Trieste (Italy). After working on 2D colloidal nanocrystals for optoelectronics at the University of Hamburg (UHH), he obtained his MSc degree in Process and Materials Engineering and the title of Engineer at the University of Trieste. Since 2018 he has moved to Germany and has joined the research group of Prof. Sebastian Kruss. Here he has been carrying out his PhD research, whose focus is set on the development of novel 2D nanomaterials for biomedical applications.

Sebastian Kruss

Sebastian Kruss received his PhD in bio-physical chemistry at Heidelberg University and the Max Planck Institute for Intelligent Systems (with Prof. Joachim Spatz). He then moved to the Massachusetts Institute of Technology (with Prof. Michael Strano), where he worked on carbon nanomaterials. After heading an independent research group at Göttingen University (2015–2020), he became professor of physical chemistry at Ruhr-Universität Bochum and Attract group leader at Fraunhofer IMS. His research focuses on novel materials, fluorescence spectroscopy and microscopy, biosensors, and cell biophysics.

thermal therapy (PTT) have been reported especially for graphene, graphene oxide (GO), reduced graphene oxide (rGO), silicate clays, layered double hydroxides (LDHs), TMDs, transition metal oxides (TMOs), graphitic carbon nitride (g-C_3N_4), hexagonal boron nitride (h-BN), transition metal carbides and carbonitrides (MXenes), 2D monoelemental materials (Xenes) and metal–organic frameworks (MOFs).[16–18] In terms of NS preparation, bottom-up synthetic techniques (*e.g.* chemical vapor deposition (CVD), epitaxial growth and wet chemical methods[12,19]) can produce high quality crystals with the drawback, however, of higher costs and more demanding experimental conditions.[9,10] Among the top-down methods, more scalable techniques include wet ball milling and high-pressure homogenization for which high shear processing is employed.[10,20] Scalability is a clear advantage also shared by liquid-phase exfoliation (LPE).[8–10] Furthermore, this technique allows size control and subsequent chemical modification of the exfoliated nanosheets (fundamental for *e.g.* drug delivery and sensing applications), as well as solution-based processing (*e.g.* inkjet printing and spray coating). For these reasons, LPE of layered nanomaterials holds high interest for applications, including multifunctional composites, electronics, biomedicine, energy generation and storage.[8,9]

It is well known that fluorescence imaging in the near-infrared (NIR, typically defined in the wavelength region of ≈750–1700 nm) allows higher tissue penetration and contrast due to the reduction of scattering, absorption and autofluorescence displayed by biological samples within this window.[21–24] NIR-emitting organic dyes such as cyanines[25,26] (*e.g.* indocyanine green, ICG[27]) and modified boron dipyrromethenes (BODIPYs[28–31]) have been successfully employed as fluorophores of versatile chemistry for numerous studies. Additionally, NIR-fluorescent nanomaterials characterized by higher photostability have been also reported. Among them, single-walled carbon nanotubes (SWCNTs[32–43]) have been used to detect small signaling molecules, proteins and lipids. They can be chemically tailored and allow spatiotemporal imaging of analytes such as neurotransmitters or identification of bacteria. In general, however, the amount of available fluorophores that emit fluorescence in the NIR is low, and most of them are affected by low QY, low photostability and/or biocompatibility issues.[23,27,44–48] For this reason, the scientific interest towards the preparation of novel NIR dyes and nanomaterials for biological imaging is very high.

The silicates Egyptian Blue ($CaCuSi_4O_{10}$, EB), Han Blue ($BaCuSi_4O_{10}$, HB) and Han Purple ($BaCuSi_2O_6$, HP) embrace a fascinating historical background and exciting photophysical and chemical properties. EB is regarded as the most ancient artificial pigment made by man. With its origins dated back to Ancient Egypt (≈2500 BC), this phyllosilicate has been extensively employed throughout history in decoration of artworks (*e.g.* the well-known Bust of Queen Nefertiti).[49–53] HB and HP, on the other side, were mostly employed in the times of the Qin and Han dynasties (≈220 BC–220 AD), as witnessed by *e.g.* the Terracotta Warriors of the tomb of Emperor Qin Shihuangdi in Xi'an.[54] The manufacturing of these pigments shares common traits,[49,55,56] historically focused on salt-flux methods. These typically require long reaction times, yet they yield large crystals at not excessive reaction temperatures.[49,57] Alternatively, flux-less solid-state synthesis is usually less time-consuming and can lead to lower amounts of glassy matrix surrounding the crystals, however they require higher temperatures and tend to produce smaller crystallites.[52,57–63] Synthesis in molten carbonates has proven so far inefficient, resulting in the production of *e.g.* azurite and malachite.[64] In search of a better control over morphology and size while working more "green" (*i.e.* at relatively mild temperatures and pressures), hydrothermal processes have been successfully established.[65–68] Additionally, also sol–gel methods,[69] solution combustion synthesis (SCS)[70] and pseudomorphosis routes from a synthetic layered sodium silicate[71] have been reported.

Thanks to their layered crystal structure, these silicates can be easily exfoliated into 2D nanomaterials (NS). Most interestingly, EB-NS, HB-NS and HP-NS seem to retain most of their bulk features after down-scaling: a robust (photo)chemical stability, a bright NIR emission, a broad visible (Vis)-NIR absorption range and a high biocompatibility are just some of their most appealing characteristics. In recent years, a growing number of studies has been devoted to the collection of novel insights on the optoelectronic properties of these nanomaterials. Furthermore, the typically high aspect ratio of 2D nanomaterials, next to the previously mentioned features of EB, HB and HP, have raised interest for these silicates among researchers of diverse scientific backgrounds. Apparently unrelated modern technological fields such as smart inking, latent fingermark detection, batteries, multifunctional biocomposites, biological sensors and labeling agents are making use of EB-NS, HB-NS and HP-NS (Fig. 1).

Crystallography and exfoliation routes

The blue-purple pigments EB, HB and HP (Fig. 2a) are layered homologue silicates with similar crystal structure. EB's natural analogue is the mineral cuprorivaite, whose tetragonal crystal structure (spacegroup $P4/ncc$), first determined by Pabst *et al.* in 1959, consists of parallel layers of silicate weakly held together by the presence of interlayer calcium ions in an eight-fold coordination geometry (Fig. 2b).[49,61,81,82] The copper ions, tightly shielded within the silicate framework, are arranged in a square planar coordination geometry (D_{4h}). Except for the substitution of the Ca^{2+} ions with Ba^{2+} ones, HB (whose natural analogue is the mineral effenbergerite) displays the same structure.[61,82,83] The tetragonal crystal structure of HP (for which suggested space groups at room temperature include $I\bar{4}m2$[68,84,85] and $I4_1/acd$[66,86]) is, instead, less rich in silica and presents a chemically labile Cu–Cu bond. The weaker stability especially towards weak acids shown by HP (whose natural mineral analogue is colinowensite) is likely due to this characteristic metal–metal bond.[55,56,68,85,87,88] For EB, HB and HP alike, the weaker out-of-plane bonds enable exfoliation of these lamellar structures into NS. Up to now, the main

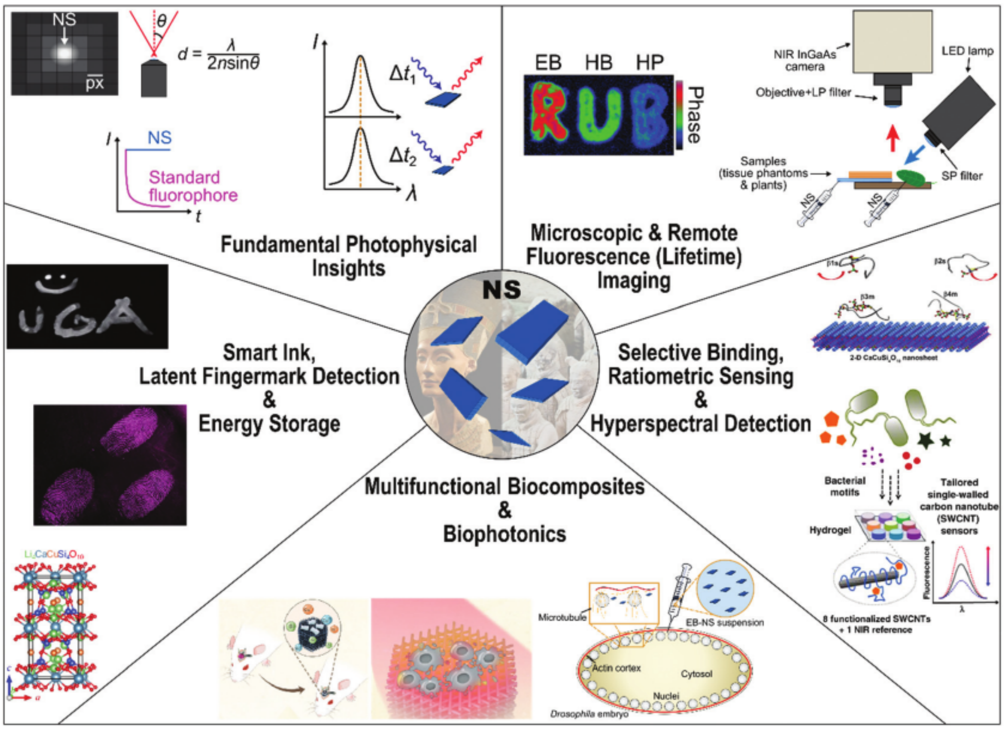

Fig. 1 Fundamental insights and applications of silicate nanosheets. Due to their layered crystal structures, Egyptian Blue ($CaCuSi_4O_{10}$, EB), Han Blue ($BaCuSi_4O_{10}$, HB) and Han Purple ($BaCuSi_2O_6$, HP) can be easily exfoliated into nanosheets (NS). These 2D nanomaterials display numerous interesting properties that make them versatile platforms for multiple technological fields. Adapted with permission from ref. 72 and 73. Copyright 2020 Springer Nature. Reproduced with permission from ref. 74 and 75. Copyright 2021 Royal Society of Chemistry. Reproduced with permission from ref. 76. Copyright 2018 John Wiley and Sons. Reproduced with permission from ref. 77. Copyright 2021 John Wiley and Sons. Reproduced with permission from ref. 78. Copyright 2016 Elsevier. Reproduced with permission from ref. 57. Copyright 2014 Journal of Visualized Experiments. Reproduced with permission from ref. 79. Copyright 2009 Philip Pikart. Reproduced with permission from ref. 80. Copyright 2011 Kevin A. McGill.

techniques employed for this task have included prolonged hot stirring (Fig. 2c(i)), probe ultrasonication (Fig. 2c(ii)), bath sonication (Fig. 2c(iii)) and ball milling (Fig. 2c(iv)). Despite applying in some cases high local mechanical (shear) stress, the exfoliation routes reported so far seem not to have significantly affected the crystallinity of the samples, thus retaining the materials' identity and properties (as shown, for example, for the hot stirring method in Fig. 2d).

Although multiple synthetic routes for EB, HB and HP have been reported (Tables 1–3), several studies rely on commercially available bulk powders as starting material. These are produced following the salt-flux method and they typically appear in the form of several μm-large platelets. On their surfaces, the characteristic steps, ridges and terraces of such lamellar materials can be easily observed (Fig. 3a). A first robust example of exfoliation of so-synthesized EB was demonstrated by Johnson-McDaniel *et al.* *Via* simple stirring in hot water over several days, EB-NS could be produced. This prolonged hot stirring, followed by a shorter bath sonication step in an organic solvent, led to μm-sized sheets down to ≈1 nm in thickness, *i.e.* monolayer regime[57,89] (Fig. 3b and c). Shortly after this seminal study, Salguero *et al.* applied a similar protocol to produce EB-NS with lateral size ranging from hundreds of nm to several μm. While exfoliation of high aspect ratio EB-NS proved to be quite straightforward, the same did not apply to HB. Indeed, proper exfoliation of this material required probe ultrasonication and bath sonication in organic solvents.[57,90] When dealing with minerals such as silicates, a common way to reduce crystal size is milling. Borisov *et al.* published the first employment of ball milling on EB.[91] While the dimensions of such crushed crystallites could enable the desired material applications, the lateral sizes obtained with this technique once again lied in the μm rather than in the nm range. The previously mentioned pivotal works inspired a series of follow-up studies which featured size reduction of EB and HB (Tables 1 and 2). While most of these publications mainly presented NS in a similar (μm) size range, the one from Shahbazi *et al.* stood out due to the higher degree of monodispersity and higher amount of small (<200 nm) EB-NS (Fig. 3d): their approach consisted in a modified version of the Johnson-McDaniel protocol with the additional employment of a cationic lipophilic surfactant (cetrimonium bromide, CTAB).[92] High energy exfoliation can quite simply yield NS structures down to few tenths in nm in lateral size that, despite the irregular morphologies typical of fragmentation, still display a homogeneous elemental distribution (Fig. 3e–h).[77] Further

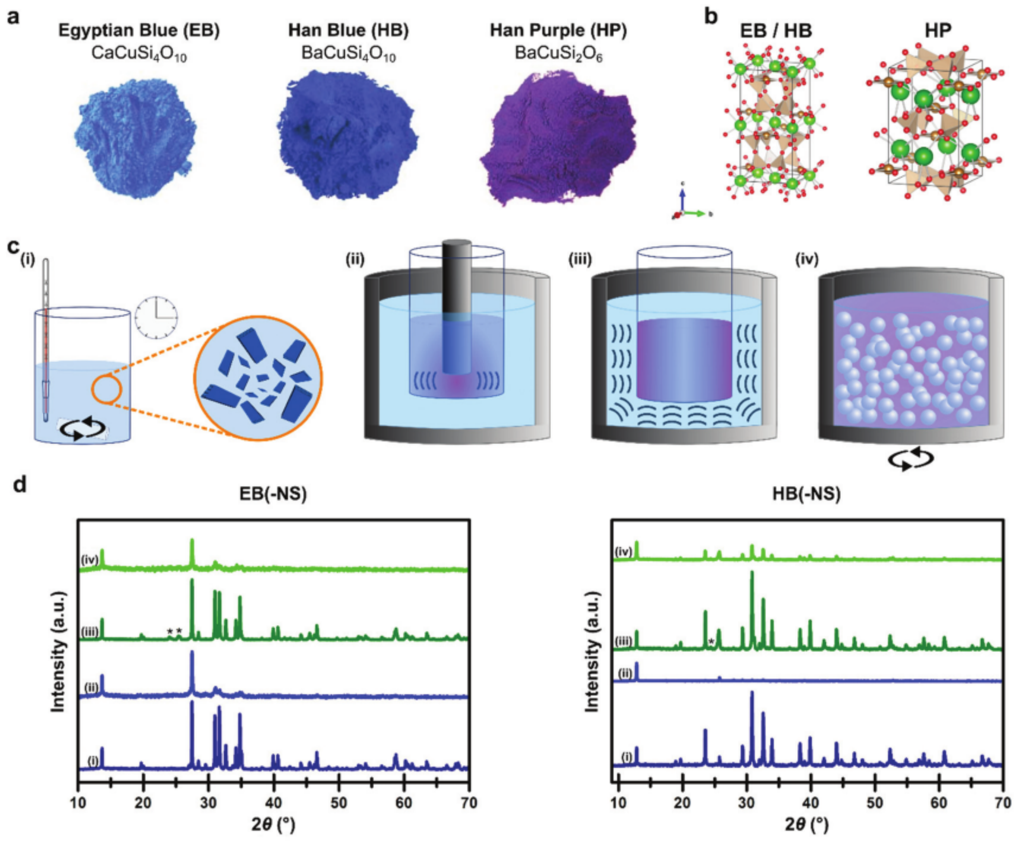

Fig. 2 A class of layered silicates: Egyptian Blue (EB), Han Blue (HB) and Han Purple (HP). (a) Picture of bulk powders of EB, HB and HP. Adapted with permission from ref. 55. Copyright 2007 Royal Society of Chemistry. (b) Schematic of the crystal structures of EB, HB and HP: except for Si (depicted as tetrahedra), all other elements are represented as spheres of color green for Ca (EB) and Ba (HB and HP), bronze for Cu, and red for O. Reproduced with permission from ref. 72. Copyright 2020 Springer Nature. (c) Illustration of the most employed techniques used to exfoliate these layered silicates into NS. Long stirring in hot water (i), tip (ii) and bath (iii) sonication in water/organic solvents, and wet milling in water/organic solvents (iv). (d) Powder X-ray diffractometry (XRD) of bulk (i and iii) and exfoliated (ii and iv) EB and HB: the starting materials were synthesized either *via* melt-flux (i) or solid-state (iii) methods, whereas EB-NS and HB-NS were respectively prepared by prolonged stirring in hot water and (ultra)sonication in *N*-vinyl pyrrolidone (NVP). Asterisks represent silica impurities. Adapted with permission from ref. 57. Copyright 2014 Journal of Visualized Experiments.

progress in the direction of smaller sizes and more thorough statistics was later reported by Selvaggio *et al.*, who established a hybrid protocol consisting of wet ball milling and tip sonication. With this approach, also HP-NS in the nm range and with just a few layers of thickness were obtained and fully characterized for the first time (Fig. 3i, j and Table 3).[72,74]

Fundamental (photo)physical insights: from bulk to nano

EB, HB and HP display outstanding photophysical properties thanks to the shared presence of Cu^{2+} in their lattices.[93] These ions represent the only color center in the crystals and determine the common features of the spectra of EB, HB and HP. As described by Pozza *et al.*,[85] the square planar geometry of Cu^{2+} originates from lattice constraints and the Jahn–Teller effect. Within the frame of ligand-field theory, the silicates are thus characterized by three distinct absorption transitions: $^2B_{1g} \rightarrow {}^2A_{1g}$, $^2B_{1g} \rightarrow {}^2E_g$ and $^2B_{1g} \rightarrow {}^2B_{2g}$. These are parity-forbidden d–d transitions which are nevertheless (weakly) allowed thanks to coupling with unsymmetrical vibrational modes. The resulting absorption features cover a broad green-red region of the visible spectrum ($^2B_{1g} \rightarrow {}^2A_{1g}$, $^2B_{1g} \rightarrow {}^2E_g$, $\lambda \approx$ 450–800 nm) and extend till the beginning of the NIR window ($^2B_{1g} \rightarrow {}^2B_{2g}$, $\lambda \approx$ 800–850 nm).[49,61,91] The fluorescence, on the other side, is uniquely ascribed to the $^2B_{2g} \rightarrow {}^2B_{1g}$ transition and has been reported in the ranges of $\lambda \approx$ 920–960 nm. As a result of ligand-field changes induced by the larger size of Ba^{2+} ions (compared to Ca^{2+}), the emissions of HP and HB are slightly red-shifted (with HB stretching up to 1000 nm).[85,94–96]

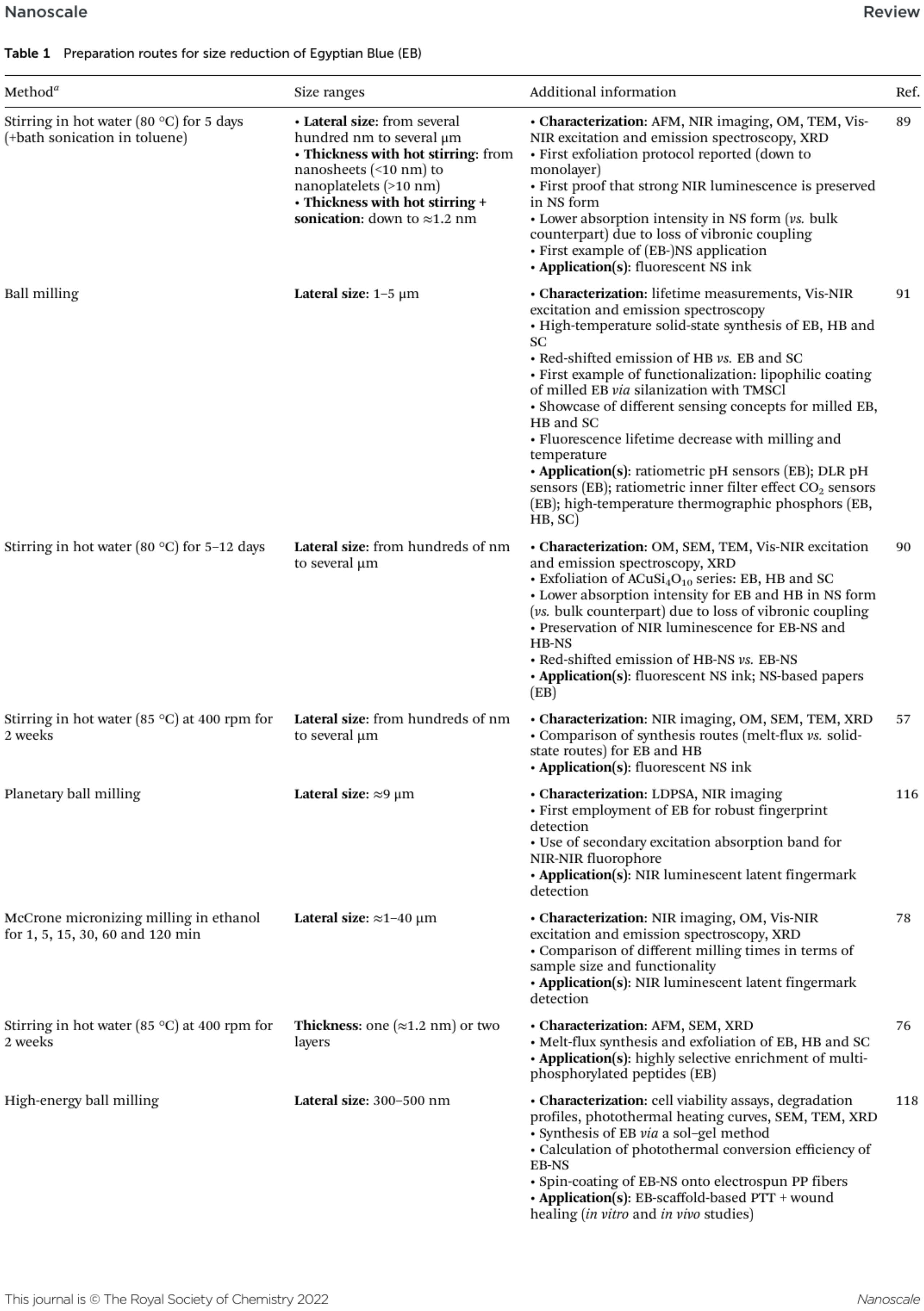

Table 1 Preparation routes for size reduction of Egyptian Blue (EB)

Method[a]	Size ranges	Additional information	Ref.
Stirring in hot water (80 °C) for 5 days (+bath sonication in toluene)	• **Lateral size**: from several hundred nm to several μm • **Thickness with hot stirring**: from nanosheets (<10 nm) to nanoplatelets (>10 nm) • **Thickness with hot stirring + sonication**: down to ≈1.2 nm	• **Characterization**: AFM, NIR imaging, OM, TEM, Vis-NIR excitation and emission spectroscopy, XRD • First exfoliation protocol reported (down to monolayer) • First proof that strong NIR luminescence is preserved in NS form • Lower absorption intensity in NS form (*vs.* bulk counterpart) due to loss of vibronic coupling • First example of (EB-)NS application • **Application(s)**: fluorescent NS ink	89
Ball milling	**Lateral size**: 1–5 μm	• **Characterization**: lifetime measurements, Vis-NIR excitation and emission spectroscopy • High-temperature solid-state synthesis of EB, HB and SC • Red-shifted emission of HB *vs.* EB and SC • First example of functionalization: lipophilic coating of milled EB *via* silanization with TMSCl • Showcase of different sensing concepts for milled EB, HB and SC • Fluorescence lifetime decrease with milling and temperature • **Application(s)**: ratiometric pH sensors (EB); DLR pH sensors (EB); ratiometric inner filter effect CO_2 sensors (EB); high-temperature thermographic phosphors (EB, HB, SC)	91
Stirring in hot water (80 °C) for 5–12 days	**Lateral size**: from hundreds of nm to several μm	• **Characterization**: OM, SEM, TEM, Vis-NIR excitation and emission spectroscopy, XRD • Exfoliation of $ACuSi_4O_{10}$ series: EB, HB and SC • Lower absorption intensity for EB and HB in NS form (*vs.* bulk counterpart) due to loss of vibronic coupling • Preservation of NIR luminescence for EB-NS and HB-NS • Red-shifted emission of HB-NS *vs.* EB-NS • **Application(s)**: fluorescent NS ink; NS-based papers (EB)	90
Stirring in hot water (85 °C) at 400 rpm for 2 weeks	**Lateral size**: from hundreds of nm to several μm	• **Characterization**: NIR imaging, OM, SEM, TEM, XRD • Comparison of synthesis routes (melt-flux *vs.* solid-state routes) for EB and HB • **Application(s)**: fluorescent NS ink	57
Planetary ball milling	**Lateral size**: ≈9 μm	• **Characterization**: LDPSA, NIR imaging • First employment of EB for robust fingerprint detection • Use of secondary excitation absorption band for NIR-NIR fluorophore • **Application(s)**: NIR luminescent latent fingermark detection	116
McCrone micronizing milling in ethanol for 1, 5, 15, 30, 60 and 120 min	**Lateral size**: ≈1–40 μm	• **Characterization**: NIR imaging, OM, Vis-NIR excitation and emission spectroscopy, XRD • Comparison of different milling times in terms of sample size and functionality • **Application(s)**: NIR luminescent latent fingermark detection	78
Stirring in hot water (85 °C) at 400 rpm for 2 weeks	**Thickness**: one (≈1.2 nm) or two layers	• **Characterization**: AFM, SEM, XRD • Melt-flux synthesis and exfoliation of EB, HB and SC • **Application(s)**: highly selective enrichment of multi-phosphorylated peptides (EB)	76
High-energy ball milling	**Lateral size**: 300–500 nm	• **Characterization**: cell viability assays, degradation profiles, photothermal heating curves, SEM, TEM, XRD • Synthesis of EB *via* a sol–gel method • Calculation of photothermal conversion efficiency of EB-NS • Spin-coating of EB-NS onto electrospun PP fibers • **Application(s)**: EB-scaffold-based PTT + wound healing (*in vitro* and *in vivo* studies)	118

Table 1 *(Contd.)*

Method[a]	Size ranges	Additional information	Ref.
• Stirring in hot water (85 °C) for 11 days • Stirring in hot water + CTAB (85 °C) for 11 days • Stirring in methanol + CTAB/PA/*n*-DA for 1 day • McCrone micronizing milling in ethanol	• **Lateral size**: <200 nm, but also unexfoliated particles (≈10 μm) • **Thickness**: <5 nm, but also unexfoliated particles	• **Characterization**: AFM, DLS, FTIR, NIR emission spectroscopy, NIR imaging, SEM • Lipophilic coating of EB with CTAB/PA/*n*-DA • **Application(s)**: NIR luminescent latent fingermark detection	92
Ball milling (as in ref. 91)	n.a.	• **Characterization**: lifetime measurements, Vis-NIR emission spectroscopy • Lipophilic coating of EB *via* silanization (as in ref. 91) • Incorporation of silanized EB into an emulsion system composed of aza-BODIPYs (indicators), hydrogel (dye incorporation), PDMS (host material) and ion barriers • **Application(s)**: DLR ammonia sensors	115
• Planetary ball milling in water at 900 rpm for 1 h + tip sonication in water/isopropanol at 60–72 W for 1–6 h • Tip sonication in isopropanol at 72 W for 6 h	• **Lateral size**: 20–300 nm • **Thickness**: 1–13 nm	• **Characterization**: AFM, cell viability assays, fluorescence saturation and polarization measurements, lifetime measurements, NIR imaging, reflectance spectroscopy, SEM, STEM, Vis-NIR excitation and emission spectroscopy, zeta potential • Exfoliation of EB, HB and HP • Evaluation of EB-NS' photostability towards exfoliation and several analytes • Video-rate fluorescence imaging of EB-NS with Si-based camera • Fluorescence imaging of resolution-limited EB-NS • Size-fluorescence correlation measurements of EB-NS down to few tenths of nm • **Application(s)**: *in vivo* microrheology of embryos of fruit flies (EB-NS); remote NIR fluorescence imaging in plants (EB-NS)	72
Planetary ball milling at 900 rpm for 2 h + tip sonication at 30 W for 2 h (both steps in water)	n.a.	• **Characterization**: NIR emission spectroscopy, NIR imaging • Design of sensing platforms for multiplexed detection of metabolites and virulence factors • Spectral encoding for differentiation of bacteria cell lines • **Application(s)**: ratiometric sensing of bacteria	73
Ultrasonication in NMP at 500 W for 12 h	• **Lateral size**: <100 nm • **Thickness**: ≈2–4 nm	• **Characterization**: AFM, cell viability assays, degradation profiles, photothermal heating curves, SEM, TEM, UV-Vis-NIR absorbance spectroscopy, XRD • Synthesis of EB *via* a sol–gel method • Calculation of photothermal conversion efficiency of EB-NS • Incorporation of EB-NS into shape memory polymer PT • **Application(s)**: biodegradable NIR-II-responsive shape-memory composite for wound healing (*in vitro* and *in vivo* studies)	119
Milling in ethanol for 30 min	**Lateral size**: ≈100 nm	• **Characterization**: FTIR, SEM, voltage profiles and cycling performances, XAS, XRD • Lithiation causes a conversion reaction of EB into amorphous mixed oxides with Cu nanoclusters • **Application(s)**: anode material for Li-ion batteries	75
Tip sonication in water for 96 h	• **Lateral size**: ≈800 nm • **Thickness**: >5 nm	• **Characterization**: AFM, cell viability assays, DLS, photothermal heating curves, Raman spectroscopy, SEM, TEM, Vis-NIR absorbance spectroscopy, XPS, XRD • Solid-state synthesis of EB • Incorporation of EB-NS into 3D-printed $CaCO_3$–PCL scaffold • **Application(s)**: EB-scaffold-based PTT + bone regeneration (*in vitro* and *in vivo* studies)	77

Table 1 *(Contd.)*

Method[a]	Size ranges	Additional information	Ref.
Planetary ball milling at 900 rpm for 1 h + tip sonication at 72 W for 6 h (both steps in water)	• **Lateral size**: ≈20–800 nm • **Thickness**: ≈1–350 nm	• **Characterization**: AFM, cell viability assays, LDPSA, lifetime measurements, NIR imaging, reflectance spectroscopy, SEM, STEM, Vis-NIR excitation and emission spectroscopy • Exfoliation of EB, HB and HP • Evaluation of photostability of NS *vs.* pH, ionic environments, buffer and prolonged excitation • Fluorescence imaging of resolution-limited EB-NS, HB-NS and HP-NS • Time and frequency-domain fluorescence lifetime spectroscopy • Microscopic and macroscopic lifetime-encoded imaging • **Application(s)**: remote NIR fluorescence imaging through tissue	74
• Horizontal bead milling at 3000 rpm for 4 h • Stirring in water at 400 rpm for 15 days • Three-roll milling in 2 auxiliary media	n.a. (derived coefficients of size, compactness, regularity and circuitry are employed)	• **Characterization**: NIR imaging, OM, QY, SEM, XRD • Synthesis of EB *via* dry calcination method • Investigation of relationship between dispersing methods and photoluminescence • **Application(s)**: luminescent solar concentrator	127
Ultrasonication in water at 1 kW for 5 h	• **Lateral size**: ≈200 nm • **Thickness**: ≈4–6 nm	• **Characterization**: AFM, cell viability assays, degradation profiles, photothermal heating curves, SEM, TEM, UV-Vis-NIR absorbance spectroscopy, XRD • Synthesis of EB *via* a sol–gel method • Calculation of photothermal conversion efficiency of EB-NS • Incorporation of EB-NS into shape memory polymer PT • **Application(s)**: biodegradable NIR-II-responsive shape-memory composite for endometrial regeneration (*in vitro* and *in vivo* studies)	120

Abbreviations: AFM = atomic force microscopy, aza-BODIPY = aza-boron-dipyrromethene, CTAB = cetrimonium bromide, DLR = dual-lifetime referencing, DLS = dynamic light scattering, EB = Egyptian Blue, EB-NS = Egyptian Blue nanosheet(s), FTIR = Fourier transform infrared spectroscopy, HB = Han Blue, HB-NS = Han Blue nanosheet(s), HP = Han Purple, HP-NS = Han Purple nanosheet(s), LDPSA = laser diffraction particles size analyzer, n.a. = not available, *n*-DA = *n*-dodecylamine, NIR = near-infrared, NIR-II = second near-infrared window for (bio)imaging, NMP = 1-methyl-2-pyrrolidone, NS = nanosheet(s), OM = optical microscopy, PA = palmitic acid, PCL = polycaprolactone, PDMS = polydimethylsiloxane, PP = poly(ε-caprolactone) + poly(ᴅ,ʟ-lactic acid), PT = poly(ᴅ,ʟ-lactide-*co*-trimethylene carbonate), PTT = photothermal therapy, QY = quantum yield, rpm = revolutions per minute, SC = strontium copper tetrasilicate, SEM = scanning electron microscopy, STEM = scanning transmission electron microscopy, TEM = transmission electron microscopy, TMSCl = trimethylsilyl chloride, UV = ultraviolet, Vis = visible, *vs.* = *versus*, XAS = X-ray absorption spectroscopy, XPS = X-ray photoelectron spectroscopy, XRD = X-ray diffractometry. [a] Centrifugation, filtration and/or decanting steps are not reported.

Furthermore, the parity-forbidden nature of the electronic transition of the copper ion leads to a remarkably long excited state lifetime (τ). Although different sample preparation routes are known to affect the value of τ, the decay time still lies in the µs range for EB, HB and HP alike, regardless of the synthetical procedure: more specifically, $\tau_{EB} \approx$ 100–150 µs, $\tau_{HB} \approx$ 60–100 µs, $\tau_{HP} \approx$ 6–30 µs.[74,85,95–97] Another outstanding feature of this class of silicates is represented by the quantum yield (QY). Accorsi *et al.* were the first to report a QY of bulk EB: ≈10.5%,[95] a value which is considerably high if compared to typical NIR fluorophores.[23] In a similar way, promising QYs for HB have also been measured ($QY_{HB} \approx$ 6.9% was reported for hydrothermally synthesized HB[67]), whereas the presence of the Cu–Cu bond in HP leads to a clear quantum efficiency decrease ($QY_{HP} \approx$ 0.9%, again synthesized through a hydrothermal approach[66]). By employing a novel technique based on temperature measurements in full sunlight instead of the traditional de Mello method,[98] Berdahl *et al.* measured even higher QYs for EB and (La and Li doped) HB, with values of EB exceeding 70%.[97] Additional theoretical studies have highlighted the potential benefits of material doping,[99,100] and provided further insights towards electronic and magnetic properties of bulk EB, HB and HP.[49,101] For example, the works by García-Fernández *et al.* have explained that, in order to fully understand the hue of EB and HB, the presence of a normally neglected internal electric field and the contribution of sand in the production process are of paramount importance.[102,103] Furthermore, a bright and broadband photon up-conversion of EB and HB has been demonstrated by Chen *et al.*, showing that emission in the Vis region is possible *via* pumping with a NIR laser diode.[63,104] Binet *et al.* have also very recently further investigated the origins of the NIR luminescence of EB and shown that it can be more efficiently excited in the UV range; this is possible given the existence of four UV-excited emissions that are most likely determined by the presence of trapped excitons of different origins.[105] HP, on the other side,

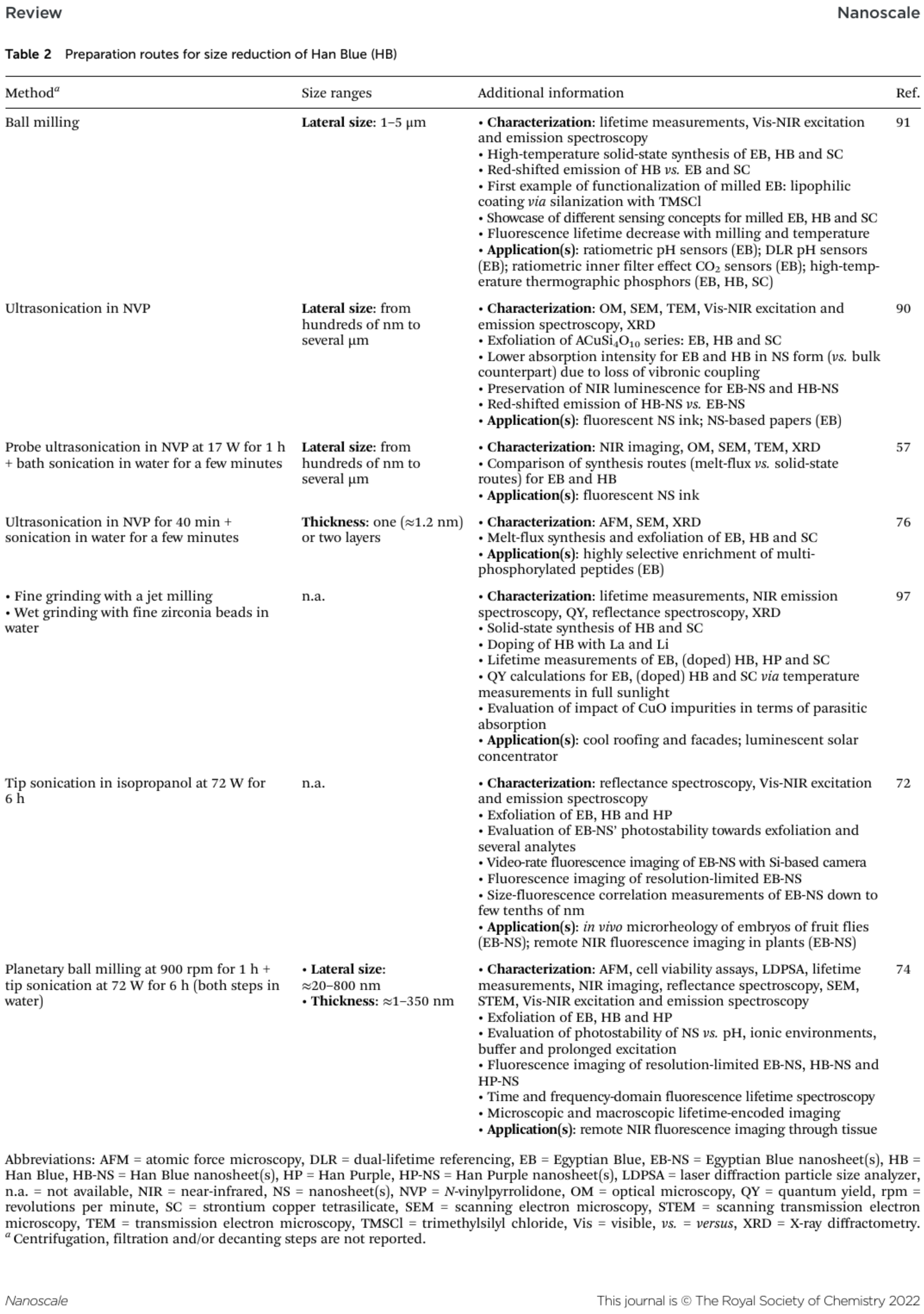

Table 2 Preparation routes for size reduction of Han Blue (HB)

Method[a]	Size ranges	Additional information	Ref.
Ball milling	**Lateral size:** 1–5 μm	• **Characterization:** lifetime measurements, Vis-NIR excitation and emission spectroscopy • High-temperature solid-state synthesis of EB, HB and SC • Red-shifted emission of HB *vs.* EB and SC • First example of functionalization of milled EB: lipophilic coating *via* silanization with TMSCl • Showcase of different sensing concepts for milled EB, HB and SC • Fluorescence lifetime decrease with milling and temperature • **Application(s)**: ratiometric pH sensors (EB); DLR pH sensors (EB); ratiometric inner filter effect CO_2 sensors (EB); high-temperature thermographic phosphors (EB, HB, SC)	91
Ultrasonication in NVP	**Lateral size**: from hundreds of nm to several μm	• **Characterization**: OM, SEM, TEM, Vis-NIR excitation and emission spectroscopy, XRD • Exfoliation of $ACuSi_4O_{10}$ series: EB, HB and SC • Lower absorption intensity for EB and HB in NS form (*vs.* bulk counterpart) due to loss of vibronic coupling • Preservation of NIR luminescence for EB-NS and HB-NS • Red-shifted emission of HB-NS *vs.* EB-NS • **Application(s)**: fluorescent NS ink; NS-based papers (EB)	90
Probe ultrasonication in NVP at 17 W for 1 h + bath sonication in water for a few minutes	**Lateral size**: from hundreds of nm to several μm	• **Characterization**: NIR imaging, OM, SEM, TEM, XRD • Comparison of synthesis routes (melt-flux *vs.* solid-state routes) for EB and HB • **Application(s)**: fluorescent NS ink	57
Ultrasonication in NVP for 40 min + sonication in water for a few minutes	**Thickness**: one (≈1.2 nm) or two layers	• **Characterization**: AFM, SEM, XRD • Melt-flux synthesis and exfoliation of EB, HB and SC • **Application(s)**: highly selective enrichment of multi-phosphorylated peptides (EB)	76
• Fine grinding with a jet milling • Wet grinding with fine zirconia beads in water	n.a.	• **Characterization**: lifetime measurements, NIR emission spectroscopy, QY, reflectance spectroscopy, XRD • Solid-state synthesis of HB and SC • Doping of HB with La and Li • Lifetime measurements of EB, (doped) HB, HP and SC • QY calculations for EB, (doped) HB and SC *via* temperature measurements in full sunlight • Evaluation of impact of CuO impurities in terms of parasitic absorption • **Application(s)**: cool roofing and facades; luminescent solar concentrator	97
Tip sonication in isopropanol at 72 W for 6 h	n.a.	• **Characterization**: reflectance spectroscopy, Vis-NIR excitation and emission spectroscopy • Exfoliation of EB, HB and HP • Evaluation of EB-NS' photostability towards exfoliation and several analytes • Video-rate fluorescence imaging of EB-NS with Si-based camera • Fluorescence imaging of resolution-limited EB-NS • Size-fluorescence correlation measurements of EB-NS down to few tenths of nm • **Application(s)**: *in vivo* microrheology of embryos of fruit flies (EB-NS); remote NIR fluorescence imaging in plants (EB-NS)	72
Planetary ball milling at 900 rpm for 1 h + tip sonication at 72 W for 6 h (both steps in water)	• **Lateral size:** ≈20–800 nm • **Thickness:** ≈1–350 nm	• **Characterization**: AFM, cell viability assays, LDPSA, lifetime measurements, NIR imaging, reflectance spectroscopy, SEM, STEM, Vis-NIR excitation and emission spectroscopy • Exfoliation of EB, HB and HP • Evaluation of photostability of NS *vs.* pH, ionic environments, buffer and prolonged excitation • Fluorescence imaging of resolution-limited EB-NS, HB-NS and HP-NS • Time and frequency-domain fluorescence lifetime spectroscopy • Microscopic and macroscopic lifetime-encoded imaging • **Application(s)**: remote NIR fluorescence imaging through tissue	74

Abbreviations: AFM = atomic force microscopy, DLR = dual-lifetime referencing, EB = Egyptian Blue, EB-NS = Egyptian Blue nanosheet(s), HB = Han Blue, HB-NS = Han Blue nanosheet(s), HP = Han Purple, HP-NS = Han Purple nanosheet(s), LDPSA = laser diffraction particle size analyzer, n.a. = not available, NIR = near-infrared, NS = nanosheet(s), NVP = *N*-vinylpyrrolidone, OM = optical microscopy, QY = quantum yield, rpm = revolutions per minute, SC = strontium copper tetrasilicate, SEM = scanning electron microscopy, STEM = scanning transmission electron microscopy, TEM = transmission electron microscopy, TMSCl = trimethylsilyl chloride, Vis = visible, *vs.* = *versus*, XRD = X-ray diffractometry.

[a] Centrifugation, filtration and/or decanting steps are not reported.

Table 3 Preparation routes for size reduction of Han Purple (HP)

Method[a]	Size ranges	Additional information	Ref.
Tip sonication in isopropanol at 72 W for 6 h	n.a.	• **Characterization**: reflectance spectroscopy, Vis-NIR excitation and emission spectroscopy • Exfoliation of EB, HB and HP • Evaluation of EB-NS' photostability towards exfoliation and several analytes • Video-rate fluorescence imaging of EB-NS with Si-based camera • Fluorescence imaging of resolution-limited EB-NS • Size-fluorescence correlation measurements of EB-NS down to few tenths of nm • **Application(s)**: *in vivo* microrheology of embryos of fruit flies (EB-NS); remote NIR fluorescence imaging in plants (EB-NS)	72
Planetary ball milling at 900 rpm for 1 h + tip sonication at 72 W for 6 h (both steps in water)	• **Lateral size**: ≈20–800 nm • **Thickness**: ≈1–350 nm	• **Characterization**: AFM, cell viability assays, LDPSA, lifetime measurements, NIR imaging, reflectance spectroscopy, SEM, STEM, Vis-NIR excitation and emission spectroscopy • Exfoliation of EB, HB and HP • Evaluation of photostability of NS *vs.* pH, ionic environments, buffer and prolonged excitation • Fluorescence imaging of resolution-limited EB-NS, HB-NS and HP-NS • Time and frequency-domain fluorescence lifetime spectroscopy • Microscopic and macroscopic lifetime-encoded imaging • **Application(s)**: remote NIR fluorescence imaging through tissue	74

Abbreviations: AFM = atomic force microscopy, EB = Egyptian Blue, EB-NS = Egyptian Blue nanosheet(s), HB = Han Blue, HB-NS = Han Blue nanosheet(s), HP = Han Purple, HP-NS = Han Purple nanosheet(s), LDPSA = laser diffraction particle size analyzer, n.a. = not available, NIR = near-infrared, NS = nanosheet(s), rpm = revolutions per minute, SEM = scanning electron microscopy, STEM = scanning transmission electron microscopy, Vis = visible, *vs.* = *versus*. [a] Centrifugation, filtration and/or decanting steps are not reported.

possesses unique spin gapped antiferromagnetic properties due to its characteristic Cu–Cu dimers.[66,106–110]

Properties as the ones discussed above already clearly highlight the potential of bulk EB, HB and HP. When it comes to down-sizing a material, most of the times the hope is that the promising bulk properties are either retained or even improved by becoming tunable, size-dependent features. With regards to the effect of down-scaling, it was hypothesized that EB could turn into a direct band-gap semiconductor and work as a mechano-sensor if its thickness were reduced down to the monolayer regime (≈1 nm).[87,96] However, only in the last years thorough insights on fundamental properties of EB-NS, HB-NS and HP-NS have been collected. The seminal studies of Johnson-McDaniel *et al.*[89] and Salguero *et al.*[90] first demonstrated that NIR fluorescence of EB and HB is preserved when the silicates are exfoliated down to µm-large NS of monolayer thickness. With the goal of understanding how the absorption/excitation and fluorescence features vary at the nanoscale, Selvaggio *et al.* carried out a thorough characterization of milled and tip-sonicated EB-NS, HB-NS and HP-NS.[72,74] By observing the 1D emission (Fig. 4a) and 2D excitation–emission spectra (Fig. 4b), it could be confirmed that the bulk features are retained in the NS samples. By means of NIR fluorescence microscopy, the bleaching behavior of these silicates could be compared to state-of-the-art fluorophores. EB-NS, HB-NS and HP-NS were extremely stable and could all be imaged for up to 2 h without any significant effect on the emitted fluorescence intensity (Fig. 4c). On the other side, the signal of a standard visible fluorophore rhodamine B decreased quickly. An important step forward in comprehending the photophysics of these nanomaterials was represented by NIR fluorescence microscopy of resolution-limited NS (Fig. 4d). A bright, fluorescent signal could indeed be detected for EB-NS, HB-NS and HP-NS also with sizes below Abbe's resolution limit (corresponding to <500 nm for the considered emission wavelengths). *Via* correlation studies based on dual SEM-NIR imaging and particle tracking, Selvaggio *et al.* furthermore showed that EB-NS down to just few tenths of nm still fluoresce. Next to the robustness of fluorescence intensity, the versatility of fluorescence lifetime[111] could be showcased, too. Time-correlated single photon counting measurements (TCSPC, Fig. 4e) yielded lifetime values τ which were on one side lower than the bulk counterparts, but on the other side still in the µs range. Frequency-domain lifetime imaging at both microscopic (Fig. 4f) and macroscopic (Fig. 4g) scales additionally underlined an important and promising aspect of EB-NS, HB-NS and HP-NS: the potential for lifetime engineering. Indeed, NS of different sizes led to subpopulations of different lifetime values within the lifetime-encoded images. Next to that, both at microscopic and macroscopic (remote) lifetime setups, it was possible to clearly distinguish the signals of EB-NS, HB-NS and HP-NS, which would otherwise be undistinguishable *via* standard imaging acquisitions based on fluorescence intensity. The above-mentioned results, together with the lack of fluorescence polarization of the NS, their facile remote detection and their biocompatible nature justify the employment of these exfoliated silicates in numerous technological fields, as described in the next section.[72,74]

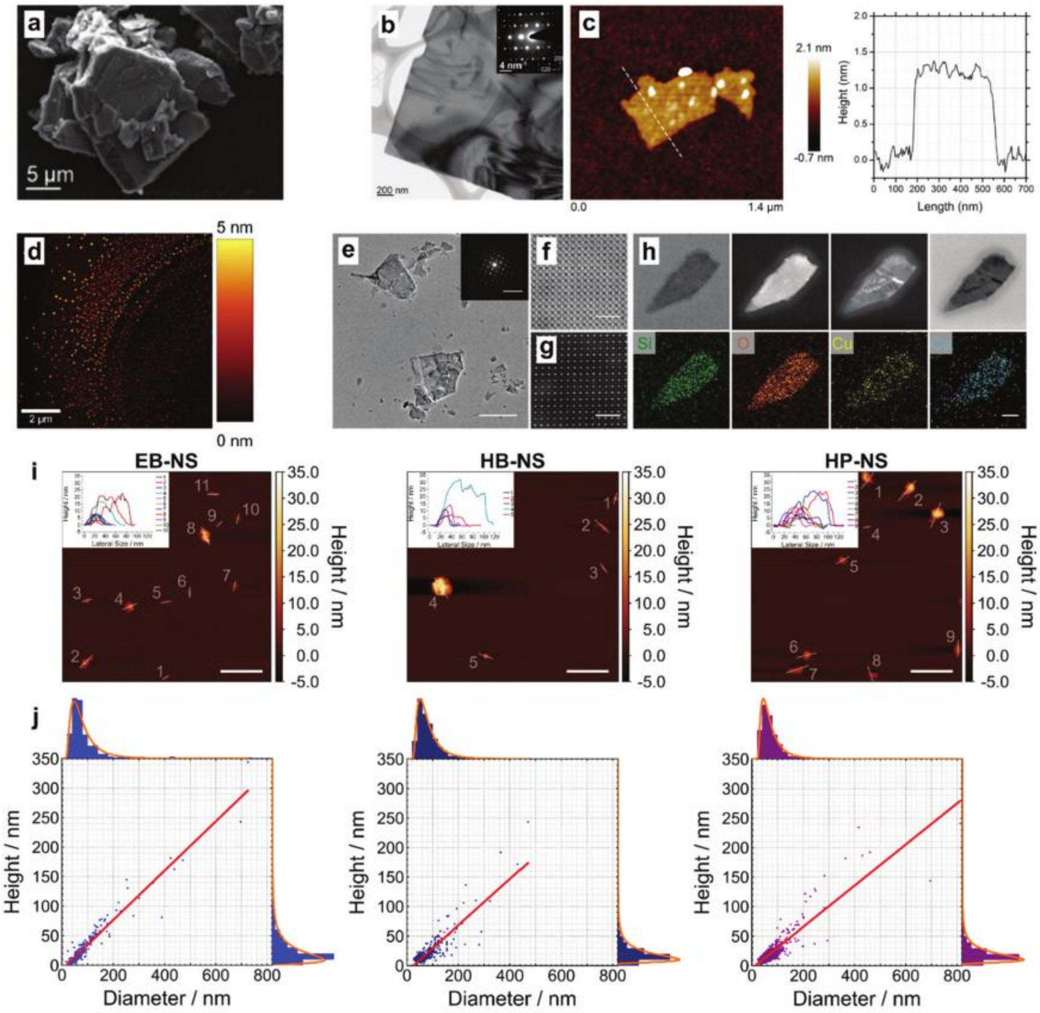

Fig. 3 Exfoliation into nanosheets (NS) and morphological characterization. (a) Scanning electron microscopy (SEM) performed on commercial (bulk) EB. Reproduced with permission from ref. 90. Copyright 2014 Springer Nature. (b) Transmission electron microscopy (TEM) image and selected area electron diffraction (SAED) pattern of EB-NS exfoliated *via* prolonged stirring in hot water followed by ultrasonication in toluene. Reproduced with permission from ref. 89. Copyright 2013 American Chemical Society. (c) Top and lateral view of a monolayer of EB-NS (exfoliated as in (b)) obtained *via* atomic force microscopy (AFM). Reproduced with permission from ref. 89. Copyright 2013 American Chemical Society. (d) Topographical AFM image showing high monodispersity of small EB-NS achieved after a modified version of the prolonged exfoliation in hot water. Reproduced with permission from ref. 92. Copyright 2020 Elsevier. (e) SEM image and SAED pattern of EB-NS, which were exfoliated *via* prolonged tip sonication in water. Scale bar = 1 μm and 10 nm^{-1}, respectively. Reproduced with permission from ref. 77. Copyright 2021 John Wiley and Sons. (f and g) Bright- and dark-field scanning transmission electron microscopy (STEM) pictures of EB-NS (exfoliated as in (e)). Scale bar = 2 nm. Reproduced with permission from ref. 77. Copyright 2021 John Wiley and Sons. (h) TEM (dark-field) and STEM (bright-field) photographs of a single EB-NS (exfoliated as in (e)) and the corresponding elemental mapping. Scale bar = 50 nm. Reproduced with permission from ref. 77. Copyright 2021 John Wiley and Sons. (i) Exemplary AFM measurements of EB-NS, HB-NS and HP-NS exfoliated *via* planetary ball milling and tip sonication in water. Scale bar = 200 nm. Reproduced with permission from ref. 74. Copyright 2021 Royal Society of Chemistry. (j) Size distribution of EB-NS, HB-NS and HP-NS from AFM measurements (exfoliation as in (i)) represented as scatter plots with linear fits and as histograms with log–normal fits. Reproduced with permission from ref. 74. Copyright 2021 Royal Society of Chemistry.

Applications in state-of-the-art technologies

EB, HB and HP are not merely pigments of historical interest, but also materials of high promise for numerous applications. The earliest and perhaps most straightforward example of exploitation of their photophysical properties has been their detection in ancient artifacts. Indeed, thanks to a broad excitation range, a strong NIR fluorescence and a long excited state lifetime, the signals of HB, HP and, above all, of the highly chemically stable EB can be easily discriminated in art-

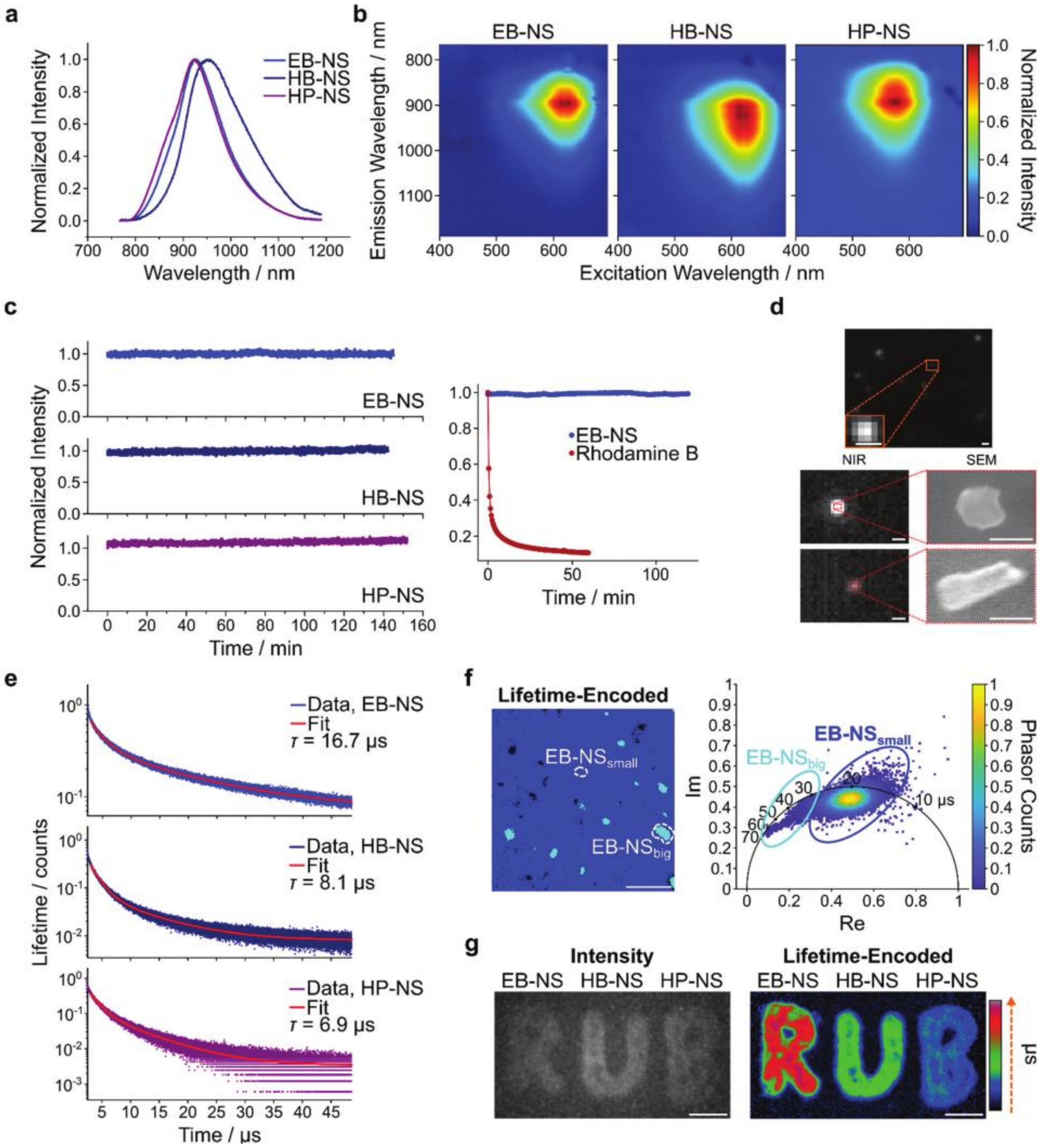

Fig. 4 Photophysical properties of exfoliated silicate nanosheets. (a) 1D fluorescence spectra of EB-NS, HB-NS and HP-NS with emission maxima between $\lambda \approx 920-950$ nm (λ_{exc} = 561 nm). (b) 2D excitation–emission spectra of EB-NS, HB-NS and HP-NS, showing maximal absorption at $\lambda \approx$ 630 nm, 620 nm and 680 nm respectively, as well as no significant alteration compared to the bulk fluorescent features. (c) Photobleaching experiments show that the fluorescence signals are stable over prolonged excitation (t > 2 h, output power ≈ 100–180 mW) in contrast to standard organic fluorophores (*e.g.* rhodamine B). (d) Near-infrared (NIR) fluorescence microscopy and NIR-SEM correlative imaging of resolution-limited EB-NS. Scale bar = 1 μm (NIR) and 200 nm (SEM). (e) Time correlated single photon counting (TCSPC) curves of nanosheets for lifetime measurements and the corresponding double-exponential fits. (f) Microscopic frequency-domain fluorescence lifetime imaging (FLIM) of EB-NS displaying size-dependence. Color-coding is given by the corresponding phasor plot. Scale bar = 5 μm. (g) Macroscopic FLIM of the logo of the Ruhr-University of Bochum (RUB) written with NS ink: while the signals of EB-, HB- and HP-NS appear undistinguishable according to the intensity channel, the lifetime clearly enables NS identification. Scale bar = 5 mm. Reproduced with permission from ref. 72. Copyright 2020 Springer Nature. Reproduced with permission from ref. 74. Copyright 2021 Royal Society of Chemistry.

works from other pigments.[50–53,95,112–114] However, exciting speculations about the employment of bulk EB, HB and HP in diverse technological fields have been made, including telecommunications, lasers, sensing/labelling for bioimaging, component of cool roofing and facades, luminescent solar concentrators and more.[50,55,58,59,66,69,91,95,97]

With regards to the down-sized EB, HB and HP, several applications for photonics have been theorized and demonstrated (Tables 1–3). For example, Borisov *et al.* have showcased applications of ball-milled EB, HB and a strontium homologue ($SrCuSi_4O_{10}$, SC) as optical chemosensors.[91] Indeed, milled and silanized EB could be successfully employed in pH sensors with a ratiometric design: aza-BODIPYs were used as indicators due to their pH-sensitive luminescence, whereas the bright and stable NIR fluorescence of EB was used as reference (Fig. 5a(i)). The bright long-lived luminescence of EB enables a further sensing technique: dual lifetime referencing (DLR). Based on this concept, a fiber-optic DLR-pH sensor with an aza-BODIPY and EB respectively as indicator and reference material was fabricated (Fig. 5a(ii)). Their long excited state lifetime, as well as their characteristic high (photo)chemical stability and their inertness to oxygen, define EB and other copper silicate phosphors as optimal DLR references. Furthermore, Borisov *et al.* demonstrated that μm-sized EB can be incorporated into ratiometric inner filter effect CO_2 sensors (Fig. 5a(iii)). In this case, EB appeared as an ideal reference due to the broad excitation spectrum, which mostly overlaps with the one of *m*-cresol purple, *i.e.* the indicator (Fig. 5a(iv)). According to this sensing scheme, considering that *m*-cresol's absorption is responsive to different pressures of CO_2, the fluorescence intensity of EB results accordingly modulated. Finally, Borisov *et al.* showed a temperature dependence of the luminescence decay time of EB, HB and SC. Due to moderate dependence at ambient T and improved sensitivity at high T (*i.e.* $T \approx 100–400$ °C), these materials allow intrinsic T compensation of the sensing materials and present excellent suitability as high-temperature thermographic phosphors (Fig. 5a (v)). Inspired by the approach of Borisov *et al.*, Maierhofer *et al.*[115] have afterwards published another example of DLR sensor based on ball-milled and silanized EB. In this case, the silicate was embedded into an emulsion system for which three different aza-BODIPYs were tested as indicator materials to detect ammonia. Thanks to a fluorescence quenching mechanism based on the deprotonation of the hydroxy group of the dyes, gaseous NH_3 could be detected throughout a broad range of concentrations (Fig. 5b). Milling has also been used by Tyler *et al.*[75] to yield EB-NS of lateral size ≈ 100 nm for energy storage applications. More specifically, it has been shown that EB-NS can be employed as anode material for Li-ion batteries displaying decent values of reversible capacity, high coulombic efficiencies and an increase in capacity with cycling time (Fig. 5c). Most interestingly, X-ray diffractometry (XRD), Fourier transform infrared spectroscopy (FTIR) and X-ray absorption spectroscopy (XAS) have confirmed that lithiation leads to a conversion reaction of EB-NS into amorphous mixed oxides with copper nanoclusters.

Perhaps the most versatile type of NS photonics application has been presented by Johnson-McDaniel *et al.*[57,89] and Salguero *et al.*[90] with the preparation of smart inks. *Via* prolonged hot stirring and ultrasonication, high aspect ratio EB-NS and HB-NS could be produced and their colloidal dispersions could be employed as NS ink. As proof-of-principle experiments and to highlight the applicability of solution-processable NS, square patterns were printed (Fig. 5d(i and ii)) and free-standing NS samples were prepared (Fig. 5d(iii)). Despite the exfoliation, inks of EB-NS and HB-NS were still strongly fluorescent in the NIR, thus suggesting that these materials could be employed for *e.g.* NIR-based biomedical imaging, IR light-emitting devices such as telecommunication platforms, and security ink formulations.

Another technological sector where EB-NS' outstanding properties led to a high interest of the scientific community is latent fingermark detection. For this task, it is crucial to employ powders which yield the maximum contrast in relation to the surface they are applied onto. Considered the inhomogeneity of most imaged samples (Fig. 5e(i)), fingerprint dusting powders which additionally display luminescence can further facilitate this task. Most of the commercially available materials, however, fluoresce in the visible with excitation in the UV range. Due to the strong background interference given by the frequent presence of *e.g.* inks, binders and coatings on the investigated backgrounds (*e.g.* banknotes), the signal-to-noise ratio is typically limited. As King *et al.*[116] pointed out, the benefit of employing a powder whose fluorescence lies in the NIR region would be substantial. A further improvement would be represented by excitation at NIR wavelengths. As described in the previous sections, EB-NS can be excited both in the visible and in the NIR regions ($\lambda_{max,NIR} \approx 780$ nm). The high chemical–physical stability and its robustness to exfoliation make EB-NS excellent candidates for latent fingermark detection (Fig. 5e(ii–v)). Similarly to King *et al.*,[116] Errington *et al.*[78] tested EB-NS on different surfaces and compared the results to state-of-the-art dusting powders. Additionally, the effect of different milling conditions was tested. Significant progress in terms of sensitivity, selectivity and adhesion was achieved by Shahbazi *et al.*[92] In their work it was found that a lipophilic coating of EB-NS with cetrimonium bromide (CTAB, Table 4) can endow the exfoliated silicates with a higher attraction towards oily components and moisture common to fingermark secretions. In conclusion, lipophilic coatings and exfoliation routes appear very promising for this application.[117]

Especially in the last 5 years, several works have been published by numerous research groups regarding applications of EB-NS, HB-NS and HP-NS for biomedical purposes. As already mentioned in the introductory section, there is a high scientific interest in developing new NIR-emitting dyes and nanomaterials for biological imaging due to the achievable higher tissue penetration and contrast, as well as due to the current scarcity of available NIR fluorophores. In 2020 and 2021, Selvaggio *et al.*[72,74] demonstrated that EB-NS, HB-NS and HP-NS can be robustly employed as NIR fluorophores for biophotonics. Next to characterization measurements focused on

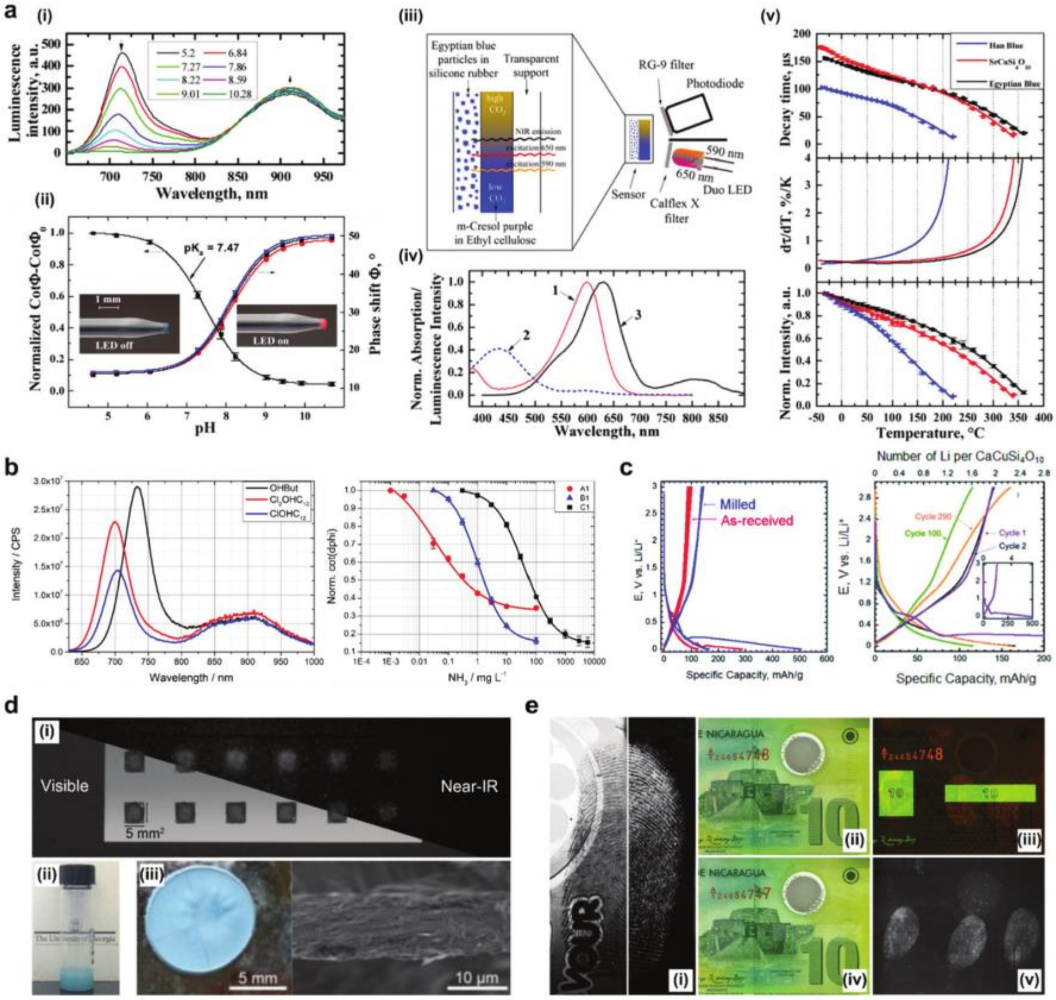

Fig. 5 Photonics and energy storage applications. (a) Effect of pH dependence on ratiometric (i) and dual lifetime referenced (DLR, ii) pH sensors consisting in aza-BODIPY as indicator and silanized, micrometer-sized EB as reference (in a hydrogel matrix). EB has also been employed for ratiometric inner filter effect CO_2 sensors (iii), where the good overlap of absorption features of EB and deprotonated *m*-cresol purple (MCP) was exploited (iv). 1 = Deprotonated MCP (low pCO_2), 2 = protonated MCP (high pCO_2), 3 = EB. Furthermore, the temperature dependence of luminescence intensity and decay time of EB, HB and the strontium homologue ($SrCuSi_4O_{10}$) highlight potential as T sensors (v). Reproduced with permission from ref. 91. Copyright 2013 American Chemical Society. (b) Fluorescence spectra and calibration curves of exemplary optical DLR ammonia sensors composed by three protonated aza-BODIPY dyes and silanized and milled EB (same exfoliation and functionalization protocol as in (a)). Reproduced with permission from ref. 115. Copyright 2020 Springer Nature. (c) Galvanostatic cycling of unprocessed and milled EB displaying improved lithiation and delithiation capacities after milling. The decrease in capacity observed in the first cycles is likely due to a conversion reaction leading to amorphization of EB. Reproduced with permission from ref. 75. Copyright 2021 Royal Society of Chemistry. (d) Visible (Vis) and near-infrared (NIR) picture of square patterns (i) printed with fluorescent EB-NS ink (ii). Macro-sized samples such as free-standing paper of EB-NS (iii) could be fabricated *via* solution-processing techniques (top and lateral view are shown). Reproduced with permission from ref. 89. Copyright 2013 American Chemical Society. Reproduced with permission from ref. 90. Copyright 2014 Springer Nature. (e) Latent fingermark detection carried out with a commercially available fingerprint dusting powder (bichromatic, (i), left panel) and micronized EB ((i), right panel) on a Fanta® can. Additionally, comparison between Vis-NIR (Redwop, (ii and iii)) and NIR–NIR (planetary ball milled EB, (iv and v)) fluorescent latent fingermark detection on polymer banknotes further underlines the benefit of NIR. Reproduced with permission from ref. 78 and 116. Copyright 2016 Elsevier.

the exfoliation protocols, proof-of-principle applications were reported to show how the bright and photostable NIR emission of the NS enables fluorescence microscopy and remote imaging of biological samples. Although the NIR-II wavelength region ($\lambda \approx 1000$–1700 nm) is typically more desirable for higher tissue penetration, the NIR-I window ($\lambda \approx 750$–1000 nm), within which the emission of EB-NS, HB-NS and HP-NS is located, allows strong fluorescent signals to be detected also by non-specialized and cheaper equipment (*e.g.* visible Si-based cameras rather than the expensive InGaAs ones). Indeed, a Si-based camera was employed to image EB-NS after injection into fruit fly embryos (*Drosophila melano-*

gaster, Fig. 6a(i)). Thanks to the lack of bleaching displayed by the NS and the absence of sample autofluorescence, long-term imaging with frame rates of 10 Hz could be performed. In this way, *in vivo* particle tracking revealed active processes within the developing embryos (Fig. 6a(ii)). EB-NS could also be easily detected in a simple and non-optimized home-made remote detection setup. Indeed, the emission brightness of EB-NS after infiltration into plant leaves was intense enough to withstand leaf autofluorescence and reach the detector from a distance > 10 cm (Fig. 6b). Furthermore, remote EB-NS signals observed at this setup were much stronger than other state-of-the-art NIR fluorophores, including single-walled carbon nanotubes (SWCNTs) and indocyanine green (ICG). By means of tissue phantom experiments performed with a NIR (InGaAs) camera, it was additionally proven that the fluorescence of EB-NS, HB-NS and HP-NS could be detected through several layers of meat, thus underlining their potential for deep tissue imaging (Fig. 6c).

While the bright and photostable NS fluorescence presents clear advantages for labeling of biological systems, it also presents several benefits as reference signal for ratiometric sensing of biomolecules. This concept was recently demonstrated for the case of remote detection of bacterial strains by Nißler *et al.*,[73] who developed NIR fluorescent nanosensor arrays composed of SWCNTs and EB-NS. According to this sensor design, different SWCNTs were chemically modified so to detect released metabolites and virulence factors, whereas the EB-NS worked as reference signal. The nanomaterials were embedded into hydrogel disks, which were then exposed to isolates of six clinically relevant bacteria (Fig. 6d(i)). By following the fluorescence modulation over time, these multiplexed nanosensors yielded spatially and spectrally encoded patterns of the analyzed pathogens (Fig. 6d(ii)). With the implementation of principal component analysis (PCA), a fingerprint and identification of different bacterial strains could be achieved (Fig. 6d(iii)). The successful remote detection of such sensors paves the way towards the creation of smart implants and sensing technologies, which could allow faster *in situ* diagnostics of infections.

Biomedical applications of NS are definitely not limited to exploiting their bright NIR fluorescence. Yang *et al.*[76] showed in 2018 that high aspect ratio EB-NS of just a few layers of thickness are highly selective towards multi-phosphopeptides. In several pH and buffer conditions, EB-NS managed to selectively bind to the tetra-phosphorylated peptides β3m and β4m without enriching the mono-phosphopeptides β1s and β2s (Fig. 7a). The same effect was not observed when testing HB-NS and the Sr homologue SC-NS. This could indicate that the high specific surface area of EB-NS with numerous Ca^{2+} ions is responsible for its higher selectivity. Direct measurements of phosphopeptides *via* mass spectrometry (MS) are normally affected by low sensitivity and ionization efficiency. Mono-phosphorylated peptides are preferentially ionized, thus dominating in the measured spectrum. Even if several strategies have been developed for separation of mono- and multi-phosphopeptides, only few of the materials designed so far have proven to efficiently distinguish them. For these reasons, the highly selective EB-NS can be defined as very promising substrates for the study of protein phosphorylation.

Several studies have shown that EB-NS absorb NIR irradiation (as a result of the d–d electronic transitions) and convert it into heat. The high photothermal conversion

Table 4 Functionalization strategies

Material	Method[a]	Additional information	Ref.
EB	Lipophilic coating *via* silanization: • Ball milling • Stirring in anhydrous THF + TMSCl for 30 min	• **Characterization**: lifetime measurements, Vis-NIR excitation and emission spectroscopy • High-temperature solid-state synthesis of EB, HB and SC • Red-shifted emission of HB *vs.* EB and SC • Showcase of different sensing concepts for milled EB, HB and SC • Fluorescence lifetime decrease with milling and temperature • **Application(s)**: ratiometric pH sensors (EB); DLR pH sensors (EB); ratiometric inner filter effect CO_2 sensors (EB); high-temperature thermographic phosphors (EB, HB, SC)	91
EB	Lipophilic coating (protocol #1): • Stirring in hot water + CTAB (85 °C) for 11 days Lipophilic coating (protocol #2): • Stirring in methanol + CTAB/PA/*n*-DA for 1 day	• **Characterization**: AFM, DLS, FTIR, NIR emission spectroscopy, NIR imaging, SEM • **Application(s)**: NIR luminescent latent fingermark detection	92
EB	Lipophilic coating *via* silanization (as in ref. 91)	• **Characterization**: lifetime measurements, Vis-NIR emission spectroscopy • Incorporation of silanized EB into an emulsion system composed of aza-BODIPYs (indicators), hydrogel (dye incorporation), PDMS (host material) and ion barriers • **Application(s)**: DLR ammonia sensors	115

Abbreviations: AFM = atomic force microscopy, aza-BODIPY = aza-boron-dipyrromethene, CTAB = cetrimonium bromide, DLR = dual-lifetime referencing, DLS = dynamic light scattering, EB = Egyptian Blue, FTIR = Fourier transform infrared spectroscopy, HB = Han Blue, *n*-DA = *n*-dodecylamine, NIR = near-infrared, PA = palmitic acid, PDMS = polydimethylsiloxane, SC = strontium copper tetrasilicate, SEM = scanning electron microscopy, THF = tetrahydrofuran, TMSCl = trimethylsilyl chloride, Vis = visible, *vs.* = *versus*. [a] Centrifugation, filtration and/or decanting steps are not reported.

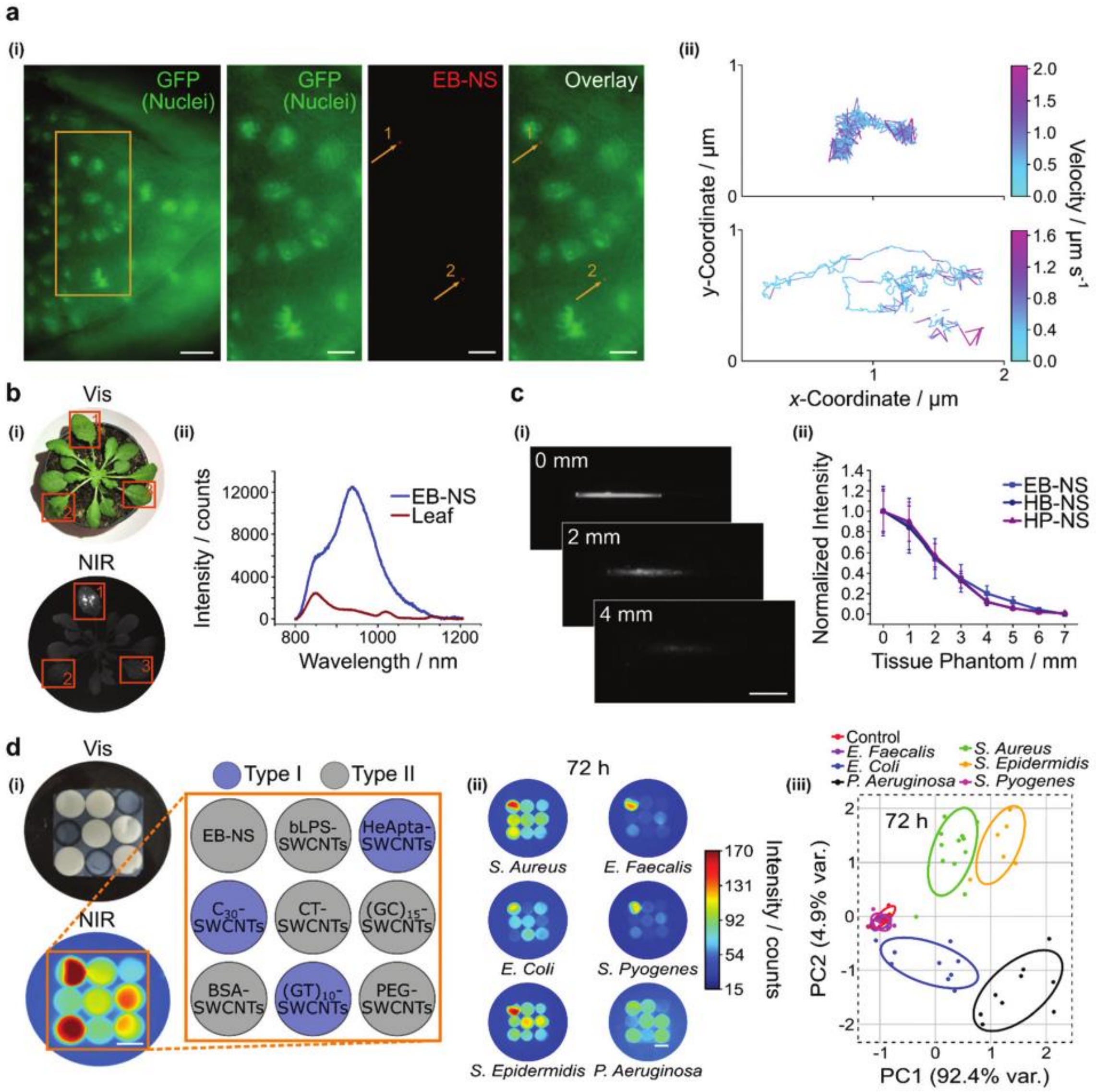

Fig. 6 Nanosheet-assisted imaging for biomedical applications. (a) Two EB-NS imaged inside a fruit fly embryo (*Drosophila melanogaster*, (i)) expressing Histone2Av-GFP that allows visible (Vis) labeling of the nuclei. The orange rectangle shows the magnified area. The GFP (Vis) and the EB-NS (NIR) channels are colored in green and red, respectively. Exemplary color-coded trajectories of the instantaneous velocity of two tracked EB-NS (ii) are shown, too. Scale bar = 10 µm (overview) and 5 µm (other channels). Reproduced with permission from ref. 72. Copyright 2020 Springer Nature. (b) Remote NIR fluorescence imaging of EB-NS (frame 1) infused into an Arabidopsis plant (i). As a comparison, single-walled carbon nanotubes (SWCNTs, frame 2) and buffer (frame 3) were infused as well. NIR fluorescence spectroscopy performed on an infused leaf (ii) shows that the signal of EB-NS stands out compared to leaf autofluorescence. Reproduced with permission from ref. 72. Copyright 2020 Springer Nature. (c) Remote NIR fluorescence imaging of several layers of tissue phantom beneath which (EB-)NS-filled capillary tubes were laid (i). Corresponding plots of normalized mean gray value of NS signal *vs.* tissue phantom thickness (ii) describe signal penetration. Scale bar = 10 mm. Error bar = standard deviation, normalized over the maximum value of mean pixel intensity within a ROI from one image. Reproduced with permission from ref. 74. Copyright 2021 Royal Society of Chemistry. (d) Vis and NIR pictures of a hydrogel (HG) array in which EB-NS serves as reference signal and modified SWCNTs serve as sensors (i). An exemplary image showing fluorescence response fingerprint of six pathogens after 72 h (ii) is presented. *Via* principal component analysis (PCA, iii), discrimination of bacterial strains with remote NIR imaging of such sensing platforms could be robustly achieved, as outlined by the representative 72 h plot. Scale bar = 0.5 cm. Reproduced with permission from ref. 73. Copyright 2020 Springer Nature.

efficiency of EB-NS (which has been calculated to be in the range of ≈34–42%[118–120]) and their robust photostability suggest that EB-NS have high potential as agent for photothermal therapy (PTT). Furthermore, release of bioactive Cu^{2+} and SiO_4^{4-} ions from EB-NS promotes angiogenesis and re-epithelization. In this way, EB-NS can carry out a crucial task also in

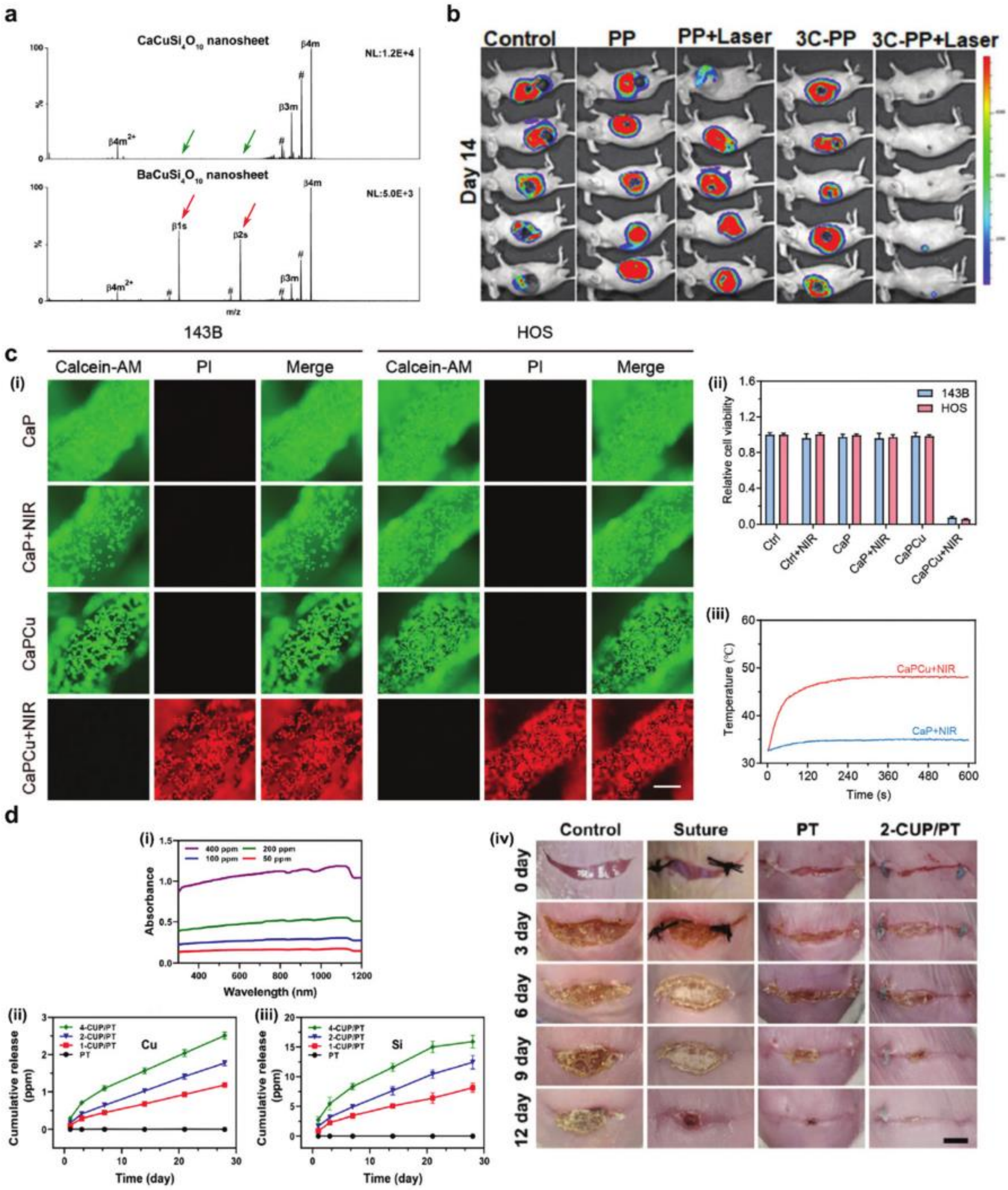

Fig. 7 Biomaterial applications of nanosheet-based markers. (a) EB-NS bind selectively multiphosphopeptides *e.g.* in contrast to HB-NS, which is useful for mass spectrometry (MS). Adapted with permission from ref. 76. Copyright 2018 John Wiley and Sons. (b) Fluorescence images of melanoma-bearing mice proving the efficiency of photothermal therapy (PTT) with irradiated EB-NS scaffold (3C-PP + laser). Reproduced with permission from ref. 118. Copyright 2019 Elsevier. (c) Confocal fluorescence with live-dead staining (i) and viability assays (ii) of osteosarcoma (OS) cells undergoing PTT with EB-NS-decorated 3D-printing scaffolds (CaPCu + NIR). Local temperature increase (iii) also enables tumor size reduction in mice. Scale bar = 200 μm. Reproduced with permission from ref. 77. Copyright 2021 John Wiley and Sons. For (b and c): Control/Ctrl = no scaffold nor laser; PP, PP + laser/CaP = scaffolds without EB-NS; 3C-PP/CaPCu = EB-NS scaffold without irradiation. (d) Absorbance spectrum (i) of aqueous dispersions of EB-NS (CUP/PT). The broad absorption features and the Cu^{2+} (ii) and SiO_4^{4-} (iii) release curves of EB-NS embedded in a shape-memory polymer (SMP) support the self-knotting and angiogenesis stimulation properties of the resulting biocomposite (PT = SMP without EB-NS). Treatment of skin wounds with commercial suture, PT and the CUP/PT composite confirms the better performance of the latter (iv). Scale bar = 0.5 cm. Reproduced with permission from ref. 119. Copyright 2021 Elsevier.

terms of cancer surgery-induced and chronic wound healing. Within this frame, Yu *et al.*[118] have recently reported a multifunctional biocomposite made of electrospun fibers on whose surface EB-NS were spin-coated. *In vitro* and *in vivo* experiments on tumor-bearing mice showed that such platforms could simultaneously allow cell proliferation (due to their biocompatible nature) and effectively kill skin tumor cells, in this way aiding tissue reconstruction (Fig. 7b). Similarly promising results have been obtained by He *et al.*,[77] who embedded EB-NS into a 3D-printed scaffold (CaPCu) and observed successful PTT and tissue regeneration in osteosarcoma (OS) cell lines (Fig. 7c). By means of mRNA transcriptome analysis, He *et al.* also observed a regulatory effect of CaPCu on genes relevant for cell death, proliferation and bone development. Some other works have almost exclusively focused on the beneficial properties of ion release from EB. Although Zhang *et al.*[121] did not explicitly describe an exfoliation protocol, they reported the preparation of a novel fibrous EB-containing membrane in combination with the flavonoid quercetin for hair regeneration in burned skin. Going further in the direction of wound healing, other studies have implemented advanced materials science concepts for the design of the novel multifunctional composites. The papers from Yang *et al.*[119] and Dong *et al.*[120] describe two works that share similar traits: in both cases, a biocomposite (CUP/PT) based on EB-NS (CUP) and a shape-memory polymer (poly(D,L-lactide-*co*-trimethylene carbonate), PT) was prepared. The ability of EB-NS to convert NIR-II light into heat was exploited to trigger the shape-memory behavior of PT. As previously mentioned, the use of NIR-II light ($\lambda \approx$ 1000–1700 nm) in place of NIR-I wavelengths ($\lambda \approx$ 750–1000 nm) is beneficial because it allows higher tissue penetration. In this way, under low power irradiation, Yang *et al.*[119] reported an outstanding self-knotting ability of CUP/PT, which was exploited for the design of sutures. The simultaneous sustained release of EB-NS ions (Cu^{2+} and $SiO_4{}^{4-}$) could furthermore lead to *in vitro* and *in vivo* stimulation of angiogenesis, thus enabling a “smart” wound healing approach (Fig. 7d). Tubular CUP/PT composites were similarly employed *in vitro* and *in vivo* by Dong *et al.*[120] as intelligent antiadhesion barrier for intrauterine adhesions with the capacity of simultaneously stimulating endometrial regeneration.

Conclusions

Egyptian Blue (EB), Han Blue (HB) and Han Purple (HP) are materials that have an ancient history and have been used by famous past civilizations. Next to the cultural heritage in world-known artworks, these silicates have recently gained a new life thanks to their outstanding chemical and photophysical properties. This interest has been moving from the bulk material to the nanoscale counterparts. Indeed, the layered crystal structures of EB, HB and HP allow exfoliation down to 2D nanomaterials, *i.e.* nanosheets (NS), which retain the most relevant features while benefiting from their reduced size and high aspect ratio. Several works have outlined exfoliation routes which yield NS structures down to monolayer thicknesses, however most of them do not describe the obtained size distribution, are time-consuming and/or report NS diameters of several microns. These issues can constitute limiting factors for certain applications and should thus be addressed in future works. For instance, if NS sizes are not small enough (nm range), the employment in biological systems could be hindered in terms of uptake and biocompatibility. Long exfoliation protocols might instead represent an obstacle for scalability of the prepared samples, thus resulting less appealing for industrial applications. Focus on more sophisticated and at the same time more efficient methods of exfoliation (*e.g.* surfactant-mediated sonication) might enable a stronger control over the obtained NS sizes, and therefore allow further tailoring of layer thickness. In this way, it could be experimentally investigated whether the fluorescence of NS monolayers can be affected by the chemical environment around the more exposed copper ions and/or by applied strain, as foreseen by past theoretical studies. Although some fundamental photophysical insights have been gained in the last years, there are still many open questions and, thus, several directions of research worth following next. For instance, it is clear that the synthesis has a strong impact on fundamental photophysical properties (*e.g.* quantum yield), therefore its full comprehension and control could lead to immediate benefits in numerous applications. To this end, also size-fluorescence correlation studies and robust quantum yield measurements of well-defined samples are of paramount importance to assess the full potential of novel NIR fluorophores. Furthermore, tailoring of material doping and employment of novel/alternative excitation (*e.g.* UV) and detection (*e.g.* fluorescence lifetime) methods could respectively allow to tune the photophysics and further extend the applicability of these materials, as already indicated by recently published works. In terms of material doping, the incorporation of defect states could perhaps lead to novel properties similar to quantum defects in SWCNTs.[122–124] Moreover, tailoring of surface chemistry is a crucial step to improve water solubility and allow targeting of molecules of interest, as required for *e.g.* drug delivery and image-guided surgery. Although first examples of functionalization have been reported in literature, this topic is currently still mostly unexplored and therefore demands attention (Table 4).[125,126] Nevertheless, numerous publications have already clearly highlighted the extreme versatility and high promise of EB-NS, HB-NS and HP-NS for multiple and diverse technological fields, including smart inking, energy storage, biological imaging and sensing, photothermal cancer therapy, tissue engineering and more. It is therefore our strong belief that many exciting chapters featuring these novel nanomaterials are soon to be written.

Conflicts of interest

There are no conflicts to declare.

Acknowledgements

This work was funded by the Deutsche Forschungsgemeinschaft (DFG, German Research Foundation) under Germany's Excellence Strategy—EXC 2033-390677874—RESOLV. This work was further supported by the "Center for Solvation Science ZEMOS" funded by the German Federal Ministry of Education and Research BMBF and by the Ministry of Culture and Research of Nord Rhine-Westphalia. We also would like to acknowledge support from the VW Foundation.

References

1 A. K. Geim and K. S. Novoselov, The rise of graphene, *Nat. Mater.*, 2007, **6**, 183–191, DOI: **10.1038/nmat1849**.

2 A. K. Geim, Graphene: Status and Prospects, *Science*, 2009, **324**, 1530–1534, DOI: **10.1126/science.1158877**.

3 K. S. Novoselov, D. Jiang, F. Schedin, T. J. Booth, V. V. Khotkevich, S. V. Morozov and A. K. Geim, Two-dimensional atomic crystals, *Proc. Natl. Acad. Sci. U. S. A.*, 2005, **102**, 10451–10453, DOI: **10.1073/pnas.0502848102**.

4 K. S. Novoselov, A. K. Geim, S. V. Morozov, D. Jiang, Y. Zhang, S. V. Dubonos, I. V. Grigorieva and A. A. Firsov, Electric Field Effect in Atomically Thin Carbon Films, *Science*, 2004, **306**, 666–669, DOI: **10.1126/science.1102896**.

5 M. Chhowalla, H. S. Shin, G. Eda, L. J. Li, K. P. Loh and H. Zhang, The chemistry of two-dimensional layered transition metal dichalcogenide nanosheets, *Nat. Chem.*, 2013, **5**, 263–275, DOI: **10.1038/nchem.1589**.

6 A. Kumar and C. Huei, Synthesis and Biomedical Applications of Graphene: Present and Future Trends, in *Advances in Graphene Science*, InTech, 2013. DOI: **10.5772/55728**.

7 G. R. Bhimanapati, Z. Lin, V. Meunier, Y. Jung, J. Cha, S. Das, D. Xiao, Y. Son, M. S. Strano, V. R. Cooper, L. Liang, S. G. Louie, E. Ringe, W. Zhou, S. S. Kim, R. R. Naik, B. G. Sumpter, H. Terrones, F. Xia, Y. Wang, J. Zhu, D. Akinwande, N. Alem, J. A. Schuller, R. E. Schaak, M. Terrones and J. A. Robinson, Recent Advances in Two-Dimensional Materials beyond Graphene, *ACS Nano*, 2015, **9**, 11509–11539, DOI: **10.1021/acsnano.5b05556**.

8 V. Nicolosi, M. Chhowalla, M. G. Kanatzidis, M. S. Strano and J. N. Coleman, Liquid exfoliation of layered materials, *Science*, 2013, **340**, 72–75, DOI: **10.1126/science.1226419**.

9 Q. H. Wang, K. Kalantar-Zadeh, A. Kis, J. N. Coleman and M. S. Strano, Electronics and optoelectronics of two-dimensional transition metal dichalcogenides, *Nat. Nanotechnol.*, 2012, **7**, 699–712, DOI: **10.1038/nnano.2012.193**.

10 H. Tao, Y. Zhang, Y. Gao, Z. Sun, C. Yan and J. Texter, Scalable exfoliation and dispersion of two-dimensional materials-an update, *Phys. Chem. Chem. Phys.*, 2017, **19**, 921–960, DOI: **10.1039/c6cp06813h**.

11 J. N. Coleman, M. Lotya, A. O'Neill, S. D. Bergin, P. J. King, U. Khan, K. Young, A. Gaucher, S. De, R. J. Smith, I. V. Shvets, S. K. Arora, G. Stanton, H. Y. Kim, K. Lee, G. T. Kim, G. S. Duesberg, T. Hallam, J. J. Boland, J. J. Wang, J. F. Donegan, J. C. Grunlan, G. Moriarty, A. Shmeliov, R. J. Nicholls, J. M. Perkins, E. M. Grieveson, K. Theuwissen, D. W. McComb, P. D. Nellist and V. Nicolosi, Two-dimensional nanosheets produced by liquid exfoliation of layered materials, *Science*, 2011, **331**, 568–571, DOI: **10.1126/science.1194975**.

12 D. V. Talapin, J. S. Lee, M. V. Kovalenko and E. V. Shevchenko, Prospects of colloidal nanocrystals for electronic and optoelectronic applications, *Chem. Rev.*, 2010, **110**, 389–458, DOI: **10.1021/cr900137k**.

13 M. M. R. Moayed, T. Bielewicz, M. S. Zöllner, C. Herrmann and C. Klinke, Towards colloidal spintronics through Rashba spin-orbit interaction in lead sulphide nanosheets, *Nat. Commun.*, 2017, **8**, 2–8, DOI: **10.1038/ncomms15721**.

14 S. Dogan, T. Bielewicz, Y. Cai and C. Klinke, Field–effect transistors made of individual colloidal PbS nanosheets, *Appl. Phys. Lett.*, 2012, **101**, 073102, DOI: **10.1063/1.4745786**.

15 S. Dogan, T. Bielewicz, V. Lebedeva and C. Klinke, Photovoltaic effect in individual asymmetrically contacted lead sulfide nanosheets, *Nanoscale*, 2015, **7**, 4875–4883, DOI: **10.1039/c4nr06957a**.

16 D. Chimene, D. L. Alge and A. K. Gaharwar, Two-Dimensional Nanomaterials for Biomedical Applications: Emerging Trends and Future Prospects, *Adv. Mater.*, 2015, **27**, 7261–7284, DOI: **10.1002/adma.201502422**.

17 T. Hu, X. Mei, Y. Wang, X. Weng, R. Liang and M. Wei, Two-dimensional nanomaterials: fascinating materials in biomedical field, *Sci. Bull.*, 2019, **64**, 1707–1727, DOI: **10.1016/j.scib.2019.09.021**.

18 M. Derakhshi, S. Daemi, P. Shahini, A. Habibzadeh, E. Mostafavi and A. A. Ashkarran, Two-Dimensional Nanomaterials beyond Graphene for Biomedical Applications, *J. Funct. Biomater.*, 2022, **13**, 27, DOI: **10.3390/jfb13010027**.

19 M. Nasilowski, B. Mahler, E. Lhuillier, S. Ithurria and B. Dubertret, Two-Dimensional Colloidal Nanocrystals, *Chem. Rev.*, 2016, **116**, 10934–10982, DOI: **10.1021/acs.chemrev.6b00164**.

20 M. Stöter, S. Rosenfeldt and J. Breu, Tunable Exfoliation of Synthetic Clays, *Annu. Rev. Mater. Res.*, 2015, **45**, 129–151, DOI: **10.1146/annurev-matsci-070214-020830**.

21 A. M. Smith, M. C. Mancini and S. Nie, Second window for in vivo imaging, *Nat. Nanotechnol.*, 2009, **4**, 710–711, DOI: **10.1038/nnano.2009.326**.

22 E. A. Owens, M. Henary, G. El Fakhri and H. S. Choi, Tissue-Specific Near-Infrared Fluorescence Imaging, *Acc. Chem. Res.*, 2016, **49**, 1731–1740, DOI: **10.1021/acs.accounts.6b00239**.

23 G. Hong, A. L. Antaris and H. Dai, Near-infrared fluorophores for biomedical imaging, *Nat. Biomed. Eng.*, 2017, **1**, 1–9, DOI: **10.1038/s41551-016-0010**.

24 A. Spreinat, G. Selvaggio, L. Erpenbeck and S. Kruss, Multispectral near infrared absorption imaging for histology of skin cancer, *J. Biophotonics*, 2020, **13**, e201960080, DOI: **10.1002/JBIO.201960080**.

25 A. Mishra, R. K. Behera, P. K. Behera, B. K. Mishra and G. B. Behera, Cyanines during the 1990s: a review, *Chem. Rev.*, 2000, **100**, 1973–2011, DOI: **10.1021/cr990402t**.

26 L. Feng, W. Chen, X. Ma, S. H. Liu and J. Yin, Near-infrared heptamethine cyanines (Cy7): From structure, property to application, *Org. Biomol. Chem.*, 2020, **18**, 9385–9397, DOI: **10.1039/d0ob01962c**.

27 J. A. Carr, D. Franke, J. R. Caram, C. F. Perkinson, M. Saif, V. Askoxylakis, M. Datta, D. Fukumura, R. K. Jain, M. G. Bawendi and O. T. Bruns, Shortwave infrared fluorescence imaging with the clinically approved near-infrared dye indocyanine green, *Proc. Natl. Acad. Sci. U. S. A.*, 2018, **115**, 4465–4470, DOI: **10.1073/pnas.1718917115**.

28 A. Loudet and K. Burgess, BODIPY dyes and their derivatives: Syntheses and spectroscopic properties, *Chem. Rev.*, 2007, **107**, 4891–4932, DOI: **10.1021/cr078381n**.

29 G. Ulrich, R. Ziessel and A. Harriman, The chemistry of fluorescent bodipy dyes: Versatility unsurpassed, *Angew. Chem., Int. Ed.*, 2008, **47**, 1184–1201, DOI: **10.1002/anie.200702070**.

30 A. Patra, L. J. Patalag, P. G. Jones and D. B. Werz, Extended Benzene-Fused Oligo-BODIPYs: In Three Steps to a Series of Large, Arc-Shaped, Near-Infrared Dyes, *Angew. Chem., Int. Ed.*, 2021, **60**, 747–752, DOI: **10.1002/anie.202012335**.

31 G. Selvaggio, R. Nißler, P. Nietmann, A. Patra, L. J. Patalag, A. Janshoff, D. B. Werz and S. Kruss, NIR-emitting benzene-fused oligo-BODIPYs for bioimaging, *Analyst*, 2022, **147**, 230–237, DOI: **10.1039/D1AN01850G**.

32 J. Ackermann, J. T. Metternich, S. Herbertz and S. Kruss, Biosensing with Fluorescent Carbon Nanotubes, *Angew. Chem., Int. Ed.*, 2022, **61**, e202112372, DOI: **10.1002/anie.202112372**.

33 S. Kruss, A. J. Hilmer, J. Zhang, N. F. Reuel, B. Mu and M. S. Strano, Carbon nanotubes as optical biomedical sensors, *Adv. Drug Delivery Rev.*, 2013, **65**, 1933–1950, DOI: **10.1016/j.addr.2013.07.015**.

34 D. Meyer, A. Hagemann and S. Kruss, Kinetic Requirements for Spatiotemporal Chemical Imaging with Fluorescent Nanosensors, *ACS Nano*, 2017, **11**, 4017–4027, DOI: **10.1021/acsnano.7b00569**.

35 N. E. Kallmyer, M. S. Abdennadher, S. Agarwal, R. Baldwin-Kordick, R. L. Khor, A. S. Kooistra, E. Peterson, M. D. McDaniel and N. F. Reuel, Inexpensive Near-Infrared Fluorimeters: Enabling Translation of nIR-Based Assays to the Field, *Anal. Chem.*, 2021, **93**, 4800–4808, DOI: **10.1021/acs.analchem.0c03732**.

36 G. Bisker, J. Dong, H. D. Park, N. M. Iverson, J. Ahn, J. T. Nelson, M. P. Landry, S. Kruss and M. S. Strano, Protein-targeted corona phase molecular recognition, *Nat. Commun.*, 2016, **7**, 1–14, DOI: **10.1038/ncomms10241**.

37 J. P. Giraldo, H. Wu, G. M. Newkirk and S. Kruss, Nanobiotechnology approaches for engineering smart plant sensors, *Nat. Nanotechnol.*, 2019, **14**, 541–553, DOI: **10.1038/s41565-019-0470-6**.

38 M. Kim, C. Chen, P. Wang, J. J. Mulvey, Y. Yang, C. Wun, M. Antman-Passig, H.-B. Luo, S. Cho, K. Long-Roche, L. V. Ramanathan, A. Jagota, M. Zheng, Y. Wang and D. A. Heller, Detection of ovarian cancer via the spectral fingerprinting of quantum-defect-modified carbon nanotubes in serum by machine learning, *Nat. Biomed. Eng.*, 2022, **6**, 267–275, DOI: **10.1038/s41551-022-00860-y**.

39 A. Antonucci, J. Kupis-Rozmysłowicz and A. A. Boghossian, Noncovalent Protein and Peptide Functionalization of Single-Walled Carbon Nanotubes for Biodelivery and Optical Sensing Applications, *ACS Appl. Mater. Interfaces*, 2017, **9**, 11321–11331, DOI: **10.1021/acsami.7b00810**.

40 R. Nißler, F. A. Mann, P. Chaturvedi, J. Horlebein, D. Meyer, L. Vukovic, S. Kruss, L. Vuković and S. Kruss, Quantification of the Number of Adsorbed DNA Molecules on Single-Walled Carbon Nanotubes, *J. Phys. Chem. C*, 2019, **123**, 4837–4847, DOI: **10.1021/acs.jpcc.8b11058**.

41 A. Spreinat, M. M. Dohmen, J. Lüttgens, N. Herrmann, L. F. Klepzig, R. Nißler, S. Weber, F. A. Mann, J. Lauth and S. Kruss, Quantum Defects in Fluorescent Carbon Nanotubes for Sensing and Mechanistic Studies, *J. Phys. Chem. C*, 2021, **125**, 18341–18351, DOI: **10.1021/ACS.JPCC.1C05432**.

42 F. A. Mann, N. Herrmann, F. Opazo and S. Kruss, Quantum Defects as a Toolbox for the Covalent Functionalization of Carbon Nanotubes with Peptides and Proteins, *Angew. Chem., Int. Ed.*, 2020, **59**, 17732–17738, DOI: **10.1002/anie.202003825**.

43 M. Dinarvand, E. Neubert, D. Meyer, G. Selvaggio, F. A. Mann, L. Erpenbeck and S. Kruss, Near-Infrared Imaging of Serotonin Release from Cells with Fluorescent Nanosensors, *Nano Lett.*, 2019, **19**, 6604–6611, DOI: **10.1021/acs.nanolett.9b02865**.

44 G. Hong, S. Diao, A. L. Antaris and H. Dai, Carbon Nanomaterials for Biological Imaging and Nanomedicinal Therapy, *Chem. Rev.*, 2015, **115**, 10816–10906, DOI: **10.1021/acs.chemrev.5b00008**.

45 O. T. Bruns, T. S. Bischof, D. K. Harris, D. Franke, Y. Shi, L. Riedemann, A. Bartelt, F. B. Jaworski, J. A. Carr, C. J. Rowlands, M. W. B. Wilson, O. Chen, H. Wei, G. W. Hwang, D. M. Montana, I. Coropceanu, O. B. Achorn, J. Kloepper, J. Heeren, P. T. C. So, D. Fukumura, K. F. Jensen, R. K. Jain and M. G. Bawendi, Next-generation in vivo optical imaging with short-wave infrared quantum dots, *Nat. Biomed. Eng.*, 2017, **1**, 0056, DOI: **10.1038/s41551-017-0056**.

46 S. He, J. Song, J. Qu and Z. Cheng, Crucial breakthrough of second near-infrared biological window fluorophores: design and synthesis toward multimodal imaging and theranostics, *Chem. Soc. Rev.*, 2018, **47**, 4258–4278, DOI: **10.1039/C8CS00234G**.

47 Z. Lei and F. Zhang, Molecular Engineering of NIR-II Fluorophores for Improved Biomedical Detection, *Angew. Chem., Int. Ed.*, 2021, **60**, 16294–16308, DOI: **10.1002/anie.202007040**.

48 Y. Fan, P. Wang, Y. Lu, R. Wang, L. Zhou, X. Zheng, X. Li, J. A. Piper and F. Zhang, Lifetime-engineered NIR-II nanoparticles unlock multiplexed in vivo imaging, *Nat. Nanotechnol.*, 2018, **13**, 941–946, DOI: **10.1038/s41565-018-0221-0**.

49 T. E. Warner, *Synthesis, Properties and Mineralogy of Important Inorganic Materials*, John Wiley & Sons, Ltd, 2011, DOI: **10.1002/9780470976012**.

50 A. Sgamellotti and C. Anselmi, An evergreen blue. Spectroscopic properties of Egyptian blue from pyramids to Raphael, and beyond, *Inorg. Chim. Acta*, 2022, **530**, 120699, DOI: **10.1016/j.ica.2021.120699**.

51 A. Masic and M. Nicola, NIR Luminescence and Composition of Egyptian Blue as Markers in Archaeometric Evaluations, *Microsc. Microanal.*, 2021, **27**, 3004–3006, DOI: **10.1017/s1431927621010448**.

52 M. Nicola, L. M. Seymour, M. Aceto, E. Priola, R. Gobetto and A. Masic, Late production of Egyptian blue: synthesis from brass and its characteristics, *Archaeol. Anthropol. Sci.*, 2019, **11**, 5377–5392, DOI: **10.1007/s12520-019-00873-w**.

53 L. M. Seymour, M. Nicola, M. Kessler, C. Yost, A. Bazzacco, A. Marello, E. Ferraris, R. Gobetto and A. Masic, On the production of ancient Egyptian blue: multi-modal characterization and micron-scale luminescence mapping, *PLoS One*, 2020, 1–13, DOI: **10.1371/journal.pone.0242549**.

54 S. S. Patel, Purple reign – How ancient Chinese chemists added color to the Emperor's army, *Archaeology*, 2007, **60**, 25–27.

55 H. Berke, The invention of blue and purple pigments in ancient times, *Chem. Soc. Rev.*, 2007, **36**, 15–30, DOI: **10.1039/b606268g**.

56 H.-G. Wiedemann and H. Berke, Chemical and Physical Investigations of Egyptian and Chinese Blue and Purple, *Monum. Sites*, 2015, **3**, 154–171, DOI: **10.11588/monstites.2001.0.22351**.

57 D. Johnson-McDaniel and T. T. Salguero, Exfoliation of Egyptian Blue and Han Blue, Two Alkali Earth Copper Silicate-based Pigments, *J. Visualized Exp.*, 2014, 1–10.

58 X. Q. Song, W. Lei, F. Wang, T. Chen, S. W. Ta, Z. X. Fu and W. Z. Lu, Phase evolution, crystal structure, and microwave dielectric properties of gillespite-type ceramics, *J. Am. Ceram. Soc.*, 2021, **104**, 1740–1749, DOI: **10.1111/jace.17564**.

59 G. Muungani, V. Moodley and W. E. van Zyl, Solid-state synthesis of the phyllosilicate Effenbergerite ($BaCuSi_4O_{10}$) for electrochemical sensing of ciprofloxacin antibiotic in pharmaceutical drug formulation, *J. Appl. Electrochem.*, 2022, **52**, 285–297, DOI: **10.1007/s10800-021-01633-2**.

60 A. Kiss, H. A. Stretz, A. Ueda and R. Mu, Synthesis of Egyptian Blue and mechanisms, *J. Phys. Chem. Solids*, 2022, 110738, DOI: **10.1016/j.jpcs.2022.110738**.

61 E. Kendrick, C. J. Kirk and S. E. Dann, Structure and colour properties in the Egyptian Blue Family, $M_{1-x}M'_xCuSi_4O_{10}$, as a function of M, M′ where M, M′ = Ca, Sr and Ba, *Dyes Pigm.*, 2007, **73**, 13–18, DOI: **10.1016/j.dyepig.2005.10.006**.

62 S. K. Barbar, K. R. Patel and S. Kumar, Structural, optical and magnetic properties of $MCuSi_4O_{10}$ (M = Ba and Sr) blue pigments, *J. Mater. Sci.: Mater. Electron.*, 2017, **28**, 3716–3724, DOI: **10.1007/s10854-016-5978-z**.

63 R. Gao, A. Shi, Z. Cao, X. Chu, A. Wang, X. Lu, C. Yao and X. Li, Construction of 2D up-conversion calcium copper silicate nanosheet for efficient photocatalytic nitrogen fixation under full spectrum, *J. Alloys Compd.*, 2022, **910**, 164869, DOI: **10.1016/j.jallcom.2022.164869**.

64 G. A. Mazzocchin, D. Rudello, C. Bragato and F. Agnoli, A short note on Egyptian blue, *J. Cult. Herit.*, 2004, **5**, 129–133, DOI: **10.1016/j.culher.2003.06.004**.

65 D. Johnson-McDaniel, S. Comer, J. W. Kolis and T. T. Salguero, Hydrothermal Formation of Calcium Copper Tetrasilicate, *Chem. – Eur. J.*, 2015, **21**, 17560–17564, DOI: **10.1002/chem.201503364**.

66 Y. Chen, Y. Zhang and S. Feng, Hydrothermal synthesis and properties of pigments Chinese purple $BaCuSi_2O_6$ and dark blue $BaCu_2Si_2O_7$, *Dyes Pigm.*, 2014, **105**, 167–173, DOI: **10.1016/j.dyepig.2014.01.017**.

67 Y. Chen, M. Shang, X. Wu and S. Feng, Hydrothermal synthesis, hierarchical structures and properties of blue pigments $SrCuSi_4O_{10}$ and $BaCuSi_4O_{10}$, *CrystEngComm*, 2014, **16**, 5418–5423, DOI: **10.1039/c3ce42394h**.

68 D. A. Corona-Martínez, J. C. Rendón-Angeles, L. A. Gonzalez, Z. Matamoros-Veloza, K. Yanagisawa, A. Tamayo and J. R. Alonso, Controllable synthesis of $BaCuSi_2O_6$ fine particles via a one-pot hydrothermal reaction with enhanced violet colour hue, *Adv. Powder Technol.*, 2019, **30**, 1473–1483, DOI: **10.1016/j.apt.2019.04.023**.

69 T. Tian, C. Wu and J. Chang, Preparation and in vitro osteogenic, angiogenic and antibacterial properties of cuprorivaite ($CaCuSi_4O_{10}$, Cup) bioceramics, *RSC Adv.*, 2016, **6**, 45840–45849, DOI: **10.1039/C6RA08145B**.

70 A. Panagopoulou, K. Karanasios and G. Xanthopoulou, Ancient Egyptian Blue ($CaCuSi_4O_{10}$) Pigment by Modern Solution Combustion Synthesis Method, *Eurasian Chem. – Technol. J.*, 2016, **18**, 31, DOI: **10.18321/ectj390**.

71 P. Loch, T. Martin, M. Grüner, G. Kaupp, W. Schwieger and J. Breu, Synthesis of Large Platelets of Egyptian Blue via Pseudomorphosis after NaRUB-18, *Z. Anorg. Allg. Chem.*, 2020, **646**, 1570–1574, DOI: **10.1002/zaac.202000203**.

72 G. Selvaggio, A. Chizhik, R. Nißler, L. Kuhlemann, D. Meyer, L. Vuong, H. Preiß, N. Herrmann, F. A. Mann, Z. Lv, T. A. Oswald, A. Spreinat, L. Erpenbeck, J. Großhans, V. Karius, A. Janshoff, J. Pablo Giraldo and S. Kruss, Exfoliated near infrared fluorescent silicate nanosheets for (bio)photonics, *Nat. Commun.*, 2020, **11**, 1495, DOI: **10.1038/s41467-020-15299-5**.

73 R. Nißler, O. Bader, M. Dohmen, S. G. Walter, C. Noll, G. Selvaggio, U. Groß and S. Kruss, Remote near infrared identification of pathogens with multiplexed nanosensors, *Nat. Commun.*, 2020, **11**, 5995, DOI: 10.1038/s41467-020-19718-5.

74 G. Selvaggio, M. Weitzel, N. Oleksiievets, T. A. Oswald, R. Nißler, I. Mey, V. Karius, J. Enderlein, R. Tsukanov and S. Kruss, Photophysical properties and fluorescence lifetime imaging of exfoliated near-infrared fluorescent silicate nanosheets, *Nanoscale Adv.*, 2021, **3**, 4541–4553, DOI: 10.1039/d1na00238d.

75 J. L. Tyler, R. L. Sacci, J. Ning, D. R. Mullins, K. Liang, J. Nanda, J. Sun and M. Naguib, Egyptian blue: from pigment to battery electrodes, *RSC Adv.*, 2021, **11**, 19885–19889, DOI: 10.1039/d1ra00956g.

76 S. S. Yang, H. X. Yu, Z. Z. Wang, H. L. Liu, H. Zhang, X. Yu, W. Shang, G. Q. Chen and Z. Y. Gu, An Exfoliated 2D Egyptian Blue Nanosheet for Highly Selective Enrichment of Multi-Phosphorylated Peptides in Mass Spectrometric Analysis, *Chem. – Eur. J.*, 2018, **24**, 2024, DOI: 10.1002/chem.201705595.

77 C. He, C. Dong, L. Yu, Y. Chen and Y. Hao, Ultrathin 2D Inorganic Ancient Pigment Decorated 3D-Printing Scaffold Enables Photonic Hyperthermia of Osteosarcoma in NIR-II Biowindow and Concurrently Augments Bone Regeneration, *Adv. Sci.*, 2021, **8**, 1–10, DOI: 10.1002/advs.202101739.

78 B. Errington, G. Lawson, S. W. Lewis and G. D. Smith, Micronised Egyptian blue pigment: A novel near-infrared luminescent fingerprint dusting powder, *Dyes Pigm.*, 2016, **132**, 310–315, DOI: 10.1016/j.dyepig.2016.05.008.

79 P. Pikart, Picture of the Nefertiti bust in Neues Museum, Berlin, Picture of the Nefertiti bust in Neues Museum, Berlin, https://en.wikipedia.org/wiki/File:Nofretete_Neues_Museum.jpg#filelinks, accessed 8 April 2022.

80 K. McGill, Terracotta Army, nr. Xi'an, Terracotta Army, nr. Xi'an, https://commons.wikimedia.org/wiki/File:Terracotta_Army_(6143564816).jpg, accessed 8 April 2022.

81 A. Pabst, Structures of some tetragonal sheet silicates, *Acta Crystallogr.*, 1959, **12**, 733–739, DOI: 10.1107/s0365110x5900216x.

82 B. C. Chakoumakos, J. A. Fernandez-Baca and L. A. Boatner, Refinement of the Structures of the Layer Silicates $MCuSi_4O_{10}$ (M = Ca, Sr, Ba) by Rietveld Analysis of Neutron Powder Diffraction Data, *J. Solid State Chem.*, 1993, **103**, 105–113.

83 G. Giester and B. Rieck, Effenbergerite, $BaCu[Si_4O_{10}]$, a new mineral from the Kalahari Manganese Field, South Africa: description and crystal structure, *Mineral. Mag.*, 1994, **58**, 663–670, DOI: 10.1180/minmag.1994.058.393.17.

84 L. W. Finger, R. M. Hazen and R. J. Hemley, $BaCuSi_2O_6$: a new cyclosilicate with four-membered tetrahedral rings, *Am. Mineral.*, 1989, **74**, 952–955.

85 G. Pozza, D. Ajò, G. Chiari, F. De Zuane and M. Favaro, Photoluminescence of the inorganic pigments Egyptian blue, Han blue and Han purple, *J. Cult. Herit.*, 2000, **1**, 393–398, DOI: 10.1016/S1296-2074(00)01095-5.

86 K. M. Sparta and G. Roth, Reinvestigation of the structure of $BaCuSi_2O_6$ – Evidence for a phase transition at high temperature, *Acta Crystallogr., Sect. B: Struct. Sci.*, 2004, **60**, 491–495, DOI: 10.1107/S0108768104011644.

87 Y. Chen, M. Kan, Q. Sun and P. Jena, Structure and Properties of Egyptian Blue Monolayer Family: $XCuSi_4O_{10}$ (X = Ca, Sr, and Ba), *J. Phys. Chem. Lett.*, 2016, **7**, 399–405, DOI: 10.1021/acs.jpclett.5b02770.

88 B. Rieck, H. Pristacz and G. Giester, Colinowensite, $BaCuSi_2O_6$, a new mineral from the Kalahari Manganese Field, South Africa and new data on wesselsite, $SrCuSi_4O_{10}$, *Mineral. Mag.*, 2015, **79**, 1769–1778, DOI: 10.1180/minmag.2015.079.7.04.

89 D. Johnson-Mcdaniel, C. A. Barrett, A. Sharafi and T. T. Salguero, Nanoscience of an Ancient Pigment, *J. Am. Chem. Soc.*, 2013, **135**, 1677–1679, DOI: 10.1021/ja310587c.

90 T. T. Salguero, D. Johnson-McDaniel, C. A. Barrett, A. Sharafi, R. Weimar and T. Blevins, Nanoscience of Metal Silicate-Based Pigments, *MRS Proc.*, 2014, **1618**, 161–166, DOI: 10.1557/opl.2014.465.

91 S. M. Borisov, C. Würth, U. Resch-Genger and I. Klimant, New Life of Ancient Pigments: Application in High-Performance Optical Sensing Materials, *Anal. Chem.*, 2013, **85**, 9371–9377, DOI: 10.1021/ac402275g.

92 S. Shahbazi, J. V. Goodpaster, G. D. Smith, T. Becker and S. W. Lewis, Preparation, characterization, and application of a lipophilic coated exfoliated Egyptian blue for near-infrared luminescent latent fingermark detection, *Forensic Chem.*, 2020, **18**, 100208, DOI: 10.1016/j.forc.2019.100208.

93 X. Feng, L. Lin, R. Duan, J. Qiu and S. Zhou, Transition metal ion activated near-infrared luminescent materials, *Prog. Mater. Sci.*, 2022, 100973, DOI: 10.1016/j.pmatsci.2022.100973.

94 D. Ajò, G. Chiari, F. De Zuane, M. Favaro and M. Bertolin, Photoluminescence of some blue natural pigments and related synthetic materials, 5th Int. Conf. non-destructive testing, Microanal. methods Environ. Eval. study Conserv. Work. art, 1996, 37–47.

95 G. Accorsi, G. Verri, M. Bolognesi, N. Armaroli, C. Clementi, C. Miliani and A. Romani, The exceptional near-infrared luminescence properties of cuprorivaite (Egyptian blue), *Chem. Commun.*, 2009, 3392–3394.

96 Y. J. Li, S. Ye, C. H. Wang, X. M. Wang and Q. Y. Zhang, Temperature-dependent near-infrared emission of highly concentrated Cu^{2+} in $CaCuSi_4O_{10}$ phosphor, *J. Mater. Chem. C*, 2014, **2**, 10395–10402, DOI: 10.1039/c4tc01966k.

97 P. Berdahl, S. K. Boocock, G. C. Y. Chan, S. S. Chen, R. M. Levinson and M. A. Zalich, High quantum yield of the Egyptian blue family of infrared phosphors ($MCuSi_4O_{10}$, M = Ca, Sr, Ba), *J. Appl. Phys.*, 2018, **123**, 193103, DOI: 10.1063/1.5019808.

98 J. C. de Mello, H. F. Wittmann and R. H. Friend, An improved experimental determination of external photoluminescence quantum efficiency, *Adv. Mater.*, 1997, **9**, 230–232, DOI: 10.1002/adma.19970090308.

99 S. Jose and M. L. Reddy, Lanthanum-strontium copper silicates as intense blue inorganic pigments with high near-infrared reflectance, *Dyes Pigm.*, 2013, **98**, 540–546, DOI: **10.1016/j.dyepig.2013.04.013**.

100 Y. Zhuang and S. Tanabe, Forward and back energy transfer between Cu^{2+} and Yb^{3+} in $Ca_{1-x}CuSi_4O_{10}$:Yb_x crystals, *J. Appl. Phys.*, 2012, **112**, 093521, DOI: **10.1063/1.4765013**.

101 R. J. Ford and M. A. Hitchman, Single crystal electronic and EPR spectra of $CaCuSi_4O_{10}$, a synthetic silicate containing copper(II) in a four-coordinate, planar ligand environment, *Inorg. Chim. Acta*, 1979, **33**, L167–L170, DOI: **10.1016/S0020-1693(00)89436-0**.

102 P. García-Fernández, M. Moreno and J. A. Aramburu, Origin of the exotic blue color of copper-containing historical pigments, *Inorg. Chem.*, 2015, **54**, 192–199, DOI: **10.1021/ic502420j**.

103 P. García-Fernández, M. Moreno and J. A. Aramburu, Origin of the Anomalous Color of Egyptian and Han Blue Historical Pigments: Going beyond the Complex Approximation in Ligand Field Theory, *J. Chem. Educ.*, 2016, **93**, 111–117, DOI: **10.1021/acs.jchemed.5b00288**.

104 W. Chen, Y. Shi, Z. Chen, X. Sang, S. Zheng, X. Liu and J. Qiu, Near-Infrared Emission and Photon Energy Upconversion of Two-Dimensional Copper Silicates, *J. Phys. Chem. C*, 2015, **119**, 20571–20577, DOI: **10.1021/acs.jpcc.5b04819**.

105 L. Binet, J. Lizion, S. Bertaina and D. Gourier, Magnetic and New Optical Properties in the UV-visible Range of the Egyptian Blue Pigment Cuprorivaite $CaCuSi_4O_{10}$, *J. Phys. Chem. C*, 2021, **125**, 25189–25196, DOI: **10.1021/acs.jpcc.1c06060**.

106 M. Jaime, V. F. Correa, N. Harrison, C. D. Batista, N. Kawashima, Y. Kazuma, G. A. Jorge, R. Stern, I. Heinmaa, S. A. Zvyagin, Y. Sasago and K. Uchinokura, Magnetic-field-induced condensation of triplons in Han Purple pigment $BaCuSi_2O_6$, *Phys. Rev. Lett.*, 2004, **93**, 6–9, DOI: **10.1103/PhysRevLett.93.087203**.

107 S. E. Sebastian, N. Harrison, C. D. Batista, L. Balicas, M. Jaime, P. A. Sharma, N. Kawashima and I. R. Fisher, Dimensional reduction at a quantum critical point, *Nature*, 2006, **441**, 617–620, DOI: **10.1038/nature04732**.

108 S. E. Sebastian, P. A. Sharma, M. Jaime, N. Harrison, V. Correa, L. Balicas, N. Kawashima, C. D. Batista and I. R. Fisher, Characteristic Bose-Einstein condensation scaling close to a quantum critical point in $BaCuSi_2O_6$, *Phys. Rev. B: Condens. Matter Mater. Phys.*, 2005, **72**, 1–4, DOI: **10.1103/PhysRevB.72.100404**.

109 S. Allenspach, P. Puphal, J. Link, I. Heinmaa, E. Pomjakushina, C. Krellner, J. Lass, G. S. Tucker, C. Niedermayer, S. Imajo, Y. Kohama, K. Kindo, S. Krämer, M. Horvatić, M. Jaime, A. Madsen, A. Mira, N. Laflorencie, F. Mila, B. Normand, C. Rüegg, R. Stern and F. Weickert, Revealing three-dimensional quantum criticality by Sr substitution in Han purple, *Phys. Rev. Res.*, 2021, **3**, 023177, DOI: **10.1103/PhysRevResearch.3.023177**.

110 Y. Sasago, K. Uchinokura, A. Zheludev and G. Shirane, Temperature-dependent spin gap and singlet ground state in $BaCuSi_2O_6$, *Phys. Rev. B: Condens. Matter Mater. Phys.*, 1997, **55**, 8357–8360, DOI: **10.1103/PhysRevB.55.8357**.

111 M. Y. Berezin and S. Achilefu, Fluorescence lifetime measurements and biological imaging, *Chem. Rev.*, 2010, **110**, 2641–2684, DOI: **10.1021/cr900343z**.

112 G. Verri, The spatially resolved characterisation of Egyptian blue, Han blue and Han purple by photo-induced luminescence digital imaging, *Anal. Bioanal. Chem.*, 2009, **394**, 1011–1021, DOI: **10.1007/s00216-009-2693-0**.

113 D. Comelli, V. Capogrosso, C. Orsenigo and A. Nevin, Dual wavelength excitation for the time-resolved photoluminescence imaging of painted ancient Egyptian objects, *Heritage Sci.*, 2016, **4**, 1–8, DOI: **10.1186/s40494-016-0090-5**.

114 P. Mirti, L. Appolonia, A. Casoli, R. P. Ferrari, E. Laurenti, A. Amisano Canesi and G. Chiari, Spectrochemical and structural studies on a roman sample of Egyptian blue, *Spectrochim. Acta, Part A*, 1995, **51**, 437–446, DOI: **10.1016/0584-8539(94)E0108-M**.

115 M. Maierhofer, V. Rieger and T. Mayr, Optical ammonia sensors based on fluorescent aza-BODIPY dyes—a flexible toolbox, *Anal. Bioanal. Chem.*, 2020, **412**, 7559–7567, DOI: **10.1007/s00216-020-02891-3**.

116 R. S. P. King, P. M. Hallett and D. Foster, NIR-NIR fluorescence: A new genre of fingermark visualisation techniques, *Forensic Sci. Int.*, 2016, **262**, e28–e33, DOI: **10.1016/j.forsciint.2016.03.037**.

117 S. Shahbazi, J. V. Goodpaster, G. D. Smith, T. Becker and S. W. Lewis, Studies into exfoliation and coating of Egyptian blue for application to the detection of latent fingermarks, ChemRxiv, 2021, 1–27.

118 Q. Yu, Y. Han, T. Tian, Q. Zhou, Z. Yi, J. Chang and C. Wu, Chinese sesame stick-inspired nano-fibrous scaffolds for tumor therapy and skin tissue reconstruction, *Biomaterials*, 2019, **194**, 25–35, DOI: **10.1016/j.biomaterials.2018.12.012**.

119 C. Yang, R. Zheng, M. R. Younis, J. Shao, L.-H. Fu, D.-Y. Zhang, J. Lin, Z. Li and P. Huang, NIR-II light-responsive biodegradable shape memory composites based on cuprorivaite nanosheets for enhanced tissue reconstruction, *Chem. Eng. J.*, 2021, **419**, 129437, DOI: **10.1016/j.cej.2021.129437**.

120 C. Dong, C. Yang, M. R. Younis, J. Zhang, G. He, X. Qiu, L. Fu, D. Zhang, H. Wang, W. Hong, J. Lin, X. Wu and P. Huang, Bioactive NIR–II Light–Responsive Shape Memory Composite Based on Cuprorivaite Nanosheets for Endometrial Regeneration, *Adv. Sci.*, 2022, **2102220**, 2102220, DOI: **10.1002/advs.202102220**.

121 Z. Zhang, Q. Dai, Y. Zhang, H. Zhuang, E. Wang, Q. Xu, L. Ma, C. Wu, Z. Huan, F. Guo and J. Chang, Design of a Multifunctional Biomaterial Inspired by Ancient Chinese Medicine for Hair Regeneration in Burned Skin, *ACS Appl.*

Mater. Interfaces, 2020, **12**, 12489–12499, DOI: 10.1021/acsami.9b22769.

122 F. A. Mann, P. Galonska, N. Herrmann and S. Kruss, Quantum defects as versatile anchors for carbon nanotube functionalization, *Nat. Protoc.*, 2022, **17**, 727–747, DOI: 10.1038/s41596-021-00663-6.

123 A. H. Brozena, M. Kim, L. R. Powell and Y. Wang, Controlling the optical properties of carbon nanotubes with organic colour-centre quantum defects, *Nat. Rev. Chem.*, 2019, **3**, 375–392, DOI: 10.1038/s41570-019-0103-5.

124 X. He, H. Htoon, S. K. Doorn, W. H. P. Pernice, F. Pyatkov, R. Krupke, A. Jeantet, Y. Chassagneux and C. Voisin, Carbon nanotubes as emerging quantum-light sources, *Nat. Mater.*, 2018, **17**, 663–670, DOI: 10.1038/s41563-018-0109-2.

125 C. Yang, M. R. Younis, J. Zhang, J. Qu, J. Lin and P. Huang, Programmable NIR-II Photothermal-Enhanced Starvation-Primed Chemodynamic Therapy using Glucose Oxidase-Functionalized Ancient Pigment Nanosheets, *Small*, 2020, **16**, 1–10, DOI: 10.1002/smll.202001518.

126 M. C. Gomes, Â. Cunha, T. Trindade and J. P. C. Tomé, The role of surface functionalization of silica nanoparticles for bioimaging, *J. Innovative Opt. Health Sci.*, 2016, **9**, 1–16, DOI: 10.1142/S1793545816300056.

127 P. Sobik, O. Jeremiasz, P. Nowak, A. Sala, B. Pawłowski, G. Kulesza-Matlak, A. Sypień and K. Drabczyk, Towards Efficient Luminescent Solar Energy Concentrator Using Cuprorivaite Infrared Phosphor ($CaCuSi_4O_{10}$)—Effect of Dispersing Method on Photoluminescence Intensity, *Materials*, 2021, **14**, 3952, DOI: 10.3390/ma14143952.

4.3.3 Publication Synopsis

The main goal of this **Review Manuscript** was to provide the scientific community with all the necessary tools to embrace the rising field of EB-NS, HB-NS and HP-NS. To start with, a short overview is given on 2D nanomaterials **(Section 4.2)** and NIR fluorophores **(Section 4.1)**, with particular focus on their applications in the biomedical field. Next, the synthesis routes for the preparation of bulk EB, HB and HP are discussed. While the original protocols were based on the salt-flux method[174,180,181,185] and commercial powders are still mainly prepared in this way, alternatives have been established: these include flux-less solid-state synthesis[177,185,188–193], hydrothermal processes[194–197], sol-gel methods[198], solution combustion synthesis[199] and pseudomorphosis routes[200]. These different approaches lead to crystals of different morphologies and can directly affect the chemical and photophysical properties of the resulting products. Next, the crystal structures of EB, HB and HP are illustrated: while EB and HB display identical crystal structures except for the substitution of the Ca^{2+} ion (EB) with Ba^{2+} (HB and HP), HP is also less rich in silica and presents a Cu-Cu bond[174,180,181,191,201–204]. The common trait shared by all three players is given by the fact that the silicate layers are held together by Ca^{2+}/Ba^{2+} ions *via* weak out-of-plane bonds; for this reason, these materials are prone to exfoliation into 2D (nano)materials, topic which is described next in the **Review Manuscript**. Preparation of exfoliated NS has been reported only very recently, with Johnson-McDaniel *et al.* [183,185] and Salguero *et al.*[184] being the first research groups to provide a simple protocol to yield EB-NS and HB-NS. These were obtained *via* either prolonged stirring in hot water (EB) or ultrasonication methods in organic solvents (HB) and led to high aspect ratio NS which were several µm large. Following these studies, other means to achieve nanocrystals of these materials have been reported and are listed in the **Review Manuscript**. These include milling and alternative methods based on ultrasounds, which have been employed in **Manuscript II**, **Manuscript III** and **Manuscript IV**.

It is crucial to understand, however, that it is not only about how small we can get, but also what happens to the material properties of EB, HB and HP when down-scaled. The following section in the **Review Manuscript** sums up the most relevant findings about the photophysics of the bulk materials. Among them it is worth mentioning here that, as described in **Section 4.3.1**, the Cu^{2+} ion in square planar geometry acts as color center and its electronic configuration results in a broad Vis-NIR excitation range ($\lambda \approx 450$-850 nm) and an intense NIR emission ($\lambda \approx 920$-960 nm)[174,182,191]. This NIR fluorescence is slightly red-shifted for HB and HP compared to EB due to ligand-field changes determined by the larger size of Ba^{2+} ions, and can thus stretch till the beginning of the NIR-II window ($\lambda \approx 1000$ nm)[182,205,206]. HP also presents extraordinary magnetic properties given by the Cu-Cu dimer[195,207–211], whereas very recent studies have indicated that up-conversion of EB and HB is possible[193,212] and that excitation of EB in the UV can lead to an even stronger NIR emission[213]. To this end, the **Review Manuscript** further outlines two outstanding properties of the NIR fluorescence of EB, HB and HP, which is given by the quantum yield (QY) and the lifetime (τ): the former has been reported to be significantly high for EB (QY ≈ 10.5%[206]) and high for HB (QY ≈ 6.9%[196]), whereas the decay time lies in the µs range for all three silicates ($\tau_{EB} \approx 100$-150 µs,

τ_{HB} ≈ 60-100 µs, τ_{HP} ≈ 6-30 µs[182,206,214–216]). Although these and several other properties of the bulk silicates already appear extremely promising, the real breakthrough, which also represents the cardinal point in the **Review Manuscript**, is that the bright and NIR fluorescence of EB, HB and HP is retained in the NS form. This discovery, first shown by Johnson-McDaniel *et al.*[183,185] and Salguero *et al.*[184] for EB and HB, has been then further investigated and also applied to HP in following works (including **Manuscript II**, **Manuscript III** and **Manuscript IV**). It has been shown that the NIR fluorescence does not bleach and is stable at different pH values, different ionic concentrations and in the presence of molecules which are known to alter the emission of similar fluorophores. Furthermore, fluorescence lifetime of NS samples still lies in the µs range and allows simple detection even in home-made remote setups. Quite surprisingly, also resolution-limited particles (diameter < 500 nm) are still fluorescent, and this result again strongly indicates the robustness of NS fluorescence.

After describing some bulk and NS photophysical properties as the ones reported above, the **Review Manuscript** focuses on the employment of these silicates in state-of-the-art technologies. Indeed, in recent years the unique features of nanostructured EB, HB and HP have gained increasing interest in the scientific community, leading to the most diverse set of applications. Studies in the field of photonics have exploited the NIR fluorescence to create smart ink[183–185] and efficient latent fingermark dusting powder[217–220], while others have used the stable emission of EB as a reference signal for sensing schemes based on ratiometric detection[221,222]. Most of the efforts, however, have been put into employing such novel nanomaterials in biomedicine. The fluorescence of EB-NS could be detected in fruit fly embryos, in plants and through tissue phantoms **(Manuscript II, Manuscript III)**, and could furthermore allow ratiometric sensing of bacterial strains together with single-walled carbon nanotube sensors[223]. However, the use of EB-NS has not been limited to its NIR fluorescence: numerous studies have indeed demonstrated that, thanks to their high aspect ratio, biocompatibility, good photothermal conversion efficiency and controlled release of bioactive Cu^{2+} and SiO_4^{4-} ions, EB-NS can also be employed for selective enrichment of multi-phosphopeptides[224], photothermal therapy[225,226] and tissue engineering[227,228].

Finally, the reported **Review Manuscript** outlines some future directions of research and open questions. While most of them concern the photophysics of EB-NS, HB-NS and HP-NS (*e.g.* QY measurements, size-fluorescence correlation, material doping, *etc*.), an important missing piece of the puzzle is represented by surface functionalization. This topic has so far not received the attention it deserves[219,221,222] and should therefore be addressed as soon as possible, given that it could immediately expand the already broad portfolio of NS applications in state-of-the-art technologies **(Manuscript IV)**.

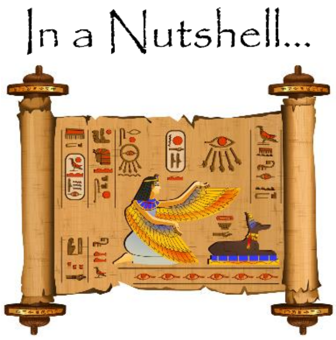

- ✓ Egyptian Blue ($CaCuSi_4O_{10}$, EB), Han Blue ($BaCuSi_4O_{10}$, HB) and Han Purple ($BaCuSi_2O_6$, HP) are layered silicates that can be easily exfoliated into 2D nanomaterials (*i.e.* nanosheets, NS).
- ✓ The bright and long-lived NIR fluorescence of the bulk materials, which originates from the Cu^{2+} ions acting as color centers, is retained in the NS form.
- ✓ Several works have outlined the great promise of these novel nanomaterials for diverse technological fields, *e.g.* security technologies, energy storage, sensing, bioimaging, photothermal therapy, tissue engineering, *etc*.

5 | Results

5.1 Photophysical Investigations on Extended Benzene-Fused Oligo-BODIPYs as Promising Platforms for Biophotonics

5.1.1 Introduction

The broad class of organic fluorophores based on the molecular skeleton of dipyrromethene boron difluoride (BODIPY) displays promising features for multiple technological fields, including bioimaging and biosensing. As outlined with more details in **Section 4.1.3** and **Section 4.1.5**, BODIPY-derived systems are typically characterized by high chemical and thermal stability, high QYs and, in general, tunable optical properties. To this regard, several strategies for the tailoring of the spectral features have been reported. Although excitonically coupled systems[85] and aggregates[229] represent valid options, the most common approach consists in the extension of the π-conjugated scaffold[230]. Unfortunately, due to the tediousness of the synthesis of nitrogen-containing organic frameworks, the preparation of conformation-restricted BODIPY dyes was long restricted to dimers only[6]. With these motivations in mind, Patalag *et al.*[231] recently demonstrated a novel oxidative approach that yielded BODIPY oligomers up to octamer species with reasonably good yields. These oligomers, which were linked at their α-positions *via* ethano units, were then used as starting point in a follow-up publication by Patra *et al.*[6]. In this work, extended benzene-fused oligo-BODIPYs could be prepared by adding an oxidative step to the procedure described by Patalag *et al*.[231] As a result, a robust protocol consisting in a straightforward, three-step synthesis followed by a one-pot oxidation was established. With this approach, a full series of fully conjugated chromophores were prepared and their spectral features characterized **(Figure 4.4)**. Among the so-produced oligomers, the hexameric (*H*) and octameric (*O*) forms stood out for their pronounced red-shifted absorption, which lied in the NIR-I window (920 nm < λ < 960 nm). Although these features suggested the presence of NIR emission, the corresponding signals could not be detected likely due to technical limitations of the employed spectrometer.

Given the interesting photophysics of these novel systems and the high promises held by NIR-emitting fluorophores for biophotonics, it would be worth further characterizing these dyes with the aim of verifying or excluding their ability to fluoresce in the NIR. From preliminary measurements at a home-built NIR setups, the NIR emission of the *H*- and *O*-oligo-BODIPYs could indeed be confirmed. The investigations that followed led to the publication of the manuscript embedded in the next section **(Section 5.1.2, Manuscript I)**. The open questions which fueled this work were:

- What are the main spectral features of these dyes?
- Does the fluorescence depend on different solvents and/or concentrations?

- Is the NIR fluorescence of the *H*- and *O*-oligo-BODIPYs bright enough to allow robust detection both at microscopy-based and remote setups?
- Is it possible to employ these dyes for bioimaging applications?

5.1.2 NIR-Emitting Benzene-Fused Oligo-BODIPYs for Bioimaging (Manuscript I)

Publication Details

Title: “NIR-emitting benzene-fused oligo-BODIPYs for bioimaging”

Authors: **Gabriele Selvaggio**†, Robert Nißler†, Peter Nietmann, Atanu Patra, Lukas J. Patalag, Andreas Janshoff, Daniel B. Werz and Sebastian Kruss

Journal: *Analyst* **147**, 230–237 (2022)

DOI: 10.1039/D1AN01850G

†These authors contributed equally.

Author Contributions: SK and DBW conceived and designed the study. AP and LJP synthesized the dyes. RN acquired 1D and 2D spectroscopy data which was analyzed with GS. QY experiments were performed and analyzed by GS and RN. RN performed remote fluorescence detection measurements. RN, GS and PN coated the beads. PN prepared actin samples. GS and PN acquired rheological data which was analyzed by GS, PN and AJ. GS, RN and SK wrote the manuscript with contributions from all authors.

Analyst

ROYAL SOCIETY OF CHEMISTRY

PAPER

View Article Online
View Journal

Cite this: DOI: 10.1039/d1an01850g

NIR-emitting benzene-fused oligo-BODIPYs for bioimaging†

Gabriele Selvaggio, ‡[a,b] Robert Nißler, ‡[a,b] Peter Nietmann,[b] Atanu Patra,[c]
Lukas J. Patalag, [c] Andreas Janshoff, [b] Daniel B. Werz [c] and
Sebastian Kruss *[a,b,d]

Received 11th October 2021,
Accepted 1st December 2021

DOI: 10.1039/d1an01850g

rsc.li/analyst

Near-infrared (NIR) fluorophores are emerging tools for biophotonics because of their reduced scattering, increased tissue penetration and low phototoxicity. However, the library of NIR fluorophores is still limited. Here, we report the NIR fluorescence of two benzene-fused oligo-BODIPYs in their hexameric (H) and octameric (O) forms. These dyes emit bright NIR fluorescence (H: maxima 943/1075 nm, O: maxima 976/1115 nm) that can be excited in the NIR (H = 921 nm, O = 956 nm) or non-resonantly over a broad range in the visible region. The emission bands of H show a bathochromic shift and peak sharpening with increasing dye concentration. Furthermore, the emission maxima of both H and O shift up to 20 nm in solvents of different polarity. These dyes can be used as NIR ink and imaged remotely on the macroscopic level with a stand-off distance of 20 cm. We furthermore demonstrate their versatility for biophotonics by coating microscale beads and performing microrheology *via* NIR video particle tracking (NIR-VPT) in biopolymer (F-actin) networks. No photodamaging of the actin filaments takes place, which is typically observed for visible fluorophores and highlights the advantages of these NIR dyes.

Introduction

Fluorophores emitting at near-infrared (NIR) wavelengths ($700\ \text{nm} < \lambda < 1700\ \text{nm}$) have advantages compared to their counterparts in the visible range of the spectrum due to reduced scattering, photodamage, autofluorescence and absorption.[1,2] Such characteristics can be exploited especially for biological imaging, where high tissue penetration and high signal-to-noise ratios are desired.[1,3–6] However, up to now the number of available fluorophores is much smaller in the NIR compared to the visible. Furthermore, despite their high potential, most NIR fluorophores display lower quantum yields (QYs). There is therefore a high interest to design the "holy grail" of superior NIR fluorophores and pave the way for a broad range of novel and powerful tools for bioimaging.

Among the currently available NIR fluorophores, only two have so far been approved for clinical use: indocyanine green (ICG) and methylene blue (MB). Both are however emitting in the so-called NIR-I region ($700\ \text{nm} < \lambda < 900\ \text{nm}$), which, compared to regions of higher wavelengths (*i.e.* $\lambda > 900$ nm and the so-called NIR-II region with $1000\ \text{nm} < \lambda < 1700\ \text{nm}$), presents lower contrast and penetration depth in tissue.[1,7] For this reason, NIR-II emitters such as lanthanide-based nanocrystals, quantum dots (QDs), rare-earth-doped nanoparticles (RENPs), single-walled carbon nanotubes (SWCNTs) and some organic dyes have received a lot of attention in recent years.[1,5,6] For instance, NIR fluorescent SWCNTs[2] have become robust tools for targeted bioimaging and sensors applications[8,9] thanks to their fluorescence tunability[10–12] in response to analytes of interest[13,14] (*e.g.* neurotransmitters[15,16]), their established separation[10,17] and functionalization routes,[8,18] as well as the possibility to perform defect chemistry.[19–21] 2D materials such as exfoliated silicate nanosheets (NS), on the other side, stand out for their high fluorescence brightness and remarkable photostability, which make them very promising labelling agents for multiple bioimaging scenarios.[22,23] Organic fluorophores tend to have shorter emission wavelengths and limited solubility in water but they also display faster excretion kinetics and can be chemically tailored, which makes them versatile materials for bioimaging.[6] Typical NIR dyes include canonical cyanines[24,25] (*e.g.* ICG), squaraines,[26,27] diketopyrrolopyrroles,[28,29] but also modified boron dipyrro-

---

[a] *Department of Chemistry and Biochemistry, Ruhr-University Bochum, 44801 Bochum, Germany. E-mail: Sebastian.Kruss@rub.de*
[b] *Institute of Physical Chemistry, Georg-August University Göttingen, 37077 Göttingen, Germany*
[c] *Technical University of Braunschweig, Institute of Organic Chemistry, 38106 Braunschweig, Germany*
[d] *Fraunhofer Institute for Microelectronic Circuits and Systems, 47057 Duisburg, Germany*

† Electronic supplementary information (ESI) available. See DOI: 10.1039/d1an01850g

‡ These authors contributed equally.

methenes (BODIPYs).[30,31] Structural modifications of the BODIPY core (*e.g.* aza-BODIPYs,[32,33] BOIMPYs[34,35]) are known to red-shift the spectral center of the parent BODIPY (around 500 nm) up to the far-red and even NIR region. In this context, the straightforward lateral extension of the π-system[36] (*e.g.* by Knoevenagel condensation[37]) is the most prominent strategy to tune the absorption and emission energies, resulting in appealing photophysical properties for *e.g.* biological labelling, photodynamic therapy, organic photovoltaics, *etc.*[38,39]

Recently, a novel three-step synthetic protocol to yield fully conjugated, benzene-fused oligo-BODIPYs from BODIPY precursors was presented.[38] With this procedure consisting in oligomerization and one-pot oxidation steps, a full series of oligomers ranging from dimers to octamers was synthesized. These chromophores displayed high stability and broad tunability of absorption and emission energies in the NIR region. While the absorption signatures were recorded for all oligo-BODIPYs[38] (500 nm < λ_{abs} < 950 nm), tetramers and larger molecules were reported to be non-fluorescent in the NIR region, presumably due to instrumental limitations.

Herein, we demonstrate the NIR fluorescence of an hexameric (H) and an octameric (O) oligo-BODIPY species. We characterize their NIR fluorescence *via* 1D and 2D NIR-fluorescence spectroscopy, and outline their performance in remote NIR imaging as well as in NIR particle tracking within biological cytoskeleton networks.

Results and discussion

The hexamer (H) and the octamer (O) form of benzene-fused oligo-BODIPYs present a large, arc-shaped structure which displays enhanced air stability and robustness against reversible reduction and oxidation cycles[38] (Fig. 1a). Their main absorption and emission bands in dichloromethane (DCM) are centered at 921/943 nm (H) and 956/976 nm (O) (Fig. 1b). The absorption is broad, stretching from the visible to the NIR region (Fig. S1†), whereas the emission window lies roughly between 900 and 1150 nm. The fluorescence main bands are narrow, presenting full widths at half maximum (FWHM) between 650 and 800 cm^{-1} (Table 1). Relative quantum yield (QY) measurements, performed according to a protocol by Würth *et al.*,[40] were carried out with a commercially available NIR dye (IR-1048) as standard. Such measurements yielded QY values of ≈2% for H and ≈4% for O in DCM, both in a similar range compared to shorter oligo-BODIPYs.[38] Interestingly, the dye concentration changed the ratio between the two largest emission peaks. Furthermore, bathochromic shifts are observed with increasing concentrations. The main emission band exhibits a red-shift of 25 nm (H) and 28 nm (O), whereas a red-shift of 6 nm of the second band of H was detected (Tables S1–S2 and Fig. S2a–b†).[39] These bathochromic shifts are accompanied by sharpening of the emission peaks in the case of the H dye. Next to that, emission energies shifted with solvent polarity (Table S3 and Fig. S2c–d†).[38] We anticipate that the previously not reported NIR fluorescence of these oligo-BODIPYs was due to low detection efficiencies of standard spectrometers in the NIR.[38] In contrast, we used equipment optimized for the NIR range (>800 nm, see Experimental section for details).

The high photostability of these dyes and the brightness of their NIR fluorescence were demonstrated *via* stand-off imaging experiments with a home-built setup.[14] In order to be properly imaged at a macroscopic setup, fluorophores need to

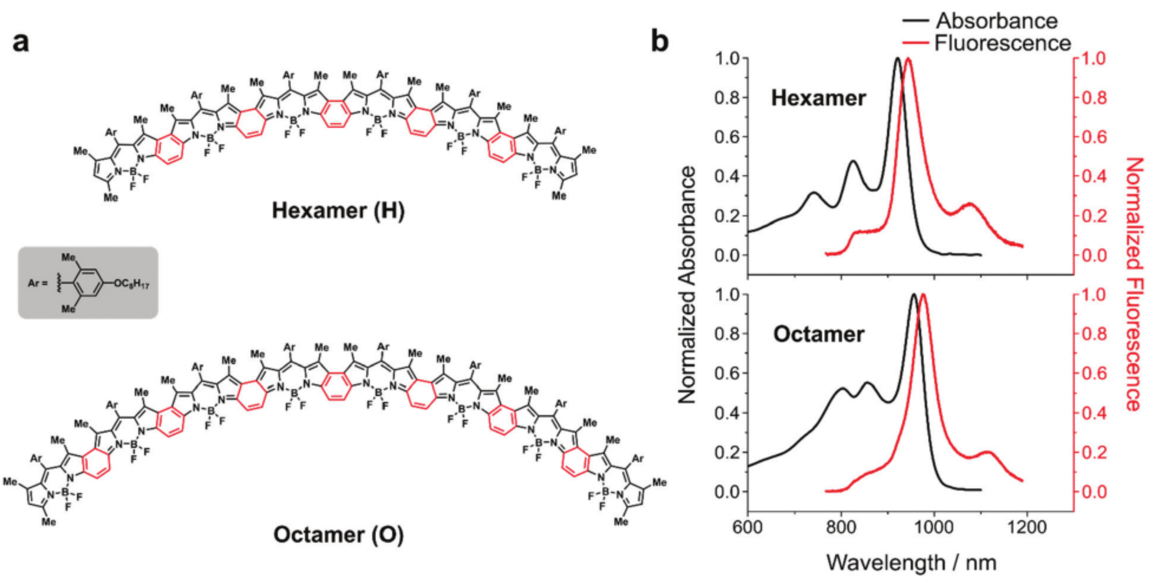

Fig. 1 NIR fluorescent organic BODIPY dyes. (a) Chemical structure of the hexamer and octamer of benzene-fused oligo-BODIPYs. (b) Visible (Vis)-near-infrared (NIR) absorbance and NIR fluorescence spectra of the hexamer- and octamer-BODIPYs in dichloromethane (DCM).

Table 1 Absorption and emission features of hexameric (H) and octameric (O) benzene-fused oligo-BODIPYs in dichloromethane (DCM). The main absorption band (λ_{abs}), the first and second emission peaks ($\lambda_{em,1}$ and $\lambda_{em,2}$), the full widths at half maximum of the mentioned signals (FWHM$_{abs}$, FWHM$_{em,1}$ and FWHM$_{em,2}$) and the Stokes shifts ($\Delta\tilde{\nu}$) are reported

Sample	λ_{abs} nm^{-1} (cm^{-1})	FWHM$_{abs}$ nm^{-1} (cm^{-1})	$\lambda_{em,1}$ nm^{-1} (cm^{-1})	FWHM$_{em,1}$ nm^{-1} (cm^{-1})	$\lambda_{em,2}$ nm^{-1} (cm^{-1})	FWHM$_{em,2}$ nm^{-1} (cm^{-1})	$\Delta\tilde{\nu}$/nm (cm^{-1})
H	921(10 858)	54.8(669)	943(10 601)	56.1(670)	1075(9301)	115.5(1201)	22(257)
O	956(10 460)	66.3(771)	976(10 247)	56.5(587)	1115(8971)	134.2(1449)	20(214)

be remarkably bright, considering that only a small fraction of emitted photons is able to reach the detector. Indeed, both H and O showed similar fluorescence intensities, which were easily observable already with low integration times, low excitation powers in the Vis (LED lamp, no laser), and both at high and low concentrations (Fig. S3† and Fig. 2a). In order to show their applicability as ink (*e.g.* for security ink technologies), letters were written on filter paper. Both O and H were clearly observable in the NIR channel, while not detectable in the visible (Fig. 2b). When imaging these samples, an efficient cut-off of emission wavelengths was obtained with long pass filters (Fig. 2c). Despite the 3× lower absolute intensity at λ_{em} > 1100 nm, both O and H were still easily imaged (the slightly higher intensity of O likely arises from local ink concentration differences, Fig. 2d). These experiments show that both O and H dyes can be used for imaging over a large range of the desired NIR spectral range. This finding is important because so far existing dyes such as ICG have been used for imaging far away from their emission maximum to get further into the NIR.[41]

In order to enhance their typically lower QYs as well as to overcome their typically limited water solubility, (NIR) organic dyes are often loaded into nano-/micrometer-sized polymeric microbeads. For this purpose, particles of different materials

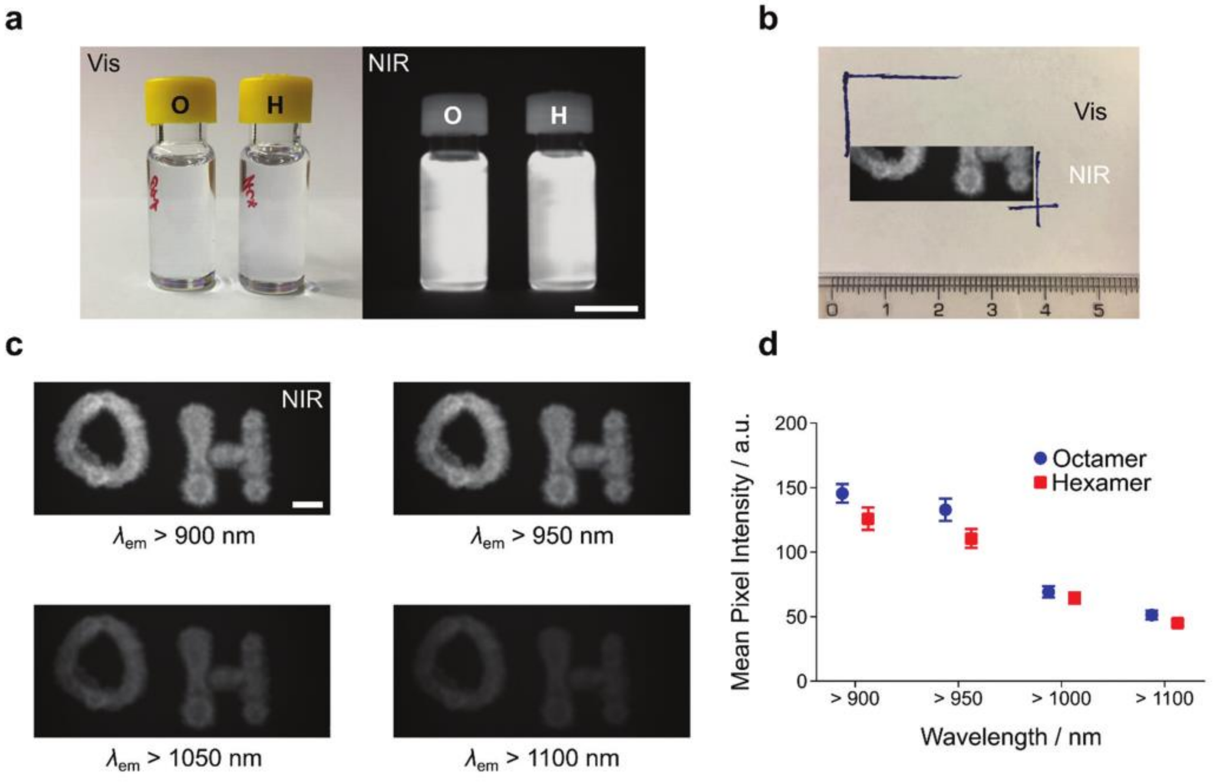

Fig. 2 Remote NIR fluorescence imaging of BODIPYs. (a) Visible and corresponding NIR fluorescence picture of the octamer-BODIPY (O) and the hexamer-BODIPY (H) in toluene. Scale bar = 1 cm. Exposure time = 500 ms. (b) BODIPY dye print on a filter paper with overlaid NIR fluorescence. The letters are only detectable in the NIR (scale in cm). (c) NIR images of the letters for different long pass emission filters (λ_{em}). Scale bar = 0.5 cm. Exposure time = 500 ms. (d) Relative signal of the two letters written in NIR at different wavelengths. The values are mean pixel intensities, evaluated from the pictures in **c**. Note that, even though the intensity decreases, there can be advantages such as less scattering or autofluorescence for using only the longer wavelengths. Error bars = standard deviation (from 5 different regions of interest within the dye print). *N* = 1 independent sample.

are commercially available. Among them, polystyrene (PS) beads appear appealing for *in vivo* imaging thanks to their mechanical stability, biocompatibility, robust synthetic protocols (miniemulsion polymerization) and broad range of sizes with narrow size distributions. Furthermore, diverse surface functionalizations are possible.[42] In terms of fluorophore incorporation techniques, the staining of particles *via* swelling represents one of the simplest options with regards to experimental complexity, yields and costs. Besides swelling, several PS loading protocols exist,[43] but BODIPY incorporation requires different approaches. The main challenge was to solubilize the BODIPY dye, without dissolving the PS beads during encapsulation (see Experimental section).

According to the images acquired at our NIR microscopic imaging setup, the coating procedure was successful: the PS particles indeed displayed a bright and uniform fluorescence with neglectable leakage (Fig. 3a and Fig. S4†). Furthermore, a staining protocol similar to the one described above could be performed on silica (SiO_2) beads. These particles are not porous and likely do not swell and therefore the dye adsorbed on the beads' surface. Nevertheless, bright and homogeneously fluorescent SiO_2 particles could be imaged, thus highlighting the versatility of our oligo-BODIPYs (Fig. S5†).

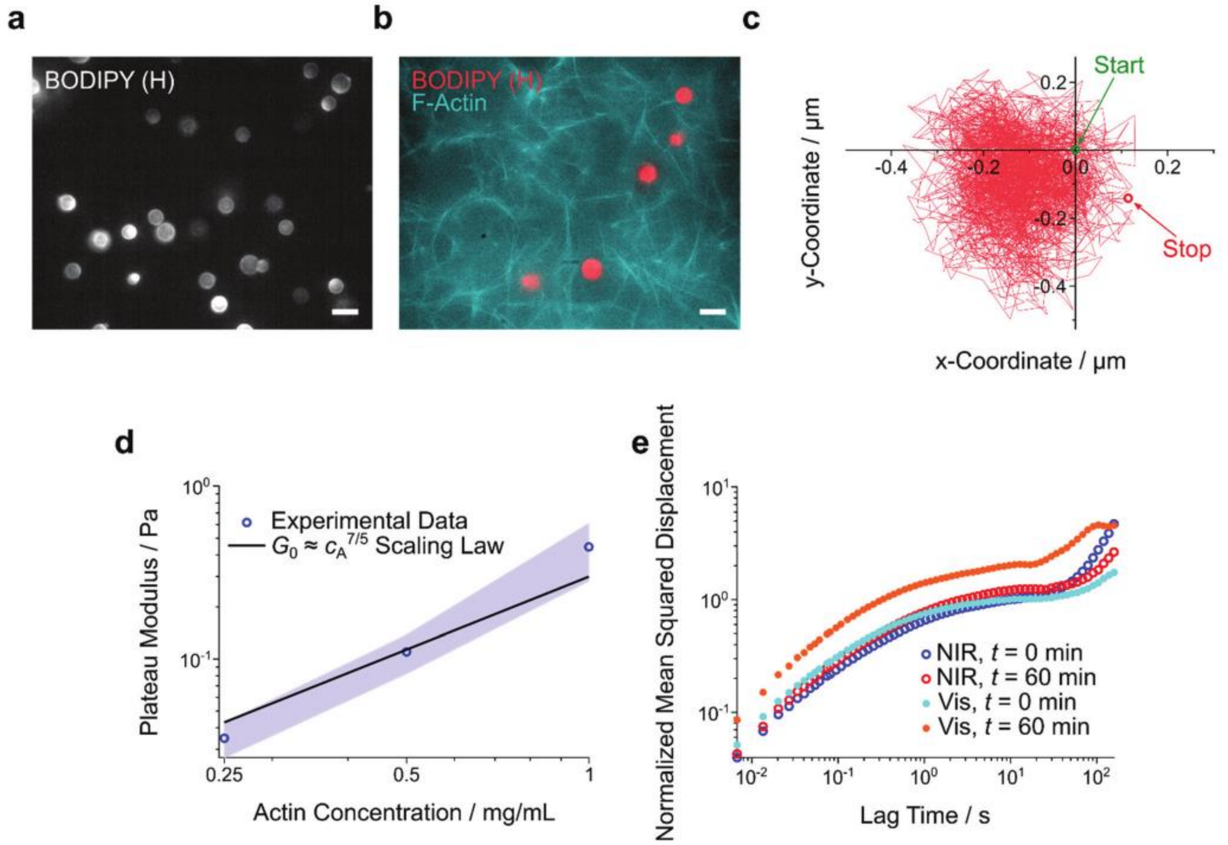

Fig. 3 NIR microrheology in actin biopolymer networks. (a) NIR fluorescence image of polystyrene (PS) beads, which were coated with the NIR dye (hexamer). Scale bar = 10 µm. (b) NIR/Vis fluorescence image of dye-coated PS beads (red) inside a F-actin network (cyan). In order to allow co-localization, the actin filaments were stained with a Vis dye. Scale bar = 10 µm. (c) An exemplary trajectory obtained after video particle tracking (VPT) of NIR dye-coated PS beads in actin networks. The initial and final bead positions are indicated by the arrows. (d) Mechanical properties of actin networks are extracted from trajectories obtained by NIR microrheology. Here, the dependence of actin concentration (c_A) on plateau modulus (G_0) is shown. The mean values (blue circles) and the corresponding standard deviations (light blue band) are plotted for the tested concentrations. The shear modulus of G_0 of such viscoelastic networks is known to scale as $G_0 \approx c_A{}^{7/5}$ (black line).[45] N = 3 independent samples. n = 11, 27, 31 beads for c_A = 0.25, 0.5 and 1 mg mL^{-1}, respectively. (e) Higher stability of actin networks using PS beads coated with our hexamer (H) dye. PS beads of same size were coated in two different ways: either with our hexamer NIR dye (NIR) or with a visible dye (Vis, *i.e.* fluorescent red PS microspheres, 545/566 nm). These two classes of beads were then separately embedded in actin network samples, and mean squared displacement (MSD) curves were obtained *via* VPT during prolonged continuous excitation. The results show that networks embedded with NIR dye-coated beads remain stable over time, which is not the case for the ones embedded with Vis dye-coated microparticles. For the continuous excitation, samples were placed under a fluorescent lamp installed on a microscope (λ_{exc} = 545 nm, measured output power ≈83 mW). The datasets were normalized to the respective t = 0 min MSD at lag time = 10 s (*i.e.* in the middle of the plateau region). NIR dataset: n = 114 beads at t = 0 min and 169 beads at t = 60 min. Vis dataset: n = 103 beads at t = 0 min and 184 beads at t = 60 min. N = 5 independent samples.

Next, we introduced the hexamer-labelled PS beads into actin networks. The globular protein actin is the most abundant cytoskeletal protein in most eukaryotic cells and it is highly important for structure and function. The mechanical (viscoelastic) properties of actin networks are therefore an active field of study, and tools that measure these properties are thus of high interest. The self-assembly of actin monomers can be easily tailored *in vitro* by *e.g.* the employment of appropriate buffers and cross-linking proteins, thus allowing for an extensive amount of studies on actin filaments and networks.[44,45] In order to perform co-localization measurements, such actin filaments can be labelled with *e.g.* visible fluorophores: in our case, bundled filaments of actin were labelled with a green-emitting dye. Thanks to the brightness of our oligo-BODIPYs as well as to the lack of autofluorescence in the NIR, the dye-labelled PS beads were still clearly distinguishable after introduction into bundled actin networks (Fig. 3b). Next, the robust (photo)stability of H allowed us to exploit its fluorescence signal to perform passive microrheology in the form of video particle tracking (VPT) of the beads (Fig. 3c). With this technique, which relies on the Generalized Stokes–Einstein relation, one can evaluate the viscoelastic properties of a system (*i.e.* our actin network) *via* the Fluctuation Dissipation Theorem. The Brownian motion of the incorporated probe particles (spheroidal microparticles, *i.e.* our beads) was quantified as mean squared displacement (MSD) and translated into shear moduli, which allowed a comparison of mechanical properties.[46] One open question is how actin concentration affects mechanical properties and this question can be answered by microrheology. Therefore, we measured the plateau modulus (G_0), *i.e.* the value of the storage modulus at the frequency for which the ratio loss/storage moduli (δ) is minimum, for three different actin concentrations. The obtained values followed a scaling law predicted *via* the Tube Model and validated experimentally for such systems[45] (Fig. 3d). Finally, the impact of different coatings of PS beads on the degradation of actin networks was studied. It is known that illumination of Vis fluorescent (PS) beads can lead to drastic softening of actin gels, likely caused by generation of free oxygen radicals and photodamage of actin.[47,48] While this mechanism might be on one side used for disintegration-triggered manipulation of actin networks, it also poses a threat and bias to most microrheological studies. With this motivation, we compared PS beads of same size with two different coatings: our H dye and a commercially available Vis control (*i.e.* fluorescent red PS microspheres, 545/566 nm, FRP5000, Lab 261). VPT analysis was performed with the camera and tracking software of an acoustic force spectroscope (AFS). In this way, MSDs could be measured at two different times: t = 0 min and t = 60 min, with continuous illumination. Our dataset displayed a clear trend: the Vis beads showed the largest increase of mean squared displacements over time, indicating a higher degree of actin softening caused by the employed Vis dye (Fig. 3e and Fig. S6–S7†). It is thus plausible that the triplet states normally responsible for generation of toxic oxygen species are not accessible or were not created around the H dye. Compared to the tested visible dye, the promising results highlight the advantage of using such versatile and robust NIR dyes for microrheology in polymeric networks and biological systems.

Conclusions

We report for the first time the NIR fluorescence of hexameric (H) and octameric (O) benzene-fused oligo-BODIPYs. Their broad excitation range and their narrow emission maxima between 940–1120 nm were studied *via* 1D and 2D spectroscopy. In different organic solvents, solvatochromic shifts appeared, whereas red-shifted emission wavelengths and peak sharpening trends were detected at higher concentrations. The NIR fluorescence of both H and O proved to be bright enough to enable stand-off detection, showing that these dyes can be used *e.g.* as security inks, for barcoding or for remote biomedical imaging. Furthermore, we demonstrated the potential of this class of BODIPYs as NIR fluorophores by coating them on silica and polystyrene microbeads. The latter could be used for NIR fluorescent video particle tracking (VPT) in biopolymer (actin) networks, without prominent actin degradation, a phenomenon occurring with conventional microrheological fluorophores.

In conclusion, thanks to their straightforward synthesis and advantageous photophysical properties, these oligo-BODIPYs are powerful tools for NIR bioimaging and photonics in general.

Experimental

UV-Vis and NIR spectroscopy

Absorption spectroscopy was performed with a JASCO V-670 device from 400 to 1100 nm in 0.2 nm steps in a 10 mm path quartz cuvette, using a ≈0.5 μM dye solution ($A_{\max} \approx 0.2$) in various solvents. The same dye solutions were transferred into glass vials and used for NIR fluorescence spectroscopy measurements, which were acquired with a Shamrock 193i spectrometer (Andor Solis Software, version 4.29.30012.0, Andor Technology Ltd) connected to an IX53 microscope (Olympus). Excitation was performed with a gem 561 laser (Laser Quantum), a Cobolt Jive laser (Cobolt AB) and a monochromator MSH150, equipped with a LSE341 light source (LOT-Quantum Design GmbH). Typical parameters for NIR fluorescence measurements were 50 mW (λ_{exc} = 561 nm) laser intensity, 200 μm spectrometer slit width and 1 s integration time, using a center wavelength of 1000 nm with a spectral grating of 150 l mm^{-1}.

A self-written Python code was used to plot the 2D spectra, which were not corrected for the spectral irradiance of the xenon lamp. Further data analysis and plotting were performed in Origin Pro 8.1.

Relative quantum yield (QY) was determined by comparison with a commercially available NIR-emissive dye (IR-1048, Sigma Aldrich, nr. 405175), following a reported protocol.[40] Fluorescence emission was acquired with a 20× NIR objective (LCPlan N 20×/0.45 IR, Olympus), measured excitation power out of the objective ≈235 mW (λ_{exc} = 561 nm) and integration time = 2 s. In short, all dyes were diluted in DCM to ≈0.1 absorption at their respective absorbance maxima. Next, absorption factors and integral photon fluxes were calculated in Origin Pro 8.1. A value of 1.412 was assigned to the refractive index of DCM at the emission wavelengths of the dyes,[49] whereas a value of 0.004 was used for the QY of IR-1048 in DCM.[50] Our calculations performed on triplicates of each dye yielded the following values (average ± standard deviation): 0.020 ± 0.004 for H, 0.044 ± 0.011 for O.

NIR camera-assisted stand-off detection

NIR stand-off detection was performed with a custom made, portable setup[14], using a XEVA (Xenics, Leuven Belgium) NIR InGaAs camera (Kowa objective, *f* = 25 mm/F1.4) and a white-light source (UHPLCC-01, UHP-LED-white, Prizmatix) equipped with a 700 nm short pass filter (FESH0700, Thorlabs) for excitation. Optical filters (FEL0900, FEL0950, FEL1050, FEL1100, ThorLabs) in a manual filter wheel (CFW6/M, Thorlabs) were mounted in front of the camera, which was equipped with an additional 900 nm long pass filter (FEL0900, Thorlabs). Stand-off distance for NIR fluorescence detection was 20 cm. For imaging of NIR dyes in vials, the following settings were chosen: integration time = 0.5 s, light intensity = 20 mW cm^{-2}. Parameters for NIR ink samples were instead: integration time = 0.5 s, light intensity = 35 mW cm^{-2}. Concentration of dyes in vials were ≈4 µM for the octamer and ≈5 µM for the hexamer solution in toluene. Approximately 10 µL of these solutions were drawn on standard filter paper to simulate the NIR ink. Light intensity was measured at 570 nm with a power meter (PM16-121, Thorlabs).

Data analysis was performed in ImageJ (v. 1.52a), whereas plotting was carried out in Origin Pro 8.1.

Coating of microbeads

The coating of polystyrene (PS) and silica (SiO_2) microspheres were performed as followed.

The following PS beads were used: Polybead® Microspheres, *d* ≈ 1.5 µm, Polysciences for rheology of different actin concentrations; PST5000, *d* ≈ 5 µm, Lab 261 for the actin degradation dataset. First, 300 µL of aqueous suspension of plain PS beads were removed from the original flask and directly mixed in a glass snap cap vial with 300 µL of methanol. The vial was placed on a heating plate at ≈50 °C and was kept under N_2 flow during all preparation steps to speed up the drying process. As soon as the solvents had evaporated, other 400 µL of methanol were introduced. After evaporation, other 300 µL of methanol were introduced and sonicated for ≈1 min. Immediately afterwards 300 µL (≈5 µM) of the hexamer dye (H) dissolved in diethyl ether was added to the PS beads-methanol suspension, mixed and directly placed for evaporation under N_2 stream. Finally, the dried beads were dispersed in 600 µL of milliQ water, and the system was bath sonicated for ≈2 min. The so-prepared H-coated PS microspheres were transferred into brown snap cap vials (to reduce the chances of photobleaching) and were stored at 4 °C.

With the previously described setup, plain SiO_2 microspheres (SS06N, *d* ≈ 6 µm, Bangs Laboratories, Inc.) were coated in a similar way. To start with, 300 µL of aqueous suspension of beads were removed from the original flask and directly mixed with 1 mL of acetonitrile. After drying, another 1 mL of acetonitrile was added. As soon as evaporation was complete, 1 mL of toluene and 300 µL (≈5 µM) of H dissolved in toluene were introduced into the glass vial. After evaporation, addition of another 1 mL of toluene and another drying step, the SiO_2 microspheres were dispersed in 1 mL of milliQ water and bath sonicated for ≈2 min. The so-prepared H-coated SiO_2 microspheres were transferred into brown snap cap vials (to reduce the chances of photobleaching) and were stored at 4 °C.

Preparation of Actin Networks

Actin (rabbit skeletal muscle, Cytoskeleton) networks were assembled at different concentrations: 0.25, 0.5 and 1 mg mL^{-1} for VPT verification, 1 mg mL^{-1} for degradation experiments, and 1.8 mg mL^{-1} for microscopy images of bundled actin. The chemicals listed below, unless explicitly mentioned, were purchased from Sigma-Aldrich.

First, the lyophilized actin powder was dissolved in ultrapure water (to 10 mg mL^{-1}). Next, the actin was introduced into a stabilizing buffer (5 mM Tris-HCl pH 8.0, 0.2 mM $CaCl_2$, 0.2 mM ATP, 5% sucrose, and 1% dextran). The system was then further diluted with freshly prepared G-buffer (2 mM Tris/HCl, 0.1 mM $CaCl_2$, 0.2 mM ATP, 0.5 mM dithiothreitol, 0.1 mM NaN_3, pH 7.8) and depolymerized (30 min on ice). Microparticles were first washed *via* centrifugation, *i.e.* the supernatant was removed and the system refilled with G-buffer ≈3–5 times. Then, the beads were added directly before the polymerization step. Similarly, for the bundled networks Alexa Fluor 488-phalloidin (Thermo Fischer) was added in this step for co-localization. The polymerization was started by adding 25% of the total volume in F-buffer (500 mM KCl, 20 mM $MgCl_2$, 50 mM EGTA, 0.1 mM NaN_3, pH 7.4) and vortexing. The samples were carefully but quickly transferred into glass chambers (*i.e.* cleaned #1 cover slips connected by 130 µm cut out double sided tape) and left to fully polymerize and equilibrate overnight at room temperature.

NIR microscopy

Our home-built NIR imaging setup consists of a 561 nm laser (Cobolt JiveTM 561 nm), a fluorescence lamp (X-Cite® 120Q, Excelitas Technologies), Olympus IX53 microscope equipped with a 100× (UPlanSApo 100×/1.35 Sil, Olympus) objective, a NIR camera (Cheetah TE1, Xenics) and a Vis camera (Zyla 5.5 sCMOS, Oxford Instruments). For NIR imaging, the laser was used as excitation source, whereas a dichroic mirror (Vis/NIR, HC BS R785 lambda/5 PV, F38-785S, AHF) and a 900 nm longpass filter (FELH0900, Thorlabs) were installed along the light path to the NIR camera. For Vis imaging at GFP wavelengths with the Zyla camera, the fluorescence lamp was employed for excitation at maximum power (≈3.8 mW, measured out of the objective with a Thorlabs S130C power sensor), and the following filters were used: ET470/40× (Set 49002, Chroma) for excitation, HC BS R488 1 lambda PV flat (F38-489, AHF) as dichroic mirror in the microscope's filter cube, the previously mentioned Vis/NIR dichroic mirror, a laser/Vis dichroic mirror (T550LPXR, 25.5 × 36 × 3 mm, Chroma), and finally ET525/50 m (Set 49002, Chroma), a Notch 561 (zet561NF F40-562, AHF) and a short-pass filter (650/SP HC, F37-650, AHF) directly mounted in front of the Vis camera.

For qualitative images of coated PS microspheres, an aliquot of bead suspension was diluted (typically, 1 : 10 in volume) with water. Then, a small volume (typically 10 μL) was removed from the diluted suspension and simply drop-casted on a #1 glass coverslip placed above the objective. Afterwards, imaging of this droplet was performed either in wet (Fig. 3a) or dried (Fig. S4†) form according to the following parameters: set laser power = 250 mW, exposure time of NIR camera = 0.1 s.

When beads were embedded in actin networks, the previously described (GFP-optimized) filters allowed the detection of the Alexa Fluor 488-labelled actin filaments. For qualitative observation of PS and SiO_2 beads embedded in ion-bundled actin networks, images were taken as follows: set laser power = 250 mW, exposure time of NIR camera = 1 s, exposure time of Vis camera = 0.02–0.03 s.

The plateau moduli of actin samples of 3 different concentrations were measured by tracking the NIR fluorescent beads over time. In this way, only the NIR camera was employed for data acquisition, which was carried out with these settings: set laser power = 250 mW, exposure time = 0.05 s, frame rate = 19 fps, total measurement time = 3 min.

Characterization images of dye-coated beads drop-casted on glass or embedded in actin networks were elaborated in ImageJ (v. 1.52a).

Bright field microscopy

Passive microrheology measurements for actin degradation experiments were performed using a bright field microscope (Lumicks, AFS) at a high frame rate (138 fps) with a 60× objective (CFI Achro-mat FF, WD = 0.3 mm, NA = 0.80, Nikon). Tracking of the microparticles was done with the AFS instrument software (Lumicks), which uses a quadrant algorithm to track ring shaped diffraction patterns in two dimensions. To avoid electrostatic interaction with the glass surfaces, the focal plane was set at heights not lower than 20 μm. Between the starting (t = 0 min) and final (t = 60 min) measurement sessions, samples were placed for continuous excitation under a fluorescent lamp (PhotoFluor II NIR, AHF) installed on an Olympus BX51 microscope. This lamp was employed at maximum intensity (λ_{exc} = 545 nm) and the light was directed to the samples through a 10× objective (MPlanFL N, Olympus) with a measured output power on the sample plane corresponding to ≈83 mW.

Microrheology analysis

For the VPT of PS beads in actin networks of different concentrations, the raw images were first despeckled and their contrast was enhanced in ImageJ (v. 1.52a). Next, a custom-made Python[51] code based on the Trackpy[52,53] package (Python v. 3.7.7, Trackpy v. 0.5.0) was used to obtain the trajectories. Typically chosen parameters for the tracking algorithm were: blob diameter = 31 pixels, memory = 10 frames, maximum displacement between consecutive frames = 25 pixels, minimum trajectory length = 3400 frames (out of 3400 total frames).

Trajectories obtained from both actin datasets (*i.e.* different actin concentrations and actin degradation) were analyzed based on the work of Crocker *et. al.*[54] with a customized variant of a MATLAB script made freely available on UMass (people.umass.edu/kilfoil) by Maria Kilfoil.

Conflicts of interest

There are no conflicts to declare.

Acknowledgements

Funded by the Deutsche Forschungsgemeinschaft (DFG, German Research Foundation) under Germany's Excellence Strategy-EXC 2033-390677874-RESOLV. We acknowledge support by the DFG *via* the Heisenberg program (S.K.). This work is supported by the "Center for Solvation Science ZEMOS" funded by the German Federal Ministry of Education and Research BMBF and by the Ministry of Culture and Research of Nord Rhine-Westphalia. We also thank Dr Lena Schnitzler for technical support during QY measurements.

References

1 G. Hong, A. L. Antaris and H. Dai, *Nat. Biomed. Eng.*, 2017, **1**, 0010.

2 S. Kruss, A. J. Hilmer, J. Zhang, N. F. Reuel, B. Mu and M. S. Strano, *Adv. Drug Delivery Rev.*, 2013, **65**, 1933–1950.

3 A. M. Smith, M. C. Mancini and S. Nie, *Nat. Nanotechnol.*, 2009, **4**, 710–711.

4 E. A. Owens, M. Henary, G. El Fakhri and H. S. Choi, *Acc. Chem. Res.*, 2016, **49**, 1731–1740.

5 J. Cao, B. Zhu, K. Zheng, S. He, L. Meng, J. Song and H. Yang, *Front. Bioeng. Biotechnol.*, 2020, **7**, 487.

6 P. Liu, X. Mu, X. D. Zhang and D. Ming, *Bioconjugate Chem.*, 2020, **31**, 260–275.

7 A. Spreinat, G. Selvaggio, L. Erpenbeck and S. Kruss, *J. Biophotonics*, 2020, **13**, e201960080.

8 A. J. Gillen and A. A. Boghossian, *Front. Chem.*, 2019, **7**, 612.

9 M. Dinarvand, S. Elizarova, J. Daniel and S. Kruss, *Chempluschem*, 2020, **85**, 1465–1480.

10 M. Zheng, *Top. Curr. Chem.*, 2017, **375**, 13.

11 R. Nißler, L. Kurth, H. Li, A. Spreinat, I. Kuhlemann, B. S. Flavel and S. Kruss, *Anal. Chem.*, 2021, **93**, 6446–6455.

12 S. M. Bachilo, M. S. Strano, C. Kittrell, R. H. Hauge, R. E. Smalley and R. B. Weisman, *Science*, 2002, **298**, 2361–2366.

13 H. Wu, R. Nißler, V. Morris, N. Herrmann, P. Hu, S. Jeon, S. Kruss and J. P. Giraldo, *Nano Lett.*, 2020, **20**, 2432–2442.

14 R. Nißler, O. Bader, M. Dohmen, S. G. Walter, C. Noll, G. Selvaggio, U. Groß and S. Kruss, *Nat. Commun.*, 2020, **11**, 5995.

15 M. Dinarvand, E. Neubert, D. Meyer, G. Selvaggio, F. A. Mann, L. Erpenbeck and S. Kruss, *Nano Lett.*, 2019, **19**, 6604–6611.

16 S. Kruss, D. P. Salem, L. Vuković, B. Lima, E. Vander Ende, E. S. Boyden and M. S. Strano, *Proc. Natl. Acad. Sci. U. S. A.*, 2017, **114**, 1789–1794.

17 F. Yang, M. Wang, D. Zhang, J. Yang, M. Zheng and Y. Li, *Chem. Rev.*, 2020, **120**, 2693–2758.

18 M. Prato, K. Kostarelos and A. Bianco, *Acc. Chem. Res.*, 2008, **41**, 275–294.

19 A. H. Brozena, M. Kim, L. R. Powell and Y. H. Wang, *Nat. Rev. Chem.*, 2019, **3**, 375–392.

20 F. A. Mann, N. Herrmann, F. Opazo and S. Kruss, *Angew. Chem., Int. Ed.*, 2020, **59**, 17732–17738.

21 A. Spreinat, M. M. Dohmen, J. Lüttgens, N. Herrmann, L. F. Klepzig, R. Nißler, S. Weber, F. A. Mann, J. Lauth and S. Kruss, *J. Phys. Chem. C*, 2021, **125**, 18341–18351.

22 G. Selvaggio, A. Chizhik, R. Nißler, L. Kuhlemann, D. Meyer, L. Vuong, H. Preiß, N. Herrmann, F. A. Mann, Z. Lv, T. A. Oswald, A. Spreinat, L. Erpenbeck, J. Großhans, V. Karius, A. Janshoff, J. P. Giraldo and S. Kruss, *Nat. Commun.*, 2020, **11**, 1495.

23 G. Selvaggio, M. Weitzel, N. Oleksiievets, T. A. Oswald, R. Nißler, I. Mey, V. Karius, J. Enderlein, R. Tsukanov and S. Kruss, *Nanoscale Adv.*, 2021, **3**, 4541–4553.

24 A. Mishra, R. K. Behera, P. K. Behera, B. K. Mishra and G. B. Behera, *Chem. Rev.*, 2000, **100**, 1973–2011.

25 L. Feng, W. Chen, X. Ma, S. H. Liu and J. Yin, *Org. Biomol. Chem.*, 2020, **18**, 9385–9397.

26 L. Hu, Z. Yan and H. Xu, *RSC Adv.*, 2013, **3**, 7667–7676.

27 C. Lambert, T. Scherpf, H. Ceymann, A. Schmiedel and M. Holzapfel, *J. Am. Chem. Soc.*, 2015, **137**, 3547–3557.

28 M. Kaur and D. H. Choi, *Chem. Soc. Rev.*, 2015, **44**, 58–77.

29 G. M. Fischer, A. P. Ehlers, A. Zumbusch and E. Daltrozzo, *Angew. Chem., Int. Ed.*, 2007, **46**, 3750–3753.

30 A. Loudet and K. Burgess, *Chem. Rev.*, 2007, **107**, 4891–4932.

31 G. Ulrich, R. Ziessel and A. Harriman, *Angew. Chem., Int. Ed.*, 2008, **47**, 1184–1201.

32 J. Killoran, L. Allen, J. F. Gallagher, W. M. Gallagher and D. F. O'Shea, *Chem. Commun.*, 2002, **317**, 1862–1863.

33 A. Kamkaew and K. Burgess, *Chem. Commun.*, 2015, **51**, 10664–10667.

34 L. J. Patalag, P. G. Jones and D. B. Werz, *Angew. Chem., Int. Ed.*, 2016, **55**, 13340–13344.

35 L. J. Patalag, M. Loch, P. G. Jones and D. B. Werz, *J. Org. Chem.*, 2019, **84**, 7804–7814.

36 K. Umezawa, A. Matsui, Y. Nakamura, D. Citterio and K. Suzuki, *Chem. – Eur. J.*, 2009, **15**, 1096–1106.

37 K. Rurack, M. Kollmannsberger and J. Daub, *Angew. Chem., Int. Ed.*, 2001, **40**, 385–387.

38 A. Patra, L. J. Patalag, P. G. Jones and D. B. Werz, *Angew. Chem., Int. Ed.*, 2021, **60**, 747–752.

39 L. J. Patalag, L. P. Ho, P. G. Jones and D. B. Werz, *J. Am. Chem. Soc.*, 2017, **139**, 15104–15113.

40 C. Würth, M. Grabolle, J. Pauli, M. Spieles and U. Resch-Genger, *Nat. Protoc.*, 2013, **8**, 1535–1550.

41 J. A. Carr, D. Franke, J. R. Caram, C. F. Perkinson, M. Saif, V. Askoxylakis, M. Datta, D. Fukumura, R. K. Jain, M. G. Bawendi and O. T. Bruns, *Proc. Natl. Acad. Sci. U. S. A.*, 2018, **115**, 4465–4470.

42 M. A. Markus, J. Napp, T. Behnke, M. Mitkovski, S. Monecke, C. Dullin, S. Kilfeather, R. Dressel, U. Resch-Genger and F. Alves, *ACS Nano*, 2015, **9**, 11642–11657.

43 T. Behnke, C. Würth, E. M. Laux, K. Hoffmann and U. Resch-Genger, *Dyes Pigm.*, 2012, **94**, 247–257.

44 H. Isambert and A. C. Maggs, *Macromolecules*, 1996, **29**, 1036–1040.

45 B. Hinner, M. Tempel, E. Sackmann, K. Kroy and E. Frey, *Phys. Rev. Lett.*, 1998, **81**, 2614–2617.

46 M. Tassieri, R. M. L. Evans, L. Barbu-Tudoran, G. N. Khaname, J. Trinick and T. A. Waigh, *Phys. Rev. Lett.*, 2008, **101**, 7–10.

47 T. Golde, C. Schuldt, J. Schnauß, D. Strehle, M. Glaser and J. Käs, *Phys. Rev. E: Stat., Nonlinear, Soft Matter Phys.*, 2013, **88**, 044601.

48 S. Van De Linde, I. Krstić, T. Prisner, S. Doose, M. Heilemann and M. Sauer, *Photochem. Photobiol. Sci.*, 2011, **10**, 499–506.

49 D. P. Shelton, *Appl. Opt.*, 2011, **50**, 4091–4098.

50 M. Casalboni, F. De Matteis, P. Prosposito, A. Quatela and F. Sarcinelli, *Chem. Phys. Lett.*, 2003, **373**, 372–378.

51 *Python*, Welcome to Python.org, https://www.python.org/, (accessed 26 November 2019).

52 J. C. Crocker and D. G. Grier, *J. Colloid Interface Sci.*, 1996, **179**, 298–310.

53 D. B. Allan, T. Caswell, N. C. Keim and C. M. van der Wel, 2019, DOI: 10.5281/zenodo.3492186.

54 J. C. Crocker, M. T. Valentine, E. R. Weeks, T. Gisler, P. D. Kaplan, A. G. Yodh and D. A. Weitz, *Phys. Rev. Lett.*, 2000, **85**, 888–891.

Electronic Supplementary Material (ESI) for Analyst.

Supplementary Information

NIR-Emitting Benzene-Fused Oligo-BODIPYs for Bioimaging

Gabriele Selvaggio[1,2,†], Robert Nißler[1,2,†], Peter Nietmann[2], Lukas J. Patalag[3], Atanu Patra[3], Andreas Janshoff[2], Daniel B. Werz[3], Sebastian Kruss[1,2,4]*

[1]Physical Chemistry II, Bochum University, Bochum, 44801, Germany

[2]Institute of Physical Chemistry, University of Göttingen, Göttingen, 37077, Germany

[3]Institute of Organic Chemistry, Technical University of Braunschweig, Braunschweig, 38106, Germany

[4]Fraunhofer Institute for Microelectronic Circuits and Systems, Duisburg, 47057, Germany

†These authors contributed equally.

*Corresponding author: sebastian.kruss@rub.de

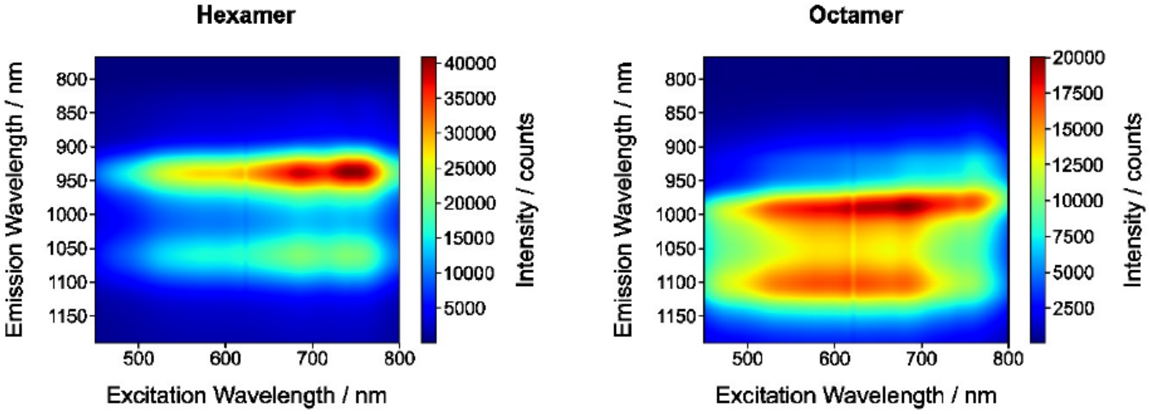

Figure S1: 2D spectra of NIR dyes. 2D excitation-emission spectra of the hexamer and octamer NIR dyes. Due to the cut-on wavelength of the dichroic mirror in our setup, the emission features resulting from excitation wavelengths > 800 nm are not measured. Therefore, the maxima for both hexamer and octamer samples are not observable.

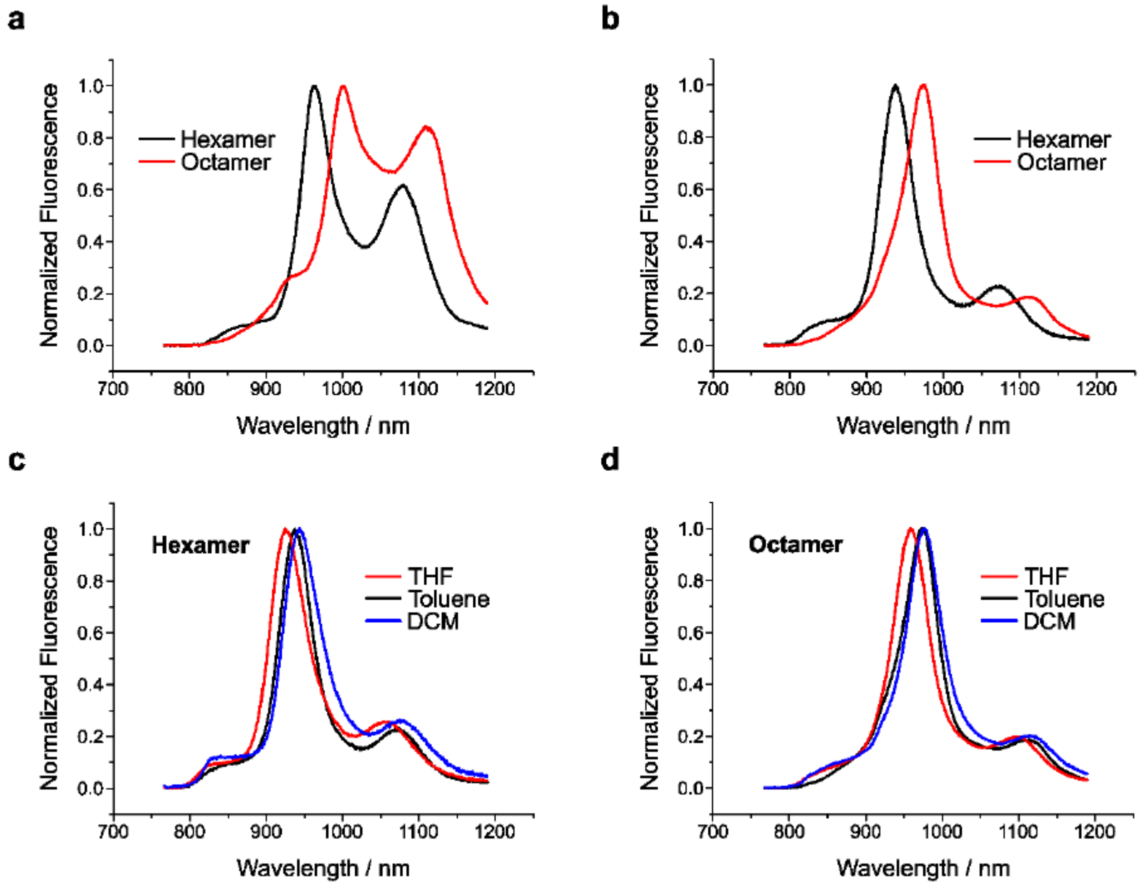

Figure S2: Concentration effects and solvatochromism. a Normalized fluorescence emission of highly concentrated samples (≈ 5 µM) of hexamer and octamer in dichloromethane (DCM). **b** Normalized fluorescence emission of diluted samples (≈ 0.5 µM) of hexamer and octamer in DCM show an altered ratio of the two largest peaks, as well as a hypsochromic shift and peak broadening, compared to more concentrated batches. **c** Solvent-dependent peak shifts in the emission profile of the hexamer-BODIPY in tetrahydrofuran (THF), toluene and DCM. **d** Solvent-dependent peak shifts in the emission profile of the octamer-BODIPY in THF, toluene and DCM.

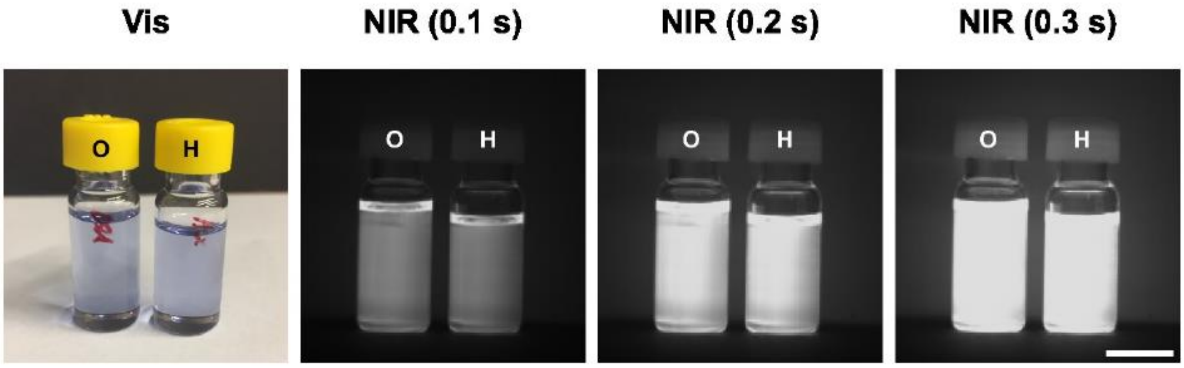

Figure S3: Stand-off NIR images of highly concentrated octamer- (O) and hexamer- (H) BODIPYs. NIR fluorescence images of highly concentrated solutions (≈ 5 µM) of octamer and hexamer dyes in toluene. Acquisition was performed with our home-built stand-off setup at maximum illumination power and at different exposure times: while *t* = 0.1 s is already sufficient to notice the bright fluorescence of the samples, with *t* = 0.3 s pixel saturation of the NIR camera starts becoming observable. Scale bar = 1 cm.

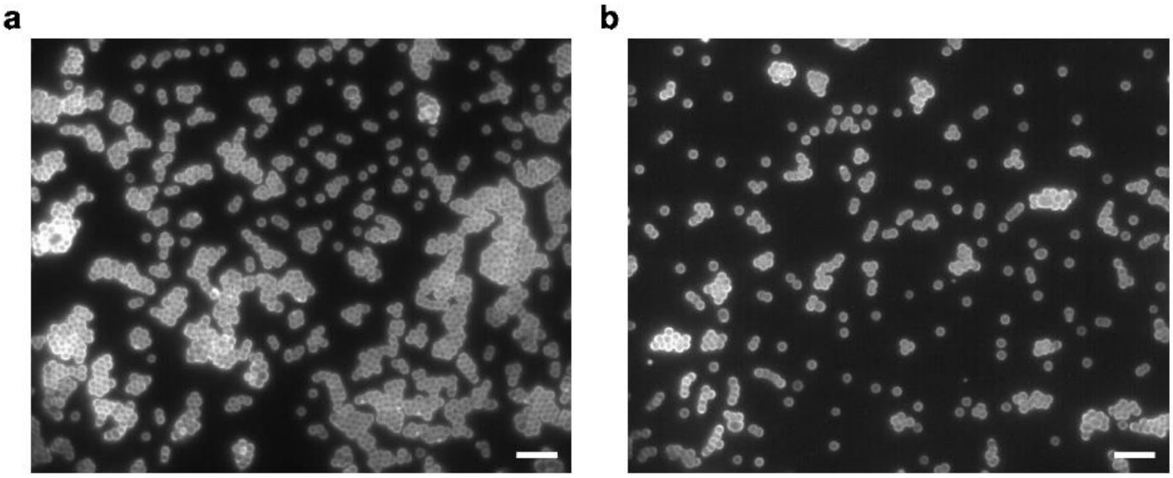

Figure S4: NIR images of hexamer-coated lower-size PS beads. NIR fluorescence images of higher (**a**) and lower (**b**) concentrations of PS beads with diameter ≈ 1.5 µm. These beads were tracked in actin networks of different concentrations thanks to their NIR fluorescent coating. Scale bar = 10 µm.

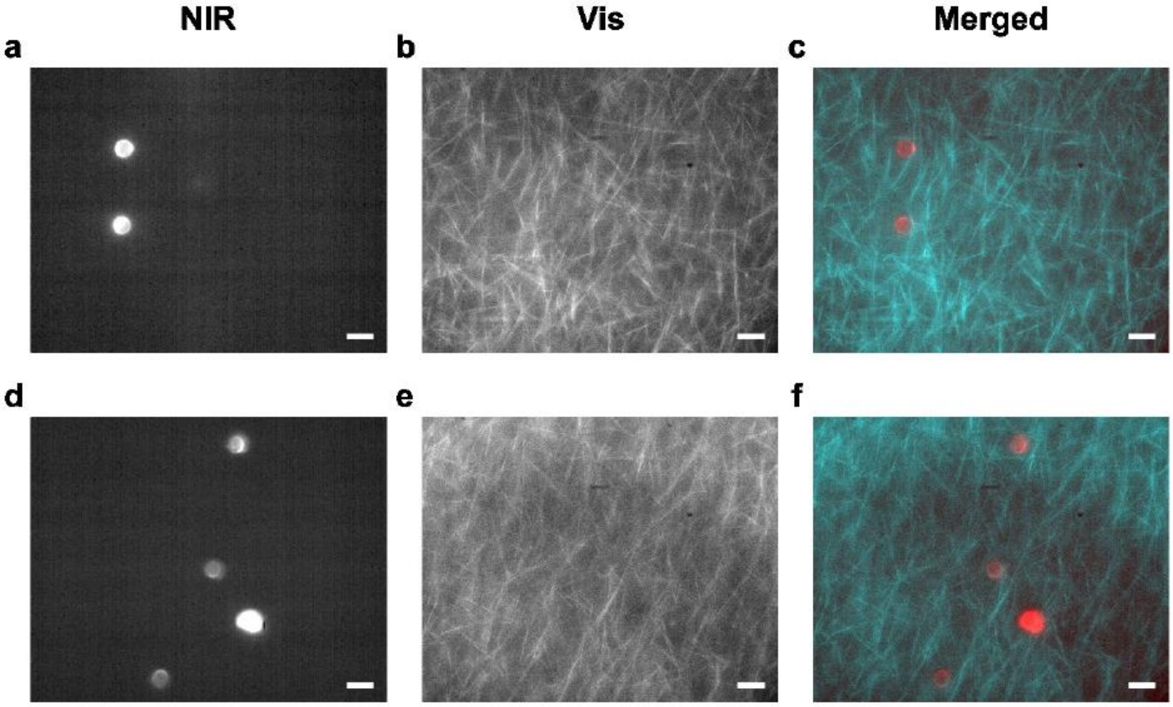

Figure S5: Coating of the hexamer-BODIPY dye on silica beads and dual-color imaging in actin networks. Besides the PS beads, also plain silica beads of diameter ≈ 6 µm were successfully coated and embedded into actin filaments, proving the versatility of the NIR dye. Different imaging channels (**a**-**c**, **d**-**f**) are shown: NIR (**a**,**d**) for detection of the hexamer-BODIPY, Vis (**b**,**e**) for detection of the actin filaments labelled with a Vis dye, and the merging of the channels in false colors (**c**,**f**) for co-localization. Scale bar = 10 µm.

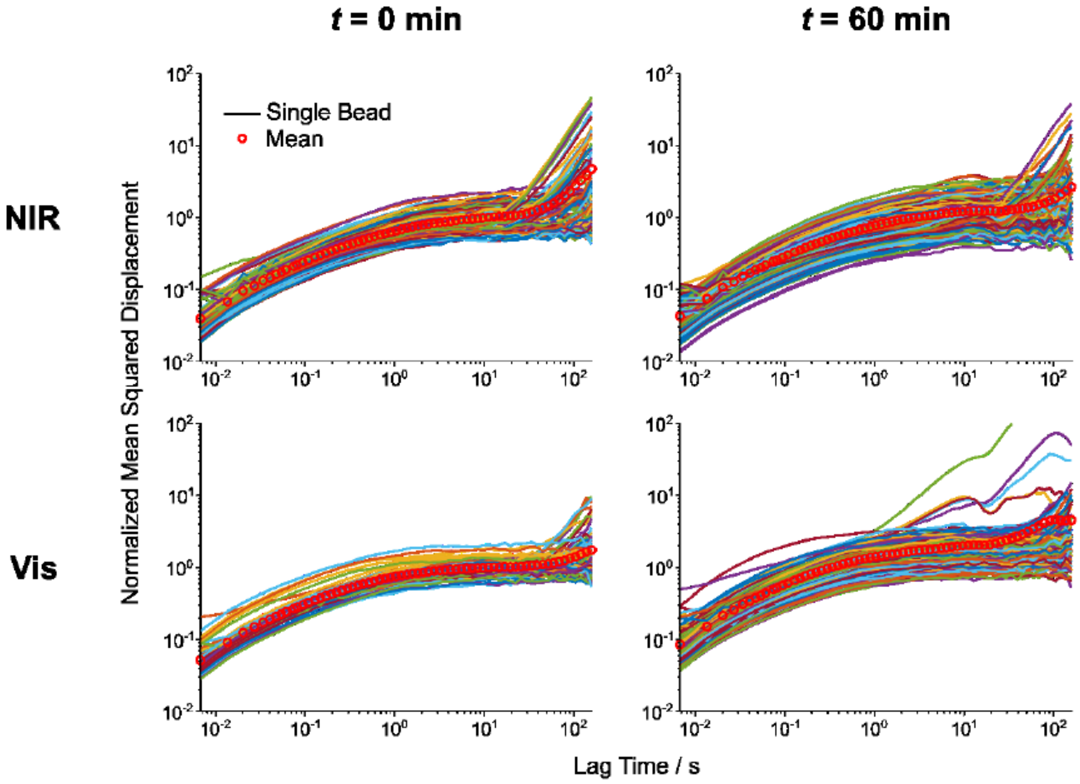

Figure S6: Single mean squared displacement (MSD) curves for actin degradation experiments. Single (colored lines) and mean (red circles) MSD curves resulting from video-particle tracking (VPT) of PS beads in actin networks after 60 min of continuous illumination. PS microspheres coated either with our NIR hexamer-BODIPY (NIR) or with a commercially available visible (Vis) dye (fluorescent red PS microspheres, 545/566 nm, FRP5000, Lab 261) were employed for this study. The 60 min datasets were normalized to the respective 0 min MSD at lag time = 10 s (*i.e.* in the middle of the plateau region). For the NIR dataset, n = 114 beads at t = 0 min and 169 beads at t = 60 min. For the Vis dataset, n = 103 beads at t = 0 min and 184 beads at t = 60 min. N = 5 independent samples.

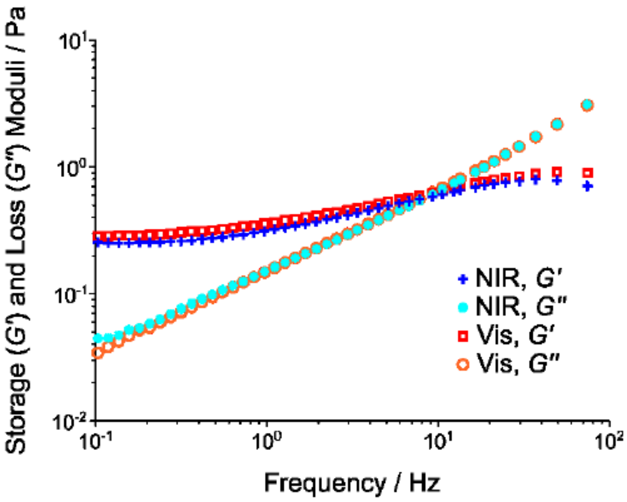

Figure S7: Storage and loss moduli for actin degradation experiments. Storage (*G'*) and loss (*G''*) moduli for both visible (Vis) and near-infrared (NIR) beads tracked in an actin network for 60 min under continuous illumination. The shown data corresponds to *t* = 0 min.

Table S1: Emission features of hexamer (H) and octamer (O) benzene-fused oligo-BODIPYs at high concentrations. The first ($\lambda_{em,1}$) and second ($\lambda_{em,2}$) emission peaks as well as the respective full widths at half maximum ($FWHM_{em,1}$ and $FWHM_{em,2}$) of highly concentrated ("high", ≈ 5 µM) dye samples in dichloromethane (DCM) are reported.

Sample	**$\lambda_{em,1\,(high)}$ / nm (cm^{-1})**	**$FWHM_{em,1\,(high)}$ / nm (cm^{-1})**	**$\lambda_{em,2\,(high)}$ / nm (cm^{-1})**	**$FWHM_{em,2\,(high)}$ / nm (cm^{-1})**
H	963 (10389)	62.6 (408.7)	1080 (9260)	93.0 (828.6)
O	1002 (9985)	68.2 (637.6)	1108 (9009)	134.7 (1069.9)

Table S2: Emission features of hexamer (H) and octamer (O) benzene-fused oligo-BODIPYs at low concentrations. The first ($\lambda_{em,1}$) and second ($\lambda_{em,2}$) emission peaks as well as the respective full widths at half maximum ($FWHM_{em,1}$ and $FWHM_{em,2}$) of diluted ("low", ≈ 0.5 µM) dye samples in dichloromethane (DCM) are reported.

Sample	**$\lambda_{em,1\,(low)}$ / nm (cm^{-1})**	**$FWHM_{em,1\,(low)}$ / nm (cm^{-1})**	**$\lambda_{em,2\,(low)}$ / nm (cm^{-1})**	**$FWHM_{em,2\,(low)}$ / nm (cm^{-1})**
H	938 (10667)	49.6 (579.5)	1074 (9315)	98.1 (1177.6)
O	974 (10264)	56.0 (594.2)	1108 (9022)	125.0 (931.3)

Table S3: Solvatochromism of hexamer (H) and octamer (O) benzene-fused oligo-BODIPYs. The first ($\lambda_{em,1}$) and second ($\lambda_{em,2}$) emission peaks of the dyes dissolved in tetrahydrofuran (THF), toluene and dichloromethane (DCM) are reported.

Sample	$\lambda_{em,1\ (THF)}$ / nm (cm^{-1})	$\lambda_{em,2\ (THF)}$ / nm (cm^{-1})	$\lambda_{em,1\ (toluene)}$ / nm (cm^{-1})	$\lambda_{em,2\ (toluene)}$ / nm (cm^{-1})	$\lambda_{em,1\ (DCM)}$ / nm (cm^{-1})	$\lambda_{em,2\ (DCM)}$ / nm (cm^{-1})
H	925 (10813)	1054 (9485)	938 (10667)	1074 (9315)	943 (10601)	1075 (9301)
O	958 (10434)	1097 (9113)	974 (10264)	1115 (9022)	976 (10247)	1115 (8971)

5.1.3 Publication Synopsis

The first fundamental result in **Manuscript I**, which set the basis for the following measurements on the investigated dyes, is represented by the detection of NIR fluorescence. This finding was confirmed by a specialized home-built equipment, which allowed 1D as well as 2D excitation-emission spectroscopy. Analysis of these datasets additionally showed that both the hexamer (*H*) and octamer (*O*) oligomers presented a broad Vis-NIR absorption. The main emission band, on the other side, was in both cases characterized by low values of full widths at half maximum (FWHM) and was located in a border region between the NIR-I and NIR-II windows (*i.e.* 900 nm < λ < 1150 nm). Both the main and the side emission bands could be shifted according to concentration and solvent nature. More precisely, significant bathochromic shifts (≈ 25-28 nm) were obtained when a higher amount of dyes was present in the system. Solvent-wise, the *H*- and *O*-dyes were dissolved in solvents of slightly increasing polarity: toluene, dichloromethane (DCM) and tetrahydrofuran (THF). While the position of the main fluorescence bands in DCM and toluene did not differ by more than 5 nm, a clear hypsochromic shift of ≈ 13-18 nm was determined in the slightly more polar THF for both *H*- and *O*-oligo-BODIPYs. Further spectroscopic analysis in **Manuscript I** focused on the evaluation of QY: for this purpose, an established protocol[232] for relative estimations was followed and the commercially available IR-1048 NIR dye was used as reference. This approach led to QY values of ≈ 2% for *H* and ≈ 4% for *O* (in DCM).

After having characterized the spectral features of the *H*- and *O*-oligo-BODIPYs, the focus of the work reported in **Manuscript I** moved to NIR fluorescence imaging. Analogously to the case of the silicate NS described in the following sections of this thesis **(Section 5.2, Section 5.3, Section 5.4)**, photostability and brightness of the fluorophores were tested at a remote imaging setup. Both *H*- and *O*-dyes displayed a bright fluorescent signal even at low integration times and excitation powers (LED lamp). Again at this stand-off system, the *H*- and *O*-oligo-BODIPYs were successfully employed as smart inks in a proof-of-principle experiment. The fluorescent signals could also endure the presence of different cut-off filters installed in front of the InGaAs camera: even when the cut-off threshold was chosen so to exclude the maxima of both emission bands (*i.e.* λ_{em} > 1100 nm), the signals from the off-peak tail fluorescence were strong enough to be robustly detected.

In the final part of **Manuscript I**, coating of polystyrene (PS) and silica (SiO_2) microbeads with the *H*-dye was carried out, and these beads were then imaged at a home-built NIR microscopy setup. Despite the diverse nature of the coating procedure (swelling for PS and surface adsorption for SiO_2), the tested *H*-oligo-BODIPY managed to homogeneously coat the substrates in both cases, yielding uniformly NIR-fluorescent beads. Furthermore, the applied coating protocol was characterized by negligible leakage, as confirmed by the absence of background signals during NIR imaging. As a proof-of-principle application of *H*-labelled PS beads in the biomedical field, these systems were introduced into actin networks. Successfully colocalized images of the NIR-emitting beads next to Vis-labelled actin filaments could be acquired thanks to the high brightness of the oligo-BODIPY and the typical lack of autofluorescence in the

NIR. Furthermore, thanks to the high photostability of the *H*-dye, video particle tracking (VPT) of the fluorescent signature of the coated beads enabled passive microrheology. Based on the Fluctuation Dissipation Theorem and according to experimentally verified literature scaling laws, the so-calculated viscoelastic properties allowed to retroactively estimate the concentrations of the imaged actin samples. Finally, to better comprehend the biocompatible aspects of the investigated oligo-BODIPYs, the effect of prolonged dye excitation (t = 60 min) on actin filaments was analyzed. For this experiment, PS beads of same size but with two different coatings were introduced into actin networks and compared: the two dyes which were chosen for the coating were the NIR-emitting hexamer and a commercially available fluorescent red control. While in the previously described actin concentration studies a NIR fluorescence-based VPT had been performed, for the actin degradation experiments a diffraction-based VPT tool installed in another device was employed instead. Given the high frame rates required to build up a robust dataset (≈ 140 fps), the employed bright-field microscope proved to be more robust for this purpose than the home-built NIR setup. During continuous illumination for t = 60 min, mean squared displacement (MSD) values were recorded at the beginning (t = 0 min) and at the end (t = 60 min) of the imaging session. The so-obtained results displayed a significantly larger increase in MSD over time for the Vis beads. Considered that higher MSD values imply a higher degree of actin softening (*i.e.* degradation), this study underlined the better performance of the *H*-oligo-BODIPY over a commercially available dye.

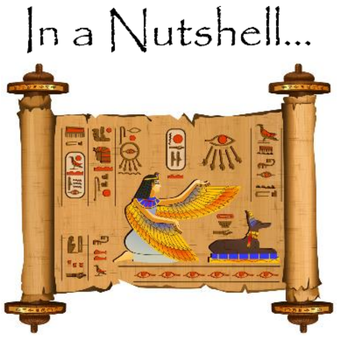

- ✓ The hexameric (*H*) and octameric (*O*) forms of extended benzene-fused oligo-BODIPYs displayed NIR fluorescence.
- ✓ Characterized spectral features included a broad Vis-NIR absorption, narrow fluorescence main bands, concentration and solvent-dependent shifts, and QYs ≈ 2-4%.
- ✓ High photostability and brightness of the NIR fluorescence of *H*- and *O*-dyes could be successfully shown at a remote detection setup.
- ✓ PS and SiO_2 beads were uniformly coated with the *H*-oligo-BODIPY and imaged *via* NIR microscopy.
- ✓ The intense fluorescence of *H*-coated beads allowed colocalized imaging with Vis-labelled actin filaments.
- ✓ Thanks to the high stability of the *H*-dye emission, fluorescence-based passive microrheology could be performed in actin networks.
- ✓ Diffraction-based video particle tracking proved that prolonged excitation of *H*-coated PS beads does not lead to significant actin degradation.

5.2 Exfoliation of Egyptian Blue and Proof-of-Principle Bioimaging Applications with EB-NS

5.2.1 Introduction

As described in **Section 4.3**, various studies have highlighted the outstanding material properties of Egyptian Blue ($CaCuSi_4O_{10}$, EB). Considered that multiple technological fields could benefit from the intense and stable near-infrared (NIR) fluorescence of this material, the interest in the scientific community has grown exponentially in the last years. The excitement around this layered silicate grew even more when Johnson-McDaniel *et al.*[183] reported the first exfoliation procedure of EB into 2D nanosheets (NS): besides the strikingly straightforward delamination protocol, the most surprising and groundbreaking finding of this work was that the NIR luminescence could be retained in EB-NS of several microns (µm) in size. This discovery clearly suggested that EB-NS could be excellent working platforms for research areas such as telecommunications, security ink formulations and biomedical imaging. Indeed, as explained in **Section 4.1** and **Section 4.2**, NIR-emitting 2D nanomaterials could be optimal candidates for biomedical applications such as fluorescence bioimaging. However, although a few papers on EB-NS had been published after the pivotal study by Johnson-McDaniel *et al.*[183], this research direction was mostly left undiscovered. Furthermore, despite the ancient origins of EB, many fundamental questions concerning its photophysical properties were still unanswered, especially concerning the dependence of fluorescence from particle size and analytes of (biological) interest. Last but not least, by the time that the work described in the upcoming **Section 5.2.2 (Manuscript II)** was performed, the exfoliation protocols available in literature were showing clear space for improvement. Some of them consisted in rather time-consuming stirring methods, which were appealing for their simplicity but presented limitations for further processing and potential industrial applications. Additionally, most of the reported procedures had yielded NS of sizes in the range of several micrometers: as pointed out in **Section 4.1.3** and **Section 4.1.4**, if the sizes at play are too large, the chances of nanoparticles being retained in the reticuloendothelial system are high, which could lead to toxicity issues and inevitably hinder translation to (pre-)clinical research. Next to that, fluorophores of larger sizes could also perturb the biological system they are introduced into, thus affecting the outcome of the measurements.

Within the scenario explained above, the study presented in the following section **(Manuscript II)** was driven by the following questions:

- Can the exfoliation procedure be improved so to yield EB-NS of diameters well below the µm range?
- Are smaller NS still fluorescent in the NIR?
- How does the NIR fluorescence of EB-NS correlate with size?
- Is the NIR fluorescence affected by *e.g.* prolonged excitation and typical quenching molecules?

- Besides the NIR fluorescence, do EB-NS display all the necessary requirements to be considered a novel NIR-emitting fluorophore for biophotonics?

5.2.2 Exfoliated Near-Infrared Fluorescent Silicate Nanosheets for (Bio)Photonics (Manuscript II)

Publication Details

Title: “Exfoliated near infrared fluorescent silicate nanosheets for (bio)photonics”

Authors: **Gabriele Selvaggio**, Alexey Chizhik, Robert Nißler, Ilyas Kuhlemann, Daniel Meyer, Loan Vuong, Helen Preiß, Niklas Herrmann, Florian A. Mann, Zhiyi Lv, Tabea A. Oswald, Alexander Spreinat, Luise Erpenbeck, Jörg Großhans, Volker Karius, Andreas Janshoff, Juan Pablo Giraldo and Sebastian Kruss

Journal: *Nat. Commun.* **11**, 1495 (2020)

DOI: 10.1038/s41467-020-15299-5

Author Contributions: SK conceived and designed the study. GS and VK performed and optimized the milling procedure. GS performed AFM experiments. GS, HP, and AS exfoliated materials and collected 1D spectra. HP and RN collected 2D spectra. AC performed single photon counting and anisotropy experiments. GS and LV performed and analyzed correlative SEM-NIR experiments. GS imaged single nanosheets and analyzed particle trajectories together with NH, IK, and AJ. GS together with RN, FAM, and ZL performed biological imaging experiments with input from LE, JPG, and JG. TAO performed cell viability experiments. DM performed calculations and simulations concerning the correction factor for diffusion of (anisotropic) EB-NS in a solvent. GS and SK wrote the manuscript with contributions from all authors.

nature COMMUNICATIONS

ARTICLE

https://doi.org/10.1038/s41467-020-15299-5 OPEN

Exfoliated near infrared fluorescent silicate nanosheets for (bio)photonics

Gabriele Selvaggio[1], Alexey Chizhik[2], Robert Nißler[1], Ilyas Kuhlemann[1], Daniel Meyer[1], Loan Vuong[3], Helen Preiß[1], Niklas Herrmann[1], Florian A. Mann[1], Zhiyi Lv[4], Tabea A. Oswald[3], Alexander Spreinat[1], Luise Erpenbeck[5], Jörg Großhans[4], Volker Karius[6], Andreas Janshoff[1], Juan Pablo Giraldo[7] & Sebastian Kruss[1]✉

Imaging of complex (biological) samples in the near-infrared (NIR) is beneficial due to reduced light scattering, absorption, phototoxicity, and autofluorescence. However, there are few NIR fluorescent materials known and suitable for biomedical applications. Here we exfoliate the layered pigment $CaCuSi_4O_{10}$ (Egyptian Blue, EB) via ball milling and facile tip sonication into NIR fluorescent nanosheets (EB-NS). The size of EB-NS can be tailored to diameters <20 nm and heights down to 1 nm. EB-NS fluoresce at 910 nm and the fluorescence intensity correlates with the number of Cu^{2+} ions. Furthermore, EB-NS display no bleaching and high brightness compared with other NIR fluorophores. The versatility of EB-NS is demonstrated by in-vivo single-particle tracking and microrheology measurements in *Drosophila melanogaster* embryos. EB-NS can be uptaken by plants and remotely detected in a low-cost stand-off detection setup. In summary, EB-NS have the potential for a wide range of bioimaging applications.

---

[1] Institute of Physical Chemistry, University of Göttingen, Göttingen 37077, Germany. [2] Third Institute of Physics, University of Göttingen, Göttingen 37077, Germany. [3] Institute of Organic and Biomolecular Chemistry, University of Göttingen, Göttingen 37077, Germany. [4] Institute of Developmental Biochemistry, Medical School, University of Göttingen, Göttingen 37077, Germany. [5] Department of Dermatology, Venereology and Allergology, University Medical Center Göttingen, Göttingen 37075, Germany. [6] Department of Sedimentology and Environmental Geology, Geoscience Center, University of Göttingen, Göttingen 37077, Germany. [7] Department of Botany and Plant Sciences, University of California, Riverside, California 92507, USA. ✉email: skruss@gwdg.de

Fluorescence imaging provides important insights into the structure, function, and dynamics of biological samples[1,2]. Imaging in the near-infrared (NIR) spectral range (800–1700 nm) promises higher tissue penetration, higher contrast, and lower phototoxicity due to reduced NIR light scattering and absorption[3–5]. However, these approaches are limited by the scarcity of NIR fluorescent materials. NIR fluorescent organic dyes such as indocyanine green (ICG) bleach and are therefore not suitable for long-term imaging[6,7]. In contrast, nanomaterials provide beneficial photophysical properties such as ultra-high photostability that would enable tracking in living systems without time constrains. NIR fluorescent nanomaterials include InAs quantum dots, lanthanide-doped nanoparticles, or semiconducting single-walled carbon nanotubes (SWCNTs)[8–12]. For example, SWCNTs have been used as building blocks for NIR imaging and as fluorescent sensors that detect small signaling molecules, proteins, or lipids[13–19]. They can be chemically tailored and have been used to reveal spatiotemporal release patterns of neurotransmitters from single cells[2,15,20–22]. However, most NIR fluorescent nanomaterials often have low quantum yields, lack biocompatibility, or are restricted to certain emission/excitation wavelengths. Therefore, there is a major need for novel NIR fluorescent and biocompatible nanomaterials for sophisticated applications such as long-time single-particle tracking in organisms or multiscale bioimaging such as stand-off detection in plants[23,24].

One of the first colored pigments created by mankind is the calcium copper silicate called Egyptian Blue ($CaCuSi_4O_{10}$, EB), which has been synthesized and used as early as 2500 BC in Ancient Egypt[25]. Current ancient works of art decorated with EB have lost none of their vibrant color, a testimony to the remarkable chemical stability of this compound. Interestingly, bulk EB displays NIR fluorescence, which was only recently identified[26,27] and attributed to a $^2B_{2g}$-$^2B_{1g}$ electronic transition of the copper ion that ranges from 910 to 930 nm[26,28]. Bulk EB shows a remarkable high quantum yield of 10.5% for a NIR emitter compared with SWCNTs, quantum dots, metal nanoclusters, and FDA-approved fluorophores such as ICG[5,28]. Recently, micrometer-sized monolayer sheets of EB were isolated by stirring in hot water for several days[29,30]. However, the remarkable properties of EB have not been explored for developing NIR luminescent nanomaterials for bioimaging applications. The layered structure of EB suggests that exfoliation procedures known from other two-dimensional (2D) materials including graphene and transition metal chalcogenides could efficiently exfoliate it[31–34]. Such 2D materials have been shown to possess promising optoelectronic properties and are a rich playground for physics and chemistry[35].

Herein, we use a facile tip sonication technique to exfoliate $CaCuSi_4O_{10}$ (EB) nanosheets (EB-NS). This procedure allows one to control the nanomaterial size/thickness and retain the unique NIR fluorescent properties of macroscopic $CaCuSi_4O_{10}$. We report the photophysical properties of EB-NS and investigate how NIR fluorescence scales with nanosheet size. Furthermore, we demonstrate the use of this material for in-vivo NIR microscopy and stand-off detection.

Results

Exfoliation of Egyptian Blue into nanosheets. The size of a nanomaterial determines its properties and interactions with the environment. For fluorescence imaging in cells or whole organisms, fluorophores should be as small as possible to not perturb the system. Exfoliation into 2D sheets is one step but it is also important to decrease the lateral size into the nanoscale. Therefore, we first reduced the size of EB by planetary ball (PB) milling and then exfoliated EB-NS via tip sonication, which allowed for the controlled decrease in height and diameter with sonication time (Fig. 1a and Supplementary Fig. 1).

Milling techniques such as PB are routinely employed for silicates[36], whereas tip sonication is a widely used method to disperse nanomaterials such as carbon nanotubes[37]. Tip sonication for 6 h in isopropanol yielded nanosheets of lateral sizes between 20 and 300 nm, and heights of around 1–13 nm (Fig. 1b–d). Atomic force microscopy (AFM) images (Fig. 1b, c) indicate that EB height correlated linearly with diameter (Fig. 1d). The height profiles of EB-NS (Fig. 1e, f) typically contain a peak, which can be explained by the convolution through the AFM tip. The smallest observed height (≈1 nm) corresponds to the monolayer of EB bulk material reported in literature[29,38,39] (Supplementary Fig. 2), but the exact height measured with AFM might vary depending on hydration and underlying substrate morphology[29]. To further purify EB-NS samples, we typically used syringe cut-off filters (0.20 µm/0.45 µm) to remove the remaining larger particles from the samples.

Photophysical properties of EB-NS. In a next step, we explored how reducing the size and dimensionality of EB into the nanoscale regime affects its luminescence properties relative to macroscopic EB powder[27]. Fluorescence quantum yields of one-dimensional materials such as SWCNTs have been shown to decrease with size, probably due to exciton diffusion and their collision with SWCNT ends[40]. Interestingly, EB fluorescence spectra did not change/shift with longer sonication times (Fig. 2a) corresponding to smaller dimensions (Fig. 1). EB-NS are extremely photostable as evidenced by the constant fluorescence emission intensity over several hours compared with the rapid bleaching of a typical organic dye (Fig. 2b). These measurements were performed on an organic dye (Rhodamin B) and on EB-NS, which were adsorbed on a glass surface under continuous excitation with a 561 nm laser (100 mW total power output) for >2 h. In addition, EB-NS show no change or shift in fluorescence emission in the presence of small redox active molecules that are known to affect the fluorescence of many dyes and fluorescent nanomaterials (Supplementary Fig. 3). EB-NS fluorescence is characterized by a large Stokes shift with a single emission maximum at ≈910 nm and an absorption maximum at ≈630 nm, as shown in the 2D excitation-emission spectrum and in the reflectance spectrum (Fig. 2c and Supplementary Fig. 4). EB-NS have a similar zeta potential (−22 mV) to spherical silica nanoparticles, which highlights that they can be dispersed and applied in aqueous solutions (Supplementary Fig. 5)[41].

To estimate the number of luminescent centers in a single EB-NS, we performed single-particle fluorescence saturation measurements of EB-NS using scanning confocal microscopy and pulsed laser excitation (20 MHz pulse rate). Only EB-NS below the resolution limit were studied (Fig. 2d, Supplementary Fig. 6, and Supplementary Table 1). Larger single sheets showed higher fluorescence intensities and could be distinguished from resolution-limited ones (see also Figs. 3 and 4). This finding complies with the hypothesis that the number of luminescent centers changes with the size of EB-NS. To better understand how fluorescence scales with excitation intensity, the laser power was stepwise increased and decreased, while fluorescence intensity was recorded. It was not possible to reach the emission saturation plateau with the maximum laser intensity. However, the nonlinear dependence between fluorescence intensity and laser power allowed us to fit the data with a fluorescence brightness saturation function (I):

$$I = I_{sat}\frac{P_{exc}}{P_{exc}+P_{sat}}, \qquad (1)$$

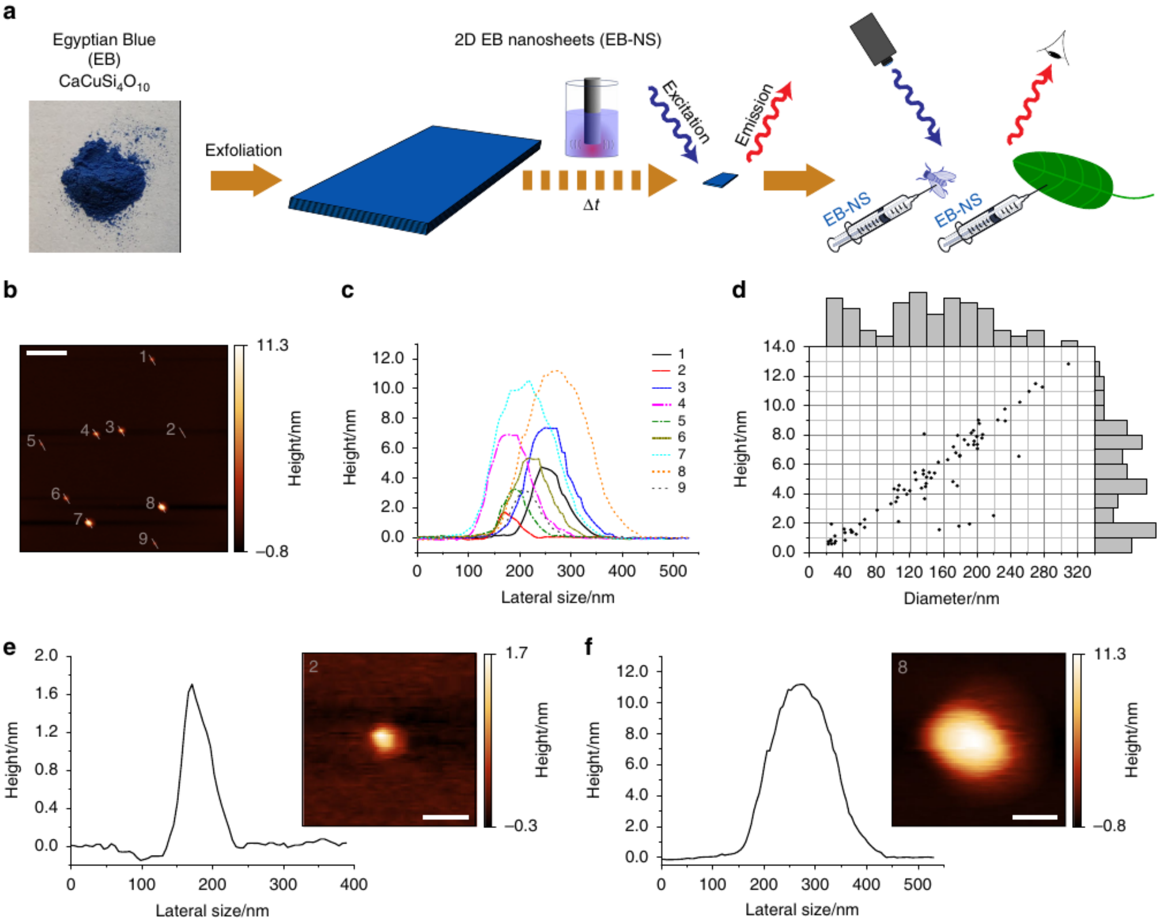

Fig. 1 Exfoliation of Egyptian Blue (EB) into Egyptian Blue nanosheets (EB-NS). a EB bulk powder ($CaCuSi_4O_{10}$, photograph taken in our lab) is exfoliated into EB-NS via tip sonication to study their near-infrared (NIR) photophysical properties. These nanostructures are furthermore used for in-vivo NIR imaging in plants and *Drosophila* embryos. **b** Representative AFM image of EB-NS. Scale bar = 1 µm. **c** Corresponding height profiles (highlighted by a white line in **b**). **d** Height and diameter distribution after 6 h of tip sonication. The bars at the axis are histograms. $n = 78$ EB-NS. **e**, **f** Height profiles and magnified images of the smallest and largest nanosheets shown in **b**. Scale bar = 100 nm.

where P_{exc} is the excitation power, P_{sat} is the saturation power, and I_{sat} is the nanoparticle luminescence intensity that can be detected at the saturation excitation power[42].

The obtained saturation values correspond to a fluorescence emission of 122×10^3 to 1250×10^3 photons s^{-1}. By taking into account factors such as the average lifetime of the excited state (≈100 µs; Supplementary Fig. 7), the quantum yield (≈0.1[28]) of bulk EB, the efficiency of the optical setup (see Supplementary Methods for an accurate calculation and Supplementary Table 1), it was thus possible to estimate the number of luminescent centers N (122–1250).

From the crystal structure of EB, it follows that there are 3.8 Cu^{2+} ions nm^{-2} of a single-layer EB-NS[43] (Supplementary Fig. 2). If every Cu^{2+} ion serves as luminescent center, these numbers would be in agreement with around 6–18 nm large (squared) single-layer EB-NS. From a resolution-limited EB-NS image, we cannot derive the lateral size and height directly. Therefore, these numbers are rather a minimum size that is in agreement with the experiment. Nevertheless, these data suggest that a large proportion, if not all, of Cu^{2+} ions act as luminescent centers. Furthermore, EB-NS showed no change of fluorescence intensity at different polarization directions (Fig. 2e) compared with a typical organic dye (Atto 488). Similar to NIR emitting lanthanide complexes, bulk EB has a long fluorescence lifetime ranging from 107 µs to 142 µs at room temperature[28,44] and this behavior is retained in EB-NS (Supplementary Fig. 7). The long fluorescence lifetime is most likely a consequence of the parity-forbidden nature of the transition, as the local D_{4h} symmetry of the Cu^{2+} ion in EB features an inversion center[27].

NIR fluorescence imaging of single EB-NS. Larger EB-NS typically exhibit a layered structure as observed in scanning electron microscopy (SEM) images (Fig. 3a, b and Supplementary Fig. 8). PB milling followed by exfoliation via tip sonication enabled us to continuously control the decrease in size of EB from large macroscopic particles to micrometer large structures down to EB-NS. These large and layered EB-NS can be imaged by a NIR fluorescence microscope, but do not show a uniform fluorescence intensity profile, indicating that differences in thickness or geometry might affect fluorescence emission intensities. EB-NS smaller than the resolution limit of light microscopy can also be imaged in the NIR (Fig. 3c, d, e). To prove this point, both a Si-based and an InGaAs camera were employed in a wide-field setup. The laser intensities in

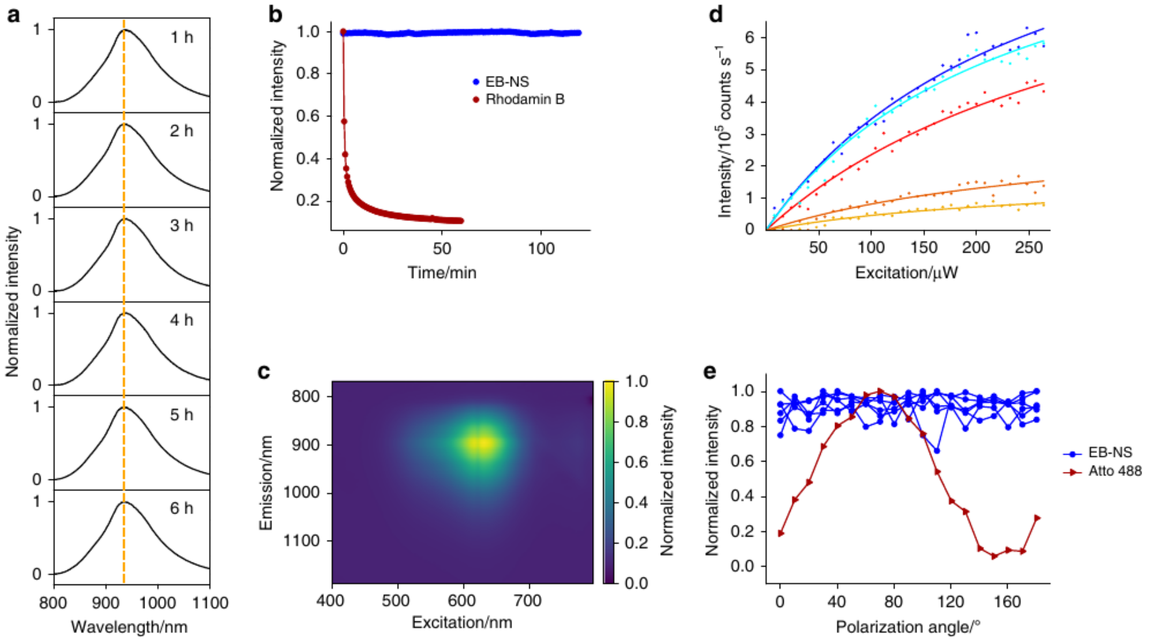

Fig. 2 NIR fluorescence properties of EB-NS. a Normalized NIR fluorescence spectra of EB-NS after different tip sonication times show no wavelength shifts. **b** EB-NS fluorescence (NIR) under continuous laser excitation (561 nm, 100 mW, corresponding to about 1 W cm^{-2}) does not bleach. In contrast, the fluorescent dye Rhodamin B (in the visible) quickly bleaches. **c** 2D excitation-emission spectrum of EB-NS. **d** Fluorescence saturation curves of different EB-NS (size below the resolution limit). **e** EB-NS display no fluorescence polarization. The dye Atto 488 is used as reference due to its distinct fluorescence polarization.

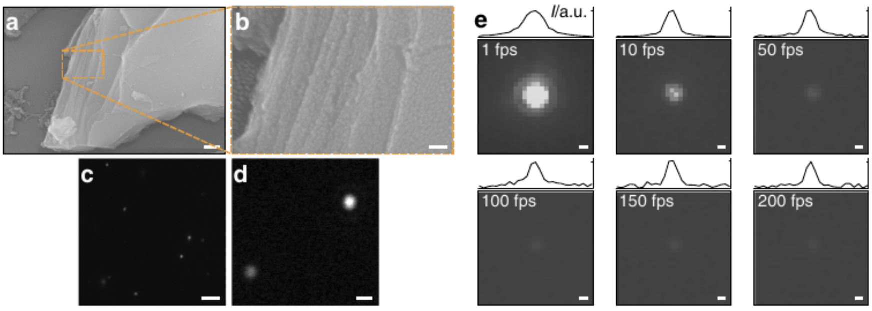

Fig. 3 SEM and NIR imaging of EB-NS. a, **b** Scanning electron microscopy (SEM) images of a larger EB particle. The blow-up clearly shows the typical lamellar structure of this material. Scale bar = 200 nm and 50 nm (respectively). **c**, **d** NIR images of EB-NS taken with a Si-based camera at increasing magnification show that single EB-NS can be resolved via NIR fluorescence microscopy down to the resolution limit of light microscopy. Excitation wavelength = 561 nm. Scale bar = 5 µm and 1 µm (respectively). **e** NIR images of a single EB-NS with a diameter below the resolution limit (≈500 nm) are captured with an InGaAs camera, optimized for NIR imaging at different frame rates up to 200 fps. The upper traces show the intensity profile of the image normalized to the maximum value. Excitation wavelength = 561 nm. Scale bar = 500 nm.

this setup corresponded to the left region (<10 µW) in the confocal setup used for saturation experiments (Fig. 2d). Si-based cameras have the highest quantum yield in the visible range and not the NIR, which limits the possible speed of imaging to around 50 fps (Fig. 3c, d and Supplementary Fig. 9). In contrast, with an InGaAs camera, resolution-limited EB-NS could be imaged at video rates up to 200 Hz (Fig. 3e). These images clearly demonstrate that the NIR fluorescence properties of macroscopic EB particles are retained in nanosheets.

Correlation between size and fluorescence intensity of EB-NS. The previous observations raise the question of how fluorescence intensity scales with size and if there is a lower limit, which is also relevant for potential bioimaging applications. Unfortunately, NIR microscopy is not able to directly assess the EB-NS size below the resolution limit. The resolution limit of light microscopy is described by the Abbe law ($\lambda/2 \approx 910$ nm$/2 \approx 450$ nm) and an exemplary resolution-limited single EB-NS is shown in Fig. 3e. The photon counting experiments from Fig. 2d show that there are many luminescent Cu^{2+} centers in one EB-NS, but because of the resolution limit it is not possible to assess the actual size. To provide an unambiguous answer, a correlative method that measures both size and fluorescence intensity of the same single nanosheet is required.

To understand whether and how nanomaterial fluorescence intensity is affected by size, we performed two independent

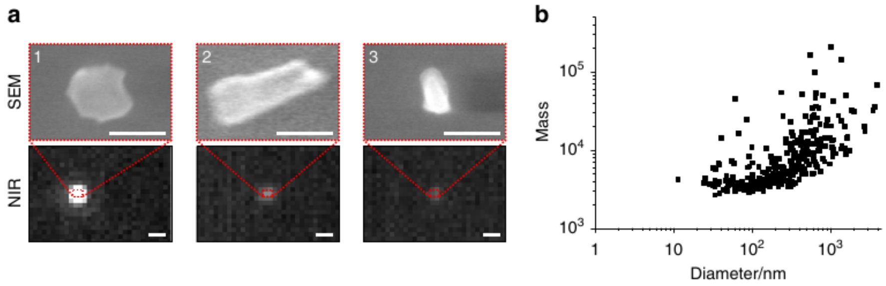

Fig. 4 Correlative measurements of size and fluorescence intensity of EB-NS. a SEM and corresponding NIR images of resolution-limited EB-NS. Scale bar = 200 nm and 1 µm (respectively). **b** Fluorescence intensity as a function of hydrodynamic diameter of EB-NS obtained by the corrected Stokes–Einstein equation. Mass stands for the total integrated brightness of the particle, and the maximum value along each trajectory was taken. From this analysis, one notices that even the smallest EB-NS (≈10 nm) still fluoresce. The general trend indicates that EB-NS of larger size are brighter. $n = 292$ EB-NS.

correlative analyses: (1) dual SEM-NIR fluorescence imaging and (2) single-particle tracking of EB-NS in a viscous glycerol solution. For the first approach, EB-NS were deposited on a glass cover slide with a grid. The labeled meshes enabled us to image the same nanostructures both under our NIR fluorescence imaging setup and under the SEM. As shown in Fig. 4a, it was thus possible to further confirm that diffraction-limited particles <200 nm (long axis) can be imaged with our protocol. Smaller EB-NS could not be found in the SEM most likely because the contrast of a thin silicate nanosheet on glass (SiO_2) is too low and the material is non-conducting. However, scanning transmission electron microscopy (STEM) images showed EB-NS down to few tenths of nanometer in agreement with the AFM data (Supplementary Fig. 10).

In the second correlative approach, single EB-NS were imaged and their fluorescence intensity quantified in a viscous glycerol solution (chosen to slow down diffusion). This method allowed us to simultaneously quantify fluorescence intensity and Brownian motion as a measure of size of the same EB-NS. For this purpose, the particle trajectories were tracked and the mean square displacement (MSD, $\langle \mathbf{r}^2 \rangle$) determined. We used the maximum value of the total integrated brightness of the tracked blob along each trajectory ("mass") as a measure of fluorescence intensity, to account for out-of-focus movement or rotations. A size equivalent can be derived from the trace of the random walk (Brownian motion) by employing the Stokes–Einstein equation. In Supplementary Figs. 11 and 12, trajectories and corresponding MSDs and NIR fluorescence images of exemplary EB-NS are shown. The trajectories (see Supplementary Fig. 11) show that the brighter particles move slower, indicating again that fluorescence intensity depends on size. To further investigate this finding, MSD curves were plotted and fitted: to estimate the EB-NS size, the fit was extended up to a certain lag time τ (25 s) and the diffusion constant (D)

$$D = \frac{\langle r^2 \rangle}{4\tau} \tag{2}$$

was calculated. The Stokes radius R is related to the diffusion constant via the Stokes–Einstein equation:

$$R = \frac{k_B T}{6\pi\eta D}, \tag{3}$$

where η is the dynamic viscosity of the solvent (Supplementary Fig. 13), T the temperature (Supplementary Fig. 14), and k_B the Boltzmann constant. As EB-NS are rather anisotropic with a large aspect ratio (Figs. 1 and 3, and Supplementary Fig. 8), one could assume that diffusion is dominated by the diameter and not the height similar to a spherical particle. Approximations that correct the Stokes–Einstein equation for anisotropy have been used, e.g., to analyze carbon nanotube diffusion and length[45]. Similarly, we approximated the EB-NS by a nanometer-sized spheroid, inspired by the work of Happel et al.[46], and confirmed the results by COMSOL simulations (see Supplementary Methods and Supplementary Fig. 15 for details). We calculated a correction factor of $A = 1.49$ and corrected the results obtained from the Stokes–Einstein by this value leading to larger hydrodynamic radii. Using this method, both fluorescence intensity and hydrodynamic radii of single EB-NS are accessible (Fig. 4b and Supplementary Figs. 16 and 17).

The sizes found in Fig. 4b are in agreement with the AFM-derived sizes in Fig. 1 but represent the (larger) hydrodynamic radii and not the actual physical particle radii (Supplementary Fig. 11). The results show again that larger EB-NS are brighter than smaller ones, indicating that fluorescence intensity correlates with the number of luminescent Cu^{2+} centers and thus the volume. The spread of data points along the fluorescence intensity axis at a given Stokes radius is most likely due to different layer numbers for sheets of similar diameter (and the already discussed out-of-focus issue as well). A power-law fit shows that fluorescence intensity scales with the square root of the diameter (Supplementary Fig. 16). However, future purification approaches that lead to samples of precise layer number and sheet diameter could increase the experimental accuracy and further enhance our understanding of how EB-NS fluorescence scales with dimension. Together with the photon counting experiments in Fig. 2, these results indicate that even the smallest EB-NS are fluorescent and fluorescence emission intensity correlates with the number of Cu^{2+} ions. Therefore, dimensionality does not appear to affect per se fluorescence properties beyond the change in the number of light-absorbing and -emitting Cu^{2+} centers.

Single-particle tracking of EB-NS in *Drosophila melanogaster* embryos. To demonstrate the potential of EB-NS for bioimaging applications, we performed single-particle tracking and microrheology measurements of EB-NS in embryos of the fruit fly *D. melanogaster*. This fly species is a widely employed model organism for studies ranging from fundamental genetics to developmental cell biology. During embryonal development the nuclei arrange in complex patterns mediated by microtubules and the actin cortex, but the underlying mechanisms and mechanics are poorly understood[47]. Following fertilization, the embryo develops as a syncytium[47] in which the nuclei arrange in a regular 2D array linked to the actin cortex of the plasma membrane (Fig. 5a).

The dynamics of the nuclei and their associated centrosomes is determined by the cortical link and internuclear interactions

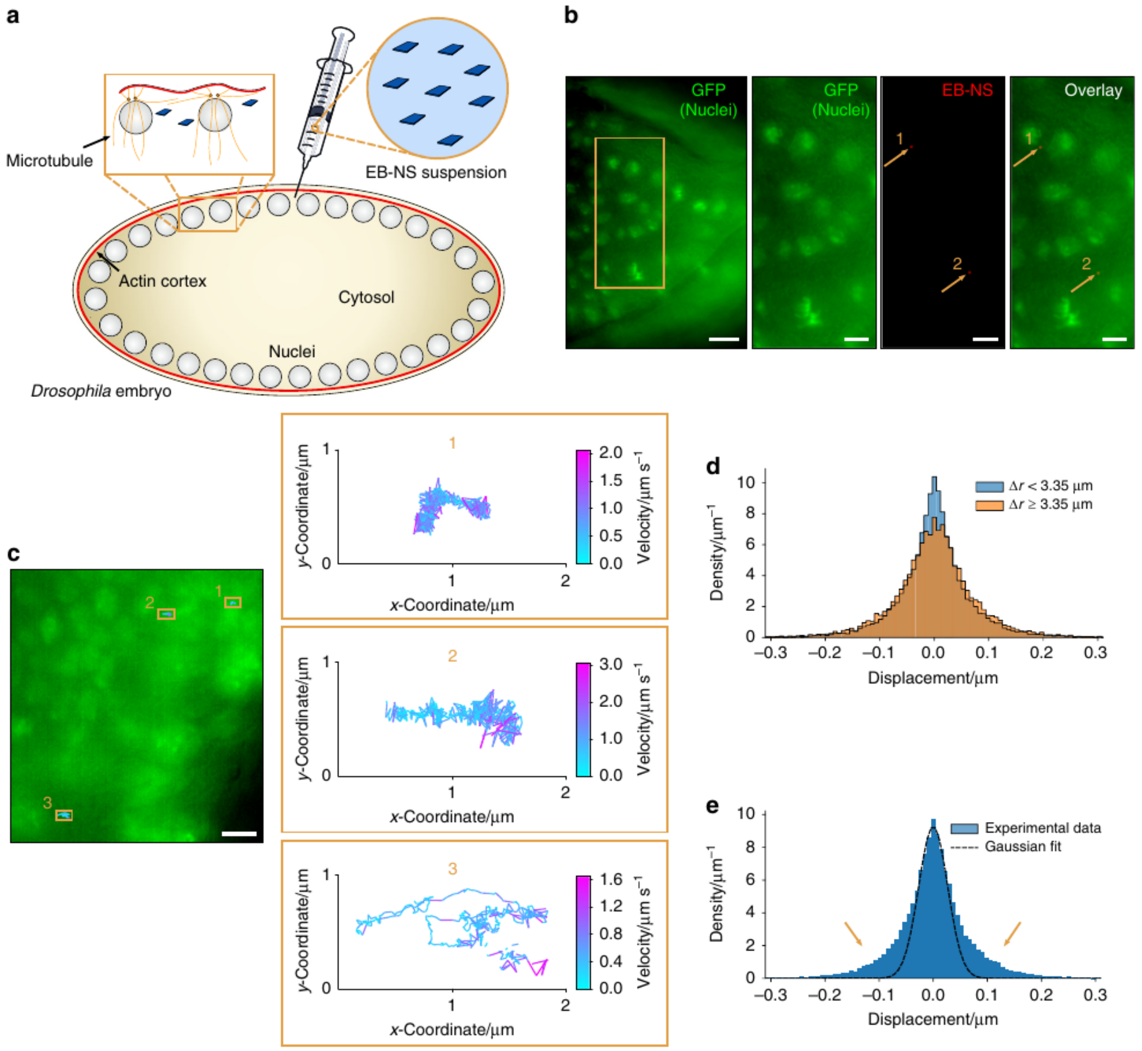

Fig. 5 In-vivo single-particle tracking and microrheology with EB-NS. a Experimental scheme for microinjection of EB-NS into syncytial *Drosophila* embryos. During the syncytial blastoderm stage, the peripheral nuclei are linked to the actin cortex of the plasma membrane (red). **b** EB-NS (red) inside a *Drosophila* embryo during gastrulation stage (stage 6) expressing Histone2Av-GFP (green) that labels the nuclei. Overview and magnified region (orange rectangle) with GFP (green), NIR EB-NS (red), and overlay channels are shown. Arrows pinpoint to the two EB-NS in this field of view. Scale bar = 10 µm (overview) and 5 µm (other channels). **c** Color-coded trajectories representing the instantaneous velocity of three tracked nanosheets moving in the space between the nuclei (lag time = 0.1 s). Particles #1, #2, and #3 have diameters (measured in the image) of 0.64 µm, 0.68 µm, and 0.52 µm, and are most likely resolution-limited. Scale bar = 5 µm. **d** Van Hove histogram of displacements of two subpopulations of injected EB-NS: close to nuclei vs. distant from nuclei. The distance (Δr) was computed for all points of all trajectories as the minimum distance to the border of any nucleus. **e** Van Hove plot of all tracked EB-NS and Gaussian fit for small displacements (range [−0.03 µm, +0.03 µm]). The tails (see arrows) of the distribution exceed the Gaussian curve, which indicates the presence of active processes in *Drosophila* that lead to larger displacements than expected from thermal motion. $n = 38$ tracked EB-NS (21 embryos).

mediated by microtubules[48]. It has been hypothesized that the viscoelastic properties and the molecular motors play a key role in this process[47]. To elucidate the micromechanical properties of the cellular matrix, we introduced EB-NS into *Drosophila* embryos and tracked single EB-NS via NIR fluorescence microscopy. Imaging in *Drosophila* is challenging due to autofluorescence in the visible region and its high sensitivity to phototoxicity; therefore, NIR imaging would be very beneficial.

For assessing the relative location of the EB-NS in *Drosophila*, mutants expressing green fluorescent protein (GFP)-labeled histones in their nuclei were used (Fig. 5b). Using this approach, we followed the traces of single EB-NS in vivo (Fig. 5b), allowing long-term imaging without bleaching or developmental abnormalities despite the high temporal resolution with frame rates of 10 Hz. In addition, the low autofluorescence in this spectral range enabled a higher contrast of the NIR EB-NS image compared to the visible GFP image (Fig. 5b). These results highlight the great advantages of a non-bleaching NIR nanoscale fluorophore compared with typical organic dyes. To further prove the potential of EB-NS as NIR fluorophore for bioimaging, we were inspired by recent studies in which NIR fluorescent carbon nanotubes were used to explore the extracellular space between

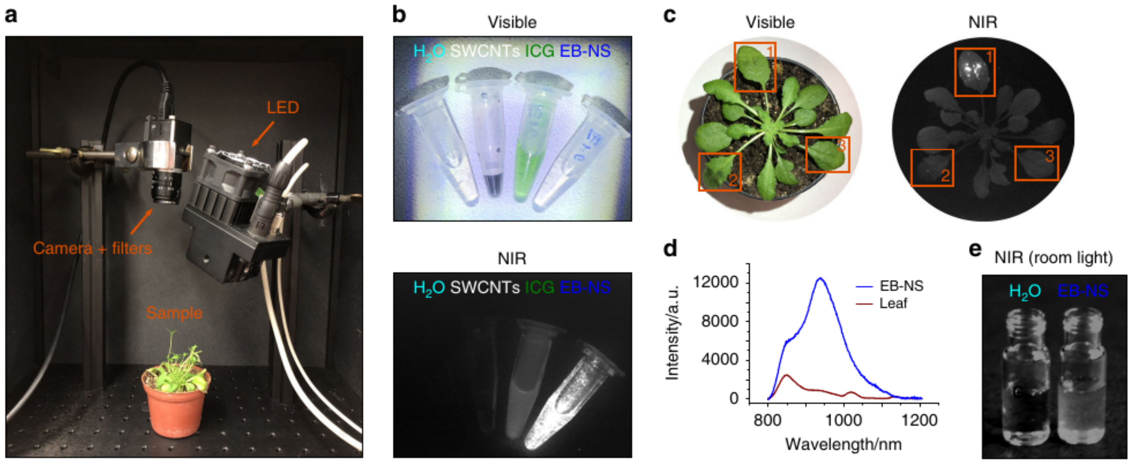

Fig. 6 Stand-off detection of EB-NS fluorescence in plants through low-cost and widely available imaging devices. a Photograph of a plant of *Arabidopsis thaliana* placed in a low-cost stand-off imaging system, which consisted of a LED, NIR filters and a Si-CMOS camera. **b** Visible and NIR fluorescence images of EB-NS (≈0.1 mg mL^{-1}) compared with other NIR nanomaterials and fluorophores at similar concentration (single-walled carbon nanotubes (SWCNTs), indocyanine green (ICG)). Water is used as negative control. **c** Visible and NIR images of an *Arabidopsis* plant, which was infused with EB-NS (frame 1), SWCNTs (frame 2), and buffer only (frame 3). **d** The NIR fluorescence spectrum of the leaf confirms the presence of EB-NS and its strong emission compared to the leaf background. Both results demonstrate the high brightness of EB-NS compared to state-of-the-art NIR nanomaterials (SWCNTs) and that this platform can be applied for stand-off detection using a low-cost optical setup. **e** The EB-NS emission can even be detected without LED excitation under room light conditions.

neurons[49]. The instantaneous velocity of the injected EB-NS moving between nuclei was therefore analyzed (Fig. 5c and Supplementary Fig. 18). The goal was to use EB-NS as a probe for the extracellular space as a function of the distance to nuclei. To best display our results, established analysis tools such as the Van Hove histogram of displacements[50] were chosen (Fig. 5d). The analysis revealed two subpopulations. EB-NS closer to nuclei showed smaller displacements, indicating a denser environment around the nuclei. EB-NS are likely to probe the mesh-size of the embryo's dense cytosol on the nanoscale and report mechanical properties on a different size scale than typical micrometer-sized beads used for microrheology[47]. Inside the embryo, one can expect active processes such as flow or motor-driven contractions ("active matter behavior"). Van Hove histograms provide access to test if there are such processes (Fig. 5e). The tails of the distribution go beyond the Gaussian function fit (thermal motion) and indicate the presence of active processes[50]. These could be, e.g., microtubules and kinesin motors (in the spindle close to the nuclei) that move the nuclei apart from each other and thereby lead to larger displacements of nearby EB-NS. Our results therefore show that EB-NS are powerful probes for studies of biological systems.

Biocompatibility and stand-off detection in living plants. In the context of biological applications, toxicity is a major concern and, e.g., a potential drawback of quantum dots that contain toxic elements and 2D materials in general[51,52]. To evaluate cytotoxicity, viability assays with EB-NS exposure to different cell lines (A549, 3T3, and MDCK-II) were performed. We observed no significant effects on the viability of these cell lines, highlighting the biocompatibility of EB-NS (Supplementary Fig. 19). In contrast, Cu^{2+} from soluble $CuSO_4$ decreased cell viability, which shows that EB-NS does not release relevant Cu^{2+} ion concentrations as expected from a stable silicate. Overall, this study demonstrates that EB-NS are powerful and biocompatible nanoprobes in living organisms for single-particle tracking and microrheology measurements in the transparent NIR window.

Another potential application of NIR fluorescent EB-NS is non-contact stand-off detection of nanoprobes in living organisms with minimal perturbation. The low autofluorescence in the NIR region provides a high contrast, but stand-off detection requires especially bright fluorophores, because only a small portion of emitted light reaches the detector. Recently, NIR fluorescent SWCNT sensors enabled plants to report to electronic devices chemical signaling processes, pollutants in the environment[53], and explosives[54]. Optical nanosensors are poised to allow the engineering of smart plants that communicate with and actuate agricultural and phenotyping devices for improving crop productivity and resource use[24].

Herein, we developed a low-cost optical setup to image the NIR emission of EB-NS from a distance >10 cm and compared it with several other NIR fluorophores. The setup consisted of a white light LED and a camera (1280 × 1024 pixels) equipped with NIR (900–920 nm) long-pass filters (Fig. 6a) corresponding to 76 µm pixel^{-1}. The high brightness of EB-NS allowed us to use a simple CMOS camera (Complementary Metal Oxide Semiconductor, Si-based) instead of expensive electrically or nitrogen-cooled InGaAs cameras (>40k €), which would have a much higher quantum yield in this spectral range. Quantum yield of Si-based cameras decrease with increasing wavelength and therefore this low-cost setup favors fluorophores with lower emission wavelength. Therefore, ICG should appear slightly brighter and SWCNTs slightly dimmer than they really are and EB-NS would be in the middle. However, the SWCNT sample also contained (6,4)-SWCNTs that emit at 870 nm. These different experimental conditions should be taken into account when assessing the performance of this low-cost setup. In the visible image (Fig. 6b), one can easily distinguish SWCNTs (black) from ICG (green), whereas the solution with EB-NS is transparent similar to the water control.

In contrast, in the corresponding NIR fluorescence image (Fig. 6b), EB-NS are significantly (2×) brighter than ICG and 10× brighter than SWCNTs (Fig. 6b and Supplementary Fig. 20). Interestingly, stand-off detection of the NIR emission of EB-NS is also possible without LED excitation: room or sunlight alone is sufficient to generate detectable NIR fluorescence from EB-NS (Fig. 6e).

Buffered EB-NS were infused into the leaves of *Arabidopsis thaliana*, a well-established plant model system (Fig. 6c, d)[53], using a standard method for nanomaterial delivery into plant leaves in-vivo[53]. The same approach was used for the infiltration of SWCNTs in separate leaves in the same plant, which served as a visual comparison with EB-NS. As it can be observed from the NIR image in Fig. 6c, plant leaves are characterized by a background autofluorescence in this wavelength region that hinders the visualization of SWCNTs fluorescence (frame 2) through a Si-based CMOS camera, whereas EB-NS can be detected with a strong fluorescence signal (frame 1). Similarly, fluorescence spectra of these leaves (Fig. 6d) show the strong EB-NS emission compared to the (autofluorescence) background. These stand-off detection experiments highlight that EB-NS can be delivered into living organisms with high background fluorescence such as plants and can be detected using low-cost and widely available stand-off imaging devices.

Discussion

Our results show that EB-NS have useful properties for NIR bioimaging applications including ultra-high photostability, high brightness for NIR fluorophores, and biocompatibility. The remarkable properties of EB-NS are retained even when the dimensions of the nanosheets are reduced. Our data indicates that most if not all copper ions serve as luminescent centers that emit NIR light. It only affects the absorption cross-section by changing the number of light-absorbing Cu^{2+} ions. In contrast, the quantum yield of NIR fluorescent SWCNTs increases with length. As a consequence, shorter SWCNTs (<100 nm) are much less bright than longer ones[40]. Therefore, SWCNTs cannot be shortened without disadvantages. Although it has been reported that for bioimaging applications the NIR-II (1000–1700 nm) windows further improves tissue penetration[5], a major advantage of the EB-NS fluorescence in the NIR-I region (800–1000 nm) is the wide availability of cameras[55,56]. Instead of expensive (>40k €), liquid nitrogen-cooled, low-resolution InGaAs-based cameras, low-cost, (1k €) high-resolution, Si-based cameras can be used for detection. In the past, (6,4)-SWCNTs with smaller diameter that emit in the NIR-I region at 870 nm have been isolated exactly for this purpose[57]. Even though the quantum yields of Si-based cameras rapidly decrease in the NIR (around 5% >900 nm), they are still able to image EB-NS using a normal microscope or a low-cost stand-off detection device. Furthermore, there exist (bulk) pigment homologs Han Blue ($BaCuSi_4O_{10}$) and Han Purple ($BaCuSi_2O_6$), which have a red-shifted emission spectrum up to 1000 nm, and they can be exfoliated into nanosheets using the same protocol as for EB (Supplementary Fig. 21). The capability of imaging EB-NS even with only room light excitation using Si-based cameras is particularly relevant for commercial applications beyond the well-equipped research laboratories or biomedical research, e.g., the engineering of smart plants for high-throughput phenotyping and precision agriculture. Another major advantage of EB-NS is their low toxicity, proven by the performed viability assays on cells (Supplementary Fig. 19). With our study, we add EB-NS to the library of 2D materials in general and especially exfoliated silicates and clays[58,59]. In the future, EB-NS and their physicochemical properties could be further investigated to find non-expected properties as in other 2D materials such as transition metal dichalcogenide nanosheets[60]. In addition, the surface chemistry could be tailored with biomolecules similar to silica nanoparticles and silicate-coated core-shell nanoparticles[61,62].

In summary, we developed a method to exfoliate the calcium copper silicate EB into nanosheets (EB-NS) and demonstrated that their NIR optical properties are retained at the nanoscale with copper ions as luminescent centers. We add a promising 2D material to the class of NIR fluorophores with ultra-high photostability, high brightness and biocompatibility. EB-NS have a large potential for demanding biological applications such as in-vivo imaging in complex biological matrices, including animal and plant model systems.

Methods

Exfoliation of Egyptian Blue. EB powder was purchased from Kremer Pigmente GmbH & Co. KG., and EB-NS were prepared as follows. If not stated otherwise, a first milling step was carried out. To produce sufficient amounts of nanoparticles, we used a PB mill (PB, Pulverisette 7 Premium Line, Fritsch, Germany) equipped with 20 mL agate beakers and 5 mm agate balls. The milling was performed in deionized water at 900 r.p.m. for up to 60 min. The resulting grainsize distribution was analyzed by laser diffraction carried out with a LS13320, Beckman&Coulter laser particle sizer (Germany). Three runs after a short tip sonication step were done. PIDS was used and an optical model R.I. 1.6/1 was applied. The so-generated and characterized EB slurry was afterwards allowed to settle down overnight and then decanted: only the supernatant portion of the slurry was dried and the so-obtained powder (visibly brighter, a consequence of the dichroism of EB[25]) was finally processed with a long-tip sonication step. In more detail, 10 mg of EB PB-milled powder was transferred to a glass vial together with 5 mL of isopropanol (Fischer Chemical, 99.98%) or milli-Q water. Tip sonication was performed in a glass vial with a Fisherbrand™ Model 120 Sonic Dismembrator (Fischer Scientific) in an ice bath for 1–6 h at 60–72 W (if not stated otherwise: typical tip sonication time and power percentage were 6 h and 60%, respectively). EB dispersions were stored at room temperature and vortexed prior to use (Vortex Mixer VV3, VWR International) for 10 s at maximum power (2500 min^{-1}, 10 W).

Atomic force microscopy. For this dataset, no PB milling step prior to tip sonication was performed. The pristine powder was ground with mortar and pestle till a visible color change could be observed, then it was tip sonicated (in isopropanol) as described in the previous section. One hundred microliters of EB-NS stock dispersion (6 h tip sonicated) were diluted 10× with isopropanol and vortexed for 10 s. Ten microliters of EB-NS were spin-coated (G3 Spin Coater, Specialty Coating Systems, Inc.) on a mica surface. The substrate was kept spinning at 500 r.p.m. (7 RCF) for 2 min (5 s of ramp time, 30 s of dwell time). An Asylum Research MFP-3D Infinity AFM (Oxford Instruments) was employed in AC mode (software version 15.01.103). Rectangular cantilevers from Opus (160AC-NA, MikroMasch Europe) were used (aluminum coating, tetrahedral tip, 300 kHz resonance frequency, force constant of 26 N m^{-1}). Image analysis was performed with Gwyddion (version 2.51).

NIR fluorescence spectroscopy. The setup consists of a monochromator (MSH-150, LOT-Quantum Design GmbH) equipped with a xenon arc lamp and a diffraction grating, an Olympus IX73 microscope with a 10× objective (UplanFLN 10×/0.30, Olympus), and a Shamrock 193i spectrograph (Andor Technology, Ltd) coupled to an array NIR detector (Andor iDUs InGaAs 491). Spectra were recorded from EB-NS dispersions at an excitation wavelength of 615 nm with an exposure time up to 5 s and a slit width up to 500 µm. The Andor SOLIS software (version 4.29.30012.0) was employed for the acquisition of spectra, which were and further analyzed with Origin Pro 8.1. For 2D spectra, EB-NS were placed on glass substrates. The excitation wavelength was scanned in 4 nm steps with the monochromator, and at each wavelength a spectrum was recorded with an integration time of 1 s at a slit width of 10 µm. The 2D spectra were corrected for the quantum efficiency of the detector and the spectral irradiance of the xenon lamp of the monochromator using a self-written Python script.

Fluorescence saturation measurements. The main components of the employed setup were a laser source (Supercontinuum laser SC400-4-20, Fianium), a photodetector (single photon avalanche diode PDM series, MPD), and a 60× objective lens (Apo N, 60×/1.49 numerical aperture (NA) oil immersion, Olympus). For this dataset, no PB milling step prior to tip sonication was performed. The pristine powder was ground with mortar and pestle till a visible color change could be observed, then it was tip sonicated (in isopropanol) as described above. Ten microliters of the supernatant of a 6 h tip-sonicated EB-NS sample (1:100 diluted in isopropanol) were spin-coated on a glass cover slide. Spin-coating parameters were the same ones chosen for AFM measurements. Despite the polydispersity of EB-NS, scanning them using a confocal microscope through the diffraction-limited focal spot of 1.49 NA objective allowed us to select only the smallest particles with sizes estimated to be not exceeding the dimensions of the focal spot. The spot size of larger EB-NS exceeded the dimensions of a diffraction-limited focal spot, thus allowing us to distinguish them from smaller particles. After selecting a particle, we measured its fluorescence intensity at different excitation powers. Excitation of nanoparticles that have relatively long excited state lifetimes of the order of 100 µs (Supplementary Fig. 7) with a laser that has high repetition rate (20 MHz) allows one to extrapolate saturation of the nanoparticle's luminescence. The solid circles in Supplementary Fig. 6a show the dependence between the brightness of the particle and the excitation power that was measured directly before the objective lens. The excitation wavelength was 640 nm. The fluorescence intensity values were normalized to the detection efficiency of the microscope, taking into account the average collection efficiency of light by the 1.49 NA objective lens (70%, given the random orientation of the emission transition dipoles), transmissivity of all the optical elements involved (~50%) and detection efficiency of the single photon avalanche diode (PDM series, MPD) in the current spectral range (~5%). It is noteworthy that as a result of the above normalization, luminescence intensity in Fig. 2d corresponds to the total number of photons emitted by the particle.

The experimental data were fitted with a typical fluorescence saturation function[63]:

$$I = I_{\mathrm{sat}}\frac{P_{\mathrm{exc}}}{P_{\mathrm{exc}} + P_{\mathrm{sat}}}, \tag{4}$$

where P_{exc} is the excitation power, P_{sat} is the saturation power, I_{sat} is the nanoparticle luminescence intensity that can be detected at the saturation excitation power. This function yields the values of P_{sat} and I_{sat} for every saturation curve measured. Supplementary Table 1 shows the obtained values.

The obtained saturation luminescence intensity values allow one to estimate the number of luminescent centers N per particle. Taking into account the average excited state lifetime τ (~100 µs, Supplementary Fig. 7) and quantum yield Φ (~0.1[28]), we recalculated the number of emitted photons I_{sat} per second into the number of centers:

$$N = \frac{I_{\mathrm{sat}}}{\Phi\tau^{-1}}. \tag{5}$$

Fluorescence polarization measurements. The setup mainly consisted of a light source (LED, Lumencor), which emitted unpolarized excitation light, a photodetector (EMCCD camera, iXon Ultra DU-897U-CS0, Andor) and a 60× objective lens (Apo N, 60×/1.49 NA oil immersion, Olympus). Measurements were performed by recording fluorescence images of individual EB-NS at different positions on a linear polarizer, which was placed in front of the camera. The sample preparation steps coincided with the ones performed for fluorescence saturation measurements. Atto 488, purchased from Atto-Tec, was used as a reference.

NIR fluorescence imaging setup. An Olympus BX53 microscope equipped with 20× (MPlanFL N 20×/0.45, Olympus) and 100× (UPlanSApo 100×/1.35 Sil, Olympus) objectives was used. A Xeva-1.7-320 NIR camera (Xenics®) and a Zyla 5.5 sCMOS camera (Oxford Instruments) were used to observe the EB-NS fluorescence excited by a 561 nm laser (Cobolt Jive™ 561 nm). Typically, a droplet of an EB-NS dispersion was put on glass slides, dried and imaged at 10–50 mW excitation power. To assess bleaching, a solution of Rhodamin B (Sigma-Aldrich) in isopropanol was prepared and a drop of this solution was put on a glass slide for imaging. Dried EB-NS were put on a separate glass slide. At a continuous excitation of 100 mW at 561 nm, images with an integration time of 100 ms were recorded 120 times every 0.5 min in the case of Rhodamin B and every 1 min with an integration time of 1 s in the case of EB-NS. For Rhodamin B the Zyla camera was used and for EB the Xenics NIR camera was used. The specified fluorescence intensity corresponds to the mean gray value of the images.

For video-rate imaging and size-fluorescence correlation experiments, a modified setup equipped with a Cheetah 640TE3 camera (Xenics NV, Belgium) was used for NIR detection. Here, the light was passed through a dichroic mirror (HC BS R785, AHF, Germany) and a long-pass filter (FELH0900, Thorlabs, Inc., USA) before reaching the camera's sensor. Images were captured with the 100× objective.

Video-rate imaging of EB-NS with an InGaAs camera. EB-NS (previously milled and tip sonicated in isopropanol) underwent a single centrifugation step (240 × g for 2 h) to remove unexfoliated material. Ten microliters of EB-NS sample were spin-coated onto a #1 glass coverslip with the following settings: 1000 r.p.m. (14 RCF) for 1 min (40 s of ramp time, 20 s of dwell time). The sample was then placed under the NIR imaging setup and pictures were taken with a 100× objective, laser power of 500 mW and exposure times in the range from 1 s to 5 ms (corresponding to frame rates ranging from 1 to 200 fps). Data analysis was performed with ImageJ (v. 1.52a) and Origin Pro 8.1 software.

Scanning electron microscopy and SEM-NIR correlation. For a first qualitative observation of exfoliated EB-NS (Fig. 3a, b), no PB milling step prior to tip sonication was performed. The pristine powder was ground with mortar and pestle till a visible color change could be observed, then it was tip sonicated (in isopropanol) as described above. Ten microliters of EB-NS suspension were drop-casted on a Si wafer. Both gold sputtering and evaporation (≈2 nm of gold layer) were tested on different samples; nevertheless, the best imaging conditions were met when no gold deposition step was performed at all. Interestingly, EB was conductive enough to be seen at SEM without gold deposition. This sample was observed under a LEO SUPRA 35 microscope (Zeiss) with an Inlens detector at 20 kV (secondary electrons).

For the SEM-NIR correlation, EB-NS (previously milled and tip sonicated in isopropanol) were centrifuged (240 × *g* for 2 h). This way unexfoliated (bulk) material could be removed. Meanwhile, a #1.5 gridded glass coverslip (Gridded Glass Coverslips Grid-50, Ibidi, Germany) was stirred for 20 min at 70 °C in a 5 : 1 : 1 solution of milli-Q water : hydrogen peroxide : ammonia. Afterwards, the substrate was dried with a nitrogen gun and, to increase the adhesion of EB-NS on its surface, plasma treatment (Zepto, Diener Electronic GmbH +Co. KG, Germany) was performed: this step included 1 min of O_2 supply and 1 min of plasma process. After cleaning the substrate as described, 10 µL of EB-NS sample were spin-coated onto it with the following settings: 1000 r.p.m. (14 RCF) for 1 min (40 s of ramp time, 20 s of dwell time). The prepared sample was then observed at the NIR imaging setup (see corresponding section for more info) with a 100× objective, 1 s of exposure time, and 500 mW of laser power. Finally, the substrate was moved to the Quattro S SEM setup (Thermo Fisher Scientific, USA) employed for the size-fluorescence correlation analysis. Typical imaging settings here were: low vacuum mode, LVD detector (Thermo Fisher Scientific, USA), high voltage = 15 kV (secondary electrons), chamber pressure = 1.25 mbar (water), high voltage = 15 kV, and spot size = 3.5. Data analysis was performed with ImageJ (v. 1.52a) and Origin Pro 8.1 software.

Correlative size-intensity measurements in glycerol. EB-NS (previously milled and tip sonicated in water) were size-selected by means of two steps of liquid cascade centrifugation:[33,64] in this way, we could get rid of unexfoliated EB and increase the monodispersity of the pellet obtained after the last step (first centrifugation = 240 × *g* for 2 h, second centrifugation = 2660 × *g* for 2 h). Glycerol (0.5 mL) (Alfa Aesar, 99+%) was then added to the dried final pellet (≈1 mg) and the sample was finally tip sonicated in an ice bath for 2 min at 60% to achieve a homogeneous redispersion. For imaging, 10–20 µL of the glycerol sample were introduced into a flow chamber (µ-Slide VI 0.5 Glass Bottom, Ibidi, Germany) and placed under our NIR imaging setup. A 100× objective was employed to observe EB-NS at 8 fps (≈50 ms exposure time, 1000 frames) with a laser power of 250 mW, which, as shown in Supplementary Fig. 14, was not overheating the sample significantly during acquisition. Particle tracking and MSD calculations were performed using a self-written Python script based on the Trackpy package[65,66] (v0.4.2 on Python v3.7.3[67]), whereas the final steps of data analysis were performed on Origin Pro 8.1 software. For identification and linking of particles into trajectories, the following parameters in Trackpy were implemented: memory = 300, minimum number of points (i.e., trajectory length) = 300, search_range (i.e., maximum displacement between consecutive frames) = 9, diameter (of the tracked blob) = 11. The tracking of the Brownian motion of an EB-NS yields the trajectory of the particle as a set of time-dependent x and y positions for N time steps of length τ. From the x and y positions, the square displacement for the n-th time step $\mathbf{r}_n^2$ is calculated as

$$r_n^2 = (x(n\cdot\tau) - x((n-1)\cdot\tau))^2 + (y(n\cdot\tau) - y((n-1)\cdot\tau))^2, \tag{6}$$

where n ranges from 1 to N. The MSD $\langle\mathbf{r}^2\rangle$ is simply the mean over all single time step values:

$$\langle\mathbf{r}^2\rangle = \frac{1}{N}\sum_{n=1}^{N}\mathbf{r}_n^2. \tag{7}$$

Assuming the diffusion is restricted to two dimensions, the diffusion coefficient D and the MSD are linked via the relation

$$D = \frac{r^2}{4\tau}. \tag{8}$$

MSD curves were fitted up to a maximum lag time of 25 s, to measure the diffusion coefficient of each particle. Finally, from the Stokes–Einstein equation, the Stokes radius R is calculated as

$$R = \frac{k_B T}{6\pi\eta D}, \tag{9}$$

where η is the dynamic viscosity of the solvent (Supplementary Fig. 13), T the temperature (Supplementary Fig. 14), and k_B the Boltzmann constant. The Stokes–Einstein equation is only strictly valid for spherical particles. Due to the high anisotropy of EB-NS, we assumed that Brownian motion is dominated by the diameter of the nanosheets and not the much smaller height.

In-vivo microrheology of *D. melanogaster* embryos. EB-NS (previously milled and tip sonicated in water) were filtered with a 0.20 µm syringe filter. To further enhance the concentration of the smallest nanosheets in the sample, the filtered sample vial was placed in a concentrator (Eppendorf® centrifugal vacuum concentrator, Eppendorf, Germany) for 45 min at 45 °C and finally bath-sonicated for 10 min to reduce agglomeration. *D. melanogaster* embryos expressing Histone2Av-GFP[68] with an age of 0–1 h were collected and dechorionated with hypochlorite for 120 s, washed with water thoroughly, aligned on a piece of agar, transferred to a coverslip coated with glue and covered with halocarbon oil (Voltalef 10 S, Lehmann & Voss) after a slight desiccation. An aliquot of suspension in water of the EB-NS sample was injected using Microinjector FemtoJet® (Eppendorf) on an inverted microscope: the injection volume is calculated according to literature[69]. After around 30 min of incubation, the sample could be moved to the NIR setup mentioned above for colocalization experiments. EB-NS were excited with the 561 nm laser (up to 500 mW), whereas a fluorescence lamp (X-Cite® 120Q, Excelitas Technologies) was used for GFP excitation. Both channels were observed through a 100× objective and recorded with a Zyla 5.5 sCMOS camera. An exposure time of 0.1 s was chosen and images on both channels were taken for 60 s (10 fps). A 2 × 2 pixel binning was performed to lower the size of acquired data and thus facilitate the following particle tracking analysis. As for the EB-NS tracking in glycerol, custom-made scripts based on Trackpy were employed to analyze the acquired frames. Only the EB data were evaluated, since the nuclei did not display any significant motion during the acquisition. Typical parameters employed for particle tracking were: memory = 300 frames (features vanishing for more than 300 frames were considered separate particles), minimum number of data points = 200, maximum displacement between frames = 9 pixels, and diameter (of the tracked blob) = 11 pixels. The perimeter of the nuclei was manually measured on ImageJ and its coordinates implemented in a self-written Python code which could assess the minimum distance of each point along a trajectory to the closest nucleus perimeter. With a separate code, instantaneous velocity plots (lag time = 0.1 s) could be evaluated and plotted. Van Hove histograms were plotted in Python, too, inspired by past works in literature[50]. The overlying Gaussian fit was performed for small displacements (range [−0.03 µm, +0.03 µm]).

Stand-off detection. NIR images were acquired with a CMOS-based DCC3240M camera (Thorlabs), equipped with a 900 nm (FEL0900, Thorlabs) and a 920 nm (LP920, Midwest Optical Systems) long-pass filter, mounted in series to exclude the visible background. A white light source (UHP, Prizmatix) connected to a 700 nm (FESH0700, Thorlabs) and a 750 nm (FESH0750, Thorlabs) short-pass filter was used for excitation. Exposure times between 50 and 100 ms were used for all acquisitions.

Single-stranded DNA (ssDNA)-modified SWCNTs were obtained by placing 125 µL (2 mg mL^{-1} in PBS) $(AT)_{15}$ ssDNA (Sigma-Aldrich) and 125 µL (6,5) chirality enriched SWCNTs (Sigma-Aldrich, Product No. 773735) (2 mg mL^{-1} in PBS) for tip sonication (15 min, 30% amplitude). The obtained suspension was centrifuged twice for 30 min at ambient temperature (16100 × *g*). The amounts of ICG (≈90%, MP Biomedicals GmbH) and of a 6 h tip-sonicated sample of EB-NS in water were ≈0.1 mg mL^{-1}.

Seeds of *A. thaliana* (Col.0 ecotype) were sown on sterilized soil (8 h, 80 °C) and stratified for 2 days in the dark at 4 °C. The plants were grown under long day length (16 h light/8 h dark) in climate-controlled growth chambers at 22 °C, 60% humidity, and light intensity of 120–150 µmol m^{-2} s^{-1}. Delivery of nanomaterials and buffer into leaves of *Arabidopsis* was performed as described by Giraldo et al.[53]. In brief, 50 µl of the desired NIR fluorophore suspension were infused through the lower (abaxial) side of the leaf lamina with a needleless syringe. Spectroscopic measurements for the presence of EB-NS in the leaf was performed using the NIR fluorescence spectroscopy setup (5 s exposure time) as described above. Regarding the imaging of EB-NS under room light excitation, 1 mL of supernatant taken from a 6 h tip-sonicated sample in water was observed. A background picture was taken and used for background subtraction.

Reporting summary. Further information on research design is available in the Nature Research Reporting Summary linked to this article.

Data availability

The data that support the findings of this study are available from the corresponding author upon reasonable request.

Code availability

The codes that support the findings of this study are available from the corresponding author upon reasonable request.

Received: 17 December 2019; Accepted: 28 February 2020;

References

1. Eggeling, C. et al. Direct observation of the nanoscale dynamics of membrane lipids in a living cell. *Nature* **457**, 1159–1162 (2009).
2. Kruss, S. et al. High-resolution imaging of cellular dopamine efflux using a fluorescent nanosensor array. *Proc. Natl Acad. Sci. USA* **114**, 1789–1794 (2017).
3. Smith, A. M., Mancini, M. C. & Nie, S. Second window for in vivo imaging. *Nat. Nanotechnol.* **4**, 710–711 (2009).
4. Owens, E. A., Henary, M., El Fakhri, G. & Choi, H. S. Tissue-Specific Near-Infrared Fluorescence Imaging. *Acc. Chem. Res.* **49**, 1731–1740 (2016).
5. Hong, G., Antaris, A. L. & Dai, H. Near-infrared fluorophores for biomedical imaging. *Nat. Biomed. Eng.* **1**, 0010 (2017).
6. Carr, J. A. et al. Shortwave infrared fluorescence imaging with the clinically approved near-infrared dye indocyanine green. *Proc. Natl Acad. Sci. USA* **115**, 4465–4470 (2018).
7. Zhu, S. et al. Molecular imaging of biological systems with a clickable dye in the broad 800- to 1,700-nm near-infrared window. *Proc. Natl Acad. Sci. USA* **114**, 962–967 (2017).
8. Bruns, O. T. et al. Next-generation in vivo optical imaging with short-wave infrared quantum dots. *Nat. Biomed. Eng.* **1**, 0056 (2017).
9. Fan, Y. et al. Lifetime-engineered NIR-II nanoparticles unlock multiplexed in vivo imaging. *Nat. Nanotechnol.* **13**, 941–946 (2018).
10. He, S., Song, J., Qu, J. & Cheng, Z. Crucial breakthrough of second near-infrared biological window fluorophores: design and synthesis toward multimodal imaging and theranostics. *Chem. Soc. Rev.* **47**, 4258–4278 (2018).
11. Hong, G., Diao, S., Antaris, A. L. & Dai, H. Carbon nanomaterials for biological imaging and nanomedicinal therapy. *Chem. Rev.* **115**, 10816–10906 (2015).
12. Kruss, S. et al. Carbon nanotubes as optical biomedical sensors. *Adv. Drug Deliv. Rev.* **65**, 1933–1950 (2013).
13. Kruss, S. et al. Neurotransmitter detection using corona phase molecular recognition on fluorescent single-walled carbon nanotube sensors. *J. Am. Chem. Soc.* **136**, 713–724 (2014).
14. Polo, E. & Kruss, S. Impact of redox-active molecules on the fluorescence of polymer-wrapped carbon nanotubes. *J. Phys. Chem. C.* **120**, 3061–3070 (2016).
15. Polo, E. et al. Control of integrin affinity by confining RGD peptides on fluorescent carbon nanotubes. *ACS Appl. Mater. Interfaces* **10**, 17693–17703 (2018).
16. Bisker, G. et al. Protein-targeted corona phase molecular recognition. *Nat. Commun.* **7**, 1–14 (2016).
17. Galassi, T. V. et al. An optical nanoreporter of endolysosomal lipid accumulation reveals enduring effects of diet on hepatic macrophages in vivo. *Sci. Transl. Med.* **10**, 1–11 (2018).
18. Mann, F., Herrmann, N., Meyer, D. & Kruss, S. Tuning selectivity of fluorescent carbon nanotube-based neurotransmitter. *Sens.* **17**, 1521 (2017).
19. Zubkovs, V., Schuergers, N., Lambert, B., Ahunbay, E. & Boghossian, A. A. Mediatorless, reversible optical nanosensor enabled through enzymatic pocket doping. *Small* **13**, 1701654 (2017).
20. Nißler, R. et al. Quantification of the number of adsorbed DNA molecules on single-walled carbon nanotubes. *J. Phys. Chem. C.* **123**, 4837–4847 (2019).
21. Mann, F. A. et al. Carbon nanotubes encapsulated in coiled-coil peptide barrels. *Chem. A Eur. J.* **24**, 12241–12245 (2018).
22. Meyer, D., Hagemann, A. & Kruss, S. Kinetic requirements for spatiotemporal chemical imaging with fluorescent nanosensors. *ACS Nano* **11**, 4017–4027 (2017).
23. Fakhri, N. et al. High-resolution mapping of intracellular fluctuations using carbon nanotubes. *Science* **344**, 1031–1035 (2014).
24. Giraldo, J. P., Wu, H., Newkirk, G. M. & Kruss, S. Nanobiotechnology approaches for engineering smart plant sensors. *Nat. Nanotechnol.* **14**, 541–553 (2019).
25. Warner, T. E. *Synthesis, Properties and Mineralogy of Important Inorganic Materials* (Wiley, 2011).
26. Ajò, D. et al. Photoluminescence of some blue natural pigments and related synthetic materials. In: *5th Int. Conf. on Non-Destructive Testing, Microanalytical Methods and Environmental Evaluation for Study and Conservation of Works of Art.* 37–47 (1996).
27. Pozza, G., Ajò, D., Chiari, G., De Zuane, F. & Favaro, M. Photoluminescence of the inorganic pigments Egyptian blue, Han blue and Han purple. *J. Cult. Herit.* **1**, 393–398 (2000).
28. Accorsi, G. et al. The exceptional near-infrared luminescence properties of cuprorivaite (Egyptian blue). *Chem. Commun.* 3392–3394 https://doi.org/10.1039/b902563d (2009).
29. Johnson-McDaniel, D., Barrett, C. A., Sharafi, A. & Salguero, T. T. Nanoscience of an ancient pigment. *J. Am. Chem. Soc.* **135**, 1677–1679 (2013).
30. Johnson-McDaniel, D. & Salguero, T. T. Exfoliation of Egyptian Blue and Han Blue, two alkali earth copper silicate-based pigments. *J. Vis. Exp.* 1–10 (2014).
31. Nicolosi, V., Chhowalla, M., Kanatzidis, M. G., Strano, M. S. & Coleman, J. N. Liquid exfoliation of layered materials. *Science* **340**, 1226419–1226419 (2013).
32. Cunningham, G. et al. Solvent exfoliation of transition metal dichalcogenides: dispersibility of exfoliated nanosheets varies only weakly between compounds. *ACS Nano* **6**, 3468–3480 (2012).
33. Backes, C. et al. Guidelines for exfoliation, characterization and processing of layered materials produced by liquid exfoliation. *Chem. Mater.* **29**, 243–255 (2017).

34. Coleman, J. N. et al. Two-dimensional nanosheets produced by liquid exfoliation of layered materials. *Science* **331**, 568–571 (2011).
35. Wang, Q. H., Kalantar-Zadeh, K., Kis, A., Coleman, J. N. & Strano, M. S. Electronics and optoelectronics of two-dimensional transition metal dichalcogenides. *Nat. Nanotechnol.* **7**, 699–712 (2012).
36. Wu, S., Karius, V., Schmidt, B. C., Simon, K. & Wörner, G. Comparison of ultrafine powder pellet and flux-free fusion glass for bulk analysis of granitoids by laser ablation-inductively coupled plasma-mass spectrometry. *Geostand. Geoanal. Res.* **42**, 575–591 (2018).
37. Bachilo, S. M. et al. Structure-assigned optical spectra of single-walled carbon nanotubes. *Science* **298**, 2361–2366 (2002).
38. Chen, Y., Kan, M., Sun, Q. & Jena, P. Structure and properties of Egyptian Blue monolayer family: XCuSi$_4$O$_{10}$ (X = Ca, Sr, and Ba). *J. Phys. Chem. Lett.* **7**, 399–405 (2016).
39. Yang, S. S. et al. An exfoliated 2D Egyptian Blue nanosheet for highly selective enrichment of multi-phosphorylated peptides in mass spectrometric analysis. *Chem. A Eur. J.* **24**, 2024 (2018).
40. Hertel, T., Himmelein, S., Ackermann, T., Stich, D. & Crochet, J. Diffusion limited photoluminescence quantum yields in 1-D semiconductors: single-wall carbon nanotubes. *ACS Nano* **4**, 7161–7168 (2010).
41. Sikora, A. et al. A systematic comparison of different techniques to determine the zeta potential of silica nanoparticles in biological medium. *Anal. Methods* **7**, 9835–9843 (2015).
42. Chaze, W., Caballina, O., Castanet, G. & Lemoine, F. The saturation of the fluorescence and its consequences for laser-induced fluorescence thermometry in liquid flows. *Exp. Fluids* **57**, 58 (2016).
43. Pabst, A. Structures of some tetragonal sheet silicates. *Acta Crystallogr.* **12**, 733–739 (1959).
44. Li, Y. J., Ye, S., Wang, C. H., Wang, X. M. & Zhang, Q. Y. Temperature-dependent near-infrared emission of highly concentrated Cu2+ in CaCuSi4O10 phosphor. *J. Mater. Chem. C.* **2**, 10395–10402 (2014).
45. Streit, J. K. et al. Measuring single-walled carbon nanotube length distributions from diffusional trajectories. *ACS Nano* **6**, 8424–8431 (2012).
46. Happel, J. & Brenner, H. The motion of a rigid particle of arbitrary shape in an unbounded fluid. *Low Reynolds Number Hydrodyn.* 159–234 (1983).
47. Wessel, A. D., Gumalla, M., Grosshans, J. & Schmidt, C. F. The mechanical properties of early *Drosophila* embryos measured by high-speed video microrheology. *Biophys. J.* **108**, 1899–1907 (2015).
48. Winkler, F. et al. Fluctuation analysis of centrosomes reveals a cortical function of Kinesin-1. *Biophys. J.* **109**, 856–868 (2015).
49. Godin, A. G. et al. Single-nanotube tracking reveals the nanoscale organization of the extracellular space in the live brain. *Nat. Nanotechnol.* **12**, 238–243 (2017).
50. Toyota, T., Head, D. A., Schmidt, C. F. & Mizuno, D. Non-Gaussian athermal fluctuations in active gels. *Soft Matter* **7**, 3234–3239 (2011).
51. Zhao, J., Zhong, D. & Zhou, S. NIR-I-to-NIR-II fluorescent nanomaterials for biomedical imaging and cancer therapy. *J. Mater. Chem. B* **6**, 349–365 (2018).
52. Martín, C., Kostarelos, K., Prato, M. & Bianco, A. Biocompatibility and biodegradability of 2D materials: graphene and beyond. *Chem. Commun.* **55**, 5540–5546 (2019).
53. Giraldo, J. P. et al. Plant nanobionics approach to augment photosynthesis and biochemical sensing. *Nat. Mater.* **13**, 400–408 (2014).
54. Wong, M. H. et al. Nitroaromatic detection and infrared communication from wild-type plants using plant nanobionics. *Nat. Mater.* **16**, 264–272 (2017).
55. Hong, G. et al. Multifunctional in vivo vascular imaging using near-infrared II fluorescence. *Nat. Med.* **18**, 1841–1846 (2012).
56. Hong, G. et al. Through-skull fluorescence imaging of the brain in a new near-infrared window. *Nat. Photonics* **8**, 723–730 (2014).
57. Antaris, A. L. et al. Single chirality (6,4) single-walled carbon nanotubes for fluorescence imaging with silicon detectors. *Small* **11**, 6325–6330 (2015).
58. Stöter, M., Rosenfeldt, S. & Breu, J. Tunable exfoliation of synthetic clays. *Annu. Rev. Mater. Res.* **45**, 129–151 (2015).
59. Tao, H. et al. Scalable exfoliation and dispersion of two-dimensional materials – an update. *Phys. Chem. Chem. Phys.* **19**, 921–960 (2017).
60. Chhowalla, M. et al. The chemistry of two-dimensional layered transition metal dichalcogenide nanosheets. *Nat. Chem.* **5**, 263–275 (2013).
61. Parak, W. J. et al. Conjugation of DNA to silanized colloidal semiconductor nanocrystalline quantum dots. *Chem. Mater.* **14**, 2113–2119 (2002).
62. Ow, H. et al. Bright and stable core-shell fluorescent silica nanoparticles. *Nano Lett.* **5**, 113–117 (2005).
63. Plakhotnik, T. & Gruber, D. Luminescence of nitrogen-vacancy centers in nanodiamonds at temperatures between 300 and 700 K: Perspectives on nanothermometry. *Phys. Chem. Chem. Phys.* **12**, 9751–9756 (2010).
64. Backes, C. et al. Production of highly monolayer enriched dispersions of liquid-exfoliated nanosheets by liquid cascade centrifugation. *ACS Nano* **10**, 1589–1601 (2016).
65. Crocker, J. C. & Grier, D. G. Methods of digital video microscopy for colloidal studies. *J. Colloid Interface Sci.* **179**, 298–310 (1996).
66. Allan, D. et al. *soft-matter/trackpy: Trackpy v0.4.2.* https://doi.org/10.5281/ZENODO.3492186 (2019).
67. https://www.python.org/.
68. Gramates, L. S. et al. FlyBase at 25: looking to the future. *Nucleic Acids Res.* **45**, D663–D671 (2017).
69. Markow, T. A., Beall, S. & Matzkin, L. M. Egg size, embryonic development time and ovoviviparity in *Drosophila* species. *J. Evol. Biol.* **22**, 430–434 (2009).

Acknowledgements

We thank the Volkswagen foundation and the life@nano cluster for funding (S.K.). We thank Dr. Burkhard Schmidt for recording reflectance spectra; Dr. Elena Polo for initial exfoliation experiments; Dr. Nelli Teske, Dr. Jeremias Sibold, and Dr. Ingo Mey for help in the acquisition of SEM images; Angela Rübeling for expert technical assistance; Wentao Peng for assistance with zeta potential measurements; and Dr. Ellen Hornung for providing us with *Arabidopsis* plants. Furthermore, we thank Dr. Florian Rehfeldt for viscosity measurements, Dr. Heidrun Sowa for input on diffractometry, and Jonathan Bodenschatz and Nils Liebe for support in IR monitoring measurements and SEM sample preparation. Some experimental work was done in collaboration with the department of cell culture, Institute for Organic and Biomolecular Chemistry, Georg-August-University Göttingen. Parts of this work was funded by the National Science Foundation under Grant Number 1817363 to J.P.G.

Author contributions

S.K. conceived and designed the study. G.S. and V.K. performed and optimized the milling procedure. G.S. performed AFM experiments. G.S., H.P., and A.S. exfoliated materials and collected 1D spectra. H.P. and R.N. collected 2D spectra. A.C. performed single photon counting and anisotropy experiments. G.S. and L.V. performed and analyzed correlative SEM-NIR experiments. G.S. imaged single nanosheets and analyzed particle trajectories together with N.H., I.K., and A.J. G.S. together with R.N., F.A.M., and Z.L. performed biological imaging experiments with input from L.E., J.P.G., and J.G.. T.A.O. performed cell viability experiments. D.M. performed calculations and simulations concerning the correction factor for diffusion of (anisotropic) EB-NS in a solvent. G.S. and S.K. wrote the manuscript with contributions from all authors.

Competing interests

The authors declare no competing interests.

Additional information

Supplementary information is available for this paper at https://doi.org/10.1038/s41467-020-15299-5.

Correspondence and requests for materials should be addressed to S.K.

Peer review information *Nature Communications* thanks Eleni Stavrinidou and the other anonymous reviewer(s) for their contribution to the peer review of this work. Peer reviewer reports are available.

Reprints and permission information is available at http://www.nature.com/reprints

Publisher's note Springer Nature remains neutral with regard to jurisdictional claims in published maps and institutional affiliations.

Supplementary Information

Exfoliated near infrared fluorescent silicate nanosheets for (bio)photonics

Selvaggio et al.

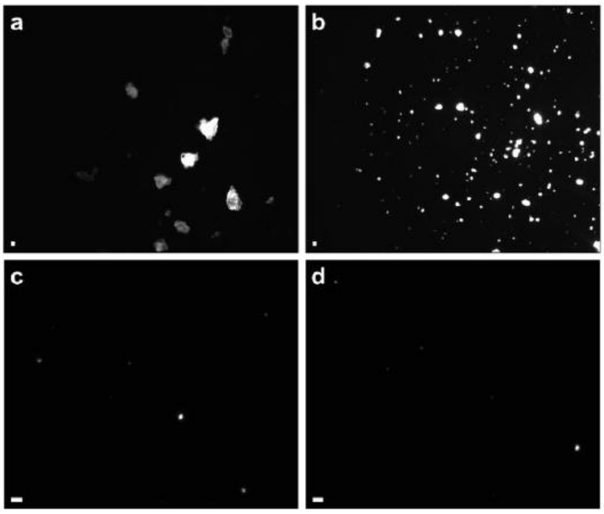

Supplementary Figure 1 NIR fluorescence images of Egyptian Blue (EB) before and after tip sonication. **a** EB bulk powder dispersed in isopropanol. **b** Egyptian Blue nanosheets (EB-NS) after 6 h of tip sonication. **c,d** EB-NS after 6 h of tip sonication and size-cut-off filtration (d = 0.45 µm). All samples were drop-casted (10 µL) on glass cover slides before imaging. Every purification step reduces the overall concentration of particles but increases monodispersity. Note that the contrast was not adjusted. Therefore, the smaller EB-NS in b-d are difficult to see (compared to the larger ones) and it looks like there are not many particles left, but when zooming in they are visible. Scale bar = 10 µm.

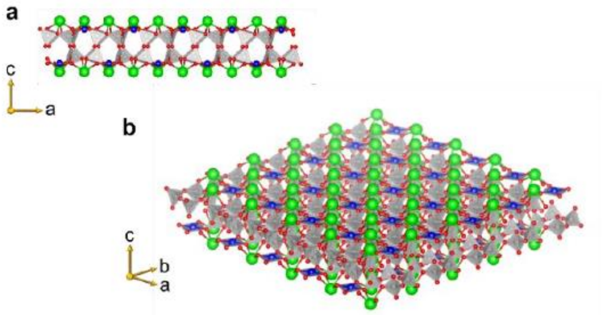

Supplementary Figure 2 Schematic of a monolayer of EB. **a** Frontal view. **b** 3D axonometric projection. For both illustrations, EB neutron powder diffraction data obtained from literature was used[1]. Si, O, Ca and Cu atoms are depicted as gray, red, green and blue spheres, respectively. Vesta (v. 3.4.4) was employed to draw the structures[2].

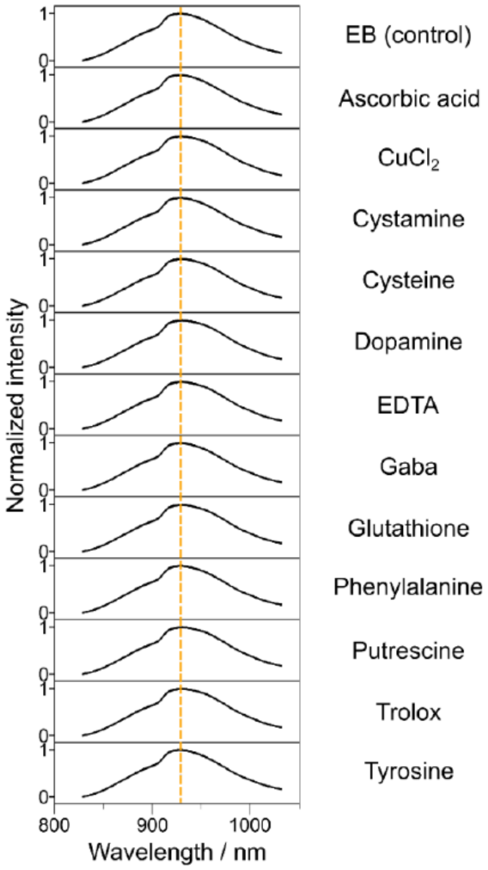

Supplementary Figure 3 Fluorescence response of EB-NS to different analytes of interest. NIR spectra of EB-NS (6 h tip sonication, 10 µg mL^{-1}) in water 10 min after addition of analytes (100 µM) that are known to affect spectra of other fluorophores. The EB-NS fluorescence did not display any significant shifts. This result further shows the stable NIR fluorescence of this nanomaterial.

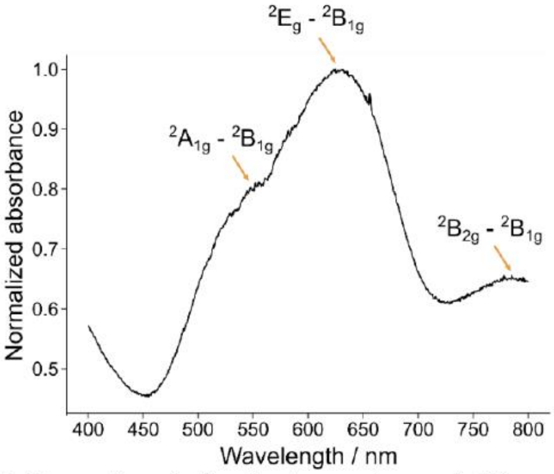

Supplementary Figure 4 Absorption (reflection) spectrum of EB powder. Three broad bands corresponding to different electronic transitions are observed (yellow arrows). The symmetry species of the orbitals involved in the transition are indicated next to the arrows. The attribution of the bands to the symmetry species was made according to the model proposed by Accorsi et al.[3].

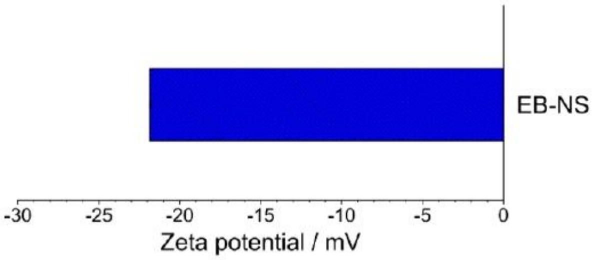

Supplementary Figure 5 Zeta potential of EB-NS. Zeta potential of EB-NS in water (2 mg mL^{-1}). The error bar corresponds to the standard deviation of triplicates.

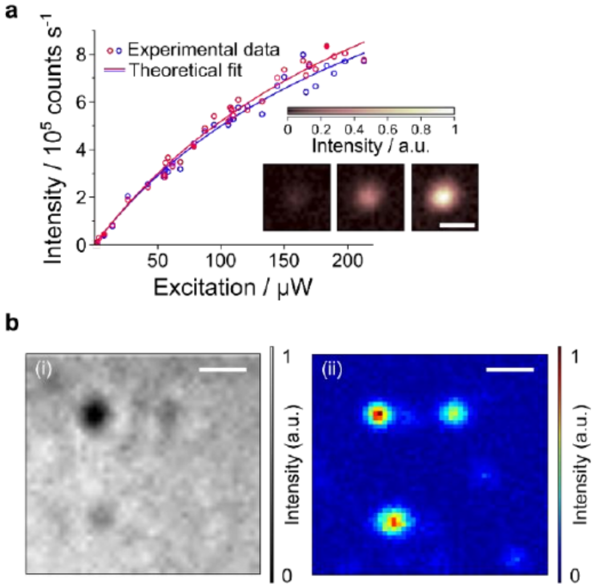

Supplementary Figure 6 NIR fluorescence saturation measurements, white light scattering and confocal scanning fluorescence images of EB-NS. **a** Fluorescence saturation measurement of a single EB-NS. Red circles show the data measured upon initial increase of excitation power, blue circles correspond to the subsequent decrease of the excitation power; red and blue lines represent the respective fits. The inset shows three images that were acquired at different excitation powers (corresponding data points are depicted with solid circles). Scale bar = 1 µm. The obtained saturation values (P_{sat}) are 276 and 252 µW. The slightly lower saturation intensity value that was obtained for the process of diminishing excitation power could be caused by heating of the sample by the excitation light, which affects the fluorescence lifetime in bulk EB[3]. The obtained saturation values correspond to a fluorescence emission of ≈ 1.95 x 10^6 photons per second. With this number we estimated the number of luminescent centers in the order of 1950 by taking into account the average lifetime of the excited state (≈ 100 µs, Supplementary Figure 7), the quantum yield (≈ 0.1[3]) of bulk EB, the quantum efficiency of the photodetector in this spectral region, the parameters of optical elements of the microscope and the acquisition time of the signal. From the crystal structure of EB it follows that there are 3.8 Cu^{2+} ions nm^{-2} of a single layer EB-NS[4] (Supplementary Figure 2). If every Cu^{2+} ion serves as luminescent center, these numbers would be in agreement with a 23 nm large (squared) single layer EB-NS. **b** White light scattering (i) and confocal scanning fluorescence (ii) images of EB-NS taken from the same area within the same sample. Scattering intensity appears not to be proportional to fluorescence intensity. The dimmest particles in (ii) are not visible in (i) due to their reduced size. Scale bar = 1 µm.

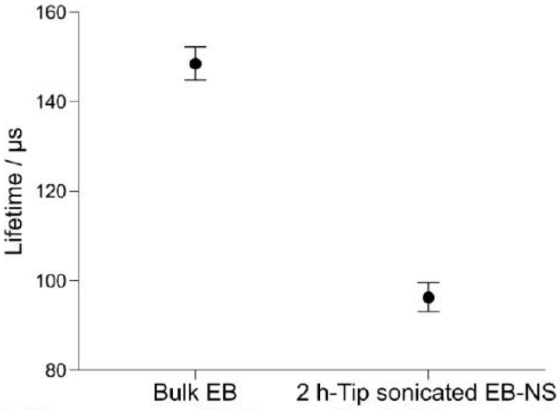

Supplementary Figure 7 Fluorescence lifetimes of bulk EB and exfoliated EB-NS. Error bars correspond to standard deviations (n = 100 repetitions performed for each sample).

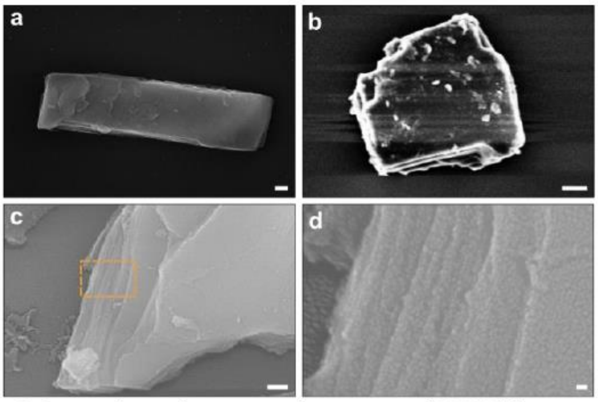

Supplementary Figure 8 Scanning electron microscopy (SEM) images of larger exfoliated EB (nano)sheets. Different samples and preparation techniques are shown. **a** No gold deposition. Scale bar = 200 nm. **b** ≈ 2 nm evaporated gold. Scale bar = 1 µm. **c** ≈ 2 nm of sputtered gold on the surface of the sample. Scale bar = 200 nm. **d** A magnified region from the inset shown in c indicates the layered structure. Scale bar = 20 nm.

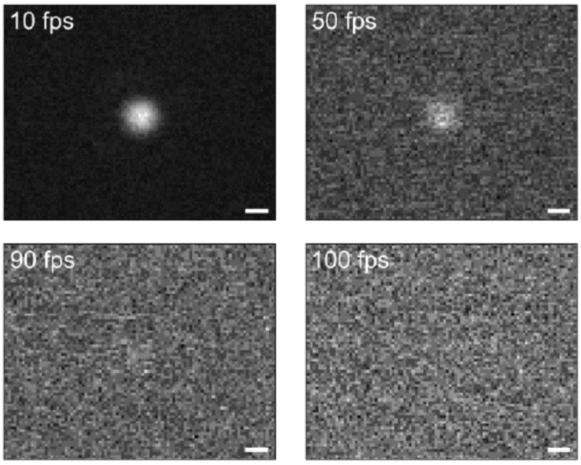

Supplementary Figure 9 Video-rate imaging of EB-NS with a Si-based camera. An EB-NS was observed with a Si-based camera (Zyla 5.5 sCMOS camera, Oxford Instruments) camera at 10 fps (≈ 100 ms), 50 fps (≈ 20 ms), 90 fps (≈ 11 ms) and 100 fps (≈ 10 ms). The quantum yield of Si-based cameras is high in the visible range, but decreases quickly in the near infrared region for wavelengths larger than 800 nm. While on one hand the particle is still visible at the two slower frame rates, it vanishes as soon as values of 90-100 fps are reached, thus highlighting the benefits of employing an InGaAs camera for NIR imaging. Scale bar = 500 nm.

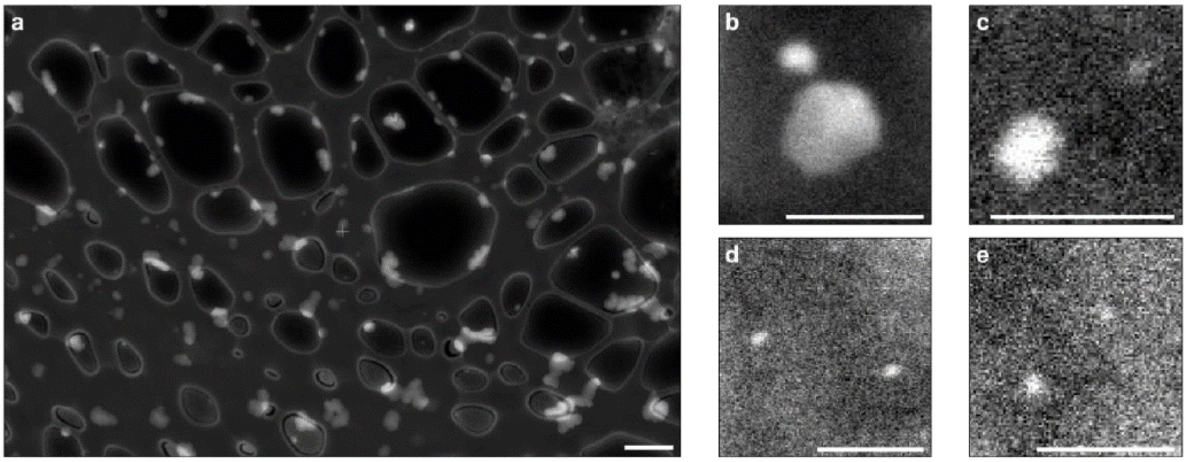

Supplementary Figure 10 Scanning Transmission Electron Microscopy (STEM) images of EB-NS. **a** Overview image of EB-NS dispersed in isopropanol and spin-coated on a TEM grid. Scale bar = 500 nm. **b-e** Blow-ups of such images of EB-NS. The EB-NS appear to agglomerate during the coating/evaporation process as often seen in TEM images. Scale bar = 100 nm.

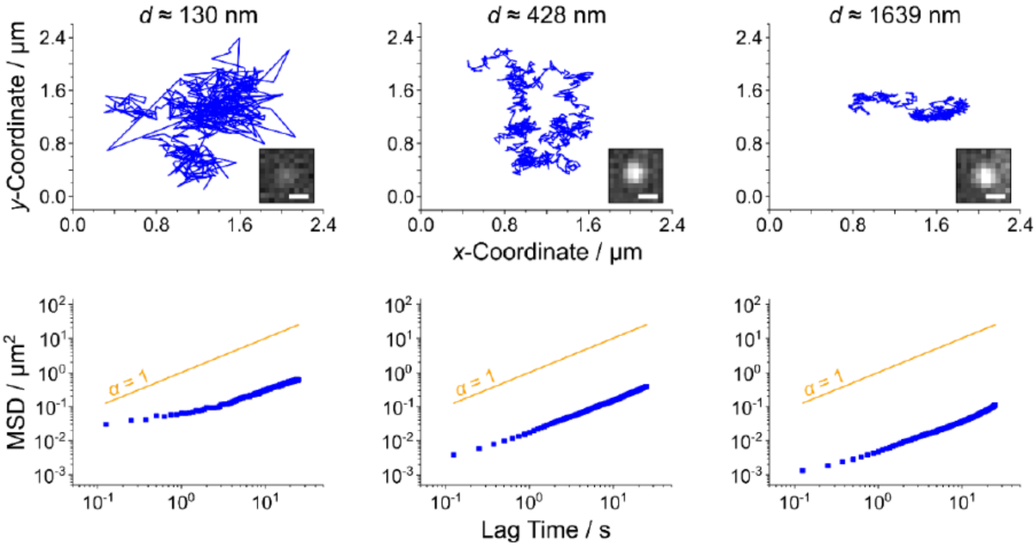

Supplementary Figure 11 Trajectories and logarithmic MSD curves of three exemplary EB-NS in glycerol. The trajectories and log-log MSDs of three particles of different sizes are shown. In the case of the largest particles, no complete filtration process was performed so that also larger particles and not only nanosheets could be present. Diameters were estimated via the protocol used for the size-fluorescence correlation analysis performed in glycerol (Figure 4). As a result, the three particles can be classified as having small, medium (< Abbe limit) and large (> Abbe limit) diameters. The size of the particles assessed (multiple times from different frames) in ImageJ (v. 1.52a) presents diameters of 0.501 µm, 0.551 µm and 0.899 µm (respectively). The Abbe limit of NIR light (900 nm) would be ≈ 450 nm. However, the particles are freely diffusing and therefore most of the time they are not perfectly in focus; the point spread functions should thus be typically bigger/distorted. Scale bar = 1 µm.

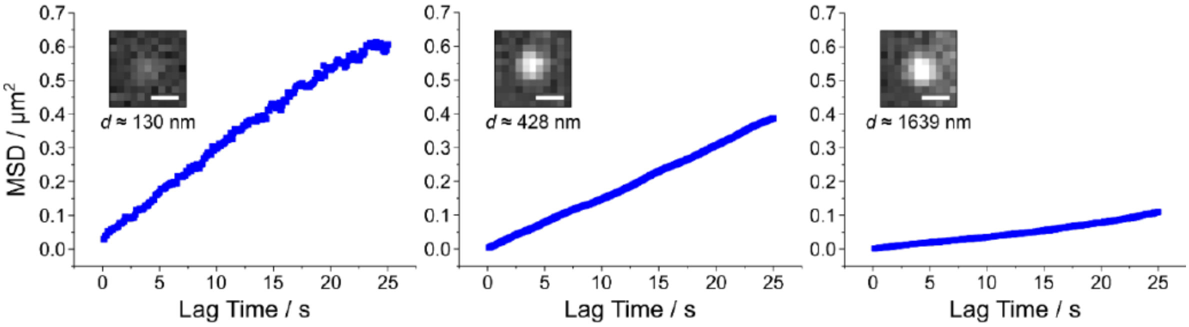

Supplementary Figure 12 Linear MSD curves of three exemplary EB-NS in glycerol. Linear MSD plots corresponding to the three EB-NS of Supplementary Figure 11 are shown. Scale bar = 1 µm.

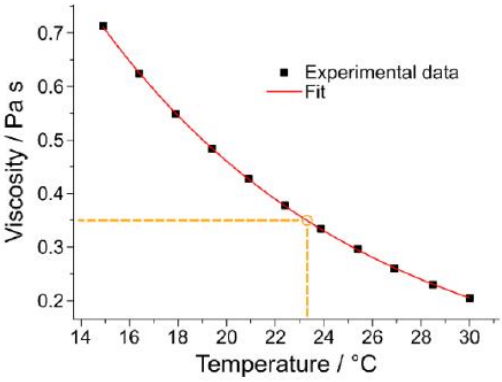

Supplementary Figure 13 Temperature sweep curve of EB-NS in glycerol. In order to independently assess the viscosity of the glycerol samples charged with EB-NS, a rheometer was used to measure viscosity for different temperatures. An exponential decay fit was chosen to interpolate the raw data ($R_2 = 0.99994$). The sample´s temperature during the NIR imaging experiments was stable and measured ≈ 23.3 °C. The corresponding viscosity value (≈ 0.35 Pa s) was taken from the plot, as indicated by the orange dashed lines.

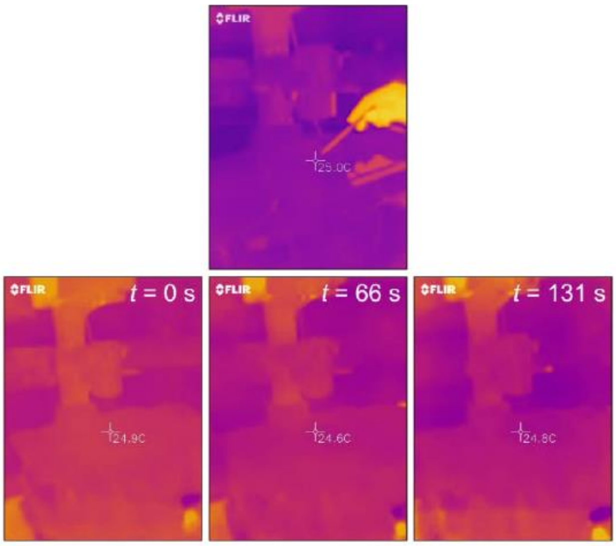

Supplementary Figure 14 IR monitoring during EB-NS tracking in glycerol. A FLIR camera (FLIR ONE Pro, FLIR Systems, Inc., USA) was employed to observe if EB-NS imaging in glycerol with a 561 nm laser heats the sample. At a laser power of 250 mW, only negligible temperature fluctuations could be observed at t = 0 s (beginning of acquisition), t = 66 s (halfway through the acquisition), and t = 131 s (end of acquisition). The first image shows a hand pointing to the sample holder.

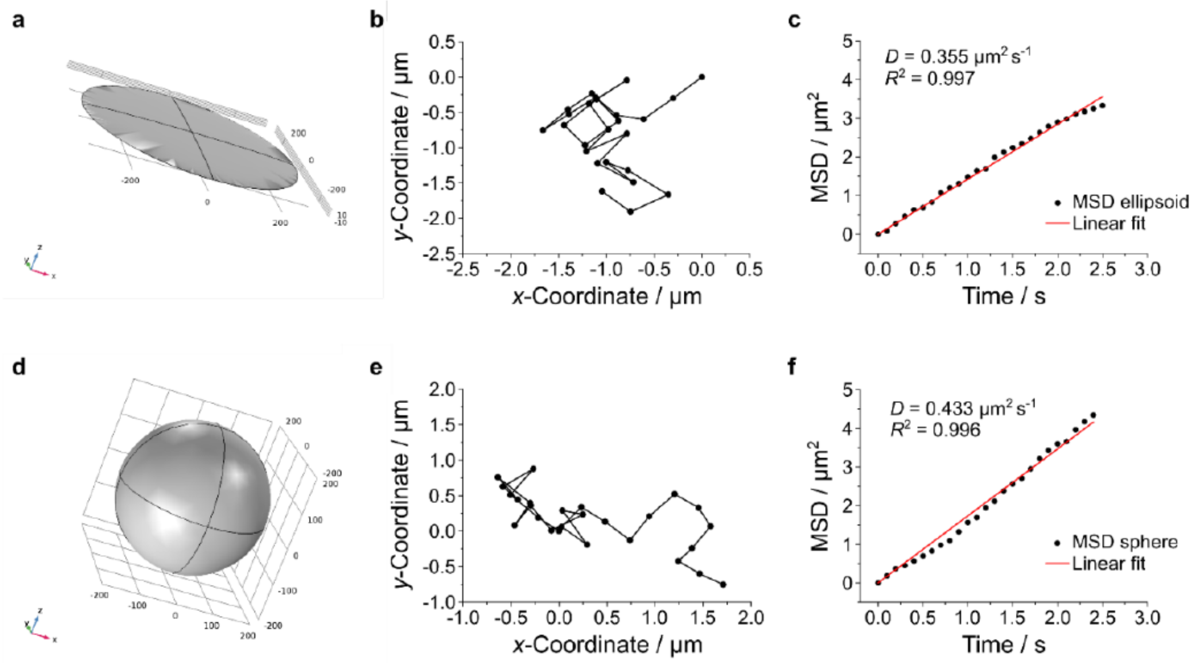

Supplementary Figure 15 Simulation to assess if the (theoretical) correction factor of the Stokes-Einstein equation for anisotropic particles is correct. **a-c** Spheroid geometry (d = 300 nm), trajectory and MSD of a simulated EB-NS during diffusion in water (T = 300 K). **d-f** Geometry, trajectory and MSD of a spherical particle during diffusion within the same environmental conditions. The radius of this spherical particle was set equivalent to the length of the maximum axis of the EB-NS spheroid, multiplied by the reciprocal of the correction factor (A) described in the Supplementary Methods (i.e. 1/A ≈ 0.67). This correction factor was derived from theoretical considerations. The MSDs yield diffusion constants (see values in c,f) which are comparable, thus confirming that the used correction factor is reasonable. Simulations were performed in COMSOL (see Supplementary Methods).

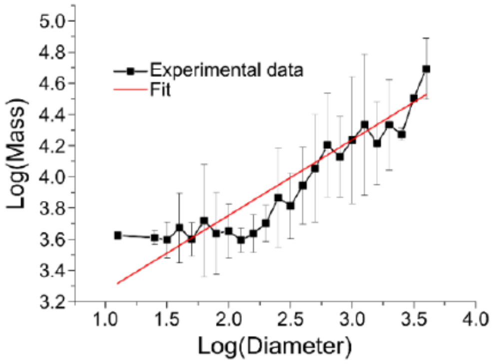

Supplementary Figure 16 Brightness vs. size of EB-NS tracked in glycerol. Mass, as defined by the Trackpy Python package[5,6] (v0.4.2 on Python v3.7.3[7]), is the total integrated brightness of the tracked blob (i.e. NIR fluorescence of an EB particle). For these plots, the maximum value along each trajectory was taken to account for the possibility of polarization-dependent excitation/emission. On the x axis, the hydrodynamic diameter obtained via the Stokes-Einstein equation (with anisotropy correction factor) is displayed. This plot is based on the same data as in Figure 4, but mean fluorescence (mass) values are taken from all data points in 0.1 steps (x-axis) to account for the potential spread in height of sheets of similar diameter. As the diameter dominates the diffusion process, this approach allows one to get a better idea if there is a scaling law. The powerlaw fit yields an exponent $\alpha \approx 0.5$ (R^2 = 0.77396), which would indicate that fluorescence of EB-NS scales with the square root of particle size. The reported plot is shown as mean ± standard deviation with a step on the x-axis of 0.1. n = 292 tracked EB-NS.

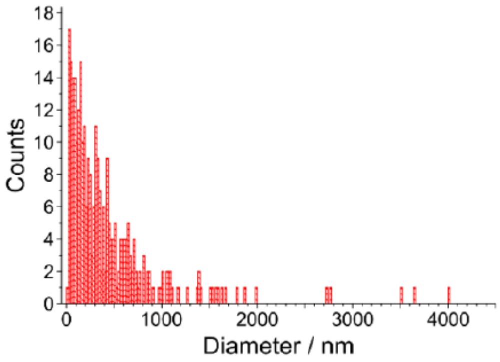

Supplementary Figure 17 Size distribution of EB-NS in glycerol. The plotted histogram presents hydrodynamic diameter values, which were obtained by size-fluorescence correlation analysis performed in glycerol (i.e. Stokes-Einstein with implementation of the correction factor, see Supplementary Methods). Bin size = 20 nm, n = 292 tracked EB-NS.

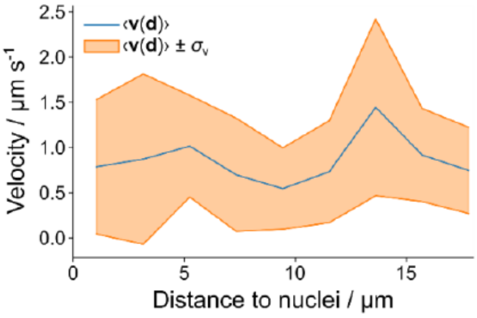

Supplementary Figure 18 Velocity of EB-NS motion vs. distance to closest nucleus in Drosophila melanogaster embryos. The mean instantaneous velocity and corresponding variance of EB-NS injected into Drosophila embryos is shown as a function of the distance to the closest nuclei encountered during particle motion. The perimeter of nuclei (observable in the GFP channel) was manually measured in ImageJ. The instantaneous velocity (lag time = 0.1 s) and the distance of every point along the trajectory to the closest nucleus were assessed via a custom-written Python script. The data set shows that one can use EB-NS to probe local velocities, but every EB-NS might have a unique mechanical environment and therefore there is not a clear trend. Bins width ≈ 2.09 µm, n = 38 tracked EB-NS (from 21 different embryos). Tracks for which the nuclei borders could not be clearly depicted were not taken into account.

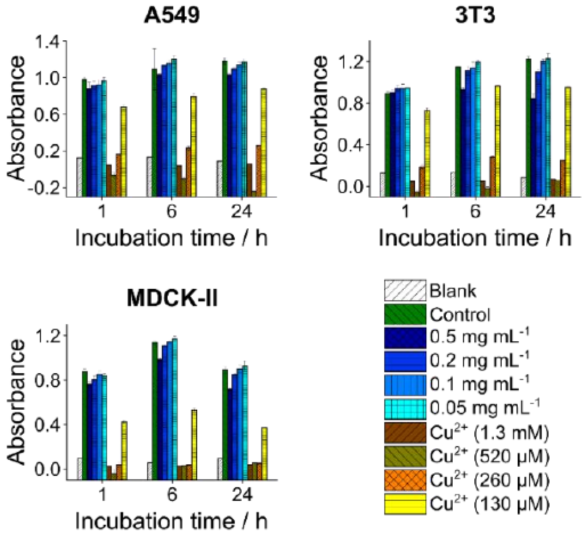

Supplementary Figure 19 Cell viability in the presence of EB-NS. Cytotoxicity of EB-NS was assessed for 3 different common cell lines (A549, NIH 3T3 and MDCK-II) using a standard assay (see Supplementary Methods). EB-NS did not show significant effects on cell viability, which indicates a high biocompatibility. As a control we used Cu^{2+} ions ($CuSO_4$), which drastically decreased viability. N = 4 independent samples (quadruplicates) for each data point, error bars correspond to standard deviation.

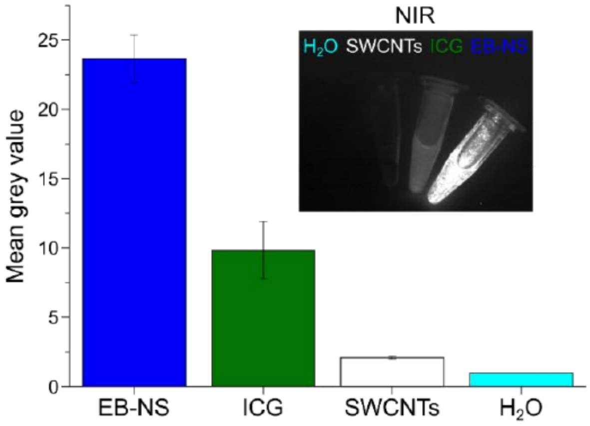

Supplementary Figure 20 Relative fluorescence intensity of different NIR fluorophores in the low-cost stand-off detection setup. Average total emission intensities (i.e. mean grey pixel values) of three different NIR fluorophores in Eppendorf tubes at similar concentration (≈ 0.1 mg mL^{-1}). Data were normalized to the water control. EB-NS, ICG and SWCNTs respectively yielded mean grey values of 23.7 ± 1.7, 9.8 ± 2.1 and 2.1 ± 0.1 (mean ± standard deviation). N = 3 independent samples.

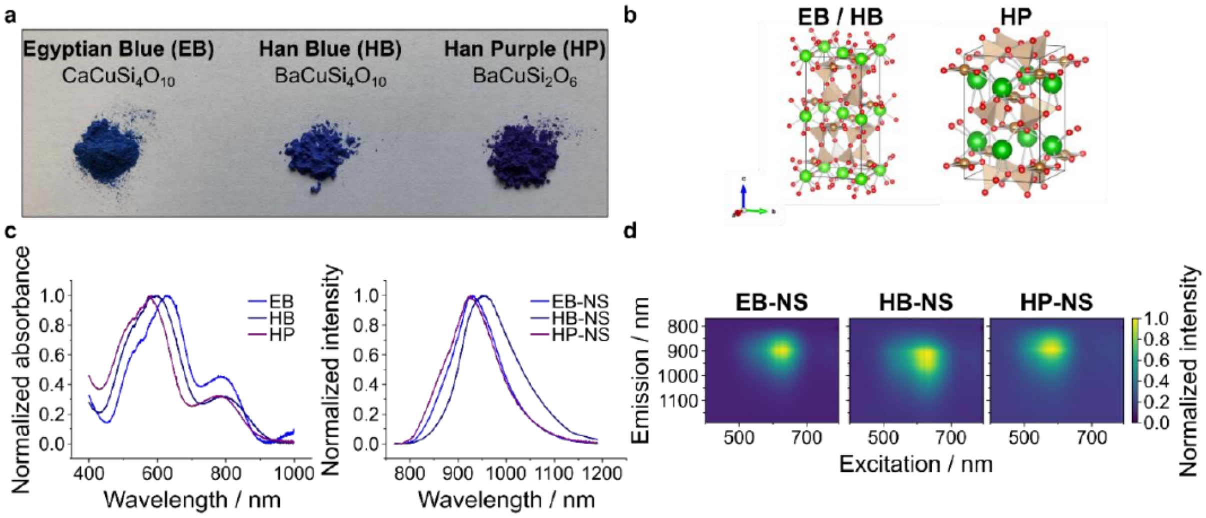

Supplementary Figure 21 Egyptian Blue (EB), Han Blue (HB) and Han Purple (HP): a family of NIR fluorophores. **a** Picture of bulk, pristine powders of EB, HB and HP. **b** Crystal structures (designed with Vesta (v. 3.4.4)[2]) of the three pigments: Ca (Ba for HB and HP) is depicted as green, Cu as bronze, O as red spheres, whereas Si is represented in its typical tetrahedral geometry. Colors were chosen according to the CPK color code (Jmol[8]). **c** Normalized absorption (reflection) of bulk EB, HB and HP powders, and 1D fluorescence spectra of EB, HB and HP nanosheets. **d** Normalized 2D excitation-emission spectra of EB-NS, HB-NS and HP-NS.

Supplementary Table 1 Fluorescence saturation measurements: saturation power, saturation luminescence intensity and number of luminescence centers per measured particle. Note that the photon numbers were corrected by the efficiency of the optical system etc. (see Supplementary Methods).

Particle number	Saturation excitation power (P_{sat}, µW)	Saturation luminescence intensity (I_{sat}, × 10^3 photons s^{-1})	Number of luminescence centers per particle
1	261	1250	1250
2	387	1135	1135
3	239	1125	1125
4	315	1008	1008
5	294	816	816
6	421	514	514
7	408	445	445
8	347	358	358
9	431	330	330
10	381	293	293
11	219	274	274
12	359	248	248
13	418	215	215
14	312	207	207
15	403	180	180
16	386	155	155
17	209	135	135
18	287	122	122

SUPPLEMENTARY METHODS

Absorption (reflection) spectra of Egyptian Blue (EB), Han Blue (HB) and Han Purple (HP) bulk powders

Absorption spectra were recorded with an AvaSpec-UV/Vis/NIR two channel broad band spectrograph (Avantes) containing a balanced deuterium-halogen lamp (AVALIGHT-DH-S-BAL). Only the signal recorded in the UV/Vis channel is shown, which is equipped with a 2048L UV/Vis spectrometer with a 25 µm slit and a 300 lines mm$_{-1}$ grid. The Avasoft-Full software was used for recording.

Zeta potential measurements

A Zetasizer Nano S device (Malvern Instruments) was employed for this experiment. The obtained dataset was analysed via the Zetasizer software.

Fluorescence saturation measurements

To estimate the number of luminescent centers in a single EB-NS, we did single particle fluorescence saturation measurements. EB-NS were deposited on the surface of standard glass cover slides. Scanning the surface with a confocal microscope through the diffraction limited focal spot of 1.49 NA objective allowed us to select only the smallest particles with sizes not exceeding the dimensions of the focal spot/resolution limit. Sizes of larger particles clearly exceeded the dimensions of a diffraction limited focal spot and allowed us to distinguish them from smaller particles. After selecting a particle, we measured its fluorescence intensity at different excitation powers. Excitation of nanoparticles that have relatively long excited state lifetimes of the order of 100 µs (Supplementary Figure 7) with a laser that has high repetition rate (20 MHz) allows one to extrapolate saturation of nanoparticle luminescence. The excitation wavelength was 640 nm. The fluorescence intensity values were normalized to the detection efficiency of the microscope, taking into account the average collection efficiency of light by the 1.49 NA objective lens (70%, given the random orientation of the emission transition dipoles), transmissivity of all the optical elements involved (~50%) and detection efficiency of the single photon avalanche diode (PDM series, MPD) in the appropriate spectral range (~5%). The experimental data were fitted with a typical fluorescence saturation function[9]:

$$I = I_{\mathrm{sat}} \frac{P_{\mathrm{exc}}}{(P_{\mathrm{exc}}+P_{\mathrm{sat}})}\,, \tag{1}$$

where P_{exc} is the excitation power, P_{sat} is the saturation power, I_{sat} is the nanoparticle luminescence intensity that can be detected at the saturation excitation power, yields the values of P_{sat} and I_{sat} for every saturation curve measured. Supplementary Table 1 shows the obtained values. The obtained saturation luminescence intensity values allow one to estimate the number of luminescent centers N per particle. Taking into account the average excited state lifetime τ (~100 µs, Supplementary Figure 7) and quantum yield Φ (~0.1[3]), we calculated the number of emitted photons I_{sat} per second into the number of centers:

$$N = \frac{I_{\mathrm{sat}}}{\Phi\tau^{-1}}\,. \tag{2}$$

Laser source: Supercontinuum laser SC400-4-20, Fianium

Photodetector: single photon avalanche diode PDM series, MPD

Objective lens: Apo N, 60×/1.49 NA oil immersion, Olympus

Fluorescence lifetime measurements

Lifetime measurements (frequency domain) were conducted in a well-plate using a Firesting oxygen meter from Pyroscience (Aachen, Germany) at room temperature. The excitation wavelength was set to 620 nm. An excitation frequency of 4 kHz and an LED intensity of 40% were employed.

Video-rate imaging of EB-NS with a Si-based camera

EB-NS (previously milled and tip sonicated in water) were filtered with a 0.2 µm syringe filter (Sartorius AG, Germany). To further enhance the concentration of the smallest nanosheets in the sample, the sample vial was placed in a concentrator (Eppendorf® centrifugal vacuum concentrator, Eppendorf, Germany) for 90 min at 50 °C and finally bath sonicated for 20 min to reduce agglomeration. 10 µL were then imaged at the fluorescence microscopy setup on a #1 glass slide with the following settings: 100x objective, 500 mW of 561 nm laser, exposure times and resulting frame rates as specified in the caption of Supplementary Figure 9.

Scanning Transmission Electron Microscopy (STEM) on EB-NS

EB-NS (previously milled and tip sonicated in water) were filtered with a 0.45 µm syringe filter (Sartorius AG, Germany) to remove the largest particles from the sample. 10 µL of the so-prepared dispersion were then drop-casted on a TEM grid (ultrathin C film supported by a Lacey carbon film on a 400 mesh Cu grid, Ted Pella Inc, USA) and imaged under a Quattro S (Thermo Fischer Scientific, USA) device with the following settings: working distance = 11.2 mm, horizontal field width = 2-7 µm, 30.00 kV, STEM3+ detector, 8-9×10^{-6} mbar.

Correlative size-intensity measurements in glycerol

EB-NS (previously milled and exfoliated/tip sonicated in water) were size-selected by means of two steps of liquid cascade centrifugation[10,11]: in this way we could get rid of unexfoliated EB and increase the monodispersity of the pellet obtained after the last step (1st centrifugation = 240g for 2 h, 2nd centrifugation = 2660g for 2 h). 0.5 mL of glycerol (Alfa Aesar, 99+%) were then added to the dried final pellet (≈ 1 mg), and the sample was finally tip sonicated in an ice bath for 2 min at 60% to achieve a homogeneous redispersion. For imaging, 10-20 µL of the glycerol sample were introduced into a flow chamber (µ-Slide VI 0.5 Glass

Bottom, Ibidi, Germany) and placed under our NIR imaging setup. A 100x objective was employed to observe EB-NS at 8 fps (≈ 50 ms exposure time, 1000 frames) with a laser power of 250 mW, which, as shown in Supplementary Figure 14, was not overheating the sample significantly during acquisition. Particle tracking and MSD calculations were performed using a self-written Python script based on the Trackpy package[5,6] (v0.4.2 on Python v3.7.3[7]), whereas the final steps of data analysis were performed on Origin Pro 8.1 software. For identification and linking of particles into trajectories, the following parameters in Trackpy were implemented: memory = 300, minimum number of points (i.e. trajectory length) = 300, search_range (i.e. maximum displacement between consecutive frames) = 9, diameter (of the tracked blob) = 11. The tracking of the Brownian motion of an EB-NS yields the trajectory of the particle as a set of time-dependent x and y positions for N time steps of length τ. From the x and y positions, the square displacement for the n-th time step $\mathbf{r}_n^2$ is calculated as

$$\mathbf{r}_n^2 = \left(\mathbf{x}(n \cdot \tau) - \mathbf{x}\left((n-1) \cdot \tau\right)\right)^2 + \left(\mathbf{y}(n \cdot \tau) - \mathbf{y}\left((n-1) \cdot \tau\right)\right)^2, \quad (3)$$

where n ranges from 1 to N. The mean square displacement $\langle \mathbf{r}^2 \rangle$ (MSD) is simply the mean over all single time step values:

$$\langle \mathbf{r}^2 \rangle = \frac{1}{N} \sum_{n=1}^{N} \mathbf{r}_n^2 \ . \quad (4)$$

Assuming the diffusion is restricted to two dimensions, the diffusion coefficient D and the MSD are linked via the relation:

$$D = \frac{\langle \mathbf{r}^2 \rangle}{4\tau} \ . \quad (5)$$

MSD curves were fitted up to a maximum lag time of 25 s in order to measure the diffusion coefficient of each particle. Finally, from the Stokes-Einstein equation, the Stokes radius R is calculated as:

$$R = \frac{k_{\mathrm{B}} T}{6 \pi \eta D} \ , \quad (6)$$

where η is the dynamic viscosity of the solvent (Supplementary Figure 13), T the temperature (Supplementary Figure 14) and k_B the Boltzmann constant. The Stokes-Einstein equation is only strictly valid for spherical particles. Due to the high anisotropy of EB-NS, one could assume that Brownian motion is dominated by the diameter of the nanosheets and not the much smaller height. However, all hydrodynamic radii were corrected to account for anisotropy (see below).

Bulk viscosity measurements of EB-NS in glycerol

In order to robustly evaluate the bulk viscosity of the glycerol samples, a stress-controlled rheometer (MCR 501, Anton Paar, Austria) that can be operated in oscillatory and rotational mode was used. For a uniform shear rate across the sample, a cone and plate geometry (diameter = 25 mm) was used and the temperature was controlled with a Peltier element. Viscosity of the sample (75 µL) was determined at a constant rotational shear stress of $d\gamma/dt = 50\ s^{-1}$ and the temperature was changed from 15 °C to 30 °C at an increment of 1 °C. To ensure reproducibility, the temperature ramp was applied three times starting at 15 °C going to 30 °C, then the reverse order, and finally again from 15 °C to 30 °C.

Estimation of the hydrodynamic radius of EB-NS

To account for the (non-spherical) asymmetry of EB-NS, a correction factor A was applied to the general Stokes-Einstein equation:

$$D = \frac{k_\mathrm{B}T}{6\pi\mu r} = A\frac{k_\mathrm{B}T}{6\pi\mu h}\,, \qquad (7)$$

where h is the length of the main axis of the particle and r is the hydrodynamic radius of a sphere of equivalent diffusivity. To estimate the correction factor, the theoretical framework of Happel et al. was used[12]. In short, the geometry of a given EB-NS was approximated with the shape of a nanometer-sized spheroid containing two symmetric long axis h (particle width) as well as a short axis a (particle height). By calculating the resistance of such a particle within a fluid of unidirectional flow parallel or perpendicular to the particle’s symmetry axis, one is able to derive an expression for the hydrodynamic radius R of a sphere with equivalent diffusivity by:

$$R_{\_} = \frac{8h}{3}\frac{1}{\left[\frac{2\varphi}{1-\varphi^2}+\frac{2(1-2\varphi^2)}{(1-\varphi^2)^{3/2}}\tan^{-1}\left(\frac{\sqrt{1-\varphi^2}}{\varphi}\right)\right]} \text{ (parallel to symmetry axis)} \quad (8)$$

and

$$R_{\perp} = \frac{8h}{3}\frac{1}{\left[-\frac{\varphi}{1-\varphi^2}-\frac{2\varphi^2-3}{(1-\varphi^2)^{3/2}}\sin^{-1}\left(\sqrt{1-\varphi^2}\right)\right]} \text{ (perpendicular to symmetry axis) , (9)}$$

with φ delineating the axis ratio $\varphi = a/h$. For φ we utilized the height/width values gained from our AFM-measurements for EB-NS (see Figure 1). A linear fit yields φ = 0.035 or $R_{\_}$ = 0.85h and $R_{\perp}$ = 0.58h, respectively. Finally, the factor A could be calculated by taking the mean of all axis values:

$$R_{\text{mean}} = \frac{R_{\_} + 2R_{\perp}}{3} = \frac{0.85 + 2\cdot 0.58}{3}h = \frac{1}{A}h \rightarrow A = 1.49 \qquad (10)$$

The actual hydrodynamic diameters of the measured EB-NS are therefore larger than expected from the pure Stokes-Einstein equation.

3D simulation of EB particle diffusion

Simulations of diffusive EB particles were performed with COMSOL (v 5.5). For this purpose, the Fluid-Structure-Interaction (fsi) package was used to create a 500 x 500 x 500 µm$_{3}$ sized, cubic water box (T = 300 K, µ = 0.001 Pa s, ρ = 997 kg m$_{-3}$, free wall boundary conditions) in which

e.g. a spheroidic “EB” particle (h = 300 nm, a = 10.44 nm, ρ = 8960 kg m$_{-3}$) was placed in its center to mimic Brownian motion. Consequently, we implemented stochastic forces applied from the fluid on the particle’s surface (**F**$_{\text{mean}}$ ≈ 1 N m$_{-2}$, approximated from test simulations to match the Stokes-Einstein relation) and started the simulation process by setting the solver step size (frame rate) to Δt = 0.1 s. The motion of the particle was then tracked by analyzing its center of mass in each step size and the traces were used to calculate the MSD and the particle's respective diffusion coefficient. This process was compared to particles of different geometry e.g. for r = 300/A = 201 nm spheres (corresponding to the correction factor expected from the theory above).

Cytotoxicity tests of EB-NS

A549, NIH 3T3 and MDCK II cell lines were employed in this study.

- A549 cell line and NIH 3T3 cell line: D10F+ (DMEM +4.5 g L^{-1} glucose with L-glutamin (4 mM), 10% fetal bovine serum and 100 µg mL^{-1} Pen-Strep), trypsin/EDTA (0.05/0.05%) solution;
- MDCK II cell line: M10F+ (EMEM with Earle's salts with L-glutamin (2 mM), 10% fetal bovine serum and 100 µg mL^{-1} Pen-Strep), trypsin/EDTA (0.25/0.05%) solution.

The cell viability (MTS) assay was performed using CellTiter 96® AQueous One Solution Cell Proliferation Assay (Promega, G3580). 2 mL (≈ 4 mg) of a 6 h-tip sonicated sample of EB-NS in water (2 mg mL^{-1}) was centrifuged (10 min, 13100 RCF). The supernatant was removed and the so-obtained pellet was re-dispersed in 400 µL, in order to reach a concentration of ≈ 10 mg mL^{-1} of EB-NS. The sample was diluted to 5% (0.5 mg mL^{-1}), 2% (0.2 mg mL^{-1}), 1% (0.1 mg mL^{-1}) and 0.5% (0.05 mg mL^{-1}).

A 13 mg mL^{-1} (i.e. 52 mM) water solution of $CuSO_4 \cdot 5H_2O$ (98%, J&K Scientific) was used as a reference to assess the maximum sensitivity of the cells to Cu^{2+} ions. 0.2% (100 µM) corresponds to the copper amount in 2% of the 2 mg mL^{-1} EB-NS dispersion (i.e. 0.04 mg mL^{-1} of EB-NS). Therefore 2.5% (1.3 mM), 1% (520 µM), 0.5% (260 µM) and 0.25% (130 µM) correspond to the EB-NS concentrations of 0.5 mg mL^{-1}, 0.2 mg mL^{-1}, 0.1 mg mL^{-1}, 0.05 mg mL^{-1}, respectively. The Cu^{2+} concentrations for this experiment have been shown to cause varying degrees of cytotoxicity in literature[13]. 2% (v/v) deionized water was employed as positive control. Cells were initially incubated in a 96-well plate at 1.2×10^3 cells per well for 24 h in M10F- Media at 37 °C and 7.5% CO_2 (MDCK II), or in D10F-Media at 37 °C and 5% CO_2 (A549 and NIH 3T3). A suspension of EB-NS was diluted to the different concentrations in appropriate media and added to the cells to be incubated for 1, 6 or 24 h. Viability of the cell samples was determined by MTS-assay.

1D and 2D fluorescence spectra of EB, HB and HP

6 h-tip sonicated EB, HB and HP samples in isopropanol were centrifuged for 2 h at 240g to remove unexfoliated bulk material. 200 µL of each supernatant were then placed in a 96-well-plate and the excitation wavelength of the monochromator was set at 615 nm for all samples. For the acquisition of 2D spectra, the following parameters were employed: excitation wavelength range = 400-800 nm, steps = 5 nm, integration time = 3 s. 2D Spectra were normalized to the maximum intensity and corrected for the quantum efficiency of the detector as well as the spectral irradiance of the xenon lamp of the monochromator using a self-written Python script.

SUPPLEMENTARY REFERENCES

1. Chakoumakos, B. C., Fernandez-Baca, J. A. & Boatner, L. A. Refinement of the Structures of the Layer Silicates. J. Solid State Chem. **103**, 105–113 (1993).

2. Momma, K. & Izumi, F. VESTA 3 for three-dimensional visualization of crystal, volumetric and morphology data. J. Appl. Crystallogr. **44**, 1272–1276 (2011).

3. Accorsi, G. et al. The exceptional near-infrared luminescence properties of cuprorivaite (Egyptian blue). Chem. Commun. 3392–3394 (2009).

4. Pabst, A. Structures of some tetragonal sheet silicates. Acta Crystallogr. **12**, 733–739 (1959).

5. Crocker, J. C. & Grier, D. G. Methods of digital video microscopy for colloidal studies. J. Colloid Interface Sci. **179**, 298–310 (1996).

6. Allan, D. et al. soft-matter/trackpy: Trackpy v0.4.2. (2019) doi:10.5281/ZENODO.3492186.

7. Welcome to Python.org. https://www.python.org/.

8. Colors. http://jmol.sourceforge.net/jscolors/.

9. Plakhotnik, T. & Gruber, D. Luminescence of nitrogen-vacancy centers in nanodiamonds at temperatures between 300 and 700 K: Perspectives on nanothermometry. Phys. Chem. Chem. Phys. **12**, 9751–9756 (2010).

10. Backes, C. et al. Production of highly monolayer enriched dispersions of liquid-exfoliated nanosheets by liquid cascade centrifugation. ACS Nano **10**, 1589–1601 (2016).

11. Backes, C. et al. Guidelines for Exfoliation, Characterization and Processing of Layered Materials Produced by Liquid Exfoliation. (2017) doi:10.1021/acs.chemmater.6b03335.

12. Happel, J. & Brenner, H. The Motion of a Rigid Particle of Arbitrary Shape in an Unbounded Fluid. 159–234 (1983) doi:10.1007/978-94-009-8352-6_5.

13. Tchounwou, P. B., Newsome, C., Williams, J. & Glass, K. Copper-Induced Cytotoxicity and Transcriptional Activation of Met Ions Biol Med . 2008 ; 10: 285–290. Stress Genes in Human Liver Carcinoma (HepG2) Cells. Met. Ions Biol. Med. **10**, 285–290 (2008).

5.2.3 Publication Synopsis

Manuscript II presented a novel exfoliation protocol based on wet planetary ball milling and tip sonication. With this approach, EB-NS of lateral sizes roughly between 20-300 nm and thicknesses down to the monolayer (≈ 1 nm) could be prepared. Furthermore, according once again to atomic force microscopy (AFM) measurements, diameter and height of so-exfoliated EB-NS were found to scale linearly. Most importantly, several 1D and 2D spectroscopic datasets confirmed that the bulk absorption and emission properties retained their main features after downsizing the material. The strong photostability of EB-NS was first highlighted by the preservation of NIR fluorescence despite increasing hours of sonication (corresponding to decreasing sizes of NS): indeed, the signal was not only still detectable after 6 h of exfoliation, but was also not displaying any peak shift in the emission wavelength. Although the fluorescence lifetime (τ) was not fully investigated in this work, preliminary acquisitions indicated that τ values were still in the µs range, as is known to be the case for the unexfoliated silicate. Quite remarkably, the NIR emission of EB-NS was not affected by photobleaching over prolonged excitation (561 nm laser, 100 mW total output power, > 2 h): under the same conditions, organic dyes are instead prone to bleaching, as demonstrated by the standard Rhodamine B used as reference for this dataset. A further strong proof for the outstanding photostability of EB-NS was provided by the lack of changes in the fluorescence spectra after addition of several analytes (*e.g.* redox active molecules) which would typically alter the spectral features of other dyes and nanomaterials[42,71,233,234]. Another comparative study was performed with dye Atto 488 to observe whether the detected fluorescence could undergo any change at different polarization angles: while the reference dye showed the expected dependence, EB-NS did not display any fluorescence polarization.

After the set of spectroscopic characterization methods described above, the focus of **Manuscript II** moved to NIR fluorescence imaging of EB-NS. In the case of fluorescence microscopy, the physical boundary which must always be kept in mind is Abbe's resolution limit: if the emission wavelengths of EB-NS are considered, the smallest fluorescent spot that can be resolved has a diameter $d_{\mathrm{res}} \approx \lambda_{\mathrm{em}} / 2 \approx 450$ nm. As the emission peak falls in the wavelength range of $\lambda_{\mathrm{em}} \approx 930$ nm, both silicon-based and InGaAs cameras could be successfully employed for imaging experiments on EB-NS. As demonstrated with both detectors, EB-NS with sizes in the range of d_{res} could indeed retain the bright NIR emission of the bulk material. Additionally, by means of single-particle fluorescence saturation measurements, an estimation of the number of luminescent centers in a single monolayer of resolution-limited EB-NS could be made. Assuming that every copper ion (Cu^{2+}) in the crystal serves as color center, this analysis provided a size range of ≈ 6-18 nm for the imaged set of particles. More in-depth imaging studies of resolution-limited EB-NS were then carried out, yielding statistically robust answers. Despite the small particle sizes at play, fluorescence intensity was strong enough to enable signal detection with high frame rates. EB-NS could be detected with up to 50 fps by the visible camera and up to 200 fps by the NIR-optimized one. Next, two different studies were carried out in parallel to investigate the size-fluorescence correlation: one could allow a direct quantification, another one required some more sophisticated data analysis. The former method consisted in colocalizing NS at two different devices: the NIR microscopy setup and a scanning electron microscope (SEM). The latter approach, instead, was based on fluorescent particle tracking of EB-NS in a medium of known viscosity (*i.e.* glycerol): indeed, a hydrodynamic diameter of NS in Brownian motion could be calculated *via* a modified version of the Stokes-Einstein equation. More specifically, this modification consisted in the application of a correction factor which accounted for the anisotropy of 2D EB-NS and was calculated based on literature values[235] and AFM measurements. Despite the diverse definition of these two correlative measurements, the collected results led to the same crucial conclusions: NS of sizes down to just a few tenths of nm are still fluorescent.

The goal of the final part of **Manuscript II** was to test the potential of EB-NS for bioimaging applications. The typically low autofluorescence of biological samples in the NIR and the characteristic lack of bleaching of EB-NS allowed long-term *in vivo* imaging of these fluorophores within embryos of fruit flies (*Drosophila melanogaster*). By means of particle tracking measurements with increased temporal resolution (10 fps), EB-NS could be employed to probe the extracellular space between the nuclei of the developing insect. Furthermore, by analyzing the instantaneous velocities of EB-NS in the form of Van Hove histograms of displacements[236], the presence of active forces exerted by the embryos during their development could be revealed. While this dataset already highlights quite clearly the potential of EB-NS as novel NIR fluorophore, additional investigations towards biological applications were carried out, *e.g.* with regards to cytotoxicity issues. The results obtained with viability assays on three different cell lines (A549, 3T3 and MDCK-II) demonstrated that EB-NS are biocompatible materials. Finally, **Manuscript II** outlined that EB-NS present optimal characteristics not only for fluorescence (*in vivo*) microscopy, but also for remote detection at distances > 10 cm. For this dataset, a home-built stand-off setup consisting in a white LED lamp, a simple CMOS camera (complementary metal oxide semiconductor, Si-based) and the necessary NIR long-pass filters ($\lambda > 900$ nm) was employed. When imaged with this simple and low-cost optical setup, EB-NS showed a bright NIR emission compared to two routinely used NIR emitters: single-walled carbon nanotubes (SWCNTs) and indocyanine green (ICG). A further comparison between SWCNTs and EB-NS was reported after their introduction into plant leaves of *Arabidopsis thaliana.* While the emission of SWCNTs was not bright enough to overcome leaf autofluorescence (determined by chlorophyll/chlorophyll degradation products), EB-NS could be robustly imaged. A final confirmation of the robustness of NS fluorescence was given by remote detection without the LED excitation source: a signal from the silicate samples could indeed be detected also with room or sunlight illumination alone.

In conclusion, 1D and 2D absorption and emission spectra of NS of Han Blue ($BaCuSi_4O_{10}$, HB) and Han Purple ($BaCuSi_2O_6$, HP) were included in the Supplementary Information files. As extensively described in **Section 4.3**, these silicates present a layered crystal structure which is similar to the one of EB and, thus, allowed exfoliation into NS according to the same protocol. More importantly, though, both HB and HP also display promising NIR fluorescence properties which are robustly retained in the NS form. All three materials will be focused on in the following section, where the work that followed **Manuscript II** will be described **(Section 5.3, Manuscript III)**.

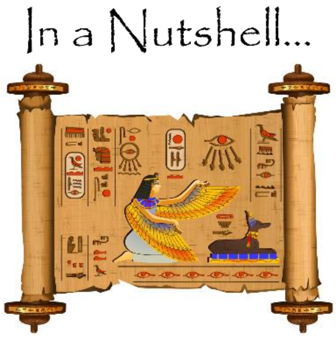

- ✓ Egyptian Blue ($CaCuSi_4O_{10}$, EB) was exfoliated into nanosheets (EB-NS) *via* wet ball milling and tip sonication.
- ✓ EB-NS retained the bright NIR fluorescence of the bulk material and could be easily imaged with both Si-based and InGaAs cameras.
- ✓ The NIR emission of EB-NS was extremely stable with regards to photobleaching, fluorescence polarization and redox active molecules.
- ✓ Size-correlation studies demonstrated that EB-NS down to few tenths of nm in size were still fluorescent.
- ✓ Cytotoxicity assays confirmed the biocompatible nature of EB-NS.
- ✓ Video-rate imaging, *in vivo* microrheology of embryos of fruit flies and remote detection in plants further underlined the high potential of EB-NS as novel NIR fluorophore.
- ✓ Analogously to EB, Han Blue ($BaCuSi_4O_{10}$, HB) and Han Purple ($BaCuSi_2O_6$, HP) were exfoliated into NS which preserved the bulk spectral features, *i.e.* broad excitation range and bright NIR fluorescence.

5.3 Optimized Exfoliation and Fluorescence Lifetime Characterization of EB-NS, HB-NS and HP-NS

5.3.1 Introduction

The work reported in the upcoming section can be considered a natural continuation of the research presented in **Manuscript II (Section 5.2.2)**. Here, more focus was set on the photophysical properties of nanosheets of Egyptian Blue ($CaCuSi_4O_{10}$, EB-NS), Han Blue ($BaCuSi_4O_{10}$, HB-NS) and Han Purple ($BaCuSi_2O_6$, HP-NS). As explained in **Section 4.3**, these three silicates share common features, including a layered crystal structure prone to exfoliation, a broad excitation range and a bright NIR fluorescence. Given their ancient origins and their presence in numerous pieces of art all over the world, past studies have already revealed some aspects of the underlying photophysics of EB, HB and HP[182]. For example, the fluorescence has been assigned to a low energy electronic transition of the shared copper ion (Cu^{2+}) in square planar coordination geometry. Furthermore, the symmetrically prohibited nature of this electronic transition leads to particularly long excited state lifetime values (τ) which lie in the range of several μs for all three materials. This long-lived fluorescence has been exploited *e.g.* to detect traces of these pigments in ancient artworks and to distinguish them from binders, varnishes and other materials; in this way, researchers in the field of history of art were able to track the evolution of synthesis and employment of EB, HB and HP over centuries[175,206,237–239]. A long fluorescence lifetime as the one owned by these materials can, however, find immediate application also in other fields, *e.g.* the biomedical sector[22,66].

Previous works have shown how EB and HB can be exfoliated into high aspect ratio NS. However, at the time when the investigations reported in **Manuscript III** (upcoming **Section 5.3.2**) were started, no past study had carried out a thorough characterization of these nanoparticles, neither with regards to their morphology nor concerning their photophysical properties. Regarding the latter, it was known that both EB-NS and HB-NS are still fluorescent, but, besides from the work reported in **Manuscript II**, works in literature had mostly focused on NS in the micrometers range. Additionally, no exfoliation of HP into HP-NS had been reported so far. As described in **Section 4.3**, some light had already been shed on how factors such as synthesis routes and material processing can affect lifetime in the bulk silicates of EB, HB and HP, however no study had so far focused on the lifetime properties in the nanoscale. Also, although FLIM had previously been carried out on the bulk silicates for non-invasive investigations of artifacts[175–178,206,237–239], this was not the case for the NS counterparts.

Considered what outlined above, the aim of the work presented in the upcoming section **(Manuscript III)** was to gather more insights with regards to the following questions:

- Can a more robust protocol of exfoliation be established in order to yield monodisperse samples of small EB-NS, HB-NS and HP-NS?

- How do these exfoliated NS look like with regards to morphology, size distribution and photophysical properties?
- Are resolution-limited NS still fluorescent for all three materials (as proven for the case of EB-NS in **Manuscript II**)?
- How does the lifetime change after exfoliation?
- Do all three NS silicates display promising photophysical and biocompatible features for state-of-the-art bioimaging applications (as proven for the case of EB-NS in **Manuscript II**)?

5.3.2 Photophysical Properties and Fluorescence Lifetime Imaging of Exfoliated Near-Infrared Fluorescent Silicate Nanosheets (Manuscript III)

Publication Details

Title: “Photophysical properties and fluorescence lifetime imaging of exfoliated near-infrared fluorescent silicate nanosheets”

Authors: **Gabriele Selvaggio**, Milan Weitzel, Nazar Oleksiievets, Tabea A. Oswald, Robert Nißler, Ingo Mey, Volker Karius, Jörg Enderlein, Roman Tsukanov and Sebastian Kruss

Journal: *Nanoscale Adv.* **3**, 4541–4553 (2021)

DOI: 10.1039/d1na00238d

Author Contributions: SK and GS conceived and designed the study. SK coordinated the study. VK and GS worked on the different exfoliation methods and studied the size distributions via LDPS. GS and MW collected and analyzed the AFM dataset. GS and IM performed SEM characterization. GS measured absorption, as well as 1D and 2D excitation and fluorescence spectra. GS acquired the NIR microscopy images. RN and GS carried out macroscopic (stand-off) fluorescence imaging experiments. RT, NO and JE performed fluorescence lifetime spectroscopy as well as microscopic FLIM. MW built the macroscopic FLIM setup and acquired the respective lifetime dataset. TO performed cytotoxicity tests. GS and SK wrote the manuscript with contributions from all authors.

Nanoscale
Advances

ROYAL SOCIETY
OF CHEMISTRY

PAPER

View Article Online
View Journal

Cite this: DOI: 10.1039/d1na00238d

Photophysical properties and fluorescence lifetime imaging of exfoliated near-infrared fluorescent silicate nanosheets†

Gabriele Selvaggio,[ab] Milan Weitzel,[b] Nazar Oleksiievets,[c] Tabea A. Oswald,[d] Robert Nißler,[ab] Ingo Mey,[d] Volker Karius,[e] Jörg Enderlein,[cf] Roman Tsukanov[c] and Sebastian Kruss*[abg]

Received 30th March 2021
Accepted 23rd June 2021

DOI: 10.1039/d1na00238d

rsc.li/nanoscale-advances

The layered silicates Egyptian Blue ($CaCuSi_4O_{10}$, EB), Han Blue ($BaCuSi_4O_{10}$, HB) and Han Purple ($BaCuSi_2O_6$, HP) emit as bulk materials bright and stable fluorescence in the near-infrared (NIR), which is of high interest for (bio)photonics due to minimal scattering, absorption and phototoxicity in this spectral range. So far the optical properties of nanosheets (NS) of these silicates are poorly understood. Here, we exfoliate them into monodisperse nanosheets, report their physicochemical properties and use them for (bio)photonics. The approach uses ball milling followed by tip sonication and centrifugation steps to exfoliate the silicates into NS with lateral size and thickness down to ≈ 16–27 nm and 1–4 nm, respectively. They emit at ≈ 927 nm (EB-NS), 953 nm (HB-NS) and 924 nm (HP-NS), and single NS can be imaged in the NIR. The fluorescence lifetimes decrease from ≈ 30–100 µs (bulk) to 17 µs (EB-NS), 8 µs (HB-NS) and 7 µs (HP-NS), thus enabling lifetime-encoded multicolor imaging both on the microscopic and the macroscopic scale. Finally, remote imaging through tissue phantoms reveals the potential for bioimaging. In summary, we report a procedure to gain monodisperse NIR fluorescent silicate nanosheets, determine their size-dependent photophysical properties and showcase the potential for NIR photonics.

Introduction

Two-dimensional (2D) nanomaterials have attracted considerable interest in light of their exceptional photophysical properties and their potential for multiple applications.[1–4] Following graphene, other 2D materials such as transition metal dichalcogenides (TMDs) have been explored.[4–6] Single layers of 2D TMDs possess a bandgap and show versatile chemistry.[1,4,7–9] Because of the very high surface area displayed by these nanostructures, TMD nanosheets (NS) have been employed in catalysis, energy storage, sensing, and electronics.[1,4,5,7,9–14]

Bottom-up synthetic techniques for 2D materials (*e.g.* chemical vapor deposition (CVD), epitaxial growth, or wet chemical methods[7,8]) enable fabrication of large-area, ultrathin and uniform layers but at high expenses.[9,14] An alternative is top-down exfoliation (or delamination), which presents several advantages. Liquid-phase exfoliation (LPE) promises scalability, subsequent chemical modification as well as simple deposition on diverse surfaces.[1,9,14] With ultrasonication, NS sizes of few hundred nanometers are achievable.[9] Scalable high shear processing techniques such as wet ball milling are also known to yield monodisperse samples and are commonly employed tools for all kind of layered materials *e.g.* sheet silicates.[14–16]

A novel class of 2D materials are (phyllo)silicates such as Egyptian Blue ($CaCuSi_4O_{10}$, EB), which is as (exfoliated) nanosheet a promising fluorophore for photonics.[17,18] This calcium copper tetrasilicate is regarded as the most ancient artificial pigment made by mankind and dates back to Ancient Egypt (≈ 2500 BC), where it was employed in artwork.[19] EB's tetragonal crystal structure (space group $P4/ncc$) consists of parallel layers of silicate tetrahedra weakly held together by the presence of interlayer calcium ions in an eight-fold coordination geometry.[20] The copper ions are placed in a square planar coordination geometry and are most likely the reason for the photophysical properties of this material. It was reported that pristine EB emits in the near-infrared (NIR) region at ≈ 910–930 nm, with a broad excitation spectrum at green-red wavelengths.[21–23] EB fluorescence is

---

[a] *Physical Chemistry II, Bochum University, Bochum, 44801, Germany. E-mail: Sebastian.Kruss@rub.de*
[b] *Institute of Physical Chemistry, University of Göttingen, Göttingen, 37077, Germany*
[c] *Third Institute of Physics, University of Göttingen, Göttingen, 37077, Germany*
[d] *Institute of Organic and Biomolecular Chemistry, University of Göttingen, Göttingen, 37077, Germany*
[e] *Department of Sedimentology and Environmental Geology, Geoscience Center, University of Göttingen, Göttingen, 37077, Germany*
[f] *Cluster of Excellence "Multiscale Bioimaging: from Molecular Machines to Networks of Excitable Cells" (MBExC), University of Göttingen, Germany*
[g] *Fraunhofer Institute for Microelectronic Circuits and Systems, Duisburg, 47057, Germany*

† Electronic supplementary information (ESI) available. See DOI: 10.1039/d1na00238d

characterized by a very high quantum yield (≈ 11%[23]) compared to typical NIR fluorescent dyes[23,24] and a long lifetime ($\tau \approx$ 100–150 μs).[22,23,25] Theoretical investigations into electronic and magnetic properties of bulk and monolayer EB have suggested that EB could turn into a direct band-gap semiconductor if its thickness is reduced down to the monolayer regime (≈ 1 nm).[19,25,26] The exfoliation of EB into μm-sized nanosheets (EB-NS) is possible by stirring in hot water over several days.[1,6,27–30]

There are also homologues of EB such as Han Blue ($BaCuSi_4O_{10}$, HB) and Han Purple ($BaCuSi_2O_6$, HP). While the former presents a crystal structure identical to EB's (except for the substitution of Ca^{2+} with Ba^{2+}), the latter is less rich in silica and presents a chemically labile Cu–Cu bond, which is likely the explanation behind a weaker stability of this compound towards weak acids.[26,31,32] HB and HP are also fluorescent in the NIR, and this can be attributed to the Cu^{2+} ions and rationalized by ligand-field theory.[22] The interesting photophysical properties of EB, HB and HP have so far been mostly exploited to classify and assess the origin of ancient artwork.[23,33,34] Nevertheless, applications have been proposed as ink, fingerprint dusting powder, scaffold for selective enrichment of phosphopeptides or luminescent solar concentrators.[27,35–39] Recently, it was shown that EB nanosheets (EB-NS) keep their NIR fluorescence properties and can serve as NIR fluorophore.[17]

In general, fluorescence methods using the NIR (800–1700 nm) benefit from reduced scattering, absorption and photodamage, leading to better image contrast and, in biological applications, to better tissue penetration.[40,41] Moreover, phototoxicity is also lower compared to other wavelengths.[24,42,43] Unfortunately, there exist only few NIR fluorophores, and most are photolabile, possess low quantum yields, or have biocompatibility issues. In contrast to organic fluorophores (*e.g.* indocyanine green (ICG)), nanomaterials such as InAs quantum dots, lanthanide-doped nanoparticles, or semiconducting single-walled carbon nanotubes (SWCNTs) offer an enhanced photostability and a handle for chemical functionalization.[44–49] Especially for SWCNTs, chemical concepts have been developed to conjugate a broad range of biomolecules, which is required for molecular recognition.[18,50–54] Nevertheless, there is a large demand for novel NIR fluorophores with better or complementary properties.

Here, we exfoliate EB, HB and HP into nanosheets (EB-NS, HB-NS and HP-NS) *via* a mixed approach of planetary ball milling (PB) and tip sonication (TS) in water. This route enables us access to NS of defined size distribution, of which we report properties including fluorescence spectra and lifetimes. Finally, we show the potential of these materials for biophotonic applications such as lifetime-encoded imaging or deep-tissue imaging.

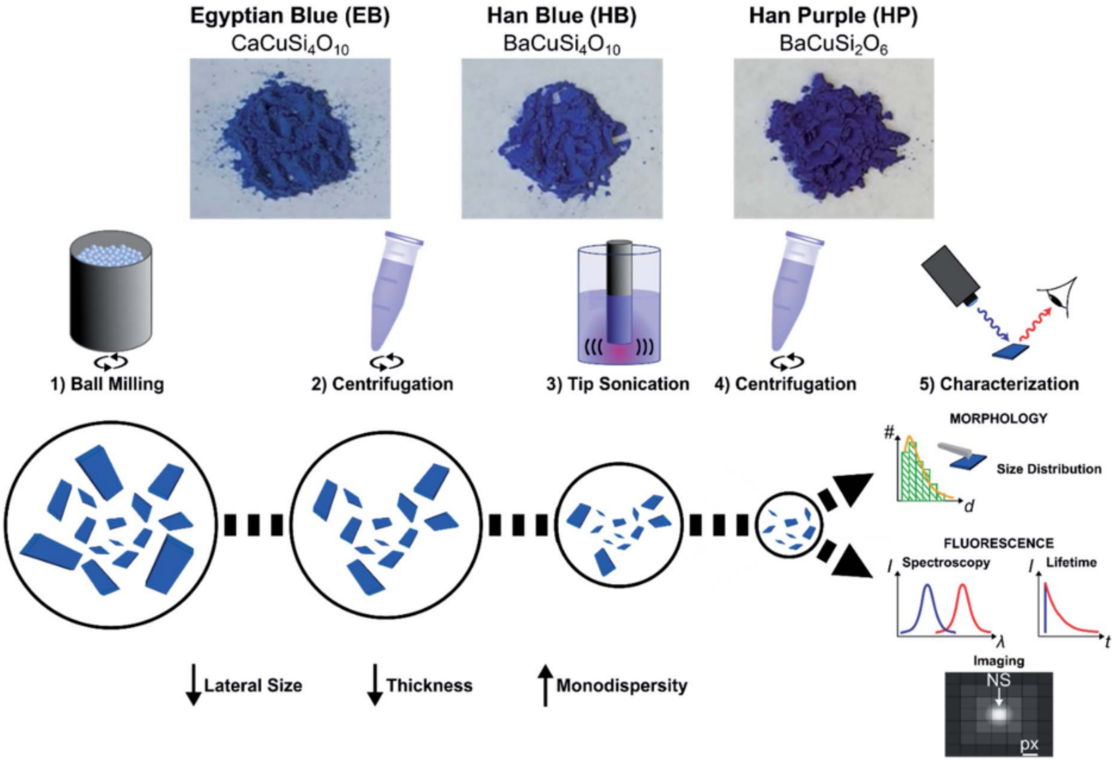

Fig. 1 Exfoliation of layered silicates into nanosheets. Bulk Egyptian Blue ($CaCuSi_4O_{10}$, EB), Han Blue ($BaCuSi_4O_{10}$, HB) and Han Purple ($BaCuSi_2O_6$, HP) are exfoliated into nanosheets (EB-NS, HB-NS and HP-NS). The bulk crystals are first reduced in size by a planetary ball mill (PB) in water. *Via* centrifugation larger particles are removed, then the supernatant is tip sonicated (6 h). An additional centrifugation step is performed to further increase monodispersity. These NS are colloidally stable and their properties such as the near-infrared (NIR) fluorescence are characterized and used for (bio)photonics.

Results and discussion

Exfoliation process and size distribution

To gain access to nanosheets of defined height and lateral size, we developed a multi-step exfoliation procedure, which was optimized for EB, HB and HP (Fig. 1).

The first step of this protocol uses planetary ball milling in water, which is frequently employed to crush minerals down to few µm-sized crystallites.[16,55] In a second step, the obtained slurry was centrifuged to remove larger particles. The supernatant (pH ≈ 10–11), which already showed an increased colloidal stability in water (Fig. S1 and S2†), contained µm-sized objects as measured by laser diffraction (Fig. S3–S6†). Next, the milled supernatant was tip sonicated to further decrease lateral size and height. Finally, the sample was centrifuged to improve monodispersity and to mainly obtain the smallest NS. The final concentration of the EB-NS, HB-NS and HP-NS was ≈ 0.5 g L^{-1} and, compared to the bulk counterparts, all samples were colloidally stable up to several days (pH ≈ 8–9, Fig. S7†). Furthermore, we observed that the colloidal stability of these NS was not significantly affected by acidic conditions and ionic environments such as physiological buffers (Fig. S8–S11†). Atomic force microscopy (AFM) and scanning electron microscopy (SEM) were used to assess size distribution and morphology of the NS. The exfoliated EB-NS, HB-NS and HP-NS show lateral sizes of few tenths of nm and heights ranging from monolayers to multilayers (Fig. 2 and S12a–f†). The data furthermore showed (Fig. S12g–i†) that lateral size increases linearly with thickness. As expected from the fragmentation of crystal structures like silicates undergoing sonication and/or milling, a log-normal function can best describe the overall trend of both lateral size and thickness of EB-NS, HB-NS and HP-NS.[55] Scanning electron microscopy (SEM) revealed additional insights into particle morphology (Fig. S13 and S14a–c†). This was also evaluated *via* scanning transmission electron microscopy (STEM, Fig. S14†). As indicated by AFM, SEM and STEM (Fig. S14d–f†), the exfoliation yields small NS with varying morphology, which could be attributed to the mechanical stress applied during milling and tip sonication. Nevertheless, we also observed NS with very regular geometry (Fig. S14d–f, S15 and S16†).

NIR spectroscopy and imaging

During transition from bulk to the nanoscale material, one could imagine that the NIR fluorescence might be damaged/destroyed. We therefore studied the NIR fluorescence of the NS.

All three bulk starting materials showed a broad absorption in the green-red region of the visible spectrum (Fig. 3 and S17†). Similarly, the NIR fluorescence of EB, HB and HP showed the known NIR emission features, with HB displaying a red-shifted fluorescence (up to 1000 nm).[21–23] This shift to longer wavelengths (Fig. 3b, e and S18†) opens possibilities in the field of *e.g.* biological imaging. Both excitation and emission features remained unaltered (Fig. 3d–f) in the NS, thus demonstrating that the exfoliation process of EB, HB and HP does not significantly alter the photophysics of these NIR fluorophores.

The fluorescence of these NS can also be detected/imaged on the single particle level in a custom-built NIR fluorescence microscope. Imaging experiments showed that the NS are relatively monodisperse, with a size below the resolution limit ($d < 500$ nm) of light microscopy (Fig. 4). Furthermore, all NS displayed no photobleaching during 2 h-long laser illumination (≈ 200 mW effective laser power) and imaging (Fig. S19†). However, some of the NS were so bright that they saturated the local pixels and looked 'larger' than the resolution limit. This finding could be explained by either differences in size (see AFM data) or agglomeration of multiple NS within resolution-limited (500×500 nm^2) regions. The question of how fluorescence scales with size is still not well understood but it likely increases with volume and requires further investigations.[17]

Fluorescence lifetime measurements in the time and frequency domains

As discussed above, bulk EB presents a high quantum yield and a long fluorescence lifetime (τ), which is the consequence of a parity-forbidden electronic transition of the copper ion.[22,23,25]

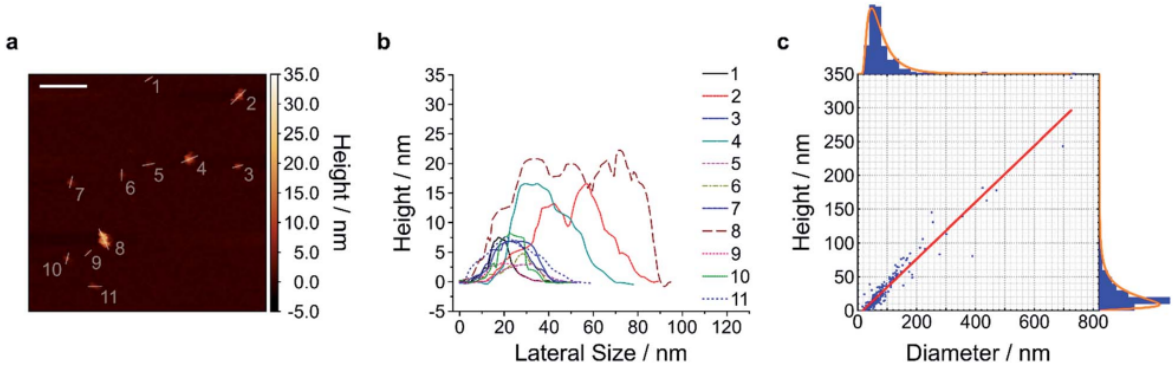

Fig. 2 Size and height of exfoliated silicate nanosheets. Exfoliated nanosheets were spin-coated on mica and imaged with atomic force microscopy (AFM) in intermittent contact mode. A representative image (a) and the respective height traces (b) and histograms with log-normal fits (c) of EB-NS are shown. The results indicate that lateral size scales linearly with height (linear fit = red line in (c)). The diameter/height values corresponding to the log-normal distributions' maxima are 47.0 nm/9.0 nm, with R^2 values of the linear fit of 0.924. $n = 245$ measured NS. The exfoliation of HB-NS and HP-NS yielded similar outcomes (Fig. S12†). Scale bar = 200 nm.

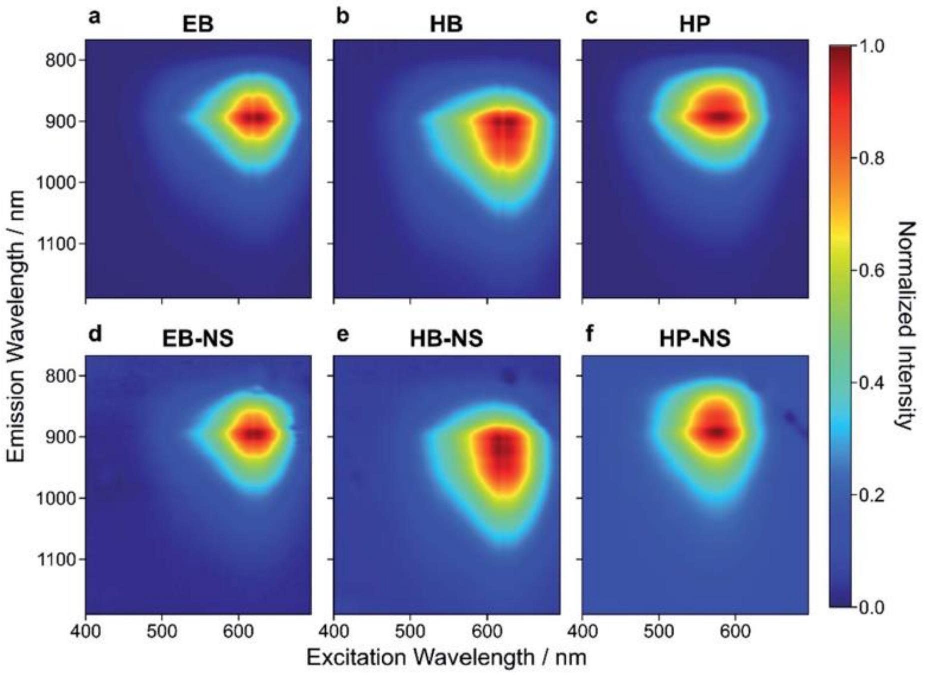

Fig. 3 Excitation–emission spectra of exfoliated silicate nanosheets. Normalized 2D excitation–emission spectra of bulk (a–c) and exfoliated (d–f) EB, HB and HP. The exfoliation procedure and decrease of size/layer number has nearly no influence on the emission spectra. Absorption is maximal at ≈ 630 nm (EB-NS), ≈ 620 nm (HB-NS) and ≈ 580 nm (HP-NS). These 2D spectra as well as 1D spectra (λ_{exc} = 561 nm, Fig. S18†) confirm emission maxima at ≈ 930 nm (EB-NS), ≈ 950 nm (HB-NS) and ≈ 920 nm (HP-NS).

To better understand what affects fluorescence lifetimes, they were measured with complementary methods. First, we used time-correlated single-photon counting (TCSPC) in a confocal setup (MicroTime 200, Picoquant) (Fig. 5a–d). We noticed that a single-exponential decay did not well describe TCSPC curves for all NS types (Fig. S20†). We therefore attributed the shorter

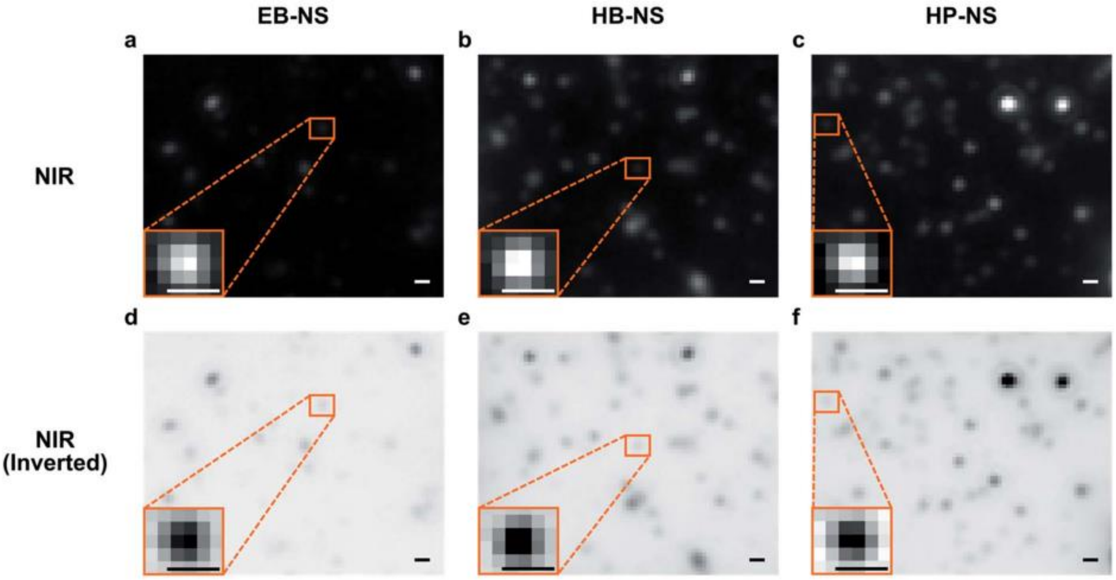

Fig. 4 Near-infrared (NIR) imaging of single silicate nanosheets. Fluorescence images of EB-NS, HB-NS and HP-NS (λ_{exc} = 561 nm) in the NIR (> 900 nm). Most nanosheets appear as resolution-limited spots (Abbe limit ≈ $\lambda_{emi}/2$). Note that some NS are so bright that they saturate the detector and appear to be larger than the resolution limit, but the AFM data proves otherwise (Fig. 2). Both normal (a–c) and inverted (d–f) grey scales are shown for better clarity. Scale bar = 1 µm.

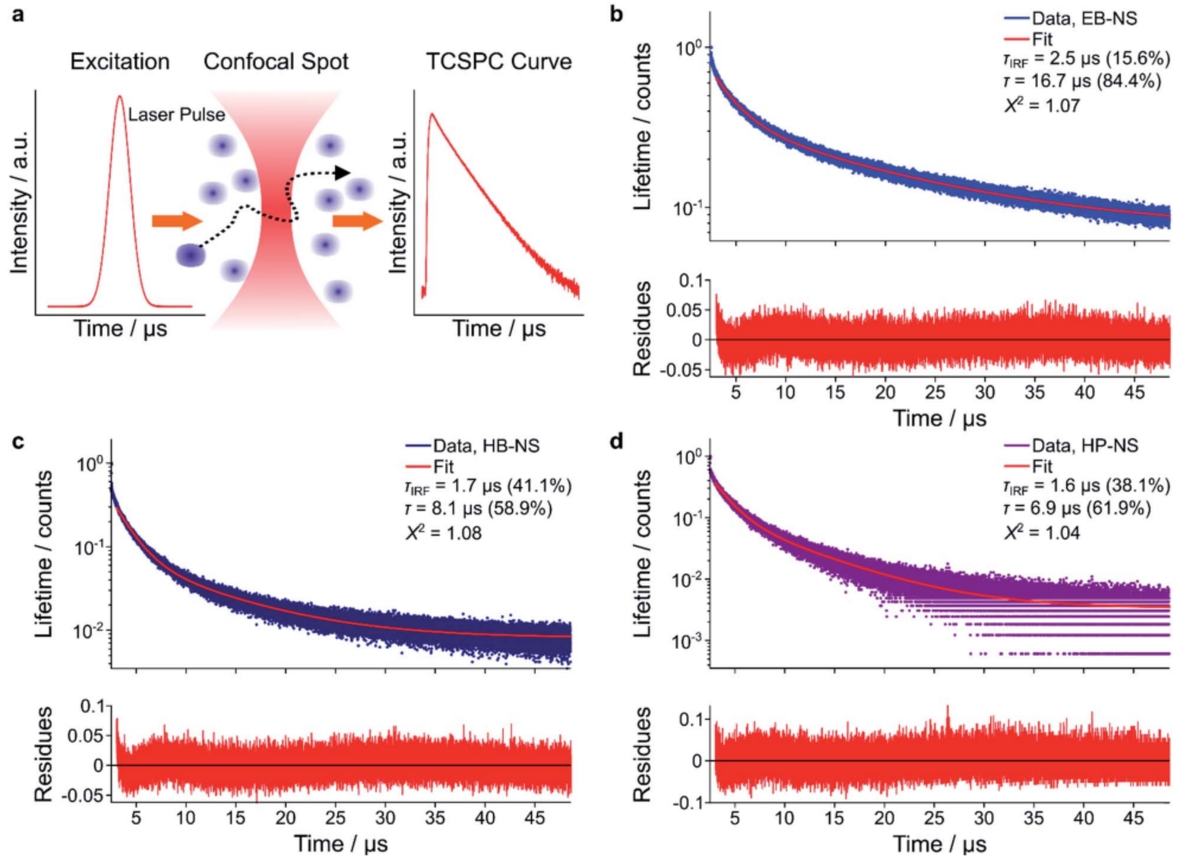

Fig. 5 Fluorescence lifetimes of silicate nanosheets. (a) Schematic of the confocal time-correlated single-photon counting (TCSPC)-based measurements of fluorescent lifetimes of single NS diffusing freely in a solution. (b–d) Exemplary decay curves of EB-NS (b), HB-NS (c) and HP-NS (d), and the corresponding bi-exponential fits. Note that the short lifetime component corresponds to the instrument response function. Fit residues are given below the plot.

component to the laser pulses (Instrument Response Function, IRF). The (longer) fluorescence lifetimes were determined to be 16.5 ± 0.25 µs, 8.25 ± 0.15 µs and 9.91 ± 0.06 µs for EB-NS, HB-NS and HP-NS, respectively.

This decrease in fluorescence lifetime from bulk (EB ≈ 130 µs, HB ≈ 60 µs, HP ≈ 25 µs) to NS was in agreement with frequency-domain measurements (Fig. S21†). An explanation for the observed decrease could be that defects or changes in symmetry either enable non-radiative decay pathways or increase the radiative rate constants.

Microscopic and macroscopic fluorescence lifetime imaging (FLIM) of nanosheets

Fluorescence lifetimes are very sensitive measurements for the environment and can also be used for multiplexing. The µs lifetimes of silicate NS are an interesting property because they are orders of magnitude longer than typical organic fluorophores (which are in the nanoseconds range).

Therefore, we built a setup for frequency-domain fluorescence lifetime imaging microscopy (FLIM).[56,57] This combination of FLIM and wide-field microscopy allows for fast FLIM with variable optical magnification. In short, the laser excitation is modulated, and from the delay of the fluorescence signal one can infer the lifetime. This way one can directly receive a fluorescence lifetime image in contrast to scanning methods that have to measure lifetimes pixel by pixel. However, the necessary time-gated camera for frequency domain measurements required a careful calibration using samples with known lifetime values. Therefore, an independent measurement of single NS lifetime was required. For calibrating the frequency domain-based lifetime camera, we used lifetime values of EB-NS obtained with the TCSPC-based method described above (Fig. 5b), and imaged a drop-casted EB-NS in a homogeneous layer on top of a glass coverslip. Then, we imaged non-homogeneous layers of all NS types (Fig. 6 and S22†).

Furthermore, due to different lifetimes of EB-NS and HP-NS, we could identify the NS type (border) based on a lifetime image of a region with both EB-NS and HP-NS (Fig. 6d–f). This identification was performed by using the corresponding phasor plot (see Materials and methods†). A phasor plot represents frequency-domain lifetime data using the measured phase

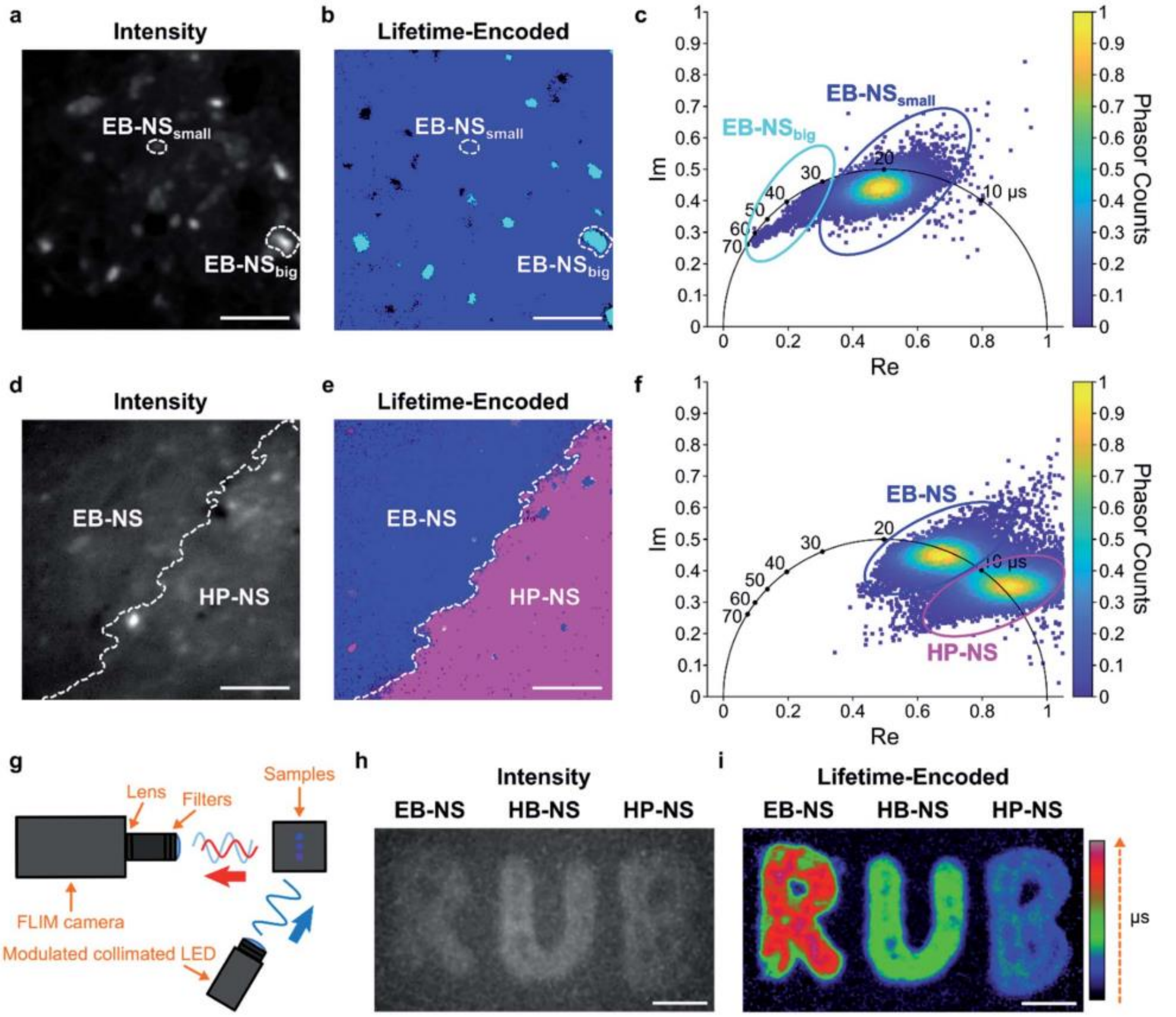

Fig. 6 Fluorescence lifetime imaging of nanosheets. (a) Fluorescence intensity image of an EB-NS solution drop-casted on a glass coverslip. Scale bar = 5 µm. (b) Frequency-domain fluorescence lifetime imaging microscopy (FLIM) of the same region as in (a), but with a color-coding that shows two sub-populations of different lifetime. Scale bar = 5 µm. (c) Corresponding phasor plot highlighting the two populations and the color-coding in (b). Species with longer lifetime appear in a light blue color and the ones with the shorter lifetime appear in a dark blue color. (d) Fluorescence intensity image of the border of stripes made from EB-NS and HP-NS. Scale bar = 5 µm. (e) FLIM image of the same region as in (d), but with a color-coding that shows the different NS according to their lifetime values. Scale bar = 5 µm. (f) Phasor plot highlighting the color-coding of the lifetimes in (e): EB-NS (longer lifetimes, blue color) and HP-NS (shorter lifetimes, purple). (g) Schematic of the macroscopic frequency-domain FLIM setup. (h) Intensity image of concentrated NS drop-casted on paper showing the logo of the Ruhr-Universität Bochum (RUB). Scale bar = 5 mm. (i) FLIM image of the same piece of paper as in (h), but with lifetime-encoded colors of EB-NS, HB-NS and HP-NS. Scale bar = 5 mm.

angle (φ) and the modulation ratio (M), calculated for each single camera pixel and defined as:

$$\mathrm{Im} = M \times \sin(\varphi), \tag{1}$$

$$\mathrm{Re} = M \times \cos(\varphi). \tag{2}$$

In our case, on such a phasor plot we could highlight two sub-populations of NS (blue and purple ovals in Fig. 6f). Then, we applied a color selection to the FLIM image (Fig. 6e). When only using the intensity image, it was not possible to identify the border between EB-NS and HP-NS (Fig. 6d). The average lifetimes of all NS types deduced from the lifetime images are: 17.6 ± 2.4 µs, 7.8 ± 1.5 µs and 4.5 ± 0.7 µs for EB-NS, HB-NS and HP-NS, respectively. Moreover, we noticed that, for each NS type, aggregates and particles with larger size exhibit slightly different lifetimes (Fig. 6a–c, S22 and S23†). In addition to microscopic FLIM, the high brightness of NS enabled macroscopic lifetime imaging (Fig. 6g). Indeed, drop-casting of ethanol dispersions of EB-NS, HB-NS and HP-NS on paper enabled us to detect their fluorescence (Fig. 6h), and to clearly distinguish them according to their uncalibrated phase lifetime (Fig. 6i). In this way, by using the NS as an ink we could encode

Table 1 Fluorescence lifetime values of EB-NS, HB-NS and HP-NS measured using confocal TCSPC-based technique[a]

Sample	τ_{TCSPC} [μs]
EB-NS	16.50 ± 0.25
HB-NS	8.25 ± 0.15
HP-NS	6.91 ± 0.06

[a] Mean ± standard deviation ($N = 3$–4 measurements).

the letters of the logo of the Ruhr-University Bochum (RUB) as lifetimes. These experiments show the huge potential for NIR FLIM and how it drastically improves the contrast, which is desirable for many imaging applications.

The lifetime values obtained using TCSPC were in good agreement with the lifetime values measured by frequency-domain FLIM (Tables 1 and S1†). Furthermore, the lifetime values measured with a simple fiber-optic sensor were in the same range, too (Table S1†). Therefore, the μs fluorescence lifetimes of these NS can be detected by methods of different complexity and potential.

Remote imaging through tissue

In a next step, we explored the potential of the NS in remote (stand-off) imaging through a tissue phantom. In such experiments, NS are imaged in a distance > 10 cm without a sophisticated optical setup or microscope (Fig. S24†). It mimics the requirements *e.g.* for image-guided surgery or remote imaging of fluorescent barcodes. We observed that the NS displayed a strong fluorescence sufficient for stand-off detection (Fig. S25–S28†). Furthermore, by monitoring the fluorescence intensity of NS solutions after addition of salts or lowering the pH, we noticed no significant decrease in the fluorescent signal (Fig. S8–S11†). Proven that these NS possess a robust and stable fluorescence, we performed a proof-of-principle experiment for biological imaging *e.g.* of vessels, by introducing EB-NS, HB-NS and HP-NS into glass capillary tubes (Fig. 7a and b).

Their intense fluorescence can be detected without a laser, *i.e.* with a simple LED (equipped with a 700 nm short-pass filter) and with a 900 nm long-pass filter in front of the NIR InGaAs camera. Next, we performed tissue phantom experiments, a standard test routinely performed in biomedical imaging (Fig. 7a and S29–S31†). The goal of this experiment was to assess the brightness of the sample through tissue slices of different thickness. Multiple 1 mm-thick chicken phantom tissues were therefore placed on top of NS-containing capillary tubes, and NIR pictures were taken (Fig. 7b and c). For each image, the intensity within a selected region of interest (ROI) was evaluated after every addition of a 1 mm-thick tissue slice. The fluorescence intensity of all silicate NS showed a similar trend (EB-NS seemed to display a slightly better performance) and was intense enough to be detected through up to 4–5 mm of tissue (Fig. 7d and e). Higher light intensities *e.g.* a laser illumination could further increase the tissue penetration. These results, together with the robustness of the fluorescence against biological analytes and pH ranges, and the high biocompatibility of EB-NS, HB-NS and HP-NS (Fig. S32–S34†), clearly demonstrate the potential of these NIR nanomaterials for biomedical imaging applications.

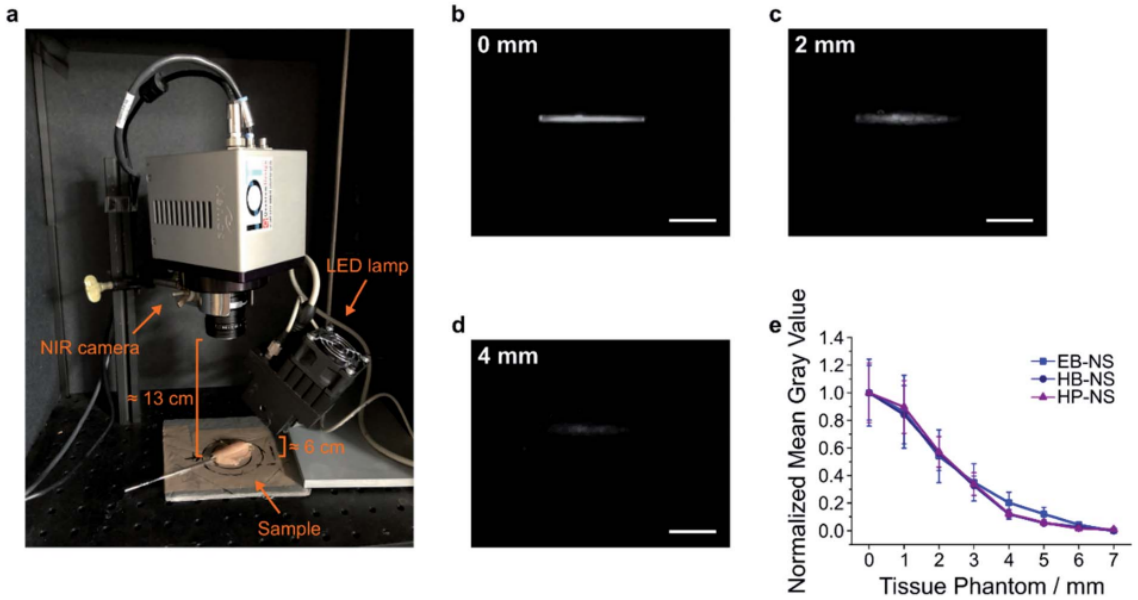

Fig. 7 Remote NIR imaging of nanosheets under tissue. (a) Picture of the NIR remote (stand-off) detection system. Capillary tubes (containing NS in water) under chicken tissue phantoms were imaged as shown in the image. (b–d) NIR image of capillary tubes filled with EB-NS under a chicken tissue of a certain thickness. Scale bar = 10 mm. (e) Normalized mean gray value of a region of interest within each image *vs.* tissue phantom thickness. Error bar = standard deviation, normalized over the maximum value of mean pixel intensity within a ROI (area ≈ 19 × 1 mm^2) from one image.

Conclusions

In this work, we developed a robust protocol to exfoliate the layered silicates EB, HB and HP *via* a combination of planetary ball milling, tip sonication, and multi-step centrifugation, obtaining nanosheets of high monodispersity (lateral size ≈ 16–27 nm and height ≈ 1–4 nm). Thorough characterization *via* AFM and SEM allowed a complete description of the morphology of these NS. In the future, the exfoliation could be further improved by using surfactants that facilitate faster exfoliation and reduction of the required mechanical forces (milling/tip sonication).

Most importantly, EB-NS, HB-NS and HP-NS retained the absorption (≈ 550–650 nm) and emission (≈ 850–1000 nm) properties of the non-exfoliated material. Therefore these NS are an addition to the library of NIR fluorescent nanomaterials beyond ICG, InAs quantum dots, lanthanide-doped nanoparticles and SWCNTs.[44–49] The fluorescence of all three NS is very bright, and single nanosheets can be easily imaged with a NIR fluorescence microscope. Therefore, single nanoparticle fluorescence applications such as microrheology or, in the future, chemical sensing[52,58–60] should be possible.

Interestingly, the fluorescence lifetimes decrease in comparison to bulk silicates, especially for EB-NS. This result indicates that lifetimes of these nanomaterials can be tailored and be used for lifetime-encoded imaging.[47] Microscopic fluorescence lifetime imaging can result in increased contrast, considering that short-lived background fluorescence can be easily removed. Furthermore, FLIM presents several advantages over standard fluorescence intensity imaging including independence from fluorescence intensity, fluorophore concentration or bleaching. Additionally, the fluorescence lifetime can be sensitive to environmental factors, which could facilitate the monitoring of functional changes in biological systems.[61] Macroscopic fluorescence lifetime imaging experiments demonstrated an additional benefit of working with such bright and robust materials, *i.e.* that they can be clearly detected and unambiguously distinguished even when using non-optimized home-built stand-off devices. The µs fluorescence lifetimes do indeed not require complicated setups as normally needed for ps- to ns-long lifetimes of other typical NIR fluorophores (*e.g.* SWCNTs). For this reason, the successful application of such NS for barcoding *e.g.* banknotes but also biological materials or even cells is within reach. The advantage of the NS' intense fluorescence was also shown by stand-off detection experiments with tissue phantoms. Considering their high biocompatibility, these NS have large potential for bioimaging.

In summary, exfoliated EB-NS, HB-NS and HP-NS possess versatile NIR fluorescence properties and pave the way for novel fluorescence (lifetime) bioimaging applications and for photonics in general.

Experimental

Exfoliation of Egyptian blue (EB), Han blue (HB) and Han purple (HP) bulk powders into nanosheets (EB-NS, HB-NS and HP-NS, respectively)

EB, HB and HP powders (respectively < 120 µm, < 40 µm and < 40 µm qualities) were purchased from Kremer Pigmente GmbH & Co. KG. For each powder, exfoliation was performed as follows.

In the milling step, 3 g of powder were introduced into a 20 mL agate beaker together with 5 mm agate balls. Deionized water was added until a slurry consistency was reached. The so-prepared agate beaker was then placed in a planetary ball mill (PB, Pulverisette 7 Premium Line, Fritsch), which was run at 900 rpm for 1 h (3 cycles of 20 min each, 5 min pause). Aliquots of the resulting milled slurry were removed from the beaker and their grain size distributions were measured by means of a laser diffraction particle sizer (LDPS, model LS13320, Beckman&Coulter). For each measurement, three runs were performed, PIDS was used, and an optical model R.I. 1.6/1 was applied. To visualize the grain size distribution, the number of particles within an individual grain size class was plotted as percentage of all particles against the central diameter of the class. In this way, the very small number of bigger particles that was present in the system does not dominate the distribution curve, as it would instead happen if volume percentages were displayed.

Following the milling step, an aliquot was poured into a Nalgene® centrifuge tube (Thermo Fisher Scientific) and water was added until an overall volume of 150 mL (dilution factor ≈ 3) was reached. Then, a first centrifugation step (Heraeus Multifuge X3R, Thermo Fisher Scientific) was performed: $T = 20\ ^\circ\mathrm{C}$, 800 rpm (150 × g), 9 min 41 s, 5 s acceleration ramp, 5 s deceleration ramp, 5 cycles. These parameters were calculated from the Stokes equation (corrected for centrifugation[62]) in order to remove particles of diameter $d > 1\ \mu\mathrm{m}$:

$$t = \frac{18 \times \eta}{(\rho_\mathrm{k} - \rho_\mathrm{w}) \times 4\pi^2 \times f^2 \times d^2} \times \ln \frac{r}{r_0}. \tag{3}$$

In eqn (3), t is the settling time [s], η the temperature-dependent dynamic viscosity of water [kg m^{-1} s^{-1}], ρ_k the grain density [kg m^{-3}], ρ_w the temperature-dependent water density [kg m^{-3}], f the rpm [s^{-1}], d the previously mentioned grain (equivalent) diameter [m], r the distance between the rotor's fulcrum and the sediment's height [cm], and r_0 the distance between the rotor's fulcrum and the suspension's surface [cm] (the last two parameters are dependent on the geometry of the employed centrifuge). At the end of each cycle, the supernatant was decanted and new water was added up to the initial volume; finally, the so-obtained supernatant dispersion (pH ≈ 10–11) was collected in a glass jar and stored at room temperature. New LDPS measurements were performed to check the efficiency of the described centrifugation step in terms of the size distribution. Aliquots of each supernatant of each of the three milled pigments were taken, dried and weighed, yielding the following concentrations: EB ≈ 2.2 g L^{-1}, HB ≈ 1.4 g L^{-1} and HP ≈ 0.6 g L^{-1}. While EB proved to be stable for up to ≈ 2 days already at this stage, milled HB and HP particles settled after a few hours.

The supernatant vials were vigorously shaken and specific volumes of them were withdrawn for the following steps. More precisely, in order to carry out the second exfoliation procedure of each silicate in a total volume of 50 mL with comparable concentrations, sample aliquots were diluted with additional

Milli-Q water until the lowest concentration among the three samples (*i.e.* HP $\approx$ 0.6 g L^{-1}) could be reached in all systems. Typically, a so-diluted milled supernatant was then poured into a 50 mL glass vial and subjected to tip sonication (Fisherbrand™ Model 120 Sonic Dismembrator, Fisher Scientific) in an ice bath for 6 h at 60% amplitude (*i.e.* 72 W).

A second and last centrifugation step followed, necessary to remove metal residues from the previous tip sonication step. Typically, the sample was introduced into a 50 mL Falcon tube, which was then centrifuged under the following conditions: T = 20 °C, 1500 rpm (526 × g), 4 min 12 s, 9 s acceleration ramp, 7 s deceleration ramp, 1 cycle. While most of the sample's volume could be efficiently decanted in this way, an additional step at 3000 rpm (2103 × g) for 1 min was performed on its last fraction in the Falcon tube (<5 mL), where the removal of the supernatant from the sediment was typically more challenging. Here also, parameters were optimized to remove particles larger than 1 μm.

The so-generated samples (EB-NS, HB-NS and HP-NS) had a pH $\approx$ 8–9, concentration of $\approx$ 0.5 g L^{-1}, measured by drying aliquots of known volume. The final sample vials were in conclusion stored at room temperature. Further characterization steps were always preceded by either vortexing (Vortex Mixer VV3, VWR International) at maximum power or by bath sonication (Branson 1800 Cleaner, Sonics Online) for 10 min. Unless explicitly stated otherwise, measurements described in this paper were performed in the same way for EB-NS, HB-NS and HP-NS, which are therefore referred to as "NS".

Atomic force microscopy (AFM)

A typical NS sample was vortexed and bath sonicated for 10 min, then 5–10 μL of undiluted solution were spin-coated (G3 Spin Coater, Specialty Coating Systems, Inc.) onto a previously Scotch-tape exfoliated mica surface according to the following parameters: 10 s of ramp time, 2000 rpm, 150 s of dwell time. An Asylum Research MFP-3D Infinity AFM (Oxford Instruments) was employed in AC mode (software version 15.01.103). Rectangular cantilevers from Opus (160AC-NA, MikroMasch Europe) were used: these were characterized by aluminum coating, a tetrahedral tip, 300 kHz resonance frequency, and a force constant of 26 N m^{-1}. For the statistical analysis, sample regions with sizes of 5 × 5 μm^2 were measured at 1.03 Hz and with 512 points per line (which corresponds to 9.8 nm of pixel size). High resolution AFM images were, on the other side, acquired on sample regions of 1 × 1 μm^2, at 0.85 Hz and with 1024 points per line (977.5 pm of pixel size). Image analysis was carried out with the software Gwyddion (version 2.51). For size distribution estimations, the mean diameter (*i.e.* mean radius $R_m \times 2 = D_m$) and the maximum height (z_{max}) obtainable in Gwyddion after height and slope thresholding were considered. Python scripts based on the module scipy.stats were run for the fitting of histograms and scatter plots: the former class of fits are log-normal distribution functions, typical for fragmentation phenomena like the ones endured by our NS with our protocols,[55] whereas the latter is represented by linear fits. The parameters of the histograms were calculated using a maximum likelihood estimation method.

Scanning electron microscopy (SEM) and scanning transmission electron microscopy (STEM)

For SEM imaging (Quattro S SEM, Thermo Fisher Scientific), highly-oriented pyrolytic graphite (HOPG, grade ZYB, Bruker) were used as substrates. HOPGs were plasma-treated (Zepto Diener Electronic GmbH +Co. KG, 1 min of O_2 supply, 1 min of plasma process) in order to clean their surfaces and increase their hydrophilicity. Next, a typical NS sample was vortexed and bath sonicated for 10 min. 10 μL of undiluted sample were spin-coated with the same parameters employed for AFM measurements. For each NS sample, the so-prepared HOPG was either imaged at the SEM as is, or a $\approx$ 4 nm-thick gold layer was evaporated (Baltec MED-020, Baltec) onto it to decrease surface charging and, thus, increase imaging contrast. The HOPG was then placed into the SEM chamber and imaged in the following conditions: high vacuum mode, voltage = 5.00 kV, spot size = 3.0, working distance = 10.0 mm, Everhart–Thornley Detector (ETD) for secondary electrons, Circular Backscatter Detector (CBS) for backscattered electrons.

STEM measurements were carried out on the same device. Typically, undiluted 5 μL of previously vortexed and bath sonicated NS were deposited and dried onto formvar-coated copper grids, stabilized with evaporated carbon film (FCF300-CU, Electron Microscopy Sciences). The parameters are the same as for SEM imaging, except for the employed detector (STEM3+).

Near-infrared (NIR) imaging at microscopy setup

The imaging setup consists of a 561 nm laser (Cobolt Jive™ 561 nm), an Olympus IX53 microscope equipped with a 100× (UPlanSApo 100×/1.35 Sil, Olympus) and a 20× (MPlanFL N 20×/0.45, Olympus) objectives, and a NIR camera (Cheetah TE1, Xenics). Along the light path leading from the microscope to the camera, a dichroic mirror (VIS/NIR, HC BS R785 lambda/5 PV, F38–785S, AHF) and a 900 nm long-pass filter (FELH0900, Thorlabs) are installed. NS droplets were imaged directly after drying on a #1 glass coverslip.

For simple characterization images, a 5 μL droplet ($\approx$ 0.5 g L^{-1}) of heavily vortexed NS was drop-casted on the imaging substrate; acquisition was performed with the 100× objective, an integration time of 0.5 s and the laser was set at an excitation power of 250 mW.

To investigate whether NS can be bleached, a long imaging session with continuous excitation was performed on 10 μL of NS sample. Acquisition settings were the following: objective = 20×, laser set power = 500 mW, measured power out of the objective $\approx$ 180 mW, acquisition time $\approx$ 2 h, exposure time = 0.5 s, frame rate = 0.3 fps.

Data acquisition was controlled by the Xenics software (v. 2.6), whereas data analysis was carried out in ImageJ (v. 1.52a) and on Origin Pro 8.1. Background subtraction (*i.e.* subtraction of dark regions within the original images) was also performed in ImageJ, but was only applied to Fig. 4.

Near-infrared (NIR) 1D and 2D spectroscopy

The spectroscopy setup presents two different light sources: a laser (Gem 561, Laser Quantum, Novanta) and a monochromator (MSH-150, LOT-Quantum Design GmbH, equipped with a xenon arc lamp and a diffraction grating). While the former was employed for the study of 1D emission profiles, the latter was used for acquisition of 2D spectra. The microscope is an Olympus IX73 with a 10× objective (UplanFLN 10×/0.30, Olympus), whereas the spectrometer is a Shamrock 193i spectrograph (Andor Technology Ltd.) coupled to an array NIR detector (Andor iDUs InGaAs 491). NS (300 µL, undiluted) were introduced into a 96-well-plate, positioned above the setup's objective; ≈ 1–3 mg of bulk (pristine) silicate powders were dispersed in the same Milli-Q water volume and measured, too. Fluorescence data was acquired *via* the Andor SOLIS software (version 4.29.30012.0).

For the 1D dataset, the exposure time was set to 1 s, the laser power to 100 mW, and the input side slit width to 500 µm. Data analysis and plotting were performed by means of the software Origin Pro 8.1; more precisely, the peak positions were evaluated *via* 1st derivative method with Savitzky–Golay smoothing (Peak Analyzer-Integrate Peaks, polynomial order = 2, points of window = 20). Full widths at half maximum (FWHM) were automatically assessed by the software at the end of this procedure.

For acquisition of 2D spectra, the monochromator light source was scanned with steps of 5 nm over a wavelength range of 400–700 nm; during a single measurement, a spectrum was recorded with an integration time of 4 s and 10 s for bulk and NS samples, respectively (input side slit width = 500 µm). The plotting as well as the correction for the quantum efficiency of the detector and for the spectral irradiance of the xenon lamp were performed using a self-written Python script.

Fluorescence lifetime measurements with time-correlated single-photon counting device

Confocal fluorescence lifetime measurements (Fig. 5a) were performed using the commercial confocal setup Microtime 200 (PicoQuant GmbH). The system is based on an Olympus IX-71 inverted microscope (Olympus Deutschland) with a side-port on the right side. The excitation unit consists of a pulsed diode laser (λ_{exc} = 640 nm, LDH-D-C-640, PicoQuant GmbH) with a repetition rate of 80 MHz. To ensure enough excitation efficiency, 100 pulses were sent together consecutively within a time of 1.25 µs with a subsequent laser-off time of 48.75 µs, during which emitted photons were collected. The total acquisition time for each measurement was 10 min. The laser power was maintained at 20 µW in the back-focal plane of the objective lens. A high-NA objective (UApoN 100× oil, 1.49 NA, Olympus) was used to focus the light inside the sample and at the same time to collect the emission photons. Collected emission light was passed through the dichroic mirror (Di01-R405/488/561/635, Semrock) and focused through a pinhole (diameter = 100 µm) for confocal detection. After the pinhole, the light was refocused onto an avalanche single photon diode (τ-SPAD, PicoQuant) using two achromatic lens doublets. A long-pass filter (647LP, Semrock) was used to block backscattered excitation light. Signals from the detector were processed by a multichannel picosecond event timer (Hydraharp 400, PicoQuant) with 16 ps time resolution.

Analysis of fluorescence lifetime decays was performed using a custom-written MATLAB routine. First, photon arrival times were read from the raw.hdd data files with MATLAB functions provided by PicoQuant. Single- and double-exponential decay functions were then used to tail-fit the TCSPC curves, within a time window from 2.6 µs till 50 µs after excitation pulse (Fig. S20† and 5b–d).

Fluorescence lifetime measurements with fiber-optic oxygen sensor

The chosen fiber-optic oxygen sensor (FireSting O_2, PyroScience GmbH) is equipped with a fluorophore (REDFLASH indicator) which is excitable at orange-red wavelengths ≈ 610–630 nm and displays an oxygen-dependent luminescence at ≈ 760–790 nm. It was used for measurements in the frequency domain (Fig. S21a†) to determine fluorescence lifetimes. Measurements were performed on dry samples: while the bulk powders were measured without prior treatment, 10 mL of NS counterparts were freeze-dried over 2 days, yielding ≈ 10–15 mg of powder. Typically, the FireSting optical probe was lowered into a Falcon tube where few mg of sample powder were positioned; the fiber was then mechanically fixed at a distance from the sample which could result in the desired signal value (intensity ≈ 14 mV, constant for all samples) with our settings (ν = 4000 Hz, LED intensity = 60%, amplification factor = 400×). Each measurement took 10 min, while data points were acquired every second; signal (and calculated lifetime) values were showing a neglectable fluctuation, thus leading to a low standard deviation (not observable by eye in Fig. S21b†). However, given the overall low signal strength when measuring with this device, the TCSPC values should be regarded as the gold-standard.

Microscopic frequency-domain fluorescence lifetime imaging

Measurements were performed using a custom-built optical setup (Fig. S35†). Light of an excitation laser with 638 nm wavelength (PhoxX+ 638-150, Omicron) was modulated with square-shaped pulses at 8 kHz frequency. Gating signal was sent by a camera to laser in order to switch it off during the camera readout time. A clean-up filter (CUF) (ZET 640/10, Chroma) was used to reject undesired wavelengths. A variable neutral density filter (ND) (NDC-50C-4-A, Thorlabs) was used for adjusting the laser power. Afterwards, the laser light was coupled into a single-mode optical fiber (SMF) (P1-460B-FC-2, Thorlabs) with a typical coupling efficiency of 50%. After exiting the fiber, the light beam was expanded by a factor of 3.6 using two telescopic lenses (TL1 and TL2). The collimated laser light was focused into the back focal plane of the objective (UAPON 100× oil, 1.49 NA, Olympus) using lens L1 (AC508-180-AB, Thorlabs). For reducing back-reflections of the excitation light, the illumination angle on the sample was varied slightly by mechanically shifting the collimated beam with a translation stage TS (LNR50M, Thorlabs) perpendicular to the optical axis. A high-performance two-axis linear stage (M-406, Newport) ensured smooth lateral sample positioning. An independent one-dimensional translation stage (LNR25/M, Thorlabs) was equipped with a differential micrometer screw (DRV3, Thorlabs) to move the objective along the optical axis for focusing. Collected fluorescence was spectrally separated from the excitation path using a multi-band dichroic mirror (DM) (Di03 R405/488/532/635, Semrock) that guided the fluorescence light towards the tube lens L2 (AC254-200-A-ML, Thorlabs). Lenses L5 (AC254-100-A, Thorlabs) and L6 (AC508-150-A-ML, Thorlabs) re-imaged the fluorescence from the image plane located after the tube lens onto the chip of an emCCD camera (iXon Ultra 897, Andor). Alternatively, lenses L3 (AC254-100-A, Thorlabs) and L4 (AC508-075-A-ML, Thorlabs) re-imaged the light onto the chip of a lifetime camera (PCO.FLIM, PCO AG). For switching the light between the two cameras, a dielectric mirror (BB1-E02, Thorlabs) was positioned on a magnetic base plate MB (KB50/M, Thorlabs) with a removable top. A band-pass filter BP (BrightLine HC 692/40, Semrock) was used to reject scattered excitation light in the emCCD detection path. Alternatively, a long-pass filter LPF (647 nm EdgeBasic, Semrock) was used for the frequency domain-based lifetime camera path. The magnification for imaging with the emCCD was 166.6×, resulting in an effective pixel size in sample space of 103.5 nm. The magnification for imaging with the lifetime camera was 83×, so that the effective pixel size in sample space was 84 nm. The total acquisition time for a single frame with lifetime information was 3.2 s and consisted of 16 consecutive sub-frames with exposure times of 200 ms each. Careful calibration was required in order to obtain absolute lifetime values using the frequency domain-based lifetime camera. The sample with an homogeneous layer of EB-NS drop-casted on top of a glass coverslip was used for calibration. The lifetime value used as a reference for calibration was obtained using a confocal TCSPC-based measurement of the same EB-NS sample. The excitation laser power was in the range of 20–30 mW.

Macroscopic frequency-domain fluorescence lifetime imaging

The macroscopic lifetime imaging setup (Fig. 6g) consists of the above mentioned PCO.FLIM camera, a lime-colored LED, and a custom-built stage to hold the sample in place. The camera is positioned at a distance of ≈ 30 cm from the sample, and is equipped with a fixed focal length objective (f = 16 mm/F1.4, Thorlabs), an 800 nm long-pass filter (FEL0800, Thorlabs), and a 920 nm band-pass filter (FB920-10, Thorlabs). The LED illuminates the sample from a distance of ≈ 15 cm with a power below 1 W (M565L3, Thorlabs). The light beam is collimated by an aspheric condenser lens (ACL2520U-A, Thorlabs) and controlled by an LED Driver (LEDD1B, Thorlabs). During data acquisition, the LED was modulated by the camera with a sine wave of 5 kHz frequency and was not turned off during pixel readout. To achieve the best possible image quality, an increased exposure time of 5 s for each of the 16 sub-frames was used and a median filter with a kernel size of 5 was applied to reduce salt-and-pepper-noise. No calibration was performed prior to the acquisition.

NIR imaging at stand-off detection setup

Our NIR custom-made stand-off detection setup[18] consists of a NIR InGaAs camera (XEVA, Xenics), a Kowa objective (f = 25 mm/F1.4), and a white light source (UHPLCC-01, UHP-LED-white, Prizmatix). The latter is equipped with a 700 nm short pass filter (FESH0700, Thorlabs) for excitation. Furthermore, a 900 nm long pass filter (FEL0900, Thorlabs) is mounted on the camera.

For imaging of EB, HB and HP water dispersions in glass vials, an exposure time of 3 s at maximum lamp intensity was employed.

Concerning sample preparation for tissue phantom experiments, 1 mL of NS batch was concentrated (Concentrator 5301, Eppendorf) for ≈ 2 h, yielding a volume of ≈ 0.1 mL with concentration of ≈ 5 g L^{-1}. After ≈ 5 min of bath sonication, a capillary tube (ringcaps® 25 µL, Hirschmann Laborgeräte GmbH & Co. KG) was dipped into the NS vial, and NS were thus sucked into the glass tube due to capillary forces. For each class of silicates, a so-prepared capillary tube was positioned onto the setup's stage at ≈ 6 cm and ≈ 13 cm away from the excitation lamp and the detection camera, respectively (Fig. S24†). Initial reference images were acquired with 0.5 s of exposure time at maximum excitation intensity. Afterwards, ≈ 1 mm-thick chicken slices were step-wise laid on top of the capillary tube, and new images with the same settings were taken after every layer's deposition.

Colloidal stability experiments were performed in cuvettes on sample volumes of ≈ 2 mL. EB-NS, HB-NS and HP-NS had a starting pH value in the range of ≈ 8–9. Prior to imaging, NS were bath sonicated for 5 min. Then, buffer solutions of pH 4 and 7 were added to some NS cuvettes in the volumes necessary to reach pH 5 and pH 7, respectively. To study the impact of ions on the colloidal stability of the NS, 200 µL of a solution of NaCl (9 g L^{-1} a typical blood concentration) were added into other cuvettes. The effect of phosphate-buffered saline (PBS) was also evaluated by adding 200 µL of 10× PBS into separate cuvettes, leading to a final 1× PBS concentration in the samples. Finally, control samples consisted in the addition of 200 µL of H_2O. Imaging was started shortly after the introduction of the mentioned aliquots in the cuvettes. Acquisition settings were: exposure time = 2 s, frame rate = 0.067 fps, LED excitation power = 50%, acquisition time ≈ 60 min, LED-cuvette distance ≈ 18 cm, camera-cuvette distance ≈ 20 cm. To assess the fluorescence intensity over time, the mean signal intensity in a central region of interest of each cuvette was measured (and normalized to the starting frame).

Except for colloidal stability experiments, background subtraction (*i.e.* subtraction of a background reference image) was performed on the acquired dataset. Data analysis of the obtained NIR pictures was carried out in ImageJ (v. 1.52a) and Origin Pro 8.1.

Preprint

This manuscript has been uploaded to a preprint server (https://doi.org/10.26434/chemrxiv.13350728.v1).

Author contributions

SK and GS conceived and designed the study. SK coordinated the study. VK and GS worked on the different exfoliation methods and studied the size distributions *via* LDPS. GS and MW collected and analyzed the AFM dataset. GS and IM performed SEM characterization. GS measured absorption, as well as 1D and 2D excitation and fluorescence spectra. GS acquired the NIR microscopy images. RN and GS carried out macroscopic (stand-off) fluorescence imaging experiments. RT, NO and JE performed fluorescence lifetime spectroscopy as well as microscopic FLIM. MW built the macroscopic FLIM setup and acquired the respective lifetime dataset. TO performed cytotoxicity tests.

Conflicts of interest

There are no conflicts to declare.

Acknowledgements

Funded by the Deutsche Forschungsgemeinschaft (DFG, German Research Foundation) under Germany's Excellence Strategy-EXC 2033-390677874-RESOLV. We acknowledge support by the DFG *via* the Heisenberg Program (S. K.). This project was supported by the VW Foundation. NO is grateful to the Deutsche Forschungsgemeinschaft (DFG) for financial support *via* Project A10 of the SFB 803. We also thank Dr Burkhard Schmidt for the acquisition of reflection spectra, Cornelia Friedrich for assistance in the Geology labs, Jutta Gerber-Nolte and Angela Rübeling for expert technical assistance. JE acknowledges support by the Deutsche Forschungsgemeinschaft (DFG, German Research Foundation) under Germany's Excellence Strategy – EXC 2067/1-390729940. The authors also acknowledge Dr Ingo Gregor for help with lifetime measurements using confocal setup and Dr Gerhard Holst from PCO AG for continuous support, advices and software updates for the PCO.FLIM camera. We thank Dr Alexey Chizhik and Dr Anna Chizhik for providing and purchasing the equipment for the optical setup.

References

1 V. Nicolosi, M. Chhowalla, M. G. Kanatzidis, M. S. Strano and J. N. Coleman, *Science*, 2013, **340**, 72–75.
2 A. K. Geim and K. S. Novoselov, *Nat. Mater.*, 2007, **6**, 183–191.
3 K. S. Novoselov, A. K. Geim, S. V. Morozov, D. Jiang, Y. Zhang, S. V Dubonos, I. V Grigorieva and A. A. Firsov, *Science*, 2004, **306**, 666–669.
4 G. R. Bhimanapati, Z. Lin, V. Meunier, Y. Jung, J. Cha, S. Das, D. Xiao, Y. Son, M. S. Strano, V. R. Cooper, L. Liang, S. G. Louie, E. Ringe, W. Zhou, S. S. Kim, R. R. Naik, B. G. Sumpter, H. Terrones, F. Xia, Y. Wang, J. Zhu, D. Akinwande, N. Alem, J. A. Schuller, R. E. Schaak, M. Terrones and J. A. Robinson, *ACS Nano*, 2015, **9**, 11509–11539.
5 M. Chhowalla, H. S. Shin, G. Eda, L. J. Li, K. P. Loh and H. Zhang, *Nat. Chem.*, 2013, **5**, 263–275.
6 J. N. Coleman, M. Lotya, A. O'Neill, S. D. Bergin, P. J. King, U. Khan, K. Young, A. Gaucher, S. De, R. J. Smith, I. V. Shvets, S. K. Arora, G. Stanton, H. Y. Kim, K. Lee, G. T. Kim, G. S. Duesberg, T. Hallam, J. J. Boland, J. J. Wang, J. F. Donegan, J. C. Grunlan, G. Moriarty, A. Shmeliov, R. J. Nicholls, J. M. Perkins, E. M. Grieveson, K. Theuwissen, D. W. McComb, P. D. Nellist and V. Nicolosi, *Science*, 2011, **331**, 568–571.
7 D. V. Talapin, J. S. Lee, M. V. Kovalenko and E. V. Shevchenko, *Chem. Rev.*, 2010, **110**, 389–458.
8 M. Nasilowski, B. Mahler, E. Lhuillier, S. Ithurria and B. Dubertret, *Chem. Rev.*, 2016, **116**, 10934–10982.
9 Q. H. Wang, K. Kalantar-Zadeh, A. Kis, J. N. Coleman and M. S. Strano, *Nat. Nanotechnol.*, 2012, **7**, 699–712.
10 M. M. R. Moayed, T. Bielewicz, M. S. Zöllner, C. Herrmann and C. Klinke, *Nat. Commun.*, 2017, **8**, 2–8.
11 S. Dogan, T. Bielewicz, Y. Cai and C. Klinke, *Appl. Phys. Lett.*, 2012, **101**(7), 073102.
12 S. Dogan, T. Bielewicz, V. Lebedeva and C. Klinke, *Nanoscale*, 2015, **7**, 4875–4883.
13 J. N. Coleman, M. Lotya, A. O'Neill, S. D. Bergin, P. J. King, U. Khan, K. Young, A. Gaucher, S. De, R. J. Smith, I. V. Shvets, S. K. Arora, G. Stanton, H. Y. Kim, K. Lee, G. T. Kim, G. S. Duesberg, T. Hallam, J. J. Boland, J. J. Wang, J. F. Donegan, J. C. Grunlan, G. Moriarty, A. Shmeliov, R. J. Nicholls, J. M. Perkins, E. M. Grieveson, K. Theuwissen, D. W. McComb, P. D. Nellist and V. Nicolosi, *Science*, 2011, **331**, 568–571.
14 H. Tao, Y. Zhang, Y. Gao, Z. Sun, C. Yan and J. Texter, *Phys. Chem. Chem. Phys.*, 2017, **19**, 921–960.
15 M. Stöter, S. Rosenfeldt and J. Breu, *Annu. Rev. Mater. Res.*, 2015, **45**, 129–151.
16 S. Wu, V. Karius, B. C. Schmidt, K. Simon and G. Wörner, *Geostand. Geoanal. Res.*, 2018, **42**, 575–591.
17 G. Selvaggio, A. Chizhik, R. Nißler, L. Kuhlemann, D. Meyer, L. Vuong, H. Preiß, N. Herrmann, F. A. Mann, Z. Lv, T. A. Oswald, A. Spreinat, L. Erpenbeck, J. Großhans, V. Karius, A. Janshoff, J. Pablo Giraldo and S. Kruss, *Nat. Commun.*, 2020, **11**, 1495.
18 R. Nißler, O. Bader, M. Dohmen, S. G. Walter, C. Noll, G. Selvaggio, U. Groß and S. Kruss, *Nat. Commun.*, 2020, **11**, 1–12.
19 T. E. Warner, *Synthesis, Properties and Mineralogy of Important Inorganic Materials*, John Wiley & Sons, Ltd, Chichester, UK, 2011.
20 A. Pabst, *Acta Crystallogr.*, 1959, **12**, 733–739.
21 D. Ajò, G. Chiari, F. De Zuane, M. Favaro and M. Bertolin, *5th Int. Conf. Non-Destructive Testing, Microanal. Methods Environ. Eval. Study Conserv. Work. Art*, 1996, pp. 37–47.
22 G. Pozza, D. Ajò, G. Chiari, F. De Zuane and M. Favaro, *J. Cult. Herit.*, 2000, **1**, 393–398.
23 G. Accorsi, G. Verri, M. Bolognesi, N. Armaroli, C. Clementi, C. Miliani and A. Romani, *Chem. Commun.*, 2009, 3392–3394.
24 G. Hong, A. L. Antaris and H. Dai, *Nat. Biomed. Eng.*, 2017, **1**, 0010.
25 Y. J. Li, S. Ye, C. H. Wang, X. M. Wang and Q. Y. Zhang, *J. Mater. Chem. C*, 2014, **2**, 10395–10402.
26 Y. Chen, M. Kan, Q. Sun and P. Jena, *J. Phys. Chem. Lett.*, 2016, **7**, 399–405.

27 D. Johnson-McDaniel, C. A. Barrett, A. Sharafi and T. T. Salguero, *J. Am. Chem. Soc.*, 2013, **135**, 1677–1679.

28 D. Johnson-McDaniel and T. T. Salguero, *J. Visualized Exp.*, 2014, 1–10.

29 G. Cunningham, M. Lotya, C. S. Cucinotta, S. Sanvito, S. D. Bergin, R. Menzel, M. S. P. Shaffer and J. N. Coleman, *ACS Nano*, 2012, **6**, 3468–3480.

30 C. Backes, T. M. Higgins, A. Kelly, C. Boland, A. Harvey, D. Hanlon and J. N. Coleman, *Chem. Mater.*, 2017, **29**, 243–255.

31 H. Berke, *Chem. Soc. Rev.*, 2007, **36**, 15–30.

32 H.-G. Wiedemann and H. Berke, 1996, 154–171.

33 G. Verri, *Anal. Bioanal. Chem.*, 2009, **394**, 1011–1021.

34 D. Comelli, V. Capogrosso, C. Orsenigo and A. Nevin, *Heritage Sci.*, 2016, **4**, 1–8.

35 S. Shahbazi, J. V. Goodpaster, G. D. Smith, T. Becker and S. W. Lewis, *Forensic Chem.*, 2020, **18**, 100208.

36 R. S. P. King, P. M. Hallett and D. Foster, *Forensic Sci. Int.*, 2016, **262**, e28–e33.

37 B. Errington, G. Lawson, S. W. Lewis and G. D. Smith, *Dyes Pigm.*, 2016, **132**, 310–315.

38 P. Berdahl, S. K. Boocock, G. C. Y. Chan, S. S. Chen, R. M. Levinson and M. A. Zalich, *J. Appl. Phys.*, 2018, **123**(19), 193103.

39 S. S. Yang, H. X. Yu, Z. Z. Wang, H. L. Liu, H. Zhang, X. Yu, W. Shang, G. Q. Chen and Z. Y. Gu, *Chem.–Eur. J.*, 2018, **24**, 2024.

40 S. Kruss, A. J. Hilmer, J. Zhang, N. F. Reuel, B. Mu and M. S. Strano, *Adv. Drug Delivery Rev.*, 2013, **65**, 1933–1950.

41 Z. Hu, W. H. Chen, J. Tian and Z. Cheng, *Trends Mol. Med.*, 2020, **26**, 469–482.

42 A. M. Smith, M. C. Mancini and S. Nie, *Nat. Nanotechnol.*, 2009, **4**, 710–711.

43 E. A. Owens, M. Henary, G. El Fakhri and H. S. Choi, *Acc. Chem. Res.*, 2016, **49**, 1731–1740.

44 J. A. Carr, D. Franke, J. R. Caram, C. F. Perkinson, M. Saif, V. Askoxylakis, M. Datta, D. Fukumura, R. K. Jain, M. G. Bawendi and O. T. Bruns, *Proc. Natl. Acad. Sci. U. S. A.*, 2018, **115**, 4465–4470.

45 S. Zhu, Q. Yang, A. L. Antaris, J. Yue, Z. Ma, H. Wang, W. Huang, H. Wan, J. Wang, S. Diao, B. Zhang, X. Li, Y. Zhong, K. Yu, G. Hong, J. Luo, Y. Liang and H. Dai, *Proc. Natl. Acad. Sci. U. S. A.*, 2017, **114**, 962–967.

46 O. T. Bruns, T. S. Bischof, D. K. Harris, D. Franke, Y. Shi, L. Riedemann, A. Bartelt, F. B. Jaworski, J. A. Carr, C. J. Rowlands, M. W. B. Wilson, O. Chen, H. Wei, G. W. Hwang, D. M. Montana, I. Coropceanu, O. B. Achorn, J. Kloepper, J. Heeren, P. T. C. So, D. Fukumura, K. F. Jensen, R. K. Jain and M. G. Bawendi, *Nat. Biomed. Eng.*, 2017, **1**, 0056.

47 Y. Fan, P. Wang, Y. Lu, R. Wang, L. Zhou, X. Zheng, X. Li, J. A. Piper and F. Zhang, *Nat. Nanotechnol.*, 2018, **13**, 941–946.

48 S. He, J. Song, J. Qu and Z. Cheng, *Chem. Soc. Rev.*, 2018, **47**, 4258–4278.

49 G. Hong, S. Diao, A. L. Antaris and H. Dai, *Chem. Rev.*, 2015, **115**, 10816–10906.

50 G. Bisker, J. Dong, H. D. Park, N. M. Iverson, J. Ahn, J. T. Nelson, M. P. Landry, S. Kruss and M. S. Strano, *Nat. Commun.*, 2016, **7**, 1–14.

51 E. Polo, T. T. Nitka, E. Neubert, L. Erpenbeck, L. Vuković and S. Kruss, *ACS Appl. Mater. Interfaces*, 2018, **10**, 17693–17703.

52 F. A. Mann, Z. Lv, J. Großhans, F. Opazo and S. Kruss, *Angew. Chem., Int. Ed.*, 2019, **58**, 11469–11473.

53 R. M. Williams, C. Lee, T. V. Galassi, J. D. Harvey, R. Leicher, M. Sirenko, M. A. Dorso, J. Shah, N. Olvera, F. Dao, D. A. Levine and D. A. Heller, *Sci. Adv.*, 2018, **4**, eaaq1090.

54 F. A. Mann, N. Herrmann, F. Opazo and S. Kruss, *Angew. Chem., Int. Ed.*, 2020, **59**, 17732–17738.

55 K. Kouroupis-Agalou, A. Liscio, E. Treossi, L. Ortolani, V. Morandi, N. M. Pugno and V. Palermo, *Nanoscale*, 2014, **6**, 5926–5933.

56 H. Chen, G. Holst and E. Gratton, *Microsc. Res. Tech.*, 2015, **78**, 1075–1081.

57 R. Franke and G. A. Holst, *Imaging, Manip. Anal. Biomol. Cells, Tissues XIII*, 2015, vol. 9328, p. 93281K.

58 L. Cognet, D. A. Tsyboulski, J. D. R. Rocha, C. D. Doyle, J. M. Tour and R. B. Weisman, *Science*, 2007, **316**, 1465–1468.

59 S. Kruss, D. P. Salem, L. Vuković, B. Lima, E. Vander Ende, E. S. Boyden and M. S. Strano, *Proc. Natl. Acad. Sci. U. S. A.*, 2017, **114**, 1789–1794.

60 D. Meyer, S. Telele, A. Zelená, A. J. Gillen, A. Antonucci, E. Neubert, R. Nißler, F. A. Mann, L. Erpenbeck, A. A. Boghossian, S. Köster and S. Kruss, *Nanoscale*, 2020, **12**, 9104–9115.

61 M. Y. Berezin and S. Achilefu, *Chem. Rev.*, 2010, **110**, 2641–2684.

62 H. Tributh and G. Lagaly, *GIT Fachz. Lab.*, 1986, **30**, 524–529.

Electronic Supplementary Material (ESI) for Nanoscale Advances.

Supplementary Information

Photophysical Properties and Fluorescence Lifetime Imaging of Exfoliated Near-Infrared Fluorescent Silicate Nanosheets

Gabriele Selvaggio, Milan Weitzel, Nazar Oleksiievets, Tabea A. Oswald,

Robert Nißler, Ingo Mey, Volker Karius, Jörg Enderlein, Roman Tsukanov,

*Sebastian Kruss**

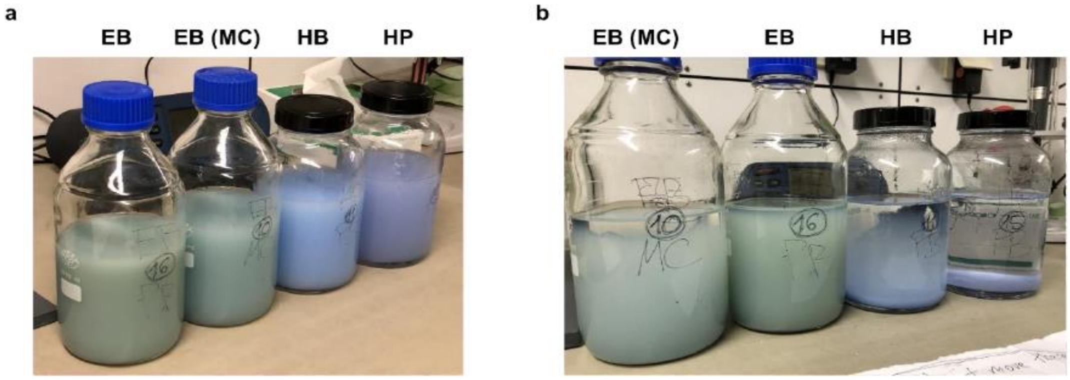

Figure S1. Colloidal stability of planetary ball (PB)/McCrone (MC) milled and centrifuged Egyptian Blue (EB), Han Blue (HB) and Han Purple (HP) a Picture of EB, HB and HP dispersions in water obtained after milling and centrifugation step #1. In addition to the standard PB technique, MC milling was also tested on EB. **b** Pictures of the same samples taken 3 days later to check the colloidal stability: while EB supernatants were still stable, HB and especially HP had started to settle down.

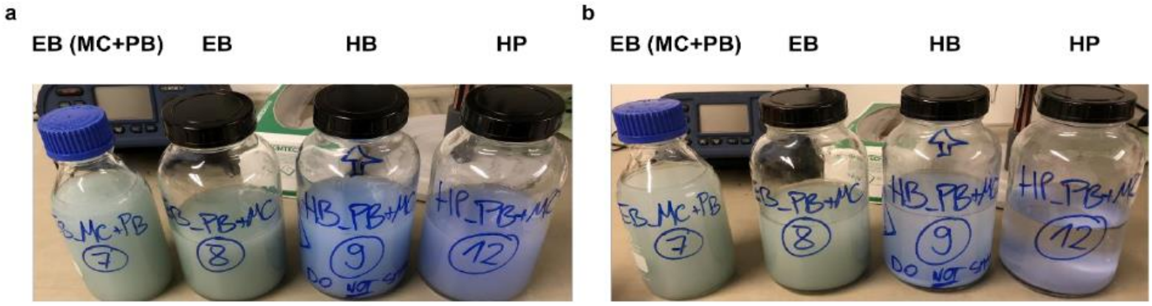

Figure S2. Colloidal stability of PB+MC/MC+PB milled and centrifuged EB, HB and HP Before choosing the planetary ball mill (PB) as best compromise for the milling step of EB, HB and HP, other techniques were tested. These included McCrone milling (MC) and mixed approaches (PB+MC, MC+PB). **a** Picture of EB, HB and HP dispersions in water obtained after mixed approaches of milling, followed by centrifugation step #1. For this dataset, MC+PB was performed only on EB. **b** Pictures of the same samples taken 1 day later to check the colloidal stability: while EB supernatants were still stable, HB and especially HP had started to settle down.

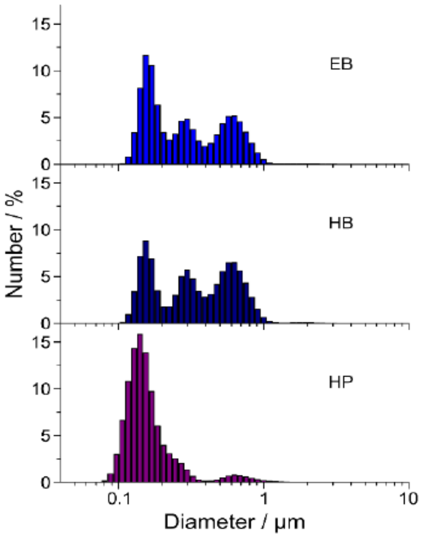

Figure S3. Size distribution of planetary ball milled (PB) EB, HB and HP after centrifugation step #1 (i.e. prior to tip sonication) Milled and centrifuged samples measured via laser diffraction particle sizer (LDPS). For EB, HB and HP alike, the efficiency of the centrifugation step is shown by the cut-off seen at ≈ 1 µm. All samples display a trimodal distribution, which is less pronounced in the case of HP. N = 1 independent sample per category, n = 3 measurement runs.

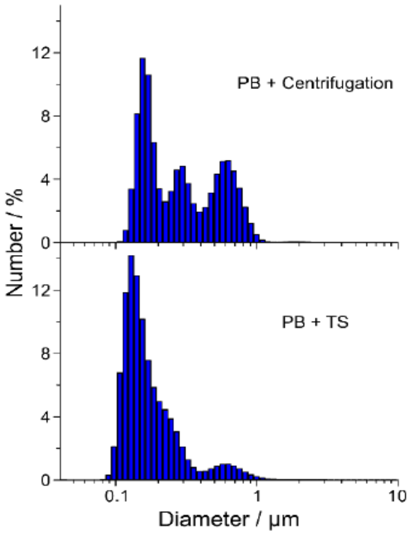

Figure S4. Effect of tip sonication (TS) on the size distribution of planetary ball milled (PB) EB Laser diffraction particle sizer (LDPS)-based analysis of only milled and milled + tip sonicated EB is presented. The former (milled) sample was centrifuged and its supernatant decanted before measurement, as described in the main manuscript text. The latter, on the other side, underwent a tip sonication step in addition to the milling one, and is then measured directly after exfoliation (as a whole, i.e. without centrifugation). When plotted in the form of histograms (number % vs. particle diameter), the LDPS dataset shows that the trimodal distribution is less pronounced after tip sonication, and its lowest extremes are shifted to lower diameter values, indicating a further size reduction. N = 1 independent sample per category, n = 3 measurement runs.

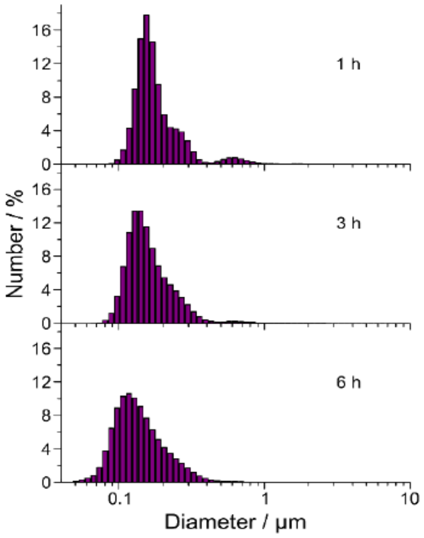

Figure S5. Monitoring of size distribution of Han Purple nanosheets (HP-NS) during tip sonication Laser diffraction particle sizer (LDPS)-based analysis shows the effect of tip sonication on the size distribution of a HP sample over time (1 h - 3 h - 6 h). When plotted in the form of histograms (number % vs. particle diameter), the LDPS dataset shows that the trimodal distribution gets less and less pronounced in time, and its lowest extremes are shifted to lower diameter values, indicating a further size reduction. N = 1 independent sample per category, n = 3 measurement runs.

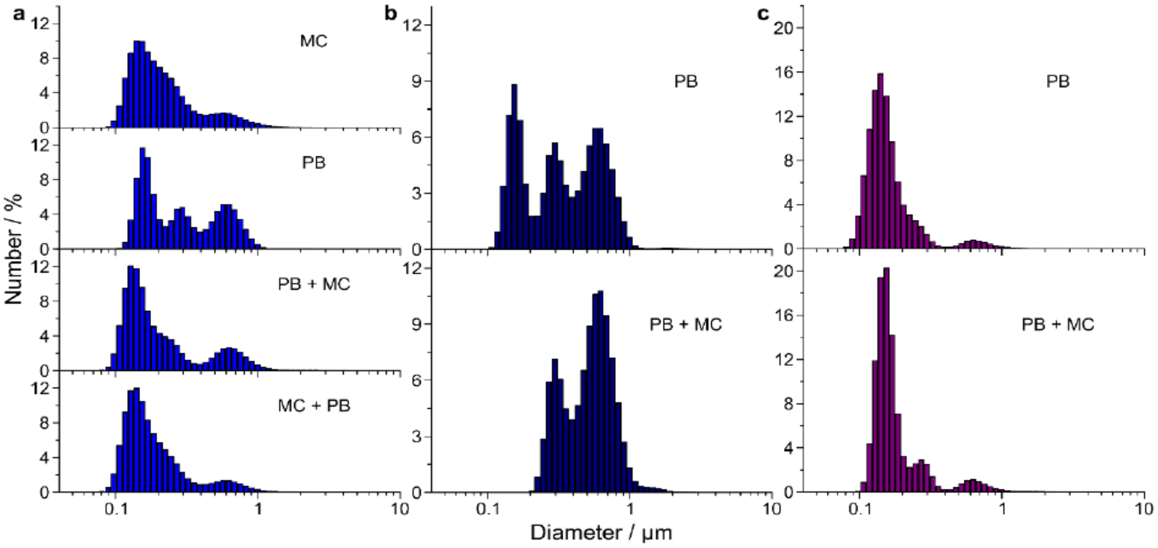

Figure S6. Comparison of exfoliation efficiency of different milling techniques Histograms (number % vs. particle diameter) obtained from a laser diffraction particle sizer (LDPS) show the obtained size distributions of EB (**a**), HB (**b**) and HP (**c**). Before measurement, all samples were centrifuged and the supernatant decanted. The efficiency of the employed centrifugation step is proven by the very low amount of particles larger than ≈ 1 µm. For EB, while the population's extremes seem to be consistent with all tested techniques, the trimodal distribution is more evident in the PB case. HB displays a much clearer difference between the tested PB and PB+MC; here, the former approach yields smaller particles and, thus, results more optimal. Finally, the HP sample does not show a pronounced difference between the previous two techniques. N = 1 independent sample per category, n = 3 measurement runs.

Figure S7. PB milled, tip sonicated and centrifuged EB-NS, HB-NS and HP-NS Self-taken photograph of the fully exfoliated samples, i.e. the final NS batches that underwent complete morphological and photophysical characterization.

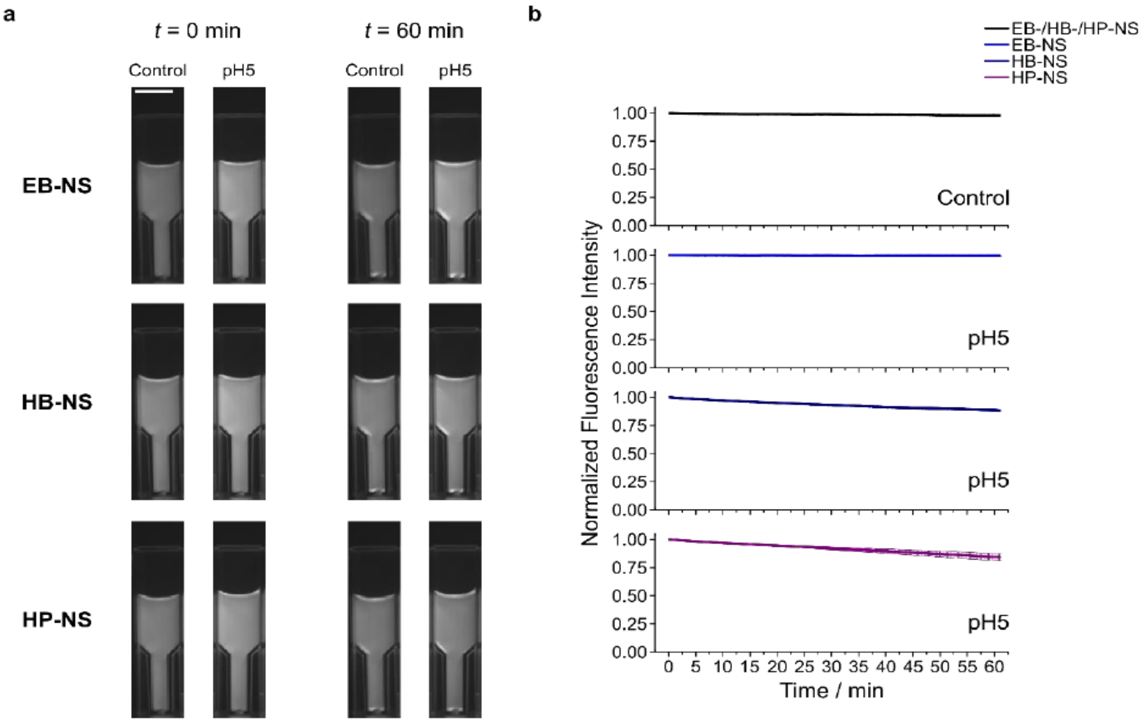

Figure S8. Colloidal stability of EB-NS, HB-NS and HP-NS in acidic conditions a Stand-off NIR fluorescence images of NS samples in cuvettes at pH 5. Measurements were taken over 1 h to assess the effect of acidic pH on the stability, i.e. the fluorescence of a central region of interest within the cuvette. Control = addition of H_2O (instead of buffer solutions). Scale bar = 1 cm. **b** Corresponding mean fluorescence intensity, normalized to the first frame. HB- and HP-NS performed worse than EB-NS. Nevertheless, all NS displayed a signal decrease not lower than 15%, thus proving to be significantly stable in such conditions. Error bars = standard deviation, N = 2 independent samples.

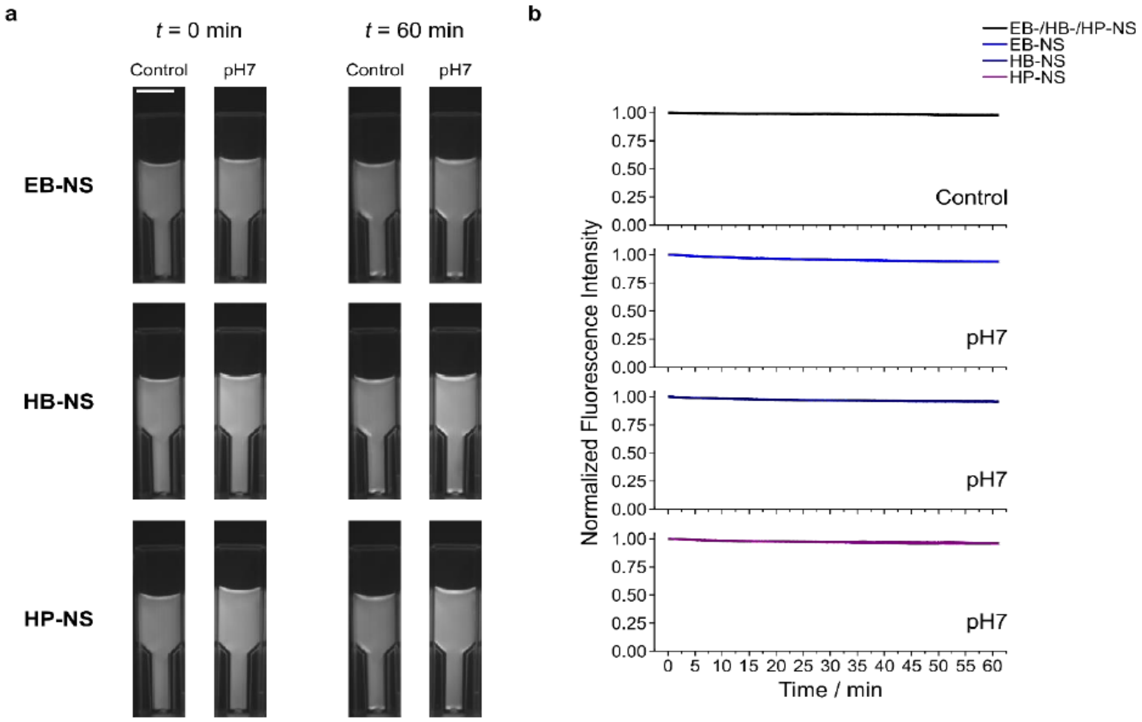

Figure S9. Colloidal stability of EB-NS, HB-NS and HP-NS at neutral pH a Stand-off NIR fluorescence images of NS samples in cuvettes at pH 7. Measurements were taken over 1 h to assess the effect of neutral pH on the stability, i.e. the fluorescence of a central region of interest within the cuvette. Control = addition of H_2O (instead of buffer solutions). Scale bar = 1 cm. **b** Corresponding mean fluorescence intensity, normalized to the first frame. All NS displayed a neglectable signal decrease, thus confirming their stability in such conditions. Error bars = standard deviation, N = 2 independent samples.

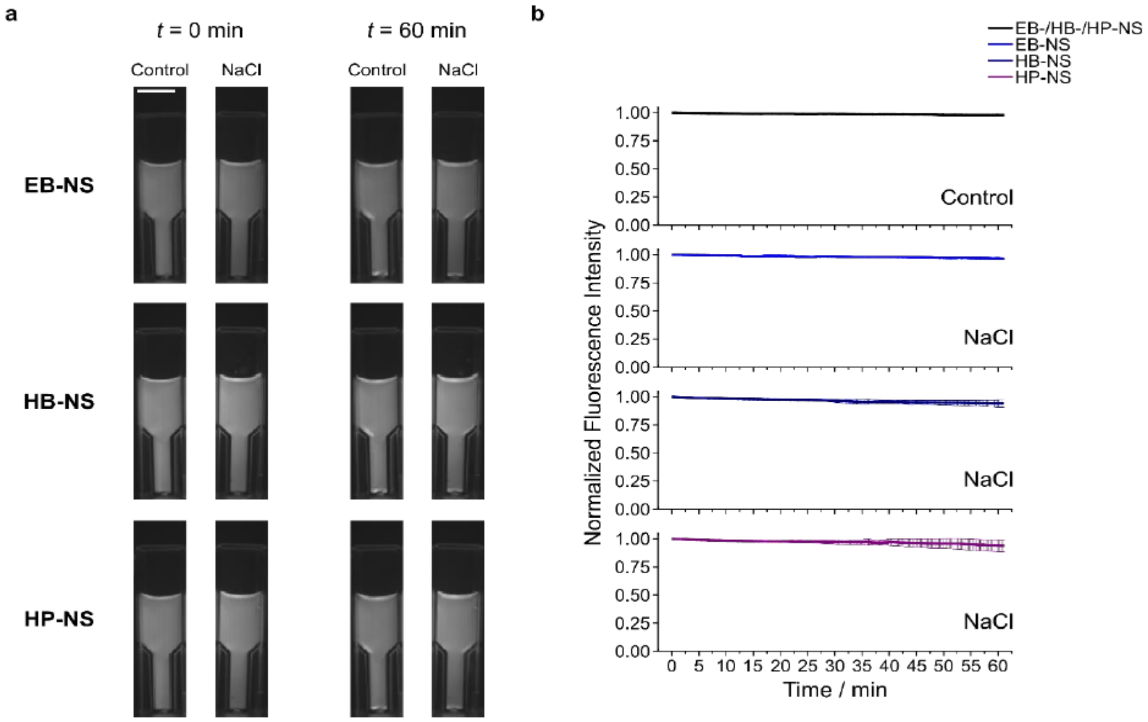

Figure S10. Colloidal stability of EB-NS, HB-NS and HP-NS in ionic environment a Stand-off NIR fluorescence images of NS samples in cuvettes in the presence of sodium chloride (NaCl). Measurements were taken over 1 h to assess the effect of ions (9 g/L NaCl, a typical concentration in blood) on the stability, i.e. the fluorescence of a central region of interest within the cuvette. Control = addition of H_2O (instead of NaCl solution). Scale bar = 1 cm. **b** Corresponding mean fluorescence intensity, normalized to the first frame. HB- and HP-NS performed slightly worse than EB-NS. Nevertheless, all NS displayed a signal decrease not lower than 15%, thus proving to be significantly stable in such conditions. Error bars = standard deviation, N = 2 independent samples.

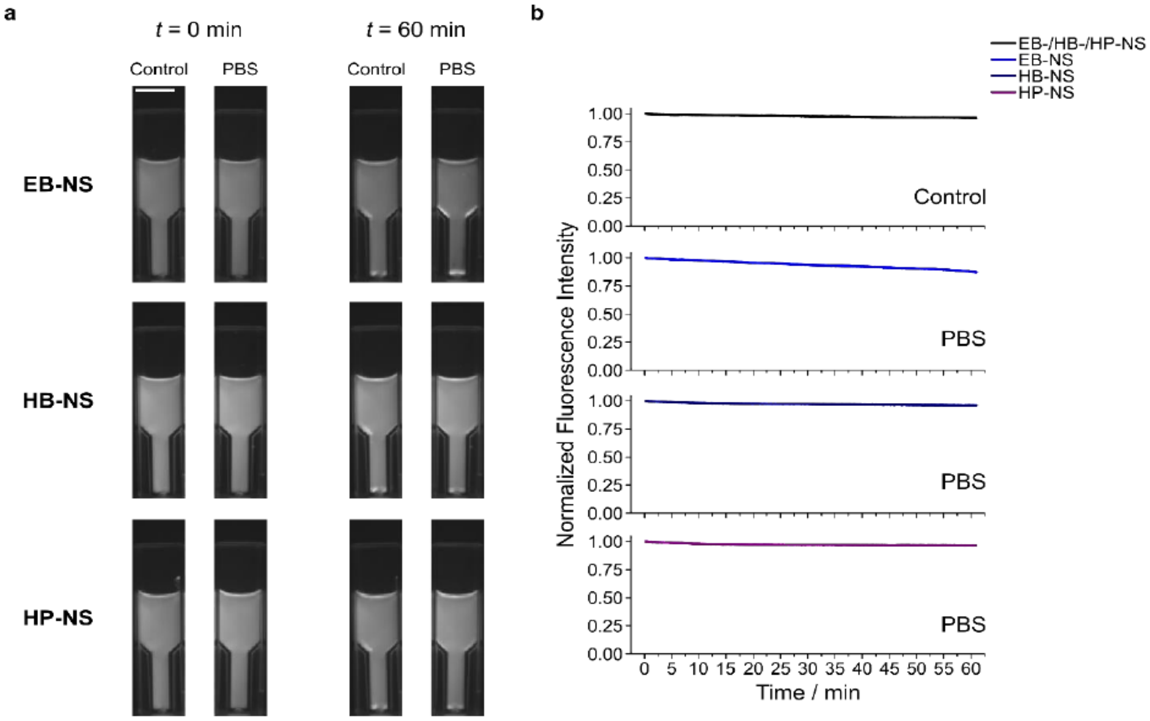

Figure S11. Colloidal stability of EB-NS, HB-NS and HP-NS in buffer solution a Stand-off NIR fluorescence images of NS samples in cuvettes in the presence of buffer (phosphate-buffered saline, PBS). Measurements were taken over 1 h to assess the effect of PBS (1x) on the stability, i.e. the fluorescence of a central region of interest within the cuvette. Control = addition of H_2O (instead of buffer). Scale bar = 1 cm. **b** Corresponding mean fluorescence intensity, normalized to the first frame. EB-NS performed slightly worse than HB- and HP-NS. Nevertheless, all NS displayed a signal decrease not lower than 15%, thus proving to be significantly stable in the presence of PBS. Error bars = standard deviation, N = 2 independent samples.

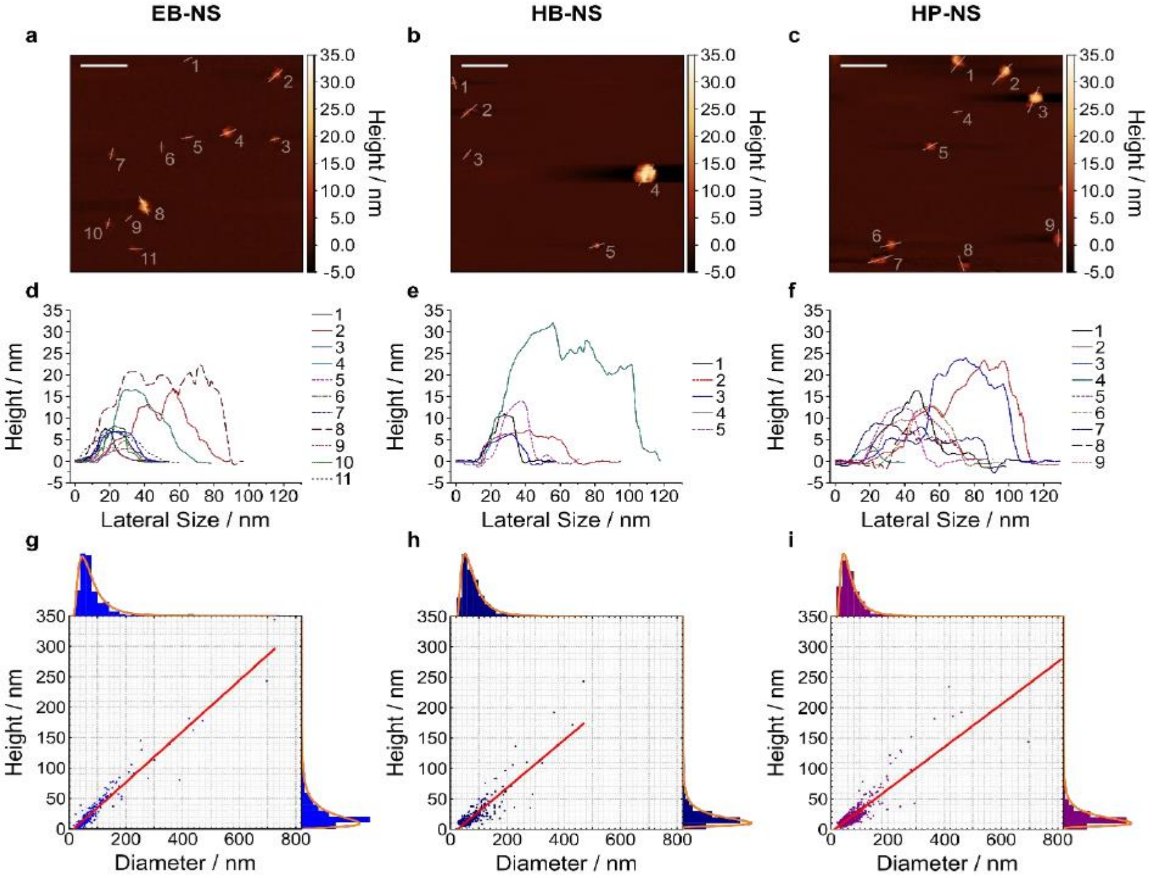

Figure S12. Size and height of exfoliated silicate nanosheets Exfoliated nanosheets were spin-coated on mica and imaged with atomic force microscopy (AFM) in intermittent contact mode. Representative images (**a-c**), height traces (**d-f**) and histograms with log-normal fits (**g-i**) of EB-NS, HB-NS and HP-NS. The results indicate that lateral size scales linearly with height (linear fit = red line in **g-i**). The diameter/height values corresponding to the log-normal distributions' maxima are 47.0 nm / 9.0 nm for EB-NS, 51.5 nm / 10.3 nm for HB-NS, and 44.4 nm / 10.4 nm for HP-NS. R^2 values of the linear fits are 0.924 (EB-NS), 0.755 (HB-NS) and 0.779 (HP-NS). Scale bar = 200 nm. n = 245, 308 and 530 for EB-NS, HB-NS and HP-NS, respectively.

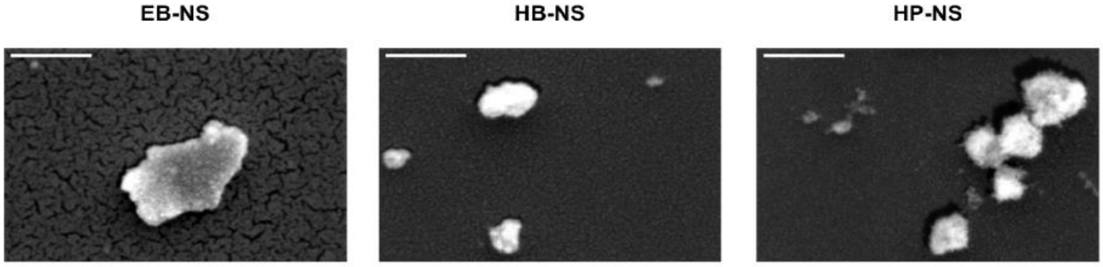

Figure S13. Scanning Electron Microscopy (SEM) images of gold-coated small NS NS with sizes comparable/smaller than the optical resolution limit for optical microscopy ($\lambda \approx 500$ nm, in our case) show a slightly improved contrast after the evaporation of gold on their surfaces. Scale bar = 500 nm.

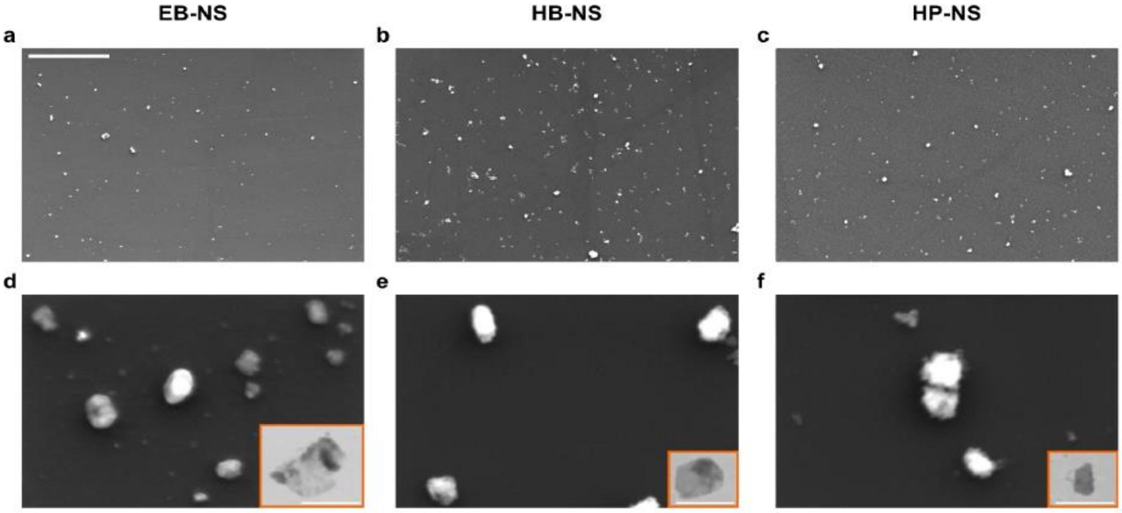

Figure S14. Morphology of nanosheets Scanning electron microscopy (SEM) and scanning transmission electron microscopy (STEM) were used to assess NS morphology**. a-c** EB-NS, HB-NS and HP-NS spin-coated on a graphite substrate. Scale bar = 5 µm. **d-f** Magnified images of the same samples to highlight the presence of particles close to/lower than the resolution limit of optical microscopy. In the lower-right window, clear 2D nanosheet structures could be observed in STEM mode. Scale bar = 500 nm.

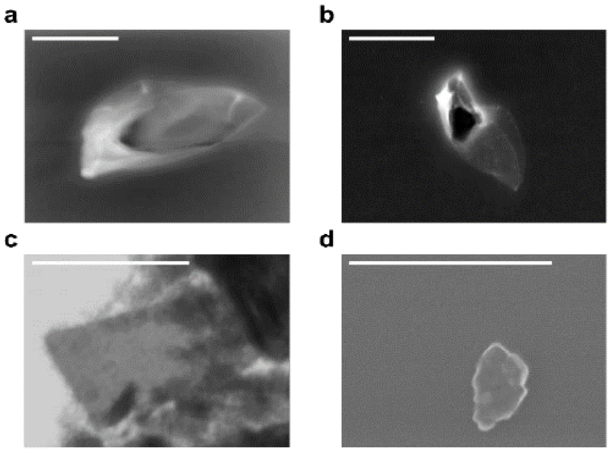

Figure S15. Scanning Transmission Electron Microscopy (STEM) images of small EB-NS **a-b** EB-NS with sizes slightly larger than Abbe's resolution limit ($\lambda \approx 500$ nm) and displaying the lamellar morphologies typically yielded by fragmentation of thicker EB particles. **c** A thin EB-NS with lateral sizes in the range of the optical resolution limit. **d** Example of an EB-NS of diameter below 500 nm. Scale bar = 500 nm.

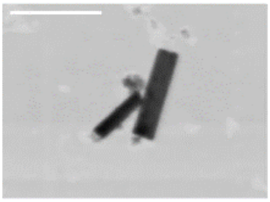

Figure S16. Scanning Electron Microscopy (STEM) images of regular 2D structures in HP-NS Regular 2D structures of HP-NS were noticed, both in SEM and STEM mode. Scale bar = 500 nm.

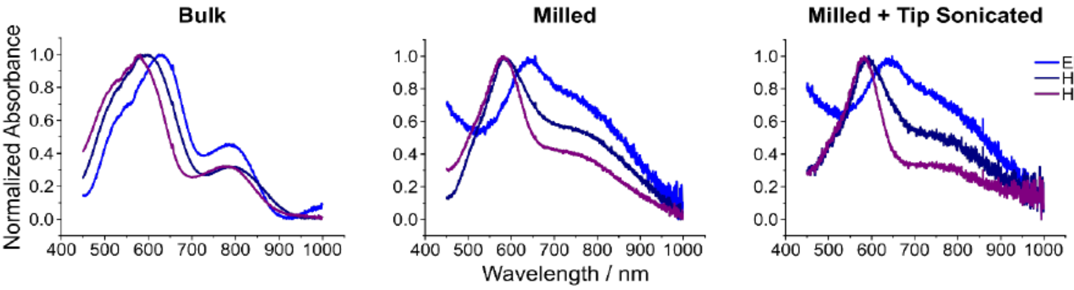

Figure S17. Absorption spectra of bulk, ball milled and fully processed nanosheets of EB, HB and HP Absorbance spectra show impact of processing. First of all, HB is the only powder to show a blue-shift after milling. The main peak position of the other samples is not altered. However, all milled powders lose some features on both the left and right shoulder of the main peak. Features on the right-handed side of the main peak of milled and milled + tip sonicated samples can still be noticed, even if they are not as pronounced as in the bulk counterpart.

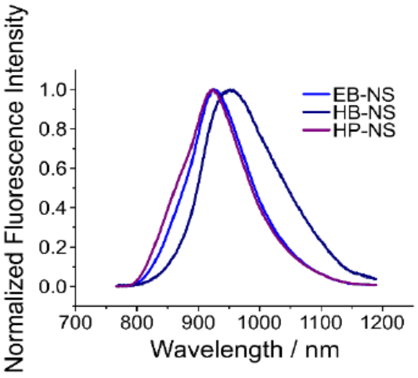

Figure S18. 1D Fluorescence Spectra of NS Normalized NIR fluorescence spectra of EB-NS, HB-NS and HP-NS are plotted. $\lambda_{\text{exc}} = 561$ nm, laser power = 100 mW and exposure time = 1 s. $\lambda_{\text{emi, EB-NS}} \approx 927.3$ nm (FWHM ≈ 115.3 nm); $\lambda_{\text{emi, HB-NS}} \approx 953.4$ nm (FWHM ≈ 146.6 nm); $\lambda_{\text{emi, HP-NS}} \approx 923.9$ nm (FWHM ≈ 123.7 nm). A slight discrepancy compared to our 2D dataset is likely the result of data correction for the quantum efficiency of the detector and for the spectral irradiance of the xenon lamp, which was here not performed; additionally, spectra normalization and background subtraction might be responsible for further slight shifts, too.

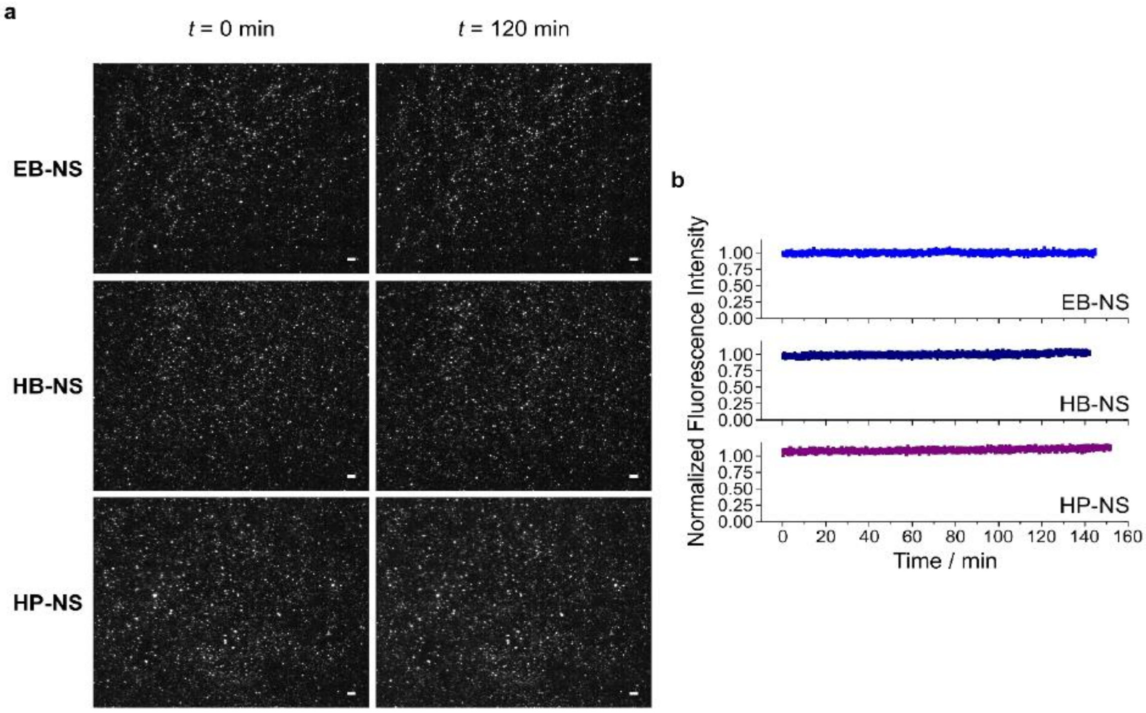

Figure S19. Photobleaching experiments at the microscopic NIR imaging setup a NS were drop-casted and dried on a glass coverslip before a prolonged ($t > 2$ h) imaging session at an effective output power of ≈ 180 mW. Scale bar = 20 µm. **b** Corresponding mean fluorescence intensity, normalized to the first frame, showing absence of bleaching for all NS. N = 1 independent sample.

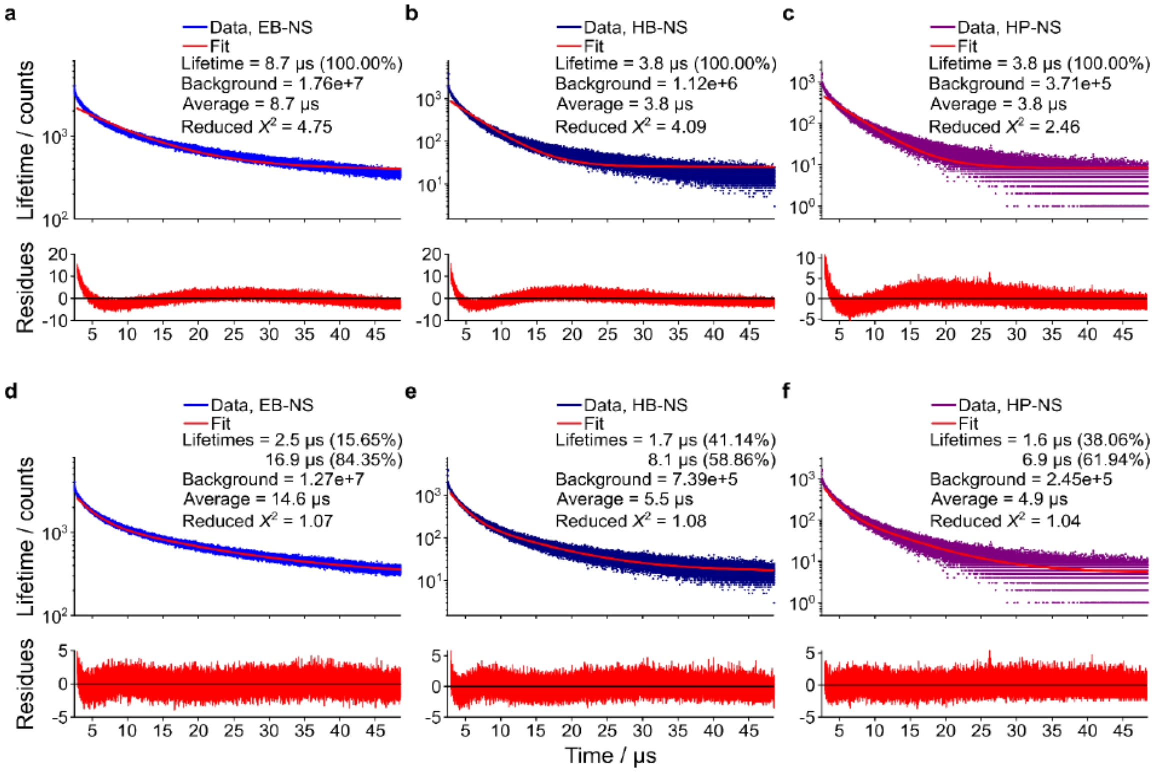

Figure S20. Characterization of the NS fluorescence lifetimes using confocal time-correlated single-photon counting (TCSPC)-based technique Exemplary TCSPC curves of EB-NS, HB-NS and HP-NS with the correspondent single- (**a**-**c**) and double-exponential (**d**-**f**) fits. The fit outputs are given on the plots. The fit residues are shown below the fit to guide the eye.

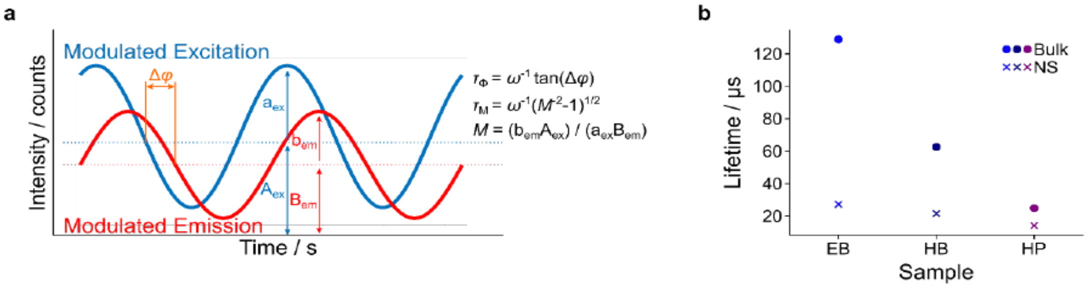

Figure S21. Characterization of fluorescence lifetimes of NS in the frequency domain **a** Schematic describing fluorescence lifetime measurements in the frequency domain. τ_ϕ and τ_M represent the lifetime values obtainable from the phase (ϕ) and the modulation (M), respectively. **b** Frequency domain measurements of bulk and corresponding NS samples of EB, HB and HP performed with a FireSting oxygen sensor device. A decrease in τ is observable for all exfoliated silicates, especially EB-NS. $\tau_{EB} = 128.89 \pm 0.45$ µs, $\tau_{EB\text{-}NS} = 27.22 \pm 0.05$ µs, $\tau_{HB} = 62.60 \pm 0.21$ µs, $\tau_{HB\text{-}NS} = 21.55 \pm 0.05$ µs, $\tau_{HP} = 24.85 \pm 0.14$ µs, $\tau_{HP\text{-}NS} = 14.14 \pm 0.04$ µs. Error bars (not visible by eye) = standard deviation. N = 1 independent sample.

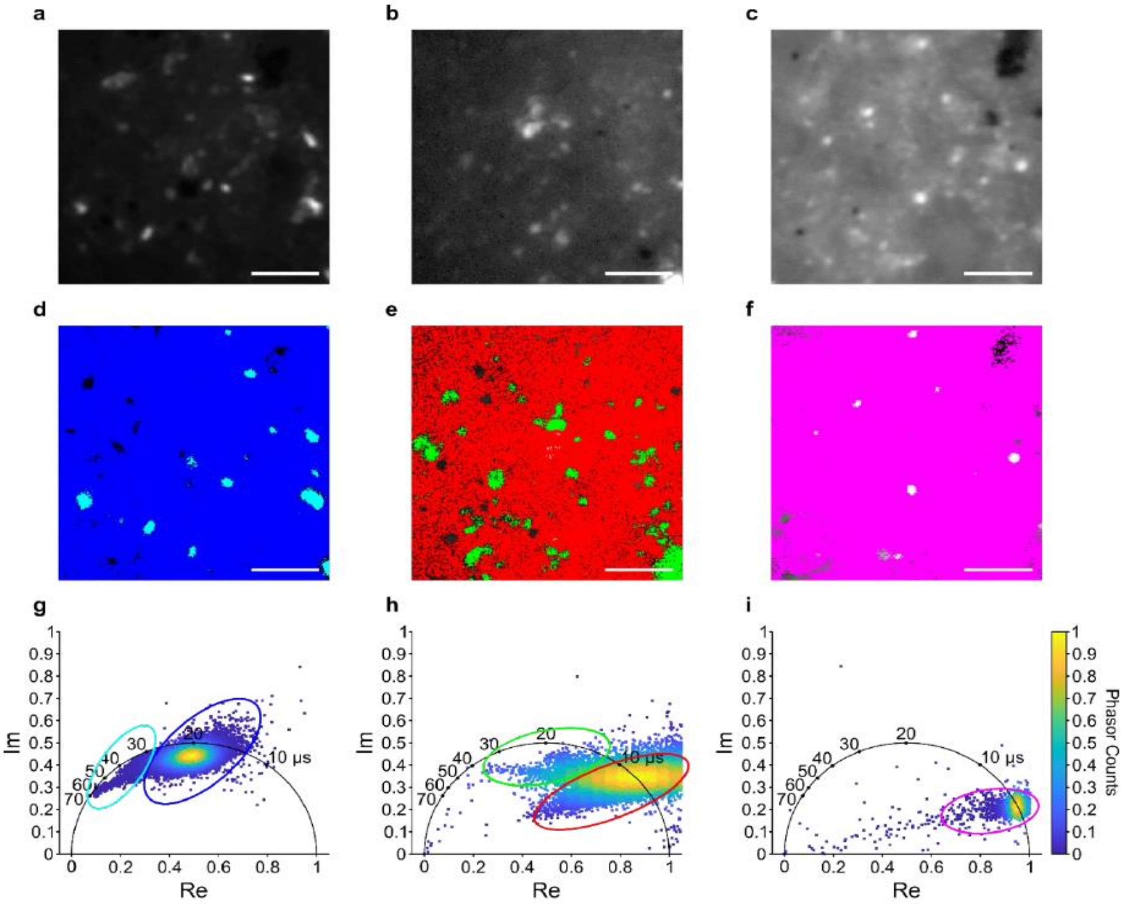

Figure S22. Fluorescence lifetime imaging (FLIM) of the three different NS types using the frequency domain FLIM images of NS drop-casted in a high concentration on top of a glass coverslip: EB-NS (**a**), HB-NS (**b**) and HP-NS (**c**). In **a**, **b** and **c** the intensity images are shown. In **d**, **e** and **f**, the corresponding FLIM images are presented. The colors correspond to a division into the sub-populations displayed in the phasor plots (**g**, **h** and **i**, respectively). Scale bar = 5 µm.

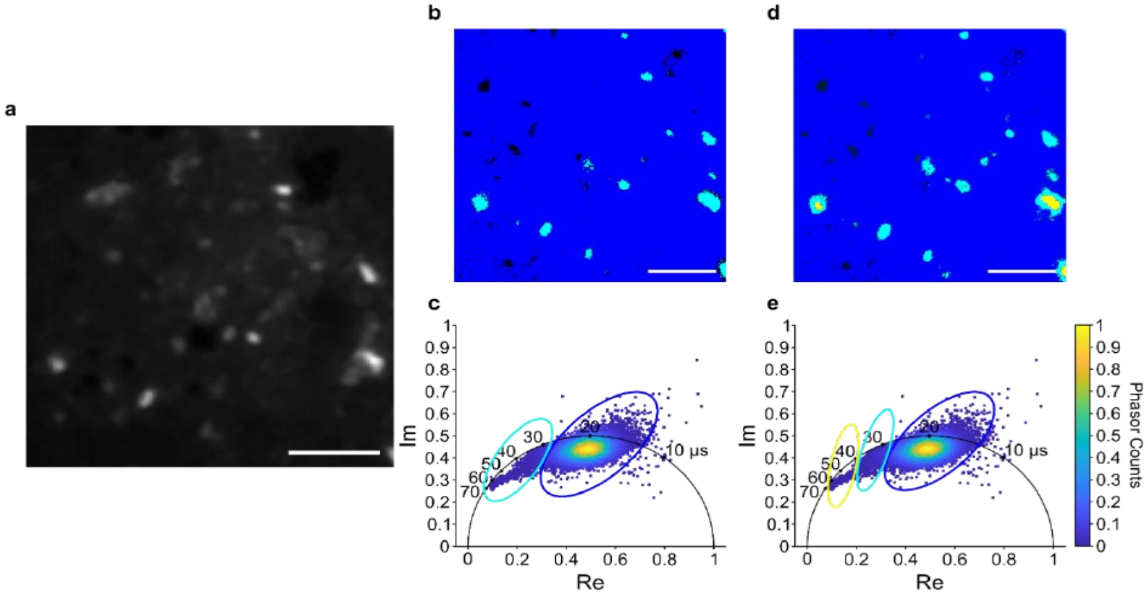

Figure S23. Lifetime-size dependency of EB-NS particles **a** FLIM image showing the fluorescence intensity of EB-NS drop-casted on top of a glass coverslip. **b** FLIM image of the same sample region in **a**, but with color scheme corresponding to the division of EB-NS into lifetime subpopulations: NS with lifetimes in the range of 15-27 µs appear in dark blue color, the ones in the range of 27-70 µs in light blue color. **c** Phasor plot illustrating the selection of the color scheme in **b**. **d** FLIM image of the same sample region in **a** and **b**, but differently divided into sub-populations: NS with lifetimes in the range of 15-27 µs appear in dark blue color, the ones in the range of 27-40 µs in light blue color and the ones in the range of 40-70 µs in yellow color. **e** Phasor plot illustrating the selection of the color scheme in **d**. Scale bar = 5 µm.

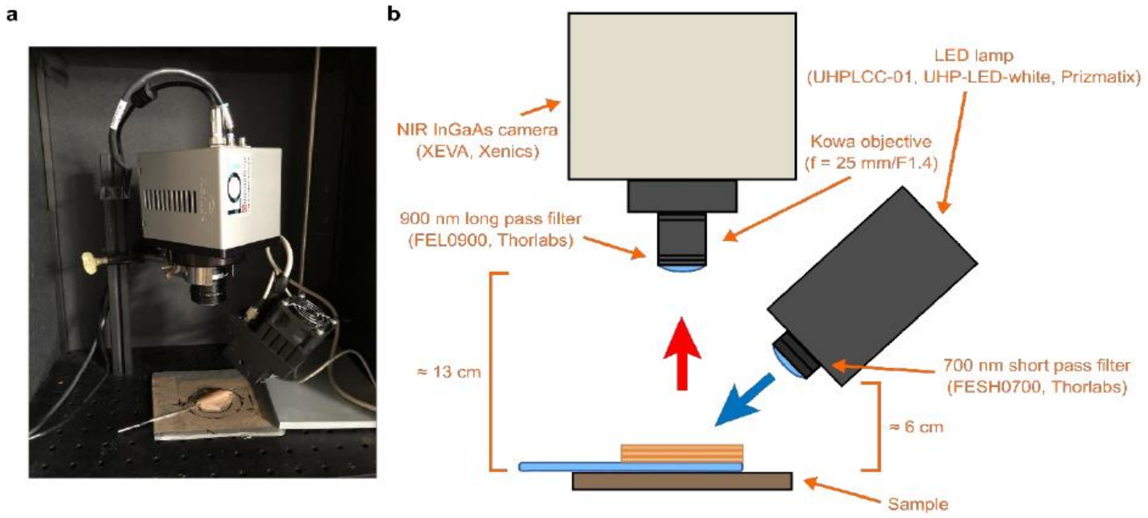

Figure S24. Schematic of home-built stand-off setup a Photo of the home-built stand-off NIR setup, configured for tissue phantom experiments. **b** Corresponding schematic showing the employed devices and filters, as well as the typical working distances.

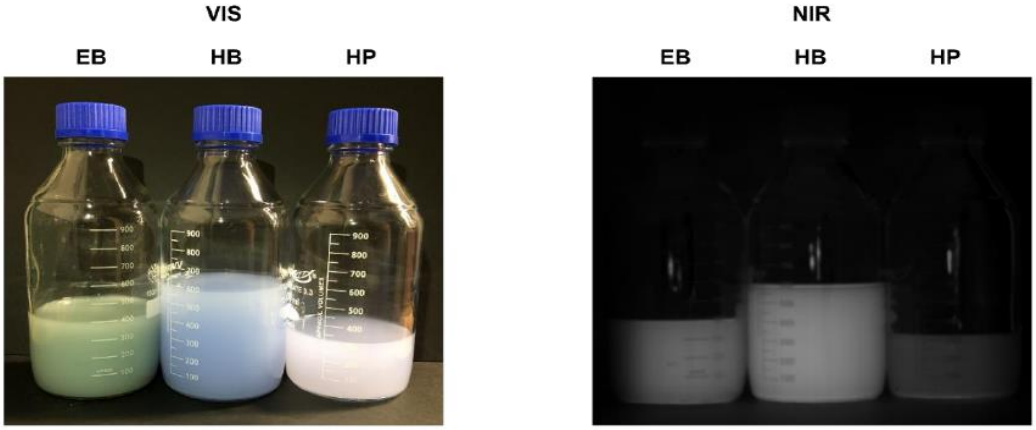

Figure S25. Stand-off imaging of PB milled and centrifuged EB, HB and HP Visible and NIR images acquired at our stand-off setup and showing samples in the exfoliation stage prior to the tip sonication step. The supernatants presented different concentrations, nevertheless they all displayed a clearly detectable fluorescence signal.

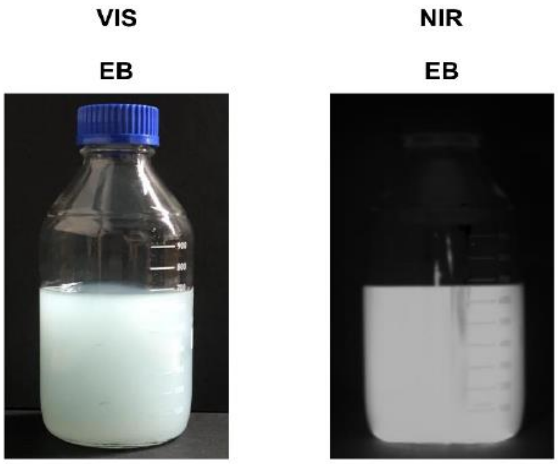

Figure S26. Stand-off imaging of MC milled and centrifuged EB Visible and NIR images acquired at our stand-off setup and showing a MC milled and centrifuged EB sample. The supernatant presented different concentrations compared to other (e.g. PB milled) batches, nevertheless the fluorescence signal was clearly detectable.

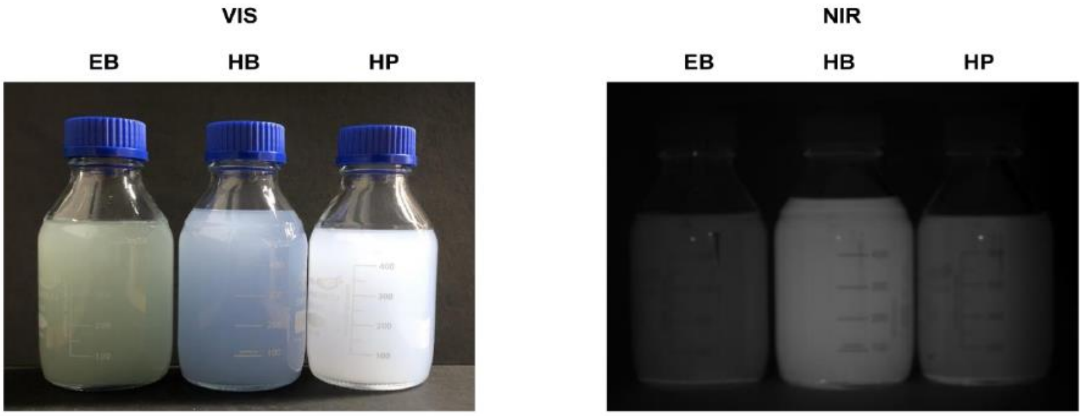

Figure S27. Stand-off imaging of PB+MC milled and centrifuged EB, HB and HP Visible and NIR images acquired at our stand-off setup and showing silicate dispersions obtained via a mixed milling approach followed by a centrifugation step. The supernatants presented different concentrations, nevertheless they all displayed a clearly detectable fluorescence signal.

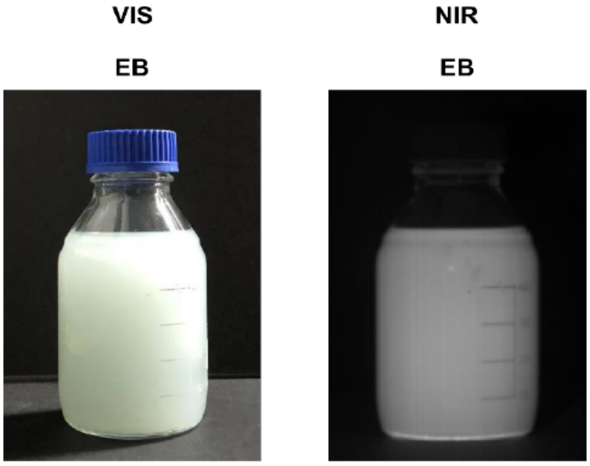

Figure S28. Stand-off imaging of MC+PB milled and centrifuged EB Visible and NIR images acquired at our stand-off setup and showing an EB dispersion obtained via a mixed milling approach followed by a centrifugation step. The supernatant presented different concentrations compared to other (e.g. PB milled) batches, nevertheless the fluorescence signal was clearly detectable.

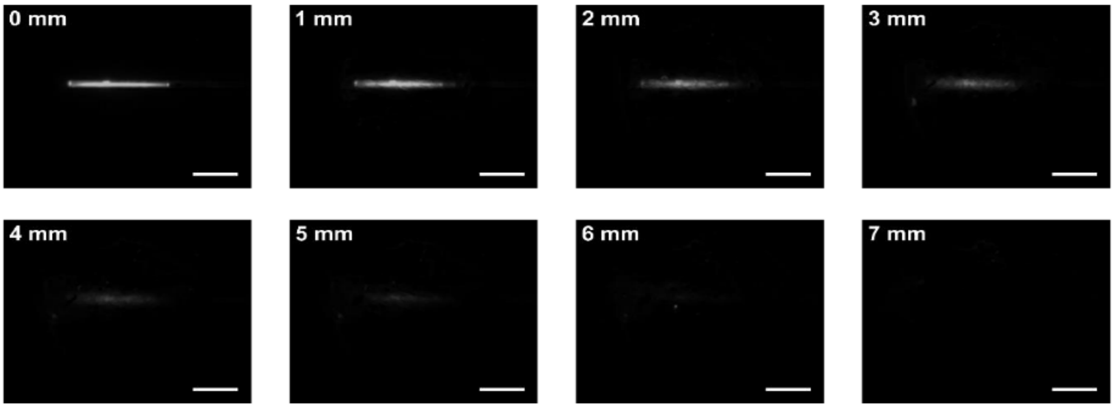

Figure S29. Tissue phantom experiments of EB-NS A concentrated solution of EB-NS (≈ 5 g/L) was sucked into capillary tubes and imaged in a stand-off detection setup. Pictures show NIR fluorescence emitted from the NS under visible excitation (white light source with a 700 nm short-pass filter). The emission signal managed to reach the NIR camera through multiple 1 mm-thick chicken phantom tissues, which were positioned on top of the capillary glass. A background image was subtracted in each image. Scale bar = 10 mm. N = 1 sample.

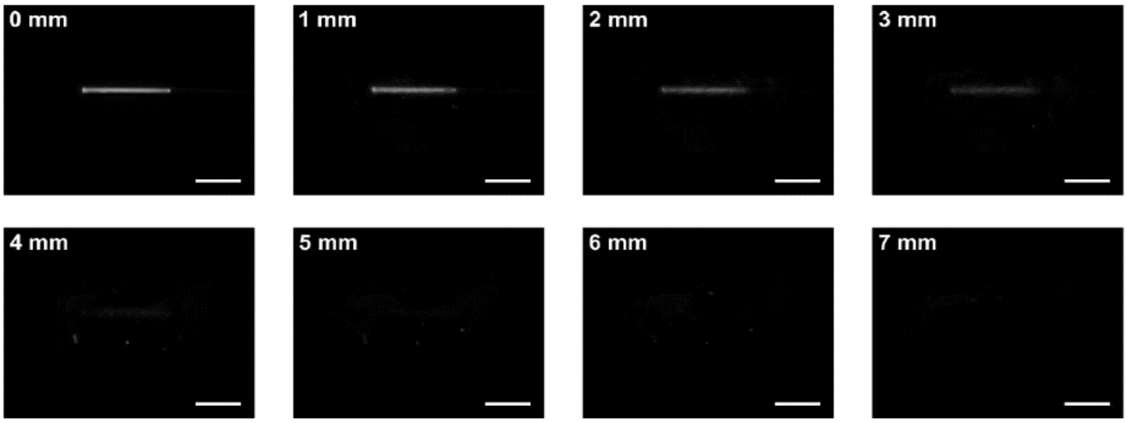

Figure S30. Tissue phantom experiments of HB-NS A concentrated solution of HB-NS (≈ 5 g/L) was sucked into capillary tubes and imaged in a stand-off detection setup. Pictures show NIR fluorescence emitted from the NS under visible excitation (white light source with a 700 nm short-pass filter). The emission signal managed to reach the NIR camera through multiple 1 mm-thick chicken phantom tissues, which were positioned on top of the capillary glass. A background image was subtracted in each image. Scale bar = 10 mm. N = 1 sample.

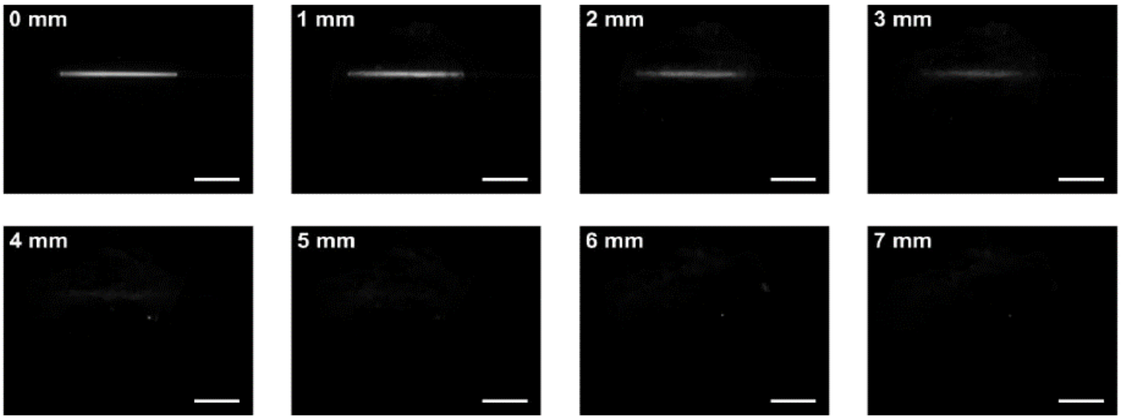

Figure S31. Tissue phantom experiments of HP-NS A concentrated solution of HP-NS (≈ 5 g/L) was sucked into capillary tubes and imaged in a stand-off detection setup. Pictures show NIR fluorescence emitted from the NS under visible excitation (white light source with a 700 nm short-pass filter). The emission signal managed to reach the NIR camera through multiple 1 mm-thick chicken phantom tissues, which were positioned on top of the capillary glass. A background image was subtracted in each image. Scale bar = 10 mm. N = 1 sample.

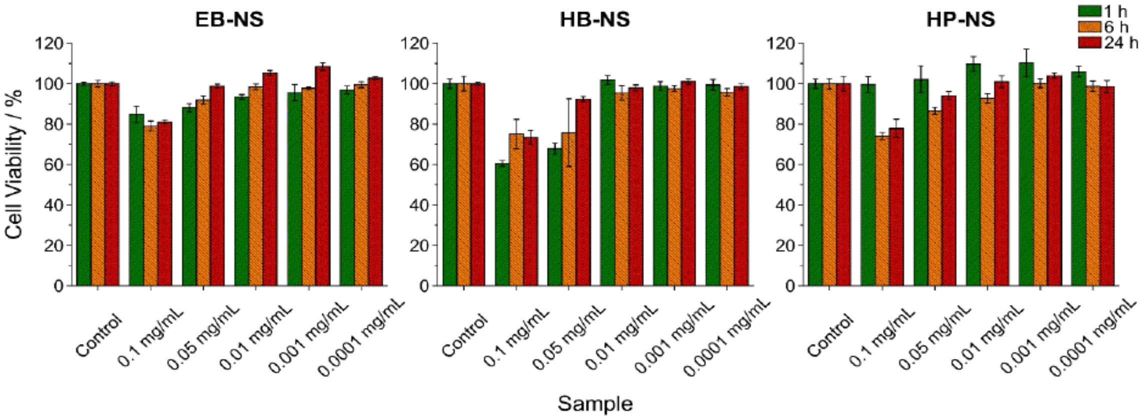

Figure S32. Cytotoxicity tests with cell line 3T3 Different concentrations of EB-NS, HB-NS and HP-NS were dispersed in cell medium and incubated with cell lines of type 3T3 for 1 h, 6 h and 24 h. NS-induced cytotoxicity was assessed via a cell proliferation assay whose absorbance at 490 nm is directly proportional to the number of living cells in the culture (expressed in the figure as % cell viability). Only at 0.1 mg/mL (0.05 mg/mL for HB-NS) cell viability decreased slightly. The biologically more relevant lower concentrations showed no effect on viability. Average values calculated from quadruplicates of each sample are plotted. Error bars = standard deviation.

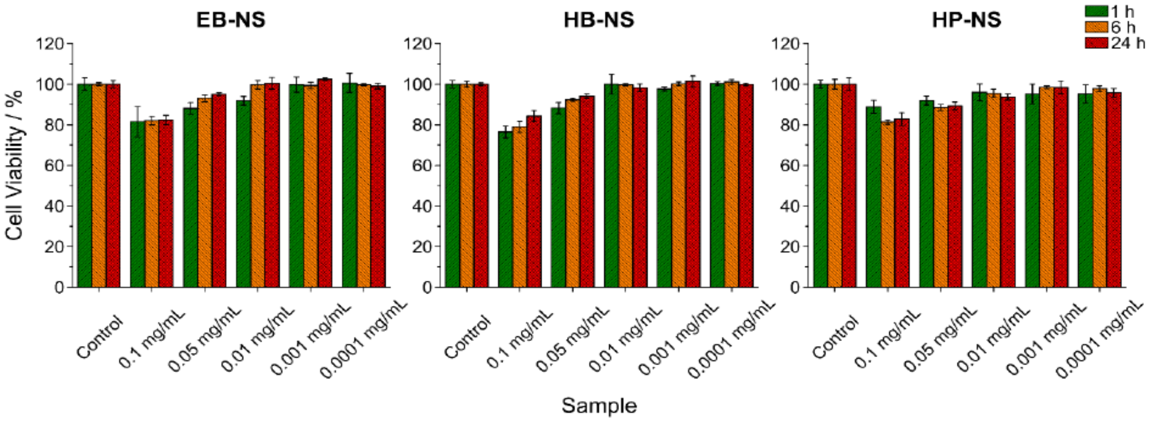

Figure S33. Cytotoxicity tests with cell line A549 Different concentrations of EB-NS, HB-NS and HP-NS were dispersed in cell medium and incubated with cell lines of type A549 for 1 h, 6 h and 24 h. NS-induced cytotoxicity was assessed via a cell proliferation assay whose absorbance at 490 nm is directly proportional to the number of living cells in the culture (expressed in the figure as % cell viability). Only at 0.1 mg/mL cell viability decreased slightly. The biologically more relevant lower concentrations showed no effect on viability. Average values calculated from quadruplicates of each sample are plotted. Error bars = standard deviation.

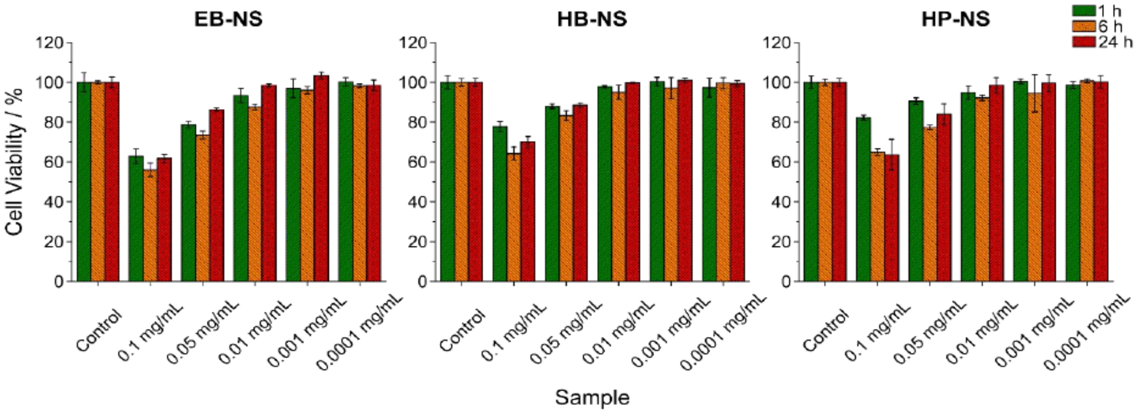

Figure S34. Cytotoxicity tests with cell line MDCK-II Different concentrations of EB-NS, HB-NS and HP-NS were dispersed in cell medium and incubated with cell lines of type MDCK-II for 1 h, 6 h and 24 h. NS-induced cytotoxicity was assessed via a cell proliferation assay whose absorbance at 490 nm is directly proportional to the number of living cells in the culture (expressed in the figure as % cell viability). Only at 0.1 mg/mL cell viability decreased slightly. The biologically more relevant lower concentrations showed no effect on viability. Average values calculated from quadruplicates of each sample are plotted. Error bars = standard deviation.

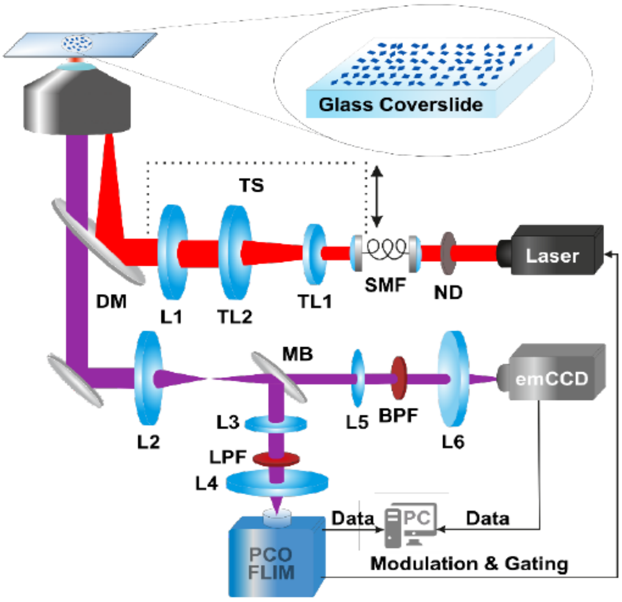

Figure S35. Microscopic fluorescence lifetime imaging (FLIM) on a home-built setup Schematic of the custom-built optical setup for FLIM imaging of NS samples using a frequency domain-based lifetime camera.

Table S1. Comparison of fluorescence lifetime values of EB-NS, HB-NS and HP-NS measured using different experimental techniques: confocal TCSPC, microscopic PCO.FLIM lifetime imaging and oxygen sensor For TCSPC measurements, the mean value and standard deviation were calculated from at least three separate measurements performed on the same samples (N = 3-4 measurements). For FLIM imaging, the lifetime values of each pixel of the acquired image were histogrammed and fitted with the single Gaussian fit; the mean lifetime and standard deviation were taken from the fit (N = 1 measurement). For the modulated LED dataset, the error bar simply corresponds to the standard deviation of the acquisition (N = 1 measurement).

Sample	τ_{TCSPC} [µs]	$\tau_{\text{FLIM imaging}}$ [µs]	$\tau_{\text{modulated LED}}$ [µs]
EB-NS	16.50 ± 0.25	17.6 ± 2.4	27.22 ± 0.05
HB-NS	8.25 ± 0.15	7.8 ± 1.5	21.55 ± 0.05
HP-NS	6.91 ± 0.06	4.5 ± 0.7	14.14 ± 0.04

SUPPLEMENTARY EXPERIMENTAL SECTION

Absorption (Reflection) Spectra of Egyptian Blue (EB), Han Blue (HB) and Han Purple (HP) Bulk and Exfoliated Powders: Bulk powders were analyzed with no prior processing. Aliquots of the milled supernatants were positioned on a watch glass under the lab hood and left to dry in air over several days. Aliquots of the fully exfoliated NS (milled and tip sonicated supernatants) were instead freeze-dried for a couple of days, due to the lower concentrations of this batch of samples. To record absorption spectra, an AvaSpec-UV/Vis/NIR two channel broad band spectrograph (Avantes) equipped with a balanced deuterium-halogen lamp (AVALIGHT-DH-S-BAL) was employed. For our purposes, only the signal recorded in the UV/Vis channel is relevant, therefore the NIR one is not shown; more precisely, the settings of the 2048L UV/Vis spectrometer included a 25 µm slit and a 300 lines/mm grid. Data acquisition and analysis were performed with the Avasoft-Full and Origin Pro 8.1 software, respectively.

Planetary Ball (PB), McCrone (MC) and Mixed Milling Approaches: EB, HB and HP powders (respectively < 120 µm, < 40 µm and < 40 µm qualities) were purchased from Kremer Pigmente GmbH & Co. KG. The standard milling procedure for the first phase of exfoliation was planetary ball (PB) milling, which was performed as follows. 3 g of powder were introduced into a 20 mL agate beaker together with 5 mm agate balls. Deionized water was added until a slurry consistency was reached. The so-prepared agate beaker was then placed in a planetary ball mill (PB, Pulverisette 7 Premium Line, Fritsch, Germany), which was run at 900 r.p.m. for 1 h (3 cycles of 20 min each, 5 min pause). Aliquots of the resulting milled slurry were removed from the beaker and their grain size distributions were measured by means of a laser diffraction particle sizer (LDPS, model LS13320, Beckman&Coulter). For each measurement, three runs were performed, PIDS was used, and an optical model R.I. 1.6/1 was applied. To visualize the grain size distribution, the number of particles within an individual grain size class was plotted as percentage of all particles against the central diameter of the class. In this way, the very small number of bigger particles present in the system does not dominate the distribution curve, as it would instead happen if volume percentage were displayed. Following the PB milling step, an aliquot was poured into a Nalgene® centrifuge tube (Thermo Fisher Scientific) and water was added until an overall volume of 150 mL (dilution factor ≈ 3) was reached. Then, a first centrifugation step (Heraeus Multifuge X3R, Thermo Fisher Scientific) was performed: T = 20°C, 800 r.p.m. (150 × g), 9 min 41 s, 5 s acceleration ramp, 5 s deceleration ramp, 5 cycles. These parameters were calculated from the Stokes Equation (corrected for centrifugation[1]) in order to remove particles of diameter $d > 1$ μm:

$$t = \frac{18 \times \eta}{(\rho_k - \rho_w) \times 4\pi^2 \times f^2 \times d^2} \times \ln \frac{r}{r_0}\,. \qquad \text{(S1)}$$

In Equation (S1), t is the settling time [s], η the temperature-dependent dynamic viscosity of water [kg m^{-1} s^{-1}], ρ_k the grain density [kg m^{-3}], ρ_w the temperature-dependent water density [kg m^{-3}], f the r.p.m. [s^{-1}], d the previously mentioned grain (equivalent) diameter [m], r the distance between the rotor's fulcrum and the sediment's height [cm], and r_0 the distance between the rotor's fulcrum and the suspension's surface [cm] (the last two parameters are dependent on the geometry of the employed centrifuge). At the end of each cycle, the supernatant was decanted and new water was added up to the initial volume; finally, the so-obtained supernatant dispersion was collected in a glass jar and stored at room temperature. New LDPS measurements were performed to check the efficiency of the described centrifugation step in terms of the resulting size distribution. Aliquots of each supernatant of each of the three milled pigments were taken, dried and weighed, yielding the following concentrations: EB ≈ 2.2 g/L, HB ≈ 1.4 g/L and HP ≈ 0.6 g/L. While EB proved to be stable for up to ≈ 2 days already at this stage, milled HB and HP particles settled after a few hours.

To understand whether better results (i.e. smaller grain size and higher monodispersity) could be obtained via techniques other than PB milling, also McCrone (MC) and a mixed milling approach were tested with some of the mentioned powders. With regards to the former, 2 g of bulk EB were added into MC beakers together with 48 agate cylinders and ≈ 7 mL of demineralized water; 2 consecutive milling cycles of 30 min each were performed (XRD-Mill McCrone, Retsch), then the slurry was washed out of the beaker to yield ≈ 45 mL of total slurry volume.

Concerning the mixed approaches, instead, the starting material was represented by the settled parts of PB and MC centrifugations (i.e. the sediment, which had been collected and dispersed in demineralized water): according to the order these millings were executed in, the samples were named "PB+MC" or "MC+PB". The former ones were prepared by loading a total volume of 10 mL of sediment slurries into the MC mill for 30 min: after washing steps, a final volume of ≈ 45 mL was collected. For "MC+PB" samples, instead, MC sediment slurries were first centrifuged according to the following settings: T = 20°C, 3000 r.p.m. (2103 × g), 5 min, 5 s acceleration ramp, 5 s deceleration ramp, 1 cycle. Next, the so-obtained volume of sediment (≈ 8 mL) was placed in PB beakers and milled as described above: after washing steps, a final volume of ≈ 45 mL could be collected.

For MC and mixed milling techniques alike, samples were diluted and centrifuged to produce the supernatant slurries, analogously to how described for the (reference) PB approach. For all exfoliation routes, size distribution measurements of "whole" and "centrifuged" samples were carried out by means of LDPS before and after the centrifugation step.

Scanning Electron Microscopy (SEM) and Scanning Electron Transmission Microscopy (STEM): For SEM imaging (Quattro S SEM, Thermo Fisher Scientific), highly-oriented pyrolytic graphite (HOPG, grade ZYB, Bruker) were used as substrates. HOPGs were plasma-treated (Zepto Diener Electronic GmbH +Co. KG, 1 min of O_2 supply, 1 min of plasma process) in order to clean their surfaces and increase their hydrophilicity. Next, a typical NS sample was vortexed and bath sonicated for 10 min. 10 µL of undiluted sample were spin-coated with the same parameters employed for AFM measurements. For each NS sample, the so-prepared HOPG was either imaged at the SEM as it is, or a ≈ 4 nm-thick gold layer was evaporated (Baltec MED-020, Baltec) onto it to decrease surface charging and, thus, increase imaging contrast. The HOPG was then placed into the SEM chamber and imaged in the following conditions: high vacuum mode, voltage = 5.00 kV, spot size = 3.0, working distance = 10.0 mm, Everhart-Thornley detector (ETD) for secondary electrons, Circular Backscatter Detector (CBS) for backscattered electrons.

STEM measurements were carried out on the same device. Typically, undiluted 5 µL of previously vortexed and bath sonicated NS were deposited and dried onto formvar-coated copper grids, stabilized with evaporated carbon film (FCF300-CU, Electron Microscopy Sciences). The parameters are the same as for SEM imaging, except for the employed detector (STEM3+).

Photobleaching Experiments at the Near-Infrared (NIR) Imaging Microscopic Setup: The imaging setup consists of a 561 nm laser (Cobolt JiveTM 561 nm), an Olympus IX53 microscope equipped with a 20x (MPlanFL N 20x/0.45, Olympus) objective, and a NIR camera (Cheetah TE1, Xenics). Along the light path leading from the microscope to the camera, a dichroic mirror (VIS/NIR, HC BS R785 lambda/5 PV, F38-785S, AHF) and a 900 nm long-pass filter (FELH0900, Thorlabs) are installed. To investigate whether NS can be bleached, a long imaging session with continuous excitation was performed on 10 µL of NS sample, previously drop-casted and dried on a #1 glass coverslip. Acquisition settings were the following: laser set power = 500 mW, measured power out of the objective ≈ 180 mW, acquisition time ≈ 2 h, exposure time = 0.5 s, frame rate = 0.3 fps. Data acquisition was controlled by the Xenics software (v. 2.6), whereas data analysis was carried out in ImageJ (v. 1.52a) and on Origin Pro 8.1.

NIR Imaging at Stand-Off Detection Setup: Our NIR custom-made stand-off detection setup[2] consists of a NIR InGaAs camera (XEVA, Xenics), a Kowa objective (f = 25 mm/F1.4), and a white light source (UHPLCC-01, UHP-LED-white, Prizmatix). The latter is equipped with a 700 nm short pass filter (FESH0700, Thorlabs) for excitation. Furthermore, a 900 nm long pass filter (FEL0900, Thorlabs) is mounted on the camera.

For imaging of EB, HB and HP water dispersions in glass vials, an exposure time of 3 s at maximum lamp intensity was employed.

Colloidal stability experiments were performed in cuvettes on sample volumes of ≈ 2 mL. EB-NS, HB-NS and HP-NS had a starting pH value in the range of ≈ 8-9. Prior to imaging, NS were bath sonicated for 5 min. Then, buffer solutions of pH 4 and 7 were added to some NS cuvettes in the volumes necessary to reach pH 5 and pH 7, respectively. To study the impact of ions on the colloidal stability of the NS, 200 µL of a solution of NaCl (9 g/L, a typical blood concentration) were added into other cuvettes. Finally, control samples consisted in the addition of 200 mL of H_2O. Imaging was started shortly after the introduction of the mentioned aliquots in the cuvettes. Acquisition settings were: exposure time = 2 s, frame rate = 0.067 fps, LED excitation power = 50%, acquisition time ≈ 60 min, LED-cuvette distance ≈ 18 cm, camera-cuvette distance ≈ 20 cm. The acquired images were processed as is, i.e. without background subtraction. To assess the fluorescence intensity over time, the mean signal intensity in a central region of interest of each cuvette was measured (and normalized to the starting frame).

Concerning sample preparation for tissue phantom experiments, 1 mL of NS batch was concentrated (Concentrator 5301, Eppendorf) for ≈ 2 h, yielding a volume of ≈ 0.1 mL with concentration of ≈ 5 g/L. After ≈ 5 min of bath sonication, a capillary tube (ringcaps® 25 µL, Hirschmann Laborgeräte GmbH & Co. KG) was dipped into the NS vial, and NS were thus sucked into the glass tube due to capillary forces. For each class of silicates, a so-prepared capillary tube was positioned onto the setup's stage at ≈ 6 cm and ≈ 13 cm away from the excitation lamp and the detection camera, respectively. Initial reference images were acquired with 0.5 s of exposure time at maximum excitation intensity. Afterwards, ≈ 1 mm-thick chicken slices were step-wise laid on top of the capillary tube, and new images with the same settings were taken after every layer's deposition.

For all acquired datasets (unless explicitly mentioned), background subtraction (i.e. subtraction of background reference image) and data analysis of the so-obtained NIR pictures were carried out in ImageJ (v. 1.52a) and Origin Pro 8.1.

Cytotoxicity Tests: Cells were initially seeded in a 96-well plate at 1.2×10^3 cells per well for 24 h in EMEM with Earle's salts with GlutaMAXTM (Gibco) and 10% FCS (BioWest) at 37°C and 7.5% CO_2 (MDCK II), or in DMEM with L-Glutamine (4 mM) and 10% FCS (BioWest) at 37°C and 5% CO_2 (A549 and NIH 3T3). Freeze-dried EB-NS, HB-NS and HP-NS were dissolved at 10 mg/mL in the appropriate media for each cell line with 100 µg/mL Penn-Strep (Biochrom). Different concentrations were subsequently added to the cells and incubated for 1, 6 or 24 h. Viability of the cell samples was determined by MTS-assay using CellTiter 96® AQueous One Solution Cell Proliferation Assay (Promega); for each sample, the absorption at 490-650 nm was measured.

SUPPLEMENTARY REFERENCES

[1] H. Tributh, G. Lagaly, GIT Fachz. Lab. **1986**, 30, 524.

[2] R. Nißler, O. Bader, M. Dohmen, S. G. Walter, C. Noll, G. Selvaggio, U. Groß, S. Kruss, Nat. Commun. **2020**, 11, 1.

5.3.3 Publication Synopsis

The exfoliation protocol described in **Manuscript III** consisted in an optimization of the approach reported in the previous work on the NS topic **(Manuscript II, Section 5.2.2)**. Wet ball milling and tip sonication were both performed in water and accompanied by centrifugation steps; these were designed in such a way to remove larger particles with a size cut-off diameter d = 1 µm. This exfoliation protocol could indeed yield EB-NS, HB-NS and HP-NS well below the micron range, with lateral sizes and thicknesses reaching minimum values down to ≈ 16-27 nm and 1-4 nm, respectively. In terms of colloidal stability, the so-obtained supernatants showed a clear improvement compared to **Manuscript II**: ranging from HP-NS to HB-NS and EB-NS, colloidal stability increased and resulted in the better performing NS being stable for up to several days. Additionally, when evaluating the resistance to acidic conditions and ionic environments (*e.g.* physiological buffers), the fluorescence of all samples did not decrease significantly in the measured time window (t = 1 h). Analogously to what observed for EB-NS alone in **Manuscript II**, lateral sizes and thicknesses scaled linearly, and the obtained NS morphologies appeared quite irregular. Concerning size distributions, log-normal functions could nicely describe the acquired statistics on diameters and heights of EB-NS, HB-NS and HP-NS.

After a first part dedicated to the morphological characterization of the silicate NS, **Manuscript III** set the focus on the spectroscopy of these materials. The most important and technologically promising finding was represented by the preservation of the bulk absorption and emission features even in the nanostructured form: more precisely, as illustrated by 2D spectra, excitation and emission were still located at wavelength ranges ≈ 550-650 nm and ≈ 850-1000 nm, respectively. Following this initial observation, more in-depth investigations on the NIR fluorescence were carried out. Single-particle fluorescence microscopy imaging confirmed the monodispersity of these samples, as most of the observed NS were resolution-limited (*i.e.* roughly d < 500 nm). Imaging during prolonged excitation (*i.e.* 561 nm laser, 2 h, ≈ 200 mW effective laser power), on the other side, showed that the emission of these fluorophores is not affected by photobleaching. Next, the fluorescence lifetime values were collected by means of two different methods: time-correlated single-photon counting (TCSPC) in a confocal setup, and frequency-domain measurements. The former allowed the estimation of τ through a double-exponential fitting, resulting in the following data: $\tau_{\text{EB-NS}}$ ≈ 17 µs, $\tau_{\text{HB-NS}}$ ≈ 8 µs and $\tau_{\text{HP-NS}}$ ≈ 7 µs. These values, which were in agreement with the frequency-domain investigations, indicated a clear decrease compared to the bulk counterparts (τ_{EB} ≈ 130 µs, τ_{HB} ≈ 60 µs and τ_{HP} ≈ 25 µs). Nevertheless, the fact that both bulk and NS lifetimes lied in the µs range represented a further confirmation for the robustness of NS fluorescence.

Towards the last part of **Manuscript III**, efforts were made in the direction of fluorescence imaging, above all lifetime-based. With a home-built, self-calibrated setup for frequency-domain FLIM in combination with wide-field microscopy, inhomogeneous layers of EB-NS, HB-NS and HP-NS were imaged. By selecting different regions within the FLIM camera's phasor plots, the lifetime channel could provide information which would have otherwise been inaccessible in the conventional (fluorescence) intensity channel. For example, border regions of EB-NS and HP-NS could be clearly identified based on the diverse *τ* values of the two materials. To this regard, the average NS lifetime values that could be extracted from the lifetime images were also in agreement with the datasets described in the spectroscopy section of **Manuscript III**. Another relevant finding which also resulted from the analysis of the FLIM phasor plots was the observed size-dependence of fluorescence lifetime: within a layer of drop-casted NS, sub-populations could in this way be defined. In a similar manner to what done with EB-NS in **Manuscript II**, remote fluorescence imaging detection was tested on all three materials, too. In this case, either an InGaAs or a FLIM camera were employed in a simpler home-built setup depending on the employed imaging mode: respectively intensity-based or lifetime-based. The former showed that NS supernatants emit a NIR fluorescence which is bright enough to be easily detected from distances > 10 cm; furthermore, no significant decrease in the fluorescent signal could be noticed after addition of salts or after lowering the pH. Lifetime-based measurements, on the other side, proved that the strong signals could also allow a clear labelling of each silicate according to the respective (uncalibrated) *τ* values.

Finally, additional studies were carried out on EB-NS, HB-NS and HP-NS to more directly test their potential use as bioimaging labels. As previously observed for EB-NS in **Manuscript II**, the results of cytotoxicity experiments on three different cell lines demonstrated the reasonable biocompatibility of all three silicate NS. Moreover, tissue phantom experiments (which are typically done to simulate *in vivo* imaging conditions) were performed at the remote detection setup mentioned above: an LED lamp and an InGaAs camera were used for excitation and signal detection, respectively. The collected images proved that the intense fluorescence of EB-NS, HB-NS and HP-NS can be detected through several layers of tissue (at least up to 4 mm), with high potential for further improvement if more optimized optical techniques were to be used.

In a Nutshell...

- ✓ Egyptian Blue (EB), Han Blue (HB) and Han Purple (HP) were exfoliated into NS *via* a mixed approach of wet ball milling and tip sonication in water.
- ✓ A size cut-off with centrifugation steps was performed, leading to NS with diameter < 1 µm.
- ✓ EB-NS, HB-NS and HP-NS retained the excitation and emission features of the bulk materials.
- ✓ Their robust NIR fluorescence did not display photobleaching and was not significantly affected by pH, ionic environments or buffer.
- ✓ Time and frequency-domain fluorescence lifetime spectroscopy measurements displayed a decrease in lifetime (τ) after exfoliation, even though the NS values still lied in the µs range.
- ✓ Microscopic and macroscopic lifetime-encoded imaging (FLIM) allowed to clearly distinguish EB-NS, HB-NS and HP-NS from one another.
- ✓ Microscopic FLIM measurements indicated the existence of sub-populations of NS within each silicate sample, which were determined by the differences in sizes among single particles.
- ✓ Cytotoxicity assays confirmed the biocompatible nature of EB-NS, HB-NS and HP-NS.
- ✓ The NS fluorescence was bright enough to be detected though several layers of tissue phantoms.

5.4 Surface Functionalization of EB-NS for Targeted Bioimaging

5.4.1 Introduction

The final section of the Results chapter of this dissertation addresses another fundamental aspect in the design of novel fluorophores: surface functionalization. The studies reported in the previously described works **(Manuscript II, Manuscript III)** have outlined with clear proof-of-principle applications how promising Egyptian Blue nanosheets (EB-NS) are for multiple technological fields, above all bioimaging and biosensing. Especially these applications would directly benefit from the tailoring of the surface chemistry on these layered silicates, as this could increase colloidal stability and allow targeting of (bio)molecules of interest[234]. In the own works described so far, EB-NS were employed as is, *i.e.* directly after exfoliation. Unfortunately, very few literature works have so far put effort into chemically functionalizing the surface of EB-NS and, in all cases, the established protocols were either non-covalent[219] or not optimal for further biomedical uses[221,222] **(Section 4.3.2, Review Manuscript)**. In the search of suitable protocols for the desired purposes, inspiration can be drawn from other silicon-based systems. The family of silicon-based nanoparticles (NPs) and biomaterials is very broad and includes versatile platforms such as nonporous colloidal silica NPs, mesoporous silica NPs, organosilica NPs, porous silicon (pSi), bioglass and silicene/silicon nanosheets. These materials have found several applications in the biomedical fields of *e.g.* drug delivery, diagnostic bioimaging, biosensing, antibacterial substrates and tissue engineering[240]. Next to their biocompatible traits, these silicon-composed (nano)systems also benefit from a well-established chemistry. Among them, the covalent grafting of accessible surface silanol groups (Si-OH) with silanes represents a very common strategy[241]. In order for the reaction to take place, the chosen organosilicon compound must display leaving groups of high reactivity on the silicon atom. From this point of view, alkoxy- (*e.g.* trialkoxysilane), halo- (*e.g.* chlorosilane), amino- (*e.g.* (3-aminopropyl)triethoxy silane, APTES) and other silanes have been employed successfully in various studies[234,242–247]. These coupling agents, however, present disadvantages including high reactivity and moisture sensitivity. In this regard, improvements have been reported with the employment of more stable allylsilanes and by means of catalytic grafting processes with methallyl- and vinylsilane precursors, however the required long reaction times can lead to decomposition of the functional groups and, thus, make these approaches less appealing for industrial application[245,248]. Within this scenario, an approach that stands out for its simplicity, robustness and versatility is the one reported by Moitra *et al.*[248] Their protocol, based on Si-H activation of hydrosilanes, enabled straightforward grafting of tailorable moieties onto the surface of silica particles.

Past studies have shown that, due to synthesis and exfoliation procedures, silanol groups can be present in significantly high amounts on the surface of EB-NS[174,177,225]. **Manuscript IV** therefore describes the application of the protocol of Moitra *et al.*[248] to EB-NS. The points that were addressed in this study were the following:

- What analytical tools can be used to robustly prove that this functionalization approach was successful?
- Are the promising photophysical properties of EB-NS retained after functionalization and/or are some new features unlocked?
- Is it possible to use this approach to bind functional groups of biological relevance on the surface of EB-NS?
- Can a proof-of-principle experiment of targeted bioimaging with the so-functionalized EB-NS be performed?

5.4.2 Covalently Functionalized Egyptian Blue Nanosheets for Near-Infrared Bioimaging (Manuscript IV)

Publication Details

Title: “Covalently Functionalized Egyptian Blue Nanosheets for Near-Infrared Bioimaging”

Authors: **Gabriele Selvaggio**†, Niklas Herrmann†, Björn Hill, Riza Dervisoglu, Sebastian Jung, Milan Weitzel, Meshkat Dinarvand, Dietmar Stalke, Loren Andreas and Sebastian Kruss

Journal: accepted on *ChemRxiv* (2022)

[Status update on 4/12/2022: revised and accepted for publication in ACS Applied Bio Materials]

DOI: 10.26434/chemrxiv-2022-20ts5

†These authors contributed equally.

Author Contributions: GS, NH and SK conceived and designed the study. SK coordinated the study. GS exfoliated EB into EB-NS. NH synthesized and characterized Pyr-Sil with support from GS. Corresponding NMR and MS data was analyzed by NH. NH and GS performed the grafting of Pyr-Sil onto EB-NS and acquired the 1D and 2D Vis-NIR spectroscopic dataset of pyrene-functionalized EBfunc. MD performed CLSM on pyrene-functionalized EBfunc samples prepared by GS and MW. Colocalization analysis of the CLSM dataset was performed by GS. ssNMR measurements were performed and analyzed by RD and LA with support from NH. GS synthesized COOH-preSil and COOH-Sil with support from DS, NH and MW. Corresponding NMR and MS data was analyzed by NH. The grafting of COOH-Sil onto EB-NS to yield COOH-functionalized EBfunc was performed by GS with support from DS and NH. BH acquired zeta potential measurements on COOH-functionalized EBfunc. BH and SJ carried out FA conjugation and cell experiments with support from GS. GS, NH and SK wrote the manuscript with contributions from all authors.

Covalently Functionalized Egyptian Blue Nanosheets for Near-Infrared Bioimaging

G. Selvaggio[1,2†], N. Herrmann[2†], B. Hill[1], R. Dervisoglu[3], S. Jung[1], M. Weitzel[2], M. Dinarvand[1,2], D. Stalke[4], L. Andreas[3], S. Kruss[1,2,5,6]

Fluorophores emitting in the near-infrared (NIR) wavelength region present optimal characteristics for photonics and especially bioimaging. Unfortunately, only few NIR fluorescent materials are known and even fewer are biocompatible. For this reason, the scientific interest in designing novel NIR fluorophores is very high. Egyptian Blue ($CaCuSi_4O_{10}$, EB) is a NIR fluorescent layered silicate that can be exfoliated into fluorescent nanosheets (EB-NS). So far, its surface chemistry has not been tailored but this is crucial for colloidal stability and biological targeting. Here, we demonstrate covalent surface functionalization of EB nanosheets (EBfunc) *via* Si-*H* activation using hydrosilanes with variable functionalities. EB-NS were first grafted with the visible fluorescent pyrene (Pyr) moieties to prove conjugation by colocalization of the Vis/NIR fluorescence on the (single) EB-NS level. The same procedure was performed and validated with carboxyl group (COOH)-containing hydrosilanes. These groups can serve as generic handle for further (bio)functionalization of the EB-NS surface. Finally, folic acid (FA) was conjugated to these COOH-functionalized EB-NS to target folic acid receptor-expressing cancer cells. These results highlight the potential of this surface chemistry approach to modify EB-NS and enable targeted NIR imaging for biomedical applications.

Introduction

After the discovery of graphene, two-dimensional (2D) nanomaterials have become an emerging class in science[1–3]. They provide numerous opportunities for electronics, catalysis, optics and (gas) storage on the nanoscale and beyond[1–9]. Furthermore, their use in biomedical applications is a main focus for researchers[10–15]. Classes of 2D nanomaterials which have proven successful in biomedicine include graphene, transition metal dichalcogenides (TMDs), layered double hydroxides (LDHs), silicate clays, transition metal oxides (TMOs), hexagonal boron nitride (hBN) and many more[16–18]. Hydrophobicity and the chemical inertness of most 2D nanomaterials are challenges especially for biological applications, in aqueous environments. Especially inorganic materials *e.g.* metal sulfides, chalcogenides and silicates require additional surface chemistry for example to guarantee colloidal stability. The tailoring of surface functionalization therefore plays a role of paramount importance for the achievement of enhanced colloidal stability, longer circulation times and improved biocompatibility. The possibility of decorating these nanomaterials with (bio)molecules of interest could furthermore allow therapeutic treatment, sensing and imaging applications[19].

Egyptian Blue ($CaCuSi_4O_{10}$, EB) is the most ancient pigment in the history of mankind, having its origins dated back to Ancient Egypt (≈ 2500 BC)[20,21]. This calcium copper tetrasilicate displays a layered crystal structure which allows to prepare nanosheets (NS) *via* simple stirring in hot water[22–27]. Most interestingly, it has been shown that the bright, stable and long-lived near-infrared (NIR) fluorescence of the bulk material ($\lambda_{em} \approx$ 910-930 nm)[25–30] is preserved in exfoliated NS down to just few tenths of nm in size[31,32]. The biocompatible nature of this class of layered silicates has been demonstrated by cell viability assays and *in vivo* studies[31]. Among them, an increasing number of publications has proven the high potential of EB-NS in the biomedical field as multi-functional platform for bioimaging[31,32], sensing[33], photothermal therapy (PTT)[34,35], tissue engineering[36,37] and more. Especially as novel NIR fluorophore, EB-NS appears of extreme interest. Fluorophores that emit in the NIR window (NIR-I: $\lambda \approx$ 750-1000 nm; NIR-II: $\lambda \approx$ 1000-1700 nm) present optimal characteristics for bioimaging due to reduced phototoxicity, scattering, absorption and autofluorescence of biological samples at these wavelengths[38–41]. Although organic dyes (*e.g.* indocyanine green[42], modified boron dipyrromethenes[43–46], *etc.*) and nanomaterials (*e.g.* quantum dots[47], silicon nanocrystals[48], single-walled carbon nanotubes[49–55], *etc.*) have been successfully implemented for numerous biological studies, their number is quite limited and in most cases they are affected by low quantum yield, low photostability and/or biocompatibility issues[40,42,47,56–59]. For these reasons, the interest in novel NIR materials is very high. Although the potential of EB-NS as NIR fluorophore has already been recognized [31,32], the next important step in this direction is tailoring of its surface chemistry. So far, the few publications which have described functionalization procedures on EB-NS have focused on lipophilic coatings. These were bond to the silicate surface either through electrostatic interactions (with *e.g.* the cationic surfactant cetyltrimethylammonium bromide, CTAB[60]) or covalently *via* silanization (with trimethylsilyl chloride, TMSCl[61,62]). Due to the non-covalent nature of the former, dynamics in the biological environment represent a challenge. The latter, on the other side, is covalent but also hydrophobic and inert, thus limited for biological applications.

[1.] *Department of Chemistry, Bochum University, Bochum, 44801, Germany.*
[2.] *Institute of Physical Chemistry, University of Göttingen, Göttingen, 37077, Germany.*
[3.] *Max-Planck-Institute for Multidisciplinary Sciences, Göttingen, 37077, Germany.*
[4.] *Institute of Inorganic Chemistry, University of Göttingen, Göttingen, 37077, Germany.*
[5.] *Fraunhofer Institute for Microelectronic Circuits and Systems, Duisburg, 47057, Germany.*
[6.] *Center for Nanointegration Duisburg-Essen (CENIDE).*

†These authors contributed equally.

**Corresponding author: sebastian.kruss@rub.de.*

Therefore, versatile chemical surface chemistry is crucial to use EB-NS *e.g.* for bioimaging.

Silicon-based nanoparticles (NPs) and materials have found several applications in the biomedical field[63–69]. These materials benefit from a well-established surface chemistry. For example, in the case of silica NPs, reactive functional moieties including the hydroxyl (-OH), carboxyl (-COOH), amine ($-NH_2$), azide ($-N_3$) and alkyl halogen groups can be covalently introduced either *via* co-condensation or by post-synthesis surface modification ("grafting"). While the former yields a more uniform distribution of functional groups, the latter does not significantly affect the size distribution and morphology of the silica NPs. The grafting procedure, which can be applied to diverse silica substrates, consists in the condensation of functionalized organosilicon compounds (typically silanes) with the accessible silanol groups (Si-OH) present on the surface of the silica-based material[70]. The most employed leaving groups in silanes are alkoxy groups (R_nSiX_{4-n}, X = OR'), but also alternatives such as halides, acyloxy and amino groups (X = halide, OCOR' and NR'_2 in R_nSiX_{4-n}) have been extensively reported. In this way, silane chemistry can robustly install strong bonds between the particle surface and (bio)molecules of interest, *e.g.* small organic molecules, fluorophores, nucleic acids, peptides, proteins, enzymes, antibodies, gold NPs, *etc.*[19,64–69]. However, the main issue with traditional alkoxy- (*e.g.* trialkoxysilane), halo- (*e.g.* chlorosilane), amino- (*e.g.* (3-aminopropyl)triethoxy silane, APTES) and acyloxysilanes coupling agents is that they are highly reactive and moisture sensitive, therefore purification steps can be challenging. A versatile alternative are hydrosilanes. These molecules are easily accessible, highly stable against moisture and allow simple purification. By choosing hydrosilanes as precursors and the strong Lewis acid tris(pentafluorophenyl)borane ($B(C_6F_5)_3$) as catalyst, *Moitra et al.*[71] have reported a promising method for surface modification of silica. This Si-*H* activation process, which has also later been adapted by *Sweetman et al.*[72] to porous silicon (pSi), can be performed at room temperature, is fast (reaction time ≈ 5 min), can be confirmed by naked eye (hydrogen release), and allows covalent binding of diverse groups.

In this work we report covalent functionalization of EB-NS *via* Si-*H* activation of hydrosilanes, followed by conjugation of EB-NS with different functional groups including folic acid (FA). We establish covalent (bio)functionalization of EB-NS and demonstrate targeted imaging of cancer cells **(Fig. 1)**.

Results

Functionalization (EBfunc) of Egyptian Blue Nanosheets (EB-NS) With Pyrene (Pyr)

Previous works have demonstrated that silanol groups are indeed accessible in significantly high numbers as a consequence of both synthesis and exfoliation procedures[22,35,73]. Our goal was to first demonstrate that this chemistry works in general and then to use it to bind biologically relevant molecules to EB-NS. To optimize the reaction conditions and to prove that this experimental procedure works on EB-NS, pyrene (Pyr) was chosen as the functional group (R). Its well-known fluorescence[74,75] acts as a visible control for the

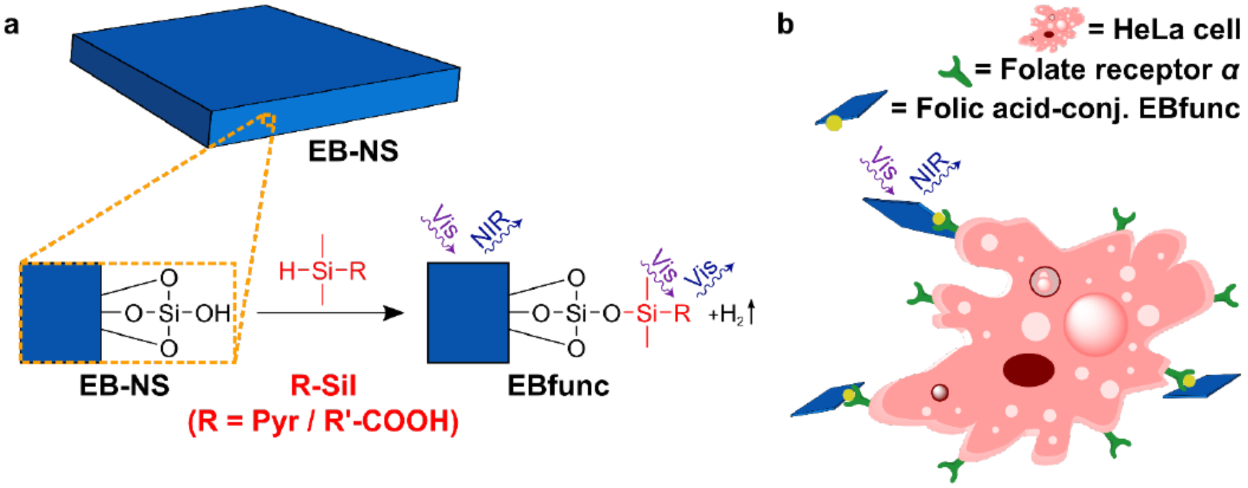

Figure 1: Surface functionalization of Egyptian Blue nanosheets for bioimaging. a *Procedure to graft hydrosilanes (R-Sil) onto the surface of Egyptian Blue nanosheets (EB-NS) via Si-H activation is illustrated. As R groups of the hydrosilanes, pyrene (Pyr) and an alkyl carboxylic acid for further conjugation were chosen. The NIR emission of EB-NS and the visible (Vis) fluorescence of Pyr are used to investigate the functionalization via colocalization. For clarity, only a small section of an EB-NS crystal with only one Si-OH on its surface is depicted.* ***b*** *EBfunc with folic acid (FA) is used to target and image FA receptors on cancer cells. Structures and objects are not to scale for better clarity.*

success of the grafting reaction. Therefore, 1-(dimethylsilyl)pyrene (Pyr-Sil) was synthesized from 1-bromopyrene and chlorodimethylsilane using a method known from literature[71] **(Fig. S1)**. The resulting silane was then reacted with EB-NS using $(C_6F_5)_3B$ as catalyst. The addition of the catalyst resulted in hydrogen evolution **(Fig. S2)**, as expected from the Si-*H* activation process and as reported in literature[71]. This observation represents a first visual indication that functionalization has been successful. After vigorous washing with dichloromethane (DCM) and hexane, the emission at visible wavelengths of the material (EBfunc) was investigated using fluorescence spectroscopy. The pyrene emission[76–78] was detected even after intense washing, thus excluding that only physisorption happened **(Fig. 2a)**. Without catalyst (noCAT) no visible fluorescence after the same washing procedure was observed, ruling out strong non-covalent binding between Pyr-Sil and EB-NS **(Fig. S3)**. Additionally, we examined whether the fluorescence of the visible- and NIR-emitting moieties (Pyr and EB-NS, respectively) changes. It is known that both radiative and non-radiative energy transfer between pyrene and other fluorescent molecules can happen if conditions such as close mutual distance and spectral overlap are met[75,79,80]. Interestingly, neither the Pyr **(Fig. 2a, Fig. S3)** nor the EB-NS **(Fig. 2b)** signals showed any significant difference compared to the starting materials[31,32]. This result shows that there is no energy transfer maybe because of the non-overlapping spectra. Nevertheless, the unchanged excitation and emission features of EB-NS once more underline the photostability of this silicate nanomaterial.

To prove functionalization on the single particle level and gain spatial information microscopy has to be used. The previously described EBfunc and noCAT powders were analyzed at a confocal laser scanning microscope (CLSM) to assess colocalization **(Fig. 3, Fig. S4-S5)**. With this method, successful functionalization can be deduced if the same particles are simultaneously observable in the bright field (BF) and in the visible fluorescence (PL) channel, meaning that fluorescent Pyr is present on the surface of the imaged nanostructure. EB-NS "as is" was chosen as one of the controls: considered that this represents pristine EB-NS which did not undergo any surface reaction and had thus no contact to pyrene, no fluorescence signal was expected here. Indeed, this control only yielded a very weak signal in the PL channel, likely determined by slight cross-talk of the CLSM optical path **(Fig. S5d,h)**. Analogously to the fluorescence spectroscopy dataset, the "noCAT" control sample was measured as well. In this case, the PL counts were slightly higher compared to the unprocessed EB-NS, yet the overall signal was very dim and colocalization was neglectable **(Fig. S5c,g)**. When measuring EBfunc, on the other side, a significantly stronger fluorescence intensity was observed over the entire sample. Furthermore, a high degree of colocalization could be measured for both larger and smaller NS structures **(Fig. 3, Fig. S5a,e)**. Indeed, the colocalization analysis indicated a comparable colocalization degree for the EB-NS and noCAT controls, whereas ≈ 2× higher values were calculated for EBfunc **(Fig. S5i)**. This dataset thus represents a further proof that Pyr is bound covalently in high number, while NS in the noCAT sample display at most a small amount of physisorbed pyrene.

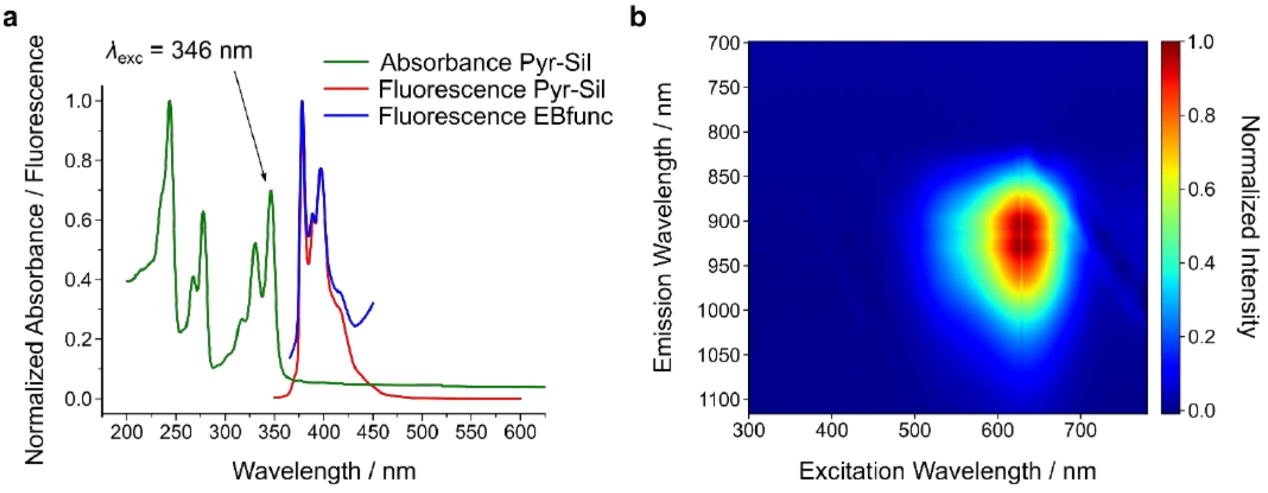

Figure 2: Proof of conjugation by absorbance and fluorescence spectroscopy. a *Pyrene has characteristic absorption features between 200-350 nm and fluorescence features between 370-400 nm which are observable in the synthesized 1-(dimethylsilyl)pyrene (Pyr-Sil). These emission features are also present in pyrene-functionalized EB-NS (EBfunc), even after several washing steps, which proves successful conjugation.* ***b*** *2D excitation-emission spectrum of EBfunc. It is not changed by the surface modification compared to EB-NS, thus highlighting on one side the robustness of EB-NS fluorescence, on the other side the absence of energy transfer between EB-NS and pyrene.*

In addition to the fluorescence studies described above, solid-state magic-angle spinning NMR analysis (MAS NMR) was performed on the previously defined EBfunc, noCAT and Pyr-Sil samples **(Fig. 4)**. Here, the signals of the 1-(dimethylsilyl)pyrene have been considered. We assigned the corresponding ^{13}C shifts of 0 ppm to the methyl and 120-140 ppm to the aromatic groups. EBfunc displayed a significant change of about +4 ppm in the chemical shift of the 0 ppm methyl groups. Furthermore, the aromatic peaks of Pyr-Sil were detected as well. Finally, no such signals were observed in the noCAT control. These findings directly prove attachment between the Si end of the Pyr-Sil and the Egyptian Blue surface. Hence, the ^{13}C MAS NMR data indicates a successful surface chemistry.

Functionalization (EBfunc) of Egyptian Blue Nanosheets (EB-NS) with Carboxyl Groups (COOH)

Next, we moved to more versatile reaction partners. 4-(dimethylsilyl)butanoic acid (COOH-Sil) was synthesized *via* a Grignard reaction from the corresponding chloro compound and carbon dioxide **(Fig. S6-S7)**. COOH-Sil was then added to EB-NS and the catalyst as previously described for Pyr-Sil, yielding in this case COOH-functionalized EB-NS (EBfunc). The grafting reaction led again to bubbling (*i.e.* hydrogen evolution), thus providing a first proof of successful covalent functionalization. When the reaction was repeated without the presence of the catalyst for the noCAT control sample, no bubbling could be observed. In a next step, after the usual washing and drying steps, zeta potential values of the EBfunc, noCAT and unprocessed EB-NS samples were measured **(Table 1)**. Acidic groups tend to dissociate in water at pH ≈ 7: although the surface of unmodified EB-NS is already negatively charged, we therefore expected the presence of carboxylic acid groups on EBfunc to further increase the amount of negative surface charges[31,81]. These can be robustly assessed *via* measurements of zeta potential, *i.e.* the electrical potential at the slipping plane of the investigated object. Indeed, the zeta potential of EBfunc (≈ -40 mV) decreased compared to noCAT and EB-NS (both ≈ -20 mV) suggesting the presence of grafted carboxyl groups on the surface of EBfunc. Furthermore, zeta potential is known to be a commonly employed tool to assess colloidal stability[82]. According to the well-established DVLO theory[83,84], the sum of van der Waals attractive and electrical double layer repulsive interactions between (nano)particles determines the

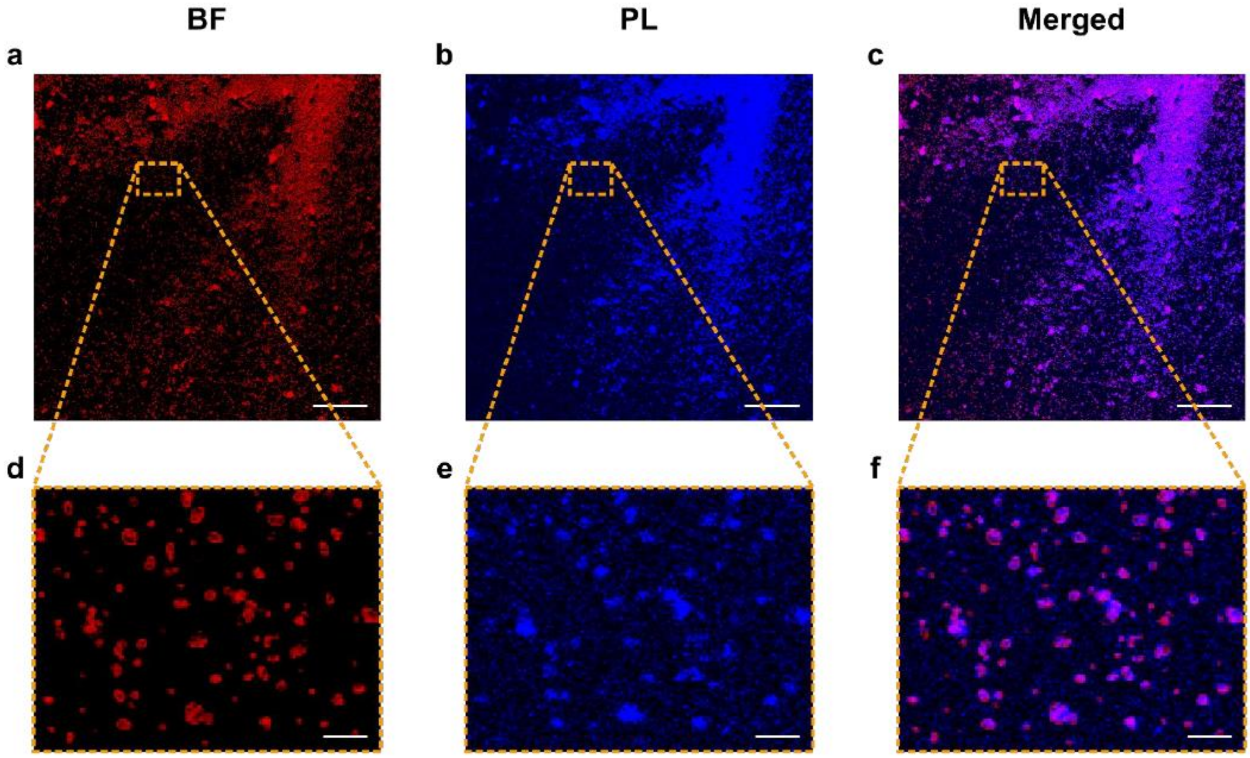

Figure 3: Proof of conjugation by optical colocalization. *Confocal laser scanning microscopy (CLSM) images of pyrene-functionalized EB-NS (EBfunc). The bright-field (BF,* ***a,d****), fluorescence (PL,* ***b,e****) and merged channels* ***(c,f)*** *of EBfunc imaged at a CLSM are shown. For both µm-sized and nm-sized EB-NS a high degree of colocalization is observed, which proves functionalization. Scale bar = 100 µm for overview images. Scale bar = 10 µm for blow-ups.*

stability of a colloidal system. In order for it to be stable and thus avoid the formation of aggregates, repulsive forces must prevail. Considered that the degree of particle repulsion is known to increase with higher absolute values of the zeta potential, this dataset also highlights a better colloidal stability of EBfunc. This lower tendency of agglomeration is of paramount importance for applications of these NS in biological systems.

Table 1: Zeta potentials of EB-NS, COOH-functionalized EB-NS (EBfunc) and folic acid-conjugated EB-NS (FA-conjugated EBfunc). *To verify the presence of carboxyl groups on the NS surface, zeta potential measurements on aliquots of EBfunc, the corresponding catalyst-free control sample (noCAT) and the unmodified EB-NS were performed. To confirm the conjugation of EBfunc with FA, zeta potential values of FA-conjugated EBfunc and the corresponding control were acquired. For both datasets, samples were dispersed in water and pH values were adjusted before measuring. N = 1 independent sample, n = 5 technical replicates.*

Sample	Zeta Potential ± Standard Deviation / mV	pH
EBfunc	-41 ± 2	6.83
noCAT	-21 ± 1	6.31
EB-NS	-20 ± 1	6.77
FA-conj. EBfunc	-38 ± 3	6.42
Control	-33 ± 2	6.11

Conjugation of Folic Acid (FA) onto COOH-Functionalized EB-NS (EBfunc)

With this functional carboxyl handle on the surface of EB-NS, classical conjugation chemistry can be used. Similar chemistries have been extensively performed for *e.g.* silica nanoparticles[19]. One interesting biomolecule is folic acid (vitamin B9, FA). This non-immunogenic, cost-efficient and stable molecule shows high affinity ($K_d \approx$ 0.1-1 nM[85,86]) to the folate receptor (FR), which tends to be up-regulated in a wide range of human cancers. For this reason, tumor-specific treatments with high selectivity are envisioned, as demonstrated by the targeting of the most widely expressed isoform FRα by means of organic molecules, antibodies and nanoparticles[85–88]. Although the COOH group in the γ position on the FA core scaffold is most often used as handle for covalent attachment, other protocols exist which target amino groups instead, without compromising the binding strength of FA to FRα[86,89–92]. Inspired by one of these procedures[91], we therefore conjugated FA to COOH-functionalized EBfunc. As a control, the same reaction but without the addition of *N*,*N'*-dicyclohexylcarbodiimide (DCC) and *N*-hydroxysuccinimide (NHS) was repeated. The success of the conjugation protocol was first assessed by means of zeta potential **(Table 1)**: the more negative values for EBfunc compared to the control indicated a higher presence of negatively charged FA on the EBfunc surface. This outcome indicates successful conjugation beyond mere physisorption.

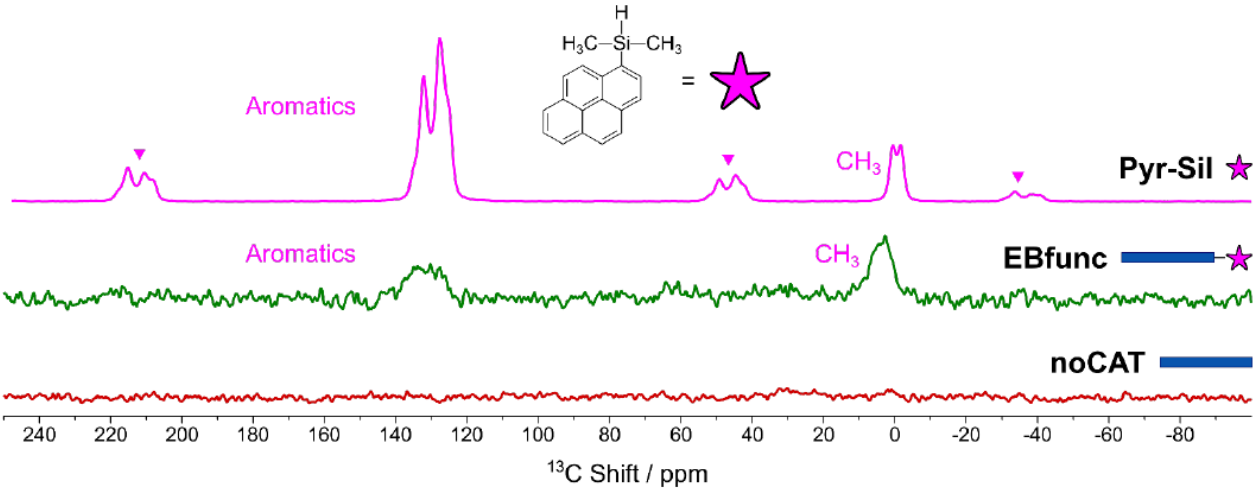

Figure 4: Proof of conjugation by solid-state nuclear magnetic resonance (ssNMR). *^{1}H-^{13}C cross-polarization (CP) magic-angle spinning (MAS) solid-state nuclear magnetic resonance (ssNMR) spectra of the 1-(dimethylsilyl)pyrene (Pyr-Sil), the pyrene-functionalized EB-NS (EBfunc) and the control sample without catalyst (noCAT) are reported. In Pyr-Sil, the peak at around 0 ppm belongs to the methyl groups attached to the Si atoms, whereas the 120-140 ppm peaks belong to the aromatic carbons of the pyrene moiety. Peaks denoted with triangles are spinning side bands. In EBfunc, the 4 ppm ^{13}C chemical shift belongs to the methyl groups and the 120-140 ppm to the aromatics from Pyr-Sil. The catalyst-free control sample shows no presence of the pyrene-silane either attached to the surface of EB-NS or free.*

Next, this novel FA-EBfunc conjugate was employed for tumor-selective targeting of HeLa cancer cells. These are epithelial cells from a cervical carcinoma which have been extensively used in biological studies and are known to express FR*α* in high amounts[85,89,91,93]. FA-conjugated EBfunc was introduced to these cell samples, which were then imaged at our home-built NIR microscopy setup. Here, colocalization experiments of the cells (phase contrast mode) and the FA-conjugated EBfunc (NIR fluorescence) were carried out **(Fig. 5)**. For the estimation of the degree of cell targeting displayed by FA-conjugated EBfunc, the positions of its NS relative to nearby cells were analyzed **(Fig. S8)**. In order to distinguish specific binding from simple physisorption, control EBfunc samples were prepared as mentioned above. Although non-specific binding events occurred, FA-conjugated EBfunc showed a higher degree of colocalization. This "background" looks different from the background one would expect from organic dyes because of the "particle" nature of EB-NS. It indicates a certain level of physisorption of non-functionalized EB-NS on cells. Nevertheless, this result suggests the presence of ligand-receptor binding events, which would be expected from the interaction between FA and the corresponding FR*α* receptors expressed by HeLa cells. In this way not only the conjugation chemistry performed on EBfunc was further confirmed, but the potential of functionalized EB-NS for bioimaging was also showcased.

Discussion

In this work a simple, robust and versatile protocol for the covalent functionalization of Egyptian Blue nanosheets (EB-NS) was described for the first time. The chosen approach, based on Si-*H* activation of hydrosilanes and adapted from the work of *Moitra et al.*[71], enables a large degree of freedom in terms of available R groups. We first demonstrated the applicability of this method on EB-NS by choosing a pyrene-bearing silane (Pyr-Sil) as precursor. A first proof of successful functionalization was given by hydrogen evolution, which could be easily observed by eye during the reaction. Next, we could exploit the visible fluorescence of pyrene to confirm its grafting onto the EB-NS surface *via* spectroscopic and imaging methods. As a final

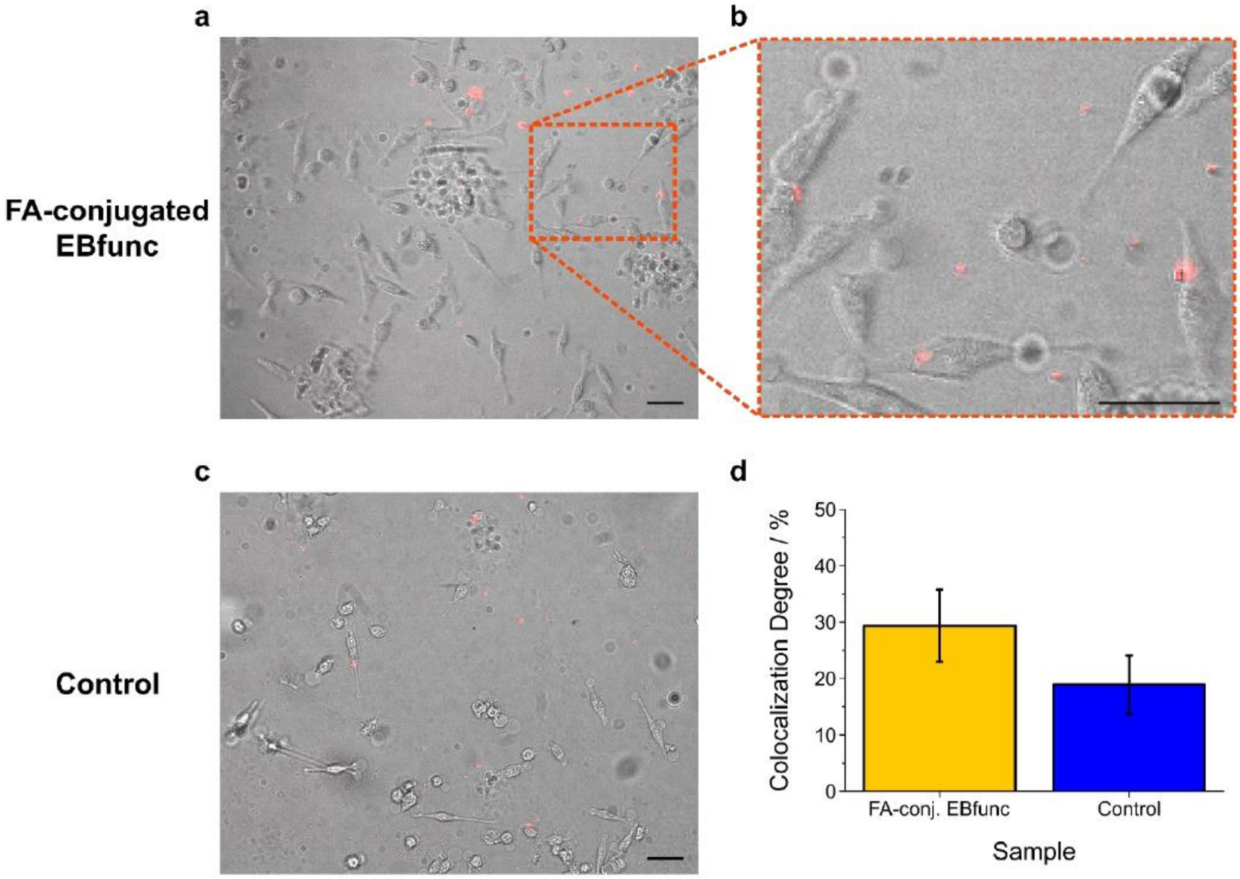

Figure 5: Targeted imaging of HeLa cells with folic acid (FA)-conjugated EBfunc. a-c *Exemplary merged microscopy images of HeLa cells (phase contrast, Vis channel, grayscale) incubated with FA-conjugated EBfunc* ***(a-b)*** *and EB-NS without FA* ***(c)*** *(fluorescence, NIR channel, red color). Scale bar = 50 µm.* ***d*** *The average colocalization highlights that EBfunc binds to a higher degree to FA expressing cells even though there is a background of non-specific adsorption. The cell labelling performance was evaluated by classifying NS particles according to their position relative to nearby cells. Data was normalized to the total number of NS present in the imaged region. Error bars = standard deviation. n = 4-5 analyzed regions of interest.*

characterization step, solid-state nuclear magnetic resonance (ssNMR) was chosen: by means of ^{1}H-^{13}C cross-polarization (CP) magic-angle spinning (MAS) measurements, the relevant signals of Pyr-Sil could be detected in the functionalized (EBfunc) sample. The versatility of this functionalization approach allowed us then to choose moieties of higher interest for *e.g.* bioimaging purposes. By following the same procedure, we explored the grafting reaction with a carboxylic acid-bearing silane (COOH-Sil). The covalent bonding of the carboxyl groups (COOH) onto the surface of EB-NS could be once more confirmed by the naked eye due to hydrogen evolution. Furthermore, zeta potential measurements clearly indicated an increased negative charge on the surface of COOH-functionalized EBfunc, which also led to an improved colloidal stability. Within the frame of biological applications, such features can result in *e.g.* an increased biocompatibility and a longer circulation time of EB *in vivo*. Finally, folic acid (FA) was linked to COOH-functionalized EBfunc *via* classical conjugation chemistry. This additional functionalization step, confirmed by zeta potential measurements, allowed NIR fluorescent labeling of cancer cells bearing folate receptors. Other NIR fluorescent nanomaterials such as SWCNTs have been successfully used for bioimaging and sensing[49,56]. A key to all these applications is versatile non-covalent and recently covalent surface chemistry[53,94,95]. It enabled imaging of neurotransmitters[96–100], reactive oxygen species[101–107], polyphenols[108], disease markers[33,53,109,110] and many other important analytes and biological targets. Translated to EB-NS, the versatile surface chemistry presented by us in this work will enable similar applications.

Conclusions

The NIR fluorescence of EB-NS offers many opportunities for biomedical applications and especially biophotonics. This work introduces a new covalent surface chemistry on EB-NS, which now provides access to numerous (bio)conjugation reactions for COOH-functionalized nanoparticles[19]. In combination with the highly promising chemical and photophysical properties of EB-NS[21], it represents an important step forward to establish EB-NS as robust and versatile fluorophore platform for NIR imaging.

Conflicts of Interest

The are no conflicts to declare.

Author Contributions

NH, GS and SK conceived and designed the study. SK coordinated the study. GS exfoliated EB into EB-NS. NH synthesized and characterized Pyr-Sil with support from GS. Corresponding NMR and MS data was analyzed by NH. NH and GS performed the grafting of Pyr-Sil onto EB-NS and acquired the 1D and 2D Vis-NIR spectroscopic dataset of pyrene-functionalized EBfunc. MD performed CLSM on pyrene-functionalized EBfunc samples prepared by GS and MW. Colocalization analysis of the CLSM dataset was performed by GS. ssNMR measurements were performed and analyzed by RD and LA with support from NH. GS synthesized COOH-preSil and COOH-Sil with support from DS, NH and MW. Corresponding NMR and MS data was analyzed by NH. The grafting of COOH-Sil onto EB-NS to yield COOH-functionalized EBfunc was performed by GS with support from DS and NH. BH acquired zeta potential measurements on COOH-functionalized EBfunc. BH and SJ carried out FA conjugation and cell experiments with support from GS. GS, NH and SK wrote the manuscript, with contributions from all authors.

Acknowledgments

This work was funded by the Deutsche Forschungsgemeinschaft (DFG, German Research Foundation) under Germany's Excellence Strategy—EXC 2033–390677874—RESOLV. This work was further supported by the “Center for Solvation Science ZEMOS” funded by the German Federal Ministry of Education and Research BMBF and by the Ministry of Culture and Research of Nord Rhine-Westphalia. We would also like to acknowledge support from the VW Foundation. We are grateful to Dr. Volker Karius and Cornelia Friedrich for granting access to their labs and for expert technical assistance. We also thank Prof. Steinem and Prof. Janshoff for support. We are also thankful to Jutta Gerber-Nolte, Angela Rübeling and all other members of the research groups of Prof. Steinem and Prof. Janshoff for the constant support. We are grateful to Laura Haberstock, Tobias Ernemann, Daniel Lüert, Tobias Heitkemper and Xiaobai Wang for providing equipment and technical assistance for synthetic chemistry. We are grateful to Niyaz Alizadeh, Dr. Antonio Del Vecchio, Dr. Fabio Pesciaioli and Dr. Leonardo Massignan for the fruitful discussions and their expert technical assistance. We also thank Dr. Lena Schnitzler, Dr. Linda Sistemich, Justus Metternich and Alexander Schrage for the fruitful discussions and technical support.

References

1 A. K. Geim and K. S. Novoselov, The rise of graphene, *Nat. Mater.*, 2007, **6**, 183–191, 10.1038/nmat1849.

2 A. K. Geim, Graphene: Status and Prospects, *Science*, 2009, **324**, 1530–1534, 10.1126/science.1158877.

3 K. S. Novoselov, A. K. Geim, S. V Morozov, D. Jiang, Y. Zhang, S. V Dubonos, I. V Grigorieva and A. A. Firsov, Electric Field Effect in Atomically Thin Carbon Films, *Science*, 2004, **306**, 666–669, 10.1126/science.1102896.

4 V. Nicolosi, M. Chhowalla, M. G. Kanatzidis, M. S. Strano and J. N. Coleman, Liquid exfoliation of layered materials, *Science*, 2013, **340**, 72–75, 10.1126/science.1226419.

5 K. S. Novoselov, D. Jiang, F. Schedin, T. J. Booth, V. V. Khotkevich, S. V. Morozov and A. K. Geim, Two-dimensional atomic crystals, *Proc. Natl. Acad. Sci. U. S. A.*, 2005, **102**, 10451–10453, 10.1073/pnas.0502848102.

6 Q. H. Wang, K. Kalantar-Zadeh, A. Kis, J. N. Coleman and M. S. Strano, Electronics and optoelectronics of two-dimensional transition metal dichalcogenides, *Nat. Nanotechnol.*, 2012, **7**, 699–712, 10.1038/nnano.2012.193.

7 H. Tao, Y. Zhang, Y. Gao, Z. Sun, C. Yan and J. Texter, Scalable exfoliation and dispersion of two-dimensional materials-an update, *Phys. Chem. Chem. Phys.*, 2017, **19**, 921–960, 10.1039/c6cp06813h.

8 A. Kumar and C. Huei, Synthesis and Biomedical Applications of Graphene: Present and Future Trends, in *Advances in Graphene Science*, InTech, 2013, 10.5772/55728.

9 G. R. Bhimanapati, Z. Lin, V. Meunier, Y. Jung, J. Cha, S. Das, D. Xiao, Y. Son, M. S. Strano, V. R. Cooper, L. Liang, S. G. Louie, E. Ringe, W. Zhou, S. S. Kim, R. R. Naik, B. G. Sumpter, H. Terrones, F. Xia, Y. Wang, J. Zhu, D. Akinwande, N. Alem, J. A. Schuller, R. E. Schaak, M. Terrones and J. A. Robinson, Recent Advances in Two-Dimensional Materials beyond Graphene, *ACS Nano*, 2015, **9**, 11509–11539, 10.1021/acsnano.5b05556.

10 W. J. Parak, D. Gerion, D. Zanchet, A. S. Woerz, T. Pellegrino, C. Micheel, S. C. Williams, M. Seitz, R. E. Bruehl, Z. Bryant, C. Bustamante, C. R. Bertozzi and A. P. Alivisatos, Conjugation of DNA to silanized colloidal semiconductor nanocrystalline quantum dots, *Chem. Mater.*, 2002, **14**, 2113–2119, 10.1021/cm0107878.

11 B. Pelaz, C. Alexiou, R. A. Alvarez-Puebla, F. Alves, A. M. Andrews, S. Ashraf, L. P. Balogh, L. Ballerini, A. Bestetti, C. Brendel, S. Bosi, M. Carril, W. C. W. Chan, C. Chen, X. X. Chen, X. X. Chen, Z. Cheng, D. Cui, J. Du, C. Dullin, A. Escudero, N. Feliu, M. Gao, M. George, Y. Gogotsi, A. Grünweller, Z. Gu, N. J. Halas, N. Hampp, R. K. Hartmann, M. C. Hersam, P. Hunziker, J. Jian, X. Jiang, P. Jungebluth, P. Kadhiresan, K. Kataoka, A. Khademhosseini, J. Kopeček, N. A. Kotov, H. F. Krug, D. S. Lee, C. M. Lehr, K. W. Leong, X. J. Liang, M. L. Lim, L. M. Liz-Marzán, X. Ma, P. Macchiarini, H. Meng, H. Möhwald, P. Mulvaney, A. E. Nel, S. Nie, P. Nordlander, T. Okano, J. Oliveira, T. H. Park, R. M. Penner, M. Prato, V. Puntes, V. M. Rotello, A. Samarakoon, R. E. Schaak, Y. Shen, S. Sjöqvist, A. G. Skirtach, M. G. Soliman, M. M. Stevens, H. W. Sung, B. Z. Tang, R. Tietze, B. N. Udugama, J. Scott VanEpps, T. Weil, P. S. Weiss, I. Willner, Y. Wu, L. Yang, Z. Yue, Q. Zhang, Q. Zhang, X. E. Zhang, Y. Zhao, X. Zhou and W. J. Parak, Diverse Applications of Nanomedicine, *ACS Nano*, 2017, **11**, 2313–2381, 10.1021/acsnano.6b06040.

12 M. V. Kovalenko, L. Manna, A. Cabot, Z. Hens, D. V. Talapin, C. R. Kagan, V. I. Klimov, A. L. Rogach, P. Reiss, D. J. Milliron, P. Guyot-Sionnnest, G. Konstantatos, W. J. Parak, T. Hyeon, B. A. Korgel, C. B. Murray and W. Heiss, Prospects of nanoscience with nanocrystals, *ACS Nano*, 2015, **9**, 1012–1057, 10.1021/nn506223h.

13 A. C. Ferrari, F. Bonaccorso, V. Fal'ko, K. S. Novoselov, S. Roche, P. Bøggild, S. Borini, F. H. L. Koppens, V. Palermo, N. Pugno, J. A. Garrido, R. Sordan, A. Bianco, L. Ballerini, M. Prato, E. Lidorikis, J. Kivioja, C. Marinelli, T. Ryhänen, A. Morpurgo, J. N. Coleman, V. Nicolosi, L. Colombo, A. Fert, M. Garcia-Hernandez, A. Bachtold, G. F. Schneider, F. Guinea, C. Dekker, M. Barbone, Z. Sun, C. Galiotis, A. N. Grigorenko, G. Konstantatos, A. Kis, M. Katsnelson, L. Vandersypen, A. Loiseau, V. Morandi, D. Neumaier, E. Treossi, V. Pellegrini, M. Polini, A. Tredicucci, G. M. Williams, B. Hee Hong, J. H. Ahn, J. Min Kim, H. Zirath, B. J. Van Wees, H. Van Der Zant, L. Occhipinti, A. Di Matteo, I. A. Kinloch, T. Seyller, E. Quesnel, X. Feng, K. Teo, N. Rupesinghe, P. Hakonen, S. R. T. Neil, Q. Tannock, T. Löfwander and J. Kinaret, Science and technology roadmap for graphene, related two-dimensional crystals, and hybrid systems, *Nanoscale*, 2015, **7**, 4598–4810, 10.1039/c4nr01600a.

14 C. Martín, K. Kostarelos, M. Prato and A. Bianco, Biocompatibility and biodegradability of 2D materials: Graphene and beyond, *Chem. Commun.*, 2019, **55**, 5540–5546, 10.1039/c9cc01205b.

15 G. Reina, J. M. González-Domínguez, A. Criado, E. Vázquez, A. Bianco and M. Prato, Promises, facts and challenges for graphene in biomedical applications, *Chem. Soc. Rev.*, 2017, **46**, 4400–4416, 10.1039/c7cs00363c.

16 D. Chimene, D. L. Alge and A. K. Gaharwar, Two-Dimensional Nanomaterials for Biomedical Applications: Emerging Trends and Future Prospects, *Adv. Mater.*, 2015, **27**, 7261–7284, 10.1002/adma.201502422.

17 T. Hu, X. Mei, Y. Wang, X. Weng, R. Liang and M. Wei, Two-dimensional nanomaterials: fascinating materials in biomedical field, *Sci. Bull.*, 2019, **64**, 1707–1727,

10.1016/j.scib.2019.09.021.

18 M. Derakhshi, S. Daemi, P. Shahini, A. Habibzadeh, E. Mostafavi and A. A. Ashkarran, Two-Dimensional Nanomaterials beyond Graphene for Biomedical Applications, *J. Funct. Biomater.*, 2022, **13**, 27, 10.3390/jfb13010027.

19 V. Biju, Chemical modifications and bioconjugate reactions of nanomaterials for sensing, imaging, drug delivery and therapy, *Chem. Soc. Rev.*, 2014, **43**, 744–764, 10.1039/c3cs60273g.

20 A. Sgamellotti and C. Anselmi, An evergreen blue. Spectroscopic properties of Egyptian blue from pyramids to Raphael, and beyond, *Inorganica Chim. Acta*, 2022, **530**, 120699, 10.1016/j.ica.2021.120699.

21 G. Selvaggio and S. Kruss, Preparation, properties and applications of near-infrared fluorescent silicate nanosheets, *Nanoscale*, , DOI:10.1039/D2NR02967G, 10.1039/D2NR02967G.

22 T. E. Warner, *Synthesis, Properties and Mineralogy of Important Inorganic Materials*, *Synthesis, Properties and Mineralogy of Important Inorganic Materials*, Wiley, Chichester, UK, 2011, 10.1002/9780470976012.

23 A. Pabst, Structures of some tetragonal sheet silicates, *Acta Crystallogr.*, 1959, **12**, 733–739, 10.1107/s0365110x5900216x.

24 B. C. Chakoumakos, J. A. Fernandez-Baca and L. A. Boatner, Refinement of the Structures of the Layer Silicates MCuSi4O10 (M = Ca, Sr, Ba) by Rietveld Analysis of Neutron Powder Diffraction Data, *J. Solid State Chem.*, 1993, **103**, 105–113.

25 D. Johnson-Mcdaniel, C. A. Barrett, A. Sharafi and T. T. Salguero, Nanoscience of an Ancient Pigment, *J. Am. Chem. Soc.*, 2013, **135**, 1677–1679, 10.1021/ja310587c.

26 D. Johnson-McDaniel and T. T. Salguero, Exfoliation of Egyptian Blue and Han Blue, Two Alkali Earth Copper Silicate-based Pigments, *J. Vis. Exp.*, 2014, 1–10.

27 T. T. Salguero, D. Johnson-McDaniel, C. A. Barrett, A. Sharafi, R. Weimar and T. Blevins, Nanoscience of Metal Silicate-Based Pigments, *MRS Proc.*, 2014, **1618**, 161–166, 10.1557/opl.2014.465.

28 G. Pozza, D. Ajò, G. Chiari, F. De Zuane and M. Favaro, Photoluminescence of the inorganic pigments Egyptian blue, Han blue and Han purple, *J. Cult. Herit.*, 2000, **1**, 393–398, 10.1016/S1296-2074(00)01095-5.

29 D. Ajò, G. Chiari, F. De Zuane, M. Favaro and M. Bertolin, Photoluminescence of some blue natural pigments and related synthetic materials, *5th Int. Conf. non-destructive testing, Microanal. methods Environ. Eval. study Conserv. Work. art*, 1996, 37–47.

30 G. Accorsi, G. Verri, M. Bolognesi, N. Armaroli, C. Clementi, C. Miliani and A. Romani, The exceptional near-infrared luminescence properties of cuprorivaite (Egyptian blue), *Chem. Commun.*, 2009, 3392–3394.

31 G. Selvaggio, A. Chizhik, R. Nißler, L. Kuhlemann, D. Meyer, L. Vuong, H. Preiß, N. Herrmann, F. A. Mann, Z. Lv, T. A. Oswald, A. Spreinat, L. Erpenbeck, J. Großhans, V. Karius, A. Janshoff, J. Pablo Giraldo and S. Kruss, Exfoliated near infrared fluorescent silicate nanosheets for (bio)photonics, *Nat. Commun.*, 2020, **11**, 1495, 10.1038/s41467-020-15299-5.

32 G. Selvaggio, M. Weitzel, N. Oleksiievets, T. A. Oswald, R. Nißler, I. Mey, V. Karius, J. Enderlein, R. Tsukanov and S. Kruss, Photophysical properties and fluorescence lifetime imaging of exfoliated near-infrared fluorescent silicate nanosheets, *Nanoscale Adv.*, 2021, **3**, 4541–4553, 10.1039/d1na00238d.

33 R. Nißler, O. Bader, M. Dohmen, S. G. Walter, C. Noll, G. Selvaggio, U. Groß and S. Kruss, Remote near infrared identification of pathogens with multiplexed nanosensors, *Nat. Commun.*, 2020, **11**, 5995, 10.1038/s41467-020-19718-5.

34 C. He, C. Dong, L. Yu, Y. Chen and Y. Hao, Ultrathin 2D Inorganic Ancient Pigment Decorated 3D-Printing Scaffold Enables Photonic Hyperthermia of Osteosarcoma in NIR-II Biowindow and Concurrently Augments Bone Regeneration, *Adv. Sci.*, 2021, **8**, 1–10, 10.1002/advs.202101739.

35 Q. Yu, Y. Han, T. Tian, Q. Zhou, Z. Yi, J. Chang and C. Wu, Chinese sesame stick-inspired nano-fibrous scaffolds for tumor therapy and skin tissue reconstruction, *Biomaterials*, 2019, **194**, 25–35, 10.1016/j.biomaterials.2018.12.012.

36 C. Yang, R. Zheng, M. R. Younis, J. Shao, L.-H. Fu, D.-Y. Zhang, J. Lin, Z. Li and P. Huang, NIR-II light-responsive biodegradable shape memory composites based on cuprorivaite nanosheets for enhanced tissue reconstruction, *Chem. Eng. J.*, 2021, **419**, 129437, 10.1016/j.cej.2021.129437.

37 C. Dong, C. Yang, M. R. Younis, J. Zhang, G. He, X. Qiu, L. Fu, D. Zhang, H. Wang, W. Hong, J. Lin, X. Wu and P. Huang, Bioactive NIR-II Light-Responsive Shape Memory Composite Based on Cuprorivaite Nanosheets for Endometrial Regeneration, *Adv. Sci.*, 2022, **2102220**, 2102220, 10.1002/advs.202102220.

38 A. M. Smith, M. C. Mancini and S. Nie, Second window for in vivo imaging, *Nat. Nanotechnol.*, 2009, **4**, 710–711, 10.1038/nnano.2009.326.

39 E. A. Owens, M. Henary, G. El Fakhri and H. S. Choi, Tissue-Specific Near-Infrared Fluorescence Imaging, *Acc. Chem. Res.*, 2016, **49**, 1731–1740, 10.1021/acs.accounts.6b00239.

40 G. Hong, A. L. Antaris and H. Dai, Near-infrared fluorophores for biomedical imaging, *Nat. Biomed. Eng.*, 2017, **1**, 1–9, 10.1038/s41551-016-0010.

41 A. Spreinat, G. Selvaggio, L. Erpenbeck and S. Kruss, Multispectral near infrared absorption imaging for histology of skin cancer, *J. Biophotonics*, 2020, **13**, e201960080, 10.1002/JBIO.201960080.

42 J. A. Carr, D. Franke, J. R. Caram, C. F. Perkinson, M. Saif, V. Askoxylakis, M. Datta, D. Fukumura, R. K. Jain, M. G. Bawendi and O. T. Bruns, Shortwave infrared fluorescence imaging with the clinically approved near-infrared dye indocyanine green., *Proc. Natl. Acad. Sci. U. S. A.*, 2018, **115**, 4465–4470, 10.1073/pnas.1718917115.

43 A. Loudet and K. Burgess, BODIPY dyes and their derivatives: Syntheses and spectroscopic properties, *Chem. Rev.*, 2007, **107**, 4891–4932, 10.1021/cr078381n.

44 G. Ulrich, R. Ziessel and A. Harriman, The chemistry of fluorescent bodipy dyes: Versatility unsurpassed, *Angew. Chemie - Int. Ed.*, 2008, **47**, 1184–1201, 10.1002/anie.200702070.

45 A. Patra, L. J. Patalag, P. G. Jones and D. B. Werz, Extended Benzene-Fused Oligo-BODIPYs: In Three Steps to a Series of Large, Arc-Shaped, Near-Infrared Dyes, *Angew. Chemie - Int. Ed.*, 2021, **60**, 747–752, 10.1002/anie.202012335.

46 G. Selvaggio, R. Nißler, P. Nietmann, A. Patra, L. J. Patalag, A. Janshoff, D. B. Werz and S. Kruss, NIR-emitting benzene-fused oligo-BODIPYs for bioimaging, *Analyst*, 2022, **147**, 230–237, 10.1039/D1AN01850G.

47 O. T. Bruns, T. S. Bischof, D. K. Harris, D. Franke, Y. Shi, L. Riedemann, A. Bartelt, F. B. Jaworski, J. A. Carr, C. J. Rowlands, M. W. B. B. Wilson, O. Chen, H. Wei, G. W. Hwang, D. M. Montana, I. Coropceanu, O. B. Achorn, J. Kloepper, J. Heeren, P. T. C. C. So, D. Fukumura, K. F. Jensen, R. K. Jain and M. G. Bawendi, Next-generation in vivo optical imaging with short-wave infrared quantum dots, *Nat. Biomed. Eng.*, 2017, **1**, 0056, 10.1038/s41551-017-0056.

48 F. Romano, S. Angeloni, G. Morselli, R. Mazzaro, V. Morandi, J. R. Shell, X. Cao, B. W. Pogue and P. Ceroni, Water-soluble silicon nanocrystals as NIR luminescent probes for time-gated biomedical imaging, *Nanoscale*, 2020, **12**, 7921–7926, 10.1039/D0NR00814A.

49 J. Ackermann, J. T. Metternich, S. Herbertz and S. Kruss, Biosensing with Fluorescent Carbon Nanotubes, *Angew. Chemie - Int. Ed.*, 2022, **61**, e202112372, 10.1002/anie.202112372.

50 S. Kruss, A. J. Hilmer, J. Zhang, N. F. Reuel, B. Mu and M. S. Strano, Carbon nanotubes as optical biomedical sensors, *Adv. Drug Deliv. Rev.*, 2013, **65**, 1933–1950, 10.1016/j.addr.2013.07.015.

51 G. Bisker, J. Dong, H. D. Park, N. M. Iverson, J. Ahn, J. T. Nelson, M. P. Landry, S. Kruss and M. S. Strano, Protein-targeted corona phase molecular recognition, *Nat. Commun.*, 2016, **7**, 1–14, 10.1038/ncomms10241.

52 J. P. Giraldo, H. Wu, G. M. Newkirk and S. Kruss, Nanobiotechnology approaches for engineering smart plant sensors, *Nat. Nanotechnol.*, 2019, **14**, 541–553, 10.1038/s41565-019-0470-6.

53 M. Kim, C. Chen, P. Wang, J. J. Mulvey, Y. Yang, C. Wun, M. Antman-Passig, H.-B. Luo, S. Cho, K. Long-Roche, L. V. Ramanathan, A. Jagota, M. Zheng, Y. Wang and D. A. Heller, Detection of ovarian cancer via the spectral fingerprinting of quantum-defect-modified carbon nanotubes in serum by machine learning, *Nat. Biomed. Eng.*, 2022, **6**, 267–275, 10.1038/s41551-022-00860-y.

54 A. Antonucci, J. Kupis-Rozmysłowicz and A. A. Boghossian, Noncovalent Protein and Peptide Functionalization of Single-Walled Carbon Nanotubes for Biodelivery and Optical Sensing Applications, *ACS Appl. Mater. Interfaces*, 2017, **9**, 11321–11331, 10.1021/acsami.7b00810.

55 N. E. Kallmyer, M. S. Abdennadher, S. Agarwal, R. Baldwin-Kordick, R. L. Khor, A. S. Kooistra, E. Peterson, M. D. McDaniel and N. F. Reuel, Inexpensive Near-Infrared Fluorimeters: Enabling Translation of nIR-Based Assays to the Field, *Anal. Chem.*, 2021, **93**, 4800–4808, 10.1021/acs.analchem.0c03732.

56 G. Hong, S. Diao, A. L. Antaris and H. Dai, Carbon Nanomaterials for Biological Imaging and Nanomedicinal Therapy, *Chem. Rev.*, 2015, **115**, 10816–10906, 10.1021/acs.chemrev.5b00008.

57 S. He, J. Song, J. Qu and Z. Cheng, Crucial breakthrough of second near-infrared biological window fluorophores: design and synthesis toward multimodal imaging and theranostics, *Chem. Soc. Rev.*, 2018, **47**, 4258–4278, 10.1039/C8CS00234G.

58 Z. Lei and F. Zhang, Molecular Engineering of NIR-II Fluorophores for Improved Biomedical Detection, *Angew. Chemie - Int. Ed.*, 2021, **60**, 16294–16308, 10.1002/anie.202007040.

59 Y. Fan, P. Wang, Y. Lu, R. Wang, L. Zhou, X. Zheng, X. Li, J. A. Piper and F. Zhang, Lifetime-engineered NIR-II nanoparticles unlock multiplexed in vivo imaging, *Nat. Nanotechnol.*, 2018, **13**, 941–946, 10.1038/s41565-018-0221-0.

60 S. Shahbazi, J. V. Goodpaster, G. D. Smith, T. Becker and S. W. Lewis, Preparation, characterization, and application of a lipophilic coated exfoliated Egyptian blue for near-infrared luminescent latent fingermark detection, *Forensic Chem.*, 2020, **18**, 100208, 10.1016/j.forc.2019.100208.

61 S. M. Borisov, C. Würth, U. Resch-Genger and I. Klimant, New Life of Ancient Pigments: Application in High-Performance Optical Sensing Materials, *Anal. Chem.*, 2013, **85**, 9371–9377, 10.1021/ac402275g.

62 M. Maierhofer, V. Rieger and T. Mayr, Optical ammonia sensors based on fluorescent aza-BODIPY dyes— a flexible toolbox, *Anal. Bioanal. Chem.*, 2020, **412**, 7559–7567, 10.1007/s00216-020-02891-3.

63 L. Ma, X. Song, Y. Yu and Y. Chen, Two-Dimensional Silicene/Silicon Nanosheets: An Emerging Silicon-Composed Nanostructure in Biomedicine, *Adv. Mater.*, 2021, **33**, 2008226, 10.1002/adma.202008226.

64 K. Wang, X. He, X. Yang and H. Shi, Functionalized silica nanoparticles: A platform for fluorescence imaging at the cell and small animal levels, *Acc. Chem. Res.*, 2013, **46**, 1367–1376, 10.1021/ar3001525.

65 D. Tarn, C. E. Ashley, M. Xue, E. C. Carnes, J. I. Zink and C. J. Brinker, Mesoporous Silica Nanoparticle Nanocarriers: Biofunctionality and Biocompatibility, *Acc. Chem. Res.*, 2013, **46**, 792–801, 10.1021/ar3000986.

66 K. K. Cotí, M. E. Belowich, M. Liong, M. W. Ambrogio, Y. A. Lau, H. A. Khatib, J. I. Zink, N. M. Khashab, J. F. Stoddart, J. Fraser, M. E. Belowich, M. Liong, M. W. Ambrogio, Y. A. Lau, K. K. Cotı, H. A. Khatib, J. I. Zink, M. Khashab and J. F. Stoddart, Mechanised nanoparticles for drug delivery, *Nanoscale*, 2009, **1**, 16–39, 10.1039/b9nr00162j.

67 T. Shimada, K. Aoki, Y. Shinoda, T. Nakamura, N. Tokunaga, S. Inagaki and T. Hayashi, Functionalization on silica gel with allylsilanes. A new method of covalent attachment of organic functional groups on silica gel, *J. Am. Chem. Soc.*, 2003, **125**, 4688–4689, 10.1021/ja034691l.

68 T. Asefa and Z. Tao, Biocompatibility of Mesoporous Silica Nanoparticles, *Chem. Res. Toxicol.*, 2012, **25**, 2265–2284, 10.1021/tx300166u.

69 M. C. Gomes, Â. Cunha, T. Trindade and J. P. C. Tomé, The role of surface functionalization of silica nanoparticles for bioimaging, *J. Innov. Opt. Health Sci.*, 2016, **9**, 1–16, 10.1142/S1793545816300056.

70 N. Takahashi, H. Hata and K. Kuroda, Exfoliation of layered silicates through immobilization of imidazolium groups, *Chem. Mater.*, 2011, **23**, 266–273, 10.1021/cm102942s.

71 N. Moitra, S. Ichii, T. Kamei, K. Kanamori, Y. Zhu, K. Takeda, K. Nakanishi and T. Shimada, Surface functionalization of silica by Si-H activation of hydrosilanes, *J. Am. Chem. Soc.*, 2014, **136**, 11570–11573, 10.1021/ja504115d.

72 M. J. Sweetman, S. J. P. McInnes, R. B. Vasani, T. Guinan, A. Blencowe and N. H. Voelcker, Rapid, metal-free hydrosilanisation chemistry for porous silicon surface modification, *Chem. Commun.*, 2015, **51**, 10640–10643, 10.1039/c5cc02689j.

73 M. Nicola, L. M. Seymour, M. Aceto, E. Priola, R. Gobetto and A. Masic, Late production of Egyptian blue: synthesis from brass and its characteristics, *Archaeol. Anthropol. Sci.*, 2019, **11**, 5377–5392, 10.1007/s12520-019-00873-w.

74 G. Bains, A. B. Patel and V. Narayanaswami, Pyrene: A probe to study protein conformation and conformational changes, *Molecules*, 2011, **16**, 7909–7935, 10.3390/molecules16097909.

75 K. Ayyavoo and P. Velusamy, Pyrene based materials as fluorescent probes in chemical and biological fields, *New J. Chem.*, 2021, **45**, 10997–11017, 10.1039/d1nj00158b.

76 H. Maeda, H. Ishida, Y. Inoue, A. Merpuge, T. Maeda and K.

Mizuno, UV absorption and fluorescence properties of fused aromatic hydrocarbons having trimethylsilyl, trimethylgermyl, and trimethylstannyl groups, *Res. Chem. Intermed.*, 2009, **35**, 939–948, 10.1007/s11164-009-0076-y.

77 Y. Niko, S. Kawauchi, S. Otsu, K. Tokumaru and G. I. Konishi, Fluorescence enhancement of pyrene chromophores induced by alkyl groups through σ-π Conjugation: Systematic synthesis of primary, secondary, and tertiary alkylated pyrenes at the 1, 3, 6, and 8 positions and their photophysical properties, *J. Org. Chem.*, 2013, **78**, 3196–3207, 10.1021/jo400128c.

78 J. Ferguson, Absorption and fluorescence spectra of crystalline pyrene, *J. Chem. Phys.*, 1958, **28**, 765–768, 10.1063/1.1744267.

79 K. C. Park, C. Seo, G. Gupta, J. Kim and C. Y. Lee, Efficient Energy Transfer (EnT) in Pyrene- and Porphyrin-Based Mixed-Ligand Metal-Organic Frameworks, *ACS Appl. Mater. Interfaces*, 2017, **9**, 38670–38677, 10.1021/acsami.7b14135.

80 N. Y. C. Chu, K. Kawaoka and D. R. Kearns, Investigation of energy-transfer mechanisms in pyrene crystals, *J. Chem. Phys.*, 1971, **55**, 3059–3067, 10.1063/1.1676546.

81 G. F. Luo, W. H. Chen, Y. Liu, J. Zhang, S. X. Cheng, R. X. Zhuo and X. Z. Zhang, Charge-reversal plug gate nanovalves on peptide-functionalized mesoporous silica nanoparticles for targeted drug delivery, *J. Mater. Chem. B*, 2013, **1**, 5723–5732, 10.1039/c3tb20792g.

82 R. J. Hunter, *Zeta Potential in Colloid Science*, *Zeta Potential in Colloid Science*, Elsevier, 1981, 10.1016/C2013-0-07389-6.

83 B. Derjaguin and L. Landau, The theory of stability of highly charged lyophobic sols and coalescence of highly charged particles in electrolyte solutions, *Acta Physicochim. URSS*, 1941, **14**, 633–52.

84 E. J. W. Verwey, Theory of the stability of lyophobic colloids, *J. Phys. Chem.*, 1947, **51**, 631–636.

85 S. Sandoval, N. Mendez, J. G. Alfaro, J. Yang, S. Aschemeyer, A. Liberman, W. C. Trogler and A. C. Kummel, Quantification of endocytosis using a folate functionalized silica hollow nanoshell platform, *J. Biomed. Opt.*, 2015, **20**, 088003, 10.1117/1.jbo.20.8.088003.

86 M. Fernández, F. Javaid and V. Chudasama, Advances in targeting the folate receptor in the treatment/imaging of cancers, *Chem. Sci.*, 2018, **9**, 790–810, 10.1039/c7sc04004k.

87 A. Friedman, S. Claypool and R. Liu, The Smart Targeting of Nanoparticles, *Curr. Pharm. Des.*, 2013, **19**, 6315–6329, 10.2174/13816128113199990375.

88 A. F. Trindade, R. F. M. Frade, E. M. S. Maçôas, C. Graça, C. A. B. Rodrigues, J. M. G. Martinho and C. A. M. Afonso, “Click and go”: simple and fast folic acid conjugation, *Org. Biomol. Chem.*, 2014, **12**, 3181–3190, 10.1039/C4OB00150H.

89 S. Mohapatra, S. K. Mallick, T. K. Maiti, S. K. Ghosh and P. Pramanik, Synthesis of highly stable folic acid conjugated magnetite nanoparticles for targeting cancer cells, *Nanotechnology*, , DOI:10.1088/0957-4484/18/38/385102, 10.1088/0957-4484/18/38/385102.

90 M. Xie, H. Shi, Z. Li, H. Shen, K. Ma, B. Li, S. Shen and Y. Jin, A multifunctional mesoporous silica nanocomposite for targeted delivery, controlled release of doxorubicin and bioimaging, *Colloids Surfaces B Biointerfaces*, 2013, **110**, 138–147, 10.1016/j.colsurfb.2013.04.009.

91 Z. Zhang, J. Jia, Y. Lai, Y. Ma, J. Weng and L. Sun, Conjugating folic acid to gold nanoparticles through glutathione for targeting and detecting cancer cells, *Bioorganic Med. Chem.*, 2010, **18**, 5528–5534, 10.1016/j.bmc.2010.06.045.

92 Y. K. Lee, Preparation and characterization of folic acid linked poly(L-glutamate) nanoparticles for cancer targeting, *Macromol. Res.*, 2006, **14**, 387–393, 10.1007/BF03219099.

93 E. Mornet, N. Carmoy, C. Lainé, L. Lemiègre, T. Le Gall, I. Laurent, R. Marianowski, C. Férec, P. Lehn, T. Benvegnu and T. Montier, Folate-equipped nanolipoplexes mediated efficient gene transfer into human epithelial cells, *Int. J. Mol. Sci.*, 2013, **14**, 1477–1501, 10.3390/ijms14011477.

94 F. A. Mann, P. Galonska, N. Herrmann and S. Kruss, Quantum defects as versatile anchors for carbon nanotube functionalization, *Nat. Protoc.*, 2022, **17**, 727–747, 10.1038/s41596-021-00663-6.

95 F. A. Mann, N. Herrmann, F. Opazo and S. Kruss, Quantum Defects as a Toolbox for the Covalent Functionalization of Carbon Nanotubes with Peptides and Proteins, *Angew. Chemie - Int. Ed.*, 2020, **59**, 17732–17738, 10.1002/anie.202003825.

96 M. Dinarvand, E. Neubert, D. Meyer, G. Selvaggio, F. A. Mann, L. Erpenbeck and S. Kruss, Near-Infrared Imaging of Serotonin Release from Cells with Fluorescent Nanosensors, *Nano Lett.*, 2019, **19**, 6604–6611, 10.1021/acs.nanolett.9b02865.

97 S. Elizarova, A. A. Chouaib, A. Shaib, B. Hill, F. Mann, N. Brose, S. Kruss and J. A. Daniel, A fluorescent nanosensor paint detects dopamine release at axonal varicosities with high spatiotemporal resolution, *Proc. Natl. Acad. Sci.*, 2022, **119**, 1–12, 10.1073/pnas.2202842119/-/DCSupplemental.Published.

98 S. Kruss, M. P. Landry, E. Vander Ende, B. M. A. A. Lima, N. F. Reuel, J. Zhang, J. Nelson, B. Mu, A. Hilmer and M. Strano, Neurotransmitter detection using corona phase molecular recognition on fluorescent single-walled carbon nanotube sensors., *J. Am. Chem. Soc.*, 2014, **136**, 713–724, 10.1021/ja410433b.

99 F. Mann, N. Herrmann, D. Meyer and S. Kruss, Tuning Selectivity of Fluorescent Carbon Nanotube-Based Neurotransmitter Sensors, *Sensors*, 2017, **17**, 1521, 10.3390/s17071521.

100 A. Spreinat, M. M. Dohmen, J. Lüttgens, N. Herrmann, L. F. Klepzig, R. Nißler, S. Weber, F. A. Mann, J. Lauth and S. Kruss, Quantum Defects in Fluorescent Carbon Nanotubes for Sensing and Mechanistic Studies, *J. Phys. Chem. C*, 2021, **125**, 18341–18351, 10.1021/ACS.JPCC.1C05432.

101 E. Polo and S. Kruss, Impact of Redox-Active Molecules on the Fluorescence of Polymer-Wrapped Carbon Nanotubes, *J. Phys. Chem. C*, 2016, **120**, 3061–3070, 10.1021/acs.jpcc.5b12183.

102 H. Jin, D. A. Heller, M. Kalbacova, J.-H. Kim, J. Zhang, A. A. Boghossian, N. Maheshri and M. S. Strano, Detection of single-molecule H2O2 signalling from epidermal growth factor receptor using fluorescent single-walled carbon nanotubes, *Nat. Nanotechnol.*, 2010, **5**, 302–309, 10.1038/nnano.2010.24.

103 N. M. Iverson, P. W. Barone, M. Shandell, L. J. Trudel, S. Sen, F. Sen, V. Ivanov, E. Atolia, E. Farias, T. P. McNicholas, N. Reuel, N. M. A. Parry, G. N. Wogan and M. S. Strano, In vivo biosensing via tissue-localizable near-infrared-fluorescent single-walled carbon nanotubes, *Nat. Nanotechnol.*, 2013, **8**, 873–880, 10.1038/nnano.2013.222.

104 J. H. Kim, C. R. Patra, J. R. Arkalgud, A. A. Boghossian, J. Zhang, J. H. Han, N. F. Reuel, J. H. Ahn, D. Mukhopadhyay and M. S. Strano, Single-molecule detection of H2O2 mediating angiogenic redox signaling on fluorescent single-walled carbon nanotube array, *ACS Nano*, 2011, **5**, 7848–7857, 10.1021/nn201904t.

105 J. Zhang, A. A. Boghossian, P. W. Barone, A. Rwei, J. H. Kim, D. Lin, D. A. Heller, A. J. Hilmer, N. Nair, N. F. Reuel and M. S. Strano, Single molecule detection of nitric oxide enabled by d(AT)15 DNA adsorbed to near infrared fluorescent single-walled carbon nanotubes, *J. Am. Chem. Soc.*, 2011, **133**, 567–581, 10.1021/ja1084942.

106 Z. W. Ulissi, F. Sen, X. Gong, S. Sen, N. Iverson, A. A. Boghossian, L. C. Godoy, G. N. Wogan, D. Mukhopadhyay and M. S. Strano, Spatiotemporal intracellular nitric oxide signaling captured using internalized, near-infrared fluorescent carbon nanotube nanosensors, *Nano Lett.*, 2014, **14**, 4887–4894, 10.1021/nl502338y.

107 J. H. Kim, D. A. Heller, H. Jin, P. W. Barone, C. Song, J. Zhang, L. J. Trudel, G. N. Wogan, S. R. Tannenbaum and M. S. Strano, The rational design of nitric oxide selectivity in single-walled carbon nanotube near-infrared fluorescence sensors for biological detection, *Nat. Chem.*, 2009, **1**, 473–481, 10.1038/nchem.332.

108 R. Nißler, A. T. Müller, F. Dohrman, L. Kurth, H. Li, E. G. Cosio, B. S. Flavel, J. P. Giraldo, A. Mithöfer and S. Kruss, Detection and Imaging of the Plant Pathogen Response by Near-Infrared Fluorescent Polyphenol Sensors, *Angew. Chemie - Int. Ed.*, 2022, **61**, 2022, 10.1002/anie.202108373.

109 Z. Yaari, Y. Yang, E. Apfelbaum, C. Cupo, A. H. Settle, Q. Cullen, W. Cai, K. L. Roche, D. A. Levine, M. Fleisher, L. Ramanathan, M. Zheng, A. Jagota and D. A. Heller, A perception-based nanosensor platform to detect cancer biomarkers, *Sci. Adv.*, 2021, **7**, 1–11, 10.1126/sciadv.abj0852.

110 R. M. Williams, C. Lee, T. V. Galassi, J. D. Harvey, R. Leicher, M. Sirenko, M. A. Dorso, J. Shah, N. Olvera, F. Dao, D. A. Levine and D. A. Heller, Noninvasive ovarian cancer biomarker detection via an optical nanosensor implant, *Sci. Adv.*, 2018, **4**, eaaq1090, 10.1126/sciadv.aaq1090.

Supplementary Information

Covalently Functionalized Egyptian Blue Nanosheets for Near-Infrared Bioimaging

G. Selvaggio[1,2†], N. Herrmann[2†], B. Hill[1], R. Dervisoglu[3], S. Jung[1], M. Weitzel[2], M. Dinarvand[1,2], D. Stalke[4], L. Andreas[3], S. Kruss[1,2,5,6]

[1]Physical Chemistry II, Bochum University, Bochum, 44801, Germany

[2]Institute of Physical Chemistry, University of Göttingen, Göttingen, 37077, Germany

[3]Max-Planck-Institute for Multidisciplinary Sciences, Göttingen, 37077, Germany

[4]Institute of Inorganic Chemistry, University of Göttingen, Göttingen, 37077, Germany

[5]Fraunhofer Institute for Microelectronic Circuits and Systems, Duisburg, 47057, Germany

[6]Center for Nanointegration Duisburg-Essen (CENIDE)

†These authors contributed equally.

*Corresponding author: sebastian.kruss@rub.de

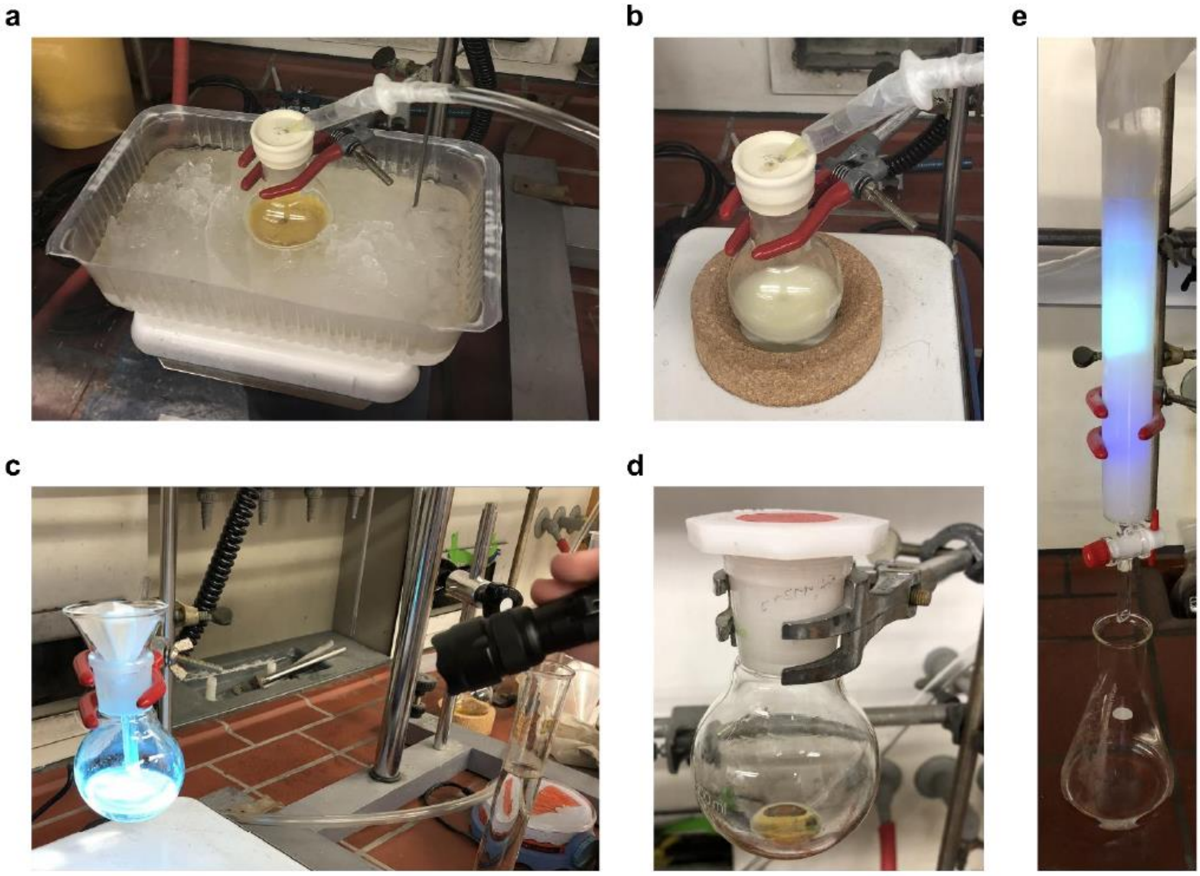

Figure S1: Synthesis of 1-(dimethylsilyl)pyrene (Pyr-Sil). a Ice-cooling of the reaction round-bottom flask (RBF) containing a stirring mixture of 1-bromopyrene, dry diethyl ether (Et_2O), dry tetrahydrofuran (THF) and n-butyllithium (^{n}BuLi, dissolved in hexane). The latter had been added dropwise to the other compounds. **b** Stirring of the mixture in **a** at room temperature for 2 h after the addition of chlorodimethylsilane. **c** Detection of the visible fluorescence of pyrene within the mixture in **a** after quenching, work-up and drying steps. **d** The crude product after removal of the solvent by means of a rotary evaporator. **e** Recognition of the product-containing fraction during silica chromatography thanks to the visible emission of pyrene.

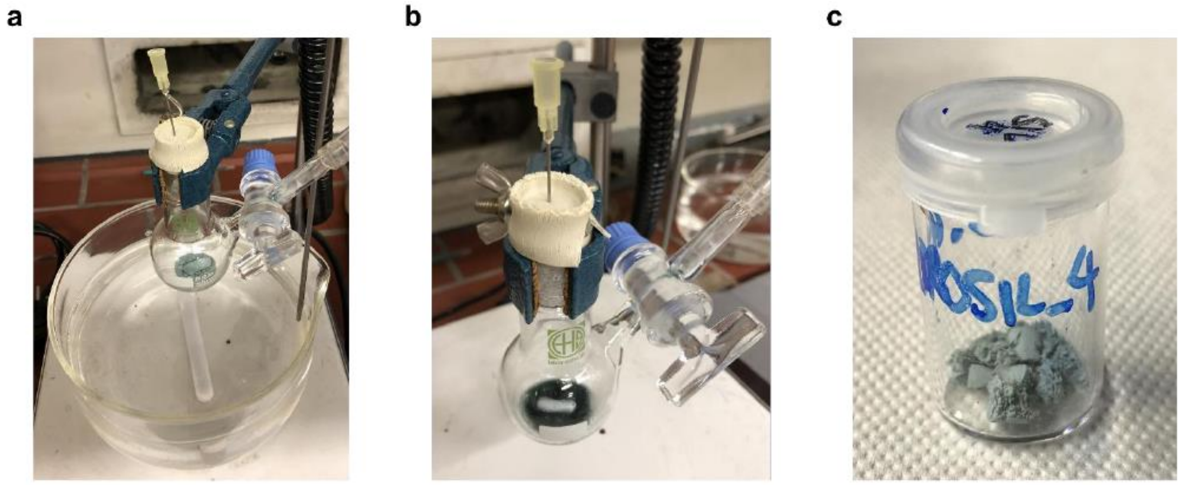

Figure S2: Preparation of pyrene-functionalized EB-NS (EBfunc). a Milled Egyptian Blue nanosheets (EB-NS) under nitrogen flow in the reaction round-bottom flask (RBF). The powder had previously undergone a prolonged drying step under vacuum to remove adsorbed water molecules. **b** Hydrogen evolution after addition of the catalyst tris(pentafluorophenyl)borane (CAT) to a stirring mixture of the EB-NS in **a**, 1-(dimethylsilyl)pyrene (Pyr-Sil) and anhydrous dichloromethane (DCM). **c** The final EBfunc sample after the grafting reaction and the following vacuum-filtration, washing and drying steps.

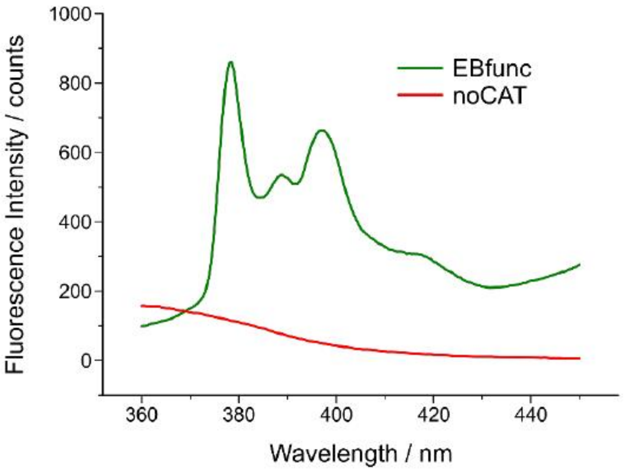

Figure S3: Fluorescence spectra of pyrene-functionalized EB-NS (EBfunc) and its control sample prepared without catalyst (noCAT). After vigorous washing, the typical fluorescence features of pyrene are retained only in the EBfunc sample, whereas they are gone in noCAT. This result indicates the presence of covalent bonds in EBfunc and, thus, proves the successful outcome of the functionalization protocol.

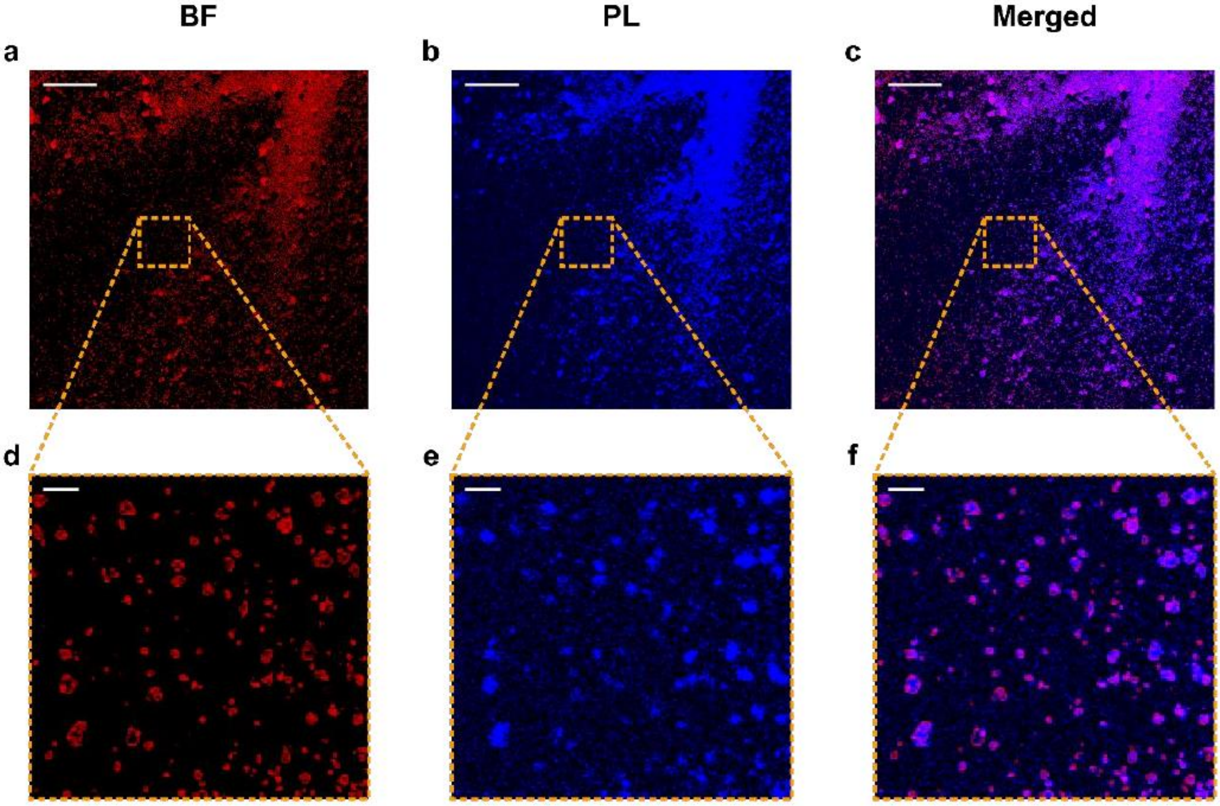

Figure S4: Confocal laser scanning microscopy (CLSM) images of pyrene-functionalized EB-NS (EBfunc). The bright-field (BF), fluorescence (PL) and merged channels of EBfunc imaged at a CLSM are shown. At both larger and smaller scales of view, a high degree of colocalization can be easily observed *for µm-* and nm-sized EB-NS alike. Scale bar = 100 *µm for overview images, scale bar* = 10 *µm for blow-*ups.

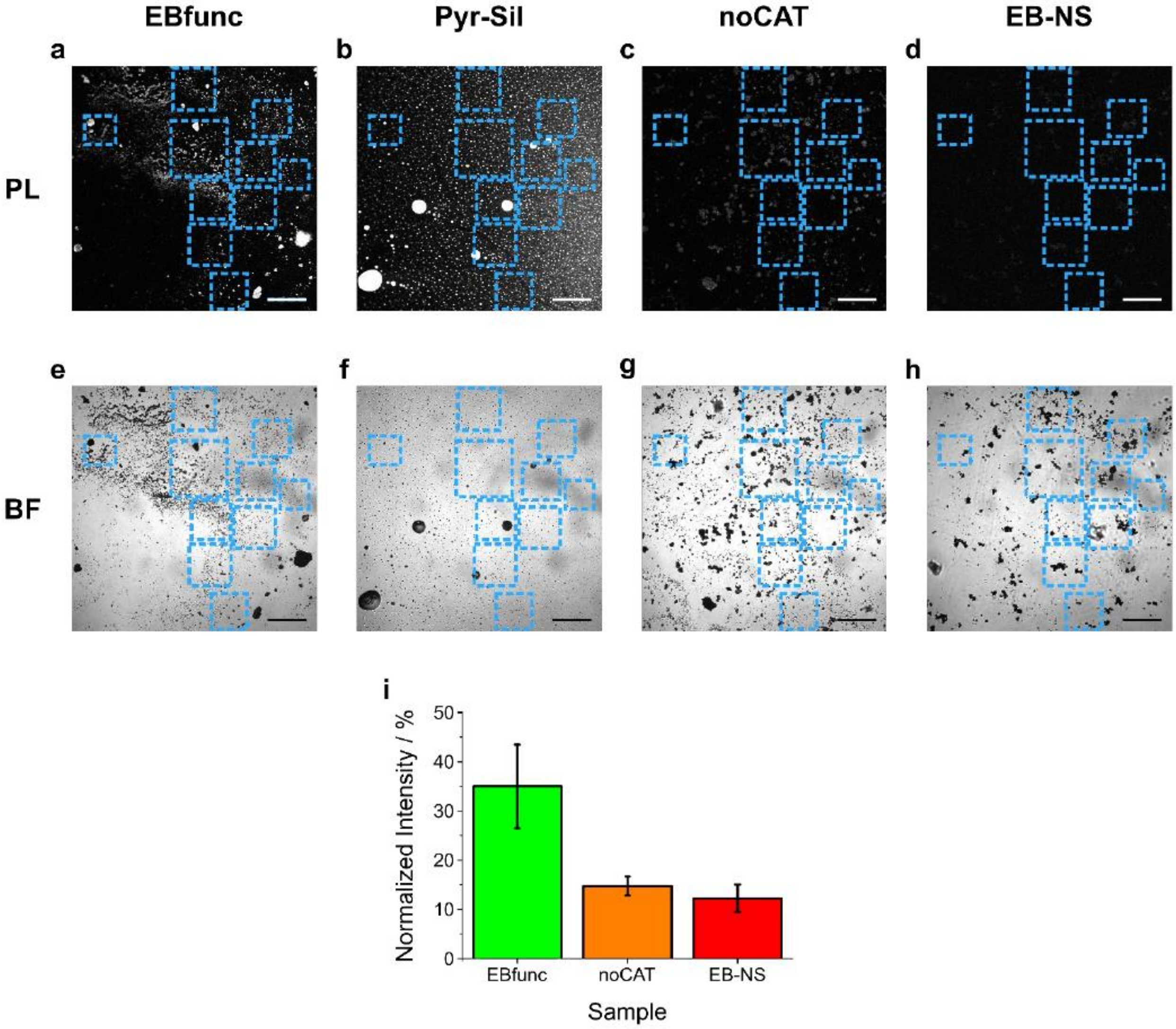

Figure S5: Confocal laser scanning microscopy (CLSM) images of pyrene-functionalized EB-NS (EBfunc) and its controls. CLSM fluorescence (PL, **a-d**) and bright-field (BF, **e-h**) channels of pyrene-functionalized EB-NS (EBfunc), pyrene-silane (Pyr-Sil), no catalyst control (noCAT) and unmodified EB-NS are shown. Yellow rectangles indicate the regions of interests (ROI) chosen for the colocalization analysis. Scale bar = 100 *µm*. **(i)** Mean signal intensity resulting from the colocalization analysis. Data is normalized to the maximum pixel brightness of the thresholded bright-field image of the corresponding ROI. Error bars = standard deviation.

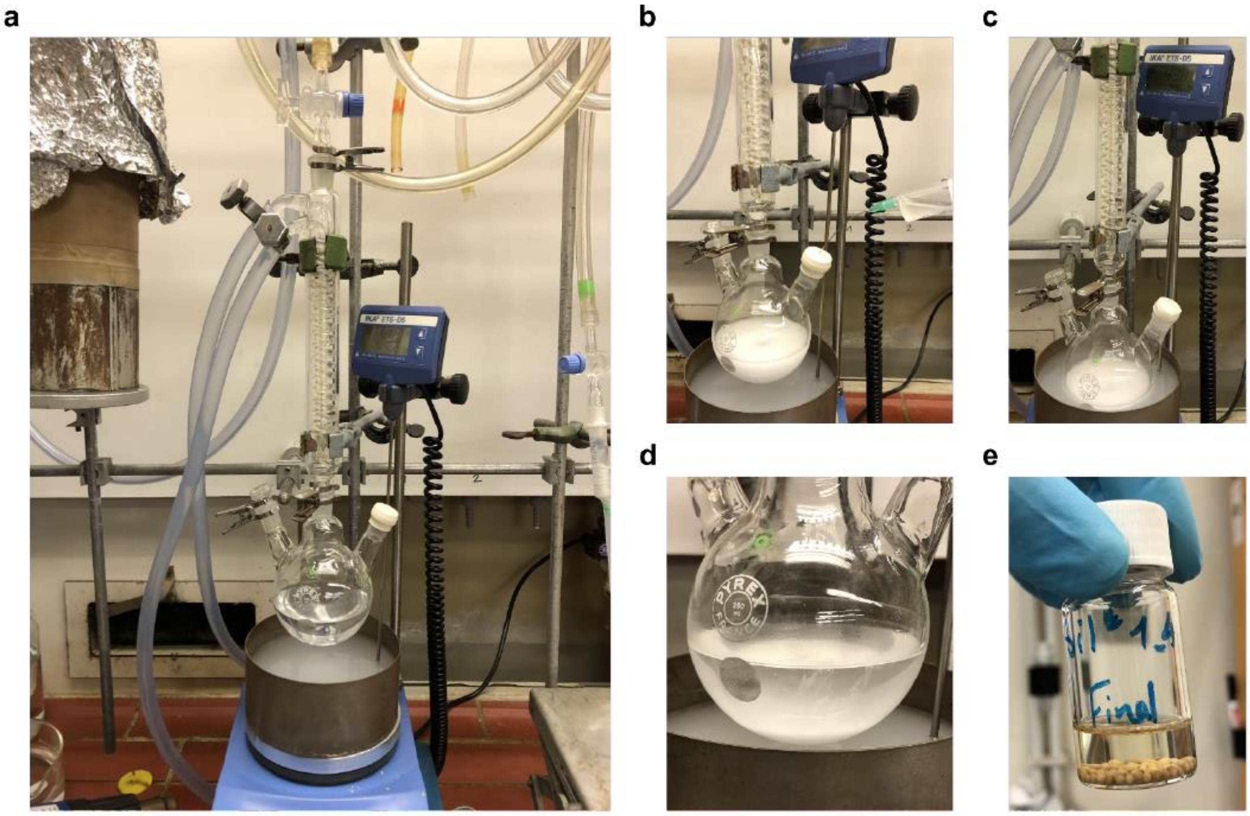

Figure S6: Synthesis of (3-chloropropyl)dimethylsilane (COOH-preSil). a Overview picture showing the employed moisture-free Schlenk setup for the synthesis of COOH-preSil. The round-bottom flask contains 100 mL of a solution of anhydrous diethyl ether (Et_2O) and lithium aluminum hydride ($LiAlH_4$). **b** Room temperature drop-wise addition of chloro(3-chloropropyl)dimethylsilane to the Et_2O-$LiAlH_4$ solution, which leads to a weak reflux and to the formation of a milky dispersion. **c** After silane addition, the system is lowered into a pre-heated bath (T = 48°C) and kept stirring for 30 min. **d** White precipitates are observable when the system is cooled down and the stirring stopped after reaction time. **e** 3A-type molecular sieves are added to the final product for sample storing.

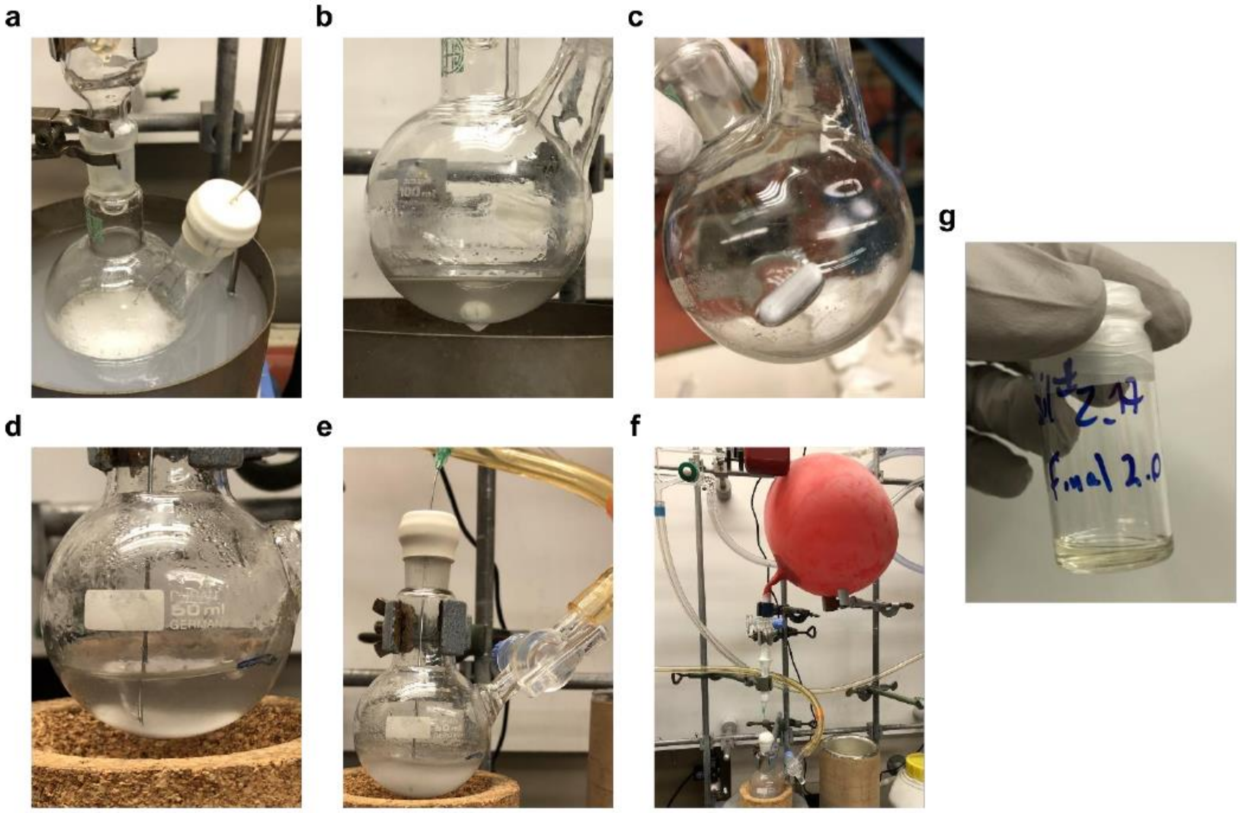

Figure S7: Synthesis of 4-(dimethylsilyl)butyric acid (COOH-Sil). a Formation of white foam symbolizing the correct start of the Grignard reaction. To keep it running, a mixture of (3-chloropropyl)dimethylsilane (COOH-preSil) and 1,2-dibromoethane (DBE) were added to the flask, where an aliquot of the same mixture had been heated up to reaction temperature (T = 70 °C) with an oil bath. **b** Appearance of the reaction volume after 2 h of stirring at 70 °C. **c** Picture of the reaction flask after the removal of the supernatant (3-(dimethylsilyl)propylmagnesium chloride, i.e. the Grignard reagent): the Mg turnings reacted almost completely. **d** Intense bubbling of CO_2 through the Grignard reagent: the needle was connected to a pressurized CO_2 tank. **e** *Formation of a white phase after* ≈ 15 min of vigorous CO_2 bubbling through the Grignard reagent. **f** Connection of a CO_2 balloon to the Grignard flask for the 24 h-stirring step. **g** Picture of the final crude product after work-up, drying steps and removal of the solvent with a rotary evaporator.

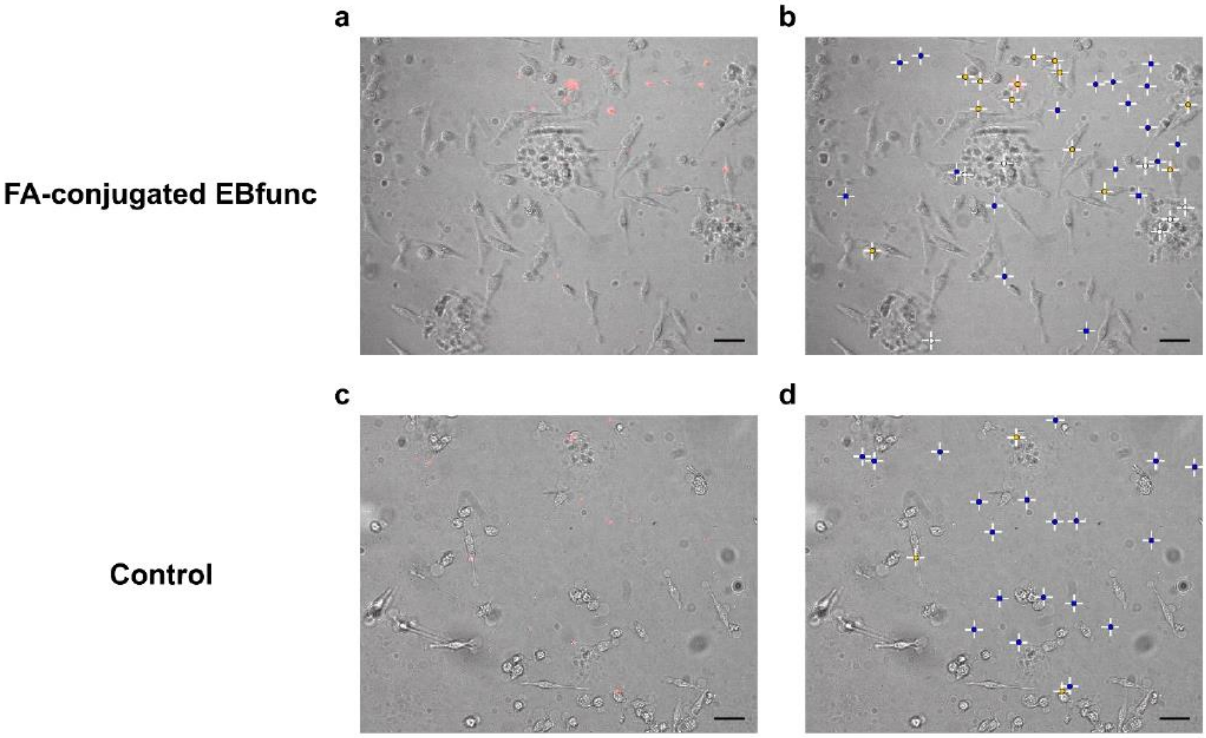

Figure S8: Targeted imaging of HeLa cells with folic acid (FA)-conjugated EBfunc. Exemplary merged images from fluorescence microscopy experiments with HeLa cells (phase contrast, Vis channel, grayscale) and NS samples (fluorescence, NIR channel, red color) are shown. The latter are FA-conjugated EBfunc **(a-b)** and the corresponding control **(c-d)**. NS that were analyzed for colocalization are color-coded based on their position relative to nearby cells **(b,d)**: colocalized (yellow) or free-standing (blue). White labels indicate NS which were excluded from statistics due to the interfering presence of biological material from cell medium. Scale bar = 50 *μm*.

MATERIALS AND METHODS

General considerations

All reactions were performed in standard glassware. Either nitrogen or argon were used as protection gas. Normal Schlenk procedures were followed for moisture- and air-sensitive reactions. All chemicals were bought from commercial suppliers (Sigma Aldrich, TCI, Acros Organics, VWR, Fisher, Carl Roth, J&K Scientific) and used as received unless stated otherwise. Thin layer chromatography was performed with pre-coated plastic sheets (0.2 mm, Polygram® Sil G/UV$_{254}$, Macherey-Nagel). Column chromatography was performed with silica (230-400 mesh, Aldrich 717185, technical grade). NMR measurements were performed in standard 5 mm NMR glass tube on a Bruker Avance III HD 300, a Bruker Avance III 400 or a Bruker Avance Neo 600 machine. The residual proton or the ^{13}C signal of the employed NMR solvents were used for internal calibration (^{1}H and ^{13}C NMR). High resolution electron ionization mass spectrometry (EI-MS) was performed on an AccuTOF (Jeol). High resolution electrospray ionization (ESI-MS) was instead measured on a micrOTOF (Bruker Daltonik) with diethyl ether (Et_2O) as solvent.

Synthesis of 1-(dimethylsilyl)pyrene (Pyr-Sil)[1]

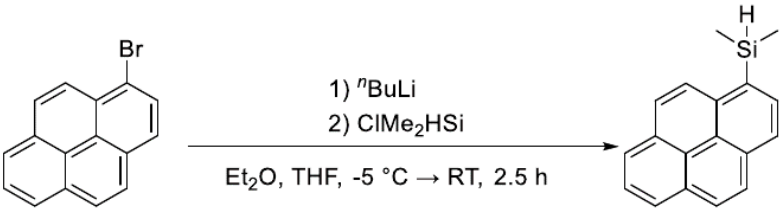

The reaction was performed under the exclusion of moisture and oxygen using nitrogen. 1-Bromopyrene (839 mg, 3.00 mmol, 1.00 eq.) was dissolved in a mixture of dry Et_2O (25 mL) and dry THF (5 mL). The solution was cooled to -5 °C and ^{n}BuLi (1.6 M solution in hexane, 1.9 mL, 3.0 mmol, 1.0 eq.) was added dropwise **(Fig. S1a)**. The resulting mixture was stirred for 30 min at -5 °C, then chlorodimethylsilane (340 mg, 400 µL, 3.60 mmol, 1.20 eq.) was added. The reaction mixture was stirred for 2 h at room temperature **(Fig. S1b)**. After the addition of HCl (10% in H_2O, 20 mL), the mixture was extracted with dichloromethane (DCM, 25 mL). The organic layer was washed with brine (25 mL), dried with anhydrous sodium sulfate (Na_2SO_4, **Fig. S1c**) and the solvent was removed under reduced pressure to yield the crude product **(Fig. S1d)**. Column chromatography (SiO_2, hexane) was performed, and the product-containing fraction was detected by its blue-green fluorescence under UV irradiation **(Fig. S1e)**. In this way a colorless solid (620 mg, 80%) was isolated.

$R_f = 0.46$ (hexane)

^{1}H NMR (600 MHz, $CDCl_3$) δ [ppm]: 8.40 (CH_{aryl}, d, J = 9.1 Hz, 1H), 8.22 (CH_{aryl}, d, J = 7.5 Hz, 2H), 8.20 (CH_{aryl}, d, J = 7.6 Hz, 1H), 8.17(CH_{aryl}, d, J = 7.5 Hz, 1H), 8.15 (CH_{aryl}, d, J = 9.1 Hz, 1H), 8.08 (CH_{aryl}, d, J = 9.0 Hz, 2H) 8.02 (CH_{aryl}, t, J = 7.6 Hz, 1H), 5.10 (SiH, h, J = 3.8 Hz, 1H), 0.62 (CH_3, d, J = 3.8 Hz, 6H).

^{13}C NMR (75 MHz, $CDCl_3$) δ [ppm]: 135.8, 133.1, 132.4, 131.4, 130.9, 128.1, 127.6, 127.6, 127.3, 126.0, 125.4, 125.3, 125.1, 125.0, 124.6, 124.3, -2.8. The two acetone signals can be attributed to the washing of the NMR tube prior to use.

These values are in accordance with the literature[1,2].

^{29}Si INEPT NMR (79 MHz, $CDCl_3$): -19.5 (s).

EI-HRMS: calc.: 260.1016 g mol^{-1} ($C_{18}H_{16}Si$), found: 260.1015 g mol^{-1}.

Another signal with m/z = 202.0773 g mol^{-1} is found, matching pyrene ($C_{16}H_{10}$). This can be explained with an 1,2-ipso H-shift taking place in the molecular cation[3].

Synthesis of (3-chloropropyl)dimethylsilane (COOH-preSil)[1,4]

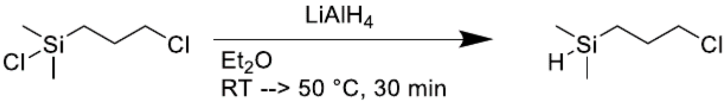

The reaction was performed with oven-dried glassware under dry argon using Schlenk techniques to exclude the presence of moisture and oxygen.

$LiAlH_4$ (4 M in Et_2O, 7.65 ml, 30.6 mmol, 1.0 eq.) was diluted in diethyl ether (93 ml) **(Fig. S6a)**. Chloro(3-chloropropyl)dimethylsilane (5.0 ml, 5.2 g, 30.6 mmol, 1.0 eq.) was added dropwise at a rate sufficient to keep the system at weak reflux. A milky dispersion started forming as soon as the injection began, accompanied by the precipitation of white agglomerates **(Fig. S6b-d)**. After complete addition, the mixture was heated to 50 °C for 30 min before cooling it down to room temperature. An ice-cooled mixture of hydrochloric acid (4 M, 60 mL) and Et_2O (40 mL) was added to the system. The organic phase was separated and the aqueous layer was extracted with dichloromethane (DCM, 4×50 mL). The combined organic extracts were dried over Na_2SO_4, and the Na_2SO_4 residues were washed with 3×50 mL of DCM. Finally, the solvent was removed under reduced pressure and the transparent-slightly yellowish crude product (i.e. (3-chloropropyl)dimethylsilane, COOH-preSil) was stored in the fridge over molecular sieves of pore size = 3 Å **(Fig. S6e)** and used without further purification.

^{1}H NMR (300 MHz, $CDCl_3$) δ [ppm]: 3.88 (Si-H, hept, J = 3.5 Hz, 1H), 3.52 (CH_2, t, J = 6.9 Hz, 2H), 1.88 – 1.75 (CH_2, m, 2H), 0.70 (CH_2, td, J = 8.5, 3.4 Hz, 2H), 0.10 (Si-CH_3, d, J = 3.6 Hz, 6H).

These values are in accordance with the literature[1].

Synthesis of 4-(dimethylsilyl)butyric acid (COOH-Sil)[1,5]

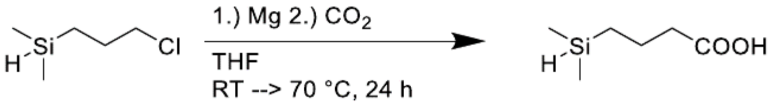

The reaction was performed with oven-dried glassware under dry argon using Schlenk techniques to exclude the presence of moisture and oxygen. Anhydrous tetrahydrofuran (THF) was prepared by drying over sodium-potassium alloy (NaK) and collected via vacuum sublimation.

A modified version of the protocol reported by Moitra et al.[1] was performed.

A solution of COOH-preSil (1.37 g, 10.0 mmol, 1.00 eq.) in THF (8 ml) and DBE (few drops) was added dropwise to activated Mg (turnings, 376 mg, 15.5 mmol, 1.54 eq.) while stirring at 70 °C. At the end of the reaction time, a light greyish dispersion was obtained **(Fig. S7b)**. The supernatant was transferred to a glass flask via cannula and the carbon dioxide (CO_2) was allowed to bubble through the collected supernatant while stirring at room temperature. This step was performed with a CO_2 tank connected to the RBF content via a needle **(Fig. S7d)**. To prevent moisture from entering the system, an empty syringe filled with cotton and the drying agent phosphorous pentoxide (P_2O_5) was fixed along the CO_2 line. The system was left stirring attached to a CO_2 balloon for 24 h **(Fig. S7f)**.

The reaction mixture was quenched with hydrochloric acid (10% HCl, 100 mL) and extracted with diethyl ether (Et_2O, 3×100 mL). The organic layer was then washed with 1×100 mL of water, 1×100 mL of brine (NaCl) and dried over Na_2SO_4, whose residues were washed with 3×50 mL of Et_2O. The solvent was removed under reduced pressure and the transparent-slightly yellowish crude product (i.e. 4-(dimethylsilyl)butyric acid, COOH-Sil) was stored in the fridge **(Fig. S7g)** and used without further purification.

^1H NMR (400 MHz, DMSO-d_6) δ [ppm]: 11.97 (br, 1H), 3.83 (s, 1H), 2.22 (q, J = 6.7 Hz, 2H), 1.52 (s, 2H), 0.67 – 0.36 (m, 2H), 0.05 (d, J = 5.5 Hz, 6H).

^{13}C NMR (101 MHz, $CDCl_3$) δ 178.27, 37.12, 20.08, 14.00, -4.46.

The proton spectra’s integrals are broadened. Both NMR spectra show additional peaks and residual THF solvent. As column chromatography was not possible, the crude product was used for grafting.

ESI-HRMS (neg. mode): calc.: 145.0690 g mol^{-1} ($C_6H_{13}O_2Si$) $[M-H]^-$, found: 145.0673 g mol^{-1}.

Exfoliation of Egyptian Blue (EB) into nanosheets (EB-NS)

EB bulk powder (3 g, < 120 µm, Kremer Pigmente GmbH & Co. KG) were introduced into an agate beaker (20 mL) together with agate balls (80 x 5 mm). Deionized water was added until a slurry consistency could be reached. The so-prepared agate beaker was then placed in a planetary ball mill (PB, Pulverisette 7 Premium Line, Fritsch), which was run at 900 r.p.m. for 1-2 h (cycles of 20 min each, 5 min pause). The so-prepared slurry was then allowed to settle for 24 h, then the supernatant was removed and the sediment was dried and stored at room temperature.

Preparation of pyrene-functionalized EB-NS (EBfunc)[1]

Grafting of 1-(dimethylsilyl)pyrene (Pyr-Sil) onto Egyptian Blue nanosheets (EB-NS) was performed in standard glass-ware under the exclusion of moisture and oxygen using nitrogen. EB-NS and Pyr-Sil were prepared as described in the corresponding sections. Anhydrous dichloromethane (DCM, 99.8%, over molecular sieves) was used as received.

In order to remove adsorbed water molecules on its surface, milled EB-NS powder (336 mg) was dried overnight under vacuum at 180°C-200°C in a 25 mL round-bottom flask (RBF). The system was then cooled down to room temperature in nitrogen atmosphere **(Fig. S2a)**, and anhydrous DCM (3 mL) was added. Next, Pyr-Sil (264 mg, theoretical 260 mg, corresponding to 1 mmol) was introduced into the RBF, and the mixture was stirred for a couple of minutes. Immediately after the addition of CAT (6 mg, theoretical 5 mg, corresponding to 0.01 mmol) and for ≈ 5 min, abundant hydrogen evolution could be observed **(Fig. S2b)**. 10 min after the introduction of CAT, the mixture was left stirring at room temperature for 2 days. After the addition of DCM (5 mL) to disperse and wash the content of the RBF, the sample mixture was vacuum-filtered using a fritted glass funnel with pore size P4 (i.e. 10-16 µm). Following rigorous washing steps with DCM (3×5 mL) and hexane (3×5 mL), necessary to exclude physisorbed Pyr-Sil, a vacuum step of 20 min was performed to dry the sample. Finally, the functionalized EB-NS powder (EBfunc, 246 mg, 73% of starting material) could be collected and stored at room temperature **(Fig. S2c)**.

The control sample without catalyst (noCAT) was performed as above, with the only difference that the addition of CAT was replaced with the introduction of 3 mL of anhydrous DCM. The system was then left stirring for 1 h, and the filtering, washing and vacuum steps were done as above, yielding the noCAT powder (269 mg, 82% of starting material).

Preparation of COOH-functionalized EB-NS (EBfunc)[1]

Grafting of 4-(dimethylsilyl)butyric acid (COOH-Sil) onto Egyptian Blue nanosheets (EB-NS) was performed with oven-dried glassware under dry argon using Schlenk techniques to exclude the presence of moisture and oxygen. EB-NS and COOH-Sil were prepared as described in the corresponding sections. Anhydrous dichloromethane (DCM) was prepared by distillation from calcium hydride and stored over molecular sieves (pore size = 3 Å).

In order to remove adsorbed water molecules on its surface, milled EB-NS powder (100 mg) was dried overnight under vacuum at 180°C in a 10 mL round-bottom flask (RBF). The system was then cooled down to room temperature in argon atmosphere, and anhydrous DCM (3 mL) was added. Next, COOH-Sil (87 mg, theoretical 73 mg, corresponding to 0.5 mmol) was introduced into the RBF, and the mixture was stirred for a couple of minutes. After the addition of CAT (4.3 mg, theoretical 2.6 mg, corresponding to 0.005 mmol), hydrogen evolution could be observed. Next, the mixture was left stirring at room temperature for 1 h. After the addition of DCM (20 mL) to disperse and wash the content of the RBF, the sample mixture was vacuum-filtered using a fritted glass funnel with pore size P4 (i.e. 10-16 µm). Following rigorous washing steps with DCM (3×5 mL) and hexane (3×5 mL), necessary to exclude physisorbed COOH-Sil, a vacuum step of 2 h was performed to dry the sample. Finally, the functionalized EB-NS powder could be collected and stored at room temperature.

The control sample without catalyst (noCAT) was performed as above, with the only difference that the addition of CAT was replaced with the introduction of 3 mL of anhydrous DCM. The system was then left stirring for 1 h, and the filtering, washing and vacuum steps were done as above, yielding the noCAT powder.

Solid-State Nuclear Magnetic Resonance (ssNMR)

Characterization via solid-state nuclear magnetic resonance (ssNMR) was performed on 5 samples: the pristine Egyptian Blue (EB) powder directly from the supplier's vial, the milled EB nanosheets (EB-NS), the pyrene-functionalized EB-NS (EBfunc), the catalyst-free counterpart of EBfunc (noCAT) and the pyrene-silane (Pyr-Sil).

^{1}H-^{13}C CP MAS NMR experiments were performed on a 14.1 T BRUKER magnet with an Avance III HD spectrometer utilizing a 4 mm HXY DVT MAS BRUKER probe. The solid samples were packed in a form of powder into the 4 mm zirconia rotors capped with vespel drive caps and no spacers were used. Rotors were spun at 12.5 kHz spinning frequency at the magic angle of 54.7° with the magnetic field. Various recycle delays were tested as the Egyptian Blue is a paramagnetic material and has, thus, a direct effect on the relaxation of NMR signals. The recycle delay for the pure Pyr-Sil and the control sample was 4 s, and the one for attached Pyr-Sil to EB-NS was 0.5 s. While we used 10240 (10k) number of scans for the pure and control samples, we employed 51200 (50k) number of scans for the functionalized sample. We used 83.3 kHz ^{1}H and 62.5 kHz ^{13}C radio frequency pulses where the CP condition was met with 58.4 kHz ^{13}C and 64kHz ^{1}H ramped 90% to 100% power on ^{1}H with a duration of 1.5 ms. During the ^{13}C channel acquisition, SPINAL64 decoupling on the ^{1}H channel with 83 kHz power was applied.

Confocal Laser Scanning Microscopy (CLSM)

Sample preparation for confocal laser scanning microscopy (CLSM) was typically performed as follows. A small aliquot of sample powder was dispersed in isopropanol (≈ 500 µL) by means of a short round of vortexing. ≈ 100-200 µL of the so-obtained dispersion were then drop-casted onto a glass-bottom petri dish, and imaging was started after the sample had dried. Measurements were carried out with a 20× objective (UPLSAPO20× NA 0.75) mounted in a FV1000 CLSM (Olympus), and DAPI filters (λ_{exc} = 405 nm, λ_{em} = 461 nm) were chosen to enable suitable excitation of pyrene and detection of its fluorescence. Images were acquired with the device software (Fluoview FV1000, v. 4.2.1.20) and processed in Fiji (v. 1.53f51)[6].

The colocalization analysis **(Fig. S5)** was performed on Fiji and its results were plotted with OriginPro 8.1 SR3 (v8.1.34.90). First, 10 regions of interests (ROIs) within the captured CLSM images were chosen in such a way that a significantly high amount of small and not agglomerated particles could be included within such areas for all measured samples, i.e. the pyrene-functionalized EB-NS (EBfunc), the pyrene-bearing silane (Pyr-Sil), the catalyst-free control (noCAT) and the unprocessed EB-NS. For each sample, the colocalization analysis therefore focused on these shared 10 ROIs only, more specifically on their bright-field (BF) and fluorescence (PL) channels. For each ROI, the BF channel was thresholded (filter = "max entropy") and then multiplied to the corresponding PL channel: in this way, if a particle was present in the BF, its corresponding PL information could be passed on, otherwise it was deleted. Next, the resulting multiplied image was converted to 8-bit and its mean (± standard deviation) pixel intensity was calculated: considered how this image had been generated, the measured signal corresponds to the fluorescence intensity of the colocalized particles only. Finally, pixel intensity (mean ± standard deviation) of the thresholded BF image was measured: this value was used to normalize the previous dataset to account for different particle density, given that the BF signal represents the highest achievable colocalization (brightness) if all filtered particles emitted maximum fluorescence.

UV-Vis Absorption & Vis Fluorescence Spectroscopy

UV-Vis absorption spectra were measured on a Jasco V670. Fluorescence spectra were acquired on a Jasco FP-6500.

For measurements of the pyrene-silane (Pyr-Sil) at the UV-Vis spectrometer, a heavily diluted aliquot of sample powder dispersed in dichloromethane (DCM) was introduced in a 10 mm path quartz cuvette. Absorption was acquired in the range of wavelengths from 200 nm to 800 nm with steps of 0.2 nm.

For measurements of pyrene-functionalized EBfunc and the corresponding noCAT sample at the fluorometer, the samples (3 mg) were dispersed in DCM (1 mL). Fluorescence spectra were then acquired with the following parameters: λ_{exc} = 346 nm, PMT = 560 V, bandwidth for excitation and emission = 3 nm, scan speed = 500 nm/min, time = 0.2 s, steps = 0.5 nm.

Near-Infrared (NIR) Spectroscopy

The spectroscopy setup consists of a monochromator (MSH-150, LOT-Quantum Design GmbH) equipped with a xenon arc lamp and a diffraction grating, an inverted microscope (Olympus IX73) equipped with a 10× objective (UplanFLN 10×/0.30, Olympus), and a spectrometer (Shamrock 193i spectrograph, Andor Technology Ltd.) coupled to an array NIR detector (Andor iDUs InGaAs 491). Fluorescence data was acquired via the Andor SOLIS software (version 4.29.30012.0).

For the acquisition of 2D excitation-emission spectra of pyrene-functionalized EBfunc, the dispersed sample in dichloromethane (DCM, 5 µL) was drop-casted onto a #1 glass coverslip. The substrate was then positioned above the setup's objective, and the measurement was started as soon as the sample had dried. The following settings were chosen: 300 nm ≤ λ_{exc} ≤ 780 nm, step = 2 nm, exposure time = 2 s, input side slit width = 500 µm. To make sure that the spectrometer would not reach saturation during the measurement, EB fluorescence with different exposure times had been checked beforehand at 630 nm. The plotting as well as the correction for the quantum efficiency of the detector and for the spectral irradiance of the xenon lamp were performed using a self-written Python script.

Preparation of Folic Acid (FA)-Conjugated Egyptian Blue Nanosheets (EBfunc)

The starting material, i.e. carboxy-functionalized EBfunc, was prepared as described in the corresponding section. Conjugation of FA with NS of EBfunc was performed according to a protocol adapted from the work by Zhang et al.[7]. Dichloromethane (analytical reagent grade, ≥ 99.8%, DCM) was purchased from Fisher Scientific GmbH. N,*N'*-dicyclohexylcarbodiimide (99%, DCC), N-hydroxysuccinimide (98%, NHS) and folic acid (≥ 97%) were purchased from Sigma-Aldrich GmbH. 1 mg of COOH-functionalized EBfunc was dispersed in 2 mL of DCM. 25 µL of DCC solution (0.05 M in DCM) and 25 µl of NHS solution (0.05 mol/L in DCM) were added into the suspension, afterwards the mixture was stirred for 1 h. 100 µl of FA solution (0.025 M in DCM) were then added and the mixture was stirred for another 16 h. After stirring, washing steps were performed twice: these consisted in first centrifuging all particles, then discarding the supernatant and finally redispersing the so-collected pellet in DCM. All particles were then centrifuged again, dried (6 h at room temperature) and dispersed in 400 µl of ultrapure water. The so-obtained dispersion was dialyzed in ultrapure water for 16 h using a Spectrapor 300 kDa membrane (Spectrum Laboratories) to remove excess FA molecules.

A control sample was prepared by repeating the reaction described above, but without the addition of DCC and NHS.

Zeta Potential Measurements

Zeta potential was analyzed using a Zetasizer Ultra ZSU5700 (Malvern Instruments GmbH). For the measurements of COOH-functionalized EBfunc and the corresponding controls **(Table 1)**, samples were dispersed in ultrapure water at a concentration of 1 mg/mL and set to a neutral pH value by addition of HCl (0.01 M). For the measurements of FA-conjugated EBfunc and the corresponding controls **(Table 1)**, 50 µl of the dialyzed dispersion were diluted in ultrapure water to a volume of 1 mL and the pH was neutralized by addition of HCl (0.01 M). For both datasets, 1 mL of the so-obtained dispersions were measured in the Zetasizer using a DTS1070 folded-capillary cuvette (Malvern Instruments GmbH) and assuming a refractive index of 1.63. The working temperature was fixed to 25 °C. Once the sample was introduced into the chamber, the time for the temperature stabilization was set to 120 s. A preinstalled measurement routine consisting of five measurements was used to obtain the average zeta potential and calculate the standard deviation.

Cell Experiments with Folic Acid (FA)-Conjugated Egyptian Blue Nanosheets (EBfunc)

The starting material, i.e. FA-conjugated EBfunc, was prepared as described in the corresponding section. HeLa cells were cultured in DMEM (Thermo Fisher Scientific) with the addition of 10% fetal calf serum, 100 units/mL penicillin, and 100 µg/mL streptomycin in a humidified 5% CO_2 atmosphere at 37 °C. For analysis of ligand-receptor binding of FA-conjugated EBfunc to FA receptors on cell surfaces, HeLa cells were seeded in glass bottom 24 well plates at a density of $2x10^4$ cells per well in 1 mL DMEM. This was done to keep the cells mostly isolated and allow an easier assessment of the colocalization degree of NS with single cells. The following day, 100 µL of the EBfunc/control sample (1:1 dilution) were added dropwisely. Cells were incubated for 2 h in a humidified 5% CO_2 atmosphere at 37 °C, carefully washed with PBS, fixed with 4% PFA for 10 min, and finally washed three times with PBS for 5 min each on an orbital shaker.

Near-Infrared (NIR) Microscopy

NIR fluorescence microscopy was performed at a home-built imaging setup consisting of an Olympus IX73 microscope (Olympus, Germany) equipped with a MPlanFL N 20×/0.45 objective (Olympus, Germany), Zyla 5.5 sCMOS VIS camera (Oxford Instruments, UK), Cheetah 640TE3 NIR-camera (Xenics NV, Belgium) and a Cobolt Jive 561 nm laser (Cobolt AB, Sweden). In terms of filters, a dichroic mirror (HC BS R785 lambda/5 PV, F38-785S, AHF) separated the visible (Vis) and the NIR optical paths; for imaging in the NIR, a 900 nm long-pass filter (FELH0900, Thorlabs) was also installed.

The HeLa-EBfunc cell samples were imaged in their well plates after fixing and washing steps. Images of the visible (Vis) channel were taken with the Zyla camera and recorded with the Andor Solis Software

(Oxford Instruments, UK); for the acquisition, phase contrast mode with top illumination was used. Images of the NIR channel were taken with the Cheetah camera and recorded with Xeneth Software 2.7 (Xenics NV, Belgium); for the acquisition, excitation with the 561 nm laser at a set power of 200 mW and an integration time of 1 s was performed.

The image analysis was performed on the NIR and Vis images as follows. After background correction and contrast/brightness adjustments, the fluorescent nanosheets of EBfunc were located and marked in the NIR images. Both NIR and Vis datasets were then converted into 8-bit format, cropped and overlaid (after calibration with a gridded reference sample) in ImageJ (1.53k). In the overlaid images, each fluorescent nanoparticle was labelled according to its position relative to the nearby HeLa cells, i.e. depending on whether it was in contact with a nearby cell or not. Finally, these values were normalized according to the number of available NS in the corresponding imaged region.

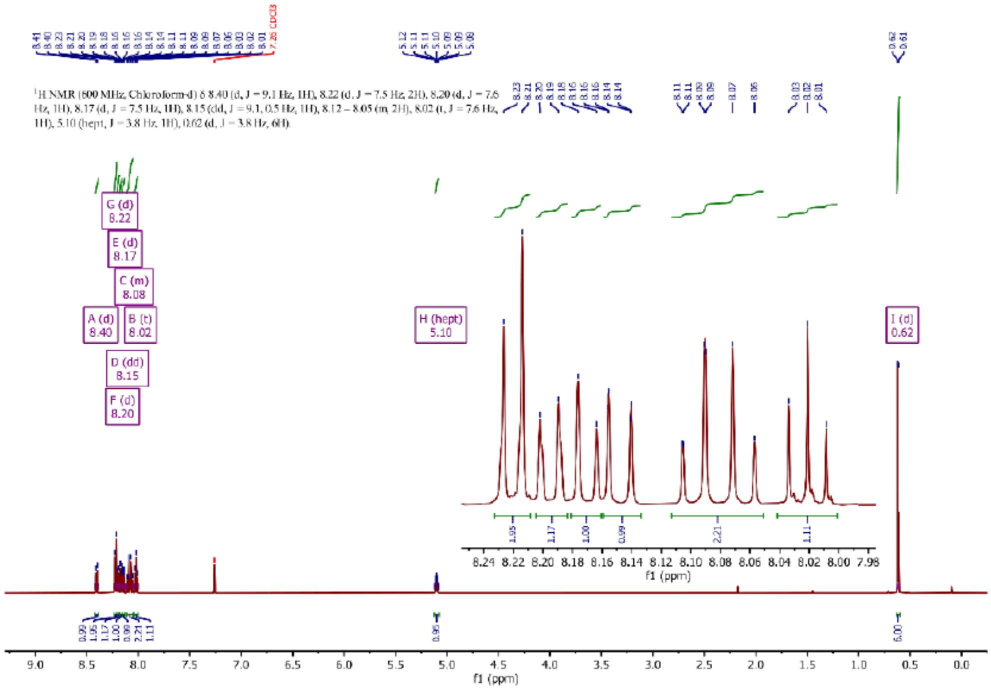

^{1}H NMR (600 MHz, Chloroform-d) δ 8.40 (d, J = 9.1 Hz, 1H), 8.22 (d, J = 7.5 Hz, 2H), 8.20 (d, J = 7.6 Hz, 1H), 8.17 (d, J = 7.5 Hz, 1H), 8.15 (dd, J = 9.1, 0.5 Hz, 1H), 8.12 – 8.05 (m, 2H), 8.02 (t, J = 7.6 Hz, 1H), 5.10 (hept, J = 3.8 Hz, 1H), 0.62 (d, J = 3.8 Hz, 6H).

Proton nuclear magnetic resonance spectrum (^{1}H-NMR) of 1-(dimethylsilyl)pyrene (Pyr-Sil) in deuterated chloroform ($CDCl_3$).

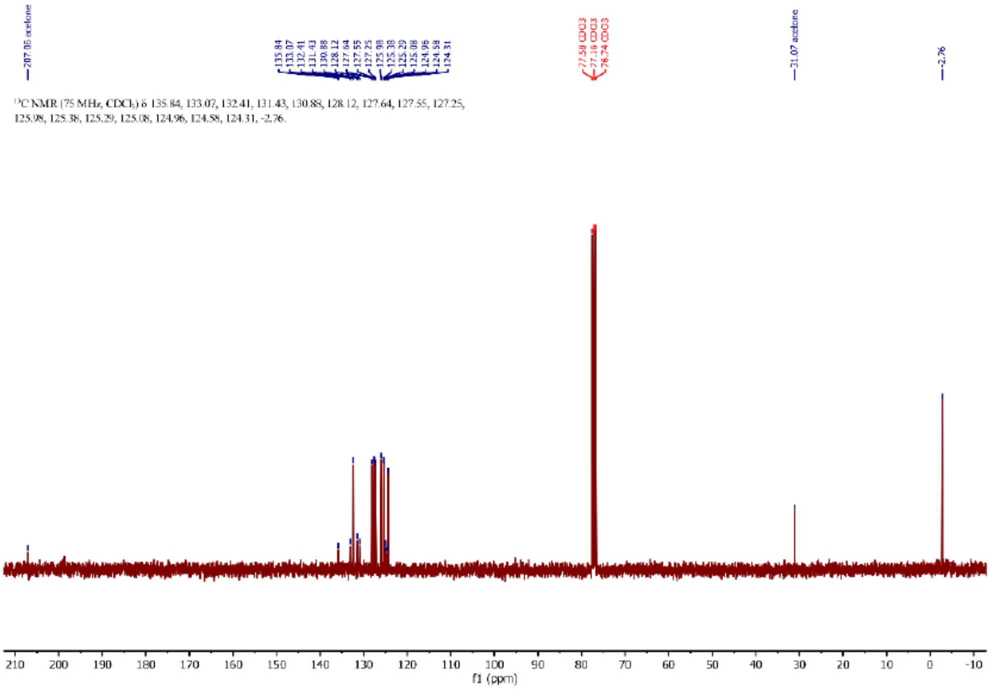

^{13}C NMR (75 MHz, $CDCl_3$) δ 135.84, 133.07, 132.41, 131.43, 130.88, 128.12, 127.64, 127.55, 127.25, 125.98, 125.38, 125.29, 125.08, 124.96, 124.58, 124.31, -2.76.

Carbon nuclear magnetic resonance spectrum (^{13}C-NMR) of 1-(dimethylsilyl)pyrene (Pyr-Sil) in deuterated chloroform ($CDCl_3$).

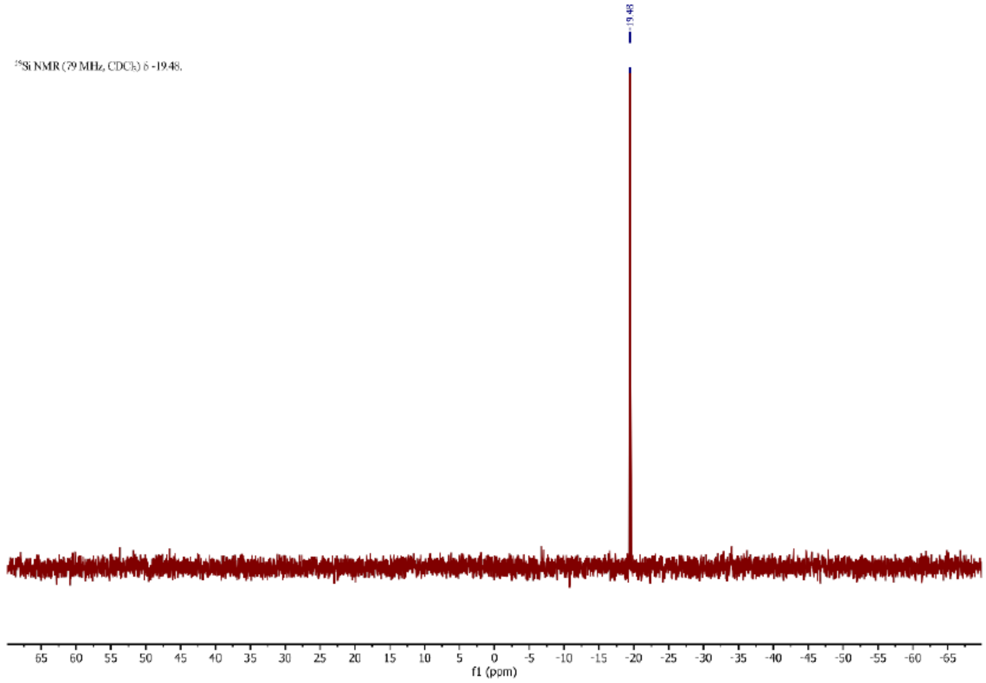

Silicon nuclear magnetic resonance spectrum (^{29}Si-NMR) of 1-(dimethylsilyl)pyrene (Pyr-Sil) in deuterated chloroform (CDCl$_3$).

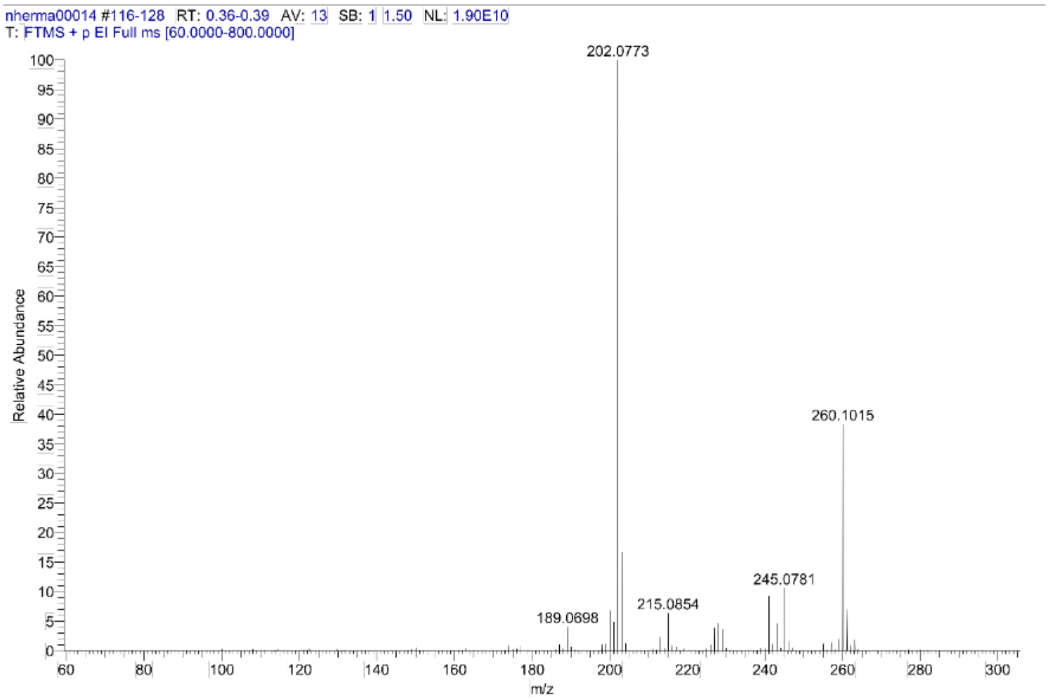

Electron ionization mass spectrum (EI-MS) of 1-(dimethylsilyl)pyrene (Pyr-Sil).

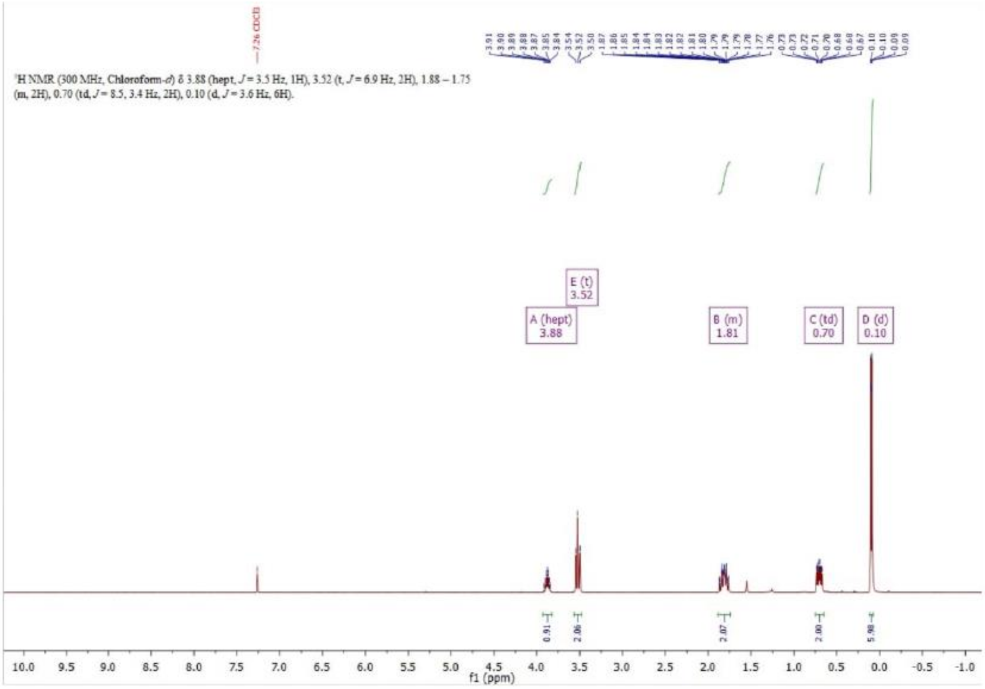

^{1}H NMR (300 MHz, Chloroform-*d*) δ 3.88 (hept, *J* = 3.5 Hz, 1H), 3.52 (t, *J* = 6.9 Hz, 2H), 1.88 – 1.75 (m, 2H), 0.70 (td, *J* = 8.5, 3.4 Hz, 2H), 0.10 (d, *J* = 3.6 Hz, 6H).

Proton nuclear magnetic resonance spectrum (^{1}H-NMR) of (3-chloropropyl)dimethylsilane (COOH-preSil) in deuterated chloroform ($CDCl_3$).

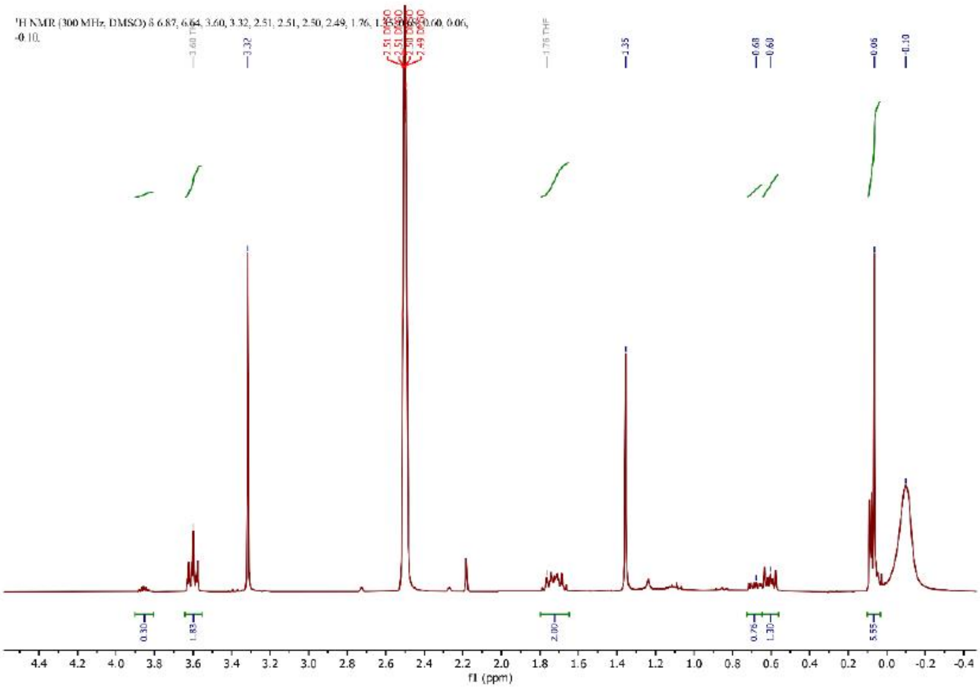

^{1}H NMR (300 MHz, DMSO) δ 6.87, 6.64, 3.60, 3.32, 2.51, 2.51, 2.50, 2.49, 1.76, 1.35, 0.68, 0.60, 0.06, -0.10.

Proton nuclear magnetic resonance spectrum (^{1}H-NMR) of (3-chloropropyl)dimethylsilane (COOH-preSil) in deuterated dimethyl sulfoxide (DMSO).

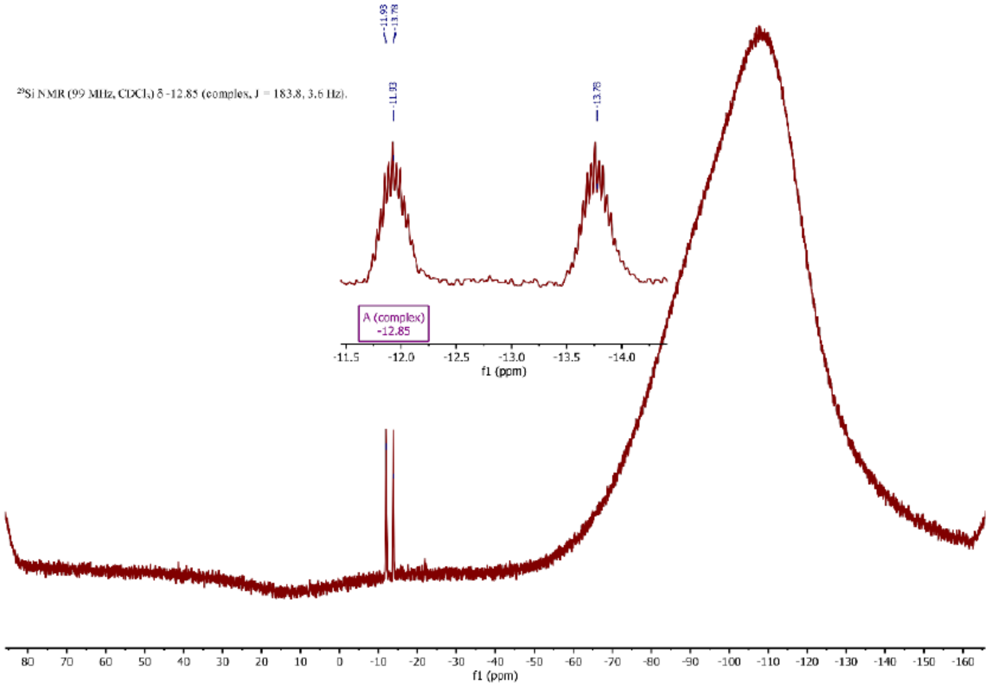

Normal silicon nuclear magnetic resonance spectrum (^{29}Si-NMR) of (3-chloropropyl)dimethylsilane (COOH-preSil) in deuterated chloroform ($CDCl_3$).

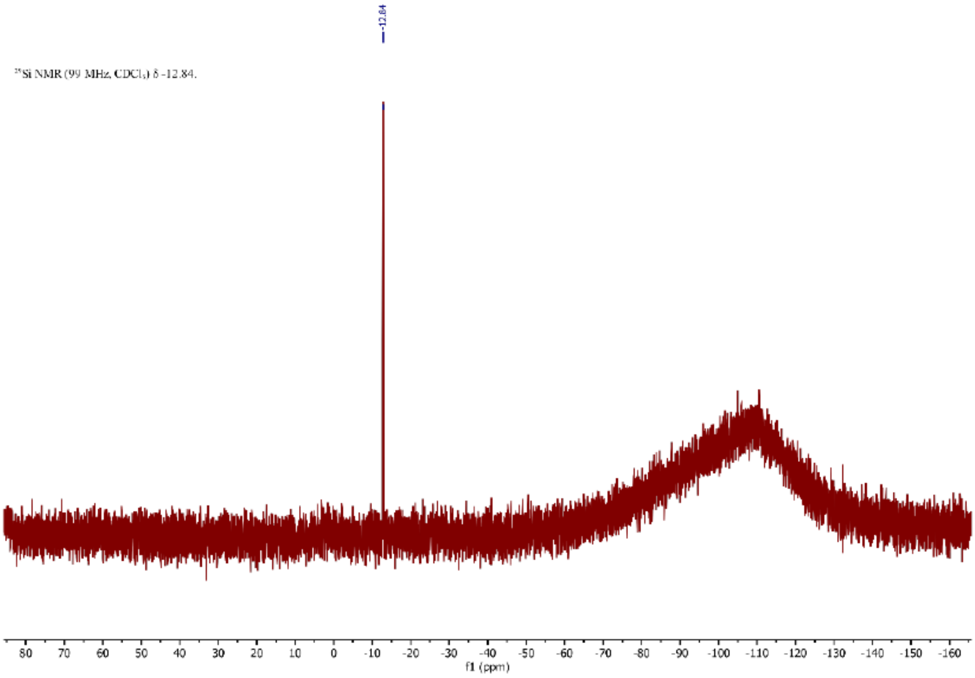

^{1}H-decoupled silicon nuclear magnetic resonance spectrum (^{29}Si-NMR) of (3-chloropropyl)dimethylsilane (COOH-preSil) in deuterated chloroform ($CDCl_3$).

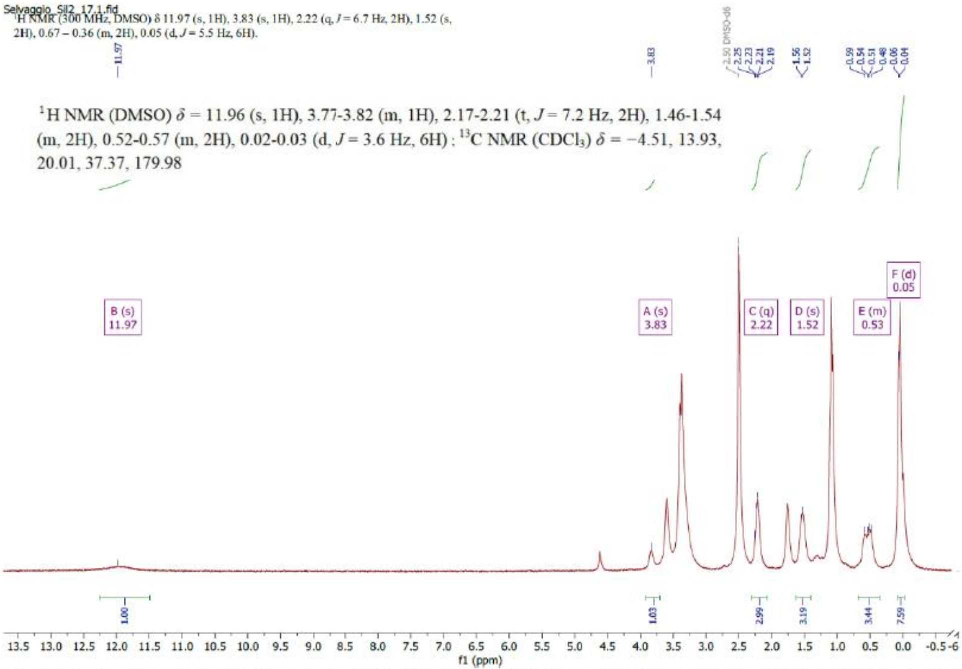

Selvaggio_Sil2_17.1.fid

^{1}H NMR (300 MHz, DMSO) δ 11.97 (s, 1H), 3.83 (s, 1H), 2.22 (q, J = 6.7 Hz, 2H), 1.52 (s, 2H), 0.67 – 0.36 (m, 2H), 0.05 (d, J = 5.5 Hz, 6H).

^{1}H NMR (DMSO) δ = 11.96 (s, 1H), 3.77-3.82 (m, 1H), 2.17-2.21 (t, J = 7.2 Hz, 2H), 1.46-1.54 (m, 2H), 0.52-0.57 (m, 2H), 0.02-0.03 (d, J = 3.6 Hz, 6H) ; ^{13}C NMR (CDCl$_3$) δ = −4.51, 13.93, 20.01, 37.37, 179.98

Proton nuclear magnetic resonance spectrum (^{1}H-NMR) of 4-(dimethylsilyl)butyric acid (COOH-Sil) in deuterated dimethyl sulfoxide (DMSO).

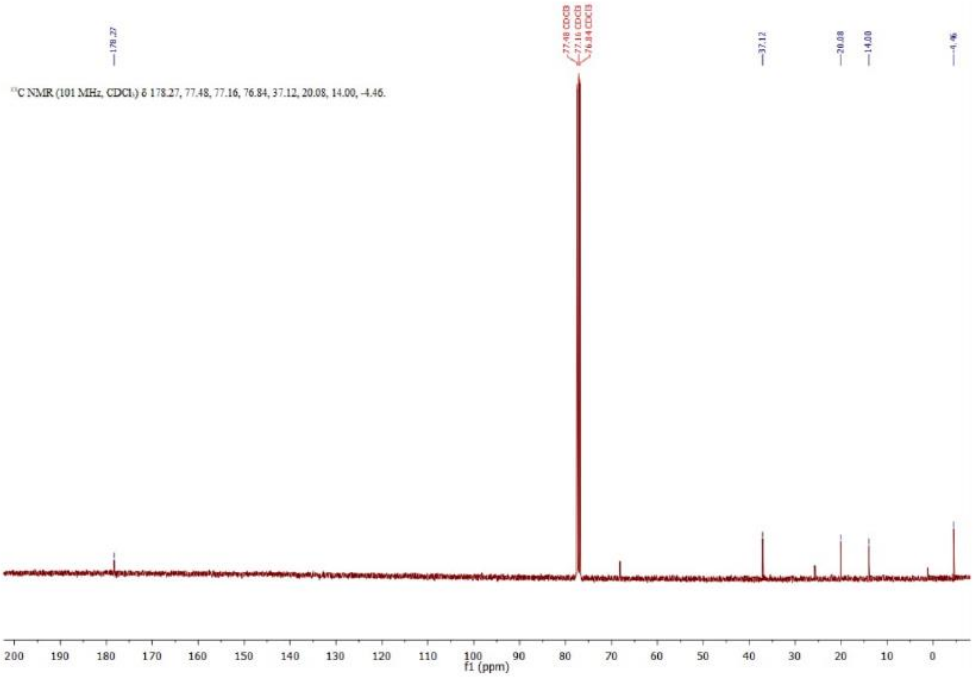

^{13}C NMR (101 MHz, CDCl$_3$) δ 178.27, 77.48, 77.16, 76.84, 37.12, 20.08, 14.00, -4.46.

Carbon nuclear magnetic resonance spectrum (^{13}C-NMR) of 4-(dimethylsilyl)butyric acid (COOH-Sil) in deuterated dimethyl sulfoxide (DMSO).

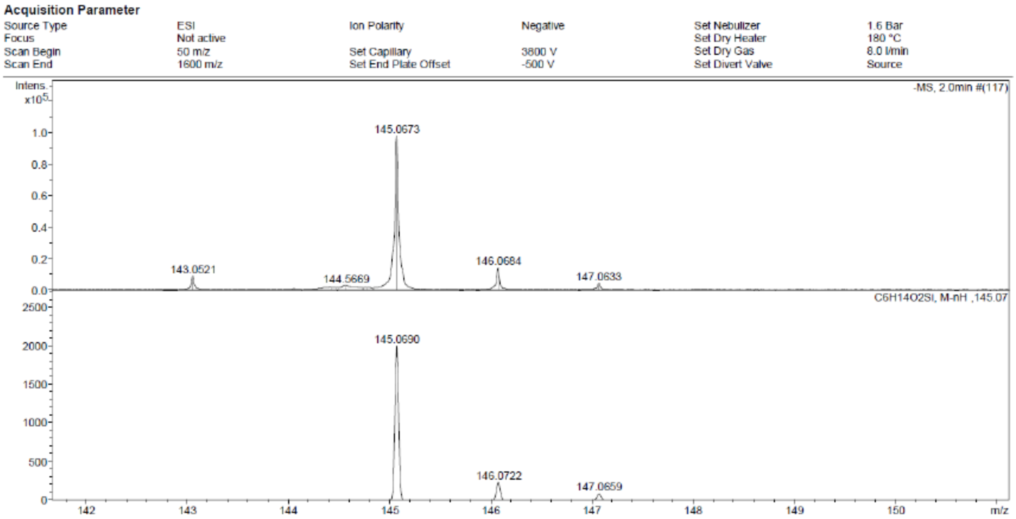

Acquisition Parameter

Source Type	ESI	Ion Polarity	Negative	Set Nebulizer	1.6 Bar
Focus	Not active			Set Dry Heater	180 °C
Scan Begin	50 m/z	Set Capillary	3800 V	Set Dry Gas	8.0 l/min
Scan End	1600 m/z	Set End Plate Offset	-500 V	Set Divert Valve	Source

Electrospray ionization mass spectrum (ESI-MS) of 4-(dimethylsilyl)butyric acid (COOH-Sil) in diethyl ether (Et_2O).

REFERENCES

1. Moitra, N. et al. Surface functionalization of silica by Si-H activation of hydrosilanes. J. Am. Chem. Soc. **136**, 11570–11573 (2014).
2. Su, B. & Hartwig, J. F. Iridium-Catalyzed, Silyl-Directed, peri -Borylation of C−H Bonds in Fused Polycyclic Arenes and Heteroarenes. Angew. Chemie Int. Ed. **57**, 10163–10167 (2018).
3. Choe, J. C. Loss of benzene from methylphenylsilane and dimethylphenylsilane molecular cations. Int. J. Mass Spectrom. **242**, 5–11 (2005).
4. Daiss, J. O. et al. N+/Si replacement as a tool for probing the pharmacophore of allosteric modulators of muscarinic M2 receptors: Synthesis, allosteric potency, and positive cooperativity of silicon-based W84 derivatives. Organometallics **21**, 803–811 (2002).
5. Steinmetz, M. G. & Udayakumar, B. S. S. Chloroplatinic acid catalyzed cyclization of silanes bearing pendant acetylenic groups. J. Organomet. Chem. **378**, 1–15 (1989).
6. Schindelin, J. et al. Fiji: an open-source platform for biological-image analysis. Nat. Methods **9**, 676–682 (2012).
7. Zhang, Z. et al. Conjugating folic acid to gold nanoparticles through glutathione for targeting and detecting cancer cells. Bioorganic Med. Chem. **18**, 5528–5534 (2010).

5.4.3 Publication Synopsis

The main finding outlined in **Manuscript IV** was that the Si-H activation approach established by Moitra *et al.*[248] could be successfully applied to a milled batch of EB-NS, therefore yielding covalently functionalized silicate nanosheets (EBfunc). To prove this important claim, a pyrene-bearing hydrosilane (1-(dimethylsilyl)pyrene, Pyr-Sil) was synthesized according to a previously reported protocol[248] and employed for a first grafting round. This decision was determined by the well-known visible emission of the corresponding R group: pyrene (Pyr)[249,250]. In this way, the plan was then to rely on these fluorescent features for a visual and spectroscopic verification of functionalization. The first strong proof of successful functionalization of EB-NS was however represented by the observed hydrogen (H_2) evolution: as expected according to the reaction mechanism[248], its beginning and termination define the start and the end of the grafting reaction. Indeed, the short timing ($t \approx 5$ min), the dehydrogenative nature and the lack of heating requirements (room temperature suffices) are some of the strong advantages of the chosen approach. As reported by Moitra *et al.*[248] for silica particles, an intense H_2 evolution (which lasted for a few minutes) could be noticed directly after the addition of the employed catalyst, *i.e.* the strong Lewis acid tris(pentafluorophenyl)borane ($B(C_6F_5)_3$, CAT). Such visible gas formation was instead absent in the case of the control sample, which was prepared by repeating the grafting reaction on another aliquot of EB-NS but without the addition of the catalyst (noCAT). This first result already indicated that the functionalization of EB-NS was likely successful. Next, as mentioned earlier, a pool of diverse characterization tools was employed to provide further confirmations. After thorough post-reaction washing steps of the NS pellets to remove physisorbed material, 1D and 2D spectroscopy were performed. While the 1D dataset revealed the presence of the typical pyrene emission features only in EBfunc, the 2D dataset showed that the characteristic NIR fluorescence of EB-NS was retained and unchanged after functionalization. Visible fluorescence imaging by means of confocal laser scanning microscopy (CLSM) was carried out next. This dataset showed significantly stronger fluorescent signals in the EBfunc samples compared to the controls (*i.e.* noCAT and unprocessed EB-NS). Moreover, after combining the information from the visible (Pyr) and bright-field (EB-NS) channels, a 2× higher colocalization degree in EBfunc compared to noCAT could be measured. Further validation of the surface chemistry was then provided by solid-state magic-angle spinning NMR analysis (MAS NMR). Here, only in the case of EBfunc the relevant signals of Pyr-Sil could be detected: these included the methyl groups and the aromatic carbons of the Pyr moiety. The noCAT control did not present these peaks, thus indicating the absence of Pyr both on the surface of EB-NS and unbound.

After having proven the functionalization of EB-NS by means of various characterization methods, **Manuscript IV** described the repetition of the same grafting reaction but with another hydrosilane: 4-(dimethylsilyl)butanoic acid (COOH-Sil). This molecule, which was synthesized *via* a Grignard reaction[248,251,252], was chosen with the intent to yield EB-NS functionalized with carboxyl groups (EBfunc). Even in this case, H_2 evolution happened only with the EBfunc sample and was not generated with the noCAT control. As a further proof of functionalization, zeta potential measurements were taken: the acquired values were significantly more negative for EBfunc (≈ -40 mV) compared to noCAT and unprocessed EB-NS (both ≈ -20 mV). This finding suggests the presence of carboxyl groups covalently bond on the surface of EBfunc only, and at the same time indicates an enhanced colloidal stability.

In the final part of **Manuscript IV**, targeted imaging experiments on cancer cells with EBfunc samples were carried out. First, folic acid (FA) was conjugated to COOH-functionalized EBfunc according to a literature protocol[253]. For this dataset, the chosen control consisted in the repetition of the conjugation reaction without addition of *N*,*N'*-dicyclohexylcarbodiimide (DCC) and *N*-hydroxysuccinimide (NHS). The outcome of the procedure was evaluated once more with zeta potential: the more negative values of FA-conjugated EBfunc compared to the control indicated a higher presence of negatively charged FA on the NS surface. Next, colocalization imaging of HeLa cells with FA-conjugated EBfunc and the control was performed at a home-built NIR microscopy setup. According to the collected data, the degree of colocalization was higher for the FA-conjugated EBfunc. Considered that HeLa cells typically display a high amount of folate receptors on their surface, the obtained results suggest the presence of ligand-receptor binding events. In this way, the performed cell experiments not only highlighted the success of the FA conjugation protocol, but also presented the first example of targeted bioimaging with EB-NS.

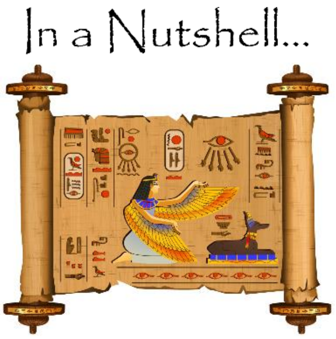

- ✓ Pyrene moieties were covalently grafted on the surface of EB-NS by means of Si-H activation of hydrosilanes.
- ✓ The NIR fluorescence of EB-NS was retained after functionalization.
- ✓ The observed hydrogen evolution and a pool of spectroscopic and imaging characterization methods confirmed the success of the grafting procedure.
- ✓ By repeating the same reaction with a hydrosilane bearing carboxyl groups, COOH-functionalized EB-NS could be prepared.
- ✓ Conjugation of folic acid on COOH-functionalized EB-NS was performed and confirmed by zeta potential measurements.
- ✓ Introduction of these novel conjugated structures into a cancer cell line demonstrated for the first time the successful employment of EB-NS for targeted bioimaging.

6 | Discussion and Outlook

6.1 Extended Benzene-Fused Oligo-BODIPYs: A Promising Addition to the BODIPY Family

Absorption and emission features of organic fluorophores strongly depend on the structure of the chromophores. For instance, conjugated BODIPY dyes display a bathochromic shift after extension of their conjugated π-system **(Section 4.1.5)**. In this regard, it was already known that dyes from the oligomer family of Patra *et al.*[6] displayed a red-shift increase with increasing length of the oligomeric structure as a result of converging HOMO-LUMO energy gaps. Nevertheless, the NIR fluorescence of the hexamer (*H*) and octamer (*O*) oligomers had not been discovered so far. The results presented in **Manuscript I** described for the first time the NIR properties of these two extended benzene-fused oligo-BODIPYs. Even though the *H*- and *O*-oligo-BODIPYs are the only ones to present clearly red-shifted features in the NIR window, the observed overall shape of the absorption and emission bands resembled the one of shorter oligomers of the same series[6]. Indeed, FWHM and Stokes shift values of *H*- and *O*-oligo-BODIPYs did not differ significantly from *e.g.* the monomeric or dimeric counterparts. This observation highlights an important advantage of the synthetic routes performed by Patra *et al.*[6]: characteristics such as the narrow emission bands, which are of interest for *e.g.* multiplexing, are not compromised by the extension of the π-conjugated scaffold.

Next, **Manuscript I** studied the solvatochromic properties of the fluorophores. The solvents used for this work were the same employed in the study by Patra *et al.*[6] In general it is known that the complex interplay of solute-solvent interactions can affect spectral features of fluorophores. Typically, non-specific and specific solute-solvent interactions are comprised in the more general definition of solvent polarity. These can be more extensively described at a macroscopic scale by the static dielectric constant (ε) and microscopically by the dipole moment of the solvent molecules (μ)[254,255]. In the case of both *H*- and *O*-oligo-BODIPYs, the emission bands were shifted to higher wavelengths with the slightly less polar toluene and DCM, thus displaying negative solvatochromism. The same trend had been already observed by Patra *et al.*[6] with the other extended benzene-fused oligo-BODIPYs. Considered that the *H*- and *O*-oligo-BODIPYs and the smaller oligomers share the same molecular building blocks, such results were expected. Still concerning spectral tunability, **Manuscript I** additionally reported red-shifts of the main emission band of *H*- and *O*-oligo-BODIPYs at higher concentrations. As briefly explained in **Section 4.1.5**, bathochromic shifts on plane conjugated systems like these are commonly attributed to J-aggregates[12]. These features were already observed in other oligomers of the same oligo-BODIPY series, so their presence in *H*- and *O*-oligo-BODIPYs would not be surprising[6,231]. However, the position of the second emission band was identical for concentrated and diluted solutions; moreover, the first emission band displayed a distortion of its shape and a decreased intensity compared to the second one. For these reasons, the observed phenomenon was more likely an artefact determined by inner-filter effect. Nevertheless, if the concentrations in **Manuscript I** will be lowered accordingly, it is likely that J-aggregates can be obtained for the *H*- and *O*-oligo-BODIPYs, too. Also considered the promising characteristics of J-aggregates for *e.g.* sensing applications **(Section 4.1.5),** it would therefore be highly interesting to further investigate this aspect.

As underlined further on in **Manuscript I**, the estimation of quantum yield (QY) is of paramount importance for a complete description of the photophysical properties of a novel fluorophore. In general, the product of QY and extinction coefficient (ε) defines the brightness, therefore the knowledge of both can allow direct comparison between different emitters. Furthermore, in conjunction with time-resolved fluorescence measurements, QYs can shed light into the photophysics of a material, as they provide a mean to determine the radiative and non-radiative decay constants[256]. Experimental setups for absolute QY estimations typically comprise three main elements: a laser beam for the excitation of the sample, a charge-coupled device (CCD) spectrometer for emission detection, and an integration sphere. This last component is crucial as its highly reflecting material allows isotropic redistribution of light and, thus, removes any angular dependence of emission[256]. Although such systems are easily available for the more common visible fluorophores, the same cannot be said for NIR emitters. Indeed, given the low quantum efficiencies of traditional Si-based spectrometers for NIR detection, QY estimations of NIR fluorophores are challenging; moreover, considered that NIR fluorophores are currently not as established in research and clinical applications as Vis-emitters, the number of NIR-optimized QY devices is limited. For these reasons, it should not surprise that QY for *H*- and *O*-dyes and the tetrameric oligo-BODIPY (whose features lied in the border region between visible and NIR wavelengths) could not be detected by Patra *et al.*[6]. For the investigations described in **Manuscript I**, the required specialized equipment was unfortunately not accessible. It was therefore decided to carry out a relative quantum yield estimation based on the protocol by Würth *et al.*[232] This analysis could be performed with more common laboratory spectrometers: this was indeed the case for the measurement of absorption, whereas a home-built NIR spectroscopy setup was employed for emission detection, given the NIR nature of the fluorescence of *H*- and *O*-oligo-BODIPYs. This method comprised calculation steps, such as the evaluation of absorption factors and integral photon fluxes, which could be made with standard analysis software. Above all, fluorophore references with similar absorption and emission features, as well as with comparable solubility in the tested solvents, were required. In this regard, a well-fitting standard for the *H*- and *O*-dyes could have been IR 140 dye. However, as commercially available alternatives, IR-1048 and IR-1061 were used. These dyes could not be dissolved in either dimethylsulfoxide (DMSO) or acetonitrile (ACN), but were soluble in dichloromethane (DCM), therefore QY measurements were carried out only in DCM. Quite importantly, because of the low fluorescent signals recorded at other excitation wavelengths with the employed setup, only one excitation mode (*i.e.* laser at $\lambda_{\text{exc}} \approx 561$ nm) could be used. Due to the low absorbance values displayed by IR-1061 at this excitation wavelength, only IR-1048 could in the end be chosen for reliable QY calculation. Despite these technical limitations, the performed analysis was thorough and the obtained results appeared reasonable when compared to the absolute QYs of the other oligomers[6]. As expected by such systems, larger structures led to lower QYs: in the work of Patra *et al.*[6], absolute values strongly decreased from the monomeric to the trimeric forms, ranging from ≈ 94% in the former case to ≈ 10% in the latter. While these observations validated the collected results, they also suggest that it would be worth performing absolute QY measurements, too. Alternatively, relative QY estimations with different reference dyes and/or excitation wavelengths should be repeated to quantitatively confirm the final values of the acquired dataset.

In the following portions of **Manuscript I**, the focus of the investigations was set on NIR fluorescence imaging. It was already known that these benzene-fused species present high chemical stability in air and enhanced robustness against reversible reduction and oxidation cycles[6]. However, the photostability was an aspect which had not been addressed so far. According to the results collected at the remote imaging detection setup, the NIR fluorescence of both *H*- and *O*-dyes was indeed stable in air and did not show photobleaching within the time window of the experiments. Furthermore, a simple LED lamp was sufficient for excitation, and clear signals could be detected from the NIR-II region after installation of the necessary long-pass filters. As reported in literature for several other commonly employed fluorophores (*e.g.* ICG[12,31]), efficient detection of the off-peak tail emissions can be clearly exploited for multiple applications. These findings indeed strongly suggest that the *H*- and *O*-oligo-BODIPYs could be implemented as smart inks for *e.g.* security technologies, barcoding or remote biomedical imaging. If higher excitation powers were to be used instead, a decrease of fluorescence intensity over time would be expected as from any organic dye if compared to *e.g.* nanomaterials **(Section 4.1.3, Section 4.1.4)**. It would however be interesting to perform photobleaching experiments with other state-of-the-art organic NIR fluorophores, considered that BODIPY-derivatives similar to the ones employed in **Manuscript I** are known to display a superior stability[42,43,87]. While qualitative trends can be ascertained quite easily, it must be kept in mind, however, that a quantitative comparison of fluorophores is always a complicated task to accomplish. Due to technical limitations, it is not trivial to obtain resonant excitation and optimal emission detection for all players in one setup, therefore absolute claims should be well reasoned: for instance, the employed filters and the detector's quantum efficiency might favor one fluorophore more than the other. Still, the strong fluorescent signal of the *H*- and *O*-dyes that was detected at both the microscopy and the remote imaging setups clearly outlined the high potential of these dyes.

In the final, more applicative part of **Manuscript I**, the coating procedures of the *H*-oligo-BODIPY on beads were described. Organic dyes are commonly coated on microbeads to enhance their typically low QYs and water solubility **(Section 4.1.5)**. Among the commercially available materials, PS beads are very promising for *in vivo* imaging applications for several reasons; these include biocompatibility, mechanical properties and tailorable syntheses with diverse surface chemistries[257]. Next to PS beads, also SiO_2 ones were successfully coated, proving the versatility of the extended benzene-fused oligo-BODIPY dye. However, the staining procedure itself needed to be tailored: while the silica beads were resistant to the employed organic solvents and thus allowed facile mixing and evaporation steps, the PS beads proved to be very sensitive. As described in the Experimental Section of **Manuscript I**, a different method was therefore followed to avoid dissolving the PS, while, at the same time, allowing dissolution of the highly unipolar NIR dyes. This method exploited the miscibility of methanol (MeOH) and diethyl ether (Et_2O), which were able to solubilize the PS beads and the oligo-BODIPY, respectively. Finally, fast evaporation steps of Et_2O could prevent any damage to the PS structure.

H-coated PS dyes prepared as described above were then introduced for microrheological proof-of-principle experiments into a biological-mimicking environment: actin networks. This globular protein plays a role of paramount importance in most eukaryotic cells and its viscoelastic properties are subject to numerous studies in the biological field[258,259]. Typically, these studies rely on video particle tracking based on the Generalized Stokes-Einstein equation and the Fluctuation Dissipation Theorem[259,260]. Within this theoretical frame, the Brownian motion of *H*-dye-labelled beads could be successfully quantified in terms of MSD and then converted to shear moduli. Those beads could in this way reveal the concentrations of the actin samples in agreement with the Tube Model's scaling law[259]: this result clearly showcased the potential of the used dyes for biological labelling. Furthermore, the following experiments performed during continuous excitation underlined the biocompatible traits of these novel NIR dyes. It is indeed known that visible organic fluorophores can generate free oxygen radicals; furthermore, prolonged excitation itself can also lead to photodamaging of actin filaments[261,262]. In most cases, both factors represent experimental issues that can compromise the outcome of microrheological studies and, in general, limit the applicability of the employed dyes. The lower degree of actin measured in **Manuscript I** for the *H*-coated beads therefore represents an additional important selling point for these fluorophores. Analogously to what observed also for other BODIPY-derivatives[43], it could be that this better performance compared to the control (Vis) dye was determined by the low yield and/or inaccessibility of triplet states. More theoretical studies could perhaps shed more light in this direction. Alternatively, the repetition of these experiments with other Vis dyes of high QY and therefore low intersystem crossing (*e.g.* rhodamines) could help to better evaluate the already high promises of extended benzene-fused oligo-BODIPYs for biophotonics.

Overall, **Manuscript I** successfully outlined the *H*- and *O*-dyes as promising NIR fluorophores for various state-of-the-art applications, including bioimaging and biosensing.

6.2 Egyptian Blue: An Ancient Pigment for Novel Bionanotechnologies

With the protocol reported in **Manuscript II**, Egyptian Blue (EB) could be exfoliated into nanosheets (NS) of diameters well below 1 µm. This result represented a clear improvement in the preparation of small nanoparticles compared to so far reported studies. As for other 2D materials, the exfoliation of the layered structure of EB is likely to be further optimized by the employment of more chemical approaches which could make use of *e.g.* surfactants and milder bath sonication[90,100,105,172]. These approaches could lead to NS of just few layers of thickness and with more regular geometries. In terms of size distribution, a more controlled cut-off by means of filtration and/or centrifugation steps could further improve monodispersity of the so-obtained samples. With the same protocol reported in **Manuscript II**, also HB and HP were exfoliated into HB-NS and HP-NS, however the focus of this work was centered on EB only. Further optimization of the exfoliation of all three silicates was addressed in a follow-up project **(Manuscript III, Section 6.3)**.

The finding that NIR fluorescence is retained in the nanosheet form is of paramount importance. It is known that size changes can strongly impact emission of other important platforms for NIR bioimaging such as SWCNTs[263] and TMDs[95,111], and therefore require attention. The finding that EB-NS did not display any peak shift in the fluorescence after exfoliation highlights the possibility of employing them as robust reference signal for *e.g.* ratiometric sensing[223,264]. Furthermore, as for the bulk materials, these NS were characterized by long fluorescence lifetime values in the µs regime (≈ 10^4 longer than QDs, ≈ 10^6 longer than SWCNTs)[66]. These are a consequence of the parity-forbidden nature of the electronic transition **(Section 4.3)**, given that the local D_{4H} symmetry of the copper ion features an inversion center[182]. Long excited state lifetime can unlock different possibilities for efficient sensing schemes, as extensively done with *e.g.* lanthanide complexes[22,66]. This direction of research was further expanded in **Manuscript III (Section 6.3)**.

It is known that bulk EB exhibits a QY ≈ 11%[206], which is exceptionally high compared to several state-of-the-art NIR fluorophores[1,2,11]. However, the QY of the exfoliated counterpart (EB-NS) has not been investigated so far and should thus be measured in future works with specialized equipment **(Section 6.1)**. Although neither absolute nor relative QY measurements were performed in **Manuscript II**, information on size-dependence of the NIR emission was provided by fluorescence saturation measurements and correlative studies. The former provided a size estimation for a typical resolution-limited NS and also showed that EB-NS were not saturated at the highest laser powers available in the employed setup (250 µW). This result suggested that the long fluorescence lifetime does not penalize the absorption of more photons, however further experiments at even higher laser power densities would shed more light in this direction. Correlative studies, on the other side, unequivocally demonstrated that EB-NS down to few tenths of nm in size still display a strong fluorescent signal. While their results represent a crucial step forward in the comprehension of how fluorescence scales with size, some points have to be addressed in the future to further refine this dataset. The SEM-NIR dual imaging, which enabled a direct visualization of fluorescent resolution-limited NS, appears to be the most straightforward and robust approach since it does not require any theoretical calculation. However, in order to not affect surface morphology, EB-NS were not coated with gold or any conductive material; this resulted in electrical charging of the NS during SEM imaging, which complicated the measurements of the smallest particles. Furthermore, this approach did not explicitly account for the height of the EB-NS structures, as it just focused on the x and y dimensions. For this reason, it would be ideal to couple a NIR detection setup to an AFM: in this way it could be possible to obtain a robust 3D dataset which accounts for the entire volume of fluorescent nanostructures. The particle tracking approach, on the other side, did not need imaging at multiple setups, however geometrical assumptions had to be made. Analogously to what done for *e.g.* SWCNTs[265], a geometrical correction factor had to be applied to the Stokes-Einstein equation to account for the anisotropic morphology of the NS. The reliability of this correction factor was cross-checked with a diffusion simulation of spherical *vs.* ellipsoid particles in a specific software (COMSOL). Moreover, to account for the temperature- and concentration-dependence of glycerol's viscosity, independent measures had to be carried out in parallel with a rheometer. A power-law fit performed on the collected data indicated that the fluorescence intensity scaled with the square root of the particle diameter. Although a trend was clearly observable and the signals for structures down ≈ 10 nm were robustly detected, a spread in the dataset with regards to the fluorescence intensity was observed. This was most likely determined by the out-of-focus movements and rotations of freely-diffusing particles, as well as by the heterogeneous NS heights. While the former aspect is an intrinsic limitation of this method, the latter could be improved with more monodisperse samples.

The high photostability of EB-NS outperformed organic dyes from several points of view. The observed lack of fluorescence shifts in the presence of redox molecules and copper chelating agents, as well as the absence of both fluorescence polarization and photobleaching represent some of the main traits that define an excellent bioimaging label. The focus of **Manuscript II** then moved to proof-of-principle bioimaging applications of EB-NS in biological systems of interest. Before targeting cellular structures with fluorophore labels, it is indeed important to verify the fluorescence behavior of EB-NS in a biological environment, both on a microscopic and macroscopic scale. Thanks to the outstanding emission features described above, it was indeed possible to perform long-term imaging of EB-NS in a simple biological *in vivo* system: embryos of fruit flies. The *Drosophila melanogaster* species is a model organism whose biological mechanisms are under constant investigations and are of high interest for fundamental genetics and developmental cell biology[266]. During their developmental stage, embryos arrange their nuclei to form regular 2D arrays linked to the actin cortex of the plasma membrane. The motion of the nuclei is mediated by microtubules and the actin cortex[267], therefore the possibility of tracking such movements with fluorescent labels is appealing. Unfortunately, *Drosophila* embryos are normally challenging to image due to autofluorescence in the visible region and the high sensitivity to phototoxicity. In light of such issues, the outstanding photophysical properties of EB-NS allowed efficient long-term imaging of the embryos *in* *vivo*. Furthermore, even though only with an InGaAs camera it was possible to perform video-rate imaging (up to 100 Hz) of EB-NS and to detect signals up to 200 fps, Si-based cameras could be quite flexibly used, too. The strong NIR-I fluorescence signal indeed allowed acquisitions with reasonably high frame rates (50 Hz) also for such detectors; in this way, a reliable MSD dataset at ≈ 10 fps could be acquired using the same camera for both NIR (EB-NS) and Vis (GFP) signals. Inspired by a recent study performed with SWCNTs[268], EB-NS could successfully probe the extracellular space between nuclei. Given that the tails of the distribution in Van Hove histograms went beyond the Gaussian function fit (*i.e.* thermal motion), the measured trajectories of EB-NS were determined by active matter behavior. These flow or motor-driven contractions could be caused by microtubules and kinesin motors in the proximity of the imaged nuclei. Furthermore, according to the collected data, EB-NS closer to the nuclei showed smaller displacements, likely due to a denser environment. Although this first *in vivo* application of EB-NS as bioimaging fluorophore clearly demonstrated the high promises of EB-NS, further improvement is likely to be achieved with surface functionalization. Indeed, as in the case of remote fluorescence bioimaging experiments in plants, injected EB-NS were not bearing any particular chemical moiety on the surface which could allow targeted imaging. Although unspecific binding proved to be enough to detect active matter behavior in the embryos and allow imaging in plants, the outlined results set the basis for further decoration of EB-NS with functional groups specifically binding to *e.g.* microtubules or other structures of interest. Such an approach could broaden the spectrum of possibilities for such class of studies. The importance of surface functionalization is further explained in **Manuscript IV (Section 6.4)**.

In remote detection setups, the bright fluorescence of EB-NS compared to *e.g.* ICG and SWCNTs further stands out. Indeed, in such stand-off setups, fluorophores must display a particularly intense emission to be robustly detected, because only a small amount of emitted light reaches the detector (≈ 20 cm distance between sample and camera). This requirement becomes even more challenging if autofluorescent samples such as plant leaves are imaged. The fact that EB-NS emit a bright fluorescence within the NIR-I window implies that also cheap home-built setups with CMOS cameras, as the one used in **Manuscript II**, can be robustly employed for such purposes. This finding further highlights the versatility of detection of EB-NS emission.

Finally, according to the performed cell toxicity assays the amount of cytotoxic Cu^{2+} released by biologically relevant concentrations of EB-NS seemed to be neglectable compared to *e.g.* $CuSO_4$. Although past studies[225–228] have reported significant release of Cu^{2+}, the employed concentrations of EB-NS were in these cases also significantly higher (difference of ≈ 1-2 orders of magnitude). Moreover, the released amount of bioactive Cu^{2+} did not present side effects in the corresponding cell studies, but rather promoted angiogenesis. The dataset collected in **Manuscript II** therefore further suggests that, under experimental conditions which are biologically relevant for *in vivo* bioimaging, the released Cu^{2+} is not cytotoxic. Nevertheless, studies with longer time windows are needed to fully verify this finding for future *in vivo* applications. It is likely that the lower ion release compared to $CuSO_4$ and the high photostability of EB-

NS towards quenching molecules are due to the fact that the copper ions are well shielded within the crystal structure and, therefore, not easily accessible.

Considered the excellent chemical and photophysical properties, as well as the proof-of-principle applications in the bioimaging field described in **Manuscript II**, EB-NS therefore present all the characteristics necessary to be regarded as outstanding NIR fluorophores for various future works.

6.3 Egyptian Blue, Han Blue and Han Purple: Novel Fluorophores for Fluorescence (Lifetime) Bioimaging and More

With the goal of increasing exfoliation yields and obtaining more uniform samples, the exfoliation method reported in **Manuscript II (Section 5.2.2)** could be further improved. **Manuscript III** presents a reliable protocol to assess well-defined NS fractions. Concerning processability, all experimental steps in this work were performed in water, so to remove the presence of organic solvents which might hinder biological applications. Concerning size distribution, the size cut-off step *via* syringe filtration was avoided: while on one side this could quite robustly yield EB-NS below *e.g.* 200 nm, the yield was unfortunately low. This inconvenience was likely due to clogging of the filter meshes by means of larger NS in the sample. For this reason, in **Manuscript III** centrifugation steps were preferred: the chosen settings, which were calculated from a corrected version of the Stokes equation[269], yielded more monodisperse samples of diameter < 1 µm. The lower tails of the so-obtained size distributions stretched down to few tenths of nm in lateral size and to the monolayer regime in height. This is the first report of these copper silicate NS with such narrow and uniform dimensions. The fact that the NS population could efficiently be described with a log-normal fitting function is a clear indication of fragmentation, which implies the presence of high (shear) stresses during milling and/or sonication. To this regard, as first observed for EB-NS in **Manuscript II**, this high-energy exfoliation protocol leads to NS of irregular morphologies. As previously suggested, promising methods for the yield of resolution-limited NS of more homogeneous geometry could be represented by milder procedures such as bath sonication together with cationic surfactants (*e.g.* CTAB[219,220]).

The focus of this dissertation is however mostly set on the photophysical properties of EB-NS, HB-NS and HP-NS. In terms of preservation of absorption and fluorescence features, the same considerations made for EB-NS in **Manuscript II** can be applied here for HB-NS and HP-NS. More precisely, neither significant excitation/emission wavelength shifts nor photobleaching events were observed. Furthermore, resolution-limited NS were still fluorescent, meaning that the photophysics of all three layered silicates is robust enough to endure exfoliation without losing the characteristic optical features. However, an important aspect necessary to get the full picture of the photophysics of these nanomaterials could not be covered in **Manuscript III**: the QY. Analogously to what was said for EB in **Section 6.2**, bulk measurements have been reported in past studies for HB (QY ≈ 6.9%[196]) and HP (QY ≈ 0.9%[195]), but are lacking for the NS counterparts. The outlined work of this thesis sets the basis on which such specialized measurements can be carried out in the future. It would certainly be interesting to compare the QY of these NS with other Si-based nanomaterials such as Si NPs[270]: these nanocrystals are known to emit a long-lived (µs range) NIR-I fluorescence whose main features (λ_{max}, QY and τ) are known to change with particle size and surface functionalization. Useful insights on the photophysics of EB-NS, HB-NS and HP-NS were nevertheless obtained by measurements of the excited state lifetime. A main portion of **Manuscript III** was dedicated to the investigation of this specific aspect of fluorescence which can be robustly exploited for bioimaging.

For a deeper understanding, both time-domain (TCSPC) and frequency-domain measurements were carried out with either advanced and customized microscopy setups or simple and commercially available detectors. To study fluorescence lifetime during frequency fluorescence lifetime imaging (FLIM) acquisitions, a specific home-built microscopy system was developed, which collected lifetime values by recording the delay of the fluorescence signal in relation to the modulated laser excitation. Differently from scanning methods where lifetimes are measured pixel by pixel, this solution allowed to directly obtain fluorescence lifetime images. The clear decrease in τ values observed in both time- and frequency-domain datasets could be ascribed to changes in the NS symmetry and/or to the presence of defects which could have been introduced during the exfoliation steps. Although amorphization of the crystal structure had been excluded according to earlier XRD investigations on milled EB-NS, the incorporation of local defects is in these circumstances possible and is known to directly affect fluorescence lifetime[221,271,272]. It could indeed be that non-radiative decay pathways were in this way enabled and/or radiative rate constants were increased. Nevertheless, the recorded lifetime values for all NS were still in the µs range and, thus, several orders of magnitude longer than typical dye-based fluorophores. Additionally, the analysis of different regions of the FLIM phasor plots shed further light towards the understanding of NS lifetime. Such plots display the frequency-domain lifetime data according to the calculated phase angle (φ) and modulation ratio (M) for each camera pixel. This revealed that the NS silicates can be easily identified according to their lifetimes and that size-dependent subpopulations exist within the samples. Quite importantly, the first finding could be confirmed also by installing the same FLIM camera in a simple home-built remote detection setup: although a quantitative analysis was not possible here due to camera calibration issues, the so-obtained uncalibrated lifetime values could still clearly show an improved contrast and an easy distinction between EB-NS, HB-NS and HP-NS. These results clearly open up several opportunities for lifetime engineering of these NS in the biomedical field[22]. For instance, the possibility to cut-off short-lived background fluorescence and yield better contrast during imaging sessions can be extremely advantageous. Besides that, fluorescence lifetime is a powerful tool for bioimaging, biosensing and multiplexing: indeed, the excited state lifetime can also be used to monitor fluorophore functional changes caused by environmental factors. In this way, FLIM represents a complementary imaging method to the traditional fluorescence intensity-based measurements[22,66].

Analogously to what done with EB-NS in **Manuscript II**, fluorescence intensity-based remote detection of HB-NS and HP-NS was tested, too. Measurements performed with an InGaAs camera confirmed once more that these silicates are robust emitters. For example, the fluorescent signal appeared stable for a period of time ranging from several minutes to hours. Moreover, fluorescence seemed to be not affected or to not display a significant decrease due to the presence of buffer, acidic pH and ionic species. In order to get more insights in this direction, follow-up works with longer time windows ($t > 1\text{-}2$ h) are recommended. More colloidal stability tests might also reveal differences among the NS samples that are known from the bulk counterparts, *e.g.* the instability of HP in the presence of even weak acids[180]. If this sensitivity of HP-NS to acidic pH were to be confirmed, the design of biosensors for applications in biological environments of variable acidity (*e.g.* leakage detection of the gastrointestinal tract) could be envisioned[10]. In terms of colloidal stability, steps forwards can certainly be made by means of surface functionalization **(Manuscript IV, Section 6.4)**. Nevertheless, a clear improvement in **Manuscript III** was already observable by naked eye compared to the work in **Manuscript II**, since sedimentation processes were significantly slowed down. This was most likely due to the higher presence of smaller NS in the new samples. Such kind of long-distance imaging modality can however also be employed to mimic the requirements for *e.g.* image-guided surgery or remote detection of fluorescent barcodes. Fluorescence intensity-based measurements performed at the same remote detection setup proved that the emission of EB-NS, HB-NS and HP-NS can be detected through several mm of tissue. Even though the collected data is definitely promising, better results could likely be achieved with higher light intensities (*e.g.* laser illumination instead of the chosen LED) and in FLIM mode (which was not performed in this work due to technical issues with the corresponding camera). Furthermore, the NIR-I nature of the NS fluorescence does not allow EB-NS, HB-NS and HP-NS to share the same optimal tissue penetration of NIR-II players, *e.g.* SWCNTs[14] **(Section 4.1)**. In this regard, the slightly red-shifted fluorescence of HB(-NS) measured in **Manuscript III** is more appealing. However, it is likely that the breakthrough in red-shifting fluorescence into the NIR-II region will be achieved by tailoring material doping, as already outlined by some promising works in literature[273–275].

In conclusion, the cytotoxicity assays performed on three different cell lines with biologically relevant NS concentrations (0.0001-0.1 mg/mL) demonstrated the biocompatible nature of all three silicates on a time scale relevant for acute toxicity. Again, longer time windows and/or elemental analysis including inductively coupled plasma-mass spectrometry (ICP-MS) or inductively coupled plasma-optical emission spectrometry (ICP-OES) could be performed in the future to validate the promising trend observed with these NS as NIR contrast agents. As hypothesized for EB-NS in **Manuscript II**, the well-shielded environment around the copper ions most likely limits their release into the cell medium compared to similar systems.

The findings reported above underline that EB-NS, HB-NS and HP-NS present the potential to be employed in future works both as robust reference signals and versatile sensors. Additional directions for sensor design could indeed be investigated, as, for instance, the detection of siderophores[276–281]. These are small high affinity chelating molecules that are produced by microorganisms (*e.g.* bacteria and fungi) for the acquisition of an essential nutrient, *i.e.* iron. Some siderophores in particular (*e.g.* pyoverdine and pyochelin) are known to bind (chelate) several other metals besides iron, including the copper ion (Cu^{2+}) present in all three silicate NS. Recent studies have shown that EB-NS can be employed as reference signal for ratiometric detection of metabolites and virulence factors (including siderophores) which were released from bacteria[223]. However, preliminary tests performed on smaller NS with pyoverdine from bacterial strains seemed to show an effect on their optical properties, suggesting that the Cu^{2+}-chelating action of pyoverdine and similar molecules might influence the photophysics of the smallest NS. Another very promising sensing concept that could be investigated in the future is represented by fluorescence manipulation with metallic nanoparticles[282–286]. It is known that such systems (*e.g.* gold NPs) are able, thanks to their strong plasmon field, to affect the fluorescence of nearby fluorophores, leading either to quenching or enhancement. This effect is highly sensitive to a large number of parameters, including the wavelength of the incident light, particle size, nature of the metallic element, distance from the nanoparticle, the surrounding medium and surface functionalization. In this way, this phenomenon could be explored for novel sensing schemes with EB-NS, HB-NS and HP-NS. However, the plethora of experimental variables that determine field-enhancement or quenching make the tailoring of this effect quite challenging. Collected preliminary results were indeed non-conclusive, as mostly random fluctuations of fluorescence of EB-NS were observed. Future works could focus on the implementation of better-defined sizes of NS and Au NPs, as well as (3D-printed) polymeric scaffolds: these structures could allow a better control over the mutual orientation of the nanoparticles and perhaps lead to applications as mechanical sensor.

As will be described in **Section 6.4**, the number of potential NS bioimaging and biosensing applications can exponentially increase as soon as the surface chemistry will be tailored. Considered the outstanding chemical and photophysical properties of the described EB-NS, HB-NS and HP-NS, it is to be expected that these novel players will be extensively employed in future works for bioimaging applications and more.

6.4 The Si-H Activation Approach: Covalent and Versatile Chemistry for Surface Functionalization of EB-NS

The core message described in **Manuscript IV** is that the already promising properties of EB-NS for the biomedical field would drastically benefit from the tailoring of surface functionalization. Silicates as well as most of the inorganic (2D) nanomaterials are indeed typically hydrophobic and chemically inert[109,111,112,234]. In order to increase colloidal stability and biocompatibility, and to specifically target biological structures, a tailored surface modification with functional handles is therefore required. In **Manuscript IV**, functionalization of EB-NS (EBfunc) with chemical moieties including pyrene (Pyr) and carboxylic acid (COOH) was performed. The chosen grafting approach, based on Si-H activation of hydrosilanes[248], presents high potential. First of all, differently from other non-covalent approaches, the robustness of covalent grafting implies that so-functionalized systems are not affected by dynamics in the biological environment. Secondly, the grafting reaction could be performed at room temperature, was fast and a reaction indicator (*i.e.* the characteristic hydrogen evolution) could be followed by eye. Furthermore, hydrosilanes present high stability and are thus easier to handle compared to other more sensitive coupling agents. Last but not least, the approach of Moitra *et al.*[248] is highly versatile, given the plethora of available functional groups that can be grafted with this method. Such broad spectrum of possibilities can lead to multiple exciting opportunities for the employment of EB-NS in biomedicine, as will be outlined in the final paragraphs of this section.

The first chemical moiety to be covalently bond on EB-NS in **Manuscript IV** was pyrene. As observable, from the acquired 2D spectra, the position of the characteristic NIR fluorescence of EB-NS was untouched after functionalization. This is a very important finding that underlines the outstanding robustness of the silicate's photophysical properties. Additionally, it also suggests the absence of energy transfer events between Pyr and EB-NS. Indeed, although both radiative and non-radiative energy transfers between pyrene and other chromophores have been extensively reported and could unlock novel interesting properties, the Pyr fluorescence and the EB-NS absorption did not display the required spectral overlap[250,287,288]. Although it seems like the photophysics of EB-NS was not affected by functionalization, follow-up works should also address QY measurements. For instance, as mentioned in **Section 6.3**, a clear dependence of QY and lifetime from functionalization was reported for NIR-emitting Si nanocrystals[270].

Besides the mentioned spectroscopy, the pyrene dataset was validated by diverse characterization tools, including fluorescence microscopy and ssNMR. The COOH-functionalized EBfunc, on the other side, was uniquely addressed in **Manuscript IV** by zeta potential measurements. Considered that acidic groups tend to dissociate in water at neutral pH, the presence of COOH on the already negatively charged surface of EB-NS could be revealed by a further decrease in the zeta potential[278,289]. Furthermore, this characterization method could confirm the increased colloidal stability after functionalization: indeed, in agreement with the DLVO theory[290,291], a higher degree of particle repulsion (*i.e.* lower formation of aggregates) results in higher absolute values of the zeta potential. Although these observations already strongly suggest the positive outcome of the grafting of carboxyl groups on EB-NS, this dataset could still benefit in future works from additional characterizations. For a more qualitative and quantitative information on the grafting yield, fluorophore coupling *via* classical amide chemistry could certainly be insightful[234,292]. A first attempt was made with amine-bearing visible fluorophores following established coupling chemistry routes[292–294]. For this task, both cyanine-3-amine (amino-Cy3) and sulfo-cyanine-3-amine (sulfo-amino-Cy3) were tested. A screening of different experimental parameters was carried out: tested coupling agents included 1-[bis(dimethylamino)methylene]-1*H*-1,2,3-triazolo-[4,5-*b*]pyridinium hexafluorophosphate (HATU)[294], *N*-ethyl-*N′*-(3-dimethylaminopropyl)-carbodiimide hydrochloride (EDC·HCl) and 1-hydroxybenzotriazole hydrate (HOBt)[293], together with the aprotic base *N,N*-diisopropylethylamine (DIPEA). Unfortunately, washing steps to remove excess (unbound) Cy3 have resulted more challenging than foreseen: indeed, even after several days of dialysis, Cy3 molecules could be detected in high amount during Vis-NIR colocalization experiments in both EBfunc and noCAT samples. This was likely due to the presence of electrostatic interactions between the negative surface charges of the silicate NS and the positively-charged amino groups of the chosen dye. For this reason, harsher washing steps with buffers of higher ionic concentration, the employment of positively-charged antagonist molecules (*e.g.* CTAB[289]) or the choice of a different fluorophore (*e.g.* OH-bearing dyes to be coupled with EB-NS *via* Fischer esterification) could represent next steps to take in the direction of successful fluorophore coupling.

In order to further prove and better quantify covalent functionalization of EB-NS with carboxyl groups, additional analytical tools can be considered in the future. X-ray photoelectron spectroscopy (XPS) is a standard technique that is routinely used to measure surface accessible groups of multiple (nano)structures, and is therefore worth testing on COOH-functionalized EBfunc. Also other techniques such as small-angle neutron scattering (SANS) and energy-dispersive X-ray spectroscopy (EDX) can typically provide information on the surface of nanomaterials[295,296]. EDX can typically perform reliable elemental mapping for several materials, however it would suffer from low sensitivities if it were to be used for the detection of COOH signals on the NS structures. Alternatively, solid-state NMR (ssNMR) could be employed analogously to what was done with the Pyr-functionalized EBfunc dataset. Although with this method it was possible to detect the relevant features of pyrene, the overall signals were however challenging to acquire and interpret. Despite the implementation of optimized acquisition settings (*e.g.* a higher number of scans), the noise could not be reduced as hoped for. This is likely due to the fact that the grafted pyrene moieties, although present, were in significantly lower numbers if compared to the entire (bulk) volume of a typical NS structure. Most likely because of the same reason, ssNMR did not result successful for the analysis of COOH-functionalized EBfunc. Considered that in this work larger EB-NS (ranging from a few microns to tenths of nm) were chosen as starting material, a possible way to increase the ssNMR could be to increment the surface area by employing NS well below 1 μm in size. Alternatively, plasma treatment of EB-NS prior to grafting could also lead to a higher number of Si-OH bonds on the surface[297,298]. Furthermore, the use of functional linkers and/or labels with isotopic patterns could help to unambiguously prove the functionalization. A simple option in this direction could be the employment of highly enriched ^{13}C-labelled CO_2 for the Grignard reaction; in this way, the expected drastic signal enhancement would allow a much easier detection of the COOH moiety.

In the final section of **Manuscript IV**, a proof-of-principle application of targeted imaging on cells was presented. The typical upregulation of the folate receptor in specific cancer cells was exploited for this study; more precisely, HeLa cells were chosen due to the characteristic high amount of FRα on their cell membranes. In this way, targeted imaging of these cells with FA-conjugated EBfunc could be verified. Although the collected results were promising and showed a clear trend, more statistics is definitely required to quantitively assess the targeting efficiency. It must be underlined, however, that labelling of HeLa cells is absolutely not the only possible outlook enabled by the performed chemistry. An alternative bioapplication of COOH-functionalized EBfunc could be represented, for example, by conjugation to a peptide sequence. It is well known that peptide-motives are straightforward to synthesize, non-immunogenic and chemically tailorable handles for biological targeting[299]. Among them, the arginine-glycine-aspartic sequence (RGD) displays high and specific affinity to $\alpha_v\beta_3$ and $\alpha_v\beta_5$ integrins, which are typically overexpressed on the membrane of tumorous cells and have thus been exploited for *e.g.* drug delivery and targeted imaging in numerous studies[289,300–304]. Established conjugation protocols that address NH_2 groups of (cyclic) RGD peptides could thus be adapted and applied to COOH-functionalized EBfunc to allow specific binding of the silicate NS to membranes of *e.g.* human leukemia HL-60 cells[130,302,305,306]. Additionally, several other viable bioconjugation routes exist[234,300]. Antibodies[307,308] and nanobodies[309–311] are extensively used in clinical applications and are in most cases conjugated *via* their lysine amines. Conjugation of single- or double-stranded DNA, which would be achievable by means of commercially available cross-linkers, represents another option that could further broaden the spectrum of probing applications in biological systems[312]. Furthermore, DNA and RNA aptamers[313,314] are also commercially available and can be engineered to bear a single accessible amine at one end of the molecule; this feature would enable a higher degree of control during the coupling steps.

While the focus was so far mostly set on labelling applications, it has to be pointed out that there can be much more to that. Indeed, surface modifications can also allow the design of sensitive nanosensors and multifunctional platforms. For instance, as performed on similar systems such as NIR-emitting silicon nanocrystals[270], the fluorescence lifetime of functionalized EB-NS[216] could additionally be investigated *in vitro* and *in vivo* in terms of *e.g.* pH dependence; next to that, time-gated biological imaging could drastically increase contrast[66]. Considered that EB-NS has been reported to be a very efficient photothermal agent[225,226], targeted imaging could be followed by treatment of tumorous cells (*e.g.* human prostate cancer cell lines[315]) or bacteria[316,317]. Although mannosilation is quite routinely performed for virus capturing and detection, a few bacterial species also present the necessary receptor on their surface; for these reasons coupling of COOH-functionalized EBfunc with *e.g.* mannosamine could lead to novel applications for both virus and bacteria detection[318–321]. Finally, the versatility of the functionalization strategy that was chosen for EBfunc can be further exploited: indeed, the same chemistry can be applied to silanes bearing various functional groups of diverse chemical nature[248]. In **Manuscript IV** carboxyl groups were grafted onto the surface of EB-NS due to foreseen improvement in colloidal stability and the numerous bioconjugation possibilities that COOH-functionalized EBfunc could be employed for, as described above. To mention some alternatives, amine-bearing allyloxycarbonyls (R = NH-Alloc) could allow peptide conjugation, whereas, by grafting azides ($R = N_3$), a standard technique for bioconjugation such as the strain-induced or copper-catalyzed azide-alkyne (Huisgen) cycloadditions could be used for *e.g.* labeling with antibodies. If thiol groups (R = SH) or pyrene were to be decided for, then respectively covalent and non-covalent conjugation to SWCNTs would become possible: in this way, the different spectral features of SWCNTs or other sensitive dyes could be exploited together with EBfunc for *e.g.* ratiometric detection and multispectral imaging.

From what outlined above, it is clear that the successfully performed covalent functionalization of EB-NS can open multiple doors in diverse research directions. Taken into account that even more (bio)conjugation options exist in literature[234] and considered the highly promising chemical and photophysical properties of EB-NS, it is to be expected that this novel fluorophore will be extensively employed in future biomedical studies.

7 | Conclusions

In the last decades, the design of novel NIR-emitting materials and molecules for biomedical applications has gained increasing interest in the scientific community. This is due to their optimal photophysical properties, which allow high tissue penetration, better contrasts and lower phototoxicity. By means of optimized preparation routes, thorough characterization studies and promising proof-of-principle applications, this doctoral thesis presented novel candidates for bioimaging and more. These belonged to two different classes of materials: BODIPY-based organic dyes and layered silicates **(Figure 7.1)**. Despite their intrinsic structural differences, the species investigated in this work shared outstanding fluorescent features and high promises for numerous state-of-the-art technological fields.

The NIR emission of the hexameric (*H*) and octameric (*O*) forms of extended benzene-fused oligo-BODIPYs were described in **Manuscript I** for the first time. 1D and 2D spectroscopy highlighted their narrow fluorescence bands as well as their broad Vis-NIR absorption, which could be tuned with different concentrations and solvents. The high photostability and brightness of these dyes allowed their robust use as smart inks in remote detection. Furthermore, efficient coating onto PS and SiO_2 microbeads enabled colocalization imaging with Vis-labelled actin filaments. Above all, *H*-coated PS beads could be successfully employed for the first bioimaging application of this group of dyes, *i.e.* fluorescent-based passive microrheology of actin filaments. Quite importantly, the continuous illumination of the hexamer did not lead to significant actin degradation, thus highlighting the biocompatible nature of this class of NIR-fluorescent BODIPY-derivatives. Although **Manuscript I** already contributed to shed further light on the photophysics and the promises of these materials, there is still much that can be done next. Having reported relative QY measurements in this work, absolute QY estimation with specialized equipment could help to better describe the properties of these dyes. If the formation of J-aggregates were to be reported, this could make the employment of these materials as NIR-II fluorophores even more promising. Additionally, the narrow fluorescent features could for example result very efficient for multiplexing schemes. Going further in the direction of potential applications, the performed remote detection imaging sessions suggest that *H*- and *O*-oligo-BODIPYs could be used for barcoding and biological labeling as well as for security technologies. As these are just few directions that can be chosen as follow-up studies of **Manuscript I**, the belief is that this work provided a significant contribution to the general landscape of NIR-emitting organic dyes.

Manuscript II demonstrated for the first time that EB-NS are to be considered highly promising novel fluorophores for biophotonics. A novel exfoliation route based on wet ball milling and tip sonication allowed to prepare NS of lateral sizes below the micron range and of just few layers of thickness. The most important finding of this work is that so-exfoliated NS retained the NIR optical properties of the bulk counterparts. By correlative studies it could be shown that this is true for EB-NS down to just few tenths of nm in diameter. Furthermore, these NS did not show photobleaching and the fluorescence properties were not affected by redox active molecules and typical quenchers. Additionally, the remarkably bright fluorescence could be easily detected in both microscopy and remote detection setups compared to state-of-the-art fluorophores. Thanks to the outstanding intensity and the NIR-I nature of EB-NS emission, high frame rates could be implemented for imaging with both a NIR-optimized InGaAs camera and a much cheaper Si-based one. Besides the barcoding and smart ink applications, **Manuscript II** paved the way for employment of EB-NS in the biomedical field. First of all it was shown that EB-NS do not present cytotoxicity in multiple cell lines. Next to that, this study was the first to report the use of EB-NS for *in vivo* microrheological measurements in fruit fly embryos. Moreover, stand-off detection in plant was easily achievable, again thanks to the NIR emission brightness which clearly overcame leaf autofluorescence. While this work set the foundations of EB-NS as biolabeling agents and clearly demonstrated their applicability with proof-of-principle experiments, it also indirectly implies that more investigations on these layered silicates are required to fully unleash their potential. Improvement of the exfoliation route (as addressed in **Manuscript III**) could lead to even smaller and more monodisperse samples. If well-defined monolayer NS were to be prepared, this could perhaps allow sensing applications in *e.g.* strain-activated systems. While the significantly long (µs range) fluorescence lifetime of the exfoliated NS might also be relied on for the design of sensors, it could certainly be exploited in FLIM mode to enhance the imaging contrast **(Manuscript III)**. Given that it is still not clear how the fluorescence of these novel fluorophores scales with size, follow-up correlative investigations would be worth performing. Considered that the reported *in vivo* experiment was carried out with unfunctionalized EB-NS, surface modification routes could further expand the range of possible biological applications of these layered silicates **(Manuscript IV)**.

In **Manuscript III**, the exfoliation protocol previously applied to EB-NS was optimized and employed also for the preparation of HB-NS and HP-NS. This work represents the first thorough characterization of NS derived from this family of layered silicates. With the chosen exfoliation procedure, monodisperse samples of EB-NS, HB-NS and HP-NS displaying resolution-limited sizes and improved colloidal stability could be obtained. Analogously to what observed earlier for EB-NS **(Manuscript II)**, also HB-NS and HP-NS retained their NIR fluorescence: the observed emission profiles, determined by the shared copper ion in squared planar coordination geometry, appeared very similar to one another, with a slightly red-shifted emission maximum for HB-NS. Quite importantly, all silicates showed no bleaching and were not significantly affected by pH and ionic environments. Furthermore, with the intention of collecting insights on the long-lived fluorescence lifetime of these materials, both lifetime spectroscopy and imaging could be robustly performed with different detection systems, also down to the single-particle level. The intense NIR-I fluorescence of all silicates also enabled easy remote detection during both intensity- and lifetime-based acquisitions. While with fluorescence intensity-based measurements it was possible to demonstrate a significantly high penetration in tissue phantoms, with lifetime-based measurements an enhanced contrast and a clear distinguishable labelling of the NS could be achieved. As required by biomedical applications, EB-NS, HB-NS and HP-NS did not display cytotoxicity at biologically relevant concentrations. These findings thus strongly highlight the potential held by these materials for biological imaging, lifetime engineering and biophotonics in general. In terms of future studies, as mentioned for EB-NS, monolayer samples could be of interest for *e.g.* sensing applications. The implementation of milder techniques such as surfactant-assisted bath sonication could in this regard be advantageous and lead to better defined shapes and sizes. Size-correlation studies and material doping strategies could additionally shed more light on the photophysics of these materials and perhaps allow deeper tissue penetration with the red-shifting of emission.

Finally, the last work described in this dissertation reported the first example of covalent and versatile functionalization of EB-NS **(Manuscript IV)**. This result was achieved by applying an established literature protocol for silica particles which was based on Si-H activation of hydrosilanes. With this surface chemistry, pyrene and carboxyl groups could be covalently bond on the surface of the layered silicates. Quite importantly, this procedure did not affect the excellent photophysical properties of EB-NS, thus once more highlighting the outstanding stability of this material. Pyrene was chosen as first chemical moiety to be tested with this approach because of its characteristic visible fluorescence. In most of the numerous characterization tools which were employed to confirm functionalization, pyrene's signature could in this way provide a robust reference signal. It was then chosen to graft carboxyl groups onto EB-NS with the same procedure because of their biological relevance. COOH-functionalized EB-NS indeed not only displayed an increased colloidal stability, but also enabled successful conjugation of folic acid and consequent targeted imaging of cancer cells. This proof-of-principle biological application is unprecedented and of high relevance for the biomedical field. Considered its covalent nature, this functionalization route is not affected by dynamics of biological environments and is, therefore, very robust. Furthermore, analogously to what done with several other established fluorophores, surface-accessible carboxyl groups can be conjugated to multiple biomolecules of interest, *e.g.* peptide sequences, antibodies, nanobodies, single- or double-stranded DNA, aptamers, *etc.* Additionally, this novel surface chemistry could extend applications well beyond labelling. Indeed, if other relevant properties of EB-NS such as the high photothermal conversion efficiency are considered, the design of multifunctional platforms for photothermal therapy as well as sensing and/or drug delivery becomes now possible. Finally, thanks to the broad library of R groups that can be grafted according to this approach, future works can branch into even more diverse directions. All considered, the study described in **Manuscript IV** defines EB-NS as a versatile novel addition to the library of NIR fluorophores.

In conclusion, this doctoral thesis established novel classes of promising NIR fluorophores for biophotonics. It advances the basic understanding of their photophysics, preparation as well as surface chemistry and showcases applications in imaging with high potential. The author's strong belief is that these new fluorophores will lead to exciting new studies in multiple state-of-the-art technologies.

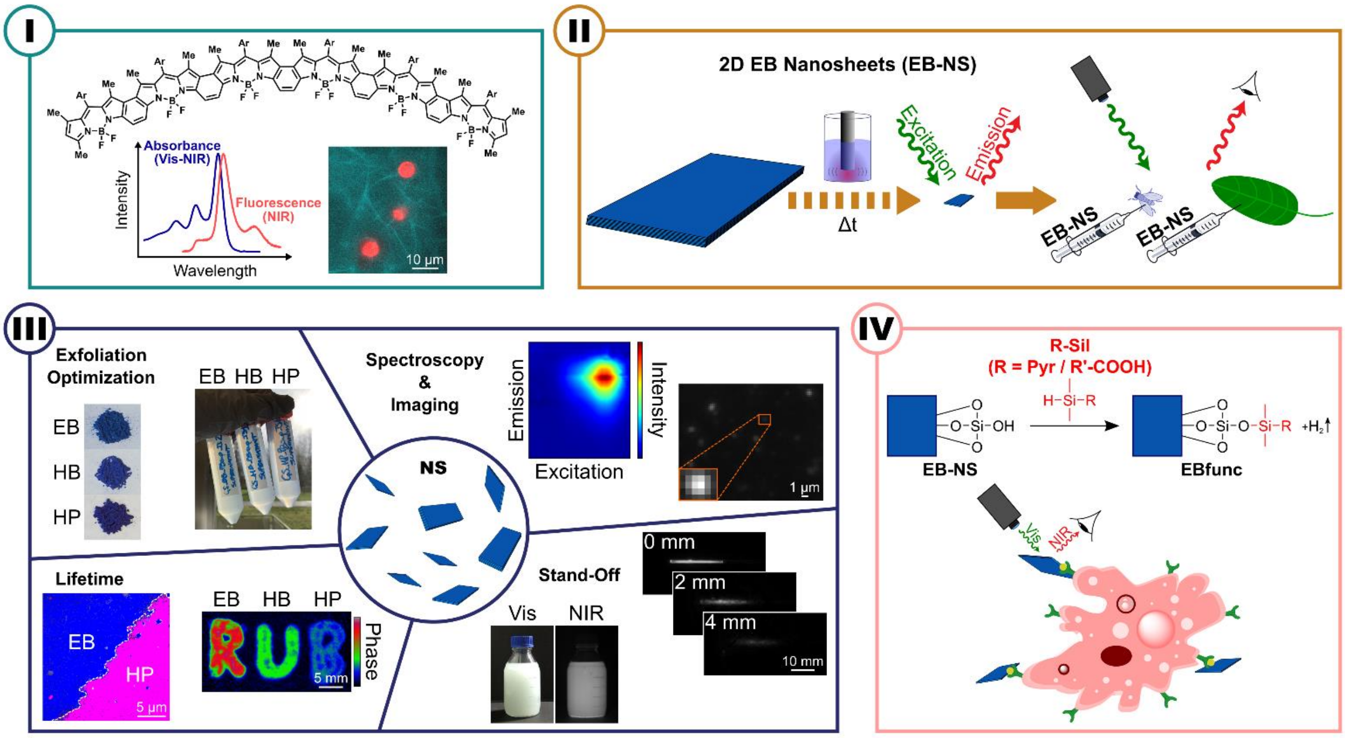

Figure 7.1 Overview of the topics described in this doctoral thesis. *This work focused on the design and characterization of novel near-infrared emitting platforms for biomedical applications.* ***Manuscript I*** *described the emission features of some extended benzene-fused oligo-BODIPYs and outlined the high potential of these organic dyes for e.g. microrheological studies of biopolymers.* ***Manuscript II*** *presented the outstanding photophysical properties of exfoliated EB-NS with proof-of-principle bioimaging applications in fruit flies and plants.* ***Manuscript III*** *further highlighted the promises of EB-NS and the homologues HB-NS and HP-NS by optimizing the exfoliation procedure and thoroughly characterizing the fluorescence properties. Finally, by means of a covalent approach,* ***Manuscript IV*** *outlined the importance of surface functionalization of EB-NS with the first reported example of targeted bioimaging of cells. Adapted with permission from ref.* [322]*. Copyright 2021 Royal Society of Chemistry. Adapted with permission from ref.* [278]*. Copyright 2020 Springer Nature. Adapted with permission from ref.* [216]*. Copyright 2021 Royal Society of Chemistry. Adapted with permission from ref.* [323]*. Copyright 2022 ChemRxiv.*

8 | References

1. Hong, G., Antaris, A. L. & Dai, H. Near-infrared fluorophores for biomedical imaging. *Nat. Biomed. Eng.* **1**, 1–9 (2017).
2. Li, C., Chen, G., Zhang, Y., Wu, F. & Wang, Q. Advanced Fluorescence Imaging Technology in the Near-Infrared-II Window for Biomedical Applications. *J. Am. Chem. Soc.* **142**, 14789–14804 (2020).
3. Benayas, A. *Near Infrared-Emitting Nanoparticles for Biomedical Applications*. *Near Infrared-Emitting Nanoparticles for Biomedical Applications* (Springer International Publishing, 2020). doi:10.1007/978-3-030-32036-2.
4. Smith, A. M., Mancini, M. C. & Nie, S. Second window for in vivo imaging. *Nat. Nanotechnol.* **4**, 710–711 (2009).
5. Selvaggio, G. & Kruss, S. Preparation, properties and applications of near-infrared fluorescent silicate nanosheets. *Nanoscale* (2022) doi:10.1039/D2NR02967G.
6. Patra, A., Patalag, L. J., Jones, P. G. & Werz, D. B. Extended Benzene-Fused Oligo-BODIPYs: In Three Steps to a Series of Large, Arc-Shaped, Near-Infrared Dyes. *Angew. Chemie - Int. Ed.* **60**, 747–752 (2021).
7. Liu, P., Mu, X., Zhang, X. D. & Ming, D. The Near-Infrared-II Fluorophores and Advanced Microscopy Technologies Development and Application in Bioimaging. *Bioconjug. Chem.* **31**, 260–275 (2020).
8. Frangioni, J. V. In vivo near-infrared fluorescence imaging. *Curr. Opin. Chem. Biol.* **7**, 626–634 (2003).
9. Diao, S. *et al.* Biological imaging without autofluorescence in the second near-infrared region. *Nano Res.* **8**, 3027–3034 (2015).
10. He, S., Song, J., Qu, J. & Cheng, Z. Crucial breakthrough of second near-infrared biological window fluorophores: design and synthesis toward multimodal imaging and theranostics. *Chem. Soc. Rev.* **47**, 4258–4278 (2018).
11. Zhao, J., Zhong, D. & Zhou, S. NIR-I-to-NIR-II fluorescent nanomaterials for biomedical imaging and cancer therapy. *J. Mater. Chem. B* **6**, 349–365 (2018).
12. Lei, Z. & Zhang, F. Molecular Engineering of NIR-II Fluorophores for Improved Biomedical Detection. *Angew. Chemie - Int. Ed.* **60**, 16294–16308 (2021).
13. Gong, L., Shan, X., Zhao, X., Tang, L. & Zhang, X. Activatable NIR-II Fluorescent Probes Applied in Biomedicine: Progress and Perspectives. *ChemMedChem* **16**, 2426–2440 (2021).
14. Hong, G. *et al.* Through-skull fluorescence imaging of the brain in a new near-infrared window. *Nat. Photonics* **8**, 723–730 (2014).
15. Diao, S. *et al.* Fluorescence imaging in Vivo at wavelengths beyond 1500 nm. *Angew. Chemie - Int. Ed.* **54**, 14758–14762 (2015).
16. Koman, V. B. *et al.* A wavelength-induced frequency filtering method for fluorescent nanosensors in vivo. *Nat. Nanotechnol.* (2022) doi:10.1038/s41565-022-01136-x.
17. Liu, Y. Y. *et al.* Versatile Types of Inorganic/Organic NIR-IIa/IIb Fluorophores: From Strategic Design toward Molecular Imaging and Theranostics. *Chem. Rev.* (2021) doi:10.1021/acs.chemrev.1c00553.
18. Welsher, K., Sherlock, S. P. & Dai, H. Deep-tissue anatomical imaging of mice using carbon nanotube fluorophores in the second near-infrared window. *Proc. Natl. Acad. Sci. U. S. A.* **108**,

8943–8948 (2011).

19. Bonis-O'Donnell, J. T. D. *et al.* Dual Near-Infrared Two-Photon Microscopy for Deep-Tissue Dopamine Nanosensor Imaging. *Adv. Funct. Mater.* **27**, 1–10 (2017).

20. Dong, B. *et al.* Facile synthesis of highly photoluminescent Ag2Se quantum dots as a new fluorescent probe in the second near-infrared window for in vivo imaging. *Chem. Mater.* **25**, 2503–2509 (2013).

21. Chen, G. *et al.* Revealing the Fate of Transplanted Stem Cells In Vivo with a Novel Optical Imaging Strategy. *Small* **14**, 1–10 (2018).

22. Fan, Y. *et al.* Lifetime-engineered NIR-II nanoparticles unlock multiplexed in vivo imaging. *Nat. Nanotechnol.* **13**, 941–946 (2018).

23. Zhu, S. *et al.* 3D NIR-II Molecular Imaging Distinguishes Targeted Organs with High-Performance NIR-II Bioconjugates. *Adv. Mater.* **30**, 1–8 (2018).

24. Huang, D. *et al.* An NIR-II Fluorescence/Dual Bioluminescence Multiplexed Imaging for In Vivo Visualizing the Location, Survival, and Differentiation of Transplanted Stem Cells. *Adv. Funct. Mater.* **29**, 1806546 (2019).

25. Hu, Z. *et al.* First-in-human liver-tumour surgery guided by multispectral fluorescence imaging in the visible and near-infrared-I/II windows. *Nat. Biomed. Eng.* **4**, 259–271 (2020).

26. Wang, F. *et al.* Light-sheet microscopy in the near-infrared II window. *Nat. Methods* **16**, 545–552 (2019).

27. Owens, E. A., Henary, M., El Fakhri, G. & Choi, H. S. Tissue-Specific Near-Infrared Fluorescence Imaging. *Acc. Chem. Res.* **49**, 1731–1740 (2016).

28. Schaafsma, B. E. *et al.* The clinical use of indocyanine green as a near-infrared fluorescent contrast agent for image-guided oncologic surgery. *J. Surg. Oncol.* **104**, 323–332 (2011).

29. Vahrmeijer, A. L., Hutteman, M., Van Der Vorst, J. R., Van De Velde, C. J. H. & Frangioni, J. V. Image-guided cancer surgery using near-infrared fluorescence. *Nat. Rev. Clin. Oncol.* **10**, 507–518 (2013).

30. Mishra, A., Behera, R. K., Behera, P. K., Mishra, B. K. & Behera, G. B. Cyanines during the 1990s: a review. *Chem. Rev.* **100**, 1973–2011 (2000).

31. Carr, J. A. *et al.* Shortwave infrared fluorescence imaging with the clinically approved near-infrared dye indocyanine green. *Proc. Natl. Acad. Sci. U. S. A.* **115**, 4465–4470 (2018).

32. Cosco, E. D., Lim, I. & Sletten, E. M. Photophysical Properties of Indocyanine Green in the Shortwave Infrared Region. *ChemPhotoChem* **5**, 727–734 (2021).

33. Zhang, R. R. *et al.* Beyond the margins: real-time detection of cancer using targeted fluorophores. *Nat. Rev. Clin. Oncol.* **14**, 347–364 (2017).

34. Choi, H. S. *et al.* Synthesis and in vivo fate of zwitterionic near-infrared fluorophores. *Angew. Chemie - Int. Ed.* **50**, 6258–6263 (2011).

35. Tummers, Q. R. J. G. *et al.* Intraoperative guidance in parathyroid surgery using near-infrared fluorescence imaging and low-dose Methylene Blue. *Surg. (United States)* **158**, 1323–1330 (2015).

36. Troyan, S. L. *et al.* The FLARE^{TM} intraoperative near-infrared fluorescence imaging system: A first-in-human clinical trial in breast cancer sentinel lymph node mapping. *Ann. Surg. Oncol.* **16**, 2943–2952 (2009).

37. Owens, E. A., Lee, S., Choi, J., Henary, M. & Choi, H. S. NIR fluorescent small molecules for intraoperative imaging. *Wiley Interdiscip. Rev. Nanomedicine Nanobiotechnology* **7**, 828–838

(2015).

38. Hyun, H. *et al.* 700-nm Zwitterionic Near-Infrared Fluorophores for Dual-Channel Image-Guided Surgery. *Mol. Imaging Biol.* **18**, 52–61 (2016).

39. te Velde, E. A., Veerman, T., Subramaniam, V. & Ruers, T. The use of fluorescent dyes and probes in surgical oncology. *Eur. J. Surg. Oncol.* **36**, 6–15 (2010).

40. Watanabe, H. *et al.* Molecular imaging of β-amyloid plaques with near-infrared boron dipyrromethane (BODIPY)-based fluorescent probes. *Mol. Imaging* **12**, 338–347 (2013).

41. Quan, L. *et al.* Near-infrared emitting fluorescent BODIPY nanovesicles for in vivo molecular imaging and drug delivery. *ACS Appl. Mater. Interfaces* **6**, 16166–16173 (2014).

42. Loudet, A. & Burgess, K. BODIPY dyes and their derivatives: Syntheses and spectroscopic properties. *Chem. Rev.* **107**, 4891–4932 (2007).

43. Ulrich, G., Ziessel, R. & Harriman, A. The chemistry of fluorescent bodipy dyes: Versatility unsurpassed. *Angew. Chemie - Int. Ed.* **47**, 1184–1201 (2008).

44. Li, Y. *et al.* Design of AIEgens for near-infrared IIb imaging through structural modulation at molecular and morphological levels. *Nat. Commun.* **11**, 1–10 (2020).

45. Sheng, Z. *et al.* Bright Aggregation-Induced-Emission Dots for Targeted Synergetic NIR-II Fluorescence and NIR-I Photoacoustic Imaging of Orthotopic Brain Tumors. *Adv. Mater.* **30**, (2018).

46. Hong, G. *et al.* Ultrafast fluorescence imaging in vivo with conjugated polymer fluorophores in the second near-infrared window. *Nat. Commun.* **5**, 1–9 (2014).

47. Liu, H. Y. *et al.* Quinoxaline-based polymer dots with ultrabright red to near-infrared fluorescence for in vivo biological imaging. *J. Am. Chem. Soc.* **137**, 10420–10429 (2015).

48. Filonov, G. S. *et al.* Bright and stable near-infrared fluorescent protein for in vivo imaging. *Nat. Biotechnol.* **29**, 757–761 (2011).

49. Shcherbakova, D. M. & Verkhusha, V. V. Near-infrared fluorescent proteins for multicolor in vivo imaging. *Nat. Methods* **10**, 751–754 (2013).

50. Soo Choi, H. *et al.* Renal clearance of quantum dots. *Nat. Biotechnol.* **25**, 1165–1170 (2007).

51. Choi, H. S. *et al.* Tissue- and Organ-Selective Biodistribution of NIR Fluorescent Quantum Dots. *Nano Lett.* **9**, 2354–2359 (2009).

52. Zhou, C. *et al.* Near-infrared emitting radioactive gold nanoparticles with molecular pharmacokinetics. *Angew. Chemie - Int. Ed.* **51**, 10118–10122 (2012).

53. Tang, L. *et al.* Theranostic Gold Nanoclusters for NIR-II Imaging and Photodynamic Therapy. *Chem. Res. Chinese Univ.* **37**, 934–942 (2021).

54. Xu, H. & Suslick, K. S. Water-soluble fluorescent silver nanoclusters. *Adv. Mater.* **22**, 1078–1082 (2010).

55. Gao, S. *et al.* Near-infrared fluorescence imaging of cancer cells and tumors through specific biosynthesis of silver nanoclusters. *Sci. Rep.* **4**, 1–6 (2014).

56. Bruns, O. T. *et al.* Next-generation in vivo optical imaging with short-wave infrared quantum dots. *Nat. Biomed. Eng.* **1**, 0056 (2017).

57. Hong, G. *et al.* In vivo fluorescence imaging with Ag2S quantum dots in the second near-infrared region. *Angew. Chemie - Int. Ed.* **51**, 9818–9821 (2012).

58. Gu, L. *et al.* In vivo time-gated fluorescence imaging with biodegradable luminescent porous silicon nanoparticles. *Nat. Commun.* **4**, 1–7 (2013).

59. Park, J. H. *et al.* Biodegradable luminescent porous silicon nanoparticles for in vivo applications. *Nat. Mater.* **8**, 331–336 (2009).

60. Tsukasaki, Y. *et al.* Synthesis and optical properties of emission-tunable PbS/CdS core-shell quantum dots for in vivo fluorescence imaging in the second near-infrared window. *RSC Adv.* **4**, 41164–41171 (2014).

61. Kong, Y. *et al.* Highly Fluorescent Ribonuclease-A-Encapsulated Lead Sulfide Quantum Dots for Ultrasensitive Fluorescence in Vivo Imaging in the Second Near-Infrared Window. *Chem. Mater.* **28**, 3041–3050 (2016).

62. Antaris, A. L. *et al.* A small-molecule dye for NIR-II imaging. *Nat. Mater.* **15**, 235–242 (2016).

63. Jiang, X., Cao, C., Feng, W. & Li, F. Nd3+-doped LiYF4 nanocrystals for bio-imaging in the second near-infrared window. *J. Mater. Chem. B* **4**, 87–95 (2016).

64. Rocha, U. *et al.* Neodymium-doped LaF3 nanoparticles for fluorescence bioimaging in the second biological window. *Small* **10**, 1141–1154 (2014).

65. Gu, Y. *et al.* High-sensitivity imaging of time-domain near-infrared light transducer. *Nat. Photonics* **13**, 525–531 (2019).

66. Berezin, M. Y. & Achilefu, S. Fluorescence lifetime measurements and biological imaging. *Chem. Rev.* **110**, 2641–2684 (2010).

67. Kruss, S. *et al.* Carbon nanotubes as optical biomedical sensors. *Adv. Drug Deliv. Rev.* **65**, 1933–1950 (2013).

68. Hong, G., Diao, S., Antaris, A. L. & Dai, H. Carbon Nanomaterials for Biological Imaging and Nanomedicinal Therapy. *Chem. Rev.* **115**, 10816–10906 (2015).

69. Crochet, J., Clemens, M. & Hertel, T. Quantum yield heterogeneities of aqueous single-wall carbon nanotube suspensions. *J. Am. Chem. Soc.* **129**, 8058–8059 (2007).

70. Welsher, K. *et al.* A route to brightly fluorescent carbon nanotubes for near-infrared imaging in mice. *Nat. Nanotechnol.* **4**, 773–780 (2009).

71. Ackermann, J., Metternich, J. T., Herbertz, S. & Kruss, S. Biosensing with Fluorescent Carbon Nanotubes. *Angew. Chemie - Int. Ed.* **61**, e202112372 (2022).

72. Bachilo, S. M. *et al.* Structure-Assigned Optical Spectra of Single-Walled Carbon Nanotubes. *Science* **298**, 2361–2366 (2002).

73. Hansen, S. F. & Lennquist, A. Carbon nanotubes added to the SIN List as a nanomaterial of Very High Concern. *Nat. Nanotechnol.* **15**, 3–4 (2020).

74. Fadeel, B. & Kostarelos, K. Grouping all carbon nanotubes into a single substance category is scientifically unjustified. *Nat. Nanotechnol.* **15**, 164–164 (2020).

75. The risks of nanomaterial risk assessment. *Nat. Nanotechnol.* **15**, 163–163 (2020).

76. Hansen, S. F. & Lennquist, A. SIN List criticism based on misunderstandings. *Nat. Nanotechnol.* **15**, 418–418 (2020).

77. Patalag, L. J. *et al.* Ultrafast Resonance Energy Transfer in Ethylene-Bridged BODIPY Heterooligomers: From Frenkel to Förster Coupling Limit. *J. Am. Chem. Soc.* **143**, 7414–7425 (2021).

78. Feng, L., Chen, W., Ma, X., Liu, S. H. & Yin, J. Near-infrared heptamethine cyanines (Cy7): From structure, property to application. *Org. Biomol. Chem.* **18**, 9385–9397 (2020).

79. Wang, L. *et al.* Hybrid Rhodamine Fluorophores in the Visible/NIR Region for Biological Imaging. *Angew. Chemie - Int. Ed.* **58**, 14026–14043 (2019).

80. Beija, M., Afonso, C. A. M. & Martinho, J. M. G. Synthesis and applications of rhodamine derivatives as fluorescent probes. *Chem. Soc. Rev.* **38**, 2410–2433 (2009).

81. Imran, M., Ramzan, M., Qureshi, A. K., Azhar Khan, M. & Tariq, M. Emerging applications of porphyrins and metalloporphyrins in biomedicine and diagnostic magnetic resonance imaging. *Biosensors* **8**, 1–17 (2018).

82. Shi, Y., Zhang, F. & Linhardt, R. J. Porphyrin-based compounds and their applications in materials and medicine. *Dye. Pigment.* **188**, 109136 (2021).

83. Huang, H., Song, W., Rieffel, J. & Lovell, J. F. Emerging applications of porphyrins in photomedicine. *Front. Phys.* **3**, 1–15 (2015).

84. Hu, L., Yan, Z. & Xu, H. Advances in synthesis and application of near-infrared absorbing squaraine dyes. *RSC Adv.* **3**, 7667–7676 (2013).

85. Lambert, C., Scherpf, T., Ceymann, H., Schmiedel, A. & Holzapfel, M. Coupled Oscillators for Tuning Fluorescence Properties of Squaraine Dyes. *J. Am. Chem. Soc.* **137**, 3547–3557 (2015).

86. Patalag, L. J., Loch, M., Jones, P. G. & Werz, D. B. Exploring the π-System of the (Aza-)BOIMPY Scaffold: Electron-Rich Pyrrole Moieties Working in Concert with Electron-Depleted Meso-Positions. *J. Org. Chem.* **84**, 7804–7814 (2019).

87. Umezawa, K., Matsui, A., Nakamura, Y., Citterio, D. & Suzuki, K. Bright, color-tunable fluorescent dyes in the Vis/NIR region: Establishment of new 'tailor-made' multicolor fluorophores based on borondipyrromethene. *Chem. - A Eur. J.* **15**, 1096–1106 (2009).

88. Rappitsch, T. & M. Borisov, S. Carbazole- and Fluorene-Fused Aza-BODIPYs: NIR Fluorophores with High Brightness and Photostability. *Chem. – A Eur. J.* (2021) doi:10.1002/chem.202100965.

89. Patalag, L. J., Jones, P. G. & Werz, D. B. BOIMPYs: Rapid Access to a Family of Red-Emissive Fluorophores and NIR Dyes. *Angew. Chemie - Int. Ed.* **55**, 13340–13344 (2016).

90. Nicolosi, V., Chhowalla, M., Kanatzidis, M. G., Strano, M. S. & Coleman, J. N. Liquid exfoliation of layered materials. *Science* **340**, 72–75 (2013).

91. Geim, A. K. & Novoselov, K. S. The rise of graphene. *Nat. Mater.* **6**, 183–191 (2007).

92. Geim, A. K. Graphene: Status and Prospects. *Science* **324**, 1530–1534 (2009).

93. Novoselov, K. S. *et al.* Two-dimensional atomic crystals. *Proc. Natl. Acad. Sci. U. S. A.* **102**, 10451–10453 (2005).

94. Novoselov, K. S. *et al.* Electric Field Effect in Atomically Thin Carbon Films. *Science* **306**, 666–669 (2004).

95. Chhowalla, M. *et al.* The chemistry of two-dimensional layered transition metal dichalcogenide nanosheets. *Nat. Chem.* **5**, 263–275 (2013).

96. Kumar, A. & Huei, C. Synthesis and Biomedical Applications of Graphene: Present and Future Trends. in *Advances in Graphene Science* (InTech, 2013). doi:10.5772/55728.

97. Bhimanapati, G. R. *et al.* Recent Advances in Two-Dimensional Materials beyond Graphene. *ACS Nano* **9**, 11509–11539 (2015).

98. Wang, Q. H., Kalantar-Zadeh, K., Kis, A., Coleman, J. N. & Strano, M. S. Electronics and optoelectronics of two-dimensional transition metal dichalcogenides. *Nat. Nanotechnol.* **7**, 699–712 (2012).

99. Tao, H. *et al.* Scalable exfoliation and dispersion of two-dimensional materials-an update. *Phys. Chem. Chem. Phys.* **19**, 921–960 (2017).

100. Coleman, J. N. *et al.* Two-dimensional nanosheets produced by liquid exfoliation of layered

materials. *Science* **331**, 568–571 (2011).

101. Talapin, D. V., Lee, J. S., Kovalenko, M. V. & Shevchenko, E. V. Prospects of colloidal nanocrystals for electronic and optoelectronic applications. *Chem. Rev.* **110**, 389–458 (2010).

102. Nasilowski, M., Mahler, B., Lhuillier, E., Ithurria, S. & Dubertret, B. Two-Dimensional Colloidal Nanocrystals. *Chem. Rev.* **116**, 10934–10982 (2016).

103. Mak, K. F., Lee, C., Hone, J., Shan, J. & Heinz, T. F. Atomically thin MoS2: A new direct-gap semiconductor. *Phys. Rev. Lett.* **105**, 136805 (2010).

104. Splendiani, A. *et al.* Emerging Photoluminescence in Monolayer MoS2. *Nano Lett.* **10**, 1271–1275 (2010).

105. Cunningham, G. *et al.* Solvent exfoliation of transition metal dichalcogenides: Dispersibility of exfoliated nanosheets varies only weakly between compounds. *ACS Nano* **6**, 3468–3480 (2012).

106. Moayed, M. M. R., Bielewicz, T., Zöllner, M. S., Herrmann, C. & Klinke, C. Towards colloidal spintronics through Rashba spin-orbit interaction in lead sulphide nanosheets. *Nat. Commun.* **8**, 2–8 (2017).

107. Dogan, S., Bielewicz, T., Cai, Y. & Klinke, C. Field–effect transistors made of individual colloidal PbS nanosheets. *Appl. Phys. Lett.* **101**, 073102 (2012).

108. Dogan, S., Bielewicz, T., Lebedeva, V. & Klinke, C. Photovoltaic effect in individual asymmetrically contacted lead sulfide nanosheets. *Nanoscale* **7**, 4875–4883 (2015).

109. Hu, T. *et al.* Two-dimensional nanomaterials: fascinating materials in biomedical field. *Sci. Bull.* **64**, 1707–1727 (2019).

110. Murali, A., Lokhande, G., Deo, K. A., Brokesh, A. & Gaharwar, A. K. Emerging 2D nanomaterials for biomedical applications. *Mater. Today* **50**, 276–302 (2021).

111. Chimene, D., Alge, D. L. & Gaharwar, A. K. Two-Dimensional Nanomaterials for Biomedical Applications: Emerging Trends and Future Prospects. *Adv. Mater.* **27**, 7261–7284 (2015).

112. Derakhshi, M. *et al.* Two-Dimensional Nanomaterials beyond Graphene for Biomedical Applications. *J. Funct. Biomater.* **13**, 27 (2022).

113. Li, B. L. *et al.* Engineered functionalized 2D nanoarchitectures for stimuli-responsive drug delivery. *Mater. Horizons* **7**, 455–469 (2020).

114. Mei, X. *et al.* Recent advancements in two-dimensional nanomaterials for drug delivery. *Wiley Interdiscip. Rev. Nanomedicine Nanobiotechnology* **12**, 1–21 (2020).

115. Yin, F. *et al.* Functionalized 2D nanomaterials for gene delivery applications. *Coord. Chem. Rev.* **347**, 77–97 (2017).

116. Lee, S. S. *et al.* Layered Double Hydroxide and Polypeptide Thermogel Nanocomposite System for Chondrogenic Differentiation of Stem Cells. *ACS Appl. Mater. Interfaces* **9**, 42668–42675 (2017).

117. Li, D., Liu, T., Yu, X., Wu, D. & Su, Z. Fabrication of graphene-biomacromolecule hybrid materials for tissue engineering application. *Polym. Chem.* **8**, 4309–4321 (2017).

118. Zheng, H. *et al.* Antibacterial applications of graphene oxides: structure-activity relationships, molecular initiating events and biosafety. *Sci. Bull.* **63**, 133–142 (2018).

119. Bolotsky, A. *et al.* Two-Dimensional Materials in Biosensing and Healthcare: From in Vitro Diagnostics to Optogenetics and beyond. *ACS Nano* **13**, 9781–9810 (2019).

120. Wang, L., Jackman, J. A., Ng, W. B. & Cho, N. J. Flexible, Graphene-Coated Biocomposite for Highly Sensitive, Real-Time Molecular Detection. *Adv. Funct. Mater.* **26**, 8623–8630 (2016).

121. Chen, W. *et al.* Black Phosphorus Nanosheet-Based Drug Delivery System for Synergistic Photodynamic/Photothermal/Chemotherapy of Cancer. *Adv. Mater.* **29**, (2017).

122. Tong, C. *et al.* PEGylated mBPEI-rGO nanocomposites facilitate hepotocarcinoma treatment combining photothermal therapy and chemotherapy. *Sci. Bull.* **63**, 935–946 (2018).

123. Jin, L. *et al.* MnO2-Functionalized Co-P Nanocomposite: A New Theranostic Agent for pH-Triggered T1/T2 Dual-Modality Magnetic Resonance Imaging-Guided Chemo-photothermal Synergistic Therapy. *ACS Appl. Mater. Interfaces* **9**, 41648–41658 (2017).

124. Li, B., Gu, Z., Kurniawan, N., Chen, W. & Xu, Z. P. Manganese-Based Layered Double Hydroxide Nanoparticles as a T1-MRI Contrast Agent with Ultrasensitive pH Response and High Relaxivity. *Adv. Mater.* **29**, (2017).

125. Wang, S. *et al.* A facile one-pot synthesis of a two-dimensional MoS2/Bi2S3 composite theranostic nanosystem for multi-modality tumor imaging and therapy. *Adv. Mater.* **27**, 2775–2782 (2015).

126. Martín, C., Kostarelos, K., Prato, M. & Bianco, A. Biocompatibility and biodegradability of 2D materials: Graphene and beyond. *Chem. Commun.* **55**, 5540–5546 (2019).

127. Goenka, S., Sant, V. & Sant, S. Graphene-based nanomaterials for drug delivery and tissue engineering. *J. Control. Release* **173**, 75–88 (2014).

128. Shen, H., Zhang, L., Liu, M. & Zhang, Z. Biomedical applications of graphene. *Theranostics* **2**, 283–294 (2012).

129. Zhu, Y. *et al.* Graphene and graphene oxide: Synthesis, properties, and applications. *Adv. Mater.* **22**, 3906–3924 (2010).

130. Guo, C. X. *et al.* RGD-peptide functionalized graphene biomimetic live-cell sensor for real-time detection of nitric oxide molecules. *ACS Nano* **6**, 6944–6951 (2012).

131. Reina, G. *et al.* Promises, facts and challenges for graphene in biomedical applications. *Chem. Soc. Rev.* **46**, 4400–4416 (2017).

132. Pattnaik, S., Swain, K. & Lin, Z. Graphene and graphene-based nanocomposites: biomedical applications and biosafety. *J. Mater. Chem. B* **4**, 7813–7831 (2016).

133. Gu, Z., Zhu, S., Yan, L., Zhao, F. & Zhao, Y. Graphene-Based Smart Platforms for Combined Cancer Therapy. *Adv. Mater.* **31**, (2019).

134. Cheng, C., Li, S., Thomas, A., Kotov, N. A. & Haag, R. Functional Graphene Nanomaterials Based Architectures: Biointeractions, Fabrications, and Emerging Biological Applications. *Chem. Rev.* **117**, 1826–1914 (2017).

135. Ji, X. *et al.* Capturing functional two-dimensional nanosheets from sandwich-structure vermiculite for cancer theranostics. *Nat. Commun.* **12**, 1–17 (2021).

136. Carrow, J. K. *et al.* Widespread changes in transcriptome profile of human mesenchymal stem cells induced by two-dimensional nanosilicates. *Proc. Natl. Acad. Sci.* **115**, 201716164 (2018).

137. Dawson, J. I. & Oreffo, R. O. C. Clay: New opportunities for tissue regeneration and biomaterial design. *Adv. Mater.* **25**, 4069–4086 (2013).

138. Su, D., Jiang, L., Chen, X., Dong, J. & Shao, Z. Enhancing the Gelation and Bioactivity of Injectable Silk Fibroin Hydrogel with Laponite Nanoplatelets. *ACS Appl. Mater. Interfaces* **8**, 9619–9628 (2016).

139. Jafarbeglou, M. M. M. M., Abdouss, M., Shoushtari, A. M. & Jafarbeglou, M. M. M. M. Clay nanocomposites as engineered drug delivery systems. *RSC Adv.* **6**, 50002–50016 (2016).

140. Long, M. *et al.* Interactions between two-dimensional nanoclay and blood cells in hemostasis.

Mater. Sci. Eng. C **105**, 110081 (2019).

141. Cao, D. *et al.* Ag-loaded MgSrFe-layered double hydroxide/chitosan composite scaffold with enhanced osteogenic and antibacterial property for bone engineering tissue. *J. Biomed. Mater. Res. - Part B Appl. Biomater.* **106**, 863–873 (2018).

142. Mei, X. *et al.* Layered double hydroxide monolayers for controlled loading and targeted delivery of anticancer drugs. *Nano Res.* **11**, 195–205 (2018).

143. Kim, J., Kim, H. & Kim, W. J. Single-Layered MoS2-PEI-PEG Nanocomposite-Mediated Gene Delivery Controlled by Photo and Redox Stimuli. *Small* **12**, 1184–1192 (2016).

144. Liu, T. *et al.* Drug delivery with PEGylated MoS2 nano-sheets for combined photothermal and chemotherapy of cancer. *Adv. Mater.* **26**, 3433–3440 (2014).

145. Zhang, Y. *et al.* Single-layer transition metal dichalcogenide nanosheet-based nanosensors for rapid, sensitive, and multiplexed detection of DNA. *Adv. Mater.* **27**, 935–939 (2015).

146. Zhang, C. *et al.* Polyphenol-Assisted Exfoliation of Transition Metal Dichalcogenides into Nanosheets as Photothermal Nanocarriers for Enhanced Antibiofilm Activity. *ACS Nano* acsnano.8b06321 (2018) doi:10.1021/acsnano.8b06321.

147. Lu, J. *et al.* Molybdenum disulfide nanosheets: From exfoliation preparation to biosensing and cancer therapy applications. *Colloids Surfaces B Biointerfaces* **194**, 111162 (2020).

148. Chen, J. *et al.* Hybrid MoSe2-indocyanine green nanosheets as a highly efficient phototheranostic agent for photoacoustic imaging guided photothermal cancer therapy. *Biomater. Sci.* **6**, 1503–1516 (2018).

149. Fan, D., Shang, C., Gu, W., Wang, E. & Dong, S. Introducing Ratiometric Fluorescence to MnO2 Nanosheet-Based Biosensing: A Simple, Label-Free Ratiometric Fluorescent Sensor Programmed by Cascade Logic Circuit for Ultrasensitive GSH Detection. *ACS Appl. Mater. Interfaces* **9**, 25870–25877 (2017).

150. Zhang, R., Yan, F. & Chen, Y. Exogenous Physical Irradiation on Titania Semiconductors: Materials Chemistry and Tumor-Specific Nanomedicine. *Adv. Sci.* **5**, (2018).

151. Fan, W. *et al.* Intelligent MnO2 Nanosheets Anchored with Upconversion Nanoprobes for Concurrent pH-/H2O2-Responsive UCL Imaging and Oxygen-Elevated Synergetic Therapy. *Adv. Mater.* **27**, 4155–4161 (2015).

152. Shang, H. *et al.* Enhancement of the photokilling effect of TiO2 in photodynamic therapy by conjugating with reduced graphene oxide and its mechanism exploration. *J. Photochem. Photobiol. B Biol.* **177**, 112–123 (2017).

153. Chen, Y. *et al.* Break-up of two-dimensional MnO 2 nanosheets promotes ultrasensitive pH-triggered theranostics of cancer. *Adv. Mater.* **26**, 7019–7026 (2014).

154. Luo, M., Fan, T., Zhou, Y., Zhang, H. & Mei, L. 2D Black Phosphorus–Based Biomedical Applications. *Adv. Funct. Mater.* **29**, (2019).

155. Tao, W. *et al.* Black Phosphorus Nanosheets as a Robust Delivery Platform for Cancer Theranostics. *Adv. Mater.* **29**, (2017).

156. Wang, H. *et al.* Ultrathin Black Phosphorus Nanosheets for Efficient Singlet Oxygen Generation. *J. Am. Chem. Soc.* **137**, 11376–11382 (2015).

157. Weng, Q. *et al.* Highly water-soluble, porous, and biocompatible boron nitrides for anticancer drug delivery. *ACS Nano* **8**, 6123–6130 (2014).

158. Yoo, S. C., Park, Y. K., Park, C., Ryu, H. & Hong, S. H. Biomimetic Artificial Nacre: Boron Nitride Nanosheets/Gelatin Nanocomposites for Biomedical Applications. *Adv. Funct. Mater.* **28**, (2018).

159. Chen, R. *et al.* Graphitic carbon nitride nanosheet@metal-organic framework core-shell nanoparticles for photo-chemo combination therapy. *Nanoscale* **7**, 17299–17305 (2015).

160. Dong, Y. *et al.* Graphitic Carbon Nitride Materials: Sensing, Imaging and Therapy. *Small* **12**, 5376–5393 (2016).

161. Xiang, M. H. *et al.* A fluorescent graphitic carbon nitride nanosheet biosensor for highly sensitive, label-free detection of alkaline phosphatase. *Nanoscale* **8**, 4727–4732 (2016).

162. Zhang, H. *et al.* SnTe@MnO2-SP Nanosheet–Based Intelligent Nanoplatform for Second Near-Infrared Light–Mediated Cancer Theranostics. *Adv. Funct. Mater.* **29**, (2019).

163. Szuplewska, A. *et al.* Future Applications of MXenes in Biotechnology, Nanomedicine, and Sensors. *Trends Biotechnol.* **38**, 264–279 (2020).

164. Han, X. *et al.* 2D Ultrathin MXene-Based Drug-Delivery Nanoplatform for Synergistic Photothermal Ablation and Chemotherapy of Cancer. *Adv. Healthc. Mater.* **7**, 1–13 (2018).

165. Tao, W. *et al.* Emerging two-dimensional monoelemental materials (Xenes) for biomedical applications. *Chem. Soc. Rev.* **48**, 2891–2912 (2019).

166. Ji, X. *et al.* A Novel Top-Down Synthesis of Ultrathin 2D Boron Nanosheets for Multimodal Imaging-Guided Cancer Therapy. *Adv. Mater.* **30**, (2018).

167. Pumera, M. & Sofer, Z. 2D Monoelemental Arsenene, Antimonene, and Bismuthene: Beyond Black Phosphorus. *Adv. Mater.* **29**, (2017).

168. Chowdhury, M. A. Metal-Organic-Frameworks as Contrast Agents in Magnetic Resonance Imaging. *ChemBioEng Rev.* **4**, 225–239 (2017).

169. Della Rocca, J., Liu, D. & Lin, W. Nanoscale Metal–Organic Frameworks for Biomedical Imaging and Drug Delivery. *Acc. Chem. Res.* **44**, 957–968 (2011).

170. Yang, J. & Yang, Y. W. Metal–Organic Frameworks for Biomedical Applications. *Small* **16**, 1–24 (2020).

171. Stöter, M., Rosenfeldt, S. & Breu, J. Tunable Exfoliation of Synthetic Clays. *Annu. Rev. Mater. Res.* **45**, 129–151 (2015).

172. Backes, C. *et al.* Guidelines for exfoliation, characterization and processing of layered materials produced by liquid exfoliation. *Chem. Mater.* **29**, 243–255 (2017).

173. Backes, C. *et al.* Production of highly monolayer enriched dispersions of liquid-exfoliated nanosheets by liquid cascade centrifugation. *ACS Nano* **10**, 1589–1601 (2016).

174. Warner, T. E. *Synthesis, Properties and Mineralogy of Important Inorganic Materials*. *Synthesis, Properties and Mineralogy of Important Inorganic Materials* (Wiley, 2011). doi:10.1002/9780470976012.

175. Sgamellotti, A. & Anselmi, C. An evergreen blue. Spectroscopic properties of Egyptian blue from pyramids to Raphael, and beyond. *Inorganica Chim. Acta* **530**, 120699 (2022).

176. Masic, A. & Nicola, M. NIR Luminescence and Composition of Egyptian Blue as Markers in Archaeometric Evaluations. *Microsc. Microanal.* **27**, 3004–3006 (2021).

177. Nicola, M. *et al.* Late production of Egyptian blue: synthesis from brass and its characteristics. *Archaeol. Anthropol. Sci.* **11**, 5377–5392 (2019).

178. Seymour, L. M. *et al.* On the production of ancient Egyptian blue: multi-modal characterization and micron-scale luminescence mapping. *PLoS One* 1–13 (2020) doi:10.1371/journal.pone.0242549.

179. S. Patel, S. Purple reign - How ancient Chinese chemists added color to the Emperor's army. *Archaeology* **60**, 25–27 (2007).

180. Berke, H. The invention of blue and purple pigments in ancient times. *Chem. Soc. Rev.* **36**, 15–30 (2007).

181. Wiedemann, H.-G. & Berke, H. Chemical and Physical Investigations of Egyptian and Chinese Blue and Purple. *Monum. Sites* **3**, 154–171 (2015).

182. Pozza, G., Ajò, D., Chiari, G., De Zuane, F. & Favaro, M. Photoluminescence of the inorganic pigments Egyptian blue, Han blue and Han purple. *J. Cult. Herit.* **1**, 393–398 (2000).

183. Johnson-Mcdaniel, D., Barrett, C. A., Sharafi, A. & Salguero, T. T. Nanoscience of an Ancient Pigment. *J. Am. Chem. Soc.* **135**, 1677–1679 (2013).

184. Salguero, T. T. *et al.* Nanoscience of Metal Silicate-Based Pigments. *MRS Proc.* **1618**, 161–166 (2014).

185. Johnson-McDaniel, D. & Salguero, T. T. Exfoliation of Egyptian Blue and Han Blue, Two Alkali Earth Copper Silicate-based Pigments. *J. Vis. Exp.* 1–10 (2014).

186. Pikart, P. Picture of the Nefertiti bust in Neues Museum, Berlin. *November 8* https://en.wikipedia.org/wiki/File:Nofretete_Neues_Museum.jpg#filelinks (2009).

187. McGill, K. Terracotta Army, nr. Xi'an. *September 13* https://commons.wikimedia.org/wiki/File:Terracotta_Army_(6143564816).jpg (2011).

188. Song, X. Q. *et al.* Phase evolution, crystal structure, and microwave dielectric properties of gillespite-type ceramics. *J. Am. Ceram. Soc.* **104**, 1740–1749 (2021).

189. Muungani, G., Moodley, V. & van Zyl, W. E. Solid-state synthesis of the phyllosilicate Effenbergerite (BaCuSi4O10) for electrochemical sensing of ciprofloxacin antibiotic in pharmaceutical drug formulation. *J. Appl. Electrochem.* **52**, 285–297 (2022).

190. Kiss, A., Stretz, H. A., Ueda, A. & Mu, R. Synthesis of Egyptian Blue and mechanisms. *J. Phys. Chem. Solids* 110738 (2022) doi:10.1016/j.jpcs.2022.110738.

191. Kendrick, E., Kirk, C. J. & Dann, S. E. Structure and colour properties in the Egyptian Blue Family, M1-xM′xCuSi4O10, as a function of M, M′ where M, M′ = Ca, Sr and Ba. *Dye. Pigment.* **73**, 13–18 (2007).

192. Barbar, S. K., Patel, K. R. & Kumar, S. Structural, optical and magnetic properties of MCuSi4O10 (M = Ba and Sr) blue pigments. *J. Mater. Sci. Mater. Electron.* **28**, 3716–3724 (2017).

193. Gao, R. *et al.* Construction of 2D up-conversion calcium copper silicate nanosheet for efficient photocatalytic nitrogen fixation under full spectrum. *J. Alloys Compd.* **910**, 164869 (2022).

194. Johnson-McDaniel, D., Comer, S., Kolis, J. W. & Salguero, T. T. Hydrothermal Formation of Calcium Copper Tetrasilicate. *Chem. - A Eur. J.* **21**, 17560–17564 (2015).

195. Chen, Y., Zhang, Y. & Feng, S. Hydrothermal synthesis and properties of pigments Chinese purple BaCuSi2O6 and dark blue BaCu2Si2O7. *Dye. Pigment.* **105**, 167–173 (2014).

196. Chen, Y., Shang, M., Wu, X. & Feng, S. Hydrothermal synthesis, hierarchical structures and properties of blue pigments SrCuSi4O10 and BaCuSi4O10. *CrystEngComm* **16**, 5418–5423 (2014).

197. Corona-Martínez, D. A. *et al.* Controllable synthesis of BaCuSi2O6 fine particles via a one-pot hydrothermal reaction with enhanced violet colour hue. *Adv. Powder Technol.* **30**, 1473–1483 (2019).

198. Tian, T., Wu, C. & Chang, J. Preparation and in vitro osteogenic, angiogenic and antibacterial properties of cuprorivaite (CaCuSi4O10, Cup) bioceramics. *RSC Adv.* **6**, 45840–45849 (2016).

199. Panagopoulou, A., Karanasios, K. & Xanthopoulou, G. Ancient Egyptian Blue (CaCuSi4O10) Pigment by Modern Solution Combustion Synthesis Method. *Eurasian Chem. J.* **18**, 31 (2016).

200. Loch, P. *et al.* Synthesis of Large Platelets of Egyptian Blue via Pseudomorphosis after NaRUB-18. *Zeitschrift fur Anorg. und Allg. Chemie* **646**, 1570–1574 (2020).

201. Pabst, A. Structures of some tetragonal sheet silicates. *Acta Crystallogr.* **12**, 733–739 (1959).

202. Chakoumakos, B. C., Fernandez-Baca, J. A. & Boatner, L. A. Refinement of the Structures of the Layer Silicates MCuSi4O10 (M = Ca, Sr, Ba) by Rietveld Analysis of Neutron Powder Diffraction Data. *J. Solid State Chem.* **103**, 105–113 (1993).

203. Giester, G. & Rieck, B. Effenbergerite, BaCu[Si4O10], a new mineral from the Kalahari Manganese Field, South Africa: description and crystal structure. *Mineral. Mag.* **58**, 663–670 (1994).

204. Rieck, B., Pristacz, H. & Giester, G. Colinowensite, BaCuSi2O6 , a new mineral from the Kalahari Manganese Field, South Africa and new data on wesselsite, SrCuSi4O10. *Mineral. Mag.* **79**, 1769–1778 (2015).

205. Ajò, D., Chiari, G., Zuane, F. De, Favaro, M. & Bertolin, M. Photoluminescence of some blue natural pigments and related synthetic materials. *5th Int. Conf. non-destructive testing, Microanal. methods Environ. Eval. study Conserv. Work. art* 37–47 (1996).

206. Accorsi, G. *et al.* The exceptional near-infrared luminescence properties of cuprorivaite (Egyptian blue). *Chem. Commun.* 3392–3394 (2009).

207. Jaime, M. *et al.* Magnetic-field-induced condensation of triplons in Han Purple pigment BaCuSi2O6. *Phys. Rev. Lett.* **93**, 6–9 (2004).

208. Sebastian, S. E. *et al.* Dimensional reduction at a quantum critical point. *Nature* **441**, 617–620 (2006).

209. Sebastian, S. E. *et al.* Characteristic Bose-Einstein condensation scaling close to a quantum critical point in BaCuSi2O6. *Phys. Rev. B - Condens. Matter Mater. Phys.* **72**, 1–4 (2005).

210. Allenspach, S. *et al.* Revealing three-dimensional quantum criticality by Sr substitution in Han purple. *Phys. Rev. Res.* **3**, 023177 (2021).

211. Sasago, Y., Uchinokura, K., Zheludev, A. & Shirane, G. Temperature-dependent spin gap and singlet ground state in BaCuSi2O6. *Phys. Rev. B* **55**, 8357–8360 (1997).

212. Chen, W. *et al.* Near-Infrared Emission and Photon Energy Upconversion of Two-Dimensional Copper Silicates. *J. Phys. Chem. C* **119**, 20571–20577 (2015).

213. Binet, L., Lizion, J., Bertaina, S. & Gourier, D. Magnetic and New Optical Properties in the UV–visible Range of the Egyptian Blue Pigment Cuprorivaite CaCuSi4O10. *J. Phys. Chem. C* **125**, 25189–25196 (2021).

214. Li, Y. J., Ye, S., Wang, C. H., Wang, X. M. & Zhang, Q. Y. Temperature-dependent near-infrared emission of highly concentrated Cu2+ in CaCuSi4O10 phosphor. *J. Mater. Chem. C* **2**, 10395–10402 (2014).

215. Berdahl, P. *et al.* High quantum yield of the Egyptian blue family of infrared phosphors (MCuSi4O10 , M = Ca, Sr, Ba). *J. Appl. Phys.* **123**, 193103 (2018).

216. Selvaggio, G. *et al.* Photophysical properties and fluorescence lifetime imaging of exfoliated near-infrared fluorescent silicate nanosheets. *Nanoscale Adv.* **3**, 4541–4553 (2021).

217. King, R. S. P., Hallett, P. M. & Foster, D. NIR-NIR fluorescence: A new genre of fingermark visualisation techniques. *Forensic Sci. Int.* **262**, e28–e33 (2016).

218. Errington, B., Lawson, G., Lewis, S. W. & Smith, G. D. Micronised Egyptian blue pigment: A novel near-infrared luminescent fingerprint dusting powder. *Dye. Pigment.* **132**, 310–315 (2016).

219. Shahbazi, S., Goodpaster, J. V., Smith, G. D., Becker, T. & Lewis, S. W. Preparation,

characterization, and application of a lipophilic coated exfoliated Egyptian blue for near-infrared luminescent latent fingermark detection. *Forensic Chem.* **18**, 100208 (2020).

220. Shahbazi, S., Goodpaster, J. V, Smith, G. D., Becker, T. & Lewis, S. W. Studies into exfoliation and coating of Egyptian blue for application to the detection of latent fingermarks. *ChemRxiv* 1–27 (2021).

221. Borisov, S. M., Würth, C., Resch-Genger, U. & Klimant, I. New Life of Ancient Pigments: Application in High-Performance Optical Sensing Materials. *Anal. Chem.* **85**, 9371–9377 (2013).

222. Maierhofer, M., Rieger, V. & Mayr, T. Optical ammonia sensors based on fluorescent aza-BODIPY dyes— a flexible toolbox. *Anal. Bioanal. Chem.* **412**, 7559–7567 (2020).

223. Nißler, R. *et al.* Remote near infrared identification of pathogens with multiplexed nanosensors. *Nat. Commun.* **11**, 5995 (2020).

224. Yang, S. S. *et al.* An Exfoliated 2D Egyptian Blue Nanosheet for Highly Selective Enrichment of Multi-Phosphorylated Peptides in Mass Spectrometric Analysis. *Chem. - A Eur. J.* **24**, 2024 (2018).

225. Yu, Q. *et al.* Chinese sesame stick-inspired nano-fibrous scaffolds for tumor therapy and skin tissue reconstruction. *Biomaterials* **194**, 25–35 (2019).

226. He, C., Dong, C., Yu, L., Chen, Y. & Hao, Y. Ultrathin 2D Inorganic Ancient Pigment Decorated 3D-Printing Scaffold Enables Photonic Hyperthermia of Osteosarcoma in NIR-II Biowindow and Concurrently Augments Bone Regeneration. *Adv. Sci.* **8**, 1–10 (2021).

227. Yang, C. *et al.* NIR-II light-responsive biodegradable shape memory composites based on cuprorivaite nanosheets for enhanced tissue reconstruction. *Chem. Eng. J.* **419**, 129437 (2021).

228. Dong, C. *et al.* Bioactive NIR-II Light-Responsive Shape Memory Composite Based on Cuprorivaite Nanosheets for Endometrial Regeneration. *Adv. Sci.* **2102220**, 2102220 (2022).

229. Chen, Z. *et al.* Near-IR Absorbing J-Aggregate of an Amphiphilic BF2-Azadipyrromethene Dye by Kinetic Cooperative Self-Assembly. *Angew. Chemie - Int. Ed.* **56**, 5729–5733 (2017).

230. Müller, M. *et al.* Tetrabenzononacene: “Butterfly Wings” Stabilize the Core. *Angew. Chemie - Int. Ed.* **59**, 1966–1969 (2020).

231. Patalag, L. J., Ho, L. P., Jones, P. G. & Werz, D. B. Ethylene-Bridged Oligo-BODIPYs: Access to Intramolecular J-Aggregates and Superfluorophores. *J. Am. Chem. Soc.* **139**, 15104–15113 (2017).

232. Würth, C., Grabolle, M., Pauli, J., Spieles, M. & Resch-Genger, U. Relative and absolute determination of fluorescence quantum yields of transparent samples. *Nat. Protoc.* **8**, 1535–1550 (2013).

233. Polo, E. & Kruss, S. Impact of Redox-Active Molecules on the Fluorescence of Polymer-Wrapped Carbon Nanotubes. *J. Phys. Chem. C* **120**, 3061–3070 (2016).

234. Biju, V. Chemical modifications and bioconjugate reactions of nanomaterials for sensing, imaging, drug delivery and therapy. *Chem. Soc. Rev.* **43**, 744–764 (2014).

235. Happel, J. & Brenner, H. The Motion of a Rigid Particle of Arbitrary Shape in an Unbounded Fluid. 159–234 (1983) doi:10.1007/978-94-009-8352-6_5.

236. Toyota, T., Head, D. A., Schmidt, C. F. & Mizuno, D. Non-Gaussian athermal fluctuations in active gels. *Soft Matter* **7**, 3234 (2011).

237. Verri, G. The spatially resolved characterisation of Egyptian blue, Han blue and Han purple by photo-induced luminescence digital imaging. *Anal. Bioanal. Chem.* **394**, 1011–1021 (2009).

238. Comelli, D., Capogrosso, V., Orsenigo, C. & Nevin, A. Dual wavelength excitation for the time-

resolved photoluminescence imaging of painted ancient Egyptian objects. *Herit. Sci.* **4**, 1–8 (2016).

239. Mirti, P. *et al.* Spectrochemical and structural studies on a roman sample of Egyptian blue. *Spectrochim. Acta Part A Mol. Spectrosc.* **51**, 437–446 (1995).

240. Ma, L., Song, X., Yu, Y. & Chen, Y. Two-Dimensional Silicene/Silicon Nanosheets: An Emerging Silicon-Composed Nanostructure in Biomedicine. *Adv. Mater.* **33**, 2008226 (2021).

241. Takahashi, N., Hata, H. & Kuroda, K. Exfoliation of layered silicates through immobilization of imidazolium groups. *Chem. Mater.* **23**, 266–273 (2011).

242. Wang, K., He, X., Yang, X. & Shi, H. Functionalized silica nanoparticles: A platform for fluorescence imaging at the cell and small animal levels. *Acc. Chem. Res.* **46**, 1367–1376 (2013).

243. Tarn, D. *et al.* Mesoporous Silica Nanoparticle Nanocarriers: Biofunctionality and Biocompatibility. *Acc. Chem. Res.* **46**, 792–801 (2013).

244. Cotí, K. K. *et al.* Mechanised nanoparticles for drug delivery. *Nanoscale* **1**, 16–39 (2009).

245. Shimada, T. *et al.* Functionalization on silica gel with allylsilanes. A new method of covalent attachment of organic functional groups on silica gel. *J. Am. Chem. Soc.* **125**, 4688–4689 (2003).

246. Asefa, T. & Tao, Z. Biocompatibility of Mesoporous Silica Nanoparticles. *Chem. Res. Toxicol.* **25**, 2265–2284 (2012).

247. Gomes, M. C., Cunha, Â., Trindade, T. & Tomé, J. P. C. The role of surface functionalization of silica nanoparticles for bioimaging. *J. Innov. Opt. Health Sci.* **9**, 1–16 (2016).

248. Moitra, N. *et al.* Surface functionalization of silica by Si-H activation of hydrosilanes. *J. Am. Chem. Soc.* **136**, 11570–11573 (2014).

249. Bains, G., Patel, A. B. & Narayanaswami, V. Pyrene: A probe to study protein conformation and conformational changes. *Molecules* **16**, 7909–7935 (2011).

250. Ayyavoo, K. & Velusamy, P. Pyrene based materials as fluorescent probes in chemical and biological fields. *New J. Chem.* **45**, 10997–11017 (2021).

251. Daiss, J. O. *et al.* N+/Si replacement as a tool for probing the pharmacophore of allosteric modulators of muscarinic M2 receptors: Synthesis, allosteric potency, and positive cooperativity of silicon-based W84 derivatives. *Organometallics* **21**, 803–811 (2002).

252. Steinmetz, M. G. & Udayakumar, B. S. S. Chloroplatinic acid catalyzed cyclization of silanes bearing pendant acetylenic groups. *J. Organomet. Chem.* **378**, 1–15 (1989).

253. Zhang, Z. *et al.* Conjugating folic acid to gold nanoparticles through glutathione for targeting and detecting cancer cells. *Bioorganic Med. Chem.* **18**, 5528–5534 (2010).

254. Valeur, B. & Berberan-Santos, M. N. *Molecular Fluorescence - Principles and Applications*. (2012).

255. Telegin, F. Y. & Marfin, Y. S. New insights into quantifying the solvatochromism of BODIPY based fluorescent probes. *Spectrochim. Acta - Part A Mol. Biomol. Spectrosc.* **255**, 119683 (2021).

256. de Mello, J. C., Wittmann, H. F. & Friend, R. H. An improved experimental determination of external photoluminescence quantum efficiency. *Adv. Mater.* **9**, 230–232 (1997).

257. Markus, M. A. *et al.* Tracking of Inhaled Near-Infrared Fluorescent Nanoparticles in Lungs of SKH-1 Mice with Allergic Airway Inflammation. *ACS Nano* **9**, 11642–11657 (2015).

258. Isambert, H. & Maggs, A. C. Dynamics and rheology of actin solutions. *Macromolecules* **29**, 1036–1040 (1996).

259. Hinner, B., Tempel, M., Sackmann, E., Kroy, K. & Frey, E. Entanglement, elasticity, and viscous

relaxation of actin solutions. *Phys. Rev. Lett.* **81**, 2614–2617 (1998).

260. Tassieri, M. *et al.* Dynamics of semiflexible polymer solutions in the highly entangled regime. *Phys. Rev. Lett.* **101**, 7–10 (2008).

261. Golde, T. *et al.* Fluorescent beads disintegrate actin networks. *Phys. Rev. E* **88**, 044601 (2013).

262. Van De Linde, S. *et al.* Photoinduced formation of reversible dye radicals and their impact on super-resolution imaging. *Photochem. Photobiol. Sci.* **10**, 499–506 (2011).

263. Hertel, T., Himmelein, S., Ackermann, T., Stich, D. & Crochet, J. Diffusion Limited Photoluminescence Quantum Yields in 1-D Semiconductors: Single-Wall Carbon Nanotubes. *ACS Nano* **4**, 7161–7168 (2010).

264. Giraldo, J. P. *et al.* A Ratiometric Sensor Using Single Chirality Near-Infrared Fluorescent Carbon Nanotubes: Application to in Vivo Monitoring. *Small* **11**, 3973–3984 (2015).

265. Streit, J. K. *et al.* Measuring single-walled carbon nanotube length distributions from diffusional trajectories. *ACS Nano* **6**, 8424–8431 (2012).

266. Wessel, A. D., Gumalla, M., Grosshans, J. & Schmidt, C. F. The mechanical properties of early drosophila embryos measured by high-speed video microrheology. *Biophys. J.* **108**, 1899–1907 (2015).

267. Winkler, F. *et al.* Fluctuation Analysis of Centrosomes Reveals a Cortical Function of Kinesin-1. *Biophys. J.* **109**, 856–868 (2015).

268. Godin, A. G. *et al.* Single-nanotube tracking reveals the nanoscale organization of the extracellular space in the live brain. *Nat. Nanotechnol.* **12**, 238–243 (2017).

269. Tributh, H. & Lagaly, G. Aufbereitung und Identifizierung von Boden- und Lagerstättentonen. I. Aufbereitung der Proben im Labor. *GIT Fachz. Lab.* **30**, 524–529 (1986).

270. Romano, F. *et al.* Water-soluble silicon nanocrystals as NIR luminescent probes for time-gated biomedical imaging. *Nanoscale* **12**, 7921–7926 (2020).

271. Kulkarni, S. K. *Nanotechnology: Principles and Practices*. *Nanotechnology: Principles and Practices* (2015). doi:10.1007/978-3-319-09171-6.

272. Lin, L. *et al.* Microfluidic fabrication of fluorescent nanomaterials: A review. *Chem. Eng. J.* **425**, 131511 (2021).

273. Jose, S. & Reddy, M. L. Lanthanum-strontium copper silicates as intense blue inorganic pigments with high near-infrared reflectance. *Dye. Pigment.* **98**, 540–546 (2013).

274. Zhuang, Y. & Tanabe, S. Forward and back energy transfer between Cu2+ and Yb3+ in Ca1−xCuSi4O10:Ybx crystals. *J. Appl. Phys.* **112**, 093521 (2012).

275. Feng, X., Lin, L., Duan, R., Qiu, J. & Zhou, S. Transition metal ion activated near-infrared luminescent materials. *Prog. Mater. Sci.* 100973 (2022) doi:10.1016/j.pmatsci.2022.100973.

276. Saha, R., Saha, N., Donofrio, R. S. & Bestervelt, L. L. Microbial siderophores: A mini review. *J. Basic Microbiol.* **53**, 303–317 (2013).

277. Budzikiewicz, H. Secondary metabolites from fluorescent pseudomonads. *FEMS Microbiol. Lett.* **104**, 209–228 (1993).

278. Selvaggio, G. *et al.* Exfoliated near infrared fluorescent silicate nanosheets for (bio)photonics. *Nat. Commun.* **11**, 1495 (2020).

279. Johnstone, T. C. & Nolan, E. M. Beyond iron: non-classical biological functions of bacterial siderophores. *Dalt. Trans.* **44**, 6320–6339 (2015).

280. Petrik, M., Zhai, C., Haas, H. & Decristoforo, C. Siderophores for molecular imaging applications.

Clin. Transl. Imaging **5**, 15–27 (2017).

281. Saha, M. *et al.* Microbial siderophores and their potential applications: a review. *Environ. Sci. Pollut. Res.* **23**, 3984–3999 (2016).

282. Tanabe, K. Field enhancement around metal nanoparticles and nanoshells: A systematic investigation. *J. Phys. Chem. C* **112**, 15721–15728 (2008).

283. Kang, K. A., Wang, J., Jasinski, J. B. & Achilefu, S. Fluorescence Manipulation by Gold Nanoparticles: From Complete Quenching to Extensive Enhancement. *J. Nanobiotechnology* **9**, 1–13 (2011).

284. Li, J. *et al.* Spectral variation of fluorescence lifetime near single metal nanoparticles. *Sci. Rep.* **6**, 21349 (2016).

285. Tabakman, S. M. *et al.* Plasmonic substrates for multiplexed protein microarrays with femtomolar sensitivity and broad dynamic range. *Nat. Commun.* **2**, (2011).

286. Seelig, J. *et al.* Nanoparticle-induced fluorescence lifetime modification as nanoscopic ruler: Demonstration at the single molecule level. *Nano Lett.* **7**, 685–689 (2007).

287. Park, K. C., Seo, C., Gupta, G., Kim, J. & Lee, C. Y. Efficient Energy Transfer (EnT) in Pyrene- and Porphyrin-Based Mixed-Ligand Metal-Organic Frameworks. *ACS Appl. Mater. Interfaces* **9**, 38670–38677 (2017).

288. Chu, N. Y. C., Kawaoka, K. & Kearns, D. R. Investigation of energy-transfer mechanisms in pyrene crystals. *J. Chem. Phys.* **55**, 3059–3067 (1971).

289. Luo, G. F. *et al.* Charge-reversal plug gate nanovalves on peptide-functionalized mesoporous silica nanoparticles for targeted drug delivery. *J. Mater. Chem. B* **1**, 5723–5732 (2013).

290. Derjaguin, B. & Landau, L. The theory of stability of highly charged lyophobic sols and coalescence of highly charged particles in electrolyte solutions. *Acta Physicochim. URSS* **14**, 633–52 (1941).

291. Verwey, E. J. W. Theory of the stability of lyophobic colloids. *J. Phys. Chem.* **51**, 631–636 (1947).

292. Valeur, E. & Bradley, M. Amide bond formation: Beyond the myth of coupling reagents. *Chem. Soc. Rev.* **38**, 606–631 (2009).

293. Bos, I., Timmerman, M. & Sprakel, J. FRET-Based Determination of the Exchange Dynamics of Complex Coacervate Core Micelles. *Macromolecules* **54**, 398–411 (2021).

294. Mann, F. A., Herrmann, N., Opazo, F. & Kruss, S. Quantum Defects as a Toolbox for the Covalent Functionalization of Carbon Nanotubes with Peptides and Proteins. *Angew. Chemie - Int. Ed.* **59**, 17732–17738 (2020).

295. Geißler, D., Nirmalananthan-Budau, N., Scholtz, L., Tavernaro, I. & Resch-Genger, U. Analyzing the surface of functional nanomaterials—how to quantify the total and derivatizable number of functional groups and ligands. *Microchim. Acta* **188**, 321 (2021).

296. Mourdikoudis, S., Pallares, R. M. & Thanh, N. T. K. Characterization techniques for nanoparticles: Comparison and complementarity upon studying nanoparticle properties. *Nanoscale* **10**, 12871–12934 (2018).

297. Sweetman, M. J. *et al.* Rapid, metal-free hydrosilanisation chemistry for porous silicon surface modification. *Chem. Commun.* **51**, 10640–10643 (2015).

298. Chu, P. K., Chen, J. Y., Wang, L. P. & Huang, N. Plasma-surface modification of biomaterials. *Mater. Sci. Eng. R Reports* **36**, 143–206 (2002).

299. Roveri, M., Bernasconi, M., Leroux, J. C. & Luciani, P. Peptides for tumor-specific drug targeting: State of the art and beyond. *J. Mater. Chem. B* **5**, 4348–4364 (2017).

300. Friedman, A., Claypool, S. & Liu, R. The Smart Targeting of Nanoparticles. *Curr. Pharm. Des.* **19**, 6315–6329 (2013).

301. Wang, F. *et al.* The functions and applications of RGD in tumor therapy and tissue engineering. *Int. J. Mol. Sci.* **14**, 13447–13462 (2013).

302. Gao, J., Wang, S., Dong, X. & Wang, Z. RGD-expressed bacterial membrane-derived nanovesicles enhance cancer therapy via multiple tumorous targeting. *Theranostics* **11**, 3301–3316 (2021).

303. Ruoslahti, E. RGD and other recognition sequences for integrins. *Annu. Rev. Cell Dev. Biol.* **12**, 697–715 (1996).

304. D'Souza, S. E., Ginsberg, M. H. & Plow, E. F. Arginyl-glycyl-aspartic acid (RGD): a cell adhesion motif. *Trends Biochem. Sci.* **16**, 246–250 (1991).

305. Zhou, A., Wei, Y., Wu, B., Chen, Q. & Xing, D. Pyropheophorbide A and c(RGDyK) comodified chitosan-wrapped upconversion nanoparticle for targeted near-infrared photodynamic therapy. *Mol. Pharm.* **9**, 1580–1589 (2012).

306. Liu, W. *et al.* Covalent RGD-Graphene-Phthalocyanine Nanocomposite for Fluorescence Imaging-Guided Dual Active/Passive Tumor Targeted Combinatorial Phototherapy. *J. Mater. Chem. B* **10**, 306–320 (2021).

307. Maynard, J. & Georgiou, G. Antibody Engineering. *Annu. Rev. Biomed. Eng.* **2**, 339–376 (2000).

308. Carter, P. J. Potent antibody therapeutics by design. *Nat. Rev. Immunol.* **6**, 343–357 (2006).

309. Muyldermans, S. Nanobodies: Natural single-domain antibodies. *Annu. Rev. Biochem.* **82**, 775–797 (2013).

310. Chakravarty, R., Goel, S. & Cai, W. Nanobody: The 'magic bullet' for molecular imaging? *Theranostics* **4**, 386–398 (2014).

311. Muyldermans, S. A guide to: generation and design of nanobodies. *FEBS J.* **288**, 2084–2102 (2021).

312. Parak, W. J. *et al.* Conjugation of DNA to silanized colloidal semiconductor nanocrystalline quantum dots. *Chem. Mater.* **14**, 2113–2119 (2002).

313. Bunka, D. H. J. & Stockley, P. G. Aptamers come of age - At last. *Nat. Rev. Microbiol.* **4**, 588–596 (2006).

314. Zhou, J. & Rossi, J. Aptamers as targeted therapeutics: Current potential and challenges. *Nat. Rev. Drug Discov.* **16**, 181–202 (2017).

315. Romanov, V. I., Durand, D. B. & Petrenko, V. A. Phage display selection of peptides that affect prostate carcinoma cells attachment and invasion. *Prostate* **47**, 239–251 (2001).

316. Chandra Ray, P., Afrin Khan, S., Kumar Singh, A., Senapati, D. & Fan, Z. Nanomaterials for targeted detection and photothermal killing of bacteria. *Chem. Soc. Rev.* **41**, 3193–3209 (2012).

317. Wang, Y., Meng, H. M. & Li, Z. Near-infrared inorganic nanomaterial-based nanosystems for photothermal therapy. *Nanoscale* **13**, 8751–8772 (2021).

318. Sarkar, B. & Jayaraman, N. Glycoconjugations of Biomolecules by Chemical Methods. *Front. Chem.* **8**, 1–27 (2020).

319. Yu, S. H., Bond, M. R., Whitman, C. M. & Kohler, J. J. Metabolic labeling of glycoconjugates with photocrosslinking sugars. in *Methods in Enzymology* vol. 478 541–562 (Elsevier Inc, 2010).

320. Cid, J. J. *et al.* Tuning of glyconanomaterial shape and size for selective bacterial cell agglutination. *J. Mater. Chem. B* **4**, 2028–2037 (2016).

321. Rodríguez-Pérez, L. *et al.* Nanocarbon-Based Glycoconjugates as Multivalent Inhibitors of Ebola Virus Infection. *J. Am. Chem. Soc.* **140**, 9891–9898 (2018).

322. Selvaggio, G. *et al.* NIR-emitting benzene-fused oligo-BODIPYs for bioimaging. *Analyst* **147**, 230–237 (2022).

323. Selvaggio, G. *et al.* Covalently Functionalized Egyptian Blue Nanosheets for Near-Infrared Bioimaging. *ChemRxiv* 1–13 (2022) doi:10.26434/chemrxiv-2022-20ts5.

9 | Acknowledgments

I am very grateful first of all to Prof. Sebastian Kruss for allowing me to work in his group and for guiding me towards professional and personal achievements that I really treasure. His mentoring skills and the constant presence are qualities that are not to be taken as granted from a supervisor. I also want to thank Prof. Dietmar Stalke and Jun.-Prof. Franziska Thomas for providing valuable feedback while following the course of my research throughout the years. I am grateful to Prof. Stalke also for putting effort into the correction of my thesis and for kindly allowing me to carry out my last experiments in his labs. Next, I thank the additional members of the Examination Board (Prof. Timo Betz, Prof. Jörg Großhans and Jun.-Prof. Anna Krawczuk) for dedicating some of their precious time to the conclusion of my PhD. I also want to thank Prof. Andreas Janshoff and Prof. Claudia Steinem for providing me with access to their lab facilities for almost the entire duration of my doctoral studies.

Most of the results described in this thesis would not have been achieved without the numerous fruitful collaborations established in these years, and I am therefore really grateful to all of them. In this regard, I want to thank Prof. Luise Erpenbeck, Prof. Juan Pablo Giraldo, Prof. Jörg Großhans, Prof. Andreas Janshoff, Prof. Jörg Enderlein, Prof. Daniel B. Werz, Prof. Dietmar Stalke, Prof. Loren Andreas and the corresponding research groups. I also want to acknowledge all the scientific staff and technicians involved in the works of this dissertation. In particular, I am grateful to Dr. Burkhard Schmidt, Dr. Florian Rehfeldt, Dr. Heidrun Sowa for their passionate scientific contributions. It was a particular pleasure to work with Dr. Roman Tsukanov and Dr. Nazar Oleksiievets, with whom I had very nice, fruitful and stimulating conversations about fluorescence lifetime and more. I am also very glad to have met and collaborated with Dr. Riza Dervisoglu: his enthusiasm and curiosity for science as well as his outgoing personality were the reasons why it was so easy and fun to work with him. Additionally, I want to send a heartfelt thanks to Dr. Volker Karius and Cornelia Friedrich for welcoming me with open arms in their Geology labs, for constantly providing me with precious technical support and for always being in the mood for a nice chat. Definitely very insightful and stimulating (online) conversations were the ones with Dr. Marco Nicola about the wonders of “Egyptian Blue & Friends”: it was a real pleasure and honor to exchange ideas and opinions with one of the main players of EB, and I am very much looking forward to finally meeting him in person at the upcoming BLUENET2022 conference in Rome.

These last four years have been an unprecedented rollercoaster of emotions for me as, I guess, is the case for most (if not all) PhD students. For sure a big THANK YOU therefore goes to the research group of Prof. Kruss. As mentioned previously for Prof. Kruss himself, not everything is to be taken as granted. I indeed believe that one should not expect to always receive full scientific cooperation and emotional support from colleagues within a research group. I am thus thankful to the “old” generation of Göttingen students: Elena Polo, Daniel Meyer, Elsa Neubert, Alexander Spreinat, Florian Mann, Niklas Herrmann, Robert Nißler, Gökhan Günay, Seren Hamsici and Meshkat Dinarvand. I am very grateful for the way they welcomed and supported me, leading in most cases to the birth of relationships well beyond the simple "coworkers" level. Worthy of a special mention are with no doubts all the great students who worked in AK Kruss and, in particular, my Bachelor and Master students Helen Preiß, Alexander Spreinat and Milan Weitzel: I consider myself very lucky from this point of view, because their outstanding work really enabled important progress in my research, so I want to send heartfelt thanks to them, too. I am also very satisfied both from a scientific and a personal point of view with the new generation of Bochum students in the Kruss lab: I really want to thank them all for making things as easy as possible for me during the group's transition from Göttingen to Bochum and, especially, for supporting me in the last months of my PhD. I am extremely confident that the future of this research group will be characterized by numerous scientific successes and joyful social moments. Speaking about joyful social moments, I am definitely lucky enough to claim that I have friends also in the research groups of Prof. Janshoff and Prof. Steinem. Several people in these groups were there when needed most, not just for technical support, but also for open-hearted conversations, stupid jokes and some well-deserved partying: these are all things I will never forget. When it comes to the "technical" support (but not only), a special mention must be made for Dr. Ingo Mey, Dr. Tabea A. Oswald, Jutta Gerber-Nolte and Angela Rübeling: their constant assistance and patience really helped me out in multiple occasions, so I really want to thank them from the bottom of my heart.

The last months of PhD have definitely been hectic and I feel that several people have played a major role to help me get through it. I want to thank the members of the research group of Prof. Stalke and Prof. Sindlinger for their technical support: in particular, I am grateful to Laura Haberstock, Tobias Ernemann, Daniel Lüert and Tobias Heitkemper. I also really want to express my gratitude to Niyaz Alizadeh, Dr. Antonio Del Vecchio, Dr. Fabio Pesciaioli, Dr. Leonardo Massignan and Dr. Silvia Zampar for their scientific knowledge and valuable friendship. I particularly want to thank my Italian friends in Göttingen (Leo, Silvia, Antonio, Fabio and Beppe) because they made me feel at home and were extremely supportive and caring even in the toughest times.

The dissertation itself deserves a few words, too. I really want to underline the amazing proof-reading job performed by my colleagues Robert, Alex and Niklas. Considering the time they spent on all these pages, I guess I owe them at least a (Belgian?) beer or two. I really appreciated the technical and moral support provided by Sarmini Nageswaran, with whom I shared the submission deadline as well as the frustrations of the writing process and the apparently endless bureaucratic struggles. Additionally, I want to acknowledge the online tool of ezgif.com and the artistic talent of Upklyak (papyrus drawing from Freepik) for allowing me to efficiently embed my manuscripts and for giving an elegant Egyptian touch to my thesis.

Going back to the roots, I want to thank my closest Italian friends from Trieste for always being there: despite the distance, I never feel alone thanks to their numerous calls and messages. The same applies to my wonderful parents, who have always supported me in every way possible and have constantly reminded me that I should always look at what lies ahead and try my best to always embrace the bright side of things. Speaking of brightness, the brightest light in these four years has been with no doubts

Nicole. She has always been there, never giving up on listening to my complaints and always putting every effort she could to cheer me up and motivate me further. I could not have asked for a more understanding and caring person to have at my side in this journey and I am truly grateful that she is part of my life. If this PhD chapter has turned out to be successful, a good portion of merit is for sure also hers.